Finite Differences and a Coupled Analytic Technique with Applications to Explosions and Earthquakes

Thesis by

Richard J. Stead

In Partial Fulfillment of the Requirements

for the Degree of

Doctor of Philosophy

California Institute of Technology

Pasadena, California

1990

(defended 27th July, 1989)

Acknowledgements

Many people contributed to my studies while I've been at Caltech, and many more have made my work possible by supporting my personal well-being. I could not possibly mention all their names here, so I apologize in advance to anyone I may overlook.

First, I thank those most directly responsible for supporting the work for this thesis. Don Helmberger was my primary advisor throughout most of this work. I also received research advice at various times from Rob Clayton, Dave Harkrider and Hiroo Kanamori. This research was supported in part by the Advanced Research Projects Agency of the U. S. Department of Defense and was monitored by the U. S. Air Force Geophysics Laboratory under Contract F19628-87-K-0028. Cindy Arvesen drafted several of the figures and digitized many of the seismograms.

Several students, past and present, have also had direct impact on my thesis research. Particularly, John Vidale got me started in finite differences, and provided the first finite difference code that I used. We have cooperated on several projects, more than are represented in this thesis. In addition, he helped arrange financial support for me for part of my time here, and assisted me during my job search. Harold Magistrale and Phyllis Ho-Liu have provided important information and helpful discussion during my work on Imperial Valley earthquakes.

The students in my class have been particularly close over the years, those in geophysics (John Louie, Ann Mori, Steve Salyards and Dave Scott) and in the rest of the division (Ken Herkenhoff, Greg Ojakangis, Carol Polansky, Carol Prentice, Dave Pickett and the rest). They have all been a fun

bunch and have provided some great moments, from the picnics our first year to the "What Do You Do with a Sixth Year Student" skit at Zilchbrau.

So many people have had a desk in my office at one time or another, I can't remember them all. I'll stick with the current group - Brad Woods, Tom Duffy and Helen Qian. These folks are always ready when you need a distraction. We're a politically active group, always checking to make sure the others remember to vote, even in minor elections. Brad provides a lot of major distractions that fall under the heading of social activities.

The computers have played a big part in my work here. Often this part was too big. I guess system responsibility here taught me some things about computers, just as being stuck in a desert without food and water teaches you about the desert. I am most grateful to those students who assisted me when I needed it, Scott King and Bruce Worden. I especially thank Doug Neuhauser for taking a job here and taking these problems away from the students.

I want to mention a few other seismo lab students before I continue. Luciana Astiz has always been a great encouragement, to myself and most of the students who were lucky enough to meet her. And I thank Joanne Yoshimura, Doug Dreger, Andrea Donnellan, Lian-she "pretty good" Zhao, and the early escapees Mike Frome and Bob Dollar just for being pals.

M-J house has been a big part of my time at Caltech. I particularly remember the days of the animal dorm with Norbert "Animal" Arndt, Steve "Fishface" Lederman, Richard "Czar" Colberg John "The Parameter" Parmeter, Tom "Tractor" Tretter and others. There is simply no other social environment like a dorm.

My spiritual life has been kept on course with the help of the people in the graduate group, originally associated with Caltech Christian Fellowship. I helped form the grad group my first year here, and since then I've gotten to know quite a few people through it. The one person I've known the longest is John McGill, who has been a source of spiritual inspiration and quite down-to-earth good times.

Last, but not least, I thank my parents who saw me off on this long trek, and who have always supported me in my goals and interests (even when the house filled up with my rocks).

Abstract

An analytic technique is developed that couples to finite difference calculations to extend the results to arbitrary distance. Finite differences and the analytic result, a boundary integral called two-dimensional Kirchhoff, are applied to simple models and three seismological problems dealing with data. The simple models include a thorough investigation of the seismologic effects of a deep continental basin. The first problem is explosions at Yucca Flat, in the Nevada test site. By modeling both near-field strong-motion records and teleseismic P-waves simultaneously, it is shown that scattered surface waves are responsible for teleseismic complexity. The second problem deals with explosions at Amchitka Island, Alaska. The near-field seismograms are investigated using a variety of complex structures and sources. The third problem involves regional seismograms of Imperial Valley, California earthquakes recorded at Pasadena, California. The data are shown to contain evidence of deterministic structure, but lack of more direct measurements of the structure and possible three-dimensional effects make two-dimensional modeling of these data difficult.

Table of Contents

Acknowledgements ii

Abstract v

General Introduction 1

Chapter1: Numerical-analytical interfacing in two dimensions with applications to modeling NTS seismograms

1.1 Introduction 5

1.2 A two-dimensional representation theorem 7

1.3 Canonical basin models 32

1.4 Application - events at Yucca Flat, Nevada Test Site 42

1.5 Discussion and Conclusions 55

References for Chapter 1 57

Chapter2: Modeling explosions with two-dimensional numerical methods

2.1 Introduction 60

2.2 Difference between 2-D and 3-D wave propagation 62

2.3 Correction factor for explosions in 2-D 64

2.4 Application to explosions on Amchitka 70

2.5 Comparison of various structure models and data 88

2.6 Comparison of various bomb sources and data 92

2.7 Conclusions 106

References for Chapter 2 108

Chapter3: The seismologic effects of a deep continental basin: a canonical study

3.1 Introduction 111

3.2 Description of the models 112

3.3 Results: comparisons of FD synthetics for SH 119

3.4 Comparison to the P-SV system 169

3.5 Discussion 189

3.6 Conclusions 193

References for Chapter 3 195

Chapter4: Numerical modeling of Imperial Valley, California earthquakes recorded at Pasadena, California

4.1 Introduction 196

4.2 Historical seismicity 206

4.3 FD modeling 234

4.4 Discussion and recommendations 275

References for Chapter 4 280

Appendix A: Analytic source function for two-dimensional finite differences 284

Appendix B: Synthetic verification of the "2D Kirchhoff" formula 291

Appendix C: Dense profiles of synthetic seismograms for basin structures 312

General Introduction

Numerical methods for waveform modeling are gaining wide acceptance in seismology. The technique of finite differences (FD) has proven to be the most successful method. This is due to its flexibility and simple implementation. The drawback to using FD for modeling is that the computation time and memory requirements increase as the square of the desired range and as the cube of the highest desired frequency. Rapidly, an ambitious modeling project will outgrow any available computer. Many problems can be categorized as locally heterogeneous. That is, the controlling structures in a model are heterogeneous in isolated regions; all of the remainder of the model is essentially homogeneous. Therefore, a full FD calculation is needed only in the heterogeneous regions. This thesis introduces an analytic technique that couples to FD to extend the results of the calculation through a homogeneous medium to arbitrary range. The variety of sources and structures that FD can be applied to are also explored.

Chapter 1 contains the development of the analytic interfacing technique which is referred to as the "2D Kirchhoff" technique. The technique is verified analytically for a whole space and demonstrated on some simple two-media models. Appendix B contains some interesting synthetic verifications of 2D Kirchhoff for complex media. The method is applied to the data set that first inspired its development, the occurrence of delayed phases that depend on small variations in source location at station MAT in Japan for explosions in Yucca Flat, Nevada. The source of the delayed phases is found to be scattered Rayleigh waves off the basin boundary in Yucca Flat, which is within a few kilometers of the explosions. Both the near-source data and teleseismic data are modeled simultaneously using a

simplified model of the structure.

Chapter 2 explores further the application of FD to nuclear explosion seismology. The local records for explosions on Amchitka Island, Alaska, are investigated for evidence of dependence on local structure and for evidence of variations in the source. Starting with a flat-layered model known to model the records well, several variations in structure are introduced, including offsets on mapped faults, velocity gradients, variation in receiver medium, and random media. The source itself is investigated by comparing different proposed source time histories for explosions (reduced displacement potentials). The shape of the cavity is investigated using an additional quadrupole term. It is found that small variations in structure have a much larger effect on the waveforms than the differences between proposed explosion time histories. It is also found for an explosion, MILROW, near the known faults, that the model with faulted structure produces the best fit. Finally, it is found that these explosions, particularly CANNIKIN, show evidence of significant cavity ellipticity.

Chapter 3 introduces the subject of earthquake modeling in regions of strong lateral heterogeneity. It is a canonical study to determine the possible effects that a strong, but realistic lateral variation would have on regional and teleseismic seismograms. A variety of variables are investigated, including source depth, distance between the source and scattering boundary, source mechanism, boundary geometry, range to receiver and receiver response. It is found that SH seismograms can be explained simply in terms of two structures, and that it may be possible to model the SH records of earthquakes in complex regions by using only the flat-layered structures at the source and receiver. The teleseismic analysis shows that only optimally

located strike-slip events will show significant evidence of scattered SH energy. The P-SV system proves much more complex, as expected. To model shallow sources accurately, detailed knowledge of the regional structure is required. Nevertheless, there are smooth variations in waveform character across the many variables that indicate a large data set may be divided into groups based on waveform with the variations indicating source depth, etc., without any knowledge of the structure. Both the SH and P-SV synthetics show evidence of the offset between the source and scattering structure, which is valuable, if accurately modeled, because essentially it places a receiver closer to the event and can improve location.

Chapter 4 presents a problem typical of those Chapter 3 is meant to address. The location is the Imperial Valley of southern California. This is an area of unusually high seismic activity, but the historical seismicity is not completely understood. The problem is a complex and unknown regional structure. A data set is introduced, and then selected calibration events from broad-band recording are compared to synthetics for a variety of models. In general, the modeling is unsuccessful. This is primarily due to the lack of structural information. The problem is such that the structure under the station PAS is not fully known, despite more than 60 years of operation as a world-class seismic observatory. Several recommendations are made on how to improve this modeling. In addition to encouraging more seismic profiling in southern California, it is important to make better use of the existing data, particularly accessing more of the old paper records than is feasible using hand-digitization. More stations need to be included in the analysis, and the current trend toward broad-band instruments will help. The view is that without clear knowledge of the structure, the waveforms need to provide

that information before modeling begins. Canonical modeling is a valuable tool here, because it can show how to divide records according to waveform and what the differences could mean.

Chapter 1

Numerical-analytical interfacing in two dimensions with applications to modeling NTS seismograms

1.1 Introduction

Seismologists have long recognized that structural complexities near seismic sources may affect teleseismic waveforms. For instance, events occurring in the Imperial Valley, California, produce extended teleseismic short-period signals lasting much longer than the source duration derived from near-in strong-motion studies, see Hartzell and Heaton (1983). Presumably, the energy trapped by the low-velocity layering scatters out the bottom of the basin when it encounters the basin edge. Recently, Vidale and Helmberger (1988), using a finite-difference scheme, had considerable success modeling a profile of the San Fernando earthquake strong-motion records that cross the Los Angeles basin. Their approach assumes two-dimensional symmetry, as displayed in Figure 1.1, but corrects for three-dimensional spreading and mimics the well-known double-couple radiation field. Essentially, the numerical excitation is matched to an asymptotic analytical source representation. Synthetics generated by this procedure match closely those generated by analytical point-source codes for the same flat-layered case (Vidale, et al., 1985). However, these solutions cannot be propagated to great distance because of computational cost. Thus, a technique is needed to interface the numerical output back into an analytical scheme such that the signals can be sent to large distances. This is the basic objective of this chapter, and we will also discuss, as a demonstration, a well-controlled

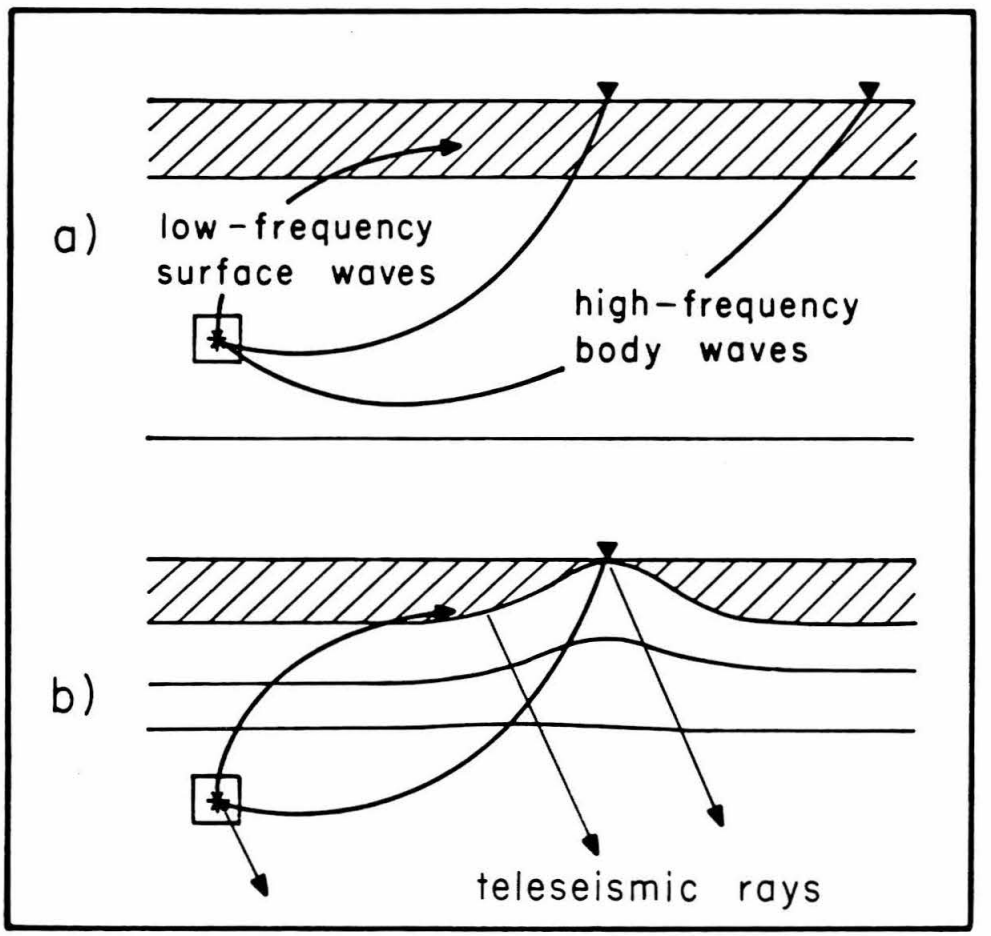

Figure 1.1. Schematic diagram displaying energy paths for a) flat-layered model versus b) laterally varying structure. The model is two-dimensional. The figure demonstrates the motivation for developing a two-dimensional teleseismic method that accounts for local structural variations.

experiment where scattered surface waves can be seen leaving the local field and reappearing as teleseismic body-wave coda.

The controlled experiment consistent with the above motivation is that of explosions fired at Yucca Flat in the Nevada Test Site. The local structure of Yucca Flat is a basin containing volcanic tuffs and alluvium (Eckren, 1968 and Houser, 1968). The events in this area have a striking complexity on teleseismic records for an explosion source (see Figure 1.2). Various studies show the structure of this region to be seismically complex (Taylor, 1983, among many others). Hart, et al. (1979) examine how the variation of amplitudes and magnitudes within Yucca Flat are dependent on source position in the valley. Recent studies have concentrated on the azimuthal variations observed in the data in both the time (Lay, Wallace and Helmberger, 1984) and frequency (Lay, 1987a) domains. Studies of these records have indicated the presence of local scattering structure (Lay, 1987b). In addition, existing strong-motion records demonstrate lateral anomalies in the propagation of seismic energy at Yucca Flat. Figure 1.3 shows the vertical velocity records from the event FLASK. The large difference in amplitude and duration of both the first arrivals and the Rayleigh waves from east to west strongly suggests that local scattering plays an important role. It is found herein that these scattered Rayleigh waves are the likely progenitors of teleseismic complexity apparent in Figure 1.2. This is consistent with the results of Lynnes and Lay (1988).

1.2 A two-dimensional representation theorem

In accordance with the motivation discussed above, we derive a two-dimensional representation theorem method similar in its application to

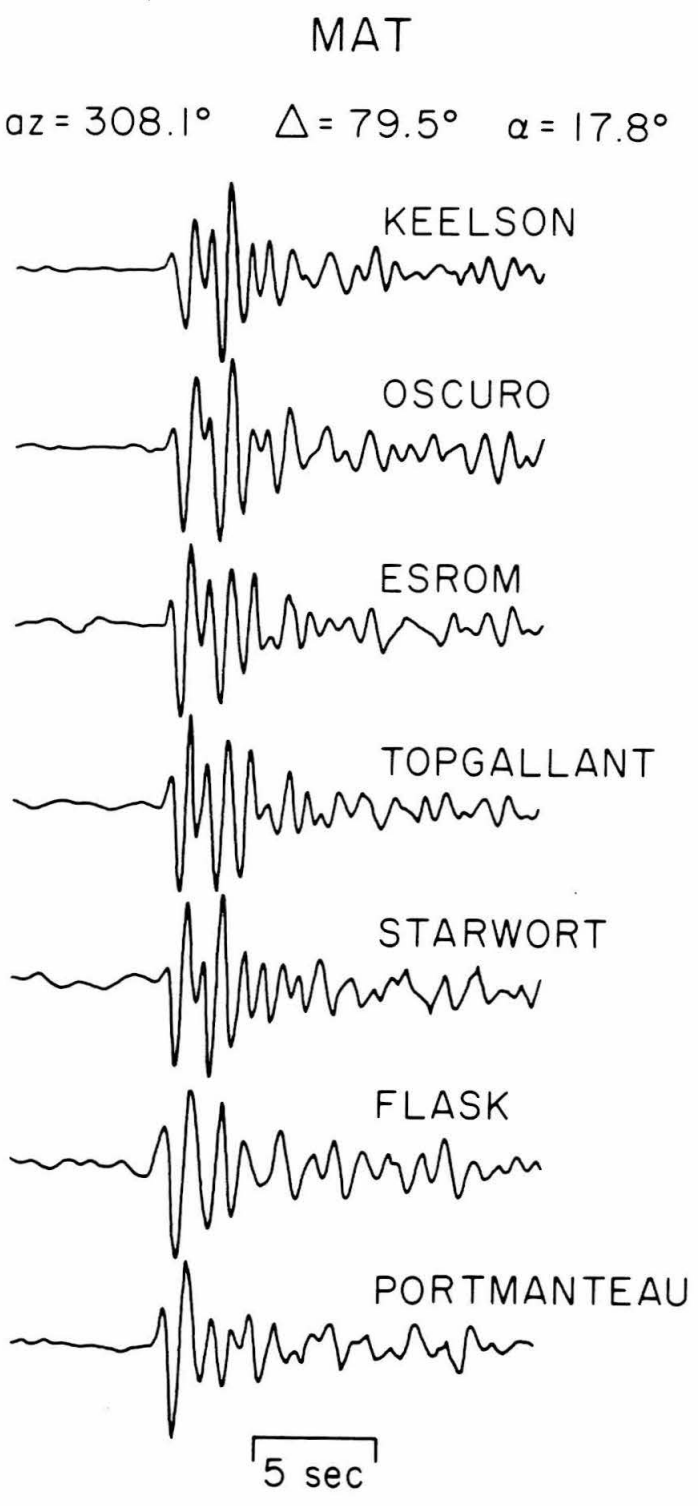

Figure 1.2. Teleseismic data at MAT. These are WWSSN short-period vertical seismograms recorded at station MAT, Japan, for seven different events at various locations within Yucca Flat (see Figure 1.18). There are very strong secondary phases appearing after P-pP. While P-pP seems relatively consistent among the records, the secondary phases are not, indicating the presence of scattering structure near the source.

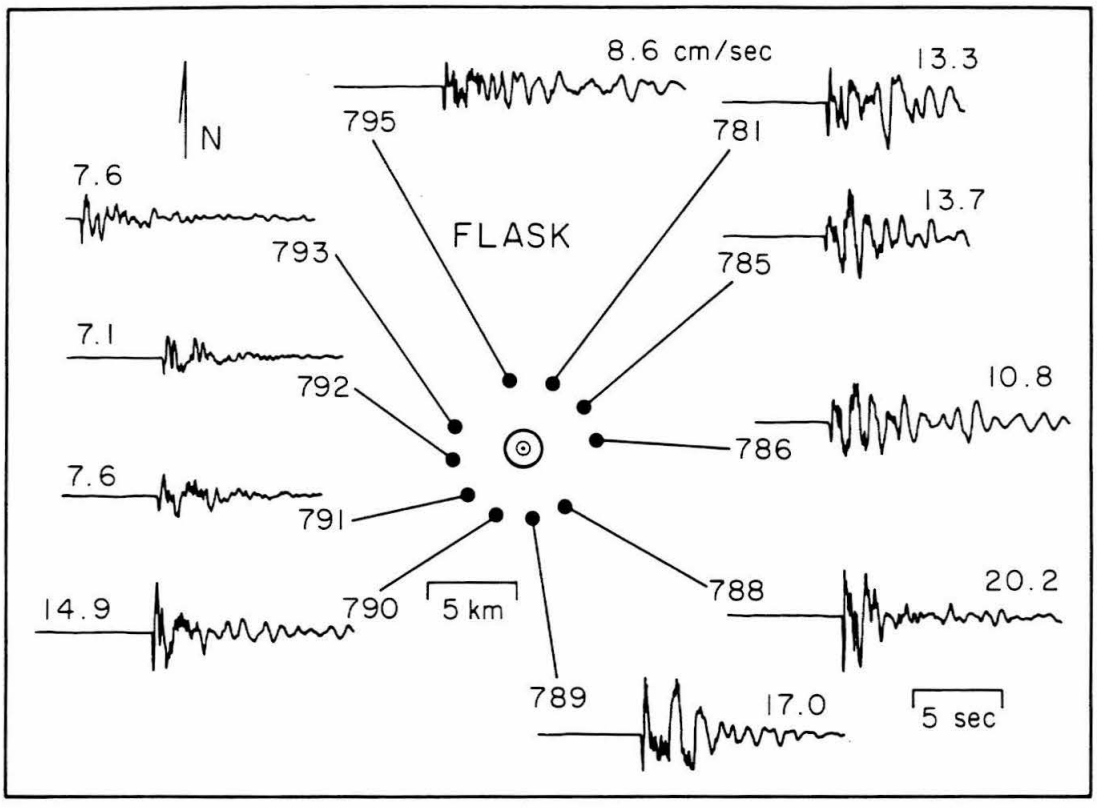

Figure 1.3. Strong motion data for FLASK. Only the vertical velocity records are shown here. The stations (781 to 795) are each marked as a dot here and also as an x on the map of Figure 1.18. The source is in the center. Such data strongly argue for lateral variation because of the strong lateral contrast in peak amplitude and duration of the Rayleigh wave.

three-dimensional Kirchhoff integration. Such an integral method allows computationally inexpensive generation of teleseismic records from complex source region calculations, particularly those of finite difference. In deriving such a method, the resulting expression must be fully elastic, require a minimum of computation time, and be readily adaptable to finite-difference methods. A straightforward approach is to parallel the derivation of three-dimensional integration methods. For more information on such integral methods in both two and three dimensions, see Baker and Copson (1950) and Mow and Pao (1971).

Starting with the two-dimensional elastic wave equation in polar coordinates,

$$\frac{\partial^2 u}{\partial r^2} + \frac{1}{r}\frac{\partial u}{\partial r} + \frac{1}{r^2}\frac{\partial^2 u}{\partial \theta^2} = \frac{1}{\alpha^2}\frac{\partial^2 u}{\partial t^2} \tag{1.1}$$

take the Laplace transform over time, ignoring the θ – dependence, and setting

$u=0$, $\frac{\partial u}{\partial t}=0$, at $t=0$, for all r, θ. Then,

$$\frac{\partial^2 \bar{u}}{\partial r^2} + \frac{1}{r}\frac{\partial \bar{u}}{\partial r} - \frac{s^2}{\alpha^2}\bar{u} = 0 \tag{1.2}$$

which has solutions like $K_0\left(\frac{sr}{\alpha}\right)$; see Hudson (1963) for example.

Thus, $\bar{u}$ depends only on r and solves

$$\left(\nabla^2 - \frac{s^2}{\alpha^2}\right)\bar{u} = 0. \tag{1.3}$$

Let w be another solution of Equation 1.2; then Green's transformation becomes

$$\int_\Gamma \left(\bar{u}\frac{\partial w}{\partial n} - w\frac{\partial \bar{u}}{\partial n} \right) dl = \iint_D \left(\bar{u}\nabla^2 w - w\nabla^2 \bar{u} \right) dA \tag{1.4}$$

$$= \iint_D \left(\bar{u}\frac{s^2}{\alpha^2} w - w\frac{s^2}{\alpha^2}\bar{u} \right) dA$$

$$= 0.$$

The geometry for this transformation is shown in Figure 1.4. Now let $w = K_0\left(\frac{sr}{\alpha}\right)$. Then for P $\notin$ D,

$$\int_\Gamma \left[\bar{u}\frac{\partial}{\partial n} K_0\left(\frac{sr}{\alpha}\right) - K_0\left(\frac{sr}{\alpha}\right)\frac{\partial \bar{u}}{\partial n} \right] dl = 0. \tag{1.5}$$

For P $\in$ D, as in Figure 1.5, the log singularity at P for $K_0\left(\frac{sr}{\alpha}\right)$ gives the result

$$\int_\Gamma \left(\bar{u}\frac{\partial w}{\partial n} - w\frac{\partial \bar{u}}{\partial n} \right) dl + \int_\sigma \left(\bar{u}\frac{\partial w}{\partial n} - w\frac{\partial \bar{u}}{\partial n} \right) dc =$$

$$\iint_{D'} \left(\bar{u}\nabla^2 w - w\nabla^2 \bar{u} \right) dA = 0. \tag{1.6}$$

Let $\hat{n} = -\bar{r}/r$ in the integral over σ; then

$$\int_\Gamma \left(\bar{u}\frac{\partial w}{\partial n} - w\frac{\partial \bar{u}}{\partial n} \right) dl = \int_\sigma \left(\bar{u}\frac{\partial w}{\partial r} - w\frac{\partial \bar{u}}{\partial r} \right) dc\,, \tag{1.7}$$

where dc is a length element on the circumference of the inner circle. Again, letting $w = K_0$, and also letting the radius, ϵ, of σ go to zero,

$$\int_\Gamma \left[\bar{u}\frac{\partial}{\partial n} K_0\left(\frac{sr}{\alpha}\right) - K_0\left(\frac{sr}{\alpha}\right)\frac{\partial \bar{u}}{\partial n} \right] dl =$$

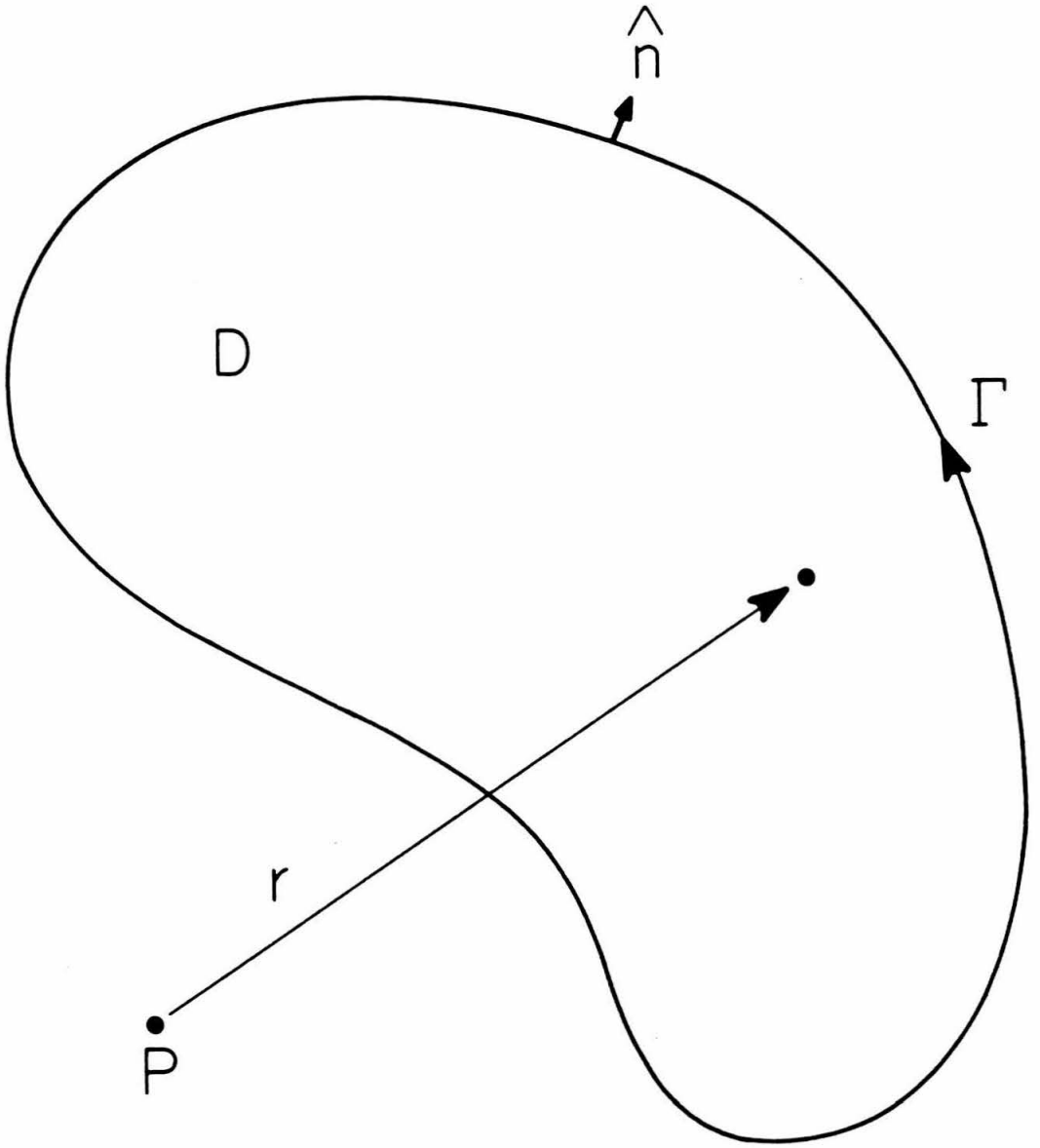

Figure 1.4. Green's transformation for P not in domain D. The contour Γ is chosen such that there are no singularities of the integrand in the area D that Γ encloses. The variable r in the transformation is the distance from P to any point on Γ or in D. The vector n is the outward directed normal to Γ.

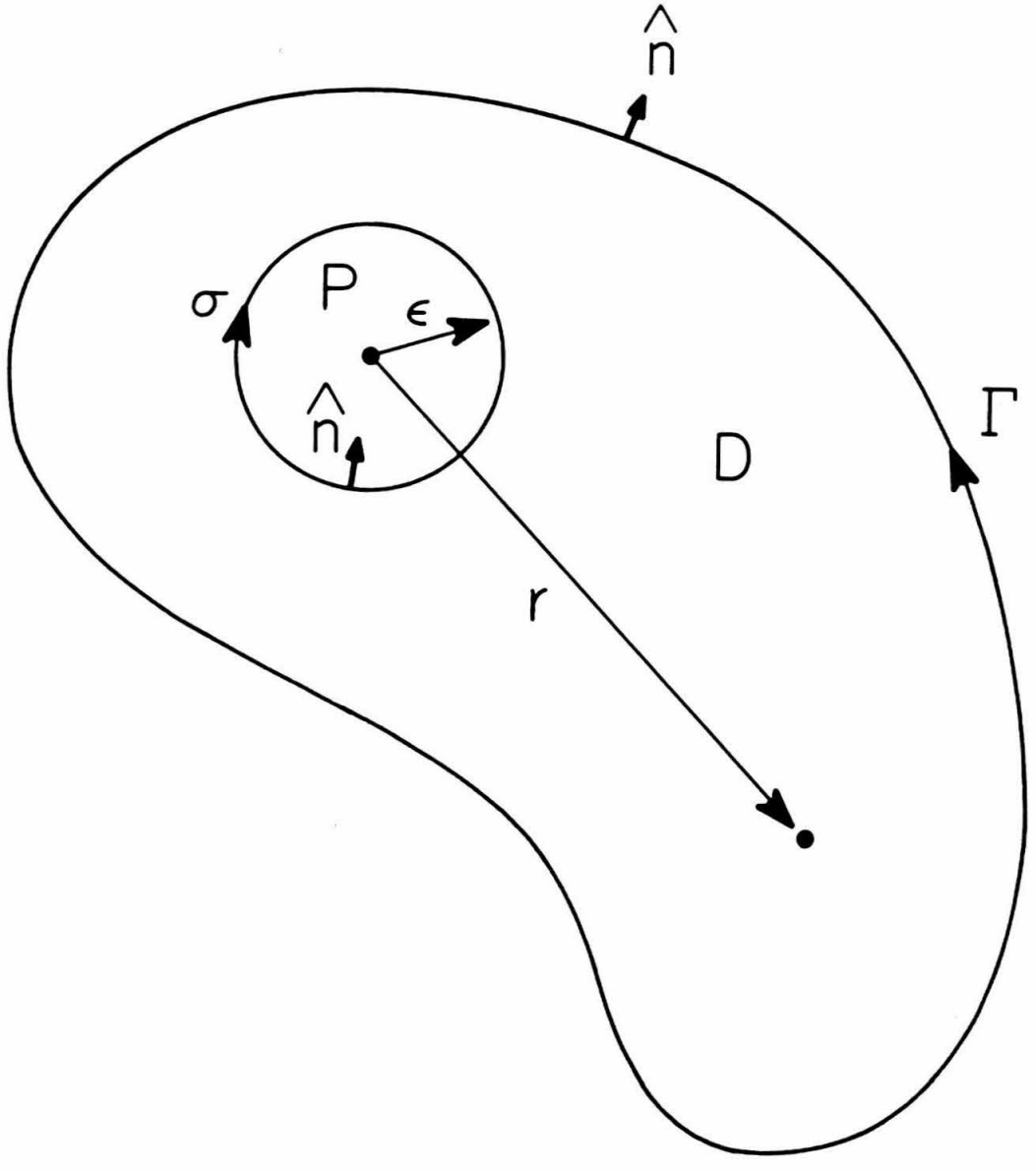

Figure 1.5. Green's transformation for P in D. Here, the contour σ is introduced in addition to Γ around the point P. Now the domain D' is that area enclosed between contour Γ and contour σ. These contours are freely deformable and σ is chosen to be circular with radius ϵ centered on point P. The limit as ϵ approaches 0 will produce the desired integral formula.

$$\lim_{\epsilon \to 0} \int_{\sigma} \left[\bar{u} \frac{\partial}{\partial r} K_0 \left(\frac{sr}{\alpha} \right) - K_0 \left(\frac{sr}{\alpha} \right) \frac{\partial \bar{u}}{\partial r} \right] dc. \tag{1.8}$$

Near P, K_0 and its derivative can be approximated as follows;

$$K_0 \left(\frac{sr}{\alpha} \right) = \frac{\pi i}{2} H_0^{(1)} \left(\frac{isr}{\alpha} \right) \sim - \log r , \tag{1.9}$$

and

$$\frac{\partial}{\partial r} K_0 \left(\frac{sr}{\alpha} \right) \sim - \frac{1}{r}. \tag{1.10}$$

If these approximations are substituted into Equation 1.8, the integral over σ is evaluated in the limit.

$$\lim_{\epsilon \to 0} \int_{\sigma} \left[\bar{u} \frac{\partial}{\partial r} K_0 \left(\frac{sr}{\alpha} \right) - K_0 \left(\frac{sr}{\alpha} \right) \frac{\partial \bar{u}}{\partial r} \right] dc = \lim_{\epsilon \to 0} - \int_{\sigma} \left(\frac{\bar{u}}{\epsilon} - \log \epsilon \frac{\partial \bar{u}}{\partial r} \right) dc$$

$$= -2\pi \bar{u} (\mathrm{P}) \tag{1.11}$$

Therefore,

$$\bar{u} (\mathrm{P}) = \frac{-1}{2\pi} \int_{\Gamma} \left[\bar{u} \frac{\partial}{\partial n} K_0 \left(\frac{sr}{\alpha} \right) - K_0 \left(\frac{sr}{\alpha} \right) \frac{\partial \bar{u}}{\partial n} \right] dl. \tag{1.12}$$

This integral can be exactly inverted to the time domain. First, take the derivative of K_0.

$$\frac{\partial}{\partial n} K_0 \left(\frac{sr}{\alpha} \right) = - \frac{s}{\alpha} K_1 \left(\frac{sr}{\alpha} \right) \frac{\partial r}{\partial n} \tag{1.13}$$

Substitute this into the integral.

$$\bar{u} (\mathrm{P}) = \frac{1}{2\pi} \int_{\Gamma} \left[\frac{s}{\alpha} \frac{\partial r}{\partial n} \bar{u} K_1 \left(\frac{sr}{\alpha} \right) + \frac{\partial \bar{u}}{\partial n} K_0 \left(\frac{sr}{\alpha} \right) \right] dl \tag{1.14}$$

Take the inverse transform.

$$u(\mathrm{P}) = \frac{1}{2\pi i}\int_{\gamma-i\infty}^{\gamma+i\infty}\frac{1}{2\pi}\int_{\Gamma}\left[\frac{s}{\alpha}\frac{\partial r}{\partial n}\bar{u}K_1\left(\frac{sr}{\alpha}\right) + \frac{\partial \bar{u}}{\partial n}K_0\left(\frac{sr}{\alpha}\right)\right] dl\ e^{st}\, ds$$

$$= \frac{1}{2\pi}\int_{\Gamma}\frac{1}{2\pi i}\int_{\gamma-i\infty}^{\gamma+i\infty}\left[\frac{s}{\alpha}\frac{\partial r}{\partial n}\bar{u}K_1\left(\frac{sr}{\alpha}\right) + \frac{\partial \bar{u}}{\partial n}K_0\left(\frac{sr}{\alpha}\right)\right] dl\ e^{st}\, ds \quad (1.15)$$

Inverting the above integral requires the use of the convolution rule, the derivative rule and the inverse transforms

$$L^{-1}(K_0(bp))\ [b>0] = (t^2-b^2)^{-1/2}\,H(t-b) \quad (1.16)$$

$$L^{-1}(K_1(bp))\ [b>0] = \frac{t}{b}\,(t^2-b^2)^{-1/2}\,H(t-b). \quad (1.17)$$

Now, taking the inverse,

$$u(\mathrm{P}) = \frac{1}{2\pi}\int_{\Gamma}\left[\frac{1}{\alpha}\frac{\partial r}{\partial n}\frac{d}{dt}\left(u * \left(\frac{\alpha t}{r}\frac{H(t-(r/\alpha))}{\sqrt{t^2-(r/\alpha)^2}}\right)\right) + \frac{\partial u}{\partial n} * \left(\frac{H(t-(r/\alpha))}{\sqrt{t^2-(r/\alpha)^2}}\right)\right] dl. \quad (1.18)$$

For simplicity, let $f(t) = (t^2-(r/\alpha)^2)^{-1/2}H(t-(r/\alpha))$.

$$u(\mathrm{P}) = \frac{1}{2\pi}\int_{\Gamma}\left[\frac{1}{r}\frac{\partial r}{\partial n}\frac{du}{dt} * (t\cdot f(t)) + \frac{\partial u}{\partial n} * f(t)\right] dl \quad (1.19)$$

Equation 1.19 may be cast in a form similar to that of conventional Kirchhoff methods. First apply the convolution identity $f(t)*g(t+c) = f(t+c)*g(t)$ with $c = -r/\alpha$.

$$u(\mathrm{P}) = \frac{1}{2\pi}\int_{\Gamma}\left[\frac{1}{r}\frac{\partial r}{\partial n}\frac{du}{dt} * ((t+\frac{r}{\alpha})f(t)) + \frac{\partial u}{\partial n} * f(t)\right] dl \quad (1.20)$$

where u is now $u(\tau)$, $\tau = t - r/\alpha$, the retarded time, and the operator $f(t) = \dfrac{H(t)}{\sqrt{t}\,\sqrt{t+2r/\alpha}}$. Rewriting this,

$$u(\mathrm{P}) = \frac{1}{2\pi}\int_\Gamma \left[f(t) * \left(\frac{\partial u}{\partial n} + \frac{1}{\alpha}\frac{\partial r}{\partial n}\frac{\partial u}{\partial t} \right) + (t \cdot f(t)) * \frac{1}{r}\frac{\partial r}{\partial n}\frac{\partial u}{\partial t} \right] dl. \qquad (1.21)$$

Bring the derivative across the convolution in the last term.

$$u(\mathrm{P}) = \frac{1}{2\pi}\int_\Gamma f(t) * \left(\frac{\partial u}{\partial n} + \frac{1}{\alpha}\frac{\partial r}{\partial n}\frac{\partial u}{\partial t} \right) dl$$

$$+ \frac{1}{2\pi}\int_\Gamma \left(\frac{1}{2\sqrt{t}} \frac{H(t)}{\sqrt{t + 2r/\alpha}} + \sqrt{t}\frac{d}{dt}\frac{H(t)}{\sqrt{t + 2r/\alpha}} \right) * \frac{u}{r}\frac{\partial r}{\partial n}\, dl \qquad (1.22)$$

Rearranging terms and taking the last time derivative,

$$u(\mathrm{P}) = \frac{1}{2\pi}\int_\Gamma f(t) * \left(\frac{\partial u}{\partial n} + \frac{u}{2r}\frac{\partial r}{\partial n} + \frac{1}{\alpha}\frac{\partial r}{\partial n}\frac{\partial u}{\partial t} \right) dl$$

$$- \frac{1}{2\pi}\int_\Gamma \left(\frac{t}{t + 2r/\alpha} f(t) \right) * \frac{u}{2r}\frac{\partial r}{\partial n}\, dl. \qquad (1.23)$$

This equation is an exact form of the representation theorem.

It is useful to approximate Equation 1.23 for large r, because $f(t)$ depends on r and therefore the convolution, which is computationally expensive, cannot be moved outside the integral. For large r, the operator $f(t)$ is dominated by $1/\sqrt{t}$; that is,

$$f(t) = \frac{H(t)}{\sqrt{t}\,\sqrt{t + 2r/\alpha}} \sim \frac{H(t)}{\sqrt{t}\,\sqrt{2r/\alpha}}, \qquad (1.24)$$

and

$$\frac{t}{t + 2r/\alpha} f(t) \sim H(t)\sqrt{t}\,(2r/\alpha)^{3/2}. \qquad (1.25)$$

Equation 1.23 then becomes

$$u(\mathrm{P}) = \frac{1}{2\pi}\frac{\sqrt{\alpha}}{\sqrt{2}}\frac{1}{\sqrt{t}} * \int_\Gamma \left[\frac{1}{\sqrt{r}} \left(\frac{\partial u}{\partial n} + \frac{u}{2r}\frac{\partial r}{\partial n} + \frac{1}{\alpha}\frac{\partial r}{\partial n}\frac{\partial u}{\partial t} \right) \right] dl$$

$$- \frac{1}{2\pi} \frac{\sqrt{\alpha}}{\sqrt{2}} \sqrt{t} * \int_\Gamma \frac{\alpha}{2r} \frac{1}{\sqrt{r}} \frac{u}{2r} \frac{\partial r}{\partial n} \, dl. \tag{1.26}$$

The second integral is similar to the second term in the first integral, except that it falls off as $1/r$ with respect to it. This means that the second integral may be ignored at large r.

$$u(\mathrm{P}) = \frac{1}{2\pi} \frac{\sqrt{\alpha}}{\sqrt{2}} \frac{1}{\sqrt{t}} * \int_\Gamma \left[\frac{1}{\sqrt{r}} \left(\frac{\partial u}{\partial n} + \frac{u}{2r} \frac{\partial r}{\partial n} + \frac{1}{\alpha} \frac{\partial r}{\partial n} \frac{\partial u}{\partial t} \right) \right] dl \tag{1.27}$$

This approximation also arises from using the asymptotic form of K_0 before inverting the transform. That is,

$$K_0 \left(\frac{sr}{\alpha} \right) \sim \frac{\sqrt{\pi\alpha}}{\sqrt{2sr}} e^{\frac{-sr}{\alpha}}. \tag{1.28}$$

Substitute Equation 1.28 into Equation 1.12, taking the appropriate derivatives, to get

$$\overline{u}(\mathrm{P}) = \frac{1}{2} \frac{1}{\sqrt{2\pi}} \int_\Gamma \frac{\sqrt{\alpha}}{\sqrt{sr}} \, e^{\frac{-sr}{\alpha}} \left[\overline{u} \left(\frac{s}{\alpha} + \frac{1}{2r} \right) \frac{\partial r}{\partial n} + \frac{\partial \overline{u}}{\partial n} \right] dl. \tag{1.29}$$

This may be inverted using the shift rule to account for the $e^{\frac{-sr}{\alpha}}$, and $L^{-1}(\sqrt{\pi/s}\,) = 1/\sqrt{t}$, to arrive at

$$u(\mathrm{P}) = \frac{1}{2\pi} \frac{1}{\sqrt{2}} \frac{1}{\sqrt{t}} * \int_\Gamma \left[\frac{\sqrt{\alpha}}{\sqrt{r}} \left(\frac{\partial u}{\partial n} + \frac{u}{2r} \frac{\partial r}{\partial n} + \frac{1}{\alpha} \frac{\partial r}{\partial n} \frac{\partial u}{\partial t} \right) \right] dl. \tag{1.30}$$

Once again, u is a function of retarded time $\tau = t - r/\alpha$, this time because of the application of the shift rule.

Equation 1.27 is comparable to the more familiar point-source Kirchhoff formula from optics (see, for example, Baker and Copson, 1950).

$$u(\mathrm{P}) = \frac{1}{4\pi} \iint_S \left(u \frac{d}{dn} \frac{1}{r} - \frac{1}{\alpha r} \frac{\partial r}{\partial n} \frac{\partial u}{\partial t} - \frac{1}{r} \frac{\partial u}{\partial n} \right) dS, \tag{1.31}$$

which can be written

$$u(\mathrm{P}) = \frac{1}{4\pi}\iint_S \frac{-1}{r}\left(\frac{\partial u}{\partial n} + \frac{u}{r}\frac{\partial r}{\partial n} + \frac{1}{\alpha}\frac{\partial r}{\partial n}\frac{\partial u}{\partial t}\right) dS. \tag{1.32}$$

Comparing Equations 1.27 and 1.32, the form is identical between the integrals, except for a factor of two on the second term. The convolution with $1/\sqrt{t}$ and the difference in scaling with distance are expected for a line source as opposed to a point source. Both integrals can be applied in similar ways. For a two-dimensional problem, the method of choice is the line-source integral.

Both the three-dimensional Kirchhoff integral and the two-dimensional integral of Equation 1.27 may be verified analytically for a whole space, by substituting into the integrals the expressions for source radiation in a whole space. This exercise also demonstrates how the formulae work with respect to time and the angle swept out over the interface. The verification of the three-dimensional Kirchhoff formula is similar to that of Hilterman (1975) except that this chapter examines transmission rather than reflection. The setup of the problem is shown in Figure 1.6, where a plane (S) is assumed to be located equidistant between the source and receiver (that is, $r_0 = r$). Conceptually, the source lights up the surface, and the surface reradiates the energy to the receiver. In this case, the transmission coefficient is unity so that only geometrical effects are tested. The integral in Laplace space is

$$\bar{\phi}(\mathrm{P}) = \frac{1}{4\pi}\iint_S e^{\frac{-sr}{\alpha}}\left[\frac{1}{r}\frac{\partial \phi(\mathrm{S})}{\partial n} + \frac{\phi(\mathrm{S})}{r^2}\frac{\partial r}{\partial n} + \frac{s}{\alpha}\frac{\phi(\mathrm{S})}{r}\frac{\partial r}{\partial n}\right] dS. \tag{1.33}$$

In this example, $\phi(\mathrm{P})$ is the potential at the observation point, and $\phi(\mathrm{S})$ is the potential on the interface S. For a symmetric point source,

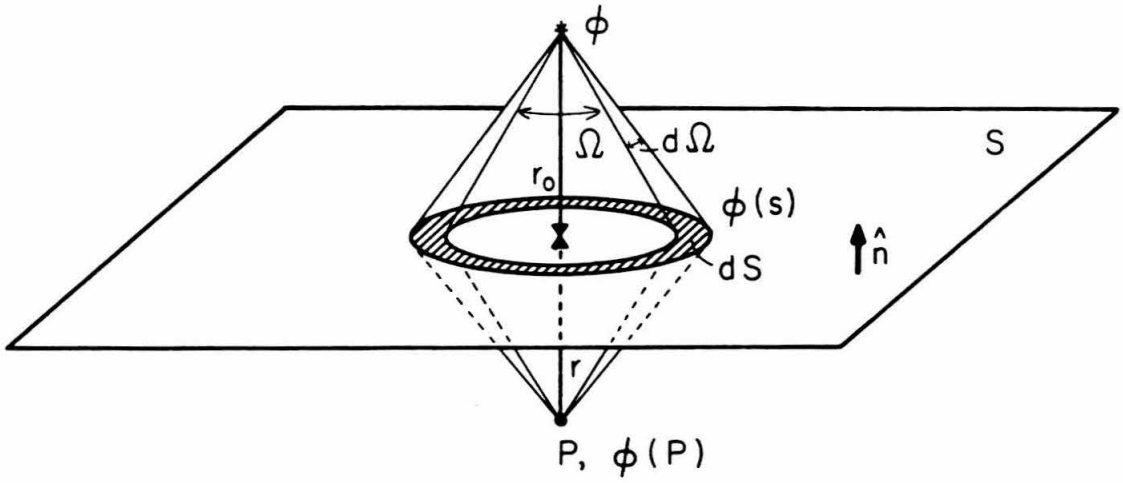

Figure 1.6. Geometry for three-dimensional analytic evaluation of the Kirchhoff integral. The interface surface is S, with solid angle Ω tracing out dS. The normal to the surface is $\hat{n}$. The source, at distance r_0 from S, generates potential ϕ, which produces signal ps on the surface. Kirchhoff integration gives the result pp at point P, at a distance r from S.

$$\phi(\mathrm{S}) = \frac{1}{r_0} e^{\frac{-sr_0}{\alpha}} \overline{f}(s). \tag{1.34}$$

Applying the chain rule to $\frac{\partial \phi(\mathrm{S})}{\partial n}$,

$$\frac{\partial \phi(\mathrm{S})}{\partial n} = \frac{\partial \phi(\mathrm{S})}{\partial r_0} \frac{\partial r_0}{\partial n} = -\left(\frac{s}{\alpha} + \frac{1}{r_0} \right) \frac{\partial r_0}{\partial n} \phi(\mathrm{S}). \tag{1.35}$$

Substituting Equations 1.34 and 1.35 into Equation 1.33 yields

$$\overline{\phi}(\mathrm{P}) = \overline{f}(s) \frac{1}{4\pi} \iint_S \frac{1}{r_0} e^{\frac{-s(r+r_0)}{\alpha}}$$

$$\left[-\frac{1}{r} \left(\frac{s}{\alpha} + \frac{1}{r_0} \right) \frac{\partial r_0}{\partial n} + \frac{1}{r^2} \frac{\partial r}{\partial n} + \frac{s}{\alpha} \frac{1}{r} \frac{\partial r}{\partial n} \right] dS. \tag{1.36}$$

Let $r_0 = r$, $\frac{\partial r_0}{\partial n} = -\frac{\partial r}{\partial n}$ and $d\Omega = \frac{1}{r^2} \frac{\partial r}{\partial n} dS$, where Ω is solid angle. Then

$$\overline{\phi}(\mathrm{P}) = \overline{f}(s) \frac{1}{2\pi} \int_\Omega e^{\frac{-2sr}{\alpha}} \left(\frac{s}{\alpha} + \frac{1}{r} \right) d\Omega. \tag{1.37}$$

Letting $t = 2r/\alpha$, $t_0 = 2r_0/\alpha$ and $d\Omega = \frac{d\Omega}{dt} dt$,

$$\overline{\phi}(\mathrm{P}) = \overline{f}(s) \frac{1}{2\pi} \int e^{-st} \left(\frac{s}{\alpha} + \frac{2}{\alpha t} \right) \frac{d\Omega}{dt} dt. \tag{1.38}$$

Inverting to the time domain,

$$\phi(\mathrm{P}) = \frac{1}{2\pi} \left(\frac{1}{\alpha} \frac{d^2\Omega}{dt^2} + \frac{2}{\alpha t} \frac{d\Omega}{dt} \right) * f(t). \tag{1.39}$$

The solid angle swept out over the surface and its derivatives as a functions of time are

$$\Omega(t) = 2\pi \left(1 - \frac{t_0}{t} \right) H(t - t_0), \tag{1.40}$$

$$\frac{d\Omega}{dt} = 2\pi \frac{t_0}{t^2} H(t-t_0), \tag{1.41}$$

and

$$\frac{d^2\Omega}{dt^2} = 2\pi \frac{t_0}{t^2}\delta(t-t_0) - 4\pi \frac{t_0}{t^3} H(t-t_0). \tag{1.42}$$

Using these expressions, Equation 1.39 becomes

$$\phi(\mathrm{P}) = \frac{1}{2\pi\alpha}\left[2\pi \frac{t_0}{t^2}\delta(t-t_0) - 4\pi \frac{t_0}{t^3} H(t-t_0) + \frac{2}{t} 2\pi \frac{t_0}{t^2} H(t-t_0)\right] * f(t)$$

$$= \frac{1}{\alpha}\frac{t_0}{t^2}\delta(t-t_0) * f(t)$$

$$= \frac{1}{\alpha}\frac{f(t-t_0)}{t_0}$$

$$\phi(\mathrm{P}) = \frac{1}{R} f(t-t_0). \tag{1.43}$$

This is the familiar geometric spreading law for a point source.

The same analysis can be performed in two dimensions (see Figure 1.7). The approximate form of the integral, as given in Equation 1.27, is used because the form is more like that of the three-dimensional case, and the analysis is more straightforward. For an appropriate correspondence, replace u inside the integral of Equation 1.27 with $\phi(\Gamma)$, the potential on the contour Γ. As above, starting with the Laplace transform of the integral (Equation 1.29), use the approximate form of the source (see Equation 1.28).

$$\phi(\Gamma) = \frac{\sqrt{\pi\alpha}}{\sqrt{2sr_0}} e^{\frac{-sr_0}{\alpha}} \overline{f}(s) \tag{1.44}$$

$$\frac{\partial\phi(\Gamma)}{\partial n} = -\frac{\sqrt{\pi\alpha}}{\sqrt{2sr_0}}\left(\frac{1}{2r_0} + \frac{s}{\alpha}\right) e^{\frac{-sr_0}{\alpha}} \frac{\partial r_0}{\partial n} \overline{f}(s) \tag{1.45}$$

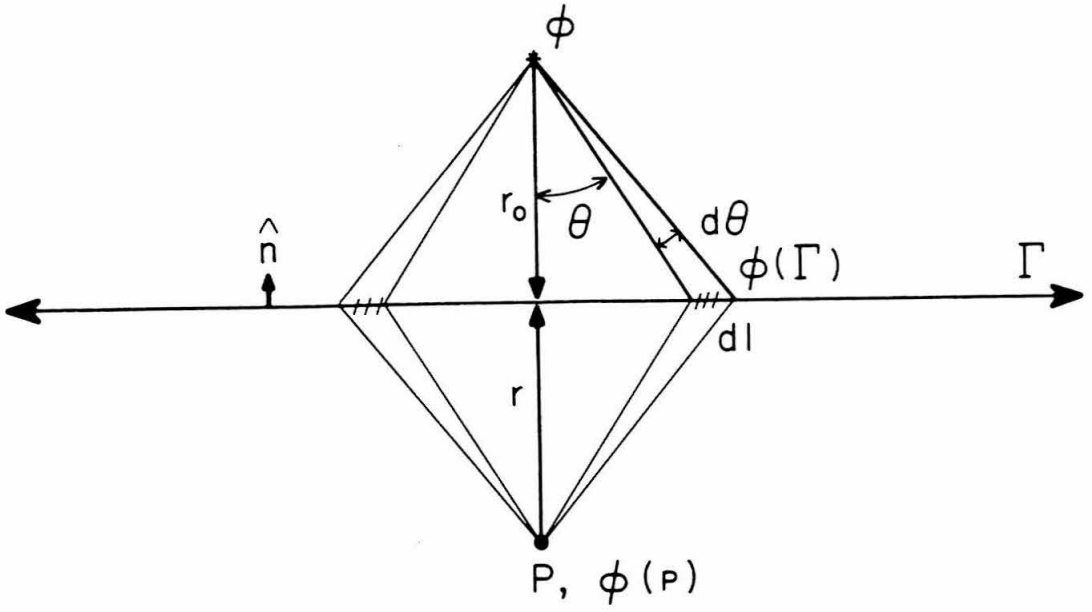

Figure 1.7. Geometry for analytic evaluation of the two-dimensional Kirchhoff integral. The line interface is Γ, with angle θ tracing out dl. The normal to the contour is $\hat{n}$. The source, at distance r_0 from Γ, generates potential ϕ, which produces signal pg on the surface. Two-dimensional Kirchhoff integration gives the result pp at point P, at a distance r from Γ.

Substitute these into Equation 1.29 to obtain

$$\bar{\phi}(\mathrm{P}) = \bar{f}(s)\frac{1}{2}\frac{1}{\sqrt{2\pi}}\int_{\Gamma}\frac{\sqrt{\alpha}}{\sqrt{sr}}\frac{\sqrt{\pi\alpha}}{\sqrt{2sr_0}}e^{\frac{-s(r+r_0)}{\alpha}}$$

$$\left[\left(\frac{s}{\alpha}+\frac{1}{2r}\right)\left(\frac{\partial r}{\partial n}-\frac{\partial r_0}{\partial n}\right)\right]dl. \tag{1.46}$$

Let $r_0=r$, $\frac{\partial r_0}{\partial n}=-\frac{\partial r}{\partial n}$ and $d\theta=\frac{1}{r}\frac{\partial r}{\partial n}dl$, where θ measures the angle from vertical, as indicated in Figure 1.7. Then

$$\bar{\phi}(\mathrm{P}) = \bar{f}(s)\frac{1}{4}\int_{\Gamma}\frac{\alpha}{sr}e^{\frac{-2sr}{\alpha}}2\left(\frac{s}{\alpha}+\frac{1}{2r}\right)\frac{\partial r}{\partial n}dl, \tag{1.47}$$

$$\bar{\phi}(\mathrm{P}) = \bar{f}(s)\frac{1}{2}\int_{\theta}\frac{\alpha}{s}e^{\frac{-2sr}{\alpha}}\left[\left(\frac{s}{\alpha}+\frac{1}{2r}\right)\right]d\theta. \tag{1.48}$$

Letting $t=2r/\alpha$, $t_0=2r_0/\alpha$ and $d\theta=\frac{d\theta}{dt}dt$,

$$\bar{\phi}(\mathrm{P}) = \bar{f}(s)\frac{1}{2}\int e^{-st}\left(1+\frac{1}{st}\right)\frac{d\theta}{dt}dt. \tag{1.49}$$

Inverting to the time domain,

$$\phi(\mathrm{P}) = \frac{1}{2}\left(\frac{d\theta}{dt}+\int_0^t\frac{1}{\tau}\frac{d\theta}{d\tau}d\tau\right)H(t-t_0)*f(t). \tag{1.50}$$

The total angle swept out over the contour as a function of time is

$$\theta(t)=2\cos^{-1}\left(\frac{t_0}{t}\right)H(t-t_0), \tag{1.51}$$

$$\frac{d\theta}{dt} = 2\frac{t_0}{t}\frac{H(t-t_0)}{\sqrt{t^2-t_0^2}}. \tag{1.52}$$

Using these expressions, Equation 1.50 becomes

$$\phi(\mathrm{P}) = \left(\frac{t_0}{t} \frac{H(t-t_0)}{\sqrt{t^2-t_0^2}} + \int_0^t \frac{1}{\tau} \frac{t_0}{\tau} \frac{H(t-t_0)}{\sqrt{\tau^2-t_0^2}} d\tau \right) H(t-t_0) * f(t)$$

$$= \left(\frac{t_0}{t} \frac{H(t-t_0)}{\sqrt{t^2-t_0^2}} + t_0 \int_{t_0}^t \frac{d\tau}{\tau^2 \sqrt{\tau^2-t_0^2}} d\tau \right) H(t-t_0) * f(t)$$

$$= \left(\frac{t_0}{t} \frac{1}{\sqrt{t^2-t_0^2}} + t_0 \frac{\sqrt{\tau^2-t_0^2}}{t_0^2 \tau} \Bigg|_{t_0}^{t} \right) H(t-t_0) * f(t)$$

$$= \frac{t_0^2 + t^2 - t_0^2}{t_0 t \sqrt{t^2-t_0^2}} H(t-t_0) * f(t)$$

$$\phi(\mathrm{P}) = \frac{t}{t_0} \frac{H(t-t_0)}{\sqrt{t^2-t_0^2}} * f(t). \tag{1.53}$$

Now, letting $t \sim t_0$,

$$\phi(\mathrm{P}) = \frac{H(t-t_0)}{\sqrt{t^2-t_0^2}} * f(t). \tag{1.54}$$

This is the familiar equation for line-source response. Note that in the three-dimensional point-source case, $d\Omega/dt = 0$ until $t = t_0$, and then jumps to $2\pi/t_0$ at $t = t_0$, gradually decreasing with time thereafter. An interface with structure behaves in a more interesting manner; see Scott and Helmberger (1983). In two dimensions, $d\theta/dt$ has a square-root singularity at $t = t_0$. In the three-dimensional extension of this case, the response at $t = t_0$ represents the integrated energy arriving at the receiver from an infinite strip

represented by the first line element. It is the integration over this infinite strip in and out of the plane of Figure 1.7 that creates the singularity.

The simplest application of two-dimensional Kirchhoff is to a medium of constant velocity set in Cartesian coordinates, with part of the contour, Γ, parallel to one of the axes (Figure 1.8). Choosing a boundary paralleling the x-axis in an (x,z) system and extending to infinity in both directions, the contour Γ may be closed at $r = \infty$ in the direction $z = +\infty$. As $r \rightarrow \infty$, the integral over this closure of Γ vanishes. The point P is chosen to be the receiver location, and all sources are outside the contour. The vector $\bar{r}$ has its origin at P and points to positions on Γ. From this information, $\hat{n} = -\hat{z}$ on the straight boundary, $\frac{\partial r}{\partial n} = \frac{z}{r}$ and $\frac{\partial}{\partial n} = -\frac{\partial}{\partial z}$. For this case, the integral from Equation 1.27 becomes

$$u\,(\mathrm{P}) = \frac{1}{2\pi}\frac{\sqrt{\alpha}}{\sqrt{2}}\frac{1}{\sqrt{t}} * \int_{-\infty}^{\infty}\left[\frac{1}{\sqrt{r}}\left(-\frac{\partial u}{\partial z} + u\frac{z}{2r^2} + \frac{z}{r\,\alpha}\frac{\partial u}{\partial t}\right)\right] dl. \tag{1.55}$$

For computation, the integral must be discretized to a finite sum. Assuming that the contributions from the ends of the boundary are small,

$$u\,(\mathrm{P}) = \frac{h}{2\pi}\frac{\sqrt{\alpha}}{\sqrt{2}}\frac{1}{\sqrt{t}} * \sum_{i=1}^{N}\left[\frac{1}{\sqrt{r_i}}\left(-\frac{\partial u}{\partial z} + u\frac{z}{2r_i^{\,2}} + \frac{z}{r_i\,\alpha}\frac{\partial u}{\partial t}\right)\right], \tag{1.56}$$

where h is the spacing between discrete line elements. If the coordinates of P are x_{P}, z_{P}, and the coordinates of the first line element are x_1, z_1, then $z = z_{\mathrm{P}} - z_1$, $x_i = x_{\mathrm{P}} - x_1 - (i-1)h$ and $r_i = \sqrt{x_i^{\,2} + z^2}$.

The above geometry is developed specifically for application with finite-difference techniques. For the acoustic case, the wave field u becomes pressure (or dilatation, Θ), and Equation 1.56 is directly applicable. For the

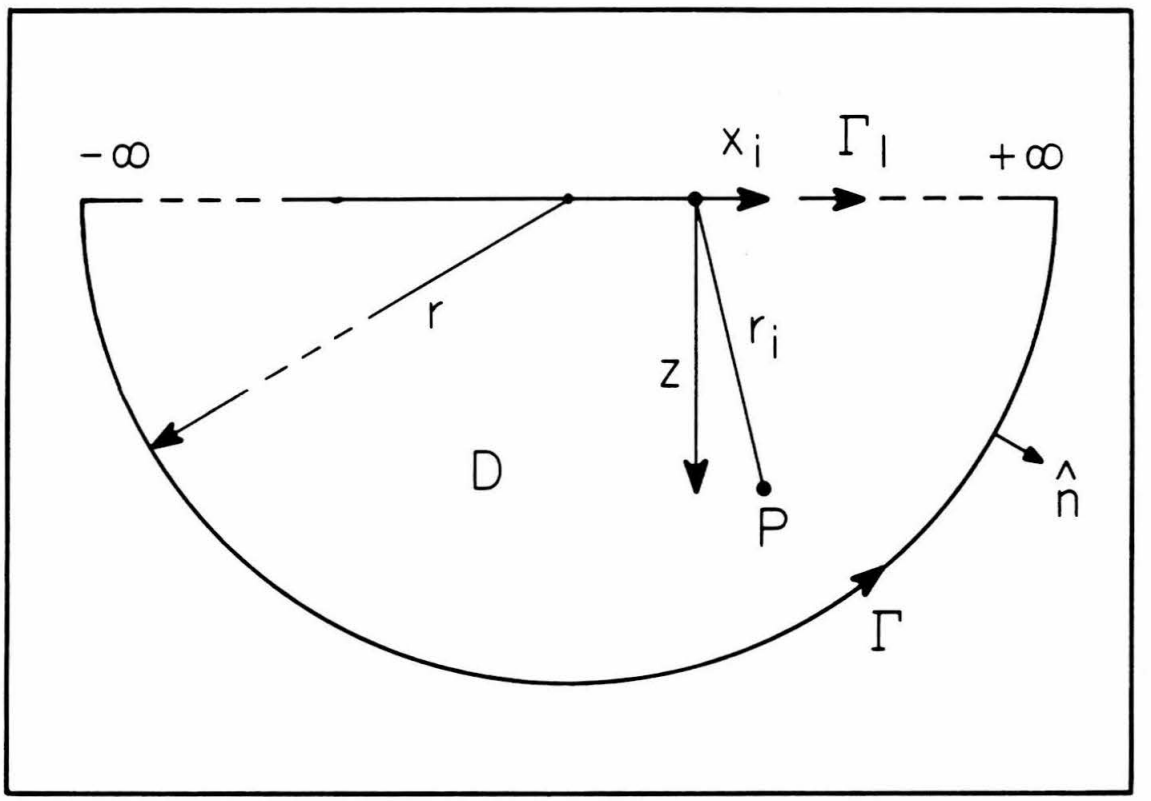

Figure 1.8. The geometry for two-dimensional Kirchhoff along a flat interface in a half space. The contour Γ has been deformed such that it follows a line Γ_1 parallel to the x axis from $x=-\infty$ to $x=+\infty$ and is closed at $r' = \infty$ (Γ_2) in the direction of $z=+\infty$. The integrand becomes trivial along Γ_2, reducing the integral to an infinite definite integral along x. This is further reduced for numerical application to a finite sum along x.

elastic case, some modifications must be made. Assuming continuous material properties across the boundary, the compressional and shear wave fields may be separated. Separating these fields following a fully elastic finite-difference calculation requires the taking of the divergence and curl of the full wave displacement field for the compressional and shear components, respectively. This can be seen from the potential form of the vector displacements, $\underline{u} = \nabla\phi + \nabla\times\underline{\psi}$. First, take the divergence, $\nabla\cdot\underline{u}_p = \nabla\cdot\nabla\phi$, and take the curl, $\nabla\times\underline{u}_s = \nabla\times\nabla\times\underline{\psi}$. Take grad and curl, respectively, of the resulting equations. Two equations now exist, one in which u is identified as the second spatial derivative of the compressional wave field with velocity as α the P-wave velocity, and a second in which u is identified as the second spatial derivative of the shear wave field with velocity as β the S-wave velocity. Returning to the wave equation, the reason for the second derivatives becomes evident. The wave equations involving the second derivatives of displacement are

$$\nabla^2\underline{u}_p = \frac{1}{\alpha^2}\frac{\partial^2\underline{u}_p}{\partial t^2} \tag{1.57}$$

$$\nabla^2\underline{u}_s = \frac{1}{\beta^2}\frac{\partial^2\underline{u}_s}{\partial t^2}. \tag{1.58}$$

Identifying the wave field u in Equation 1.27 as the second derivatives of the vector displacements $\underline{u}_p$ and $\underline{u}_s$, the wave equations allow the second spatial derivatives of $\underline{u}_p$ (P) and $\underline{u}_s$ (P) to be equated to second time derivatives, that is, accelerations. Thus, Equation 1.27 becomes two integrals, one for the P-wave field and another for the S-wave field, in each of which the required inputs are spatial derivatives of displacement (calculated in the finite-difference code), and the outputs are accelerations.

Normally, when calculating a teleseismic record in this manner, elastic or acoustic, a point source in three-dimensional geometry is the response desired. An appropriate approximate conversion, derived in Appendix A as Equation A.32, is

$$U_{\text{point}} = \frac{2}{\sqrt{R}+\sqrt{x}} \frac{1}{\sqrt{t}} * \frac{d}{dt} U_{\text{line}}. \tag{1.59}$$

This conversion is more accurate for this application than the conversion derived by Stead, et al., 1989. Here, x is the horizontal distance (as in the above derivation), and R is the total distance ($\sqrt{x^2+z^2}$) from the source to the receiver. This conversion assumes cylindrical symmetry about a vertical axis through the source. If it is applied directly to Equation 1.56, the result is as follows.

$$u\,(\mathrm{P}) = \frac{h}{2\pi} \frac{\sqrt{\alpha}}{\sqrt{2}} \frac{2}{\sqrt{R}+\sqrt{x}} \frac{d}{dt} \frac{1}{\sqrt{t}} * \frac{1}{\sqrt{t}} *$$

$$\sum_{i=1}^{N} \left[\frac{1}{\sqrt{r_i}} \left(-\frac{\partial u}{\partial z} + u \frac{z}{2{r_i}^2} + \frac{z}{r_i \alpha} \frac{\partial u}{\partial t} \right) \right] \tag{1.60}$$

This equation can be simplified by recognizing that

$$\frac{d}{dt} \frac{1}{\sqrt{t}} * \frac{1}{\sqrt{t}} * F(t) = \frac{d}{dt} \pi H(t) * F(t)$$

$$= \pi \delta(t) * F(t)$$

$$= \pi F(t). \tag{1.61}$$

Then

$$u\,(\mathrm{P}) = \frac{h}{\sqrt{R}+\sqrt{x}} \frac{\sqrt{\alpha}}{\sqrt{2}} \sum_{i=1}^{N} \left[\frac{1}{\sqrt{r_i}} \left(-\frac{\partial u}{\partial z} + u \frac{z}{2{r_i}^2} + \frac{z}{r_i \alpha} \frac{\partial u}{\partial t} \right) \right]. \tag{1.62}$$

This conversion that assumes the original line-source radiation pattern was appropriately adjusted for conversion to point source, as discussed in Appendix A.

Several assumptions are made in the above derivation. Some simple tests of the method against other analytical methods will demonstrate the accuracy of the method. Suppose we examine a simple half-space with a point source at a depth of 1 km in an elastic half-space with P-velocity 4 km/s, S-velocity 2.3 km/s and density 2.7 g/cc, and receivers at a depth of 6 km and a variety of ranges. A comparison of the new method, finite-difference and Cagniard seismograms is shown in Figure 1.9. The seismograms shown include an RDP source convolved with a Gaussian (pulsewidth is 0.24 seconds). The Gaussian is necessary in the finite-difference scheme to limit the bandwidth of the source to a range in which propagation is accurate. The records shown are velocity records, which are representative of the response of a broad-band strong-motion instrument. The response at the surface for finite differences and Cagniard are compared in Figure 1.10, demonstrating the accuracy of finite differences in modeling strong-motion records.

The synthetics for ranges less than or equal to the source depth have not been included in either Figure 1.9 or 1.10, because the line-source to point-source mapping approximation breaks down at near-vertical take-off angles; see Appendix A. The parameter k_f , used in the mapping, is fixed at 0.6 throughout this investigation, because it seems to give good agreement to other synthetic methods (Figures 1.9 and 1.10) at the take-off angles of interest in this study.

Appendix B contains further verification designed to create strong scattering points and to alter travel times.

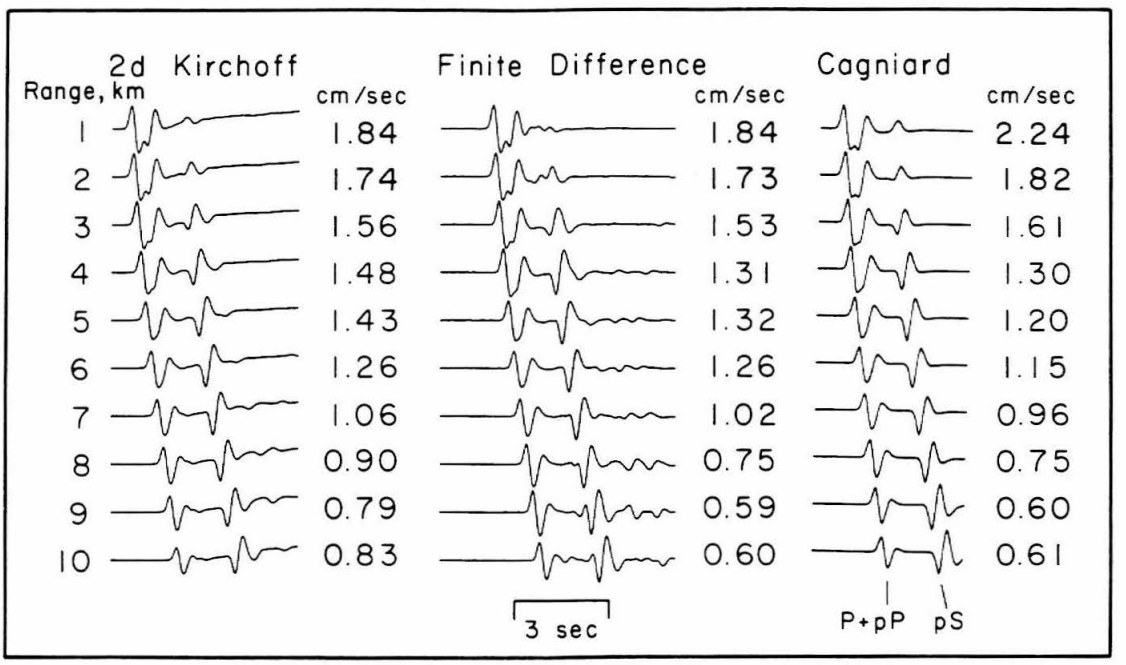

Figure 1.9. Test results for Lamb's problem. Three methods are compared in this figure: two-dimensional Kirchhoff (driven with finite differences), finite differences, and Cagniard - de Hoop. The records are vertical responses in a half-space with a source 1 km deep for deeply buried receivers (6 km) at the range of horizontal distances indicated. The velocities of the medium are 4.0 km/s P-wave and 2.3 km/s S-wave, and the density is 2.7 g/cc. The source is an explosion with RDP parameters K=12.0Hz, B=1.0 and $\psi_\infty = 10^{10}\text{cm}^3$.

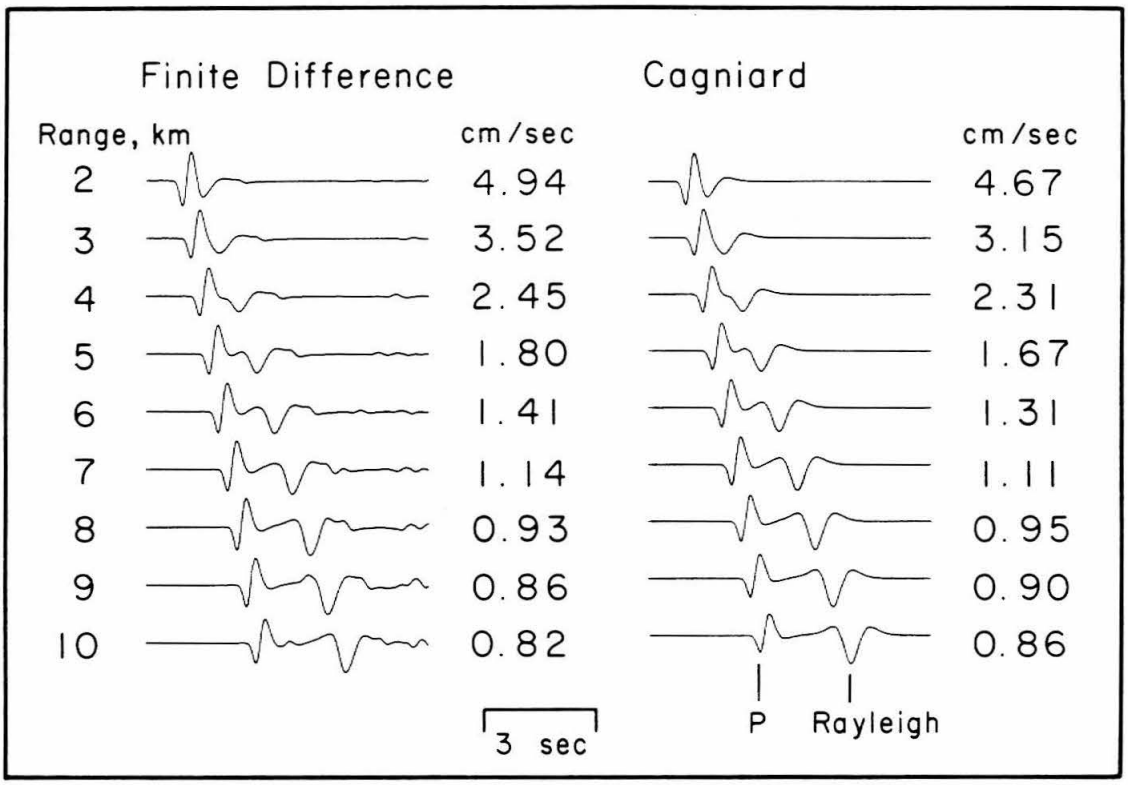

Figure 1.10. Test results for Lamb's problem. The medium is the same as that of Figure 1.9. The receivers are on the surface and only finite differences and Cagniard are compared. This demonstrates the accuracy of finite-difference strong motions.

1.3 Canonical basin models

Having demonstrated, briefly, the accuracy of the finite-difference and two-dimensional Kirchhoff methods, some canonical models of basins are examined to understand what effects various geometries may have. Four models of basin boundaries are shown in Figure 1.11; they are variations of a layer over a half-space. The half-space parameters are P-velocity 4.6 km/s, S-velocity 2.7 km/s, and density 2.7 g/cc, and are representative of crystalline rock. The layer parameters are chosen to give a P-velocity ratio of one to two, with the other parameters appropriate for a sediment with that P-velocity; P-velocity 2.3 km/s, S-velocity 1.1 km/s, density 2.0 g/cc. The source is fixed 3.75 km from the basin boundary at a depth of 0.75 km in each case (see Figure 1.11). Surface strong-motion synthetics are computed at one km intervals from the source to the edge of the model and compared with the uniform layer over a half-space model. Examination of the strong-motion synthetics in Figure 1.12 shows some of the differences between the four basin termination models. Both of the sharper basin terminations pass more energy across the termination; the gradual terminations allow waves of only about half the amplitude to pass across. Nevertheless, all the models of basin termination cause large drops in amplitude as the wave fronts cross the boundary. Part of this energy is reflected back across the basin (this energy cannot be corrected to three dimensions properly and will have higher than its true amplitude, especially as it approaches the source position), but much of it is scattered to teleseismic distances. The surface waves are not well-developed here because there is no low-velocity surface layer to reduce the direct wave and enhance amplitude and duration of the Rayleigh wave. The primary conclusion to be drawn from the strong-motion synthetics is that

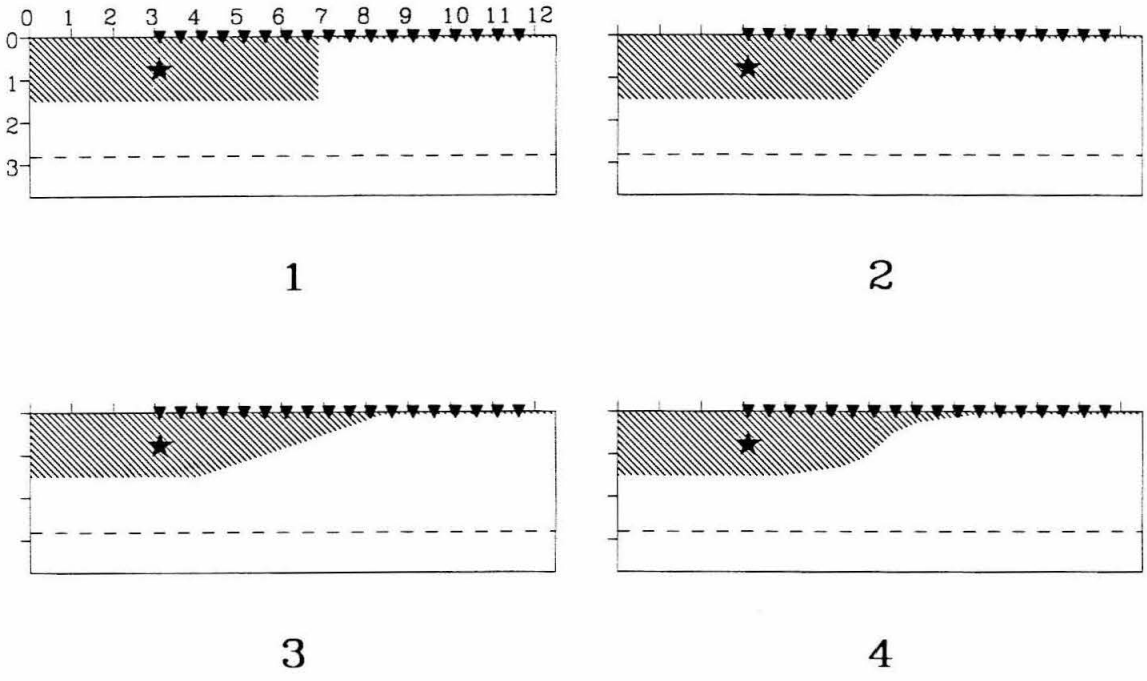

Figure 1.11. Four models of basin boundaries. These are the four canonical models which are used to demonstrate the effect of various basin terminations. The structure, apart from the boundaries, is a layer over a half-space. The layer has a P-velocity 2.3 km/s, S-velocity 1.1 km/s and density 2.0 g/cc. The half-space has a P-velocity 4.6 km/s, S-velocity 2.7 km/s and density 2.7 g/cc. The star represents the position of the source, always at a depth of 750 m. The inverted triangles are the positions of strong motion instruments. The broken line is the contour along which two-dimensional Kirchhoff is performed. The distances labeled on model 1 are in km.

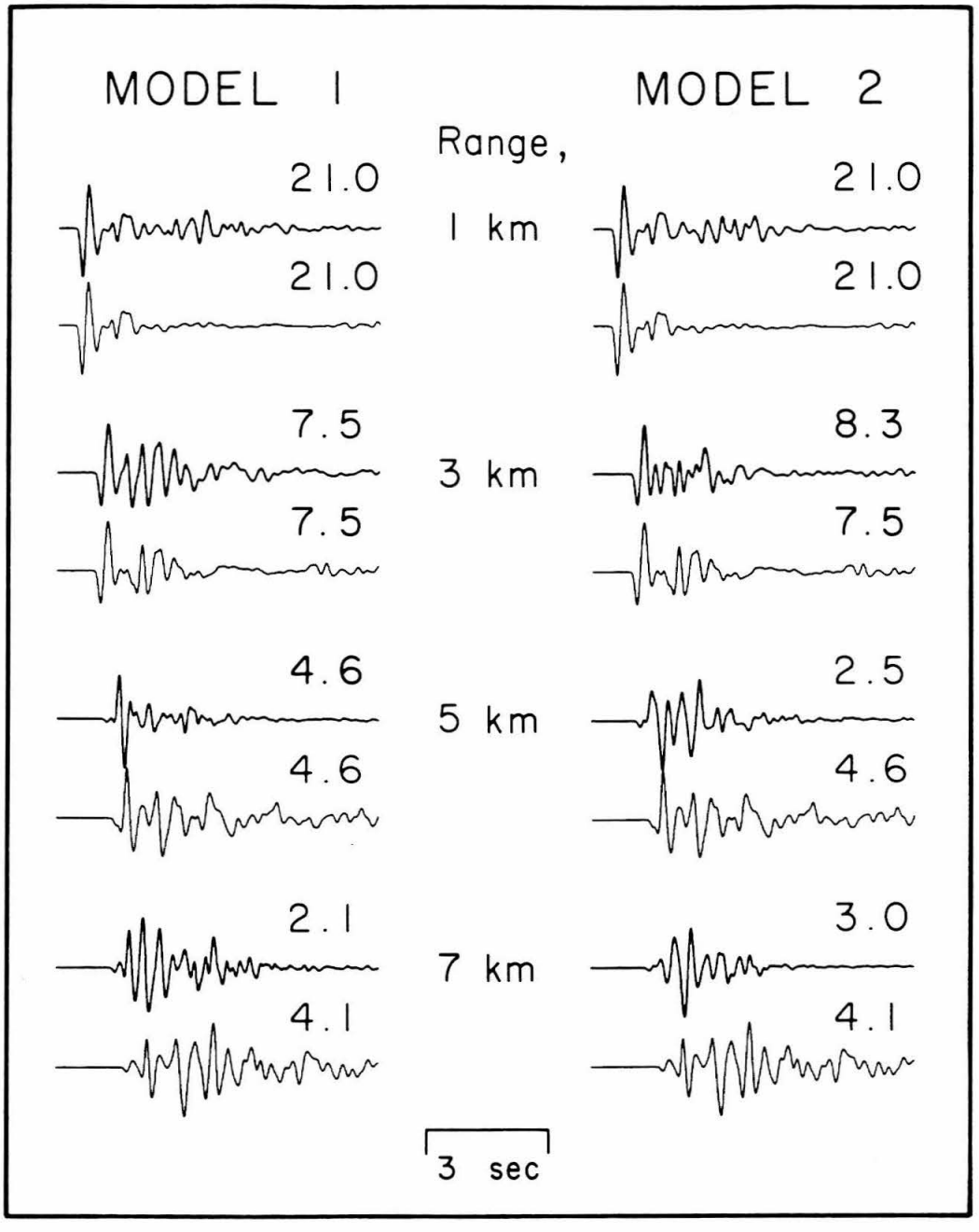

Figure 1.12a. Strong motion results for canonical basin models. These seismograms are velocity records at the surface at distances 1, 3, 5 and 7 km from the source, for models 1 and 2 shown in Figure 1.11. An RDP source with K=12, B=1, and $\psi_\infty=10^{10}$ has been used. The number to the right of each trace is the maximum amplitude in cm/s along that trace. Each trace from each model (heavy line) is compared directly to the corresponding trace for flat layers (light line). Two important observations are made. First, the amplitude of the surface wave drops abruptly at the basin boundary, and second, this drop is greatest for the least dipping boundary.

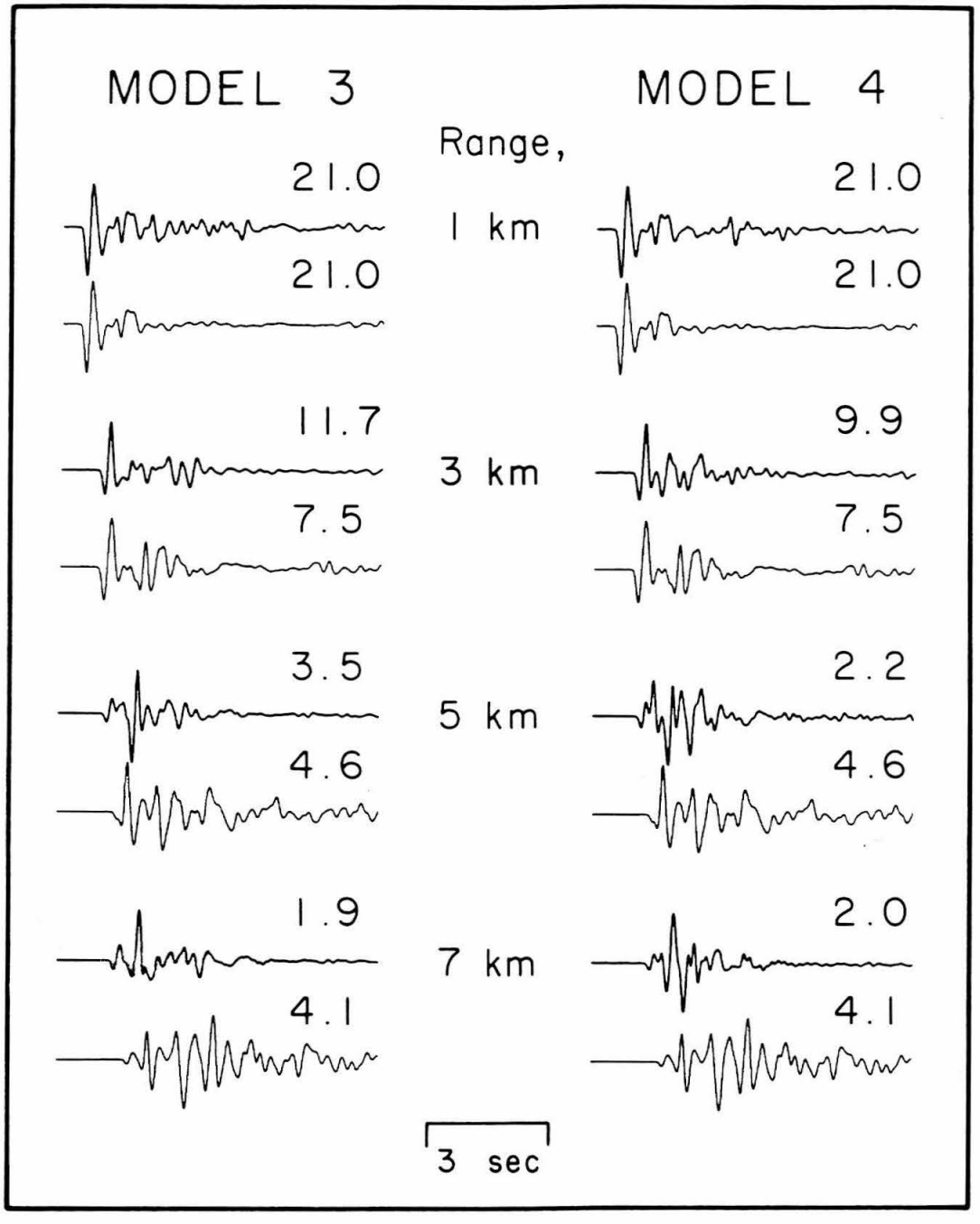

Figure 1.12b. Strong motion results for basin models. This figure is the same as Figure 1.12a, but compares models 3 and 4 shown in Figure 1.11.

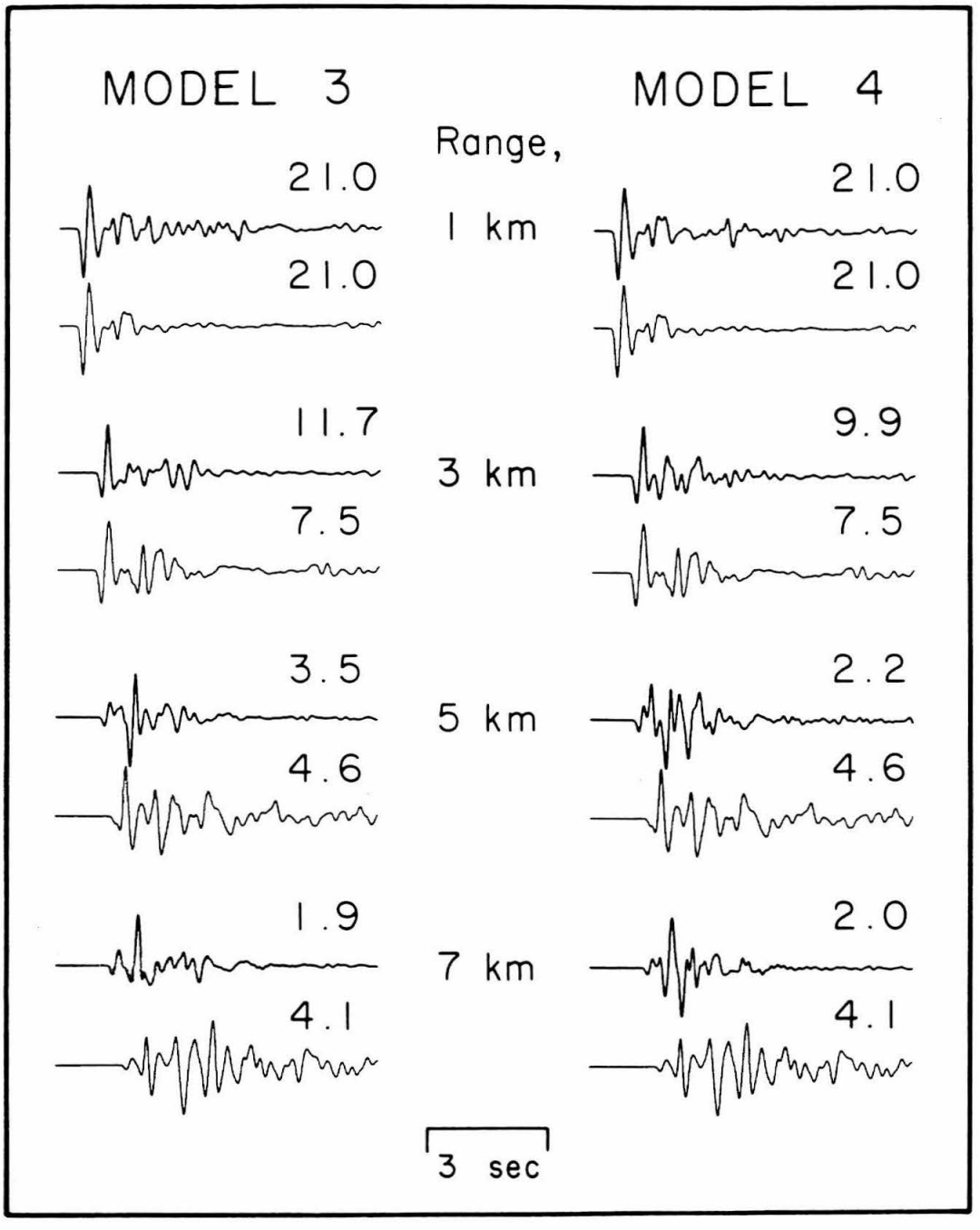

Figure 1.12b. Strong motion results for basin models. This figure is the same as Figure 1.12a, but compares models 3 and 4 shown in Figure 1.11.

gradual basin terminations will cause the greatest diminution of surface wave energy crossing that boundary, and more generally, all large contrasts across great changes in basin depth will cause large reductions in transmitted strong-motion surface waves.

Now, using the two-dimensional Kirchhoff technique derived above, the scattered energy may be examined at teleseismic distances. Figure 1.13 shows the teleseismic P-wave seismograms computed at a distance through the half-space of 1000 km from the source. These displacement records include the RDP source, a WWSSN short-period instrument response and attenuation with t^* of one. The seismograms are all normalized to the flat-layer response (that is, the response if the model at the source were extended laterally without termination). The distance of 1000 km is sufficient for these half-space teleseismic calculations because it is two orders of magnitude greater than the length of the integration contour, and therefore the waveform will no longer change with distance; only the amplitude will change by geometric spreading. This will be discussed more fully later. Differences in the synthetics for the various models consist primarily of small amplitude changes at the frequencies involved here. Even broad-band responses do not show large changes in teleseismic records (Figure 1.14). This indicates that at teleseismic distances, for explosions, velocity contrast at the boundary and the overall dimensions of the boundary are of primary importance, not the precise shape of the boundary. On the other hand, increasing the amplitude and duration of the surface wave before it interacts with the boundary increases the overall effect on the teleseismic waveform and increases the variation with boundary geometry, as we will show later.

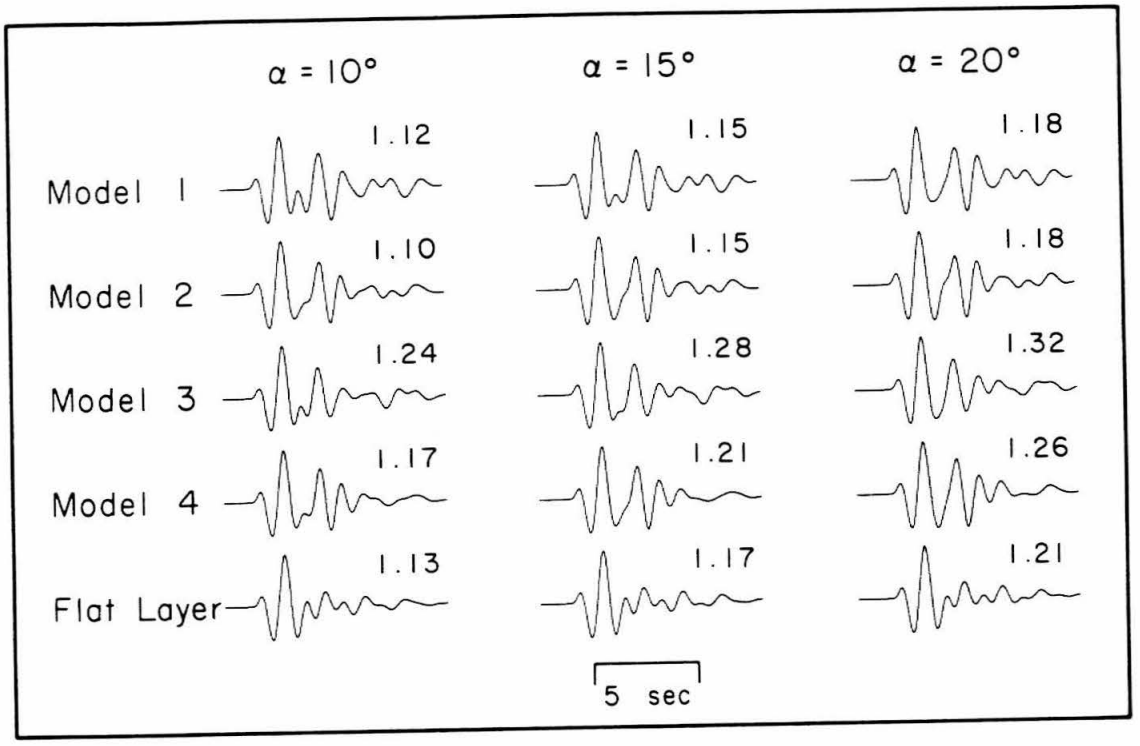

Figure 1.13. Teleseismic P-wave results for canonical basin models. These seismograms are displacement records convolved with a WWSSN short-period instrument response and include the same RDP source used in Figure 1.12. They are also convolved with a Q operator with $T^*=1$. They are at a ray length of 1000 km from the source, and at take-off angles 10°, 15° and 20°. The number to the right of each record is the peak amplitude normalized to the peak amplitude of a flat-layer model at 0° take-off angle. The simple appearance of these seismograms is misleading; they vary significantly from the flat-layer response shown as the fifth record in each series. The first four records are from the models, in order, as shown in Figure 1.11.

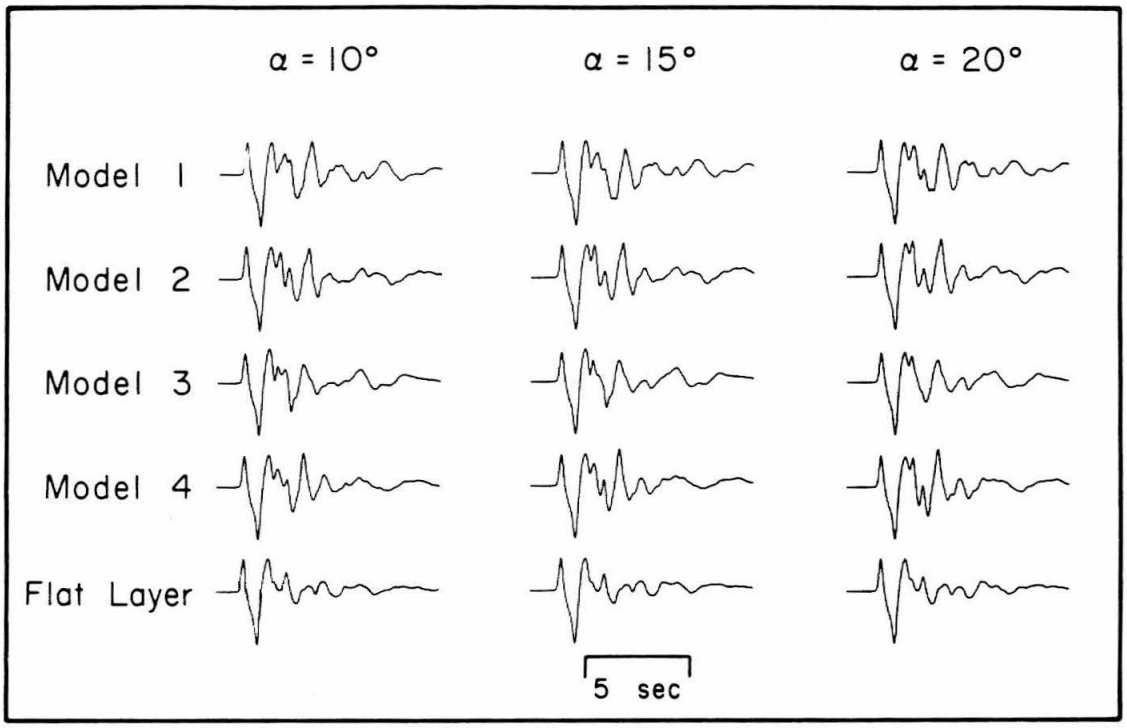

Figure 1.14. Broad-band teleseismic P-wave displacement waveforms for basin models. This is identical to Figure 1.13, except that no Q or instrument response has been convolved with the record. Differences between the records, especially secondary arrivals, are now more obvious.

Some of this scattered energy is also found as teleseismic SV-waves. Figure 1.15 shows the S-wave responses at the same teleseismic distances. These waves are of the same order of magnitude in amplitude as the scattered P-waves. Also, because they are not dominated by P and pP (pS is small at near-vertical take-off angles), they show a great deal more variation with the type of boundary chosen. Such high-amplitude scattered SV-waves could complicate the analysis of sources such as earthquakes that generate direct S-waves, and such scattered waves could be important when studying explosions, which can generate SV-waves only through structural interaction.

In demonstration of how two-dimensional Kirchhoff constructs the teleseismic waveform, Figure 1.16 shows a series of synthetic velocity seismograms at four take-off angles (5, 10, 15 and 20 degrees) for five cases in which more of the line elements along the contour are included in each subsequent calculation. That is, case 0 includes contributions from the single line element at 17 degrees take-off angle. Case 1 includes the two nearest neighbors, case 2 includes 11 elements, case 3 includes 25, and case 4 includes all elements. Up to case 2, the P-pP arrivals increase by addition of energy from a narrow range of angles providing energy propagating away from the very near vicinity of the source. Energy scattered from structure is not propagating in the direction of the receivers over this portion of the contour. The elements used in case 2 should include most of the energy for the P-pP arrival, and remaining contributions to that phase are small, as seen by comparing peak amplitudes in the remaining cases. Case 3 is the first to include significant energy from scattering. Notice that the contour elements included in case three contain all contributions from the basin boundary up to 20 degrees take-off angle. For this reason, the contributions from the remaining

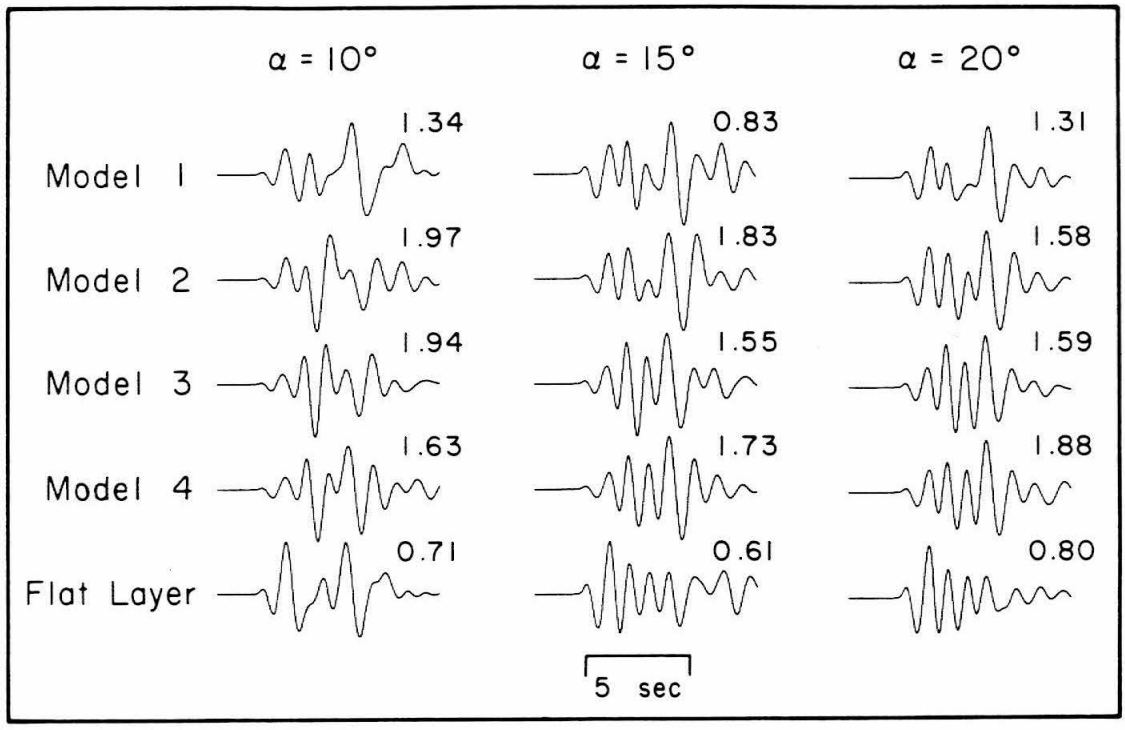

Figure 1.15. Teleseismic S-wave results for basin models. The purpose of this figure is to demonstrate the production of teleseismic S-waves, although the true character of teleseismic S-waves observed is not accurately reflected here. The figure is set up the same as Figure 1.13, but the value of T^* is far too low for the earth for S-waves. The SV-waves are partly pS, but this phase is small at small take-off angles. Much of the energy shown is the result of basin boundary interactions.

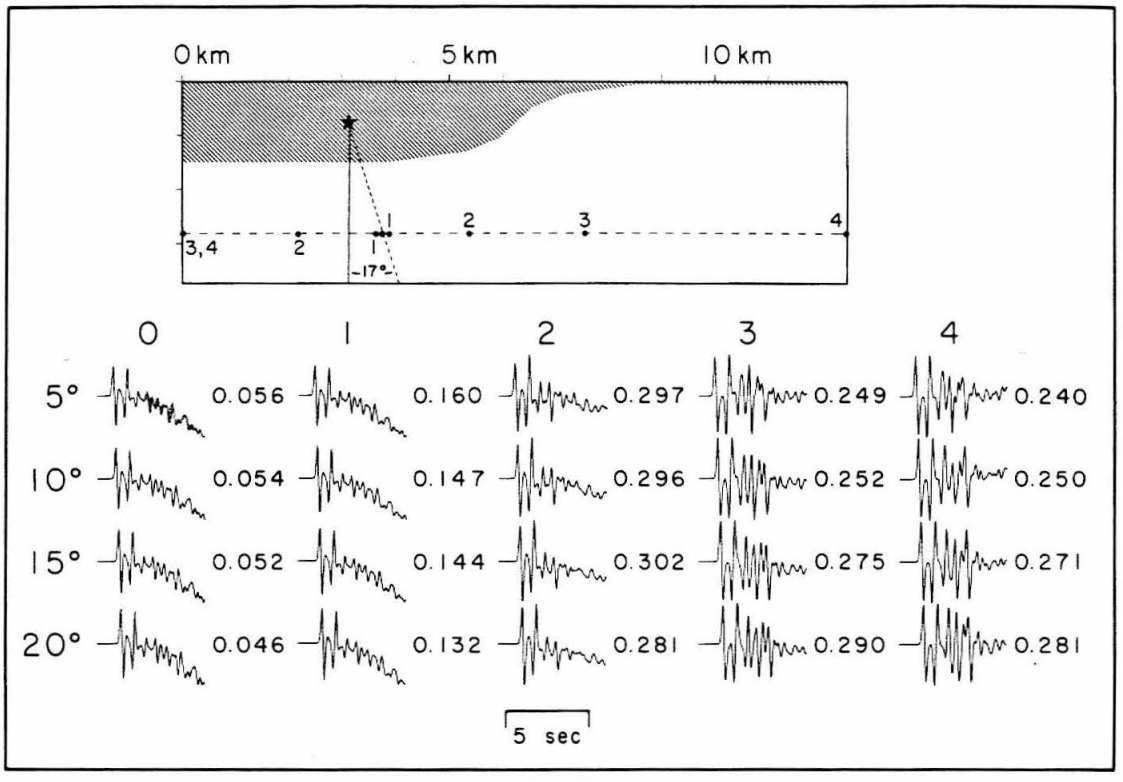

Figure 1.16. Contributions of various line elements to the final seismogram. The model is model 4 from Figure 1.11. Case 0 is the result of the contribution from one line element at 17°. Each case adds more line elements to the final seismogram. Cases 0 through 2 progressively build the P-pP arrival; case 3 adds the energy from scattering. The records in all cases are broad-band velocity records at 5, 10, 15 and 20 degrees take-off angles. They include an RDP source as described in Figure 1.12.

elements are small, and the records for case 4 differ little from those of case 3. By showing a range of take-off angles for each case, the figure demonstrates that at large distances it is more important to consider the length of the interface than the precise take-off angle.

Figure 1.17 demonstrates the effect of distance on the resulting seismograms. At the smaller distances of 5 and 10 km, the contribution from scattering propagates at a greatly different angle than the energy from the source. For receivers below the source, the scattered energy is small because it is propagating backward off the scatterer. Farther from the source, at distances of 100 and 1000 km, there is little difference between records at different distances because the take-off angles from the source and the scatterer become indistinguishable. These synthetic seismograms contain only the P-waves; if the S-waves were included, the records at 5 and 10 km would become very complicated and would differ greatly from those at teleseismic distances.

1.4 Application - events at Yucca Flat, Nevada Test Site

Since near-source structural interaction causes variations in teleseismic waveforms because of surface wave interaction, records of this scattering are likely to be quite common. Yucca Flat at Nevada Test Site (NTS) is one example of a structure that may generate these effects. The lateral variation in the Yucca Flat area is due to the basin structure of the valley. Sources at NTS are often located near the center of the valley, three to five kilometers from the basin termination. As shown in the canonical models of basins above, this situation will cause strong interaction of the surface wave with the basin boundary. At the surface, the amplitude of the surface wave will

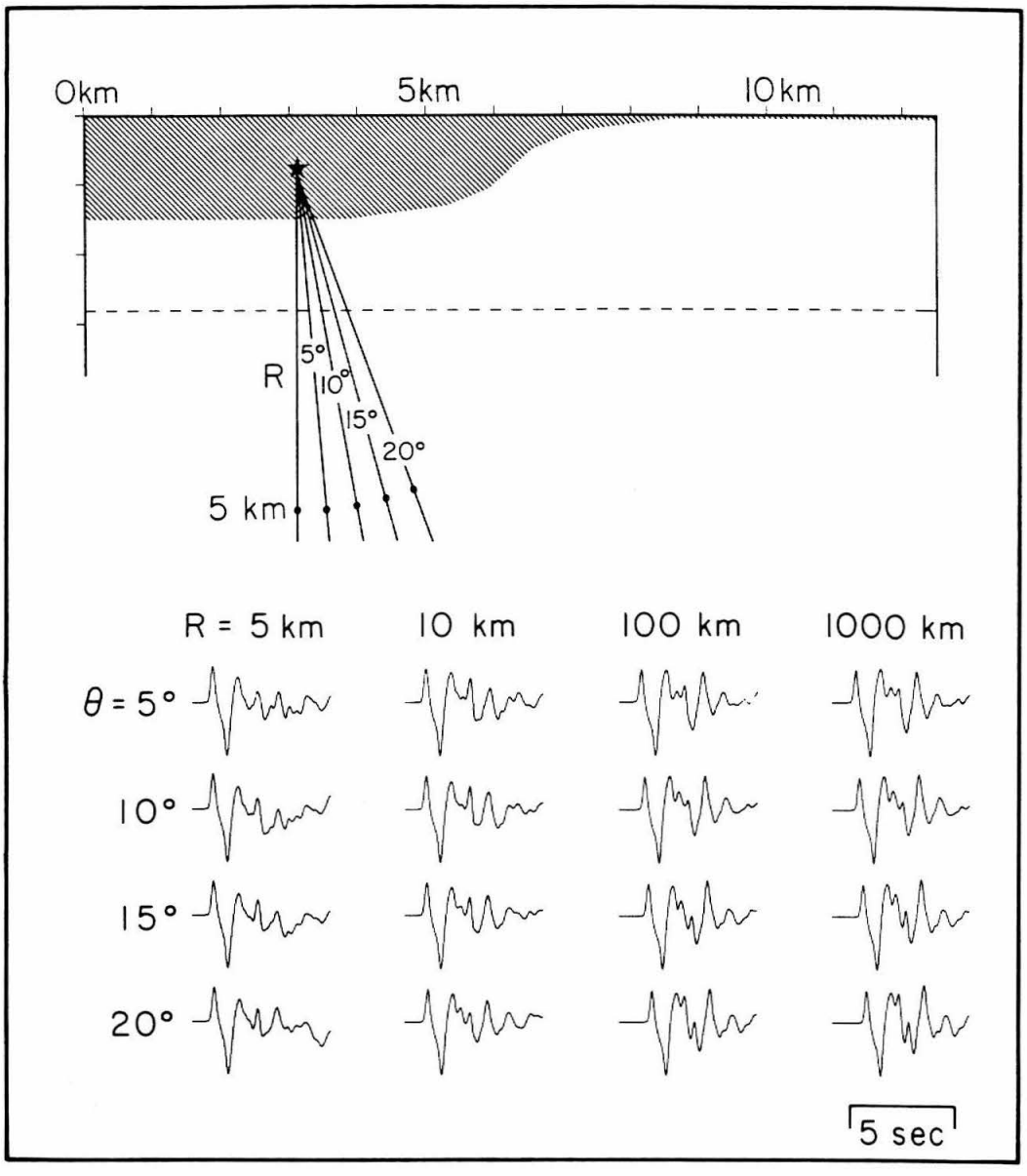

Figure 1.17. Effect of distance. The four cases represent progressively greater distance from the source (5, 10, 100 and 1000 km). These are broad-band displacement records at 5, 10, 15 and 20 degrees take-off angle. The records at 100 and 1000 km are similar, because at great distance, the source becomes indistinguishable from the scatterer in terms of take-off angle.

be reduced and the frequency content will change as the wave encounters hard rock.

As discussed above, the two-dimensional methods used in this investigation produce a three-dimensional response from point sources. The conversion derived in Appendix A requires that the source used to drive the finite-difference scheme include higher-order (non-isotropic) line-source terms (Vidale, 1986 and Vidale and Helmberger, 1987). For an explosion, these terms have radiation patterns such that the response is correct only from half the source. In the modeling below, the structure in the invalid direction is restricted to flat layers. The result of this modeling is a structure that is locally cylindrical, because the response in and out of the plane and in the invalid direction is flat-layered and has no effect on the seismograms produced.

Figure 1.18 is a map of Yucca Flat that shows the outlines of the hard rock outcrops which approximately mark the the basin boundary. Also displayed are the various event locations and a network of strong-motion recorders for one event (FLASK). Note that the locally cylindrical geometry is appropriate in the direction of the WWSSN station MAT, Japan. The line AB marks the location of a cross section shown in Figure 1.19. The cross section is a view looking south, and the positions of various sources and receivers used in this study are shown. There are three materials in this model: low-velocity alluvium, volcanic tuffs, and hard rock (Cretaceous granites and Paleozoic rocks). The large differences between the velocities of these materials is what makes lateral variation affect the teleseismic waveforms.

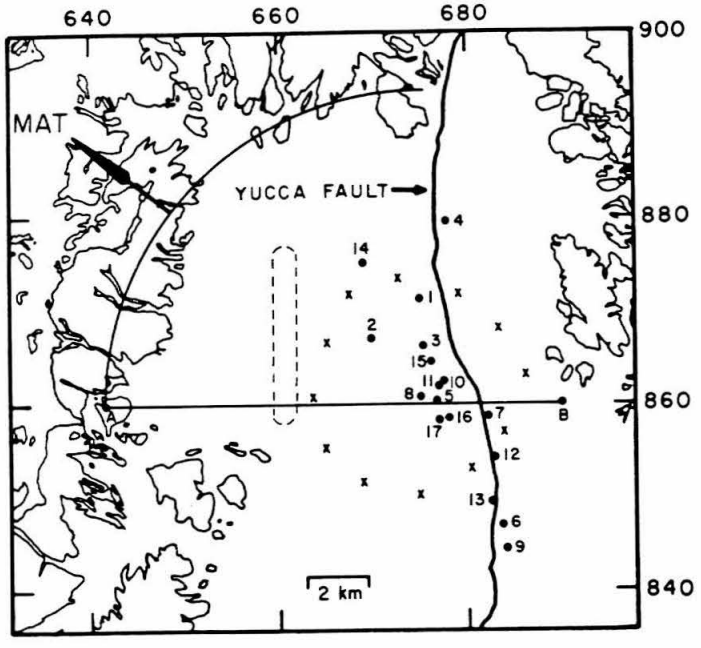

Event List

	Event	Date
1	Calabash	10/29/69
2	Carpetbag	12/17/70
3	Chiberta	12/20/75
4	Corduroy	12/3/65
5	Dumont	5/19/66
6	Escabosa	7/10/74
7	Esrom	2/4/76
8	Flask	5/26/70
9	Keelson	2/4/76
10	Knox	2/21/68
11	Lanpher	10/18/67
12	Mizzen	6/3/75
13	Oscuro	9/21/72
14	Portmanteau	8/30/74
15	Starwort	4/26/73
16	Strait	3/17/76
17	Topgallant	2/28/75

Figure 1.18. Map of Yucca Flat. The contours show the borders of hard rock outcrops. The filled circles are the locations of several events listed adjacent to the figure. Each strong motion station used to record the FLASK event (number 12) is represented by an x. The arc indicates the general shape of the basin boundary as seen from above. The arrow indicates the great-circle direction of WWSSN station MAT, Japan. The dashed line represents the approximate position of the buried basin boundary.

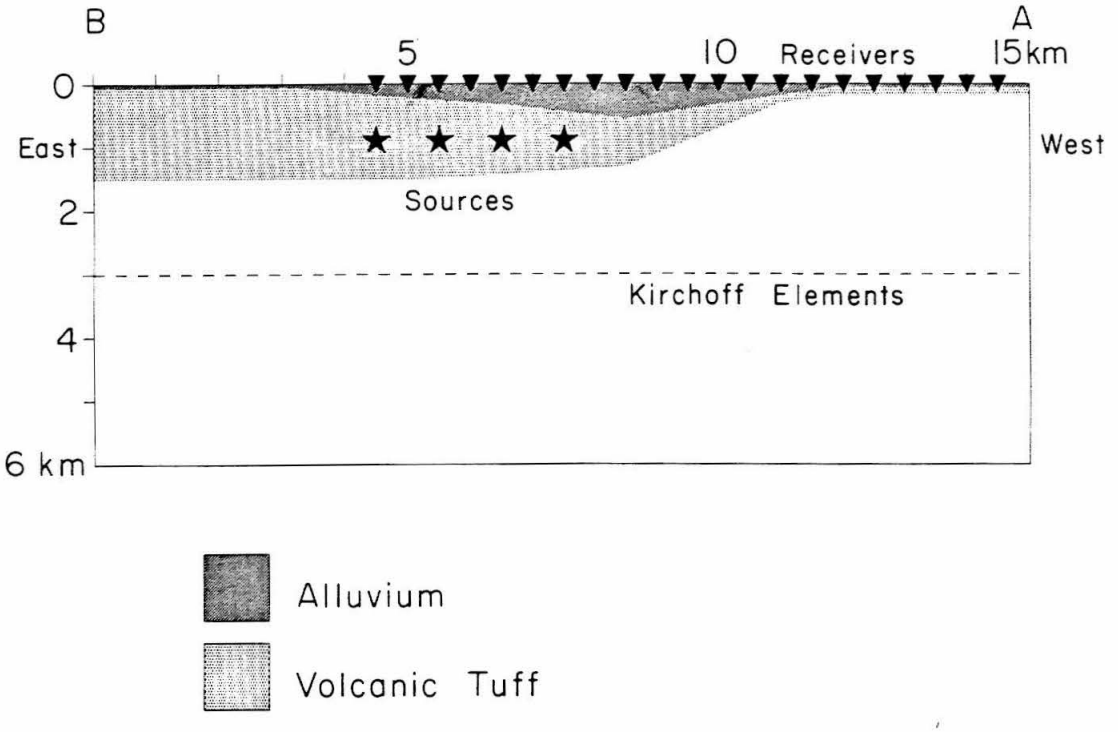

Figure 1.19. Cross section of Yucca Flat. The section is a generalization of the structure at Yucca Flat (Hayes and Murphy, 1970, Eckren, 1968, Houser, 1968). The three layers from the surface downward are alluvium, volcanic tuff and hard rock. Hard rock is a broad term used here to describe Mesozoic granitic rock and Paleozoic rocks, all of which have similar elastic properties (velocities and density). The stars indicate four different source positions used (numbered 0 to 3), all at a depth of 875 m. The inverted triangles indicate the position of the strong-motion records generated by the finite-difference calculations. The dashed line is the integration contour for the two-dimensional Kirchhoff. The alluvium, tuff and basement have P-velocities 1.5, 3.7 and 4.6 km/s, S-velocities 0.8, 2.15 and 2.7 km/s, and densities 1.9, 2.1 and 2.7 g/cc, respectively.

The local cylindrical symmetry of the resulting model is shown in Figure 1.20. The source falls on the axis of the cylinder, and the line-source to point-source conversion is valid only in the direction of the basin boundary. The seismograms generated for the source positions indicated are responses for this three-dimensional geometry.

Figure 1.3 shows some of the strong-motion data from the FLASK event. Both the locations of the receivers and the location of the event are shown on the map of Figure 1.18. (Station 787 did not record a vertical record, and station 794 was not well-recorded.) The data shown in the figure are vertical velocity records from stations three to four kilometers from the event. The basin becomes shallow between the source and the position of the westernmost stations, creating a geometry where the easternmost stations see a distant basin boundary, while those to the west see a basin boundary directly below. In the figure, the differences between the two directions is readily apparent. To the west, the amplitudes of surface waves are reduced by roughly half with respect to those to the east. It also appears that the long-period surface waves are reduced more than short-period waves. It will be shown that the energy lost from the surface waves is converted to body waves and is found on teleseismic records.

Some strong-motion synthetics for a source at position 1 are shown in Figure 1.21. Notice that as the Rayleigh wave encounters the basin boundary, the amplitude becomes roughly half and the long-period surface waves are greatly reduced. The source parameters mentioned in the figure are used in a Helmberger and Hadley (1981) reduced displacement potential. This RDP source is approximately that expected for FLASK and similar events in Yucca Flat, and is used throughout this investigation as a representative

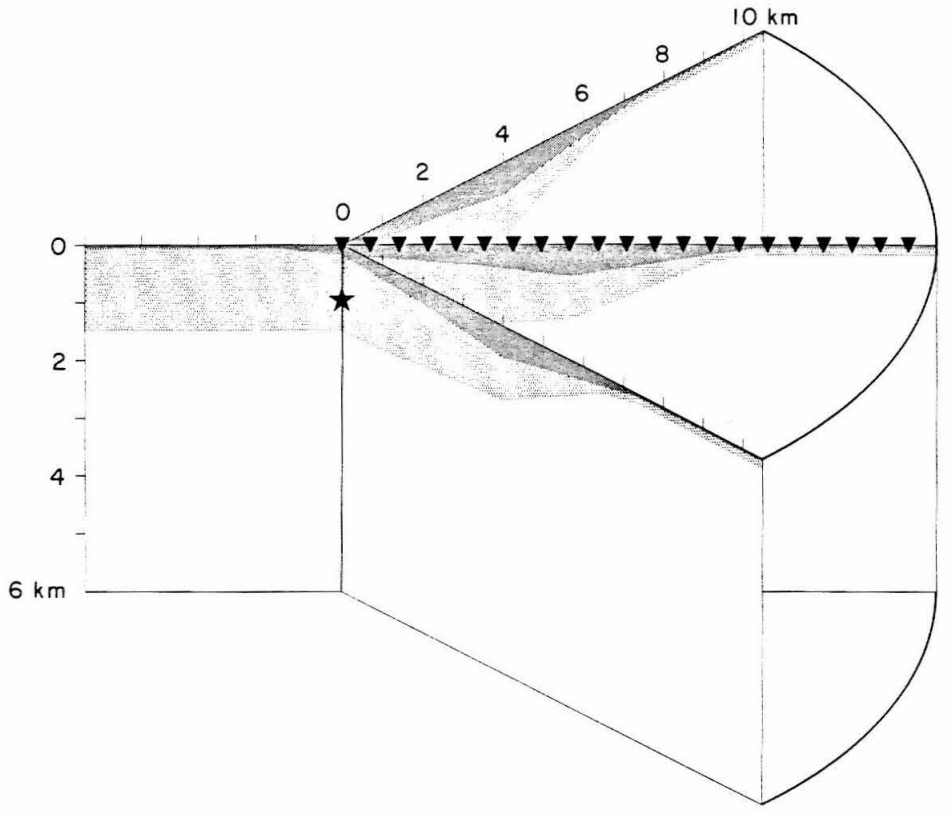

Figure 1.20. Local cylindrical symmetry. The structure of Yucca Flat is shown here as the locally cylindrical geometry assumed by the filter used to convert line-to-point responses. Comparing this to the map in Figure 1.18, local cylindrical structure is appropriate for the case of Yucca Flat.

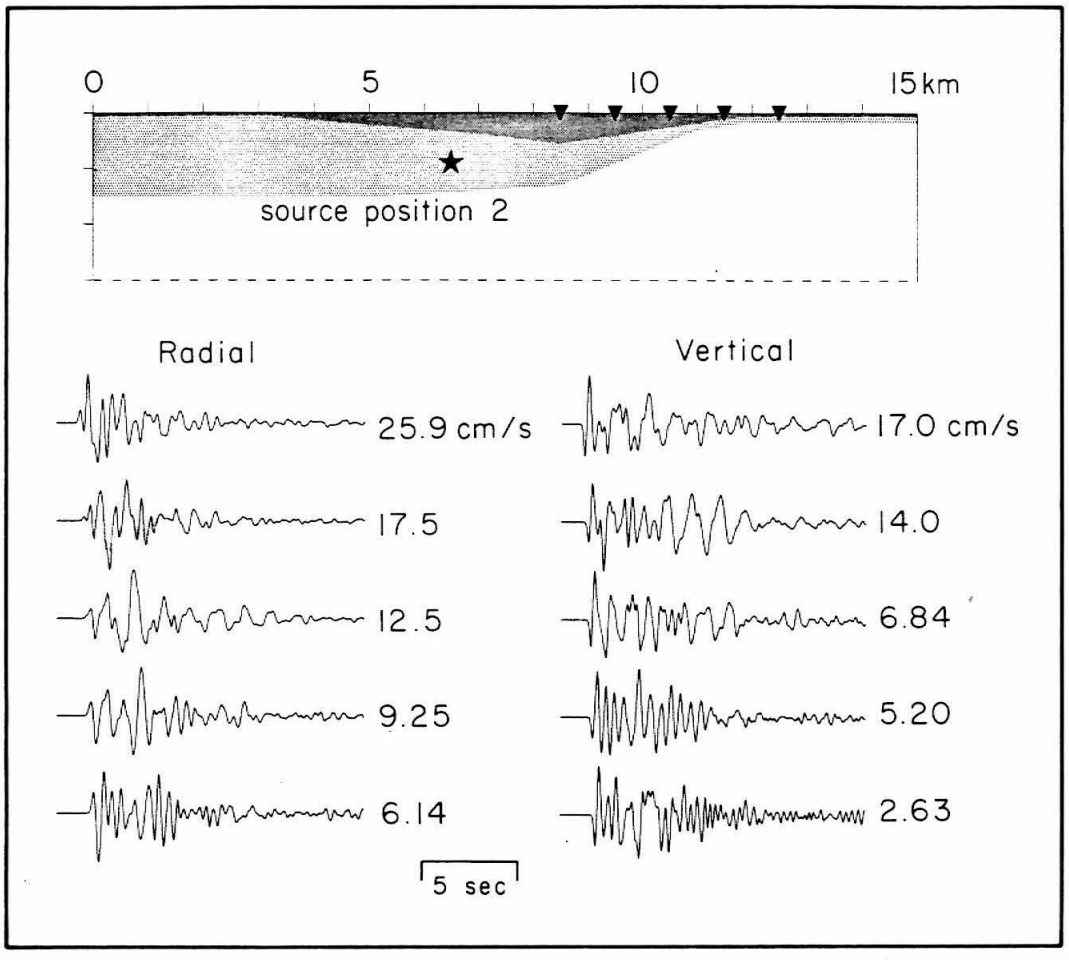

Figure 1.21. Synthetic strong-motion records for FLASK. These records, generated by the finite-difference method, include an RDP source with K=12 Hz, B=1 and $\psi_\infty=10^{10}\text{cm}^3$. These are only for source position 1 (of 0 to 3 on Figure 1.19), and for the stations shown. It is important to notice that the peak amplitude drops sharply across the boundary, that the duration of the Rayleigh wave is reduced, and that the Rayleigh wave appears to lose relatively more of the lower frequencies as it crosses the basin boundary.

source description.

Direct comparisons of various source-receiver pairs and the data are given in Figure 1.22. The data have more energy in the higher frequencies because of limitations of the finite-difference method. (The data are not filtered. This prevents the introduction of any artificial bias in the modeling.) Finite grid spacing results in a maximum frequency which can be propagated accurately. Therefore, the source used is convolved with a Gaussian window to remove higher frequencies. Nevertheless, the absolute amplitudes and many of the primary features of each record are accurately modeled. The record for station 795 is best modeled by a source at position 2 (out of positions 0 through 3 spaced one kilometer apart) at a distance of three kilometers. This is one of the better waveform fits produced by the model. Station 791 is best modeled by a source at position 3 (closest to the basin boundary) at a distance of 3.5 kilometers. Stations 791, 793 and 795 are north and east of the event. This is the range of directions, as argued from the map of Figure 1.18, which is most like a locally cylindrical geometry. Station 789 is to the south. Here, the basin boundary is farther from the source. Thus, source position 0 gives the most accurate result.

Now the two-dimensional Kirchhoff may be applied to see if this model is consistent also with the teleseismic data. Figure 1.2 shows the data set to be considered here. These are short-period WWSSN records recorded at station MAT, Japan. Seven different events from various sites within the valley are shown. (These were chosen only because they were already available in digitized form.) Notice the additional energy arriving after P-pP. This energy is present at very large amplitudes on all records except PORTMANTEAU. PORTMANTEAU occurred at the basin boundary to the northeast

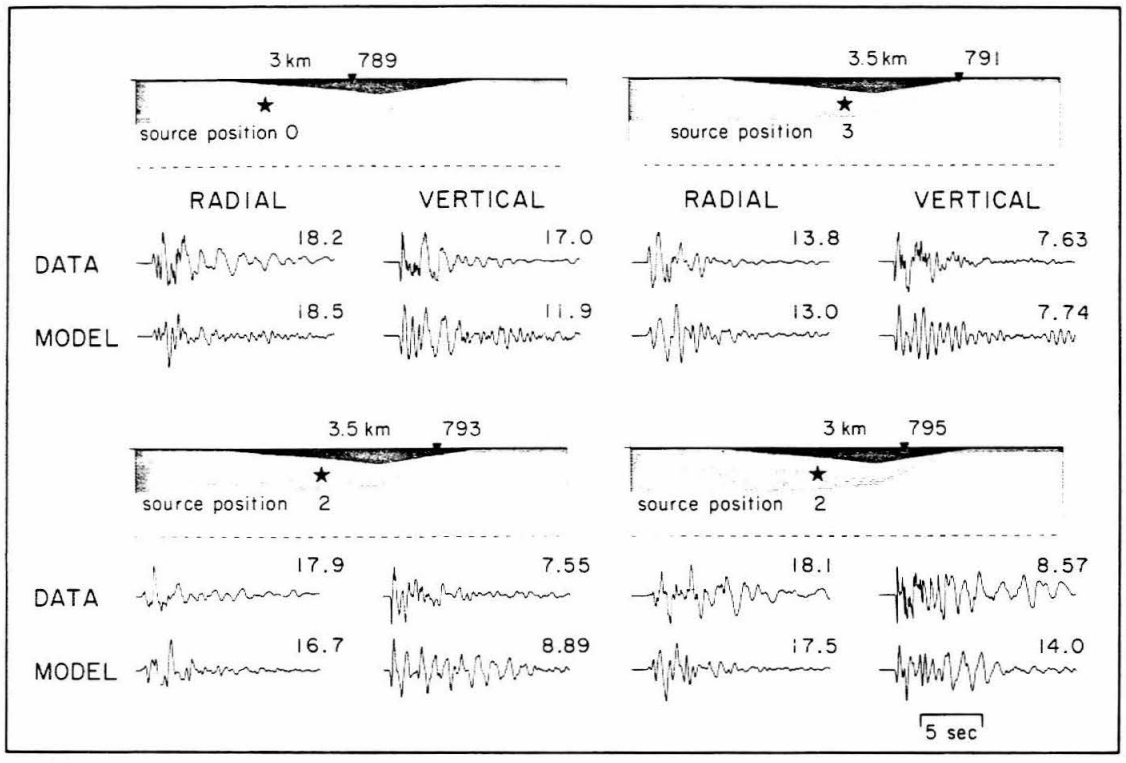

Figure 1.22. Direct comparison of strong-motion records. This figure compares some observed and synthetic strong-motion records for the FLASK event. This demonstrates that despite the simplicity of the model, the resulting strong-motion records are an accurate representation of those observed.

and therefore will lack a later basin-boundary arrival, as does the flat-layer case. Note also that while P-pP is similar for all the events, the later phases vary substantially as a function of position. Yet when sources are close together (KEELSON and OSCURO), differences are small.

Figure 1.23 shows some of the two-dimensional Kirchhoff results. These are point-source displacement records and have been convolved with a WWSSN short-period instrument response and a Q-operator with $T^*=1$. Take-off angles of 15° and 20° were chosen to bracket that appropriate for MAT (17.8°). All amplitudes are relative to the flat-layer case at a take-off angle of 0° (the flat-layer record shown is at 15°). The important observation here is that the records vary far more by moving the source one kilometer within the basin than by changing the take-off angle by five degrees. The energy causing the waveform variations comes from the conversion of surface wave energy at the basin boundary. Figure 1.24 shows a direct comparison of the data and model. KEELSON and OSCURO are modeled accurately by the same synthetic record, demonstrating repeatability, and the flat-layer comparison with PORTMANTEAU is good as expected. The agreement is very good despite the simplicity of the model, which consists of two layers over a half-space. No correction is made for mantle propagation or effects near the receiver. Only the four best fits of the seven records in Figure 1.2 are shown in Figure 1.24. The other records are not as well fit, and this is likely due to the model's simplicity. Also, note that while FLASK is modeled well for the basin boundary at the known basement high indicated by the dashed line in Figure 1.18, the position of the basin boundary that best models KEELSON and OSCURO does not correspond to the dashed line, but is closer to these sources. This indicates that greater structural complexity

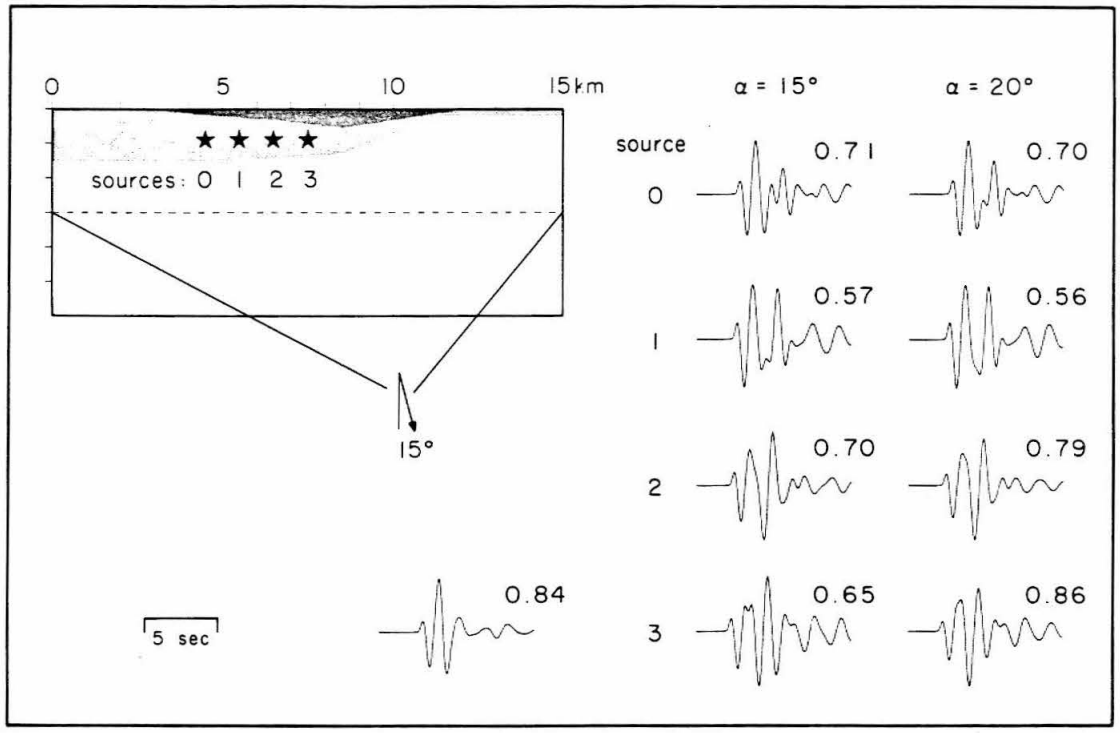

Figure 1.23. Synthetic teleseismic records for Yucca Flat events. A short-period WWSSN response and a Q operator with $T^*=1$ have been convolved into the records. The RDP source mentioned in Figure 1.21 is also included. The peak amplitudes are normalized to that for a flat-layer response at a take-off angle of 0°. (The flat-layer model is constructed by extending the velocity structure at the first source in Figure 1.19 horizontally both east and west to the grid boundaries.) The flat-layer record shown is at 15° The important observation here is that moving the source 1 km within the basin is far more important than changing the take-off angle 5°.

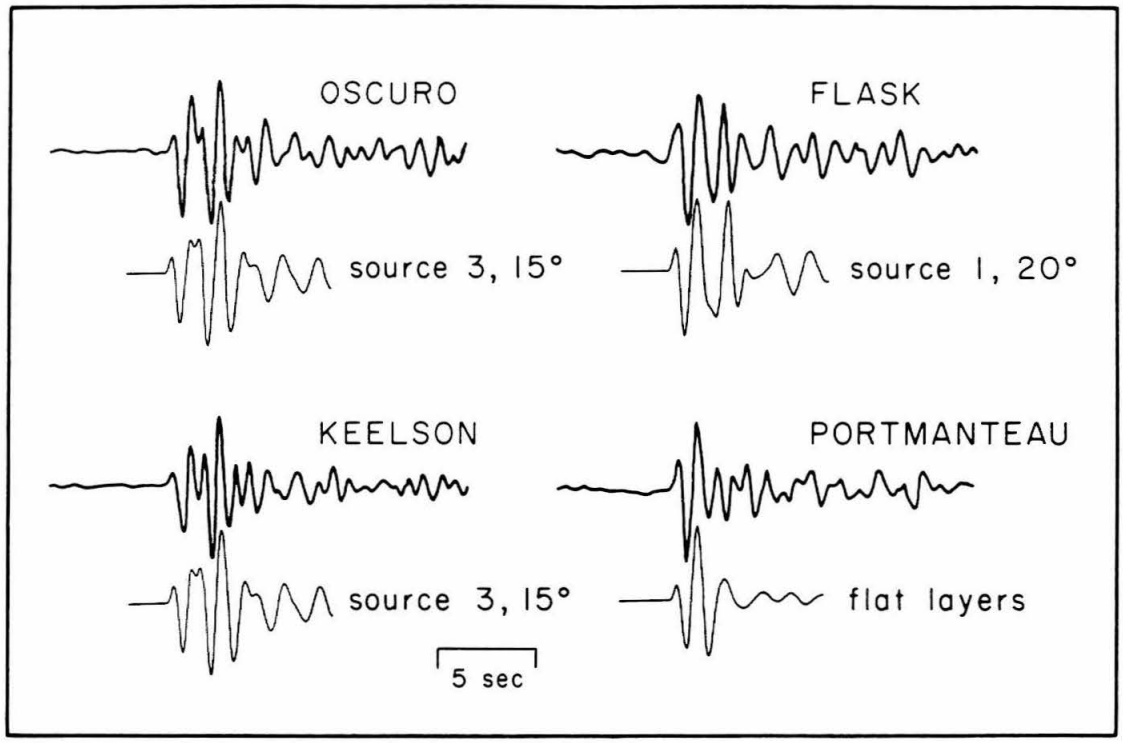

Figure 1.24. Direct comparison of teleseismic records. These comparisons demonstrate the accuracy of the new method. Although the P-waves have passed through the mantle and receiver structure, the greater part of the energy in the observed records is explained by the near-source structure at Yucca Flat. The repeatability of the method is demonstrated by KEELSON and OSCURO. These events are located close together and are modeled well by the same synthetic record.

exists within the basin than is shown in the cross section.

1.5 Discussion and conclusions

This chapter presents a new method for calculating teleseismic waveforms, using an interface of numerical and analytic computations. As presented, the two-dimensional Kirchhoff method relies entirely on local structural effects to change the teleseismic waveform. This method can be made computationally fast and efficient. The use of anisotropic sources and appropriate filtering of the resulting seismograms produce three dimensional, point-source records. The finite-difference calculation produces both surface strong-motion records and the functions needed for the teleseismic synthetics. In this way, a model of local structure can be compared with both local and teleseismic data simultaneously.

In this chapter, we concentrated on the local structural effects in modeling teleseismic waveforms. More realistic path effects can be included in the calculations by modifying Equation 1.62, using a convolution with an appropriate kernel computed by various analytical ray techniques. Such interfacing would be useful, for example, in modeling the complexities observed by Lynnes and Lay (1988).

The case for using only local structure in the teleseismic calculation is strong for Yucca Flat because the local strong-motion and teleseismic data are modeled simultaneously. Only the local structure need be considered to make a good, synthetic strong-motion seismogram. Since a local structure models well both the strong-motion records and the teleseismic records, the effect of local structure on the teleseismic waveform is substantiated. A relatively simple model of the basin at Yucca Flat produces synthetic

seismograms matching very well those observed at teleseismic and local distances. The variation of surface wave amplitude with azimuth is shown to be the result of interaction with the basin boundary. A drop in amplitude across the basin boundary occurs as surface wave energy is converted to body waves. These scattered phases are observed on teleseismic records shortly after P-pP.

References for Chapter 1

Baker, B. B. and E. T. Copson (1950), *The Mathematical Theory of Huygens' Principle* (Oxford University Press, London) pp. 36-53.

Eckren, E. B. (1968), Geologic setting of Nevada Test Site and Nellis Air Force Range, In *Nevada Test Site, GSA Memoir 110*, (ed. Eckel, E. B.) (GSA, Boulder, CO) pp. 21-33.

Hart, R. S., D. M. Hadley, G. R. Mellman and R. Butler (1979), *Seismic amplitude waveform research, Final Technical Report SGI-R-79-012* (Sierra Geophysics).

Hartzell, S. and T. Heaton (1983), Inversion of strong ground motion and teleseismic waveform data for the fault rupture history of the 1979 Imperial Valley, California earthquake, *Bull. Seism. Soc. Am.* **73**, 1553-1583.

Hays, W. W. and T. R. Murphy (1970), *The effect of Yucca Fault on seismic wave propagation, Report NVO-1163-TM-19* (Environmental Research Corporation, Las Vegas).

Helmberger, D. V. and D. M. Hadley (1981), Seismic source functions and attenuation from local and teleseismic observations of the NTS events JORUM and HANDLEY, *Bull. Seism. Soc. Am.* **71**, 51-67.

Hilterman, F. J. (1975), Amplitudes of seismic waves - a quick look, *Geophysics* **40**, 745-762.

Houser, F. N. (1968), Application of geology to underground nuclear testing, Nevada Test Site, In *Nevada Test Site, GSA Memoir 110*, (ed. Eckel, E. B.) (GSA, Boulder, CO) pp. 11-19.

Hudson, J. A. (1963), SH waves in a wedge-shaped medium, *Geophys. J. Roy. Astron. Soc.*, **7**, 517-546.

Lay, T. (1987a), Analysis of near-source contributions to early P-wave coda for underground explosions: 2. frequency dependence, *Bull. Seism. Soc. Am.* **77**, 1252-1273.

Lay, T. (1987b), Analysis of near-source contributions to early P-wave coda for underground explosions: 3. inversion for isotropic scatterers, *Bull. Seism. Soc. Am.* **77**, 1767-1783.

Lay, T., T. C. Wallace and D. V. Helmberger (1984), Effect of tectonic release on short period P waves from NTS explosions, *Bull. Seism. Soc. Am.* **74**, 819-842.

Lynnes, C. S. and T. Lay (1988), Observations of Teleseismic P-wave Coda for Underground Explosions, *PAGEOPH,* **128**, 231-249.

Mow, C. C. and Y. H. Pao (1971), *The Diffraction of Elastic Waves and Dynamic Stress Concentrations* (Report R-482-PR for United States Air Force Project Rand, Santa Monica, CA), pp. 140-171.

Scott, P. and D. Helmberger (1983), Applications of the Kirchhoff-Helmholtz integral to problems in seismology, *Geophys. J. Roy. Astron. Soc.* **72**, 237-254.

Stead, R. J., J. E. Vidale and D. V. Helmberger (1989), On modeling explosions using 2-d numerical methods, *Bull. Seism. Soc. Am.*, submitted.

Taylor, R. T. (1983), Three-dimensional crust and upper mantle structure at the Nevada Test Site, *J. Geophys. Res.* **88**, 2220-2232.

Vidale, J. E. (1986), *Application of two-dimensional finite-differencing methods to simulation of earthquakes, earth structure, and seismic hazard* (Ph.D. thesis, Calif. Institute of Tech., Pasadena).

Vidale, J. E. and D. V. Helmberger (1987), Path effects in strong motion seismology, Chapter 6 In *Methods of Computational Physics* (ed. Bolt, B.)

(Academic Press, New York) pp. 267-319.

Vidale, J. E. and D. V. Helmberger (1988), Elastic finite-difference modeling of the 1971 San Fernando, Ca. earthquake, *Bull. Seism. Soc. Am.*, **78,** 122-141.

Vidale, J. E., D. V. Helmberger and R. W. Clayton (1985), Finite-difference seismograms for SH waves, *Bull. Seism. Soc. Am.* **75**, 1765-1782.

Chapter 2

Modeling explosions with two-dimensional numerical methods

2.1 Introduction

Ideally, one would like to simulate wave propagation in the earth with 3-D numerical grids. Such experiments are, in fact, now being attempted (Stevens and Day, 1985, Reshef, et al., 1988a, Reshef, et al., 1988b). They require, however, very large amounts of computer time and allow energy to propagate only a limited number of wavelengths, so that they do not apply to many problems of geophysical interest (see, for example, Figure 13.11 of Aki and Richards, 1980, for the range of application of various methods). Numerical grids in 2-D have been used for many years to provide insight into 3-D wave propagation problems (see Boore, 1972, for example). Recently, we have developed source expressions allowing the simulation of point slip dislocations and explosions with 2-D numerical grids (Vidale, et al., 1985; Vidale and Helmberger, 1986; Stead and Helmberger, 1988; Helmberger and Vidale, 1988). These expressions are applied to a fourth-order explicit FD method. We find this method to be accurate, flexible and more efficient numerically than implicit FD or pseudo-spectral methods (pseudo-spectral methods are discussed by Reshef, et al., 1988a and Reshef, et al., 1988b, among others). The source formulations are most accurate for energy that propagates horizontally away from the source, partly because the asymptotic solution is most accurate for large range, high frequency, and non-vertical take-off angle (Vidale and Helmberger, 1986), but also because a 2-D grid does not properly simulate 3-D geometrical spreading. We describe herein a source term that

corrects for the improper geometrical spreading at most take-off angles.

We then demonstrate the use of this refinement by calculating finite difference synthetics for the Amchitka Island, Alaska blasts MILROW and CANNIKIN. The LONGSHOT blast is not considered due to the lack of near-field data. These blasts have been studied extensively by other researchers (Lay, Burdick and Helmberger, 1984, Lay, Helmberger and Harkrider, 1984, Burdick, et al., 1984, King, et al., 1974, Perret, 1973 and Toksoz and Kehrer, 1972, among many others). In this research, because the structure and the source time functions have been investigated, these blasts are a good demonstration case.

The blasts are described in detail by Perret (1973). MILROW was detonated October 2, 1969 at a depth of 1219 m. Its yield was approximately 1 Mt. CANNIKIN was detonated November 6, 1971, at a depth of 1791 m with a yield not more than 5 Mt. Both shot points were in pillow lavas beneath a varied sequence of volcanic breccias, basalts and sediments.

These events, because of their size, location and the wealth of data that were released at the time, provided seismologists a unique opportunity to study a broad range of seismological properties of nuclear explosions (Willis, et al., 1972 and Engdahl, 1972, among others). In this chapter, we will be concerned with the near-field seismic records of these blasts. The modeling of these records has been the subject of several other studies, most notably Burdick, et al. (1984) and Lay, Burdick and Helmberger (1984), where the researchers simultaneously model the near-field and teleseismic data. Here, we will take the source parameters and seismic structure from these studies as known, to demonstrate the effects of some modeling procedures made possible using finite difference (FD) wave propagation. We will not address the

close-in records of the Sandia Laboratories experiments (Perret, 1973; Perret and Breding, 1972) because our FD algorithm does not account for the spall observed in those records. We use FD in this research to demonstrate the limitations of one-dimensional (1-D) modeling and to explore the effects that realistic 2-D structures can have when superimposed on a good 1-D model.

2.2 Difference between 2-D and 3-D wave propagation

The equations for 2-D and 3-D wave propagation are similar, but there are important differences. We will examine the acoustic case, although the same arguments hold for the elastic case. In the acoustic case, the 2-D wave equation for homogeneous media is

$$P_{tt} = c^2 (P_{xx} + P_{zz}), \tag{2.1}$$

where P is pressure, c is the wave velocity, x and z are Cartesian coordinates, and subscripts indicate derivatives. The 3-D acoustic wave equation for homogeneous media is

$$P_{tt} = c^2 (P_{xx} + P_{yy} + P_{zz}), \tag{2.2}$$

where y is the third Cartesian coordinate. Cylindrical co-ordinates are also appropriate for wave propagation near a horizontal free surface. In cylindrical coordinates

$$P_{tt} = c^2 (P_{rr} + P_{zz} + \frac{P_r}{r}), \tag{2.3}$$

where r and z are the radial and vertical coordinates, and azimuthal symmetry in the wavefield is assumed. The term that is multiplied by $1/r$ becomes negligible as r becomes large, and in this case the Equations 2.1 and 2.3 are nearly equivalent.

There are several differences between waves propagating according to Equations 2.1 and 2.3. In 2-D, wave amplitude decays with geometrical spreading by $1/\sqrt{R}$, where $R = \sqrt{x^2 + z^2}$, but in 3-D, wave amplitude decays by $1/R$, where $R = \sqrt{r^2 + z^2}$. This difference can be corrected by multiplying the amplitude of seismograms produced with Equation 2.1 by $1/\sqrt{R}$, but this correction is exact only for a homogeneous medium. If the true raypath is strongly bent by velocity gradients, the appropriate R may be difficult to find. If there are several raypaths between the source and receiver, the appropriate R is ambiguous and impossible to find.

In 2-D, an impulsive burst of energy at the source results in an impulsive burst of energy at the receiver followed by a line-source tail which decays as $1/\sqrt{t}$, where t is the time after the first arrival of energy at the receiver. In 3-D, an impulsive burst of energy at the source results solely in an impulsive burst of energy at the receiver. The arrivals with a line-source tail that result from the use of a 2-D numerical grid can be restored to point-source-like impulsiveness by convolution with the time series $H(t)/\sqrt{t}$, followed by differentiation with respect to time. Here $H(t)$ is the Heaviside step function. The seismograms produced are approximately those that would result from a source on the axis of symmetry in a cylindrically symmetric medium.

The corrections above have been suggested in Vidale, et al. (1985) and Vidale and Helmberger (1986), but a further correction has been derived in Stead and Helmberger (1988) to approximate the anisotropy in geometrical spreading necessary to simulate exactly 3-D wave propagation in a 2-D numerical grid. Below, we provide physical insight into this correction.

2.3 Correction factor for explosions in 2-D

We will show that the amount of energy leaving the source region at an angle i with the vertical in the 2-D grid may be approximated by the amount of energy in the point-source case multiplied by $\sqrt{\sin i}$. The additional $\sqrt{\sin i}$ in the point-source or 3-D solution can be explained in terms of geometrical spreading, as is shown in Figure 2.1. The energy between take-off angles i_0 and $i_0 + di_0$ for the point-source becomes

$$E_P = \frac{(2\pi \sin i_0 \, r) \, r \, di_0}{2\pi \, r^2} = \sin i_0 \, di_0 \tag{2.4}$$

while for the line-source

$$E_L = \frac{2\pi \, r \, di_0}{2\pi \, r} = di_0. \tag{2.5}$$

Since energy is proportional to the square of the amplitude, we obtain the $\sqrt{\sin i}$ dependence.

If we use an isotropic explosion as the source in the 2-D model, each arrival in a record may have a different take-off angle i, but we can only correct for a constant $\sqrt{\sin i}$. The result is that the vertically traveling energy is emphasized over horizontally traveling energy in the line-source compared to the point-source case. One might ask why not simply multiply the isotropic source by $\sqrt{\sin i}$? Unfortunately, such a source does not satisfy the 2-D elastic wave equation and will not maintain the $\sqrt{\sin i}$ radiation pattern, once the energy leaves the source region, primarily because the cusp in the $\sqrt{\sin i}$ at $i = 0°$ does not satisfy the 2-D elastic wave equation.

The source functions found to be solutions to the 2-D elastic wave equation have radiation patterns of $\sin^n i \, \cos^m i$, where n and m are free parameters. An isotropic line-source explosion, for example, is the solution with

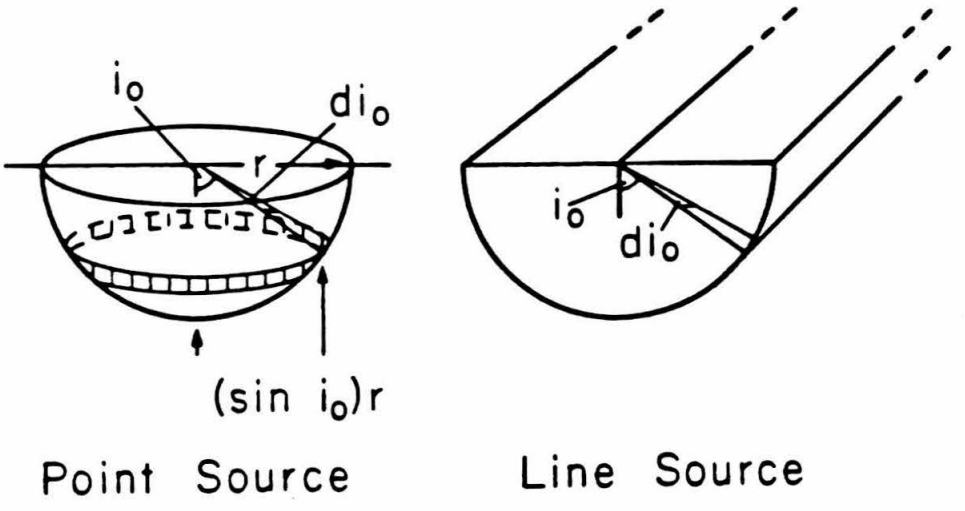

Figure 2.1 Diagrams showing energy with take-off angle i in the range $i_0 < i < i_0 + di$ for both a point-source and line-source geometry. The energy varies as sin i_0 for the point-source case but does not vary as a function of i for the line-source case.

$n = m = 0$, and the dislocation sources have $n + m = 2$ (Vidale and Helmberger, 1986; Helmberger and Vidale, 1988). Also, because of the asymptotic nature of our solutions, the compressional and shear parts of the source separate. The 2-D to 3-D correction we adopt is to add the compressional component of the horizontal force term ($n = 1$ and $m = 0$) to the isotropic explosive source. This term is added so that it decreases the amplitude of energy leaving the source vertically, but leaves unchanged the amplitude of energy leaving the source horizontally.

These two terms can be thought of as the first two terms of a Taylor series expansion of $\sqrt{\sin i}$ about the point $i = 90°$. Higher-order corrections could be added, but we choose not to, for the following reasons. The first two terms alone provide a sufficiently accurate solution, but when n or m is increased by 1, the pseudo-near-field terms in the solution grow more prominent by a factor of t; that is, the asymptotic solution diverges by another factor of t. An isotropic line-source explosion has a constant pseudo-near-field term, which is analogous to an explosion in a 3-D medium, where there may be some permanent deformation near the source. The compressional component of force described below grows with time as t, and slip dislocation sources grow with time as t^2 (see Vidale and Helmberger, 1986). Therefore, while the addition of higher-order terms in the Taylor series would make the source radiation pattern more closely resemble $\sqrt{\sin i}$, it would also add more severe pseudo-near-field terms to the displacement field in the finite difference grid.

The following solutions are for a delta function source in a whole-space (see Stead and Helmberger, 1988). Define

$$T_\alpha = \frac{R^2}{t^2 \alpha^2} \tag{2.6}$$

and

$$\Phi_\alpha = \frac{\sqrt{2}}{\sqrt{\alpha}} \frac{H(t-R/\alpha)}{\sqrt{1-T_\alpha}} \frac{1}{\pi R^2}, \tag{2.7}$$

where α is compressional wave velocity, R is the absolute distance between the source and receiver, and t is time. The analytic whole-space expressions for an isotropic explosion, which may be used as internal boundary conditions surrounding a source in a 2-D numerical grid, are

$$\begin{aligned} Q_E &= r\ \Phi_\alpha \text{ and} \\ W_E &= -z\ \Phi_\alpha , \end{aligned} \tag{2.8}$$

where r is the horizontal component of R, and is positive in the direction of the receiver, and z is the vertical component of R, and is positive downward. Q_E and W_E are the radial and vertical components of displacement.

The expressions for Q_F and W_F for a line-force, which has a sin i radiation pattern are

$$\begin{aligned} Q_F &= \frac{\alpha t}{R^2}\ \Phi_\alpha\ (\ r^2 - z^2 + T_\alpha\ z^2) \text{ and} \\ W_F &= \frac{\alpha t}{R^2}\ \Phi_\alpha\ (-2\ rz\ +\ T_\alpha\ rz)\ . \end{aligned} \tag{2.9}$$

Taken together, allowing for arbitrary combination of the terms using the parameter k_f (force ratio), the result is

$$\begin{Bmatrix} Q \\ W \end{Bmatrix} = \Phi_\alpha \left[(1 - k_f) \begin{Bmatrix} r \\ -z \end{Bmatrix} + k_f\ \frac{\alpha t}{R^2} \begin{Bmatrix} r^2 - z^2 + z^2 T_\alpha \\ (T_\alpha - 2)\ rz \end{Bmatrix} \right] . \tag{2.10}$$

The time function appropriate for an explosion, the RDP, is included by convolution after propagating the source, Q and W, through the FD grid and extracting the response, $\tilde{Q}$ and $\tilde{W}$, at the desired receiver. Thus, the

complete expression for the line-source synthetic is

$$\begin{pmatrix} \mathbf{Q}_l \\ \mathbf{W}_l \end{pmatrix} = -\frac{\partial \Psi(t)}{\partial t} * \begin{pmatrix} \tilde{Q} \\ \tilde{W} \end{pmatrix} * \mathrm{I} * \mathrm{A}, \tag{2.11}$$

where $\Psi(t) = \Psi_\infty(1-e^{-Kt})(1+Kt+...)$, and Ψ_∞ has units of volume. The function I is the instrument response, and the function A is the attenuation operator. This is similar to the moment release expression in Vidale and Helmberger (1986)

$$\begin{pmatrix} \mathbf{Q}_l \\ \mathbf{W}_l \end{pmatrix} = \frac{10^{-10}}{4\pi\rho\alpha^2}\frac{\partial M_0(t)}{\partial t} * \begin{pmatrix} \tilde{Q} \\ \tilde{W} \end{pmatrix} * \mathrm{I} * \mathrm{A}, \tag{2.12}$$

where M_0 is the earthquake moment and ρ is the density.

By judiciously mixing the explosive and force terms (varying k_f), we can modify the vertical radiation pattern of the explosion to better mimic $\sqrt{\sin i}$ in the range we desire. Figure 2.2 shows the radiation patterns that result from using $k_f = 0$, $k_f = 0.5$ and $k_f = 0.6$. These cases are compared with $\sqrt{\sin i}$ and isotropic line-source radiation patterns. Energy that leaves the source at angles near $i = 90°$ is not affected by the correction, but energy at angles near $i = 0°$ is markedly affected. The mix of explosion and line-force expressions determines where in the radiation pattern the source is most accurate. As seen in Figure 2.2, $k_f = 0.5$ is most accurate near $i = 90°$, while $k_f = 0.6$ is less accurate near $i = 90°$, but more accurate near $i = 30°$. It is clear from Figure 2.2 that only energy leaving the source at positive angles may be modeled with this corrected source.

As described in Stead and Helmberger (1988), the line-source seismograms are transformed into point-source seismograms by:

$$\begin{pmatrix} \mathbf{Q}_p \\ \mathbf{W}_p \end{pmatrix} = \frac{2}{\sqrt{R}+\sqrt{r}}\frac{d}{dt}\left(\frac{1}{\sqrt{t}} * \begin{pmatrix} \mathbf{Q}_l \\ \mathbf{W}_l \end{pmatrix} \right) \tag{2.13}$$

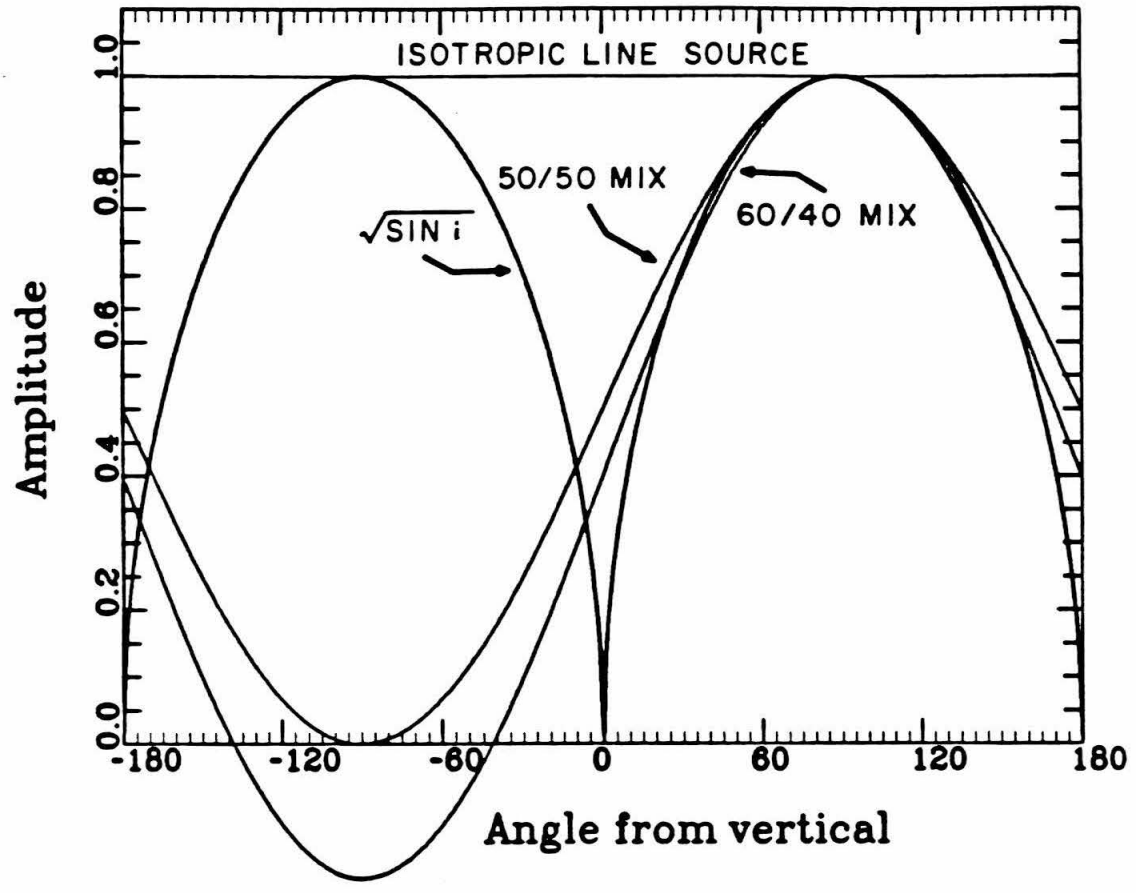

Figure 2.2 Comparison of radiation pattern for corrected and uncorrected line-source explosions. The horizontal line shows the isotropic radiation pattern which results from an uncorrected line-source explosion. The $\sqrt{\sin i}$ curve shows the best radiation pattern to simulate an point-source explosion. The two sinusoidal curves show the result of mixing a line-source force with a line-source explosion with ksubf=0.5 and ksubf=0.6 (50/50 mix and 60/40 mix, respectively). The mixed sources are meant to be accurate in the range i = +20° to +160°.

where $\mathbf{Q_p}$ and $\mathbf{W_p}$ are horizontal and vertical displacements in cm.

This correction factor will change the relative amplitude of arrivals by the $\sqrt{\sin i}$ factor shown in Figure 2.2. The effect of a $k_f = 0.5$ correction for an explosion in a half-space is shown in Figure 2.3. The corrected FD seismograms have Rayleigh waves of larger amplitude relative to the direct compressional waves than do the uncorrected seismograms, and they agree better with the seismograms generated by the Cagnaird method, which is known to be accurate (see Apsel and Luco, 1983, for example). The $\sqrt{\sin i}$ corresponds to $\sqrt{p}$, where the real part of the horizontal slowness p is $p = rt \ / \ R^2$. The correction increases the size of the Rayleigh waves because they have a greater horizontal slowness than the direct compressional waves. The correction becomes more important the more nearly vertically the energy is traveling. In modeling short-period P waves from the Nevada test site, Stead and Helmberger (1988) have found this correction to be crucial.

2.4 Application to explosions on Amchitka

We now use the corrected source to investigate the records of explosions on Amchitka Island, which is among the Rat Islands group of the Aleutian Islands in the Pacific ocean. As discussed above, the models in Burdick, et al. (1984), Lay, Burdick and Helmberger (1984) and Lay, Helmberger and Harkrider (1984) are taken here as the best 1-D approximations. Burdick, et al. (1984) show that the records from the explosion MILROW for the stations shown in Figure 2.4 can be modeled fairly well with a layered structure. The P-wave crustal model in Table 2.1 consists of 8 of the 9 layers derived by Burdick, et al. (1984) by fine-tuning the model proposed by Engdahl (1972).

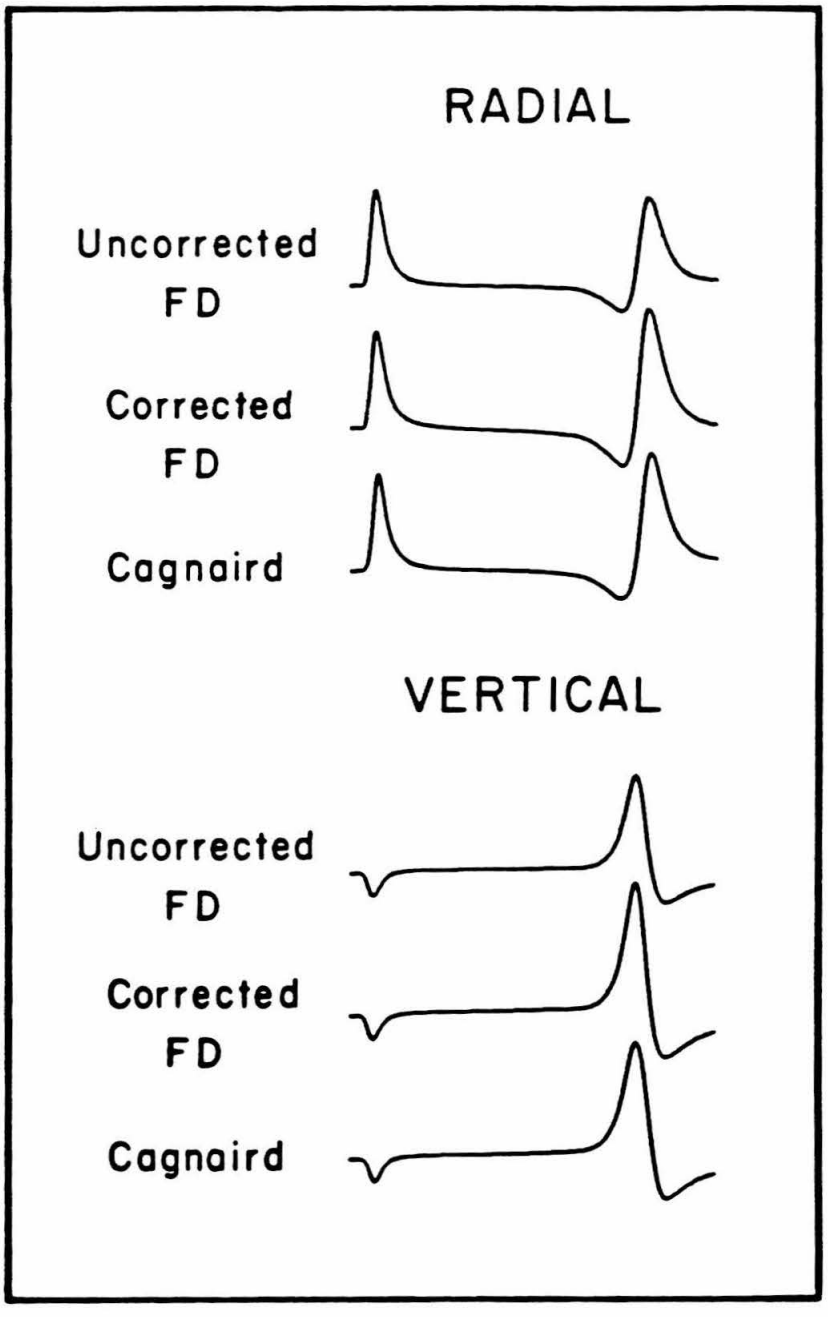

Figure 2.3 Comparison between uncorrected and corrected FD seismograms and analytic Cagnaird seismograms for an explosive point source in a half-space. The receiver is at a range 30 times the source depth to allow for the development of a Rayleigh wave that is large compared to the direct P-wave. The amplitude scale is the same for all the radial and all the vertical traces; but different between the radial and vertical components.

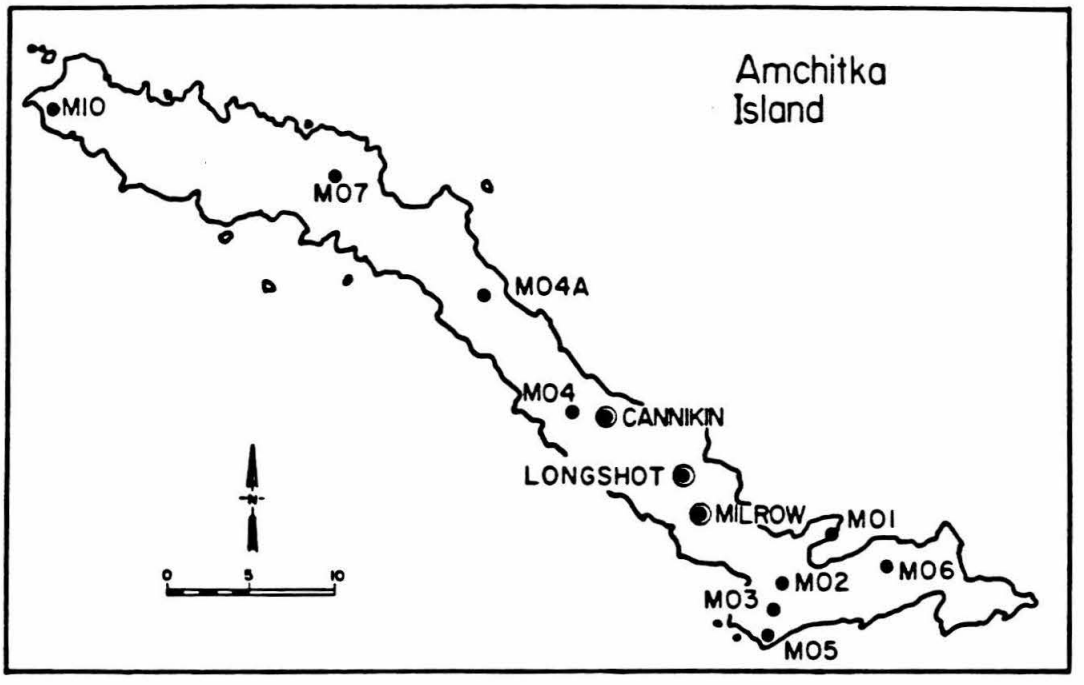

Figure 2.4 Location of the Amchitka nuclear tests and the near-field strong-motion instruments deployed to record them.

Table 2.1. Properties of sharp boundary model

Key	V_p km s^{-1}	V_s km s^{-1}	ρ g cm^{-3}	layer thickness m
A	3.0	1.7	2.5	200
B	3.7	1.9	2.5	650
C	4.2	2.0	2.5	575
D	4.7	2.0	2.5	525
E	4.9	2.1	2.55	600
F	5.35	3.1	2.55	500
G	5.5	3.2	2.6	6950
H	6.9	4.0	2.8	∞

The letters in the Key column are used in Figure 2.10.

This model predicted the observed P-wave travel times well, and the S-wave velocity structure was added in that investigation to model the Rayleigh wave arrivals. A comparison of synthetics generated by various methods including FD for the flat-layered Burdick model is discussed in Vidale and Helmberger (1986). We will be interested primarily in perturbations of this flat-layered structure and the corresponding effects on the resulting waveforms.

Geologic constraints on the structure are obtained from a report by Orphal, et al. (1970), which displays geologic cross sections from the blast to the various stations. Density, shear wave velocity and compressional wave velocity for the Amchitka sites can be obtained from well-log information, Perret (1973) and Perret and Breding (1972). Figures 2.5a through 2.5c show the S-velocity, P-velocity and density profiles chosen as models of the Amchitka structure. These models are tested below to evaluate the relative importance of various features in the available information about Amchitka structure.

The first experiment tests the effect of smoothing the layer boundaries. This is accomplished by specifying a gradient region straddling the original sharp layer boundary (see Table 2.2). The results of these trials are shown in Figure 2.6. In this figure, the synthetics for both the sharp layer boundaries and gradient boundaries are compared at two ranges for the events CANNIKIN and MILROW. The RDP source time function used is that of Helmberger and Hadley (1981),

$$\Psi(t) = \Psi_\infty \left[1 - e^{-Kt} \left(1 + Kt + 0.5(Kt)^2 - B(Kt)^3\right)\right]. \qquad (2.14)$$

The source for MILROW has K=6, B=1 and $\Psi_\infty=10^{11}$, and the source for

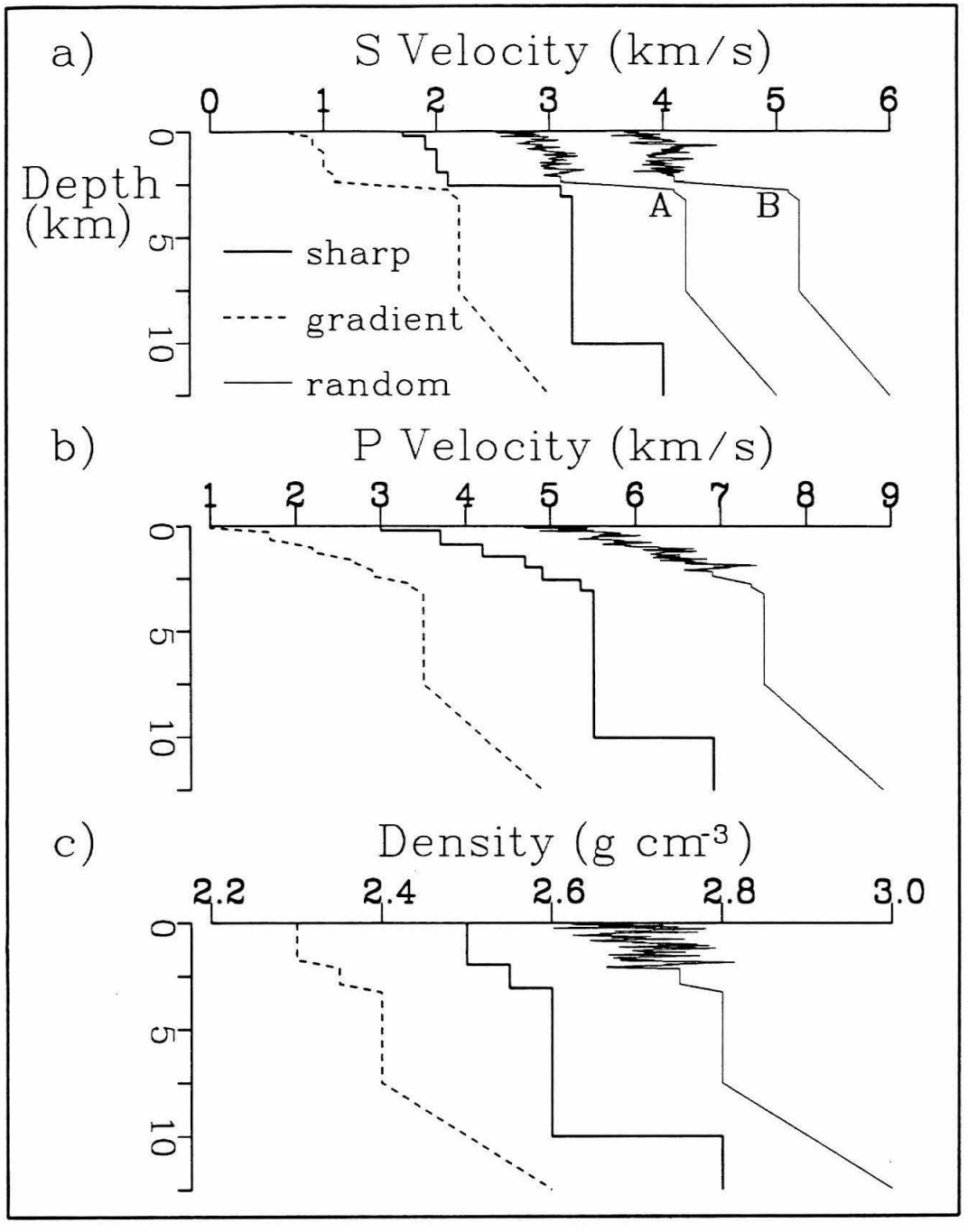

Figure 2.5 **a)** S-velocity profiles used for finite difference simulations. Three cases are shown: flat layers with sharp boundaries (sharp), gradient boundaries (gradient) and random media (random). The profile for sharp boundaries is located correctly along the velocity axis; all other profiles have been shifted 1.0 and 2.0 km/s for clarity. These models are also described in Tables 2.1, 2.2 and 2.3. Two profiles, A and B, are shown for the random media to show the variation horizontally as well as vertically; the two profiles are 12 km apart horizontally. **b)** P-velocity profiles used. The gradient and random media curves have been shifted 2.0 km/s relative to the sharp-boundary profile. **c)** Density profiles used. The curves have been shifted 0.2 g/cm^{-3} relative to the sharp-boundary profile.

Table 2.2. Properties of gradient boundary model

V_p km s^{-1}	V_s km s^{-1}	ρ g cm^{-3}	layer thickness m
3.0	1.7	2.5	100
g*	g	2.5	200
3.7	1.9	2.5	350
g	g	2.5	375
4.2	2.0	2.5	225
g	2.0	2.5	375
4.7	2.0	2.5	125
g	g	g	375
4.9	2.1	2.55	250
g	g	2.55	375
5.35	3.1	2.55	125
g	g	g	375
5.5	3.2	2.6	4250
g	g	g	5000
6.9	4.0	2.8	∞

*g = linear gradient across layer

Table 2.3. Properties of random media model

V_p	V_s	ρ	V_p variance	horizontal aspect	vertical aspect	layer thickness
km s^{-1}	km s^{-1}	g cm^{-3}	km s^{-1}	m	m	km
3.0	1.7	2.5	0.4	125	20	100
3.3	1.8	2.5	0.35	188	30	200
3.7	1.9	2.5	0.3	250	50	350
3.9	1.95	2.5	0.25	250	50	375
4.2	2.0	2.5	0.25	375	50	225
4.4	2.0	2.5	0.25	375	50	375
4.7	2.0	2.5	0.25	500	50	125
4.8	2.05	2.5	0.25	500	50	375
4.9	2.1	2.55				250
g*	g	2.55				375
5.35	3.1	2.55				125
g	g	g				375
5.5	3.2	2.6				4250
g	g	g				5000
6.9	4.0	2.8				∞

*g = linear gradient across layer

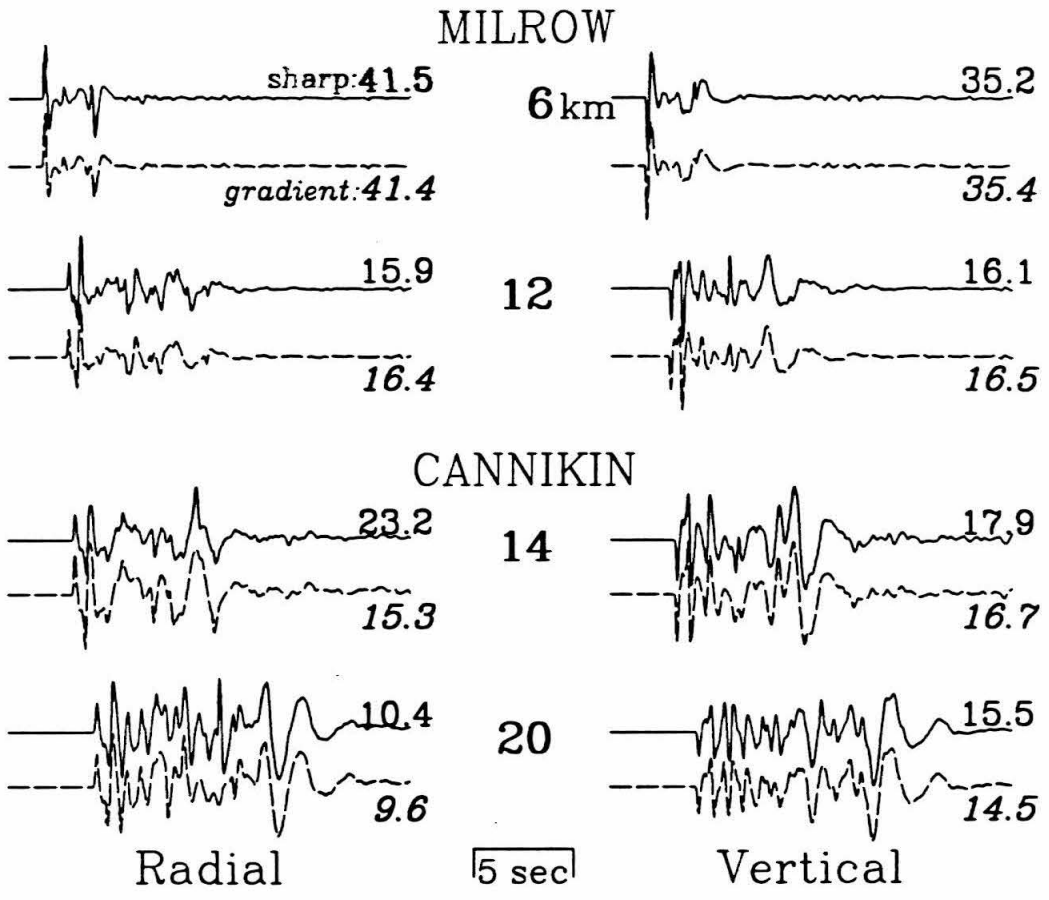

Figure 2.6 Comparison of finite difference simulations for sharp and gradient boundaries. Models are described in Figure 2.5 and Tables 2.1 and 2.2. Depths and RDP sources (H-H) are appropriate for MILROW and CANNIKIN, respectively. Ranges (given in center) are consistent with available data. Amplitudes are in cm/s.

CANNIKIN has K=9, B=0.625 and Ψ_∞=5.69$\times 10^{11}$, both as determined by Lay, Helmberger and Harkrider (1984). The most obvious effect is a change in frequency content. This is to be expected; a gradient zone appears "sharper" to low-frequency energy than to higher-frequency energy. In fact, the gradients used in this case are more effective in turning long-period energy than sharp boundaries, as shown by the larger Rayleigh waves for the CANNIKIN synthetics. Another effect is that individual reflected phases, and multiples in particular, are not large and impulsive in the gradient case. This effect is particularly evident for a phase about 7 seconds after the first arrival on the radial component of the CANNIKIN synthetics at 20 km. The large arrival for the sharp-boundary case is completely unresolved in the gradient synthetic. The apparent slowness, phase behavior and timing are consistent with a wide-angle multiple. One would expect wide-angle reflections and multiples to be affected most strongly by gradational layer boundaries. Several other similar phases exist for both MILROW and CANNIKIN synthetics at various ranges, although normally they are reduced in amplitude by about one-half and resolved for both models. Thus, late multiples can be greatly reduced in amplitude by gradients, while the direct arrivals and refractions near the first arrival are virtually unchanged. This is important to consider since observed seismic boundaries typically have some gradational character even at sharp geologic boundaries.

A second case we examine is the effect of "random" media. Observed seismic structure usually is not constant or smoothly varying with depth on scales as small as 100 meters. The media parameters are observed to fluctuate about some smoother large-scale structure. This is evident in the velocity and density logs taken from the instrument holes on Amchitka Island

(Figures 2.7a and 2.7b, adapted from Perret and Breding, 1972 and Perret, 1973). These structures correlate with the geology and are likely to be larger horizontally than vertically. To investigate the effect of such variations we add randomness to the upper layers of the gradient model discussed above (see Table 2.3). The gradient model is used as a base to avoid large, perhaps unrealistic variations in the synthetics resulting from caustics in the sharp-boundary case. The variances are larger (in percent) for the shallowest layers to allow for some effect of pressure in reducing the amplitude of variations. The randomness in the model is not as strongly varying as the observed well-log data, but is a filtered version to demonstrate the effect without requiring too fine a grid spacing for the FD model. We also permit the horizontal and vertical aspects to differ, for the reasons stated above. The aspects are essentially the mean anomaly radii in each dimension. The results are shown in Figure 2.8, compared to the gradient case. As expected, the random media scatter high-frequency energy far back into the coda; it is even seen following the arrival of the Rayleigh wave. The scattering completely obscures later multiples in the record. This has interesting implications for one-dimensional (1-D) models. Fundamentally, it means that crustal multiples from sources less than 2 km deep may not be well-behaved and should not be used to constrain 1-D velocity models. Perhaps late pulses in the near-field should not be modeled; this would be additional justification for the approach of Burdick, et al. (1984), where just the first few arrivals and the surface wave are modeled. The information contained in such coda could determine statistical properties of the medium, but little more.

The effect of site material is investigated in Figure 2.9. Site properties often vary among stations because of the erosion of fault or fold geometries

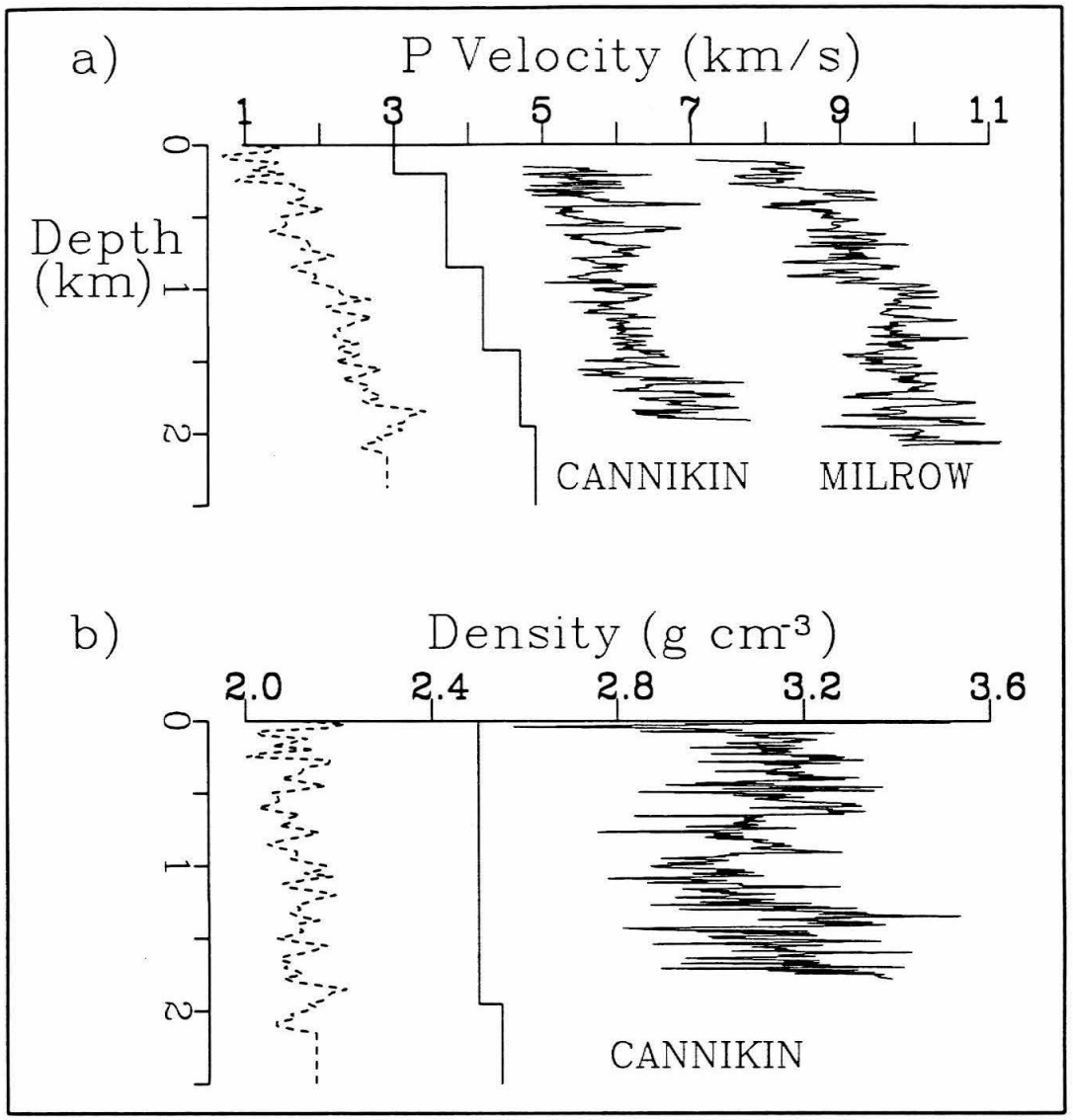

Figure 2.7 **a)** P-velocity profiles showing well-log data from Perret and Breding (1972), and Perret (1973). The heavy solid line is the sharp-boundary model and is correctly located in velocity. The dashed line is the random model used for the simulation, shifted 2.0 km/s. The light lines are the observed profiles for CANNIKIN and MILROW, shifted 2.0 and 5.0 km/s, respectively. **b)** Corresponding density profiles. Dashed line and light line are shifted 0.4 and 0.75 g/cm^{-3}, respectively. Only CANNIKIN density log is available.

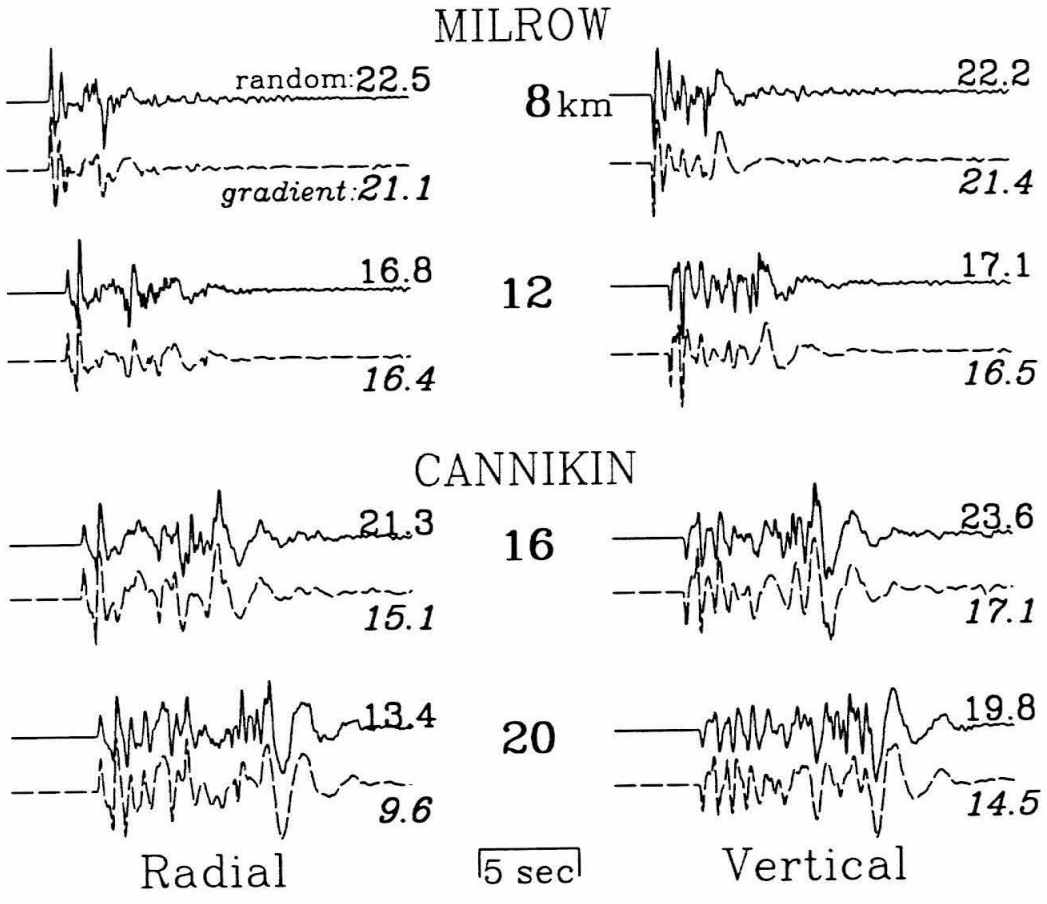

Figure 2.8 Comparison of finite difference simulations for random and gradient models. Models are described in Figure 2.5 and Tables 2.2 and 2.3. Depths and RDP sources (H-H) are appropriate for MILROW and CANNIKIN, respectively. Ranges (given in center) are consistent with available data. Amplitudes are in cm/s.

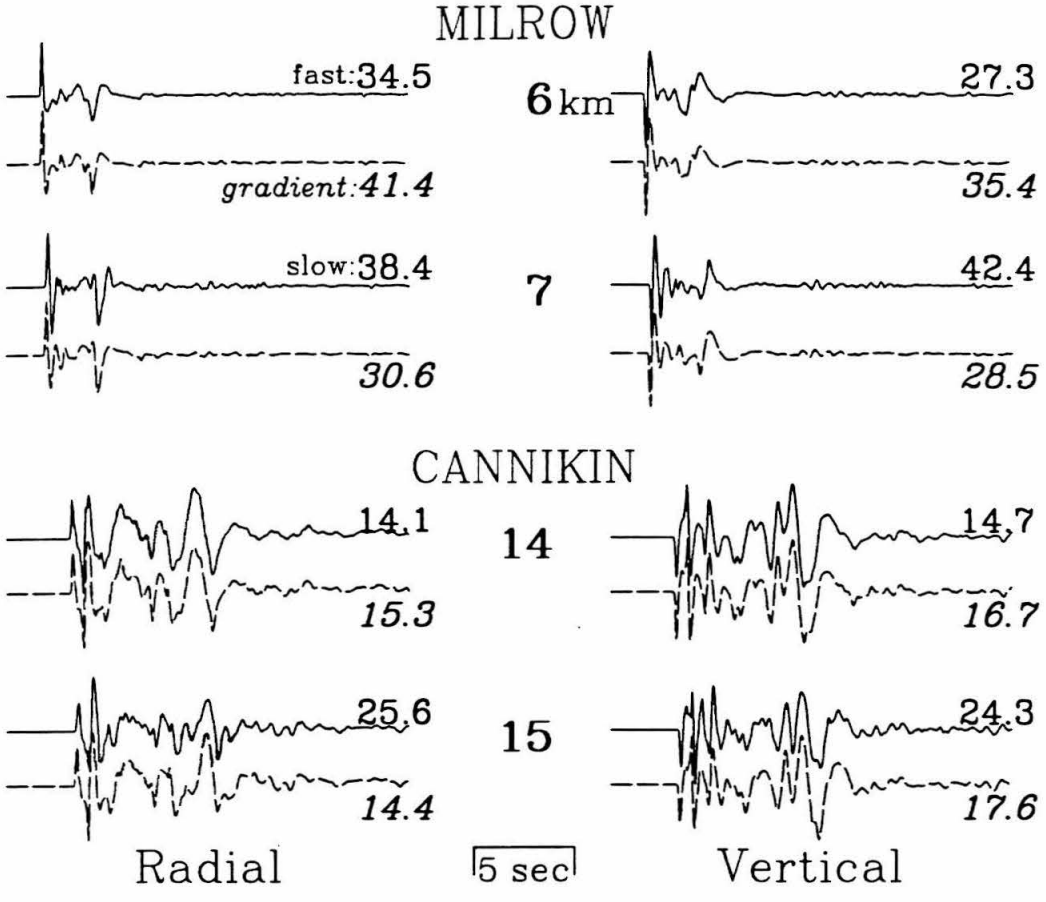

Figure 2.9 Comparison of finite difference simulations for fast and slow sites on the gradient model, and the original gradient model. See text for description of fast and slow sites. Depths and RDP sources (H-H) are appropriate for MILROW and CANNIKIN, respectively. Ranges (given in center) are consistent with available data. Amplitudes are in cm/s.

or the existence of basins, ridges and other structures. Here, we surround one station with a fast (hard) material lens 1 km in diameter, and the next station out with a slow (soft) lens, also 1 km in diameter. Both lenses are tapered somewhat with depth to mimic the generic forms for the corresponding geologic structures. That is, the fast lens is wider at its base, and the slow lens is wider at the top. The slow material has compressional wave velocity $\alpha = 2.0$ km s^{-1}, shear wave velocity $\beta = 1.13$ km s^{-1}, and density $\rho = 2.3$ g cm^{-3}, the fast material has $\alpha = 4.5$ km s^{-1}, $\beta = 2.55$ km s^{-1}, and $\rho = 2.7$ g cm^{-3}, and the top of the rest of the layer, which is 200 meters thick, has $\alpha = 3.0$ km s^{-1}, $\beta = 1.7$ km s^{-1}, and $\rho = 2.5$ g cm^{-3}. The remaining layers are the same as those listed in Table 2.2.

For both CANNIKIN and MILROW the amplitude at the receiver on the slow site is a factor of 1.5 larger than at the receiver in the same position in the plane-layered model. A simple conservation of energy argument, ignoring the transmission coefficient into the slow layer, would predict an amplification of $(v_2 \sqrt{\rho_2})/(v_1 \sqrt{\rho_1}) = 1.6$, where v is velocity and ρ is density, subscript 1 refers to the slow medium and subscript 2 refers to the top layer of the plane-layered model. When the transmission loss on entering the slow material is considered, the observed amplification factor agrees with the simple prediction. Another effect is that the particle motion for MILROW at the slow site (receiver at 7 km) is more vertical than that for the laterally homogeneous case. This is due to the greater refraction of the ray, which is due in turn to the greater velocity contrast. Small reverberations and conversions in the slow media may be seen 1 to 2 seconds after the initial pulse. At 15 km for CANNIKIN, the Rayleigh wave is not amplified as much as the initial P-wave. This is most likely due to the relative frequency

content of the waves; the Rayleigh wave (2-second period) samples a range of depths much greater than 200 meters and is therefore less affected by the contrast. At the station on the faster material, the amplitude is smaller by a factor of 1.2 versus the simple prediction of 1.5, not corrected for transmission. Thus, the simple prediction does not work well. Other factors, such as focusing, diffraction, and the free-surface interaction may be important. The direct waves and longer-period surface waves are unchanged at the ranges of 10 and 12 km (which are beyond the local station structures), although small, scattered shorter-period phases do enter the records.

The structure between the blast and station M05 (Figure 2.10) is approximated from Orphal, et al. (1970). The velocity model below the source is the same as in the sharp-boundary model, and the synthetics are compared to those of the sharp-boundary case in Figure 2.11. This result is similar to the result of the previous case in that the waveforms are quite sensitive to the structure where the rays bottom. The amplitudes differ by up to 50%. About 30% more amplitude, which translates to 70% more energy, is converted into the surface wave by the structures dipping down away from the source. This tendency of dipping layers to convert body waves to surface waves is examined in more detail in Vidale, et al. (1985). Conversely, we note here that layers dipping the opposite direction convert surface waves to body waves (Stead and Helmberger, 1988).

Shallow structure is seen to affect the amplitude of body waves as well as surface waves. These effects are difficult to model deterministically because the structures are poorly known. Derivation of a relatively detailed, flat-layered model with sharp boundaries using ray techniques may help us to understand the wave propagation involved, but should not be taken to

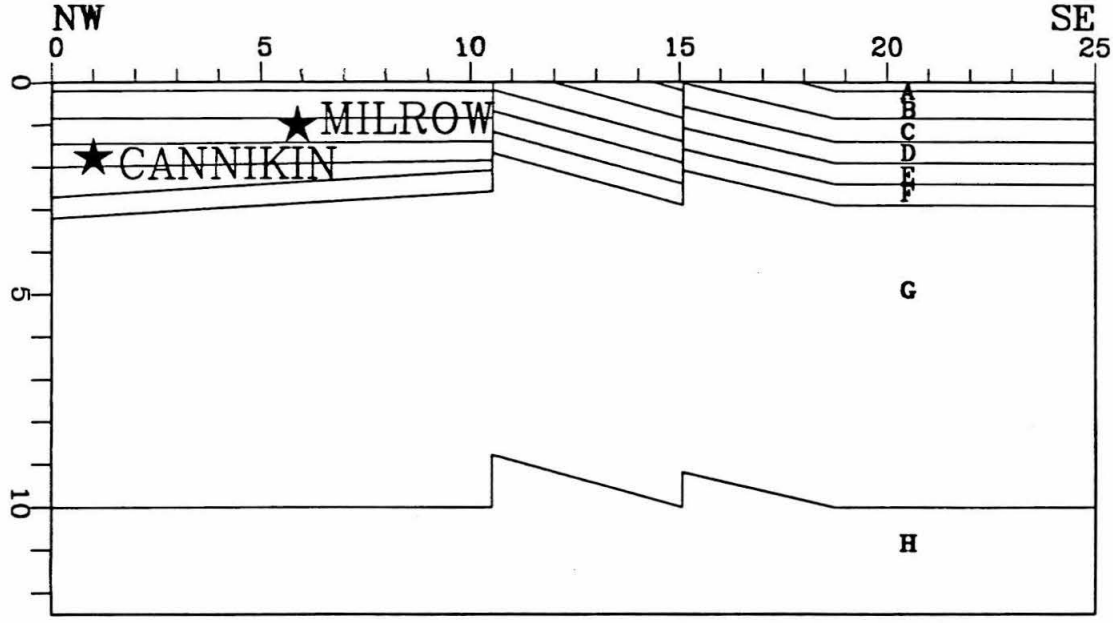

Figure 2.10 Diagram of the faulted model. The distances are in km. The fault locations and offsets are taken from Orphal, et al. (1971), for the MILROW - M05 cross section. The base model is the sharp-boundary model described in Figure 2.5 and Table 2.1, and the letters are keyed to Table 2.1. The vertical fault offsets are added to the sharp-boundary model. The dip of the layers in the region of the sources incorporates the finding of Burdick, et al. (1984) that the structure above the sources is slightly different for CANNIKIN and MILROW.

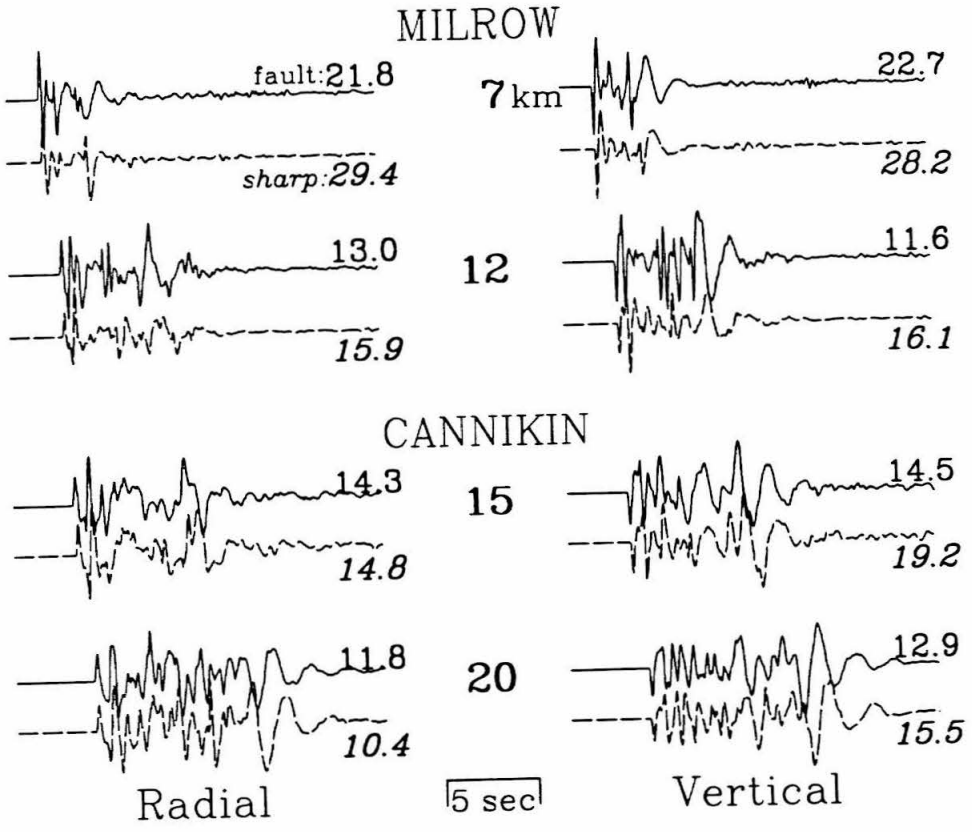

Figure 2.11 Comparison of finite difference simulations for faulted and sharp-boundary models. The sharp-boundary model is described in Figure 2.5 and Table 2.1. The faulted model is described in Figure 2.10. Depths and RDP sources (H-H) are appropriate for MILROW and CANNIKIN, respectively. Ranges (given in center) are consistent with available data. Amplitudes are in cm/s.

represent the detailed structure of the earth. Unknown shallow structure may contribute to the misfit between the synthetic seismograms and the data to be examined below.

2.5 Comparison of various structure models and data

Now we compare the synthetics for the various cases described above to the available near-field data. The purpose is to show which of the various structures result in the best fit to the data. Because the geologic structure and source functions are well-known, The criteria for a good fit are strict. Ideally, the absolute time, absolute amplitude and the waveform of each phase in the data would be identical to those in the synthetics. Here, absolute timing is important, but the amplitude of each phase is not as important. This is because of variations in the site response. We choose four stations, two for each event, as representative of the available data. For MILROW these stations are M01 and M06, at 8.0 and 11.5 km, respectively. For CANNIKIN, we choose M05 and M06 at 15.8 and 18.7 km, respectively.

Figure 2.12 shows a comparison of the radial and vertical records from station M01 for MILROW. These data are compared to the synthetic response at 8 km for four of the above models: the gradient boundaries, the sharp boundaries, the faulted geometry and the random media. The first arrival is well-modeled by both the sharp-boundary and gradient-boundary cases. This is not surprising, since Burdick, et al. (1984) fine-tuned the sharp-boundary model to the data. But the longer-period part of the signal, which includes the Rayleigh wave, is best modeled by the faulted geometry. This station is not far from the faults represented in Figure 2.10, so the effects of the faults and tilted layers are resolved in this case. In Figure 2.13,

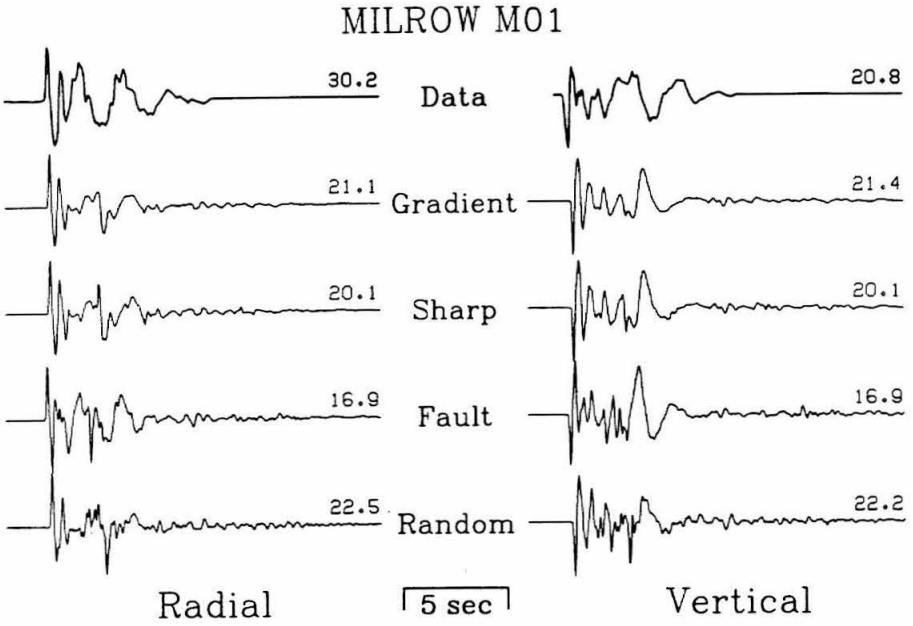

Figure 2.12 Comparison of data to four of the models previously described (Figures 2.6, 2.8, 2.9 and 2.11). Data are for station M01 for MILROW, at a range of 8.0 km. The synthetics are all at a range of 8.0 km. Amplitudes are in cm/s.

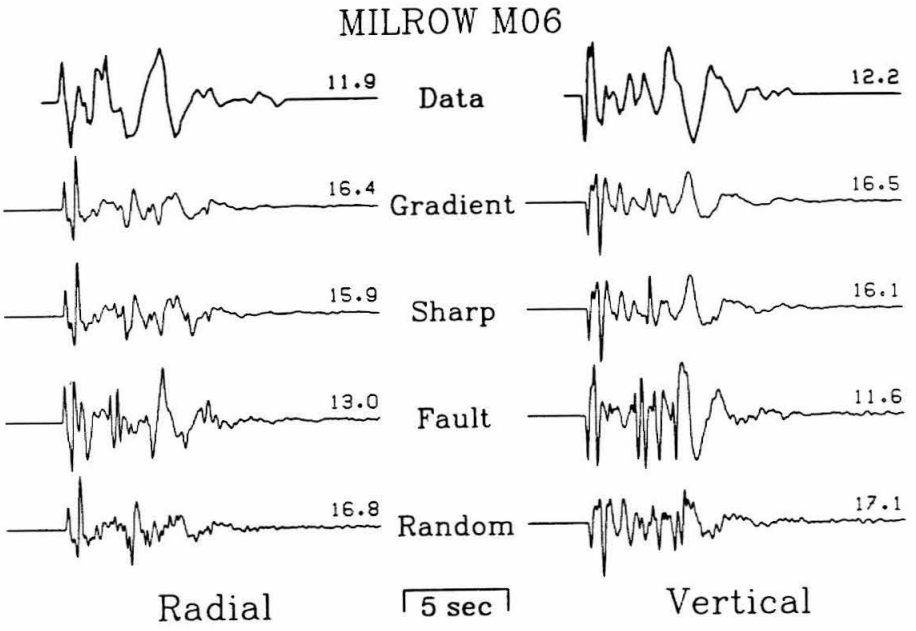

Figure 2.13 Comparison of data to four of the models previously described (Figures 2.6, 2.8, 2.9 and 2.11). Data are for station M06 for MILROW, at a range of 11.5 km. The synthetics are all at a range of 12.0 km. Amplitudes are in cm/s.

the station M06 for MILROW shows the same result; the faulted model most accurately models the data.

The CANNIKIN station M05 is compared to the synthetics in Figure 2.14. Here, the gradient model is the best fitting, according to the relative amplitude of the Rayleigh wave and its waveform. From this we infer that the effect of the faults on the larger, longer-period and more distant source CANNIKIN is not as strong as that for MILROW. In addition, the effects of sharp boundaries are clearly not present in the data. Some filtering appears necessary for the other three cases; perhaps crustal Q is important and would reduce some of the higher frequencies in the coda. Station M06 for CANNIKIN shows the same result (Figure 2.15).

2.6 Comparison of various bomb sources and data

In this section we will show that for the data we are using, structure has more effect in determining the amplitudes and shaping the waveforms than the type of RDP used. Several RDP functions have been proposed, but in this section we will show that no one source model significantly outperforms the others for the near-field body and surface waves for the explosion MILROW and CANNIKIN. The source of Helmberger and Hadley (1981) (H-H) was described above, but the sources of von Seggern and Blandford (1972) (VS-B) and Meuller and Murphy (1971) (M-M) are also frequently used in the study of explosions.

Von Seggern and Blandford (1972) postulate a source given by

$$\Psi(t) = \Psi_\infty \left[1 - e^{-K' t} \left(1 + K' t - B' (K' t)^2\right) \right] \qquad (2.15)$$

where Ψ_∞ is the source strength, and K' and B' are corner frequency and overshoot parameters similar to K and B in the H-H source.

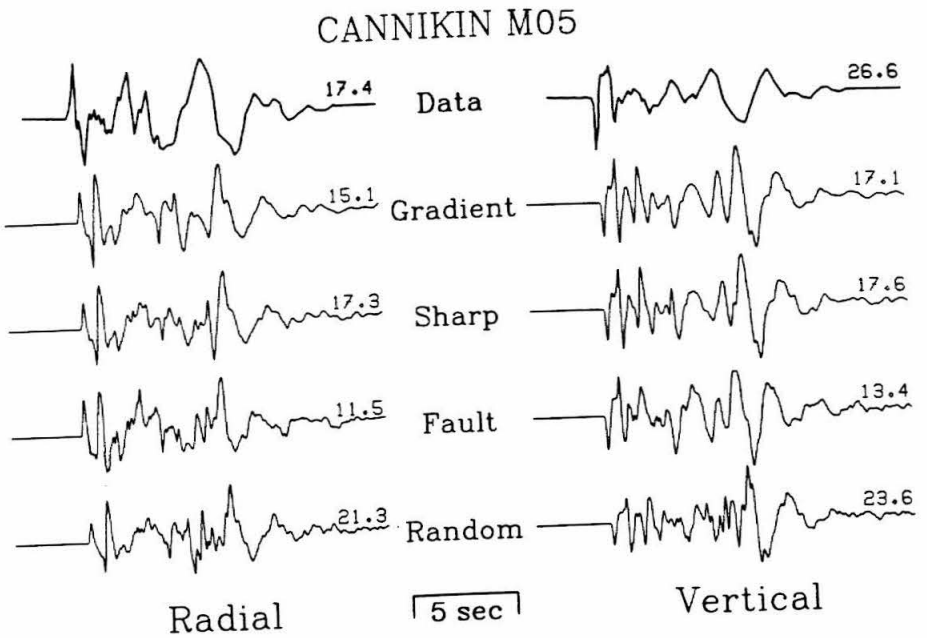

Figure 2.14 Comparison of data to four of the models previously described (Figures 2.6, 2.8, 2.9 and 2.11). Data are for station M05 for CANNIKIN, at a range of 15.8 km. The synthetics are all at a range of 16.0 km. Amplitudes are in cm/s.

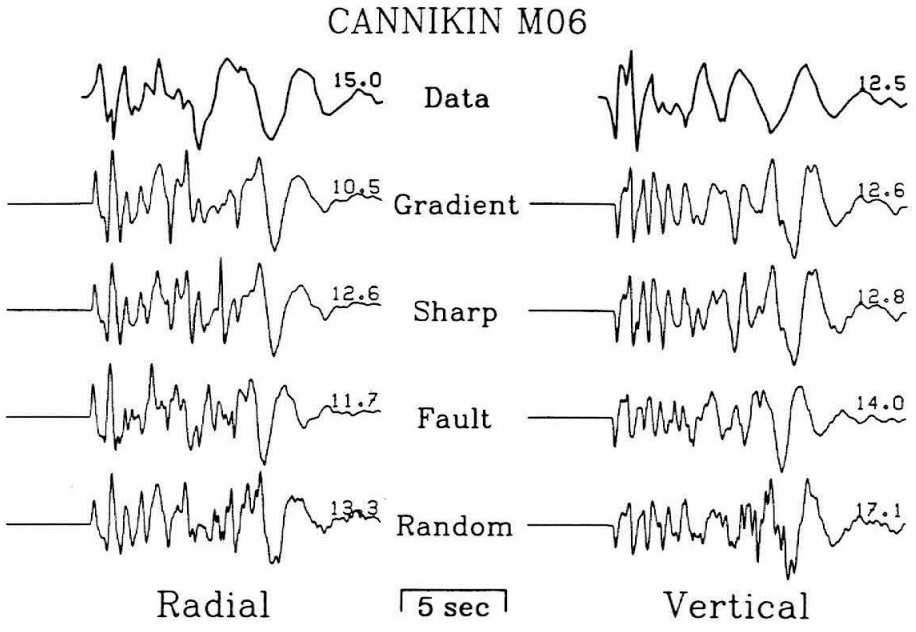

Figure 2.15 Comparison of data to four of the models previously described (Figures 2.6, 2.8, 2.9 and 2.11). Data are for station M06 for CANNIKIN, at a range of 18.7 km. The synthetics are all at a range of 19.0 km. Amplitudes are in cm/s.

Meuller and Murphy (1971) postulate a source most easily expressed as a convolution (Barker, et al., 1985):

$$\Psi(t) = \frac{r_{el}\ V_p^{\,2}}{4\ \mu}\ P(t)\ *\ F(t) \tag{2.16}$$

where the $*$ indicates convolution and $P(t)$ and $F(t)$ are as follows:

$$P(t) = \left[\ (P_{0S} - P_{0C})\ e^{-\alpha t} + P_{0C}\ \right]\ H(t) \tag{2.17}$$

and

$$F(t) = \frac{sin\,(bt)\ e^{\,at}}{\beta b}. \tag{2.18}$$

Furthermore,

$$\text{dynamic cavity pressure}\quad P_{0C} = \frac{4}{3}\ C_3\ \mu\ \left(\frac{r_c}{r_{el}}\right)^3 \tag{2.19}$$

$$\text{static cavity pressure}\quad P_{0S} = 1.5\ \rho\ g\ h \tag{2.20}$$

$$\text{elastic radius}\quad r_{el} = C_1\ \frac{Y^{0.33}}{(h\ /100)^{0.42}} \tag{2.21}$$

$$\text{cavity radius}\quad r_c = C_2\ \frac{Y^{0.29}}{(h\ /100)^{0.11}} \tag{2.22}$$

and

$$\alpha = C_4\ \omega_0 = \frac{C_4\ r_{el}}{V_p} \tag{2.23}$$

$$\beta = \frac{\lambda + 2\mu}{4\mu} \tag{2.24}$$

$$a = \frac{-\omega_0}{2\beta} \tag{2.25}$$

$$b = \frac{\omega_0}{\beta}(\beta - 0.25)^{0.5}. \tag{2.26}$$

The constants C_1 through C_4 are calibration constants dependent on the source medium and defined as follows:

$$C_1 = 200{,}000\left(\frac{A}{\rho A_{cal}}\right)^{\frac{1}{2.4}} \tag{2.27}$$

$$C_2 = 1630\ E^{0.62}\ \mu^{-0.24}\ \rho^{-0.67} \tag{2.28}$$

$$C_3 = \text{compaction factor (hard rock 1.0, tuff 0.6)} \tag{2.29}$$

$$C_4 = \text{proportionality factor (tuff 1.5, rhyolite 2.0).} \tag{2.30}$$

The amplitude calibration, A/A_{cal}, is determined using calibration events (e.g., 2.8 for salt, 2.0 for shale and 0.25 for tuff). For the other values in the equations, Y is the yield in kilotons, h is the source depth, ρ is the density, V_p is the compressional wave velocity, E is Young's modulus, and λ and μ are Lame's constants. All parameters except the yield are in cgs units. The convolution in Equation 2.16 is analytic, resulting in the following expression for the source:

$$\Psi(t) = \frac{r_{el}}{\rho b}\left\{\frac{P_0}{(a+\alpha)^2+b^2}\left[(a+\alpha)e^{at}\sin(bt) - be^{at}\cos(bt) + be^{-\alpha t}\right]\right.$$

$$\left. + \frac{P_{0C}}{a^2+b^2}\left[ae^{at}\sin(bt) - be^{at}\cos(bt) + b\right]\right\}. \tag{2.31}$$

Although the expression of Equation 2.16 is simpler, this expression is often more convenient in practice.

The three RDP representations are compared in Figure 2.16. The far-field displacement time functions for the three sources are shown at the top. There is little difference between the three traces. The RDP functions are plotted next, and the level of the permanent offset, Ψ_∞, is 1.4 x 10^{11} for the H-H and vS-B sources and 2.4 x 10^{11} for the M-M source. At the bottom are

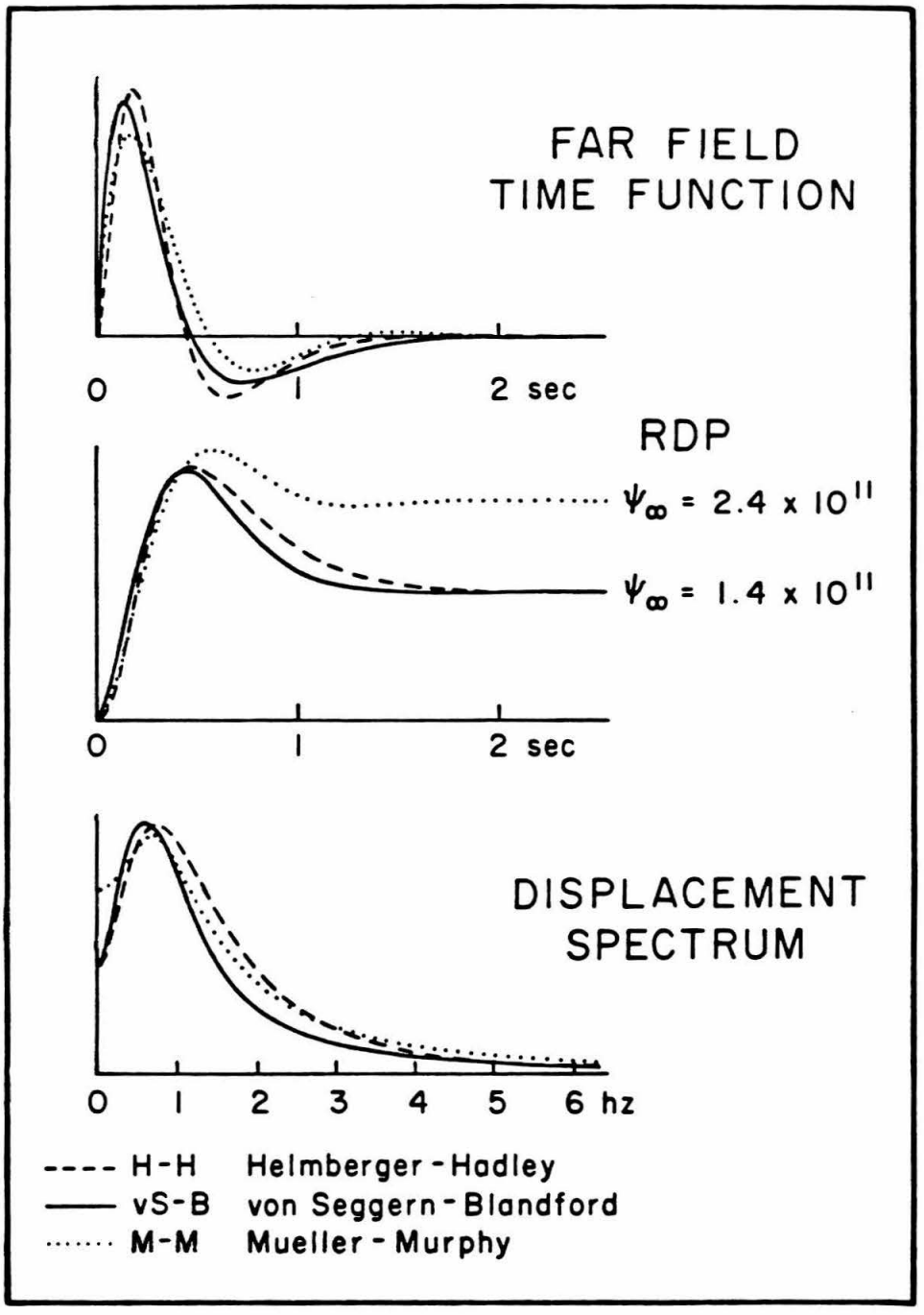

Figure 2.16 Comparisons of the Helmberger-Hadley, Meuller-Murphy, and von Seggern-Blandford RDP functions. The top graph shows the time derivative of the RDP, which is the far-field displacement time function for the 3 sources. The next graph shows the RDP's of the 3 sources. The long-period asymptote of the RDP is the Ψ_∞ of the source. The bottom graph shows the amplitude spectra of the far-field displacement time functions for the 3 sources. The parameters used for these RDP functions are listed in Table 2.4.

Table 2.4. RDP parameters

Helmberger and Hadley (1981) source

$K = 8.0\ s^{-1}$
$B = 1.0$
$\Psi_\infty = 1.4 \times 10^{11}$

von Seggern and Blandford (1972) source

$K' = 5.2\ s^{-1}$
$B' = 2.5$
$\Psi_\infty = 1.4 \times 10^{11}$

Meuller and Murphy (1971) source

Yield = 1000 Kt
h = 1200 m
$V_p = 3.4$ km/sec
$V_s = 1.7$ km/sec
$\rho = 2.1\ g/cm^3$

the spectra of the displacement time histories. The spectra are similar except that the M-M source has a higher long-period level.

The data are compared to FD seismograms computed for the M-M, vS-B, and H-H sources in Figures 2.17 and 2.18. The various source time functions are convolved with the FD impulse responses to form the seismograms in these figures. The parameters used for the three sources are given in Table 2.5. Those for the M-M source are determined by local structure, source depth and source size. The parameters for the other two sources are determined from teleseismic body and surface waves by Lay, Helmberger and Harkrider (1984).

Figure 2.17 shows the comparison for MILROW at station M01. Here, the vertical amplitudes are all within 5% of those for the data, but the fit to the radial component is not as good, primarily in terms of amplitude. There is little difference between the three RDP sources. This observation agrees with the spectra in Figure 2.16, where there is little difference between the different sources. Figure 2.18 shows the comparison for CANNIKIN at station M05. The amplitudes of the RDP seismograms are within 35% of those of the data in all cases, and within 20% in every case but one. Here, there appears to be a slight preference for the M-M formulation.

The fit to the data is good considering waveform, timing and amplitude, but the differences between the synthetics for the various sources are less than the difference between the data and any of the synthetics. The differences between the data and the synthetics are of the same order as the differences between the synthetics for different plausible structures. In this case, tilting layers that can trap more energy and local receiver effects that amplify or diminish body-wave arrivals are at least as important as

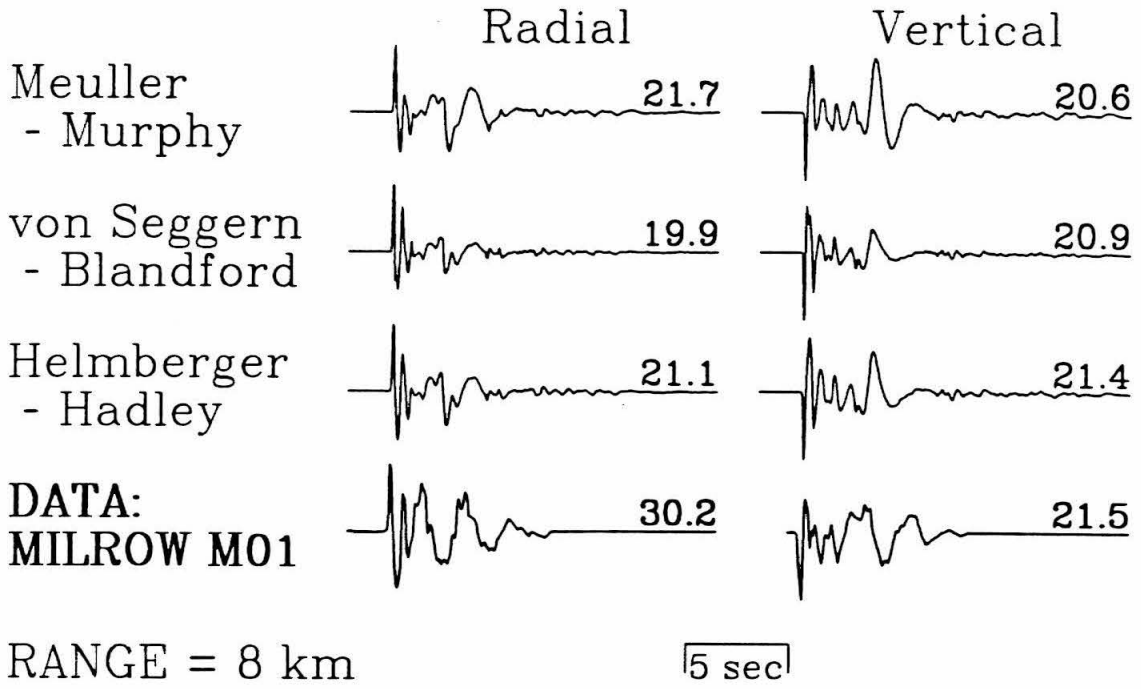

Figure 2.17 Comparison of the Meuller-Murphy, von Seggern-Blandford and Helmberger-Hadley RDP functions used with the gradient boundary model (Table 2.2). Amplitudes are in cm/s. The parameters used in the RDP functions are listed in Table 2.5.

Table 2.5. RDP parameters

Factor	MILROW	CANNIKIN
	Helmberger and Hadley (1981) source	
K (s^{-1})	9.0	6.0
B	1.0	0.625
Ψ_∞ (cm^3)	1.0×10^{11}	5.69×10^{11}
	von Seggern and Blandford (1972) source	
K′ (s^{-1})	9.0	6.0
B′	1.0	0.625
Ψ_∞ (cm^3)	1.0×10^{11}	5.69×10^{11}
	Meuller and Murphy (1971) source	
Yield (Kt)	1000	5000
h (m)	1125	1725
V_p (km s^{-1})	4.2	4.7
V_s (km s^{-1})	2.0	2.0
ρ (g cm^{-3})	2.5	2.5
A/A_{cal}	2.0	2.0
Comp. factor	0.8	0.8
Prop. factor	2.0	2.0

See text for detailed explanation of factors.

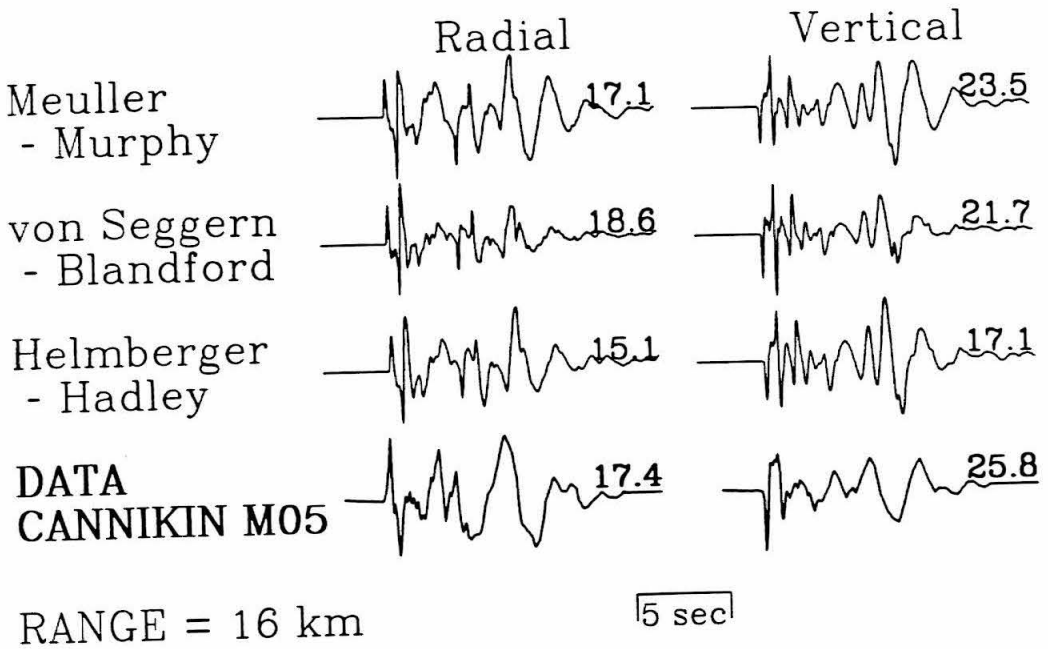

Figure 2.18 Comparison of the Meuller-Murphy, von Seggern-Blandford and Helmberger-Hadley RDP functions used with the gradient boundary model (Table 2.2). Amplitudes are in cm/s. The parameters used in the RDP functions are listed in Table 2.5.

differences in the type of RDP. Details of the structure must be better determined before details of the source time function can be resolved in the near field.

A final variation on the bomb source is the inclusion of possible source asymmetry. The motivation for investigating this effect is large variations in the ratio of first-arrival amplitude to Rayleigh-wave amplitude seen in the data, but not accurately modeled by the various approaches discussed above. Physical conditions that would lead to the formation of asymmetrical cavities are readily postulated, for example, bedding plane control or rapid vertical changes in material strength. The inclusion of asymmetry is accomplished through modification of the radiation pattern, similar to the implementation of the correction discussed above. The correction for an ellipsoidal cavity requires the introduction of S-wave radiation at the source. Figure 2.19 is the basis for the development of the correction: The correction is quadrupole-like, and for ellipsoidal cavities with a principal axis oriented vertically, this quadrupole should be well-approximated by a 45° dip-slip double-couple. We say quadrupole-like because in 3-D the pattern is radially symmetric, yet this is ideal for 2-D simulations. Double-couple sources are derived and discussed in Helmberger and Vidale (1988). When scaled for RDP instead of moment, the double-couple may be added linearly to the explosion result to produce the response from any ellipsoidal cavity in a radially symmetric medium, cavities ranging from pancakes to pencils. The explosion result should already include its correction, with k_f set for the appropriate take-off angles.

The linear combination of the two sources to provide a range of cavities from pancake to pencil may be expressed as Explosion + e $\times$ Double-Couple,

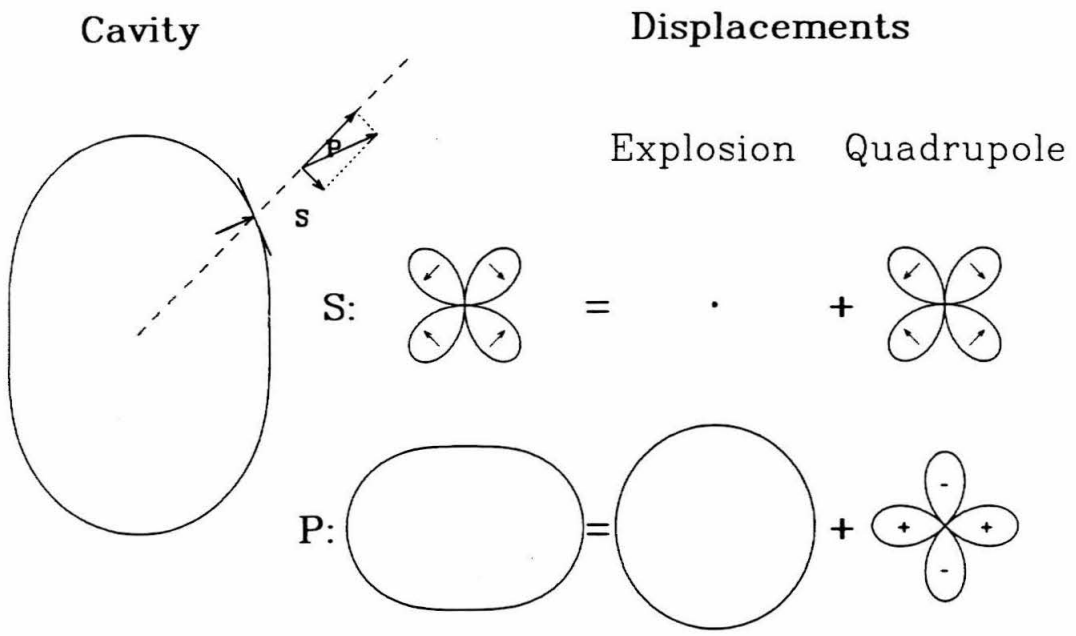

Figure 2.19 Development of a quadrupole correction for cavity asphericity. Cavity on left is ellipsoidal, with the long axis vertical. The arrow on the inside of the cavity represents the pressure acting on the cavity wall. This pressure will radiate both P- and S-wave energy, as partitioned along and normal to the propagation direction. The resultant radiation patterns are shown immediately to the right of the cavity. The P-wave pattern is elongate horizontally, because the increased radius of cavity curvature will amplify the P-wave energy, while decreased radius of curvature will diminish it. This result is further partitioned into an explosion and a quadrupole. The size of the explosion should be that for a spherical cavity of the same net volume as the ellipsoidal cavity. The quadrupole is added to this in varying amounts, depending on the amount of asphericity.

where -1 < e < 1. Note that for the pencil case (prolate), we expect a smaller teleseismic P-wave, whereas the pancake shape (oblate) enhances the P-wave. At near-regional distances the P-waves are affected less, but the surface waves are strongly affected as displayed in Figures 2.20 and 2.21. The *e* factor is set at 0.4 in these two figures for demonstration. Rayleigh waves are relatively enhanced for the prolate case. MILROW observations favor the spherical explosion with perhaps a small prolate correction for some of the stations (e.g., M04). The CANNIKIN observations strongly support a prolate correction with respect to the surface-wave development. However, the estimates are crude, taking into account the fact that the correction postulated here for ellipsoidal cavities is completely ad hoc; it has not been rigorously derived with attention to frequency dependence, coupling, anelastic material behavior, etc. Nevertheless, we believe this correction is a good first-order approach to the asphericity problem and note that because of its quadrupole nature, it may be necessary to consider when estimating tectonic release.

2.7 Conclusions

The use of two-dimensional finite difference algorithms to understand acoustic and elastic wave propagation is a powerful tool. The additional term described in this chapter to correct for the difference between two- and three-dimensional geometrical spreading significantly improves the accuracy of these numerical solutions.

Shallow station structure and lateral velocity variations have considerable effect on the synthetic records computed for the Amchitka blast MILROW. The velocity structure is shown to be at least as important as the

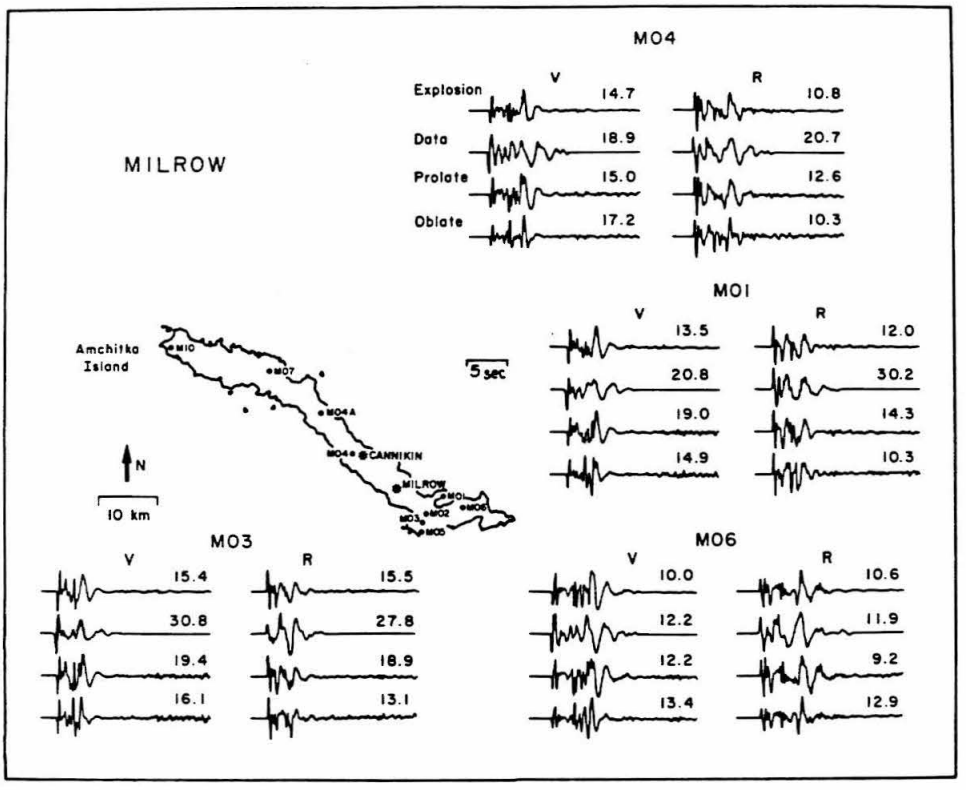

Figure 2.20 Comparison of synthetics for a spherical and aspherical cavity explosions (labeled Explosion, Prolate and Oblate) to data from MILROW. The prolate and oblate cavity synthetics are made with a quadrupole correction for asphericity, both fixed at a 40% contribution. Synthetics for all sources are scaled equivalently. Amplitudes are in cm/s. Both radial (R) and vertical (V) components are shown. The synthetics have been filtered with a $T* = 0.05$ operator and detrended to remove an exponential with time artifact of the higher-order terms of the asymptotic source expansion.

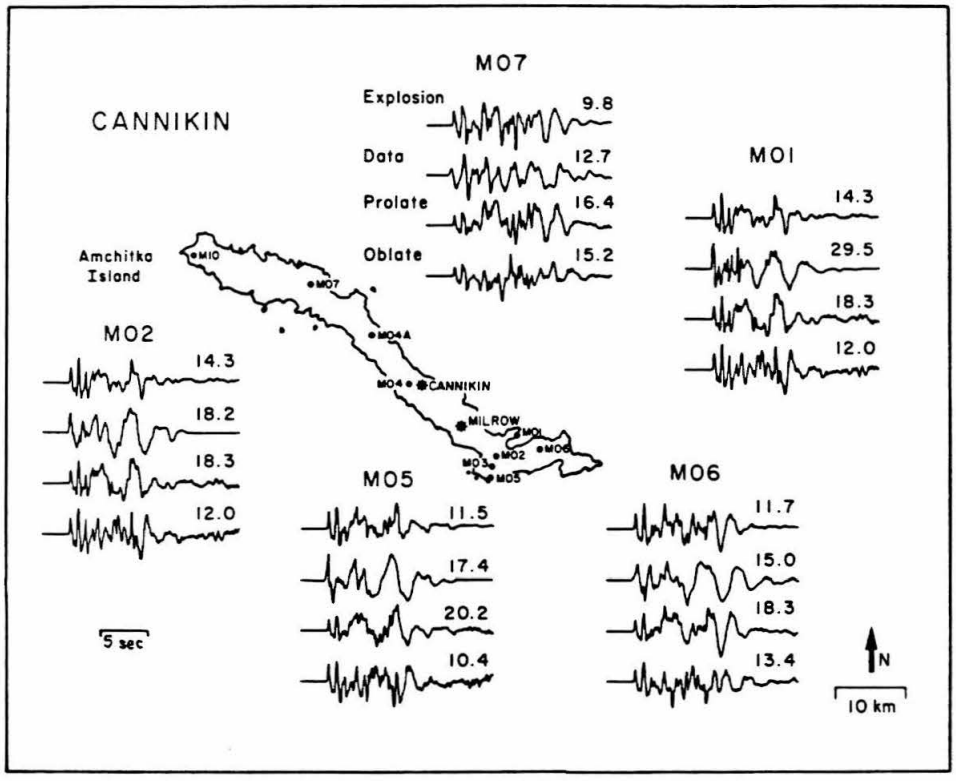

Figure 2.21 Comparison of synthetics for a spherical and aspherical cavity explosions (labeled Explosion, Prolate and Oblate) to data from CANNIKIN. Only radial components are shown. Compare Figure 2.20 (MILROW). Scaling and filtering of these synthetics are the same as in Figure 2.20.

choice of explosion time function in computing synthetic ground motion for the near-field velocity data we examine in this chapter. The medium immediately surrounding a station can greatly affect the amplitude of the observed waves, but estimating media properties at the stations from amplitude variations alone is unreliable. When possible, station structure should be determined in the field, to a depth and radius from the station consistent with the periods to be observed. Gradational boundaries are shown to fit the data better than sharp boundaries. When coupled with the effects of random media, we find that impulsive, large-amplitude arrivals in the coda are not deterministic, and can not be fit to multiples in a medium with sharp boundaries. Deterministic 2-D local structure is shown to be important for MILROW, where faults near the stations are shown to affect the surface waves.

Source asymmetry strongly affects the near-field surface waves. Such asymmetry can be modeled as the addition of a quadrupole response to the explosion response. The pancake (oblate cavity) case tends to reduce surface waves, while the prolate contribution tends to enhance surface waves. CANNIKIN favors a substantial prolate contribution and thus, smaller teleseismic m_b and larger local surface waves. A characteristic change in cavity shape from spherical to prolate (elongated vertically) for larger events could explain the change of slope in the m_b yield curves.

References for Chapter 2

Aki, K., and P. G. Richards (1980). *Quantitative Seismology, theory and methods*, W. H. Freeman and Co., San Francisco, 749.

Apsel, R. J. and J. E. Luco (1983). On the Green's functions for a layered half-space, Part II, *Bull. Seism. Soc. Amer.*, **73,** 931-952.

Barker, J. S., L. J. Burdick, and T. C. Wallace (1985). Analysis of near-field seismic waveforms from underground nuclear explosions, Scientific Report No. 1, AFGL-TR-85-0321, Woodward-Clyde Consultants, Pasadena, California, 39 pp.

Boore (1972). Finite difference methods for wave propagation in heterogeneous materials, in *Methods of Computational Physics*, vol. 2, B. Alder, S. Fernbach, and M. Rotenberg, Editors, Academic Press, New York, pp. 1-37.

Burdick, L., T. Wallace and T. Lay (1984). Modeling near-field and teleseismic observations from the Amchitka test site, *J. Geophys. Res.*, **89,** 4373-4388.

Engdahl, E. (1972). Seismic effects of the MILROW and CANNIKIN nuclear explosions, *Bull. Seism. Soc. Am.*, **62,** 1411-1423.

Helmberger, D. V., and D. Hadley (1981). Seismic source functions and attenuation from local and teleseismic observations of the NTS events JORUM and HANDLEY, *Bull. Seism. Soc. Am.*, **71,** 51-67.

Helmberger, D. V., and J. E. Vidale (1988). Modeling strong motions produced by earthquakes with two-dimensional numerical codes, *Bull. Seism. Soc. Am.*, **78,** 109-121.

King, C., A. Abo-Zena and J. Murdock (1974). Teleseismic source parameters of the LONGSHOT, MILROW and CANNIKIN nuclear explosions, *J.*

Geophys. Res., **79,** 712-718.

Lay, T., L. Burdick, and D. V. Helmberger (1984). Estimating the yields of the Amchitka tests by waveform intercorrelation, *Geophys. J. R. Astr. Soc.*, **78,** 181-208.

Lay, T., D. V. Helmberger, and D. Harkrider (1984). Source models and yield-scaling relations for underground nuclear explosions at Amchitka Island, *Bull. Seism. Soc. Am.*, **74,** 843-862.

Meuller, R. A. and J. R. Murphy (1971). Seismic characteristics of underground nuclear detonations, Part I, Seismic spectrum scaling, *Bull. Seism. Soc. Am.*, **61,** 1675-1694.

Orphal, D. L., C. T. Spiker, L. R. West, M. D. Wronski (1970). Analysis of seismic data, MILROW Event, Rept. NVO-1163-209, Environmental Research Corporation, Alexandria, Virginia, 81pp.

Perret, W. (1973). Ground motion in the vicinity of the CANNIKIN nuclear explosion, Rept. SLA-73 0043, Sandia Laboratories, Albuquerque, New Mexico, 79 pp.

Perret, W. and D. Breding (1972). Ground motion in the vicinity of an underground nuclear explosion in the Aleutian Islands: MILROW event, Rept. SL-RR-72 0668, Sandia Laboratories, Albuquerque, New Mexico, 84 pp.

Reshef, M., D. Kosloff, M. Edwards and C. Hsiung (1988a). Three-dimensional acoustic modeling by the Fourier method, *Geophysics.*, **53,** 1175-1183.

Reshef, M., D. Kosloff, M. Edwards and C. Hsiung (1988b). Three-dimensional elastic modeling by the Fourier method, *Geophysics.*, **53,** 1184-1193.

Stead, R. J., and D. V. Helmberger (1988). Numerical-analytical interfacing

in two dimensions with applications to modeling NTS seismograms. *J. Pure and Appl. Geophys.*, **128,** 101-193.

Stevens, J. L. and S. M. Day (1985). The physical basis of m_b , M_S and variable frequency magnitude methods for earthquake/explosion discrimination. *J. Geophys. Res.*, **90,** 3009-3020.

Toksoz, M. and H. Kehrer (1972). Tectonic strain release characteristics of CANNIKIN, *Bull. Seism. Soc. Am.*, **62,** 1425-1438.

Vidale, J. E., D. V. Helmberger, and R. W. Clayton (1985). Finite-difference seismograms for SH waves, *Bull. Seism. Soc. Am.*, **75,** 1765-1782.

Vidale, J. E., and D. V. Helmberger (1986). Path effects in strong motion seismology, in *Methods of Computational Physics*, Bruce Bolt, Editor, Academic Press, New York, pp. 267-319.

von Seggern, D. and R. Blandford (1972). Source time functions and spectra for underground nuclear explosions, *Geophys. J.*, **31,** 83-97.

Willis, D. E., G. D. George, K. G. Poetzl, C. E. Saltzer, A. F. Shakal, R. D. Torfin, T. L. Woodzik and C. Wolosin (1972). Seismological aspects of the CANNIKIN nuclear explosion. *Bull. Seism. Soc. Am.*, **62,** 1377-1396.

Chapter 3

The seismologic effects of a deep continental basin: a canonical study

3.1 Introduction

Tectonic regions of the earth are often associated with deep sedimentary basins. This is readily evident in California, where the Imperial Valley, San Joaquin Valley and Los Angeles Basin are all examples of deep, young continental basins. The processes that form these basins are often seismogenic. The seismologic effects of the basins on the sources near and within them is a subject of much interest (see, for example, Vidale and Helmberger, 1988, and Benz and Smith, 1988). The effects of basins are also of much interest in nuclear explosion seismology, as discussed in Chapter 1 of this thesis. Studies in both areas find that locally, basins increase the amplitude and dispersion of surface waves. In Chapter 1 of this thesis, we find that the basin termination can convert much of this surface-wave energy to body waves. These body waves then propagate teleseismically, or are available to be trapped in the crustal wave guide, reappearing at regional distances.

While the amplification effects are of direct interest in seismic hazard assessment, this study is directed primarily at discovering propagation effects, with a view toward improved assessment of historical seismicity. Many significant earthquakes have been recorded on a few instruments prior to the advent of large arrays and digital seismology. Some of these events are associated with basins and are recorded at regional or teleseismic distances. If the basin effects can be recognized in these waveforms, then more precise

locations and moment estimates can be made. Locations are improved by using the interference of basin phases and direct phases, essentially locating the event with respect to the basin boundaries. Moment estimates are improved by removing the basin overprint. Such improvements would require very precise knowledge of the basin effect.

To study the propagational effects of these deep continental basins, we apply the finite difference (FD) technique. To generate teleseismic waveforms, we use the representation theorem method developed in Chapter 1 of this thesis. We perform the FD calculation in two dimensions (2D) because of computational limitations. While a fully three-dimensional calculation would provide the most complete answer to the propagation question posed here, the 2D calculation provides valuable insight into the problem and, in many cases, is sufficient to fully model the problem. It is certainly an improvement over the one-dimensional structures which continue to dominate seismology. Such structures cannot model laterally varying structure, so common in tectonic regions, but rather give the response of some average structure. Thus, phases produced by lateral structure can be confused with variations in source time function or spatial distribution, making source discrimination from regional phases particularly difficult. The attempt here is to improve on one-dimensional modeling by identifying lateral phases, which are then available to provide source-location information.

3.2 Description of the models

To examine the problem of sources in deep, young continental basins, the models used herein are extreme cases. That is, the models have a very deep basin, 10 km, with very slow velocities. This is done to accentuate the

basin effect and to emphasize the difference between the presence and absence of a basin. To make the models more like many natural examples, the Mohorovičić discontinuity (Moho) is shallow, 25 km, typical of active tectonic regions undergoing extension or shear. Also, the Moho velocities are lower than is typical of stable continental crust. This chapter is concerned first with SH-wave propagation, and the observed effects are then compared to the P-SV system. The P-SV system will also add new features to the seismograms, because of the additional converted phases that occur in that system.

Having thus introduced the reasoning behind the creation of the models, we now examine the models in detail. The models are presented in Figure 3.1a - e. Figure 3.1a shows a basin with a steep wall. Such a model should scatter more horizontally the waves that travel across the basin. This is because the boundary appears as a plane perpendicular to the propagation direction. Some energy will scatter to all azimuths, but the vertical axis through the basin wall should be a node of scattered energy. This model is representative of fault-bounded basins, where the fault is steep. Figure 3.1b shows a basin with a shallowly dipping wall. This model should produce a very different result from the model of Figure 3.1a. The primary difference is that the shallow dip causes the energy to be incident at a small angle to the plane. For SH-waves, the shape of the boundary will affect the scattering of Love waves. For a shallow dip, Love waves of different periods will scatter at slightly different ranges, the longest periods scattering closest to the source, since these deeper waves sense the boundary slope when it first begins to turn up. We expect that for the elastic case the boundary shape has a much greater effect, on the basis of the layer over half-space canonical basin studies

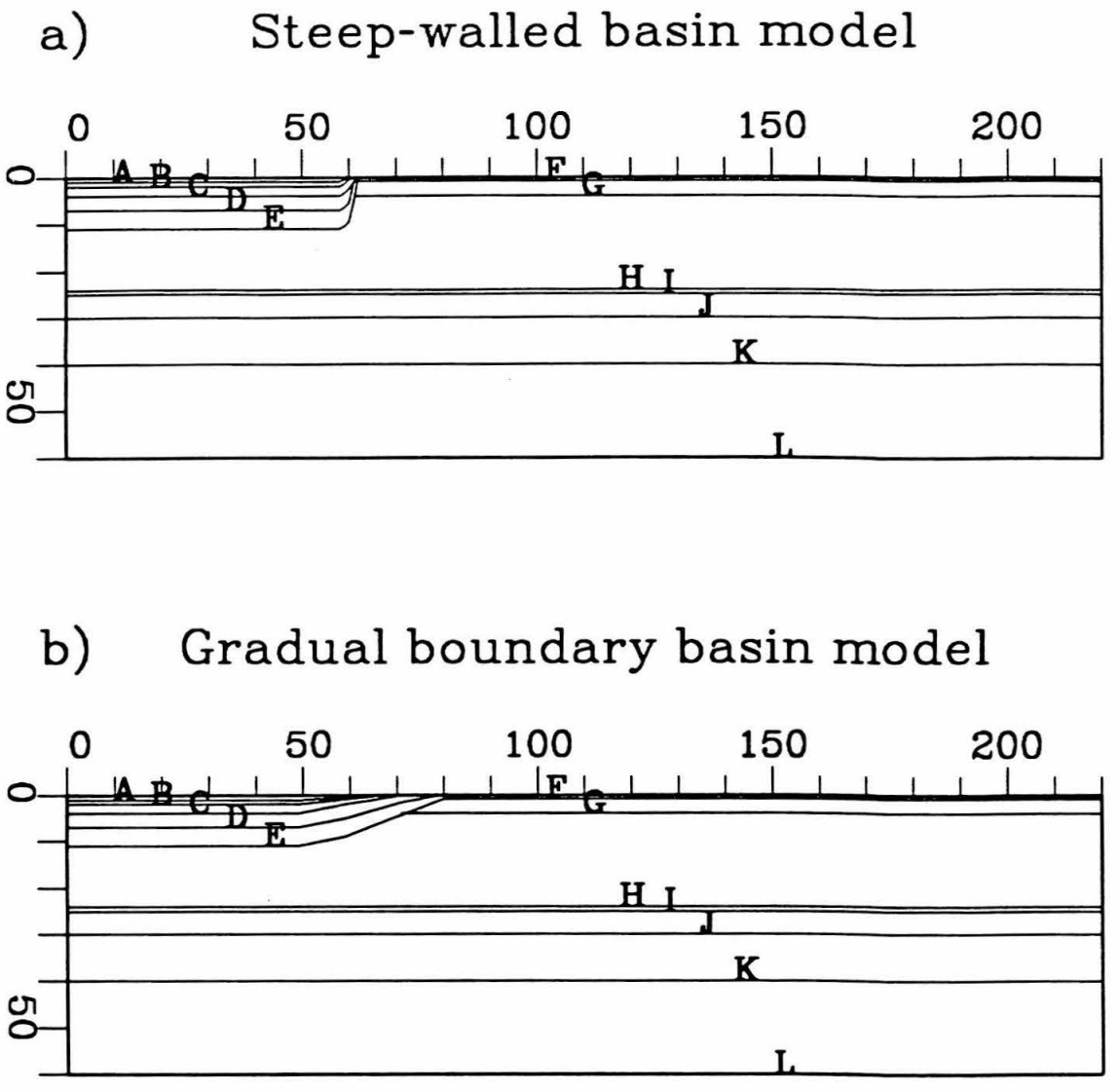

Figure 3.1 Models used in this investigation. The letters refer to the media as described in Table 3.1. There are two vertical velocity structures, the normal crust (letters F through L) and the basin structure (letters A through E followed by H through L). The Moho is the boundary between H and I. The layers below that define a negative S-velocity gradient used to simulate a long-period Sn. The surface (F) is a relatively low-velocity alluvial layer. While this layer can strongly affect the synthetics, much of the surface in tectonic regions has such a layer. The models presented are: a) steep-walled basin simulating fault-bounded basins, b) gradual boundary basin for fold- or thrust-bounded basins, c) half-space representing mantle structure up to the surface, d) flat-layered normal crust and e) flat-layered basin crust. The last three models are used as references.

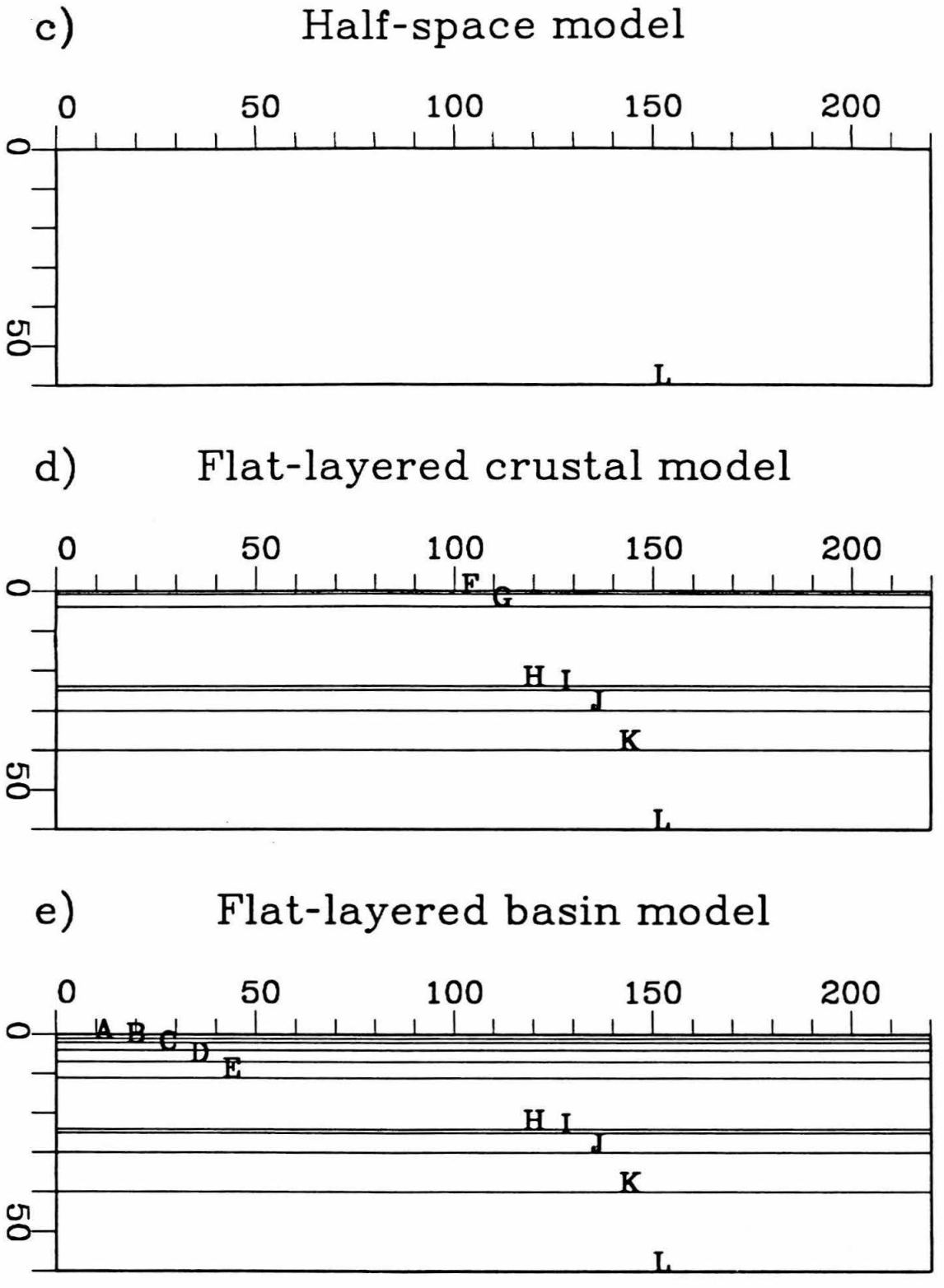

Figure 3.1 continued.

Table 3.1. Elastic constants for models

Key	V_p km s^{-1}	V_s km s^{-1}	ρ g cm^{-3}	layer thickness* km
Basin structure:				
A	2.2	1.0	1.7	1
B	3.3	1.67	2.0	1
C	4.4	2.34	2.3	2
D	5.0	2.84	2.5	3
E	5.72	3.3	2.7	4
Crustal structure:				
F	2.8	1.5	2.5	0.8
G	5.72	3.3	2.7	3.2
H	6.2	3.58	2.8	20
I	6.9	4.0	3.0	1
J	7.8	4.45	3.4	5
K	7.8	4.40	3.4	10
L	7.8	4.35	3.4	∞

*when present

in Chapter 1 of this thesis. A shallow, dipping boundary would have strong conversions such as P to S energy and Rayleigh to S energy, and this energy would be scattered along a direction dependent on the velocity contrast and dip of the boundary. For both SH and P-SV models, much of the converted energy will scatter teleseismically. Figure 3.1c shows a half-space used for comparison. Half-spaces are often used in seismology to simplify propagation effects. In some cases, such an assumption is an oversimplification. Figure 3.1d shows another model used for comparison, that of flat layers without a basin. While this is not as great a simplification as the half-space, it is nevertheless too simple to accurately model sources in the basin, especially for teleseismic records. A flat-layered model based on the basin structure is shown in 3.1e. Again, this is too simple for a full analysis because the surface waves at the farthest regional stations are most influenced by the normal crustal structure, rather than the basin structure. The velocities for these models are given in Table 3.1. The P-velocities are represented as well as S-velocities to give a full picture of the structure we seek to represent, but these are not used in this study.

Figure 3.2 shows the positions of the various sources and receivers used. A variety of sources is necessary in studying this problem, because the basin effect is strongly dependent on the source location relative to the basin boundary. The array of surface receivers is used to examine the moveout of various phases and to show the effect of the basin boundary as waves cross it. Appendix B contains some examples of these profiles for reference. The detailed moveout of phases will not be discussed here. For this study, the teleseismic wave field is sampled every five degrees of take-off angle, relative to the source. The material below the model is assumed to be a half-space,

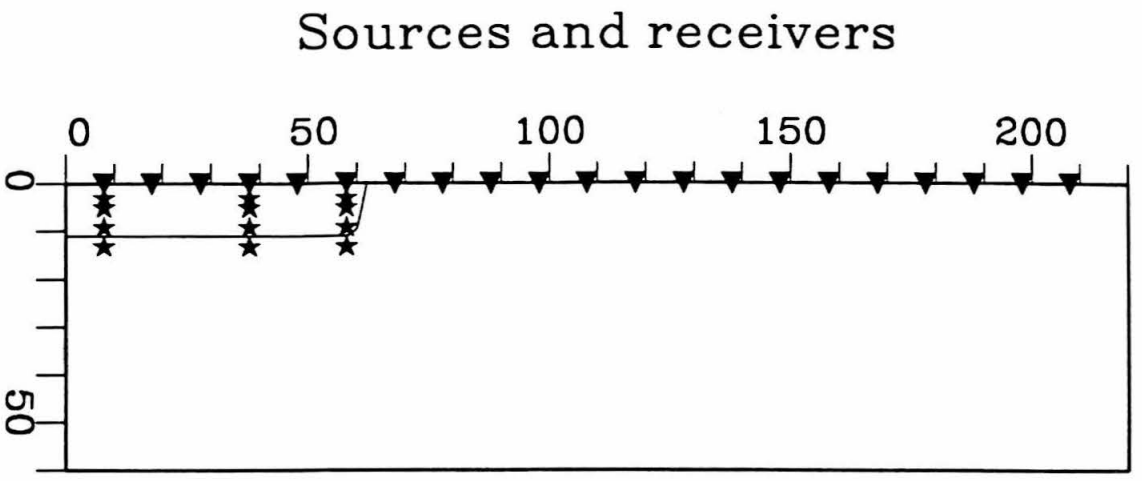

Figure 3.2 Positions of sources and receivers. The deepest boundary of the steep-walled basin is shown for reference. The stars indicate the various source positions modeled in this study. The inverted triangles indicate the selected receiver locations. The sources are at distances of 2, 22 and 52 km from the basin boundary and at depths of 3, 5, 8 and 13 km. The depths are chosen to sample the top, middle and bottom of the basin and just beneath the basin. These depths span the range of depths observed for most earthquakes in such regions. There are 21 receivers spread every 10 km starting directly above the source farthest from the basin boundary and over a range of 200 km.

as required by the formula derived in Chapter 1 of this thesis. The receiver positions are at a sufficiently large distance from the source such that waveform is independent of range.

3.3 Results: comparisons of FD synthetics for SH

In this section, we present and examine the results of the FD synthesis. We compare the synthetic seismograms produced by the models described above to each other and to the results from a half-space and a flat-layered model. The comparisons show the effect of the basin as a whole, and the effects of source position and mechanism on the result. We use the SH case because Love waves and other SH-waves are not as complex as those of the P-SV system, primarily because there is only S-energy present for the SH case, and there are no P-to-S and S-to-P conversions nor are there Rayleigh waves. Because of its simpler nature, we can expect to more fully comprehend the tangential synthetics than the radial and vertical synthetics from the P-SV system.

The numerical results are compared in Figure 3.3 for the various models: a half-space, a flat-layer case having normal crustal structure, a flat-layer case having basin structure, a 2D model with a steep-walled basin and a 2D model with a gradual basin termination. Figure 3.4 shows a comparison of teleseismic synthetics from the same runs. These introductory figures allow close inspection of features that change from one model to the next at one particular range. In this figure, the source is the deepest used in this study (13 km), which should create the least effect. The distance between the source and basin boundary is about 52 km, the longest used in this study. These have a strike-slip mechanism and show true amplitudes (in cm) for

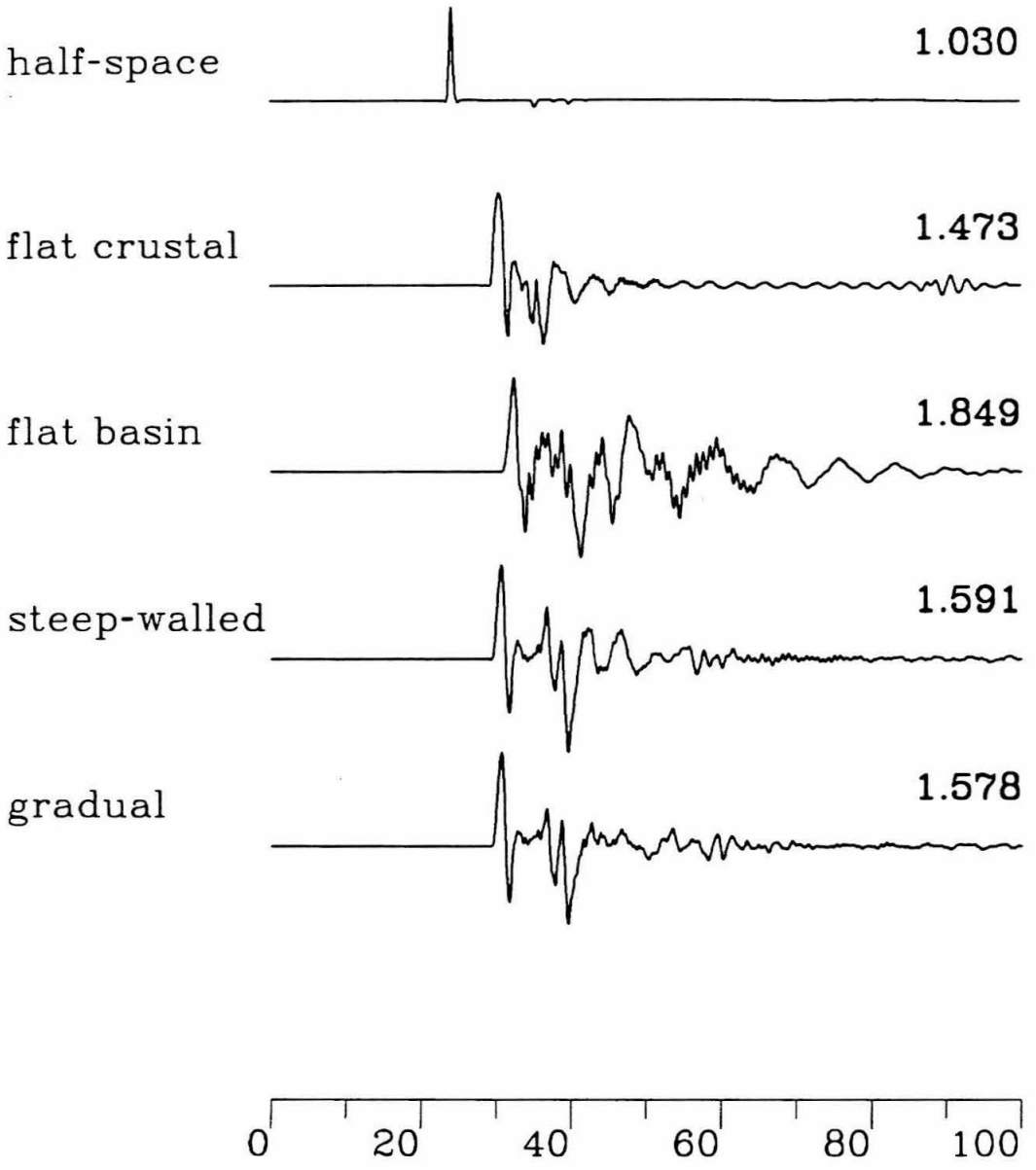

Figure 3.3 A comparison of the synthetics at 100 km range from all five models presented in Figure 3.1. The source depth is 13 km, at 52 km from the basin boundary. The mechanism is pure strike-slip and the moment is 10^{25}. The instrument response is broad-band, limited only by the maximum frequency allowed in the FD grid (about 2 Hz here). Peak amplitudes are in cm; time is in seconds.

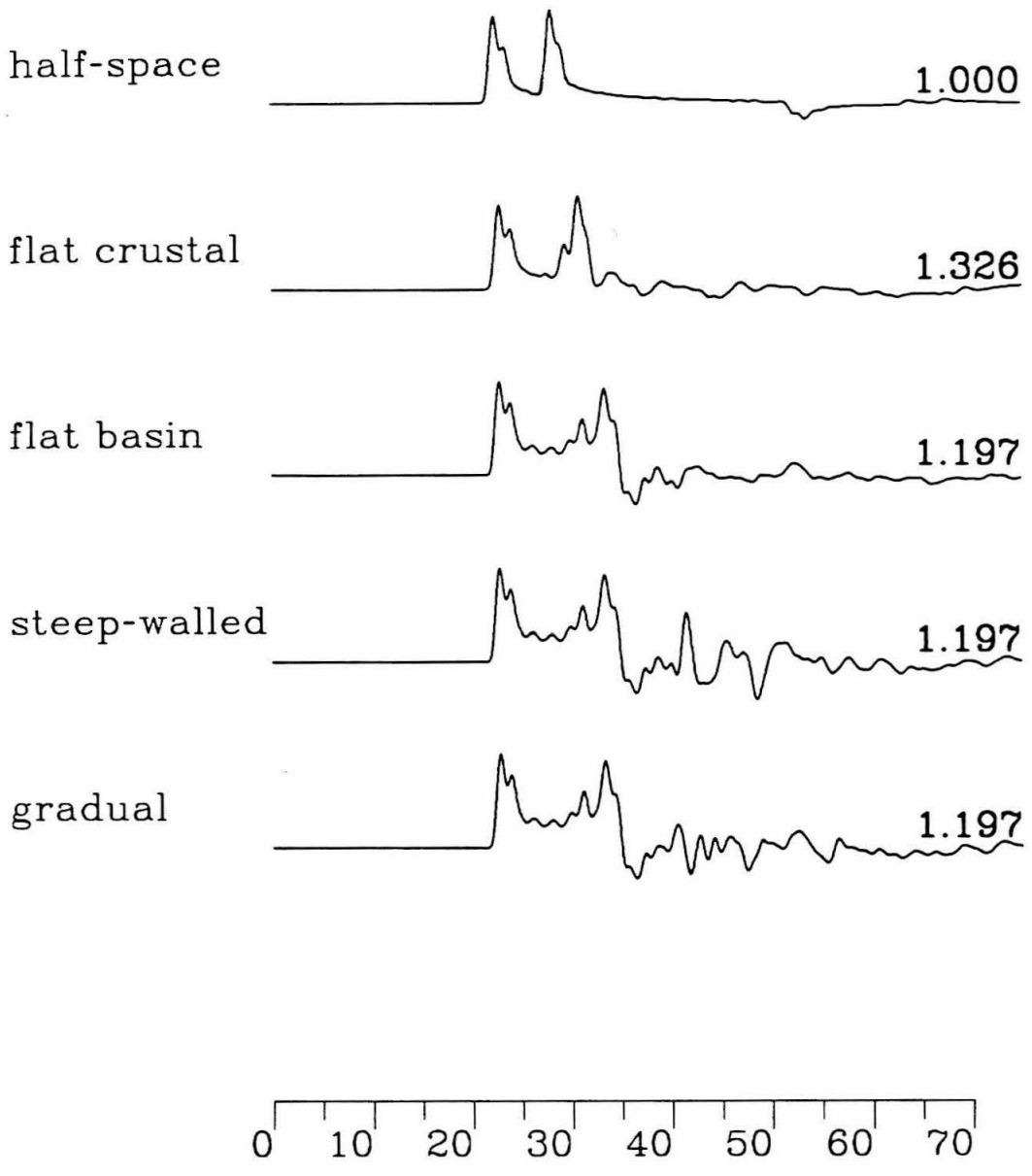

Figure 3.4 A comparison of the teleseismic synthetics at 15 degrees take-off angle. The source location and mechanism are the same as Figure 3.3. All traces are scaled to the peak amplitude of the half-space synthetic. The instrument response is broad-band, and there is no attenuation.

broad-band displacement, a moment of 10^{25} dyne-cm and a range of 100km. The teleseismic records are normalized to the half-space peak amplitude. There is no instrument response or attenuation (response is unattenuated broad-band displacement). The purpose of these figures is to demonstrate at the start just how much we can expect the seismograms to vary because of the presence of structure. To understand the details of such a figure, the models are compared against controls (half-space and flat-layered structure) and against each other.

Figure 3.5 shows a comparison between the half-space and the two flat-layered models as a function of range. The mechanism here is strike-slip and the depth is 13 km (which is below the basin structure of the second flat-layered model). As mentioned above, the amplitudes on the traces are all scaled to a moment of 10^{25} dyne-cm. The traces are broad-band displacements, containing only a Gaussian filter applied at the source to prevent grid dispersion of higher frequencies. This is evident in the form of the half-space synthetics. On the half-space synthetics some evidence of the limitations of finite-difference is visible. Note the small arrivals after the direct S-wave; these are reflections from absorbing boundary conditions. All the FD runs will have such arrivals, but these are the strongest; multiples off the absorbing boundaries from structure or the other boundaries are all geometrically smaller. Thus, the reader can judge in all the synthetics presented here exactly how much importance to place on small, late arrivals. Obviously, the arrivals must be quite small before they can be judged as possible absorbing boundary effects. Comparing the half-space to the flat-layered models, the lower velocities of the flat-layered models are evident, as well as the emergence of Love waves later in the records. This is all expected, the behavior of

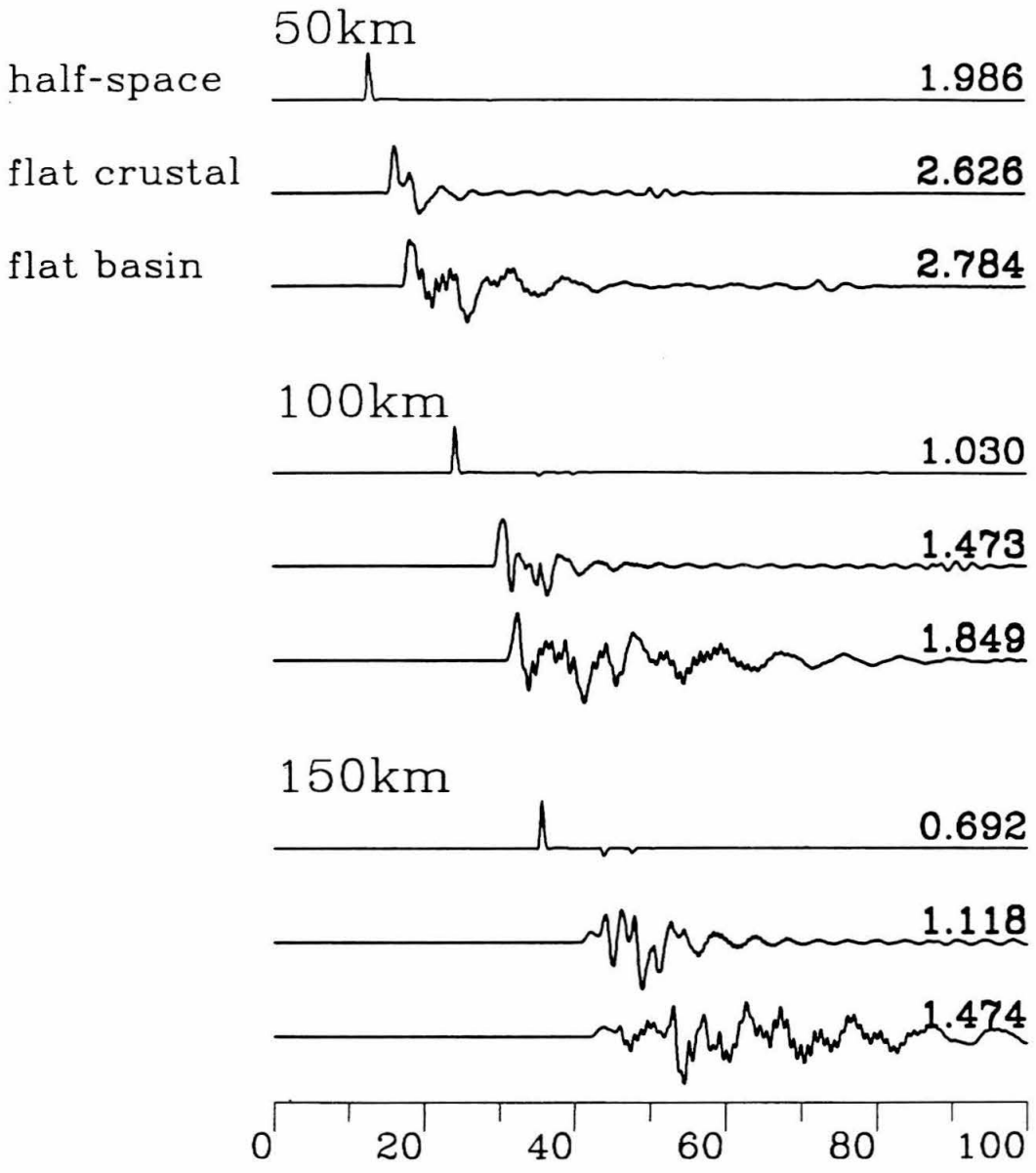

Figure 3.5 A comparison of the regional waveforms for the half-space and both flat-layered models. The source location is the same as Figure 3.3, as are the mechanism, moment and instrument. Three ranges are shown, 50, 100 and 150 km.

half-spaces and flat layers is well-known. An interesting detail about the flat-layered structures chosen here is the nature of the Love waves. For the normal crustal model, following the direct S, and the Moho and other reflections, the Love wave is a simple, low-amplitude, long-period wave, and it is relatively monochromatic. There are some complications, such as the very late wavelet traveling in the alluvial layer at the top of the model. On the other hand, the basin structure shows a much larger amplitude Love wave having a complex wave shape. The entire record is overprinted by multiples traveling primarily beneath the basin part of the structure. We also note here the effect of the negative S-velocity gradient beneath the Moho. After the Moho cross-over distance, Sn is visible. This Moho head wave is very long-period and very simple here. Such Sn waves are observed in a variety of data, and the negative gradient is included here to simulate that observation realistically.

At this point, the features expected on the regional synthetics for flat-layered structure are recognized. Now, the teleseismic synthetics as a function of take-off angle are shown in Figure 3.6. These show the waveforms expected on a short-period WWSSN instrument. The synthetics have been convolved with a t* operator with t*=4 to simulate mantle attenuation. The only noticeable feature is the delay of the phase sS, which becomes progressively later from the half-space to the basin model. This is expected because of the lower intervening velocities, and the importance of accurate source structure (vertically) is understood when interpreting such phases for depth information. Comparing Figure 3.4, the limitations of the absorbing boundaries are again visible. The small pulses echoing S and sS about 1-2 seconds back in Figure 3.4 are reflected off the side boundary. They exist

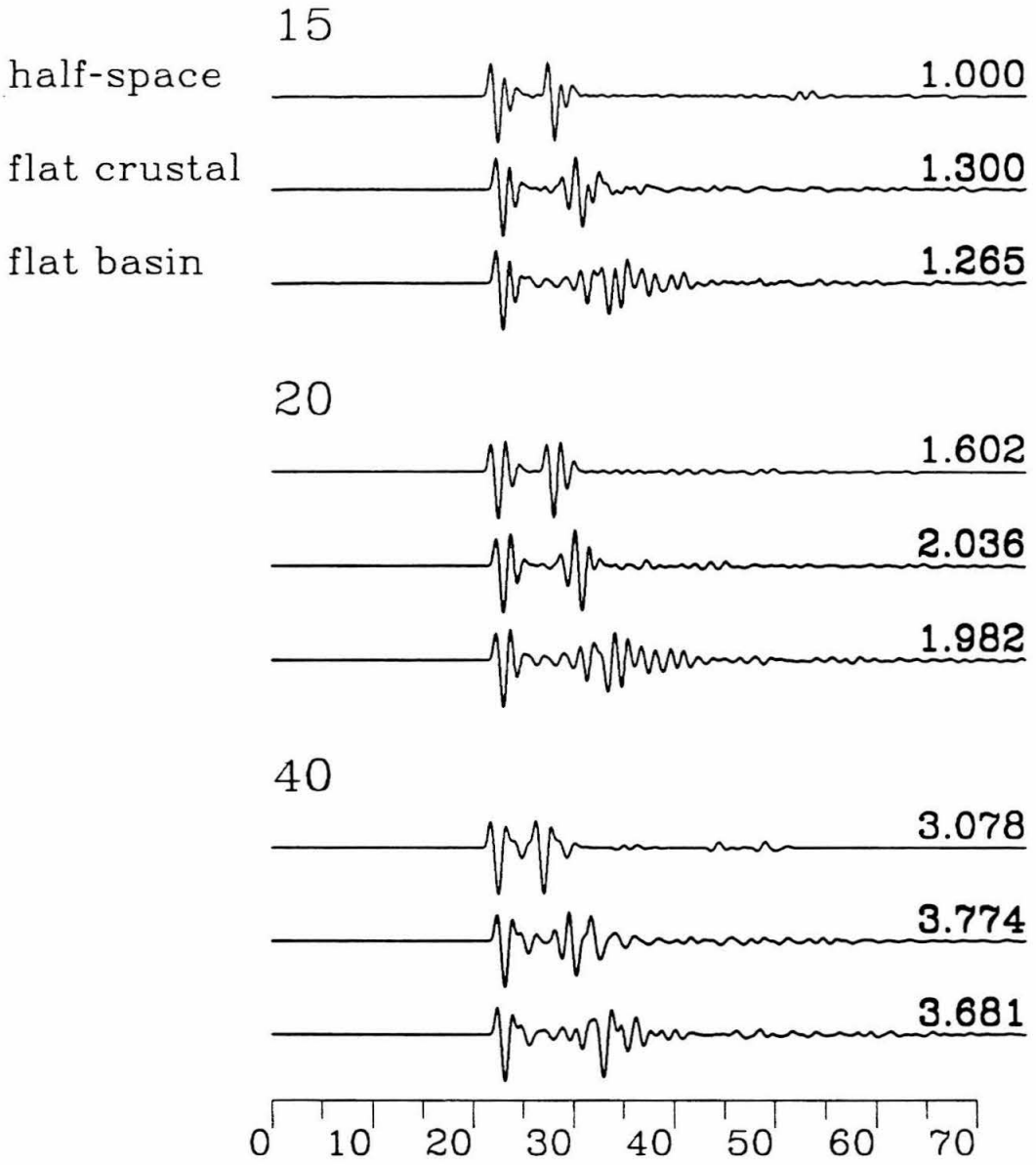

Figure 3.6 A comparison of the teleseismic waveforms for the half-space and both flat-layered models. The source location and mechanism are the same as Figure 3.4. Attenuation is provided by a t* operator with t*=4. The instrument is a short-period WWSSN response. Three take-off angles are shown, 15, 20 and 40 degrees. Only 15 and 20 degrees are appropriate for teleseismic distances; a take-off angle of 40 degrees is within the upper-mantle triplications. All traces are scaled to the peak amplitude of the first.

because the source is much closer to the side boundary than the distance from the source to the 2d Kirchhoff interface.

Of course, such short-period signals usually cannot be obtained. This is because mantle attenuation so strongly affects the periods to which the short-period WWSSN instrument is most sensitive, that the signal is below the noise level. Figure 3.7 shows a more realistic seismogram which uses a long-period WWSSN response. Here, the scattered energy from the basin boundary is not very apparent. Much more than this would be required for any modeling efforts because of the difficulty in distinguishing such a signal from long-period noise.

Now we proceed to the more complicated 2D models. Figure 3.8 shows a comparison with range between a steep-walled basin model and both flat-layered models. The source depth here is still 13 km, and the source position is far from the basin boundary, about 52 km. The interpretation is that the response is that of the flat-layered basin model up to the boundary, but that of the normal crustal model thereafter. The only other effect is a delay of free-surface multiples for the source far into the basin. These phases are the larger arrivals about 8 seconds after the direct wave. The timing of these phases matches that of the basin model, but the waveforms of the phases match the crustal model. Figure 3.9 shows the teleseismic synthetics for the same runs, using a long-period WWSSN instrument for the reasons discussed above. Note the appearance of some slight modifications to the waveforms for the sources far into the basin. This arises from the scattering of some Love wave energy at the basin boundary.

The preceding comparisons have all been done for deep sources. Deep sources are done first, because of their simplicity. Figure 3.10 shows a com-

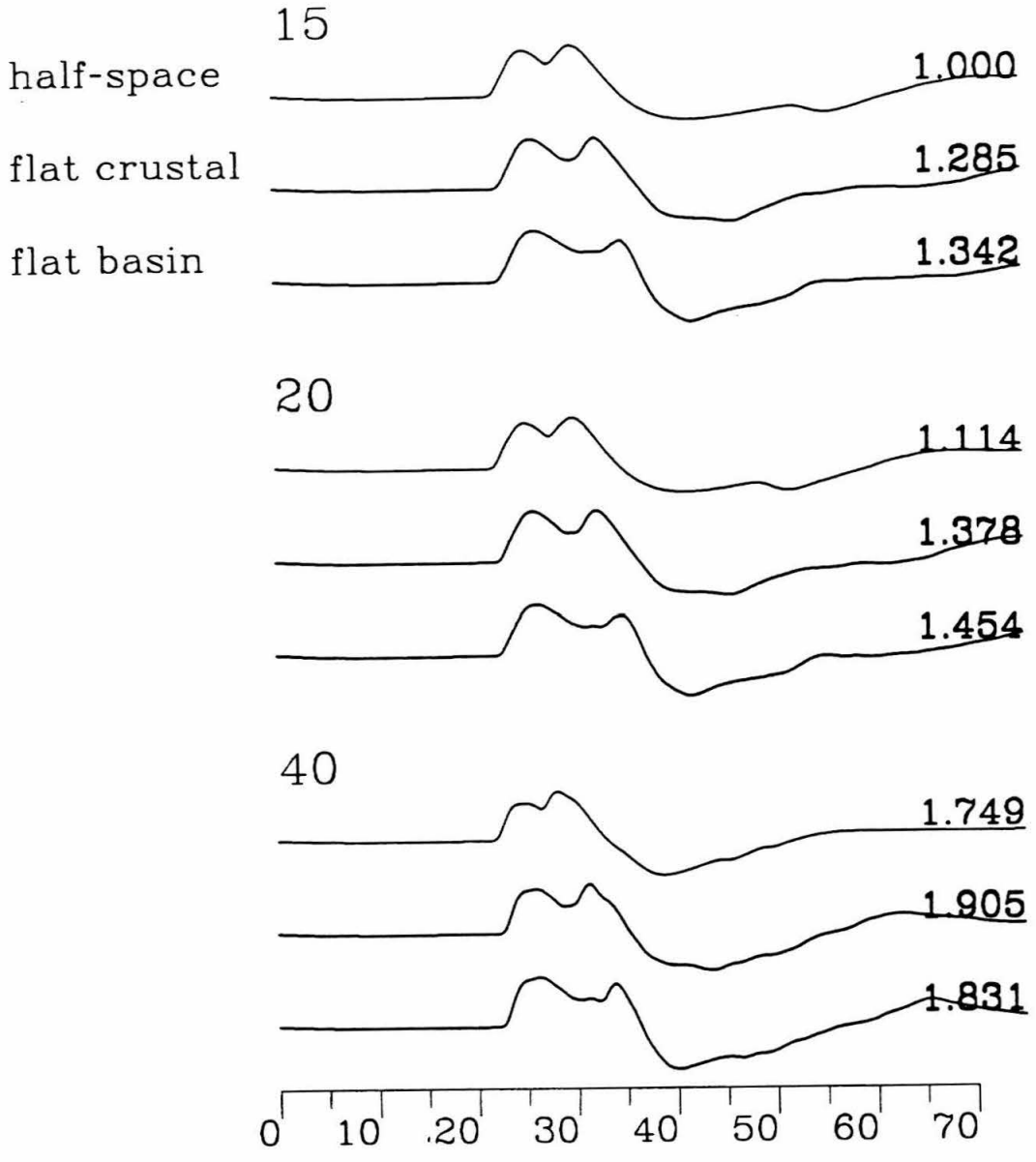

Figure 3.7 A comparison of the teleseismic waveforms for the half-space and both flat-layered models. The source location, mechanism and attenuation are the same as Figure 3.4. The instrument is a long-period WWSSN response. Three take-off angles are shown, 15, 20 and 40 degrees. Only 15 and 20 degrees are appropriate for teleseismic distances; a take-off angle of 40 degrees is within the upper-mantle triplications. All traces are scaled to the peak amplitude of the first. The peak amplitude of the first trace is 253 times that of the first trace in Figure 3.6.

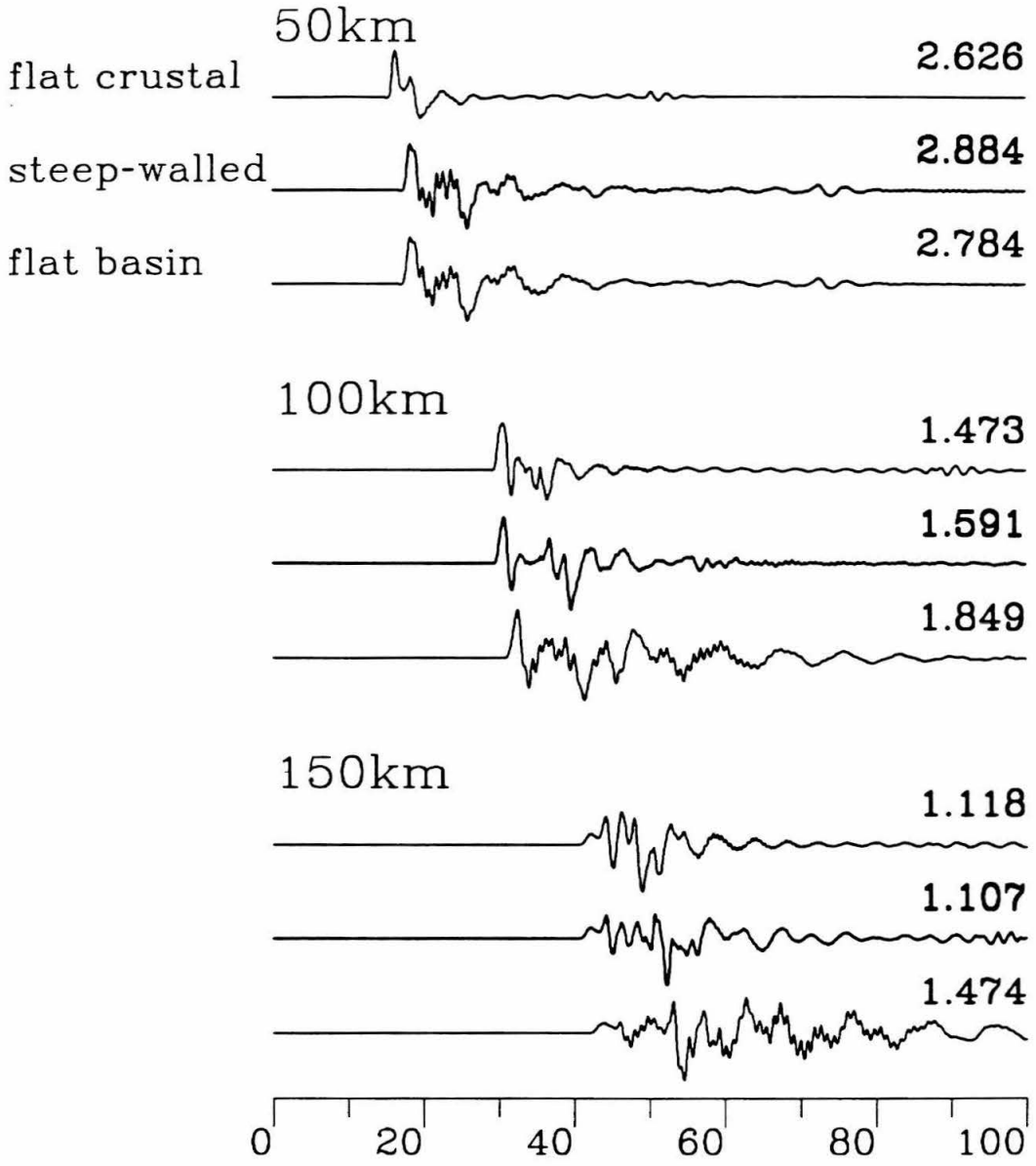

Figure 3.8 A comparison of the regional synthetics for the steep-walled basin structure and both flat-layered structures. The source location, mechanism, moment and instrument response are the same as Figure 3.3. Three ranges are shown, 50 100 and 150 km.

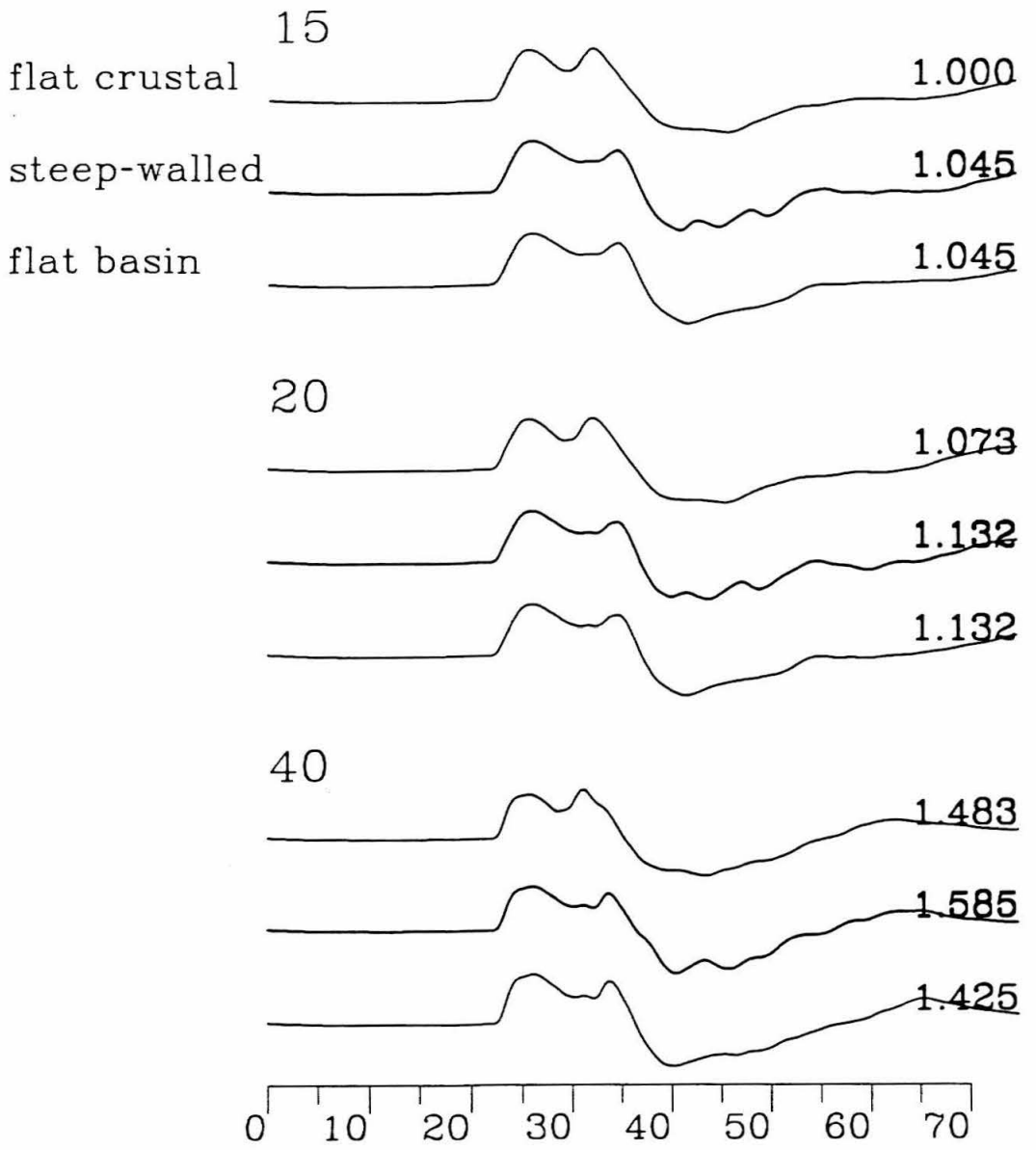

Figure 3.9 A comparison of the teleseismic synthetics for the steep-walled basin structure. The source location, mechanism, instrument and attenuation are the same as Figure 3.4. Three take-off angles are shown, 15, 20 and 40 degrees. All traces are scaled to the peak amplitude of the first. The peak amplitude of the first trace is 1.3 times that of the first trace in Figure 3.7.

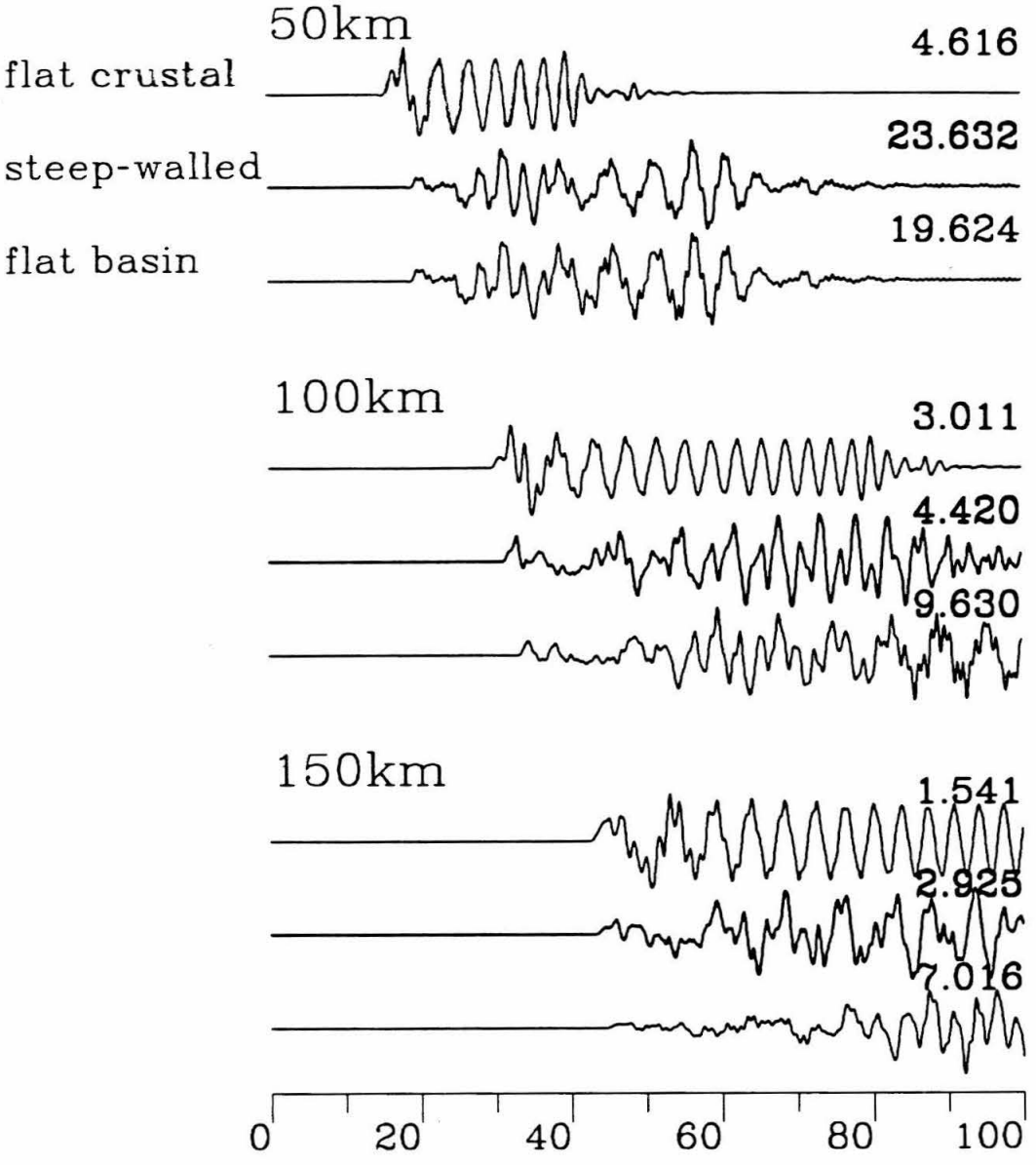

Figure 3.10 A comparison of the regional response for the steep-walled basin and both flat-layered models. The mechanism, moment and instrument are the same as Figure 3.3, but the source location is shallow, 3 km. The source is 52 km from the basin boundary. Three ranges are shown, 50, 100 and 150 km. Compare to Figure 3.8 for the effect of source depth.

parison of regional synthetics for the more interesting shallow sources. The source depth here is 3 km; the mechanism and moment remain the same as above. Immediately, one observes the greater complexity of these records, especially on the surface wave train. Yet the interpretation of these records is identical to that above for the deeper source. The response is that of the basin structure alone until the termination; then the waveform of each phase becomes more like that of the crustal model, but the timing is that of the basin model, if the phase is a free-surface multiple. This is true except for the Love wave, which seems to exhibit behavior in between that of the two flat structures, even to larger ranges. Apart from the Love wave then, these observations imply that if we understand both the structure of a basin and the structure of the crust surrounding that basin, the greater part of the record could be modeled that way. Generalized rays may be used by combining free-surface multiple rays calculated for the basin structure with the remaining rays calculated for the surrounding media. Of course, this would not completely explain the variations in the Love waves, since the amount of energy driving the Love waves for each mode in the crustal model is dependent on that transferred from the basin structure. The Love waves are also delayed due to the presence of the basin. The most dramatic results are due to the scattering of these Love waves as energy is transferred across the boundary. The scattered energy is observed teleseismically in Figure 3.11. The scattered energy following S and sS is apparent, even though the strong attenuation has eliminated the higher frequencies characteristic of the Love waves in these models. The timing of such energy in data should provide information on the distance between the source and the scattering structure, while the relative amplitude could provide information on the "strength" of

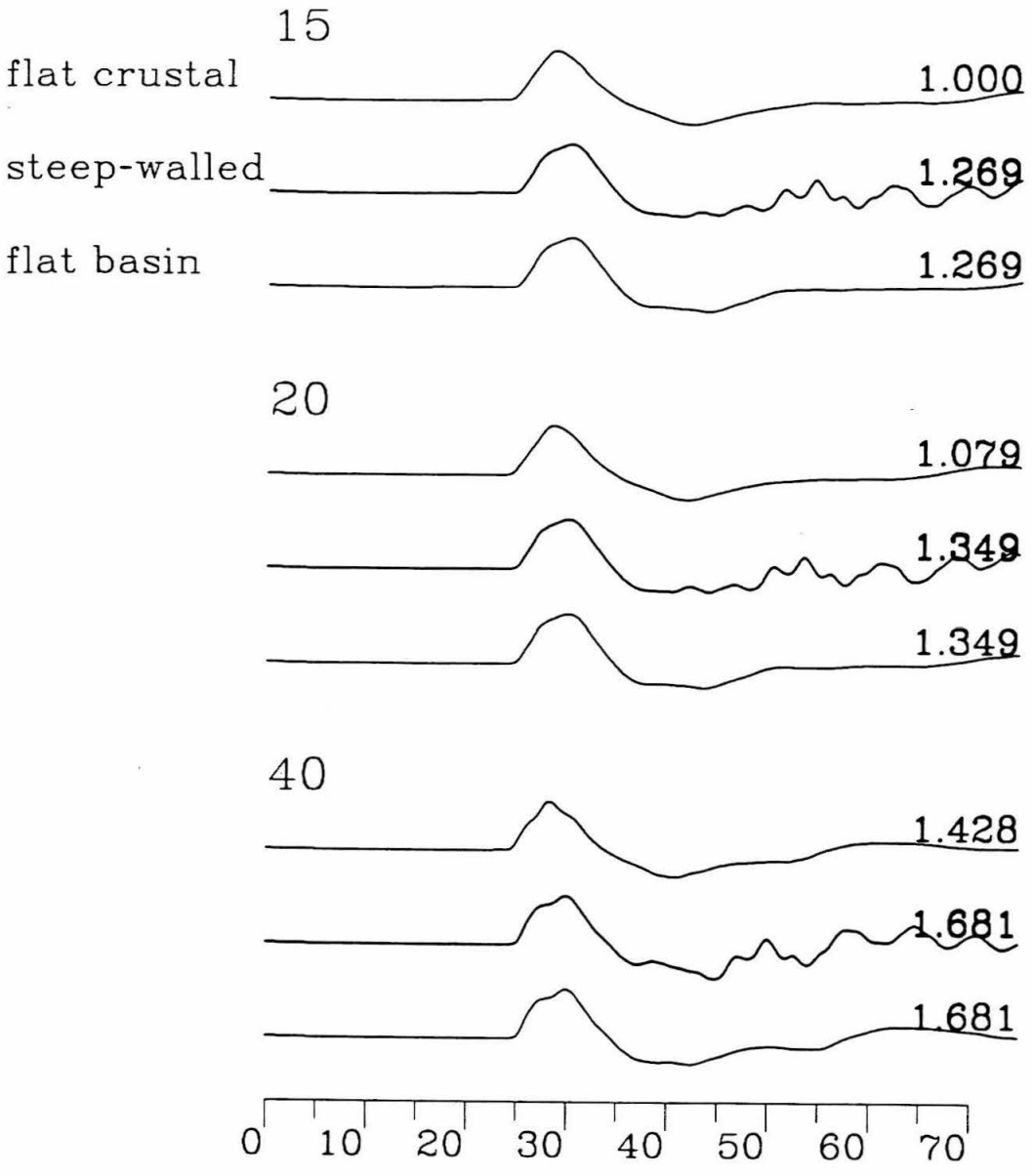

Figure 3.11 A comparison of the teleseismic synthetics for the steep-walled basin and both flat-layered models. The mechanism, attenuation and instrument are the same as Figure 3.4, but the source location is shallow, 3 km. The source is 52 km from the basin boundary. Three take-off angles are shown, 15, 20 and 40 degrees. Compare to Figure 3.9 for the effect of source depth. All traces are scaled to the peak amplitude of the first. The peak amplitude of the first trace is 2.2 times that of the first trace in Figure 3.7.

the boundary.

So far, the 2D model examined has been a steep-walled basin. Not all basins have boundaries that precipitous. Indeed, gradual terminations are arguably much more common. Does the shape of the termination affect the waveform? Chapter 1 of this thesis found evidence that the shape of the termination is important. Here too, the shape of the termination influences the waveform. Figure 3.12 compares several of the synthetics displayed above to those for a gradual termination. Differences are readily apparent, but they are not as great as might be expected. This implies that steep boundaries produce relatively simple waveforms which can be easily modeled in terms of flat-layered results, and when terminations become shallow, the waveforms change, but are well-modeled by the steep-walled basin synthetics. Therefore, identifying precise information about basin geometry in SH data from basins may be more difficult. Nevertheless, the most important information is the range between the source and the basin boundary, and that information appears to be robust. The teleseismic synthetics (Figure 3.13) show little difference in the scattered energy. This is unexpected. Different modes should "see" the basin termination at different ranges. The longest periods would be scattered earliest, while shorter periods travel farther in the basin structure. The explanation may be that the large attenuation for mantle S-waves is responsible for eliminating all but the longest period scattered energy, so there is only one phase shift for the entire record. This explanation is derived from examining unattenuated synthetics, but this cannot be done for data, so the point is moot.

Most of the above comparisons are made with sources at the same distance from the basin boundary. Varying the distance between the source and

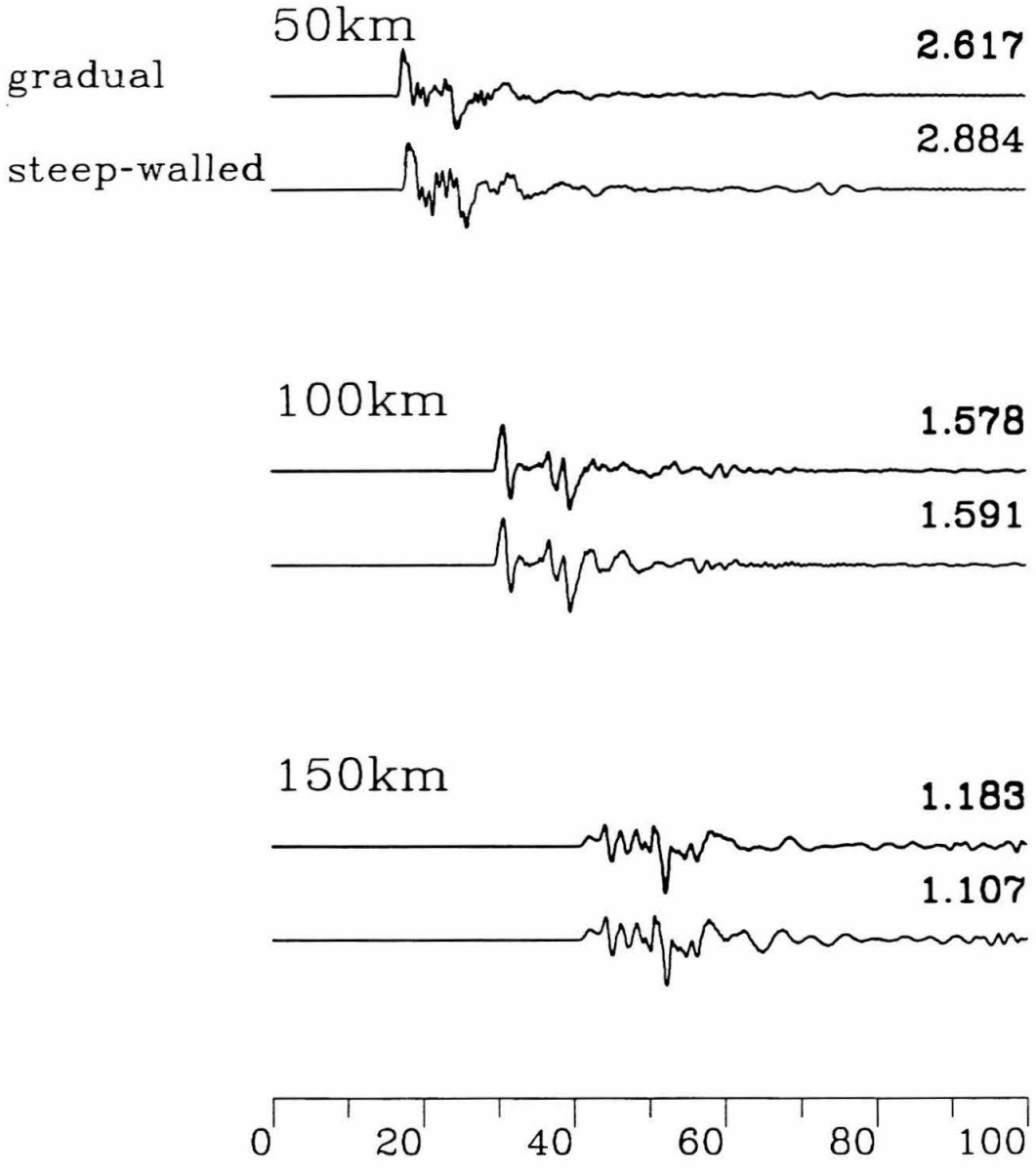

Figure 3.12a A comparison of the two basin boundaries, steep and gradual, at regional distances. The source location, depth, mechanism, instrument, moment and ranges are the same as Figure 3.8.

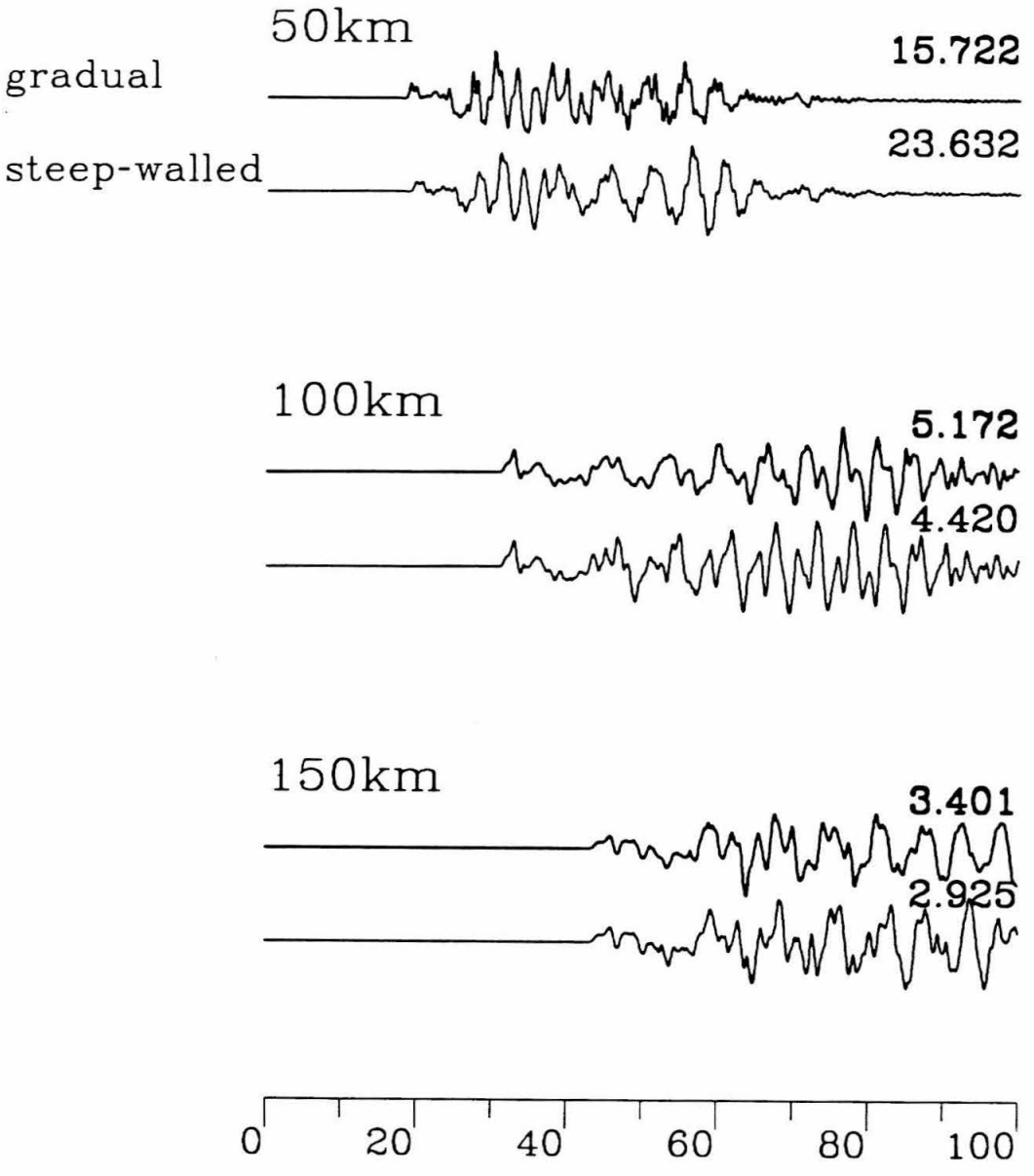

Figure 3.12b A comparison of the two basin boundaries, steep and gradual, at regional distances. The source location, depth, mechanism, instrument, moment and ranges are the same as Figure 3.10. The effect of source depth is illustrated by comparing this to Figure 3.12a.

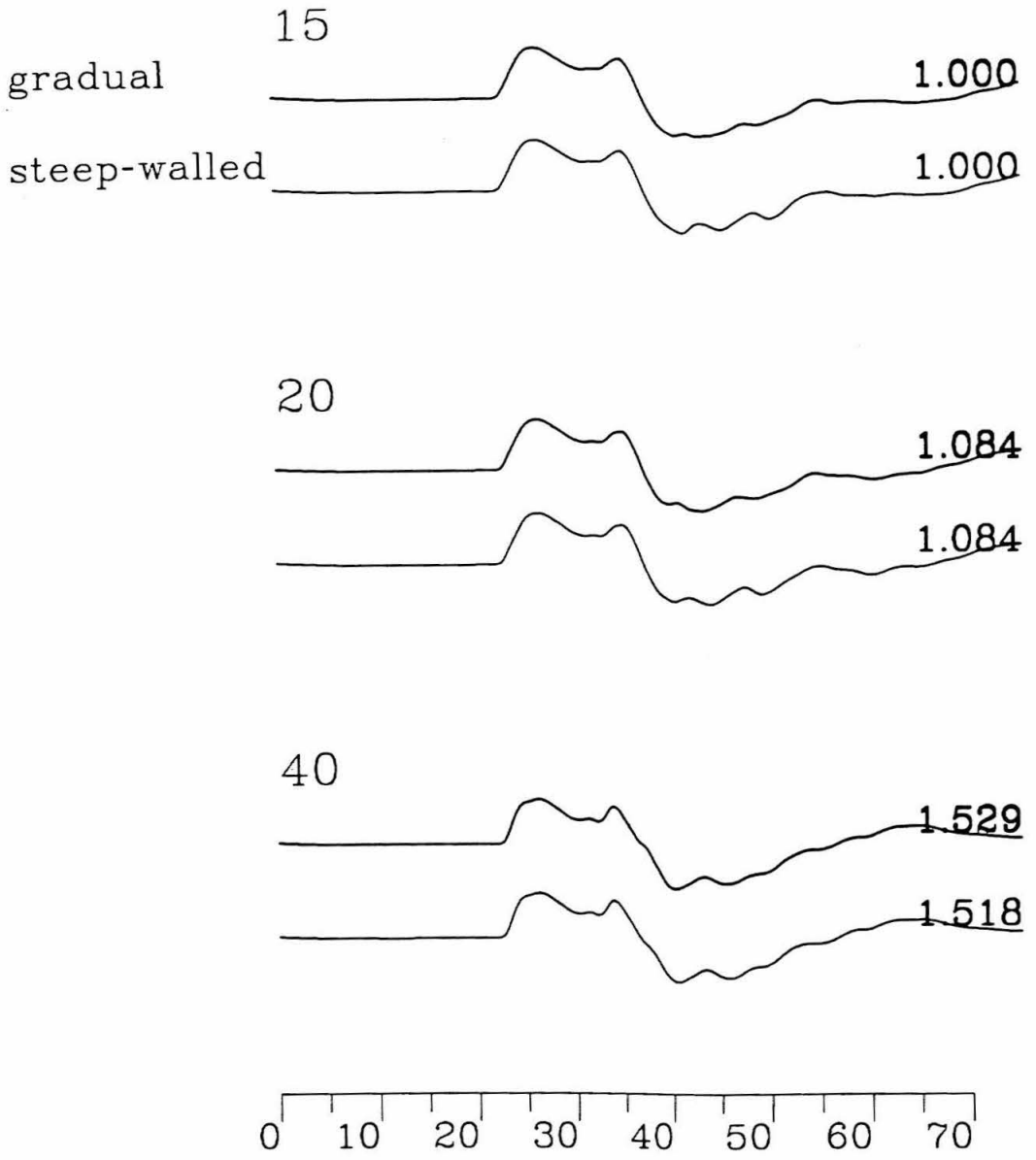

Figure 3.13a A comparison of the two basin boundaries, steep and gradual, at teleseismic distances. The source location, depth, mechanism, instrument, attenuation and take-off angles are the same as Figure 3.9.

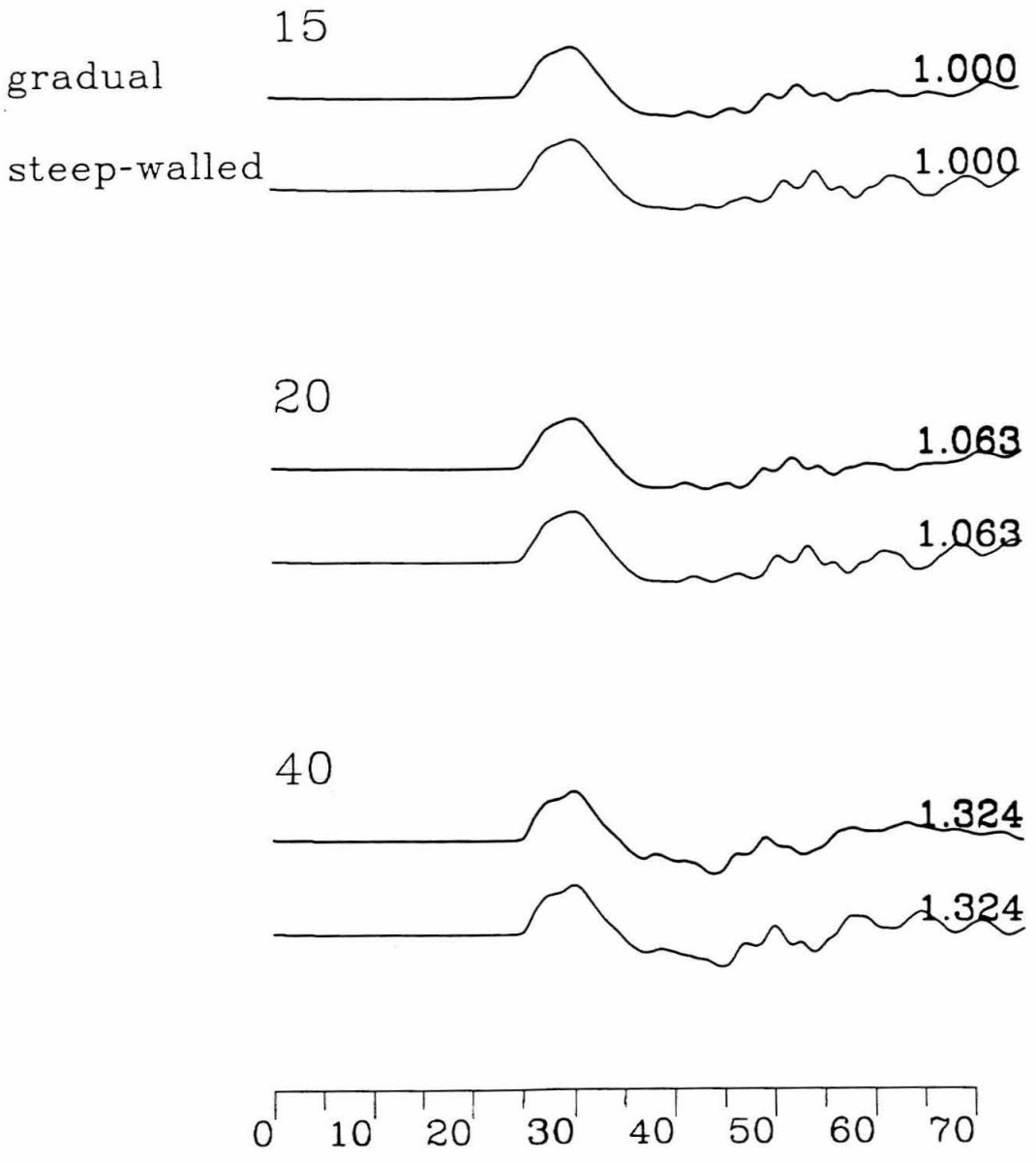

Figure 3.13b A comparison of the two basin boundaries, steep and gradual, at teleseismic distances. The source location, depth, mechanism, instrument, attenuation and take-off angles are the same as Figure 3.11. The effect of source depth is illustrated by comparing this to Figure 3.13a.

basin boundary shows how this distance is apparant in the waveforms. Figure 3.14 shows a comparison of three different source-to-boundary distances for the steep-walled basin case and a source depth of 5 km. As suggested above, the main effect here is the delay of the surface wave and of free-surface multiples. Figure 3.15 is a similar figure for the shallow basin termination. This demonstrates that despite the greater complexity of the records, the lag of phases which is due to the presence of the basin is resolved. Thus, even for a basin terminating in a non-ideal fashion, it should be possible to find evidence of the position of a source relative to a basin boundary by modeling the tangential seismograms. This would apply especially to sources with simple time-histories that are well-recorded on broad-band instruments, for the reason that it is that type of record which the synthetics presented here would model. Figure 3.16 shows the teleseismic records corresponding to Figure 3.14. The variation in phase lag, because of the variation in the distance to the basin boundary, is resolved, despite the fact that the synthetics are so long-period. For further comparison, Figure 3.17 is similar to Figure 3.16, but corresponds to Figure 3.15. Some differences are apparent between the shallow and steep termination models, and fortuitously, these differences can be greatest along teleseismic take-off angles. Nevertheless, it would be difficult to use this information to construct a structural model of the scattering boundary.

In Figure 3.18, we compare all the source positions for one range (100 km) for the steep-walled basin. Here, the effects of source position in both depth and distance from the boundary are shown. The largest differences between the records are those that are known and expected. The Love waves are very large for near-surface sources, but small for deep sources, and the

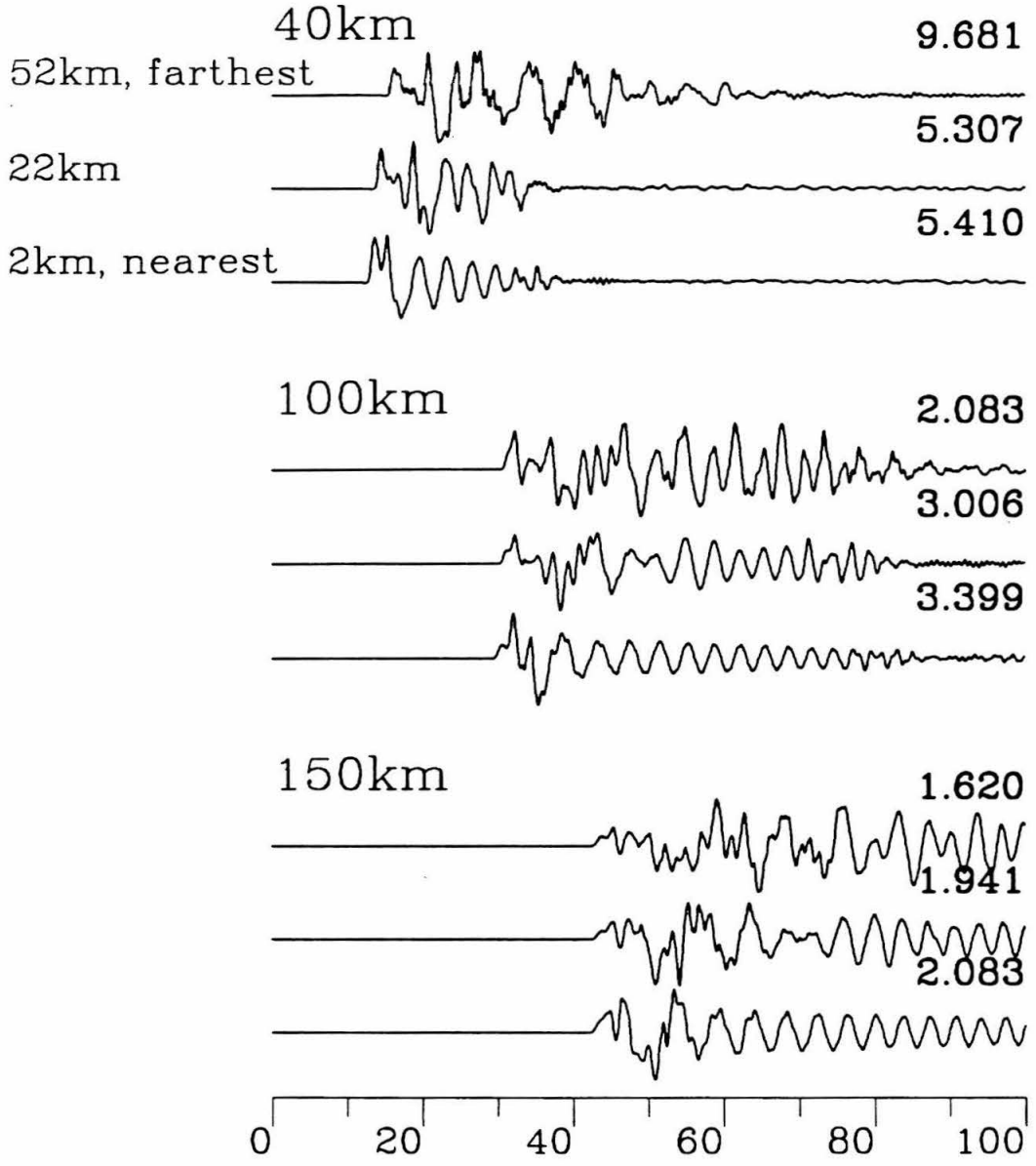

Figure 3.14 A comparison of regional synthetics to demonstrate the effect of distance between the source and basin boundary. Three of these distances are compared, 2, 22 and 52 km. The comparison is done at three ranges, 50, 100 and 150 km for a source at a depth of 5 km. The mechanism is strike-slip, with a moment of 10^{25}. The instrument is broad-band. The basin boundary here is steep.

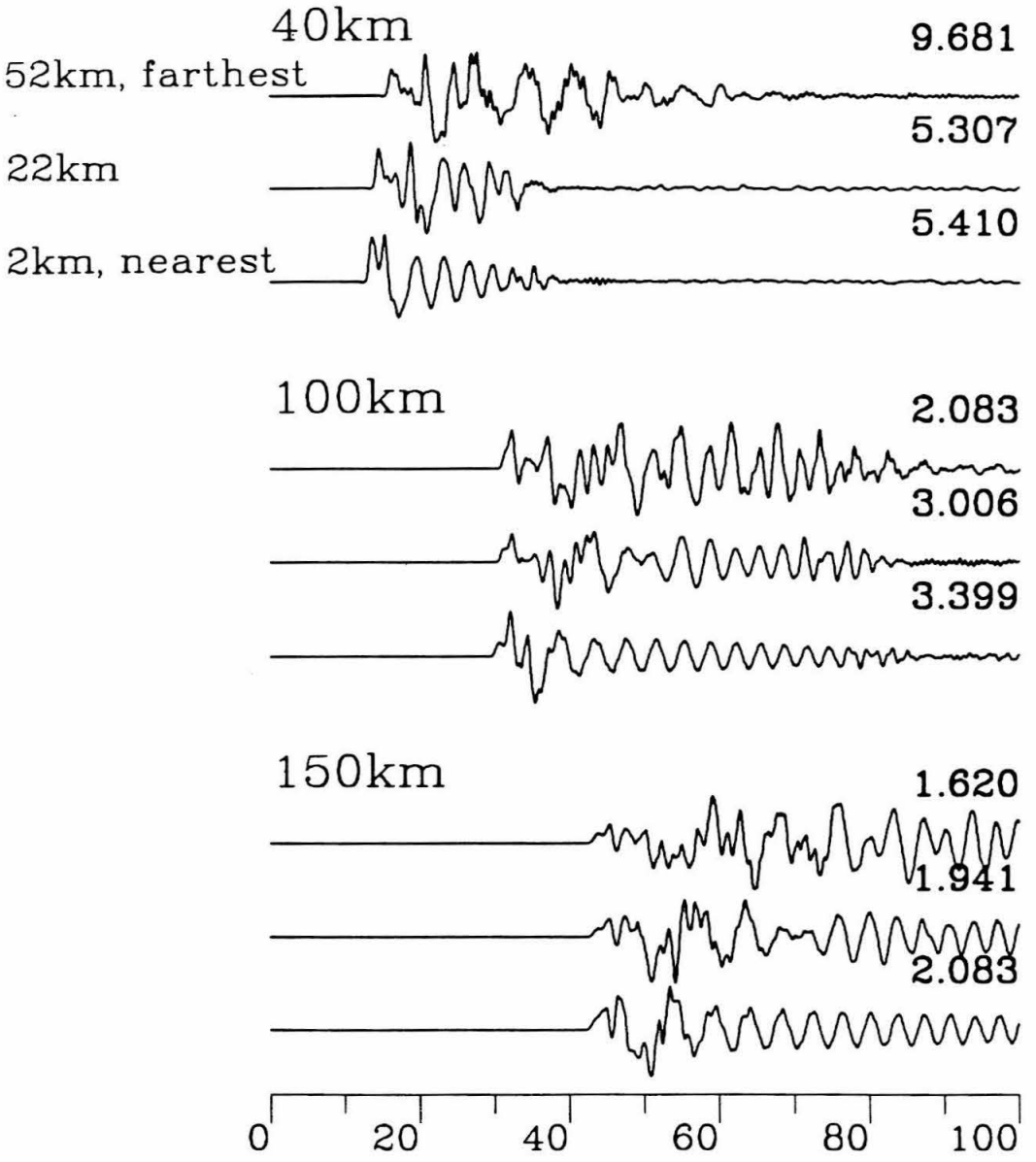

Figure 3.15 A comparison of regional synthetics to demonstrate the effect of distance between the source and basin boundary. This figure uses the gradual basin boundary and should be compared to Figure 3.14 for the effect of basin boundary type. The ranges, source positions and depths, mechanism, moment and instrument are the same as Figure 3.14.

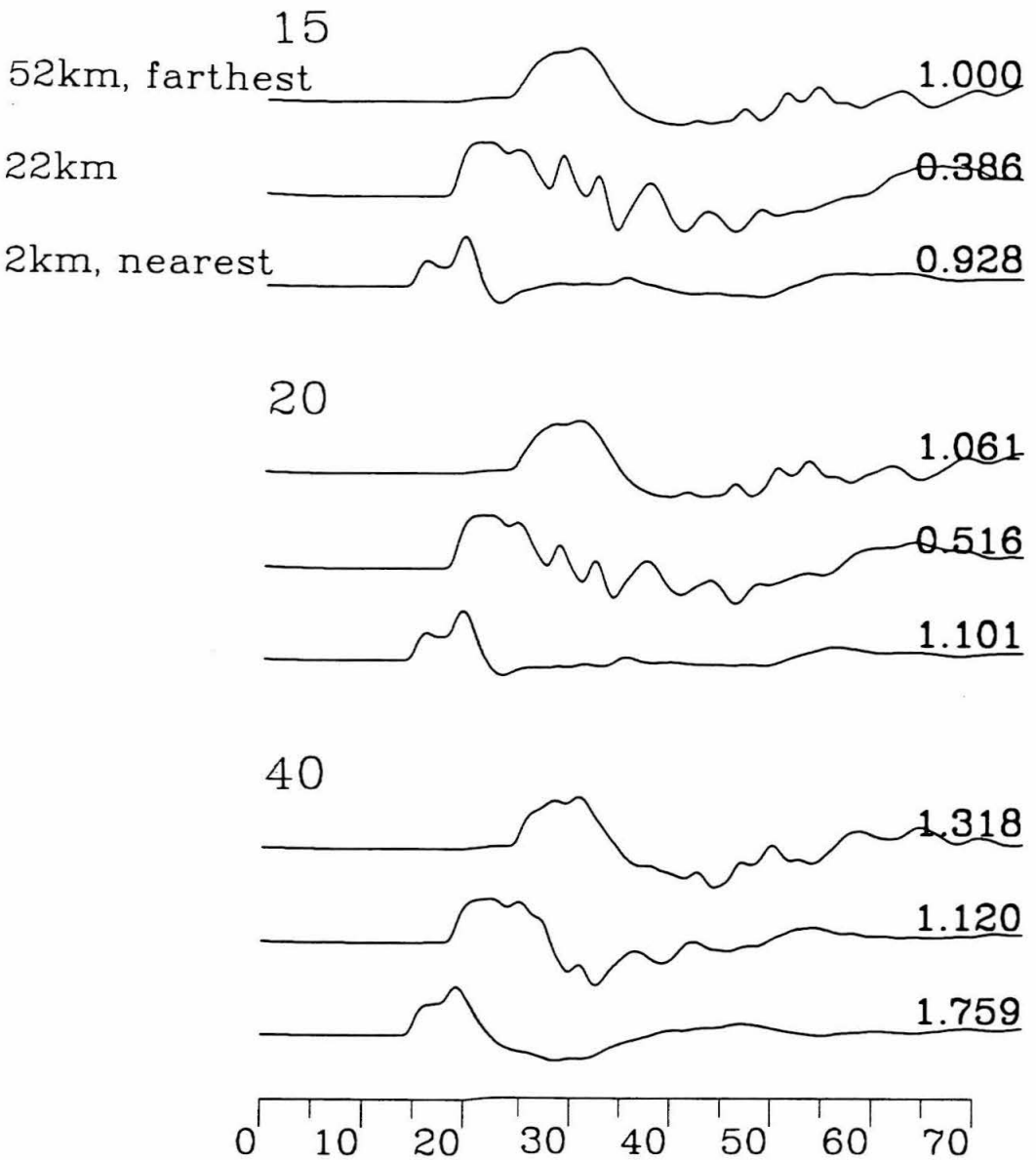

Figure 3.16 A comparison of teleseismic synthetics to demonstrate the effect of distance between the source and basin boundary. Three of these distances are compared, 2, 22 and 52 km. The comparison is done at three take-off angles, 15, 20 and 40 degrees for a source at a depth of 5 km. The mechanism is strike-slip. The instrument is a long-period WWSSN, and the mantle attenuation (T*=4) for S-waves is included. The basin boundary here is steep. The traces are all scaled to the peak amplitude of the first trace. The peak amplitude of the first trace is 1.3 times that of the first trace in Figure 3.6.

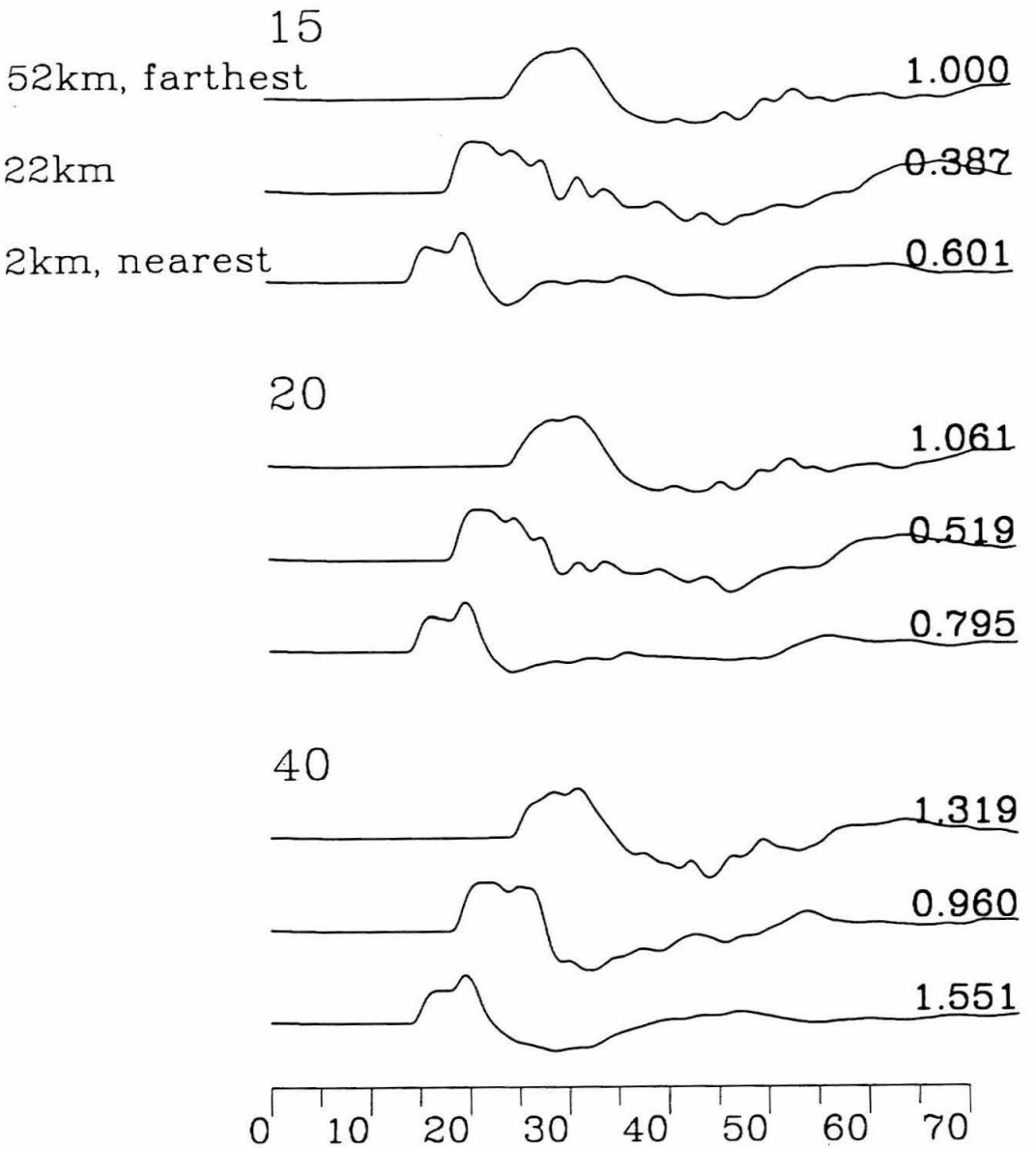

Figure 3.17 A comparison of teleseismic synthetics to demonstrate the effect of distance between the source and basin boundary. This figure uses the gradual basin boundary and should be compared to Figure 3.16 for the effect of basin boundary type. The ranges, source positions and depths, mechanism, attenuation and instrument are the same as Figure 3.16. The traces are all scaled to the peak amplitude of the first trace. The peak amplitude of the first trace is 2.6 times that of the first trace in Figure 3.16.

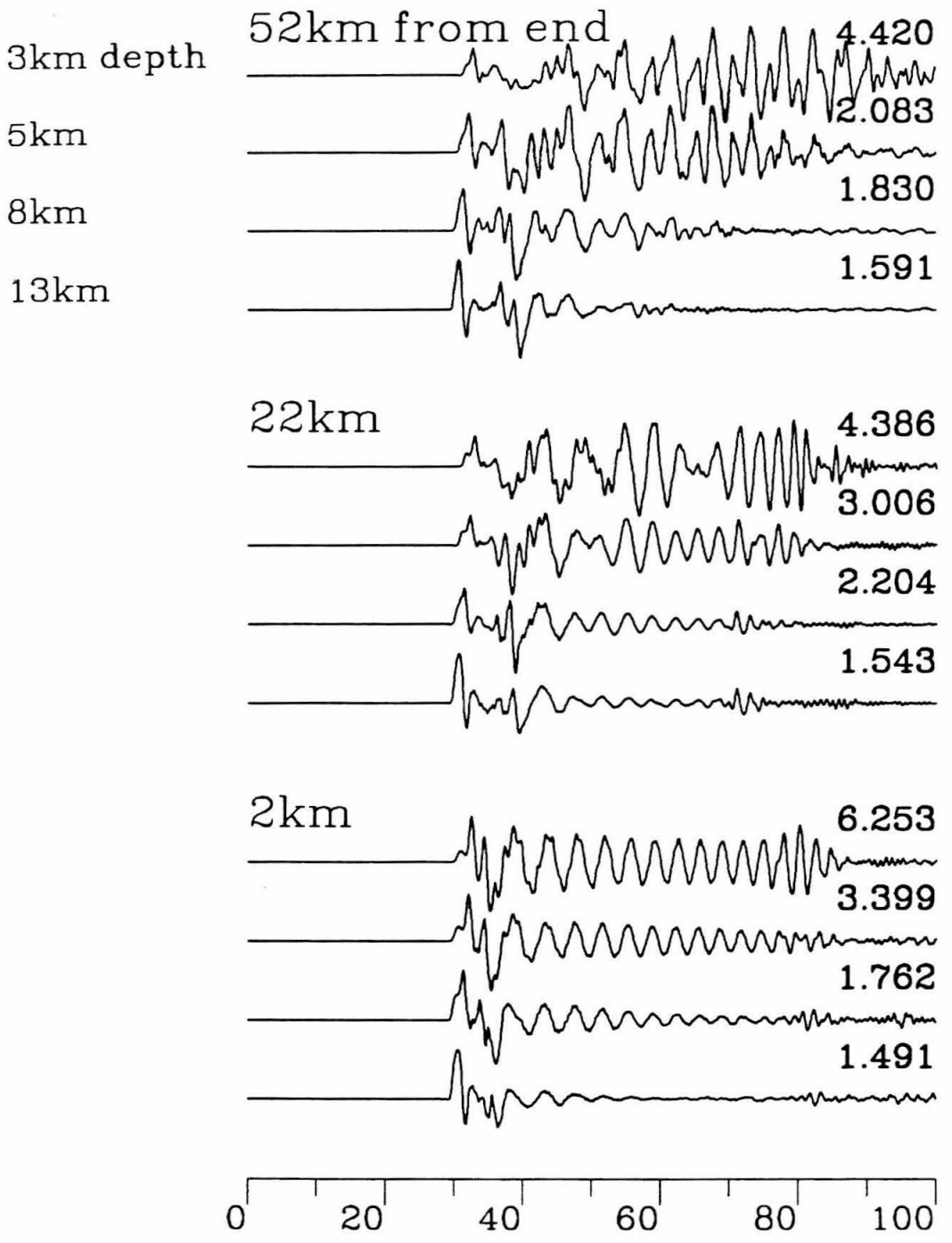

Figure 3.18 Regional synthetics for all source positions compared at one range, keeping all other variables constant. The range (source to receiver) here is 100 km. Because this is fixed, and the distance between the source and basin boundary varies, then the distance between the receiver and basin boundary varies in the opposite sense. Thus, not the receiver position, just the range, constant here. The mechanism is strike-slip with a moment of 10^{25} and the instrument is broad-band. This figure will be used as a reference for the comparisons in Figure 3.20.

cross-over distance for crustal phases changes (the mid-crustal head wave is not available for the deepest source which is below that interface). Thus, depth of the source should be resolved by examining the general character of the Love waves and modeling the initial SH-wave train (Sn, Sg and S) with an accurate layered model. The position of the source relative to the basin boundary is best examined by modeling the timing of the later S-multiples and some specific characteristics of the Love wave train (for example, duration and frequency content). Of course, modeling the Love wave train would be effective only for shallow sources, but Figure 3.18 shows that for a 3 km deep source, the Love wave is strongly dependent on the distance to the basin boundary. Figure 3.19 shows the corresponding teleseismic records for one take-off angle (15 degrees). Depth information is available in the separation between S and sS. Greater depth also seems to reduce the amount of scattered energy. This is due to the original amplitude of the Love waves being much smaller before encountering the basin boundary. At 2 km from the basin boundary, there is no apparent scattered energy. This is expected because the Love wave would not have the range necessary to develop before scattering occurs. At 52 km from the boundary, the scattered energy is quite late, approximately 30 to 50 seconds behind direct S, and is relatively low-amplitude. Again, this is due to the Love wave and its relation to the basin boundary. At a range of 52 km, the boundary is quite far from the source. Therefore, the amplitude has decayed substantially before encountering the basin boundary. The timing is correct for a Love wave traversing the slow basin. The greatest effect is for the source 22 km from the boundary. Substantial scattered energy begins to arrive within 10 seconds after direct S. This is consistent with the Love wave velocities for the model basin. The

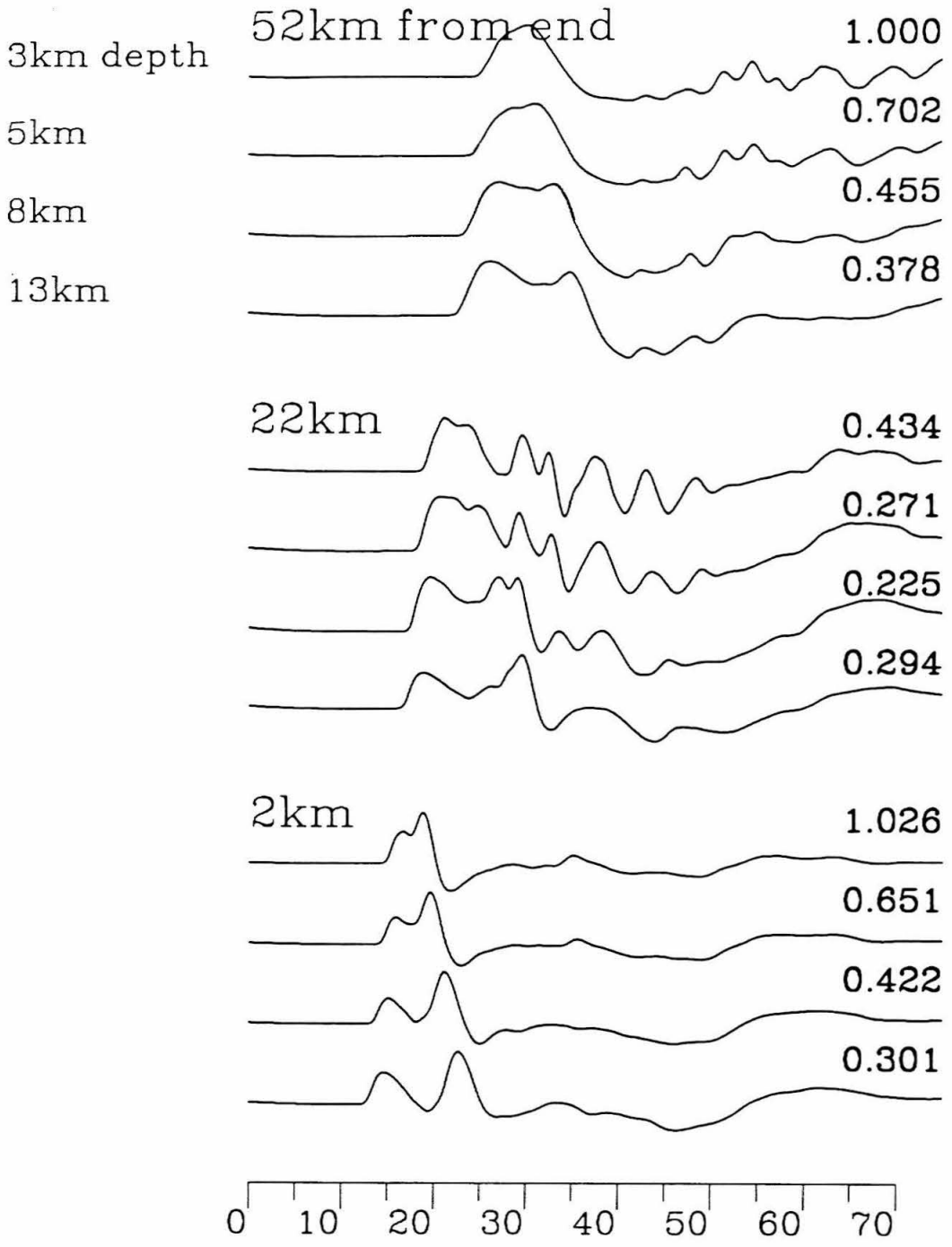

Figure 3.19 Teleseismic synthetics for all source positions compared at one take-off angle. The take-off angle here is 15 degrees. The mechanism is strike-slip; the attenuation used is T*=4. The instrument is long-period WWSSN. The traces are all scaled to the peak amplitude of the first trace. This figure will be used as a reference for the comparisons in Figure 3.21.

energy continues to affect the seismogram more than 30 seconds after direct S for the source at 3 km depth. Even the source below the basin shows obvious scattered energy, especially the broad peak following sS. In general, teleseismic work on basin-scattered SH will be restricted to a range of sources no closer to the basin boundary than the minimum distance required to form a Love wave, and at most 50 km from the boundary such that the Love wave retains sufficient energy for scattering to be observed against direct S.

At this point it is useful to explore the effects of range, instrument response, source mechanism and basin boundary geometry by comparison to the above observations from Figure 3.18. Figure 3.20 shows several collections of seismograms, each set up like Figure 3.18 but differing on some basic characteristic. Each collection is now examined in detail. The model for each is described only in how it differs from that of Figure 3.18, which has a steep-walled basin, a strike-slip mechanism (with a moment of 10^{25} dyne-cm), a broad-band response and a range of 100 km between the source and receiver.

Figure 3.20a shows the synthetics for the shallow-dipping basin boundary. Many traces show that much of the Love wave is more effectively removed by the gradual boundary. Yet, the first 10 to 15 seconds of each record is very similar to the steep-walled basin synthetics.

Figure 3.20b shows the synthetics at a range of 50 km. The source position 52 km from the basin boundary and 3 km deep shows that the Love wave in the basin structure is greatly amplified and much more dispersed. Note that since this difference disappears after the basin boundary, this energy is available to be scattered teleseismically. The effect of depth is less obvious in the first 10 seconds of the records at

Figure 3.20 Regional synthetics organized according to range, twelve source positions for each range, for a variety of cases. Each plot here shows all twelve source positions used in this study, 3, 5, 8 and 13 km depths, 2, 22 and 52 km from the basin boundary. The range (source-to-receiver distance) is held constant for each plot. Each plot may be compared to Figure 3.18 to learn the effect of a particular variable. One or two variables are changed in each case.

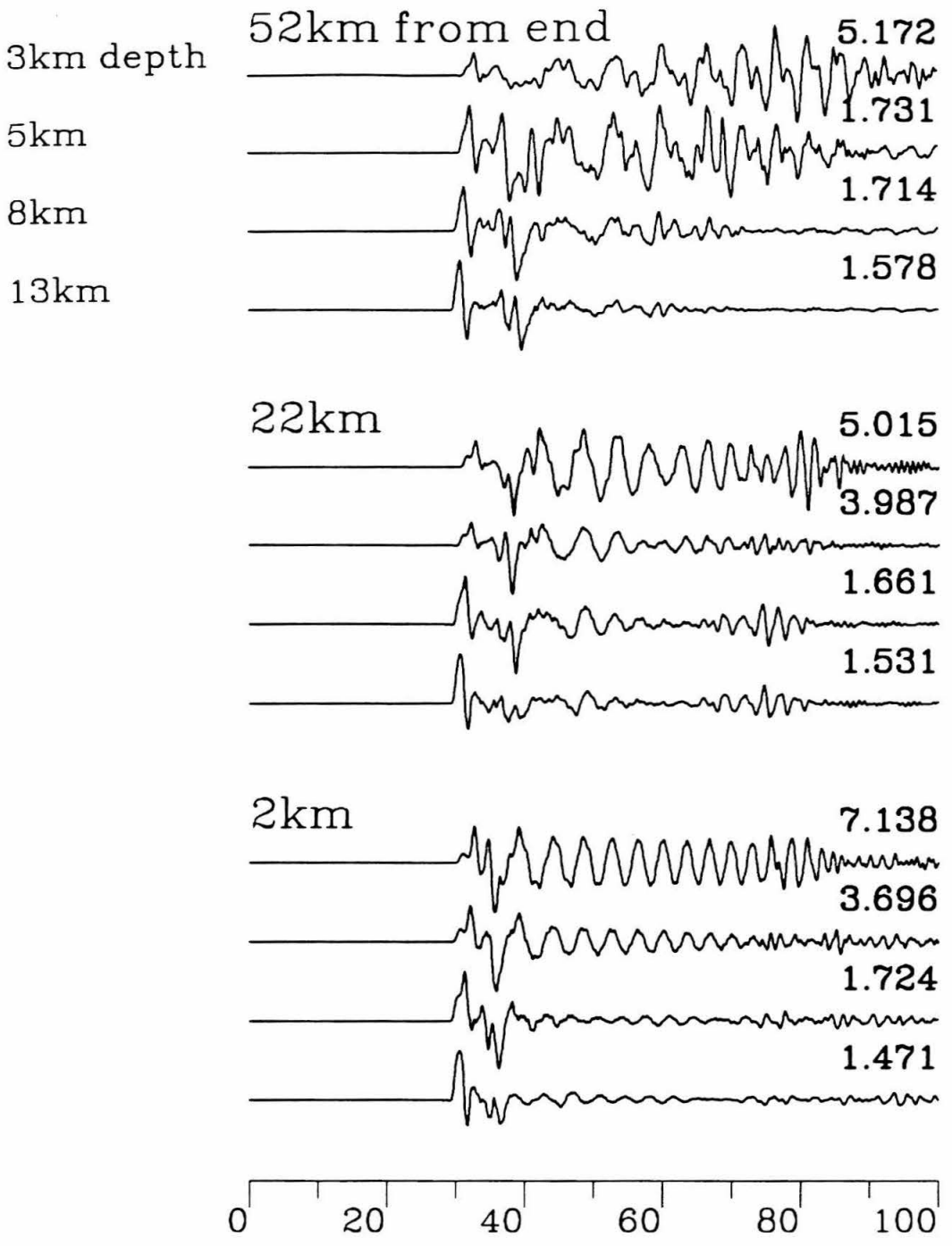

Figure 3.20 a) Effect of basin boundary dip. These synthetics are for the gradual boundary.

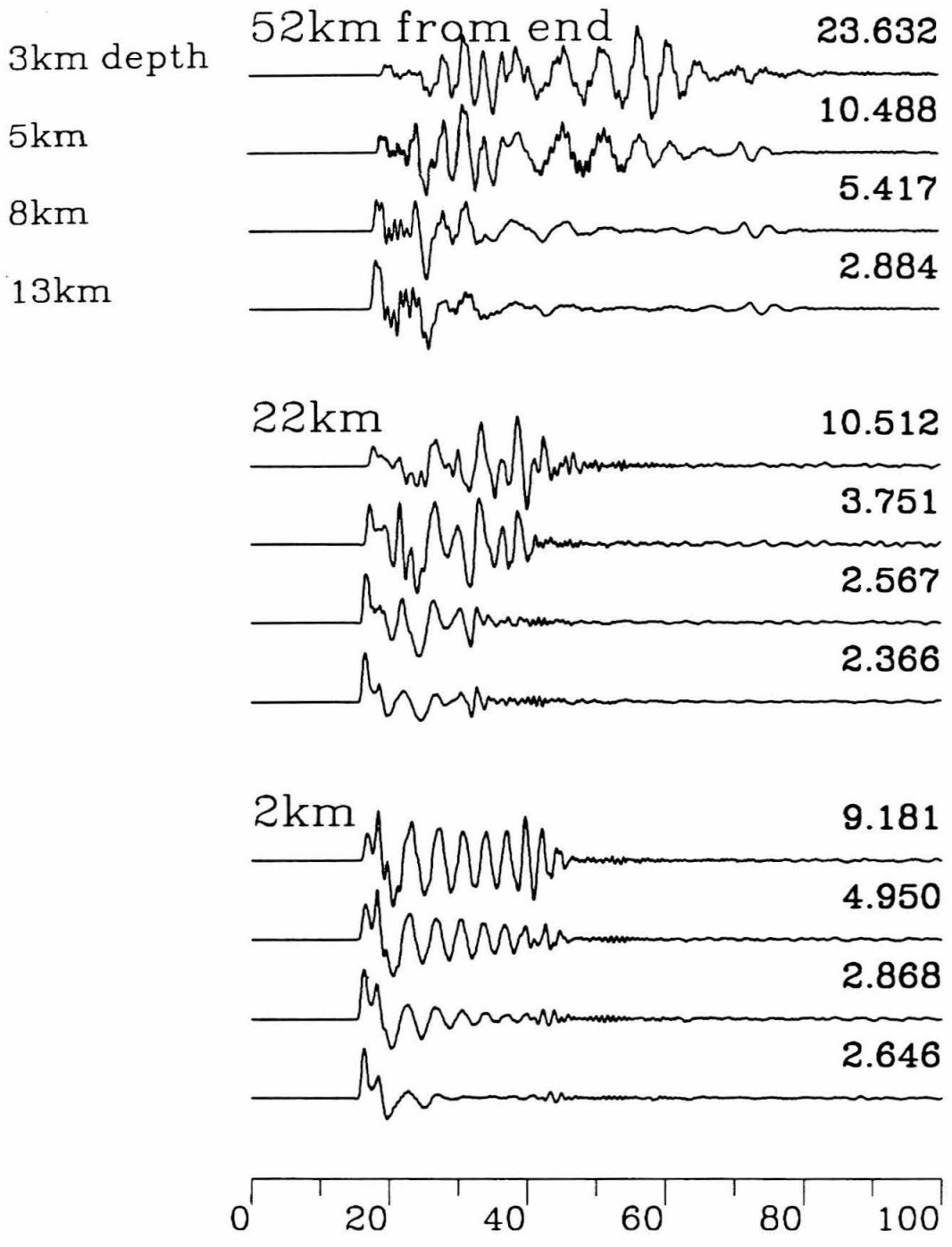

Figure 3.20 b) Effect of range. The range here is 50 km.

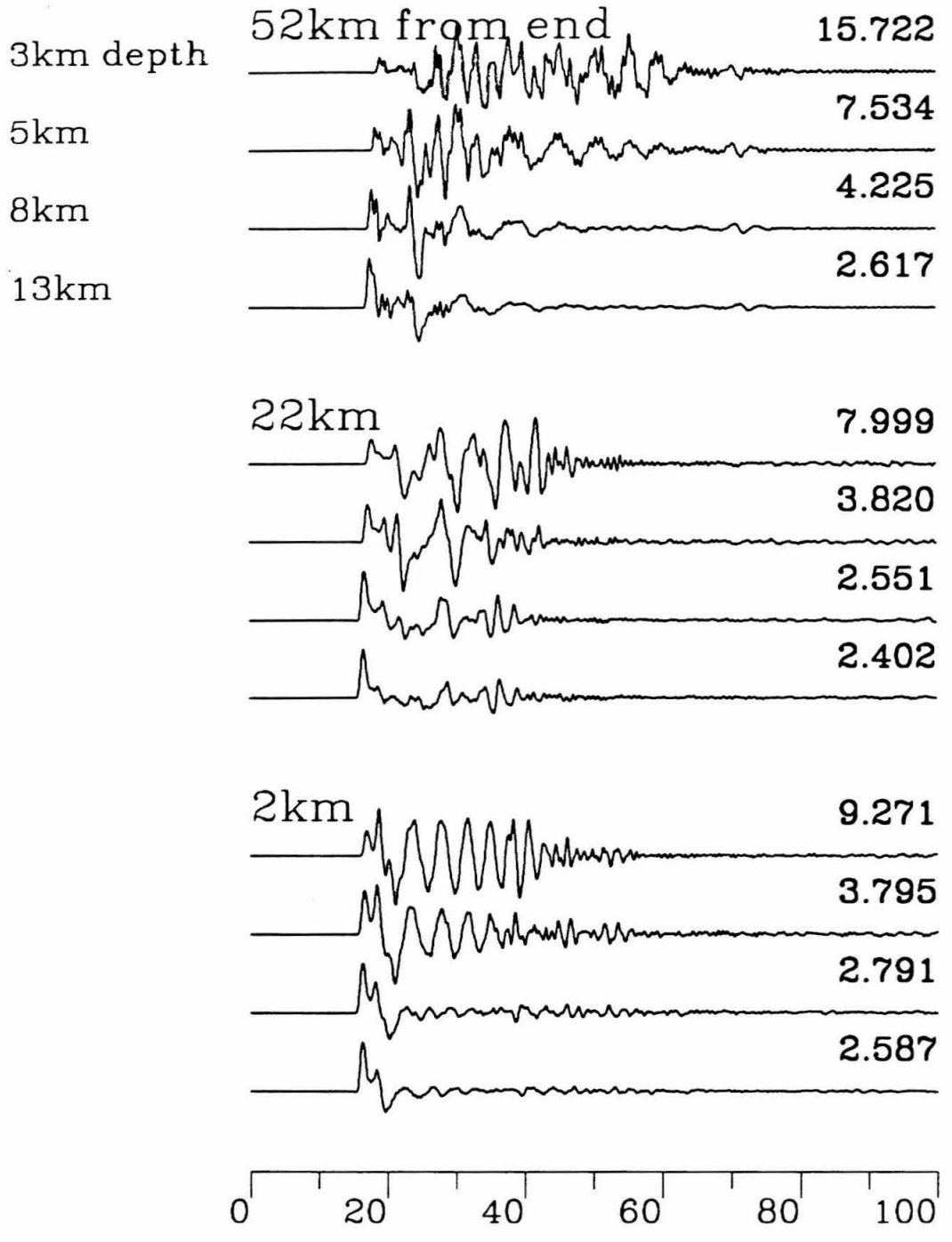

Figure 3.20 c) Effect of range and boundary dip. The range is 50 km and the boundary is gradual. Compare a) and b).

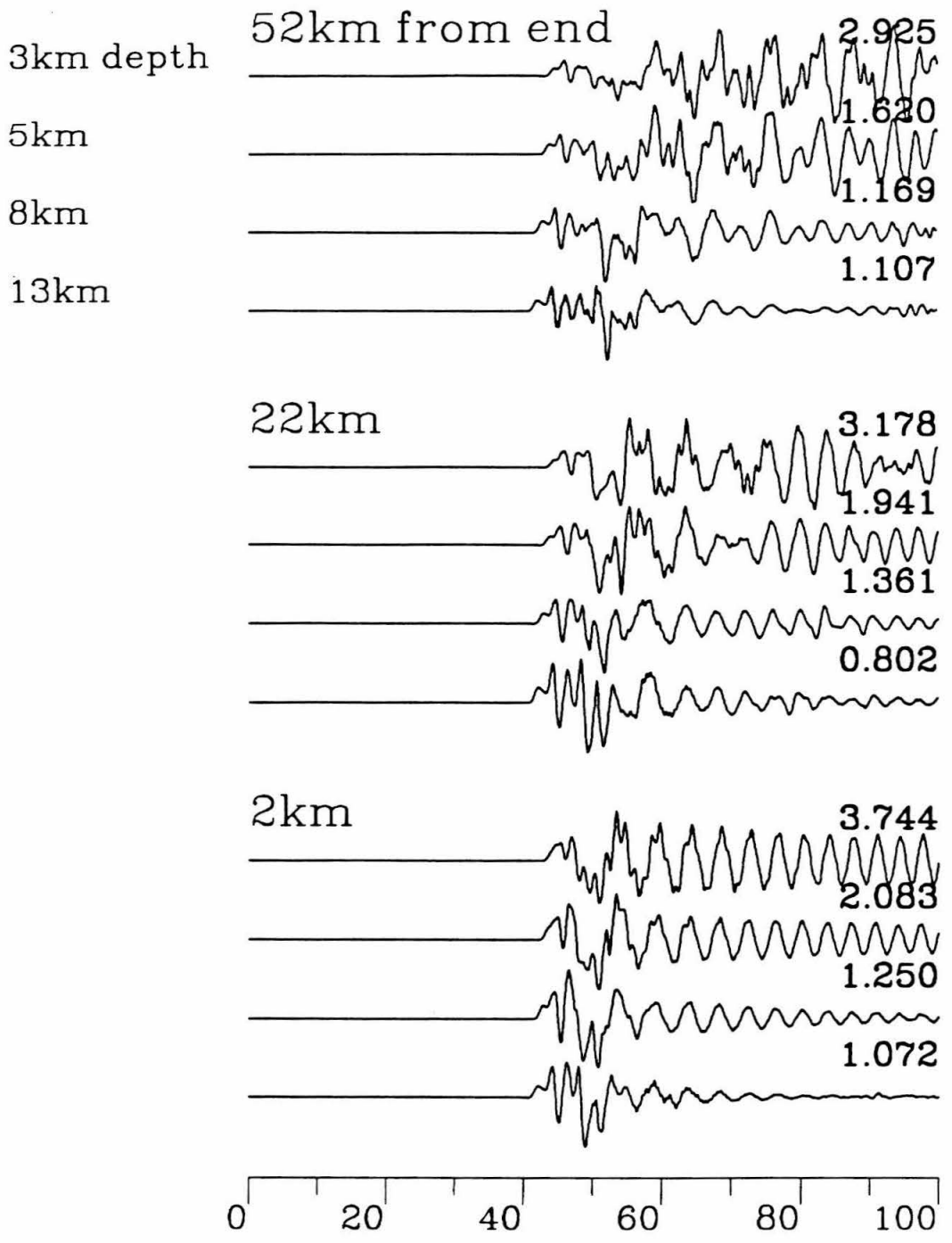

Figure 3.20 d) Effect of range. The range here is 150 km.

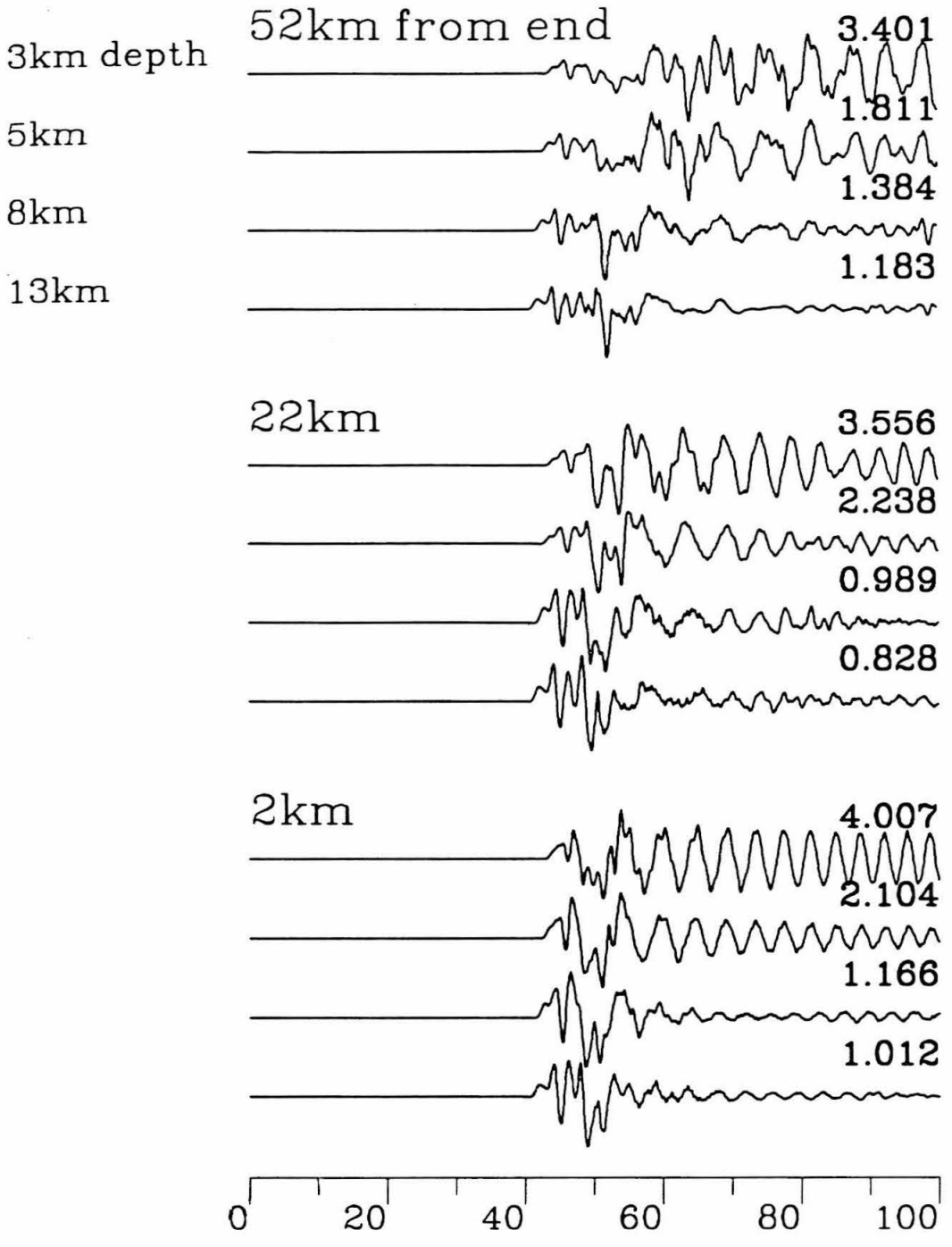

Figure 3.20 e) Effect of range and boundary dip. The range is 150 km and the boundary is gradual. Compare a) and d).

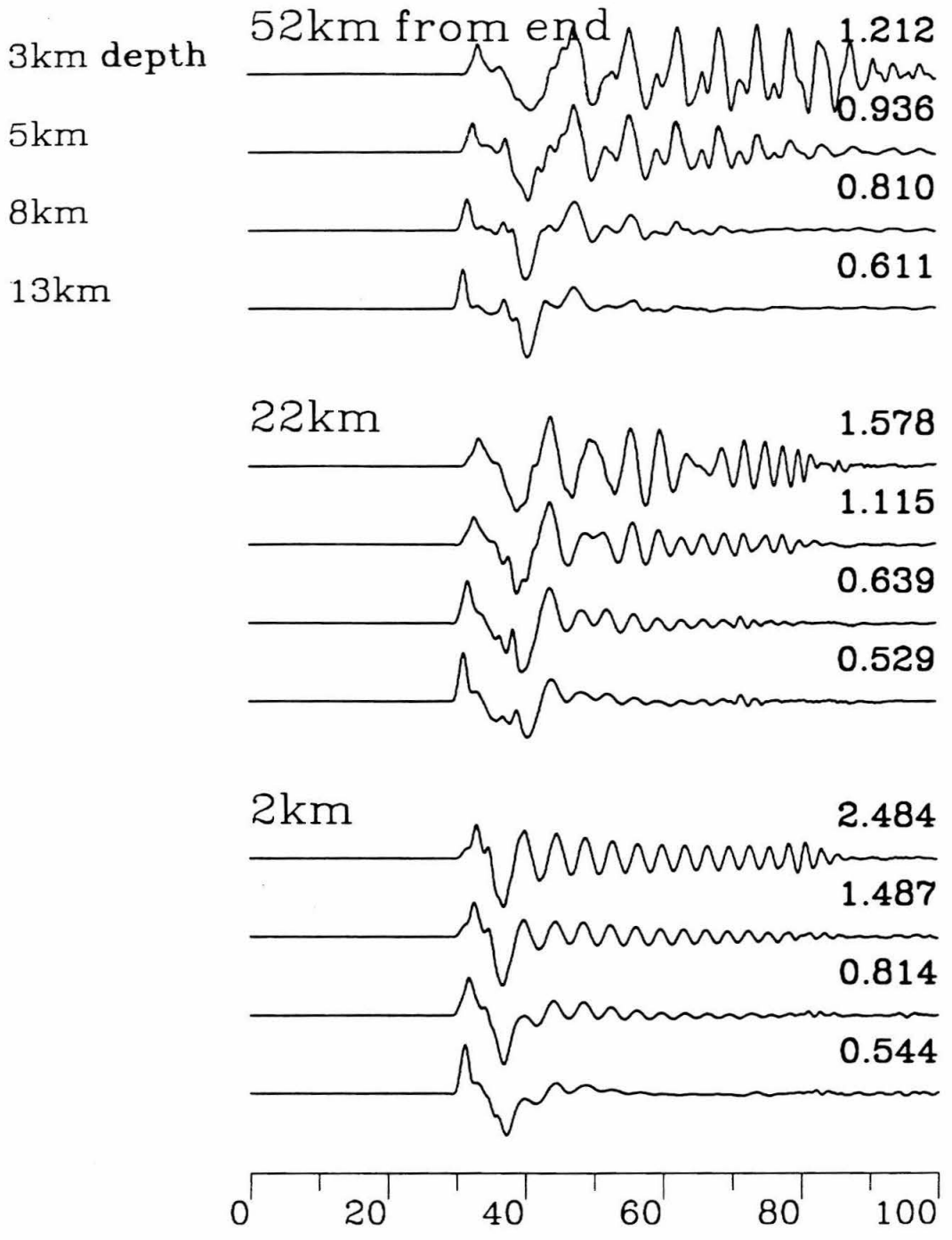

Figure 3.20 f) Effect of instrument response. The instrument here is a Press-Ewing 30-90.

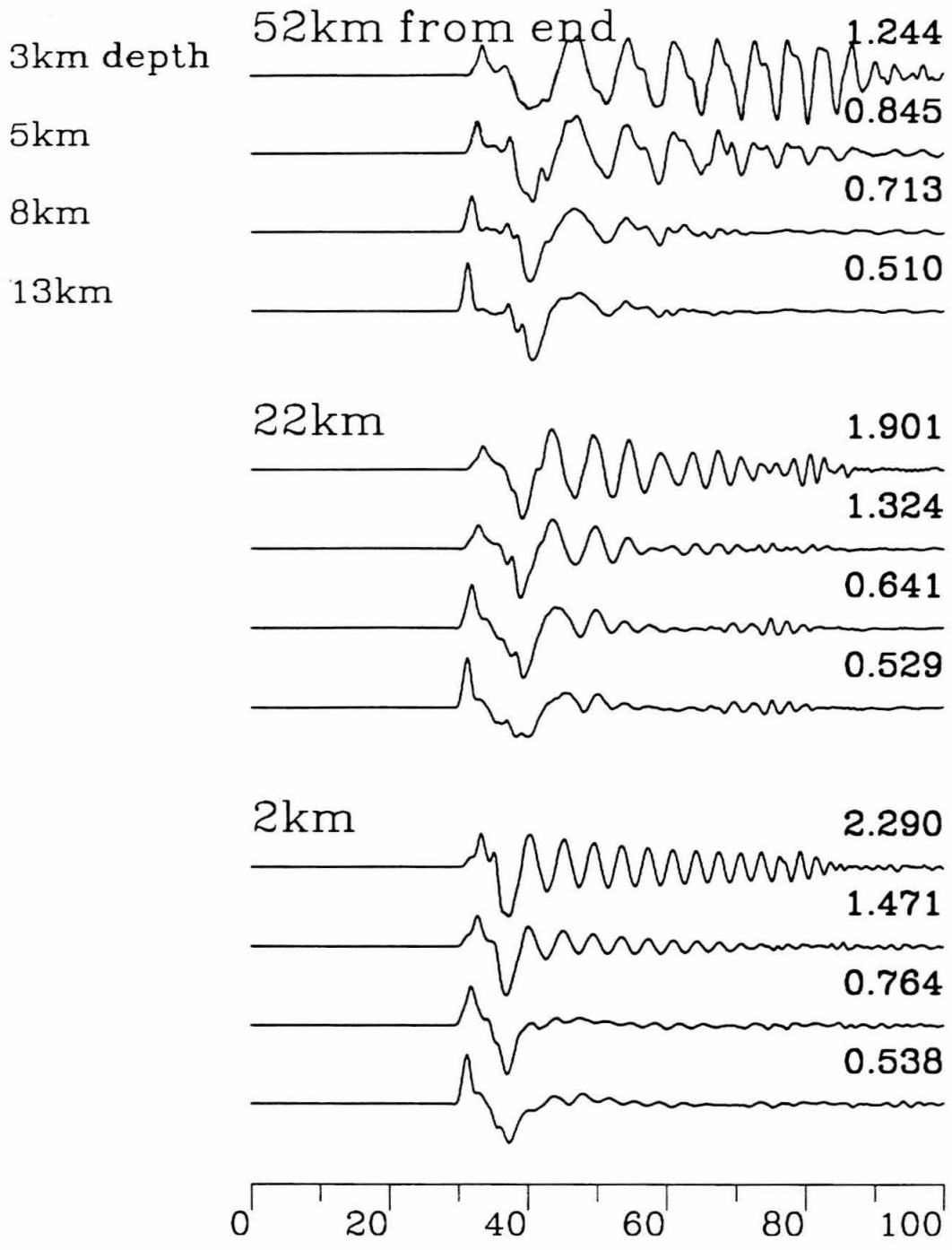

Figure 3.20 g) Effect of instrument response and basin boundary. The instrument here is a Press-Ewing 30-90; the boundary is gradual. Compare a) and f).

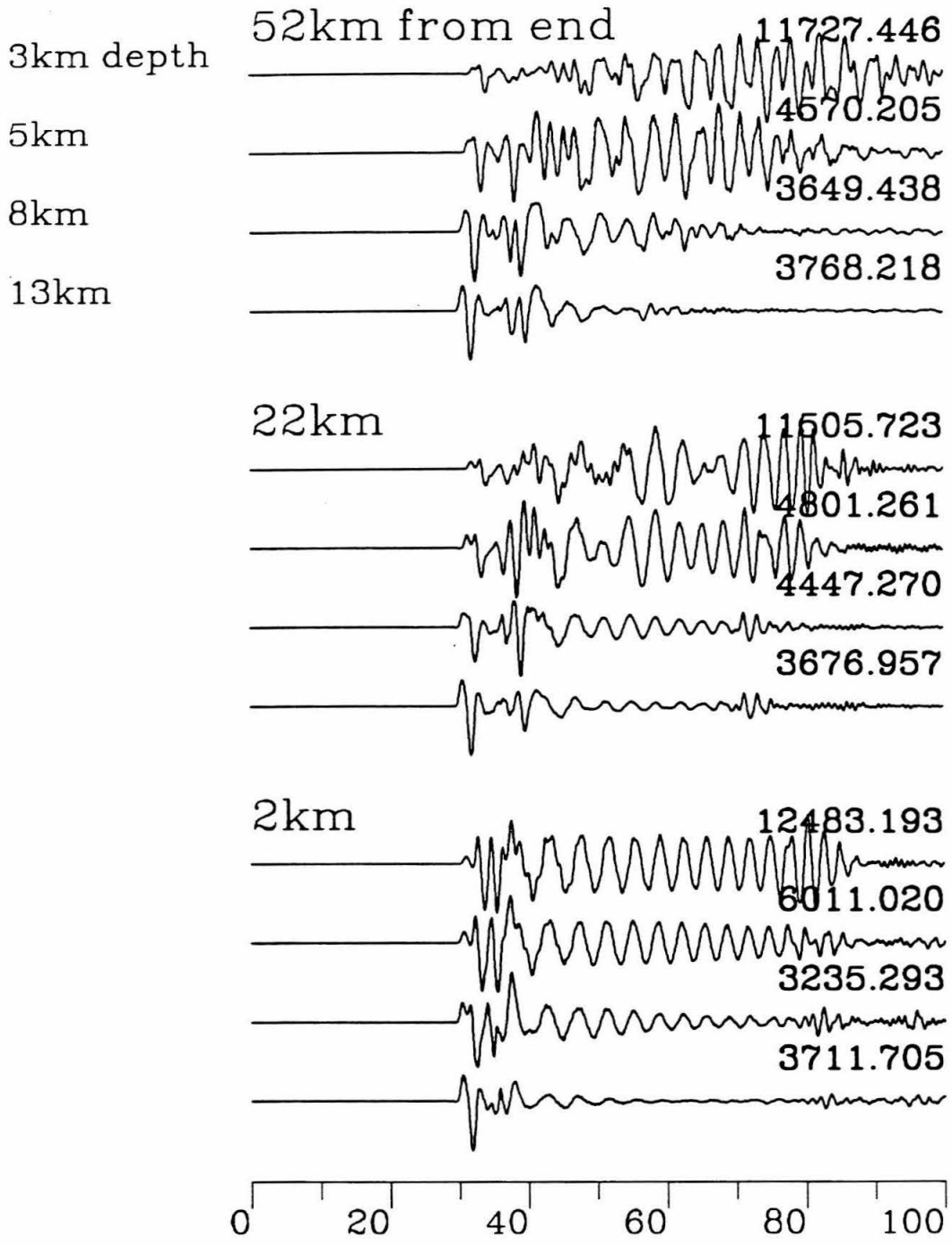

Figure 3.20 h) Effect of instrument response. The instrument here is a 6 second Wood-Anderson torsion.

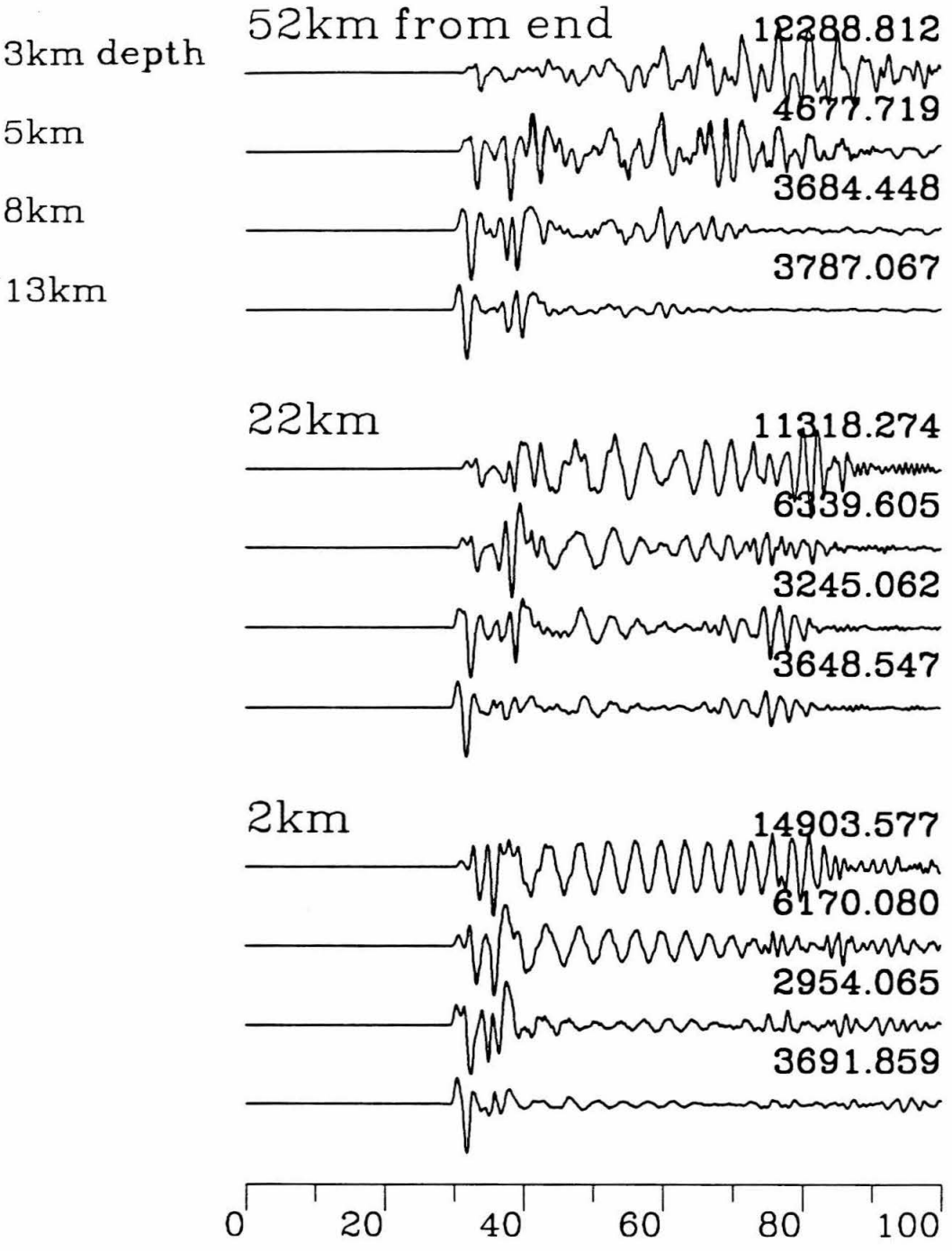

Figure 3.20 i) Effect of instrument response and basin boundary. The instrument here is a 6 second Wood-Anderson torsion; the boundary is gradual. Compare a) and h).

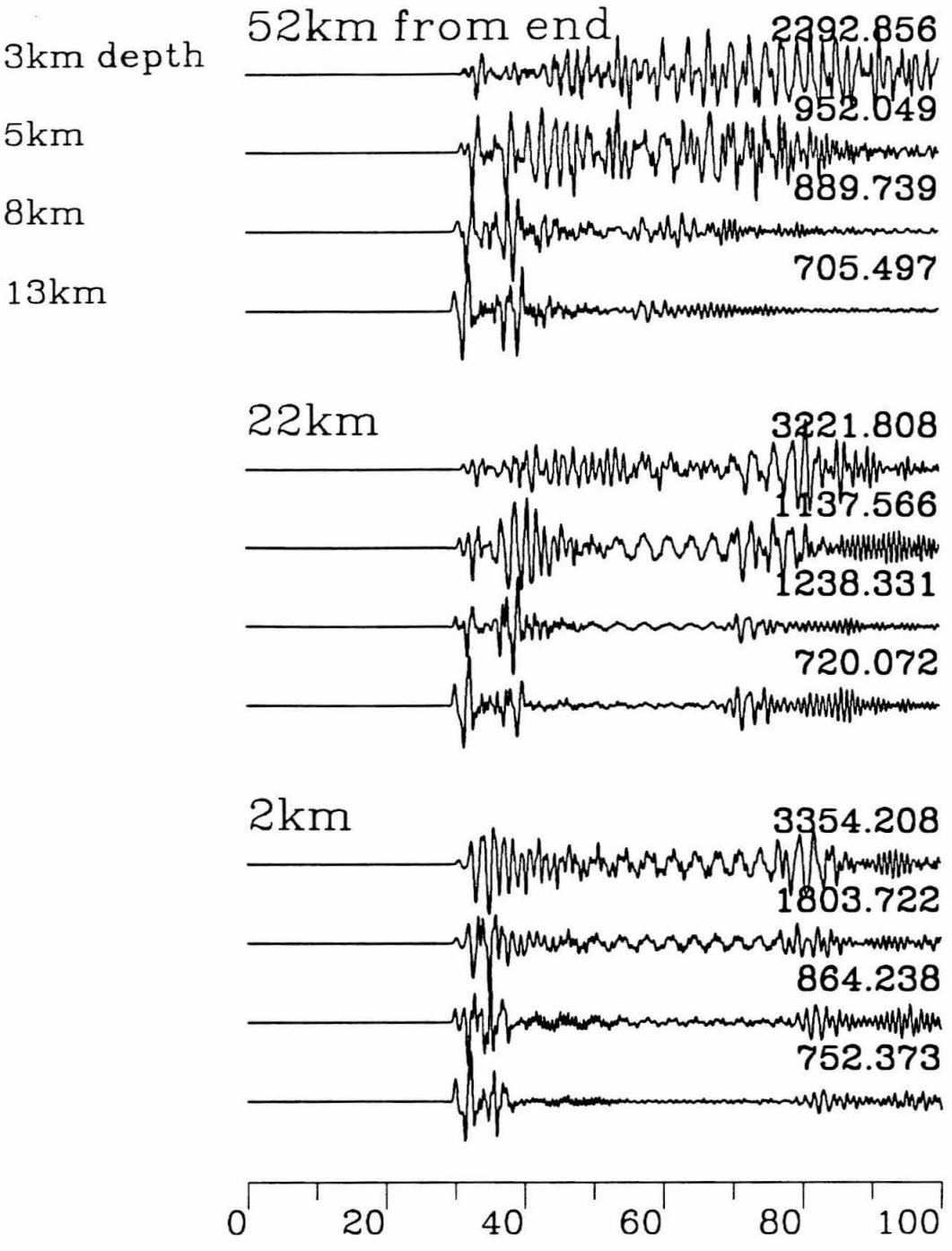

Figure 3.20 j) Effect of instrument response. The instrument here is a 0.8 second Wood-Anderson torsion.

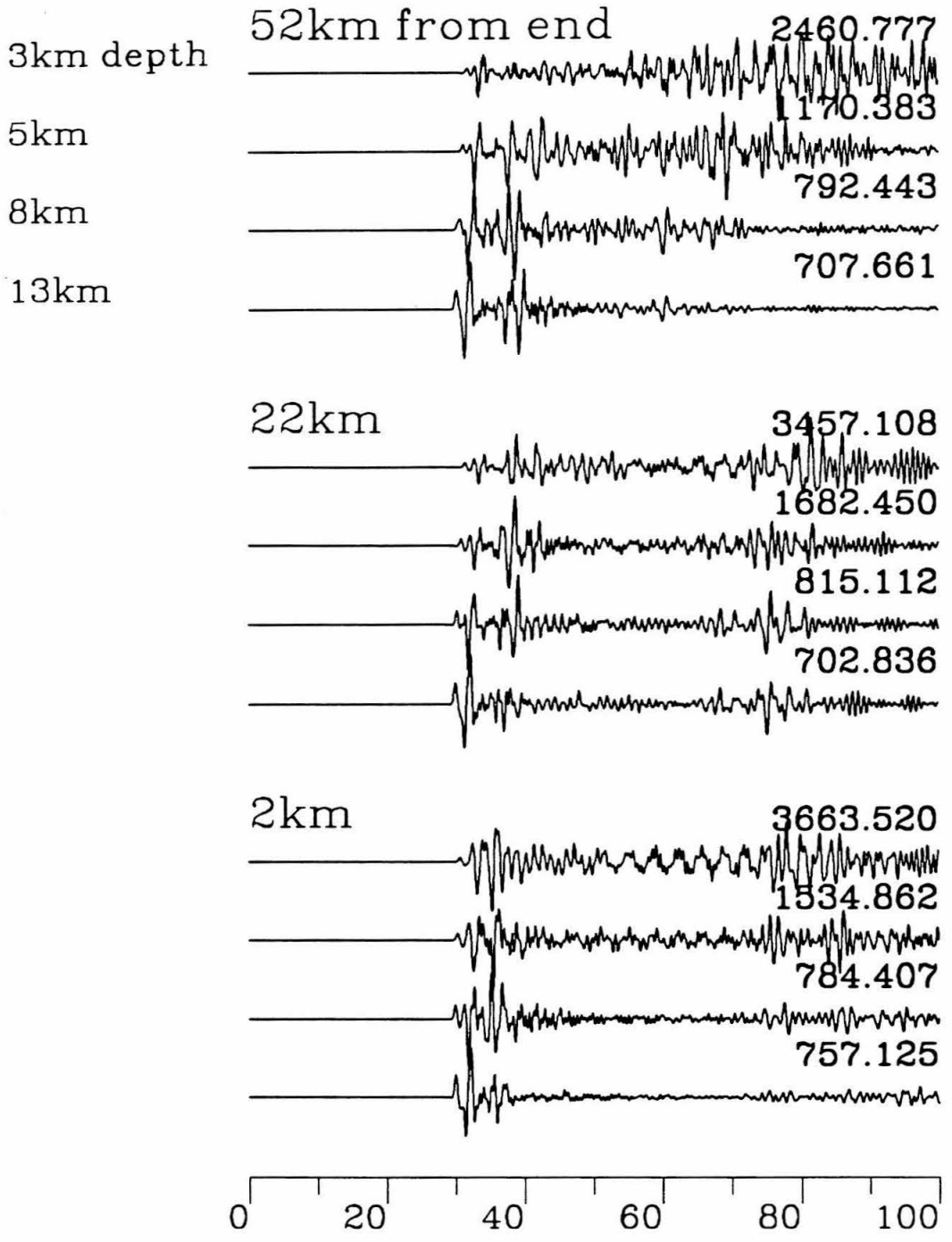

Figure 3.20 k) Effect of instrument response and basin boundary. The instrument here is a 0.8 second Wood-Anderson torsion; the boundary is gradual. Compare a) and j).

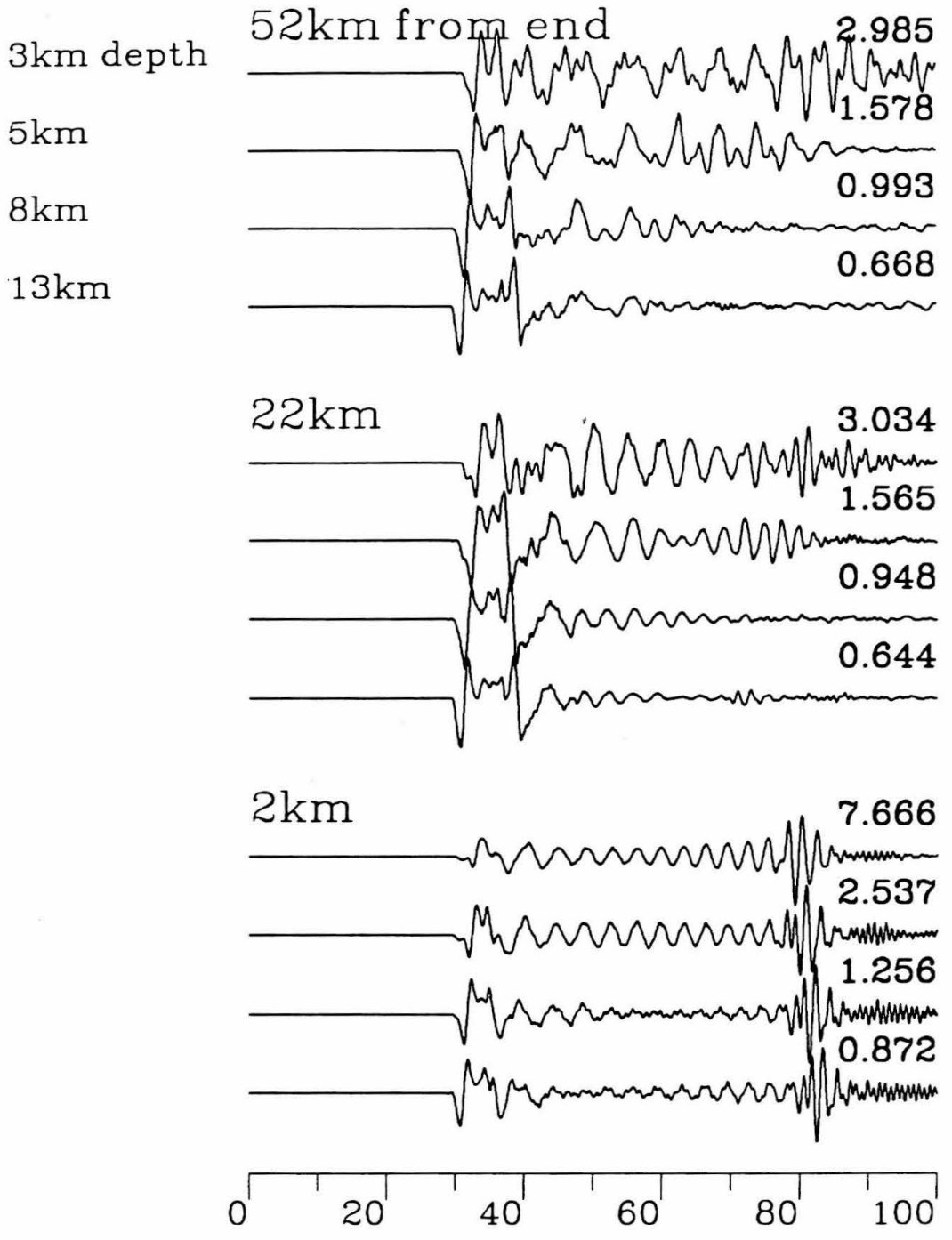

Figure 3.20 l) Effect of mechanism. The mechanism here is 90 degree dip-slip.

this range, mainly because of the lack of mid-crustal headwaves.

Figure 3.20c shows the synthetics at a range of 50 km for the gradual basin boundary. Comparing this to Figure 3.20b, we see that the longest periods have already begun to convert here at a range of 50 km from the source 52 km from the basin boundary. Also at 22 km, the waves 8 to 12 seconds back from the first arrival have been greatly affected, probably because of free surface multiples on paths intersecting the basin boundary.

Figure 3.20d shows the synthetics at a range of 150 km. The first observation is that at this range, we see Sn. The whole record is best interpreted in terms of the separate effects of the two flat-layered models as discussed above for Figure 3.8.

Figure 3.20e shows the synthetics at a range of 150 km for the gradual basin boundary. The differences between these records and Figure 3.20d is poorly resolved compared to the differences between Figures 3.20b and 3.20c. The differences are most apparent here at 8 km depth. Apparently, proximity to the basin bottom reduces the amplitudes of waves that mask the waves strongly affected by boundary geometry, at least in a relative sense. Nevertheless, it is clear that at greater ranges, the boundary geometry is poorly resolved. Of course, this may be interpreted as advantageous from a modeling perspective, since the shape of the basin boundary is no longer important.

Figure 3.20f shows the records filtered through a Press-Ewing 30-90 instrument. This is the longest-period instrument we use to examine seismograms at regional distances. The long-period response tends to wash out features in the first 10 to 15 seconds, which are important for depth

information. The distance of the source from the basin boundary is still well-resolved at these frequencies, primarily because the basin here is so slow and deep as to create a relatively large time difference for the later phases. A smaller, faster basin is not likely to be resolved at these frequencies.

Figure 3.20g shows the records for the gradual boundary filtered through a Press-Ewing 30-90 instrument. It is clear that the differences between this and Figure 3.20f are not resolved at these frequencies.

Figure 3.20h shows the records filtered through a 6 second Wood-Anderson torsion instrument. This instrument is relatively high-gain and an event of this size would clip it. The instrument response is flattest in a range of frequencies that overlap much of the frequency band contained in the original synthetics, so the waveforms very much resemble the broad-band results. Both the depth information and distance to the basin boundary are clearly resolved, both in the first 20 seconds and in the Love wave.

Figure 3.20i shows the records for the gradual boundary filtered through a 6 second Wood-Anderson torsion instrument. Compared to Figure 3.20h, the basin geometry is poorly resolved, primarily affecting the Love wave. The differences are completely unresolved for the sources 2 km from the boundary.

Figure 3.20j shows the records filtered through a standard 0.8 second Wood-Anderson torsion instrument. This is the shortest-period instrument from which we attempt to model regional seismograms. Although higher-frequency instruments are available, even at these frequencies the information is easily lost in the many swings of the pen. Because of this

confusion and the inevitable contamination of noise and off-azimuth phases, we must infer that the distance between the source and the basin boundary is poorly resolved. The depth is still resolved because that information is contained in the first few swings of the pen.

Figure 3.20k shows the records for the gradual boundary filtered through a standard 0.8 second Wood-Anderson torsion instrument. Compared to Figure 3.20j, the differences between the two models are readily apparent, but it would be difficult to measure or attribute to particular structure.

Figure 3.20l shows the records for a dip-slip mechanism. In these records, it appears that the mechanism could be resolved from a single trace. This would be due to the difference in polarity between the up-going and down-going rays. Depth is well-resolved, as is distance from the basin boundary.

Having explored the range of variables for the regional records, we now turn to the teleseismic synthetics. For this analysis, Figure 3.21 contains several collections of synthetics to explore the effects of the variables at teleseismic ranges. As above, these will be compared to Figure 3.19, and only the variables that change will be discussed. Figure 3.19 is for a strike-slip event in the steep-walled basin, recorded on a long-period WWSSN instrument at a take-off angle of 15 degrees. All the synthetics include an attenuation operator with $t^*=4$. Each plot is separately normalized to the amplitude of the first trace on the plot. The relative amplitude of the first trace on each plot to the first on Figure 3.19 is given in the captions.

Figure 3.21a shows the synthetics for the gradual basin termination. Only the sources at 3 and 5 km depth at a distance of 22 km from the basin

Figure 3.21 Teleseismic synthetics organized according to take-off angle, twelve source positions for each take-off angle, for a variety of cases. Each plot here shows all twelve source positions used in this study, 3, 5, 8 and 13 km depths, 2, 22 and 52 km from the basin boundary. The take-off angle is held constant for each plot. Each plot may be compared to Figure 3.19 to learn the effect of a particular variable. One or two variables are changed in each case.

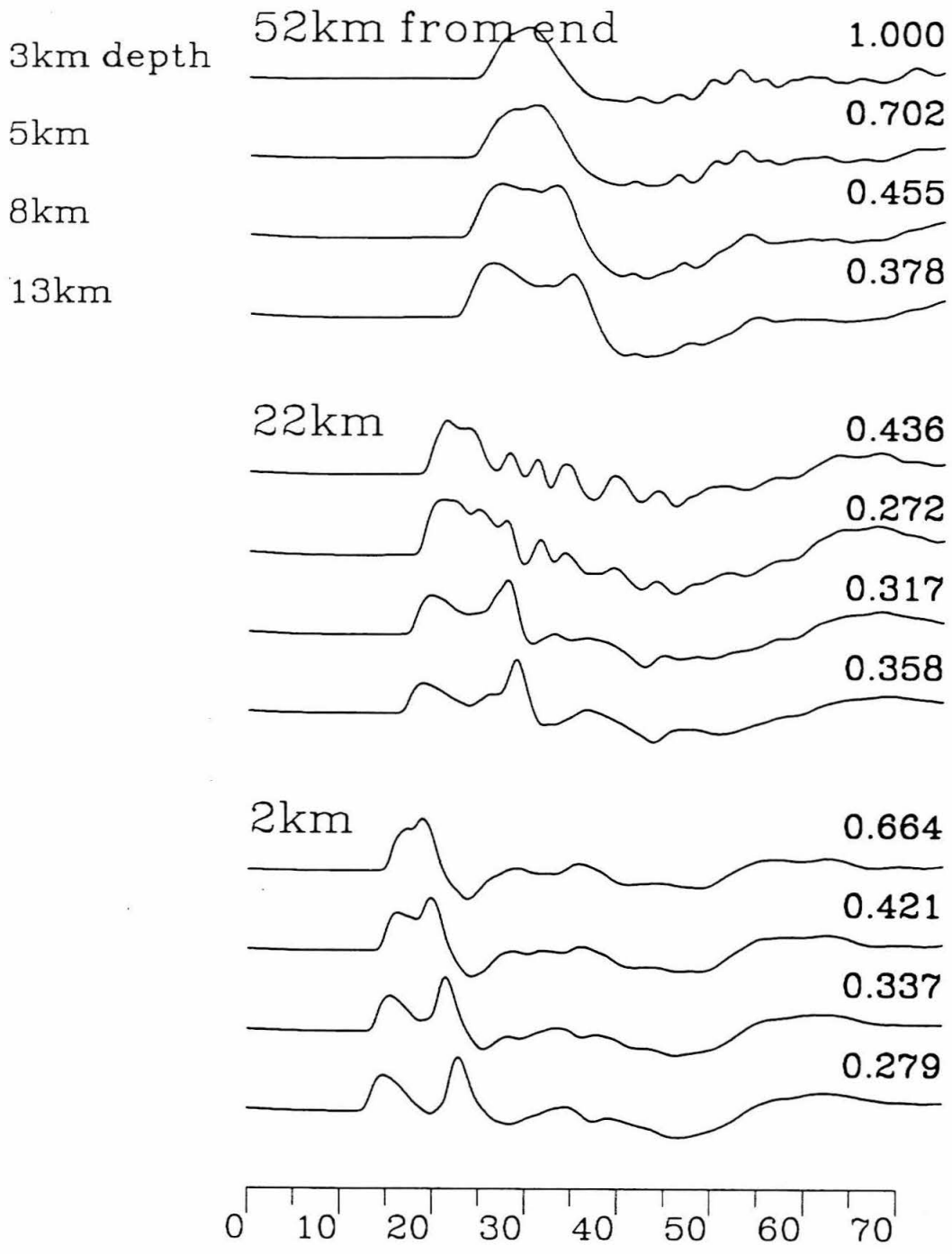

Figure 3.21 a) Effect of basin boundary dip. These synthetics are for the gradual boundary. The peak amplitude of the first trace is 0.9999 times that of the first trace in Figure 3.19.

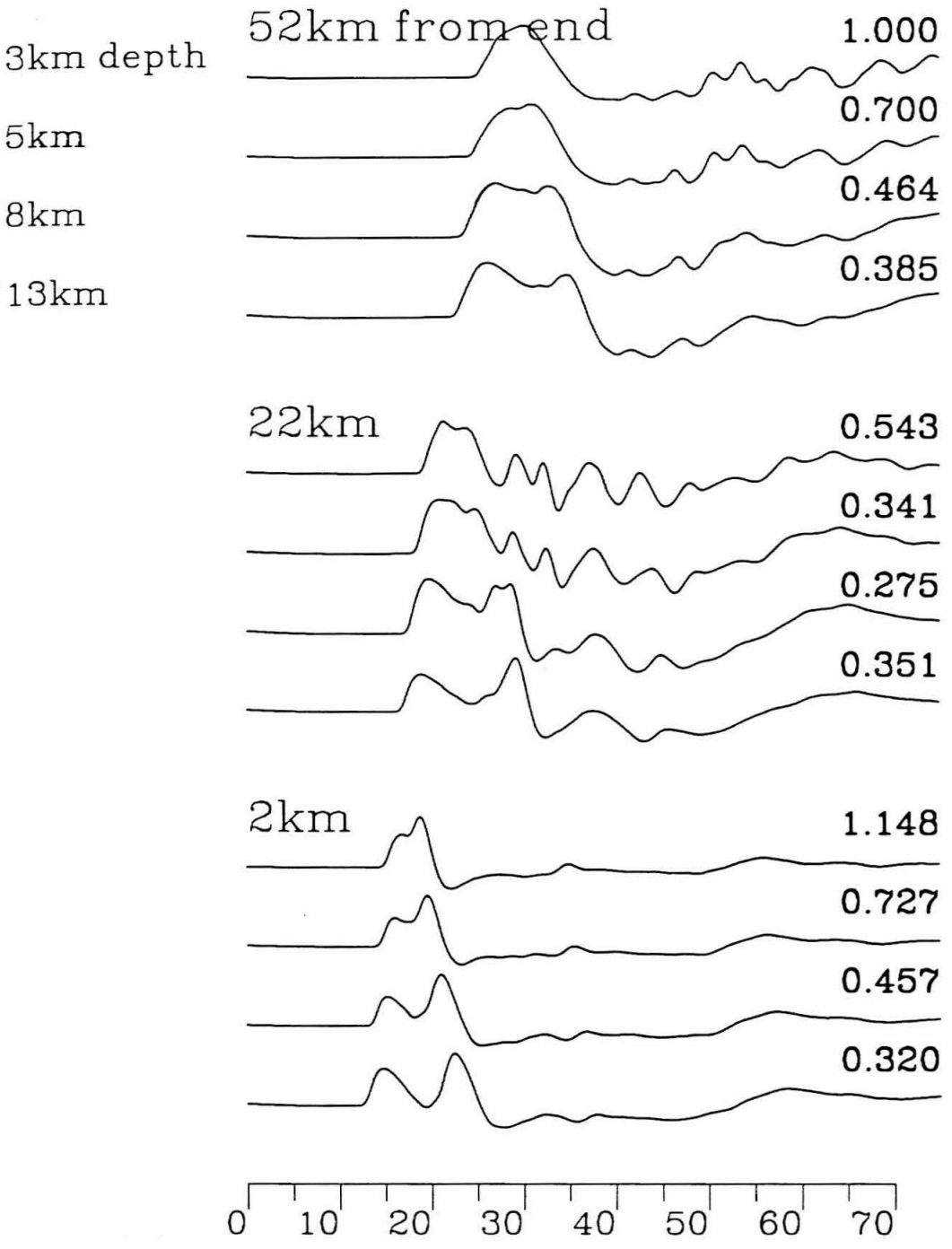

Figure 3.21 b) Effect of take-off angle. The take-off angle here is 20 degrees. The peak amplitude of the first trace is 1.06 times that of the first trace in Figure 3.19.

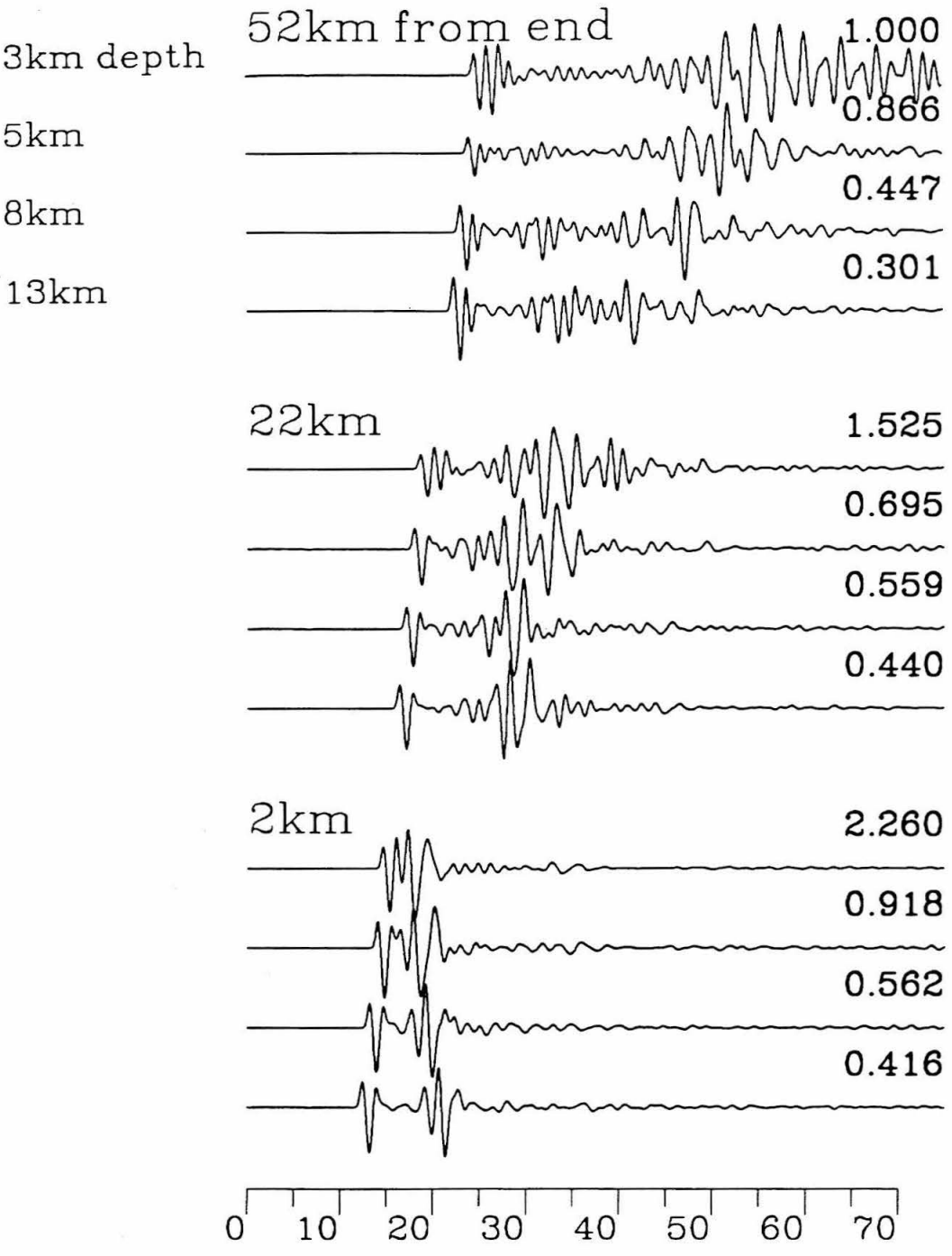

Figure 3.21 c) Effect of instrument response. The instrument here is a WWSSN short-period. The peak amplitude of the first trace is 0.0046 times that of the first trace in Figure 3.19.

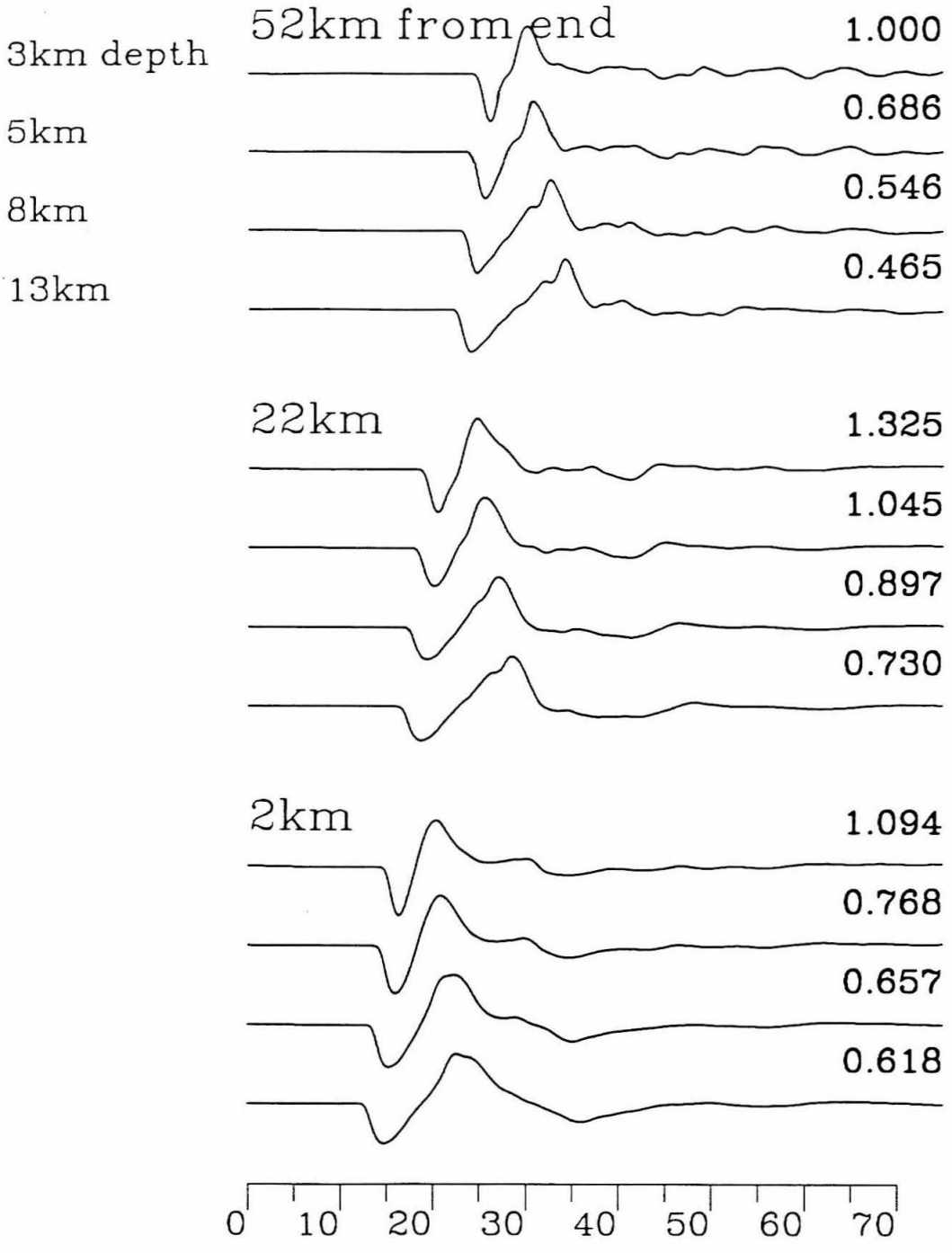

Figure 3.21 d) Effect of mechanism. The mechanism here is 90 degree dip-slip. The peak amplitude of the first trace is 1.75 times that of the first trace in Figure 3.19.

boundary can resolve the effect of boundary geometry. The effect is that steep boundaries produce more scattered SH than shallowly dipping boundaries. Apparently, the Love wave is more effective at crossing a gradual than an abrupt boundary.

Figure 3.21b shows the synthetics for a take-off angle of 20 degrees. The effect of varying take-off angle by a few degrees is negligible. Even the synthetics for 22 km offset are very similar at 15 and 20 degrees.

Figure 3.21c shows the effect of using a short-period WWSSN response. Normally, this information would be unavailable because the attenuation is so strong in the frequency range of the instrument's peak response. Therefore, noise normally dominates the S waves on this instrument at teleseismic distances. For very large events, or events that partition an unusual amount of energy into teleseismic SH, SH body phases may be observed on short-period instruments at the best sites. If such are available, it is seen in these synthetics that scattered energy will dominate the record even for an offset of 52 km.

Figure 3.21d shows the synthetics for a dip-slip source. It is noted here that the first trace of this series has a peak amplitude 3.2 times as great as that of the first trace in Figure 3.19. This contrast is due to the radiation patterns. The strike-slip mechanism is nodal along the vertical axis through the source, while the dip-slip mechanism has a peak in the radiation pattern there. So, the direct SH is much stronger for this mechanism and tends to swamp the small scattered phases. This is most obvious for the source 22 km from the boundary. The effect is made even stronger because the dip-slip mechanism is nodal along its horizontal axis, which reduces the amplitude of the Love waves. The strike-slip

mechanism has a peak there. Nevertheless, scattered energy is still plainly visible for the source at 52 km from the boundary. This is due to Love waves forming from energy at take-off angles far from horizontal, both up and down.

3.4 Comparison to the P-SV system

Now that the fundamental features of the SH synthetics are understood, we extend the analysis to P-SV synthetics. Regional FD synthetics, both radial and vertical components, for the five models (half-space, two flat-layered models and two basin models) are shown in Figure 3.22. This figure is comparable to Figure 3.3, using the same source depth (13 km), source offset from the basin boundary (52 km), and range to receiver (100 km). The mechanism is strike-slip, the instrument response is broad-band, and the moment is 10^{25} dyne-cm. Immediately, the comparison to the SH synthetics demonstrates the greater complexity of the P-SV synthetics. In addition, there is little comparison between the half-space result and any of the other synthetics. Because the half-space model does not provide much assistance in interpreting the synthetics from other structures, we do not use it for the comparisons below.

In Figure 3.23, the radial and vertical synthetics for the sharp basin termination are compared to those for both the flat-layered normal crust and the flat-layered basin crust. Since the source is located about 52 km from the basin boundary, the basin synthetic at 50 km range is almost identical to the synthetic for the flat-layered basin structure. The small difference is due to energy reflected from the steep basin boundary. At ranges of 100 and 150 km, the basin synthetics show more features of the flat-layered normal crust.

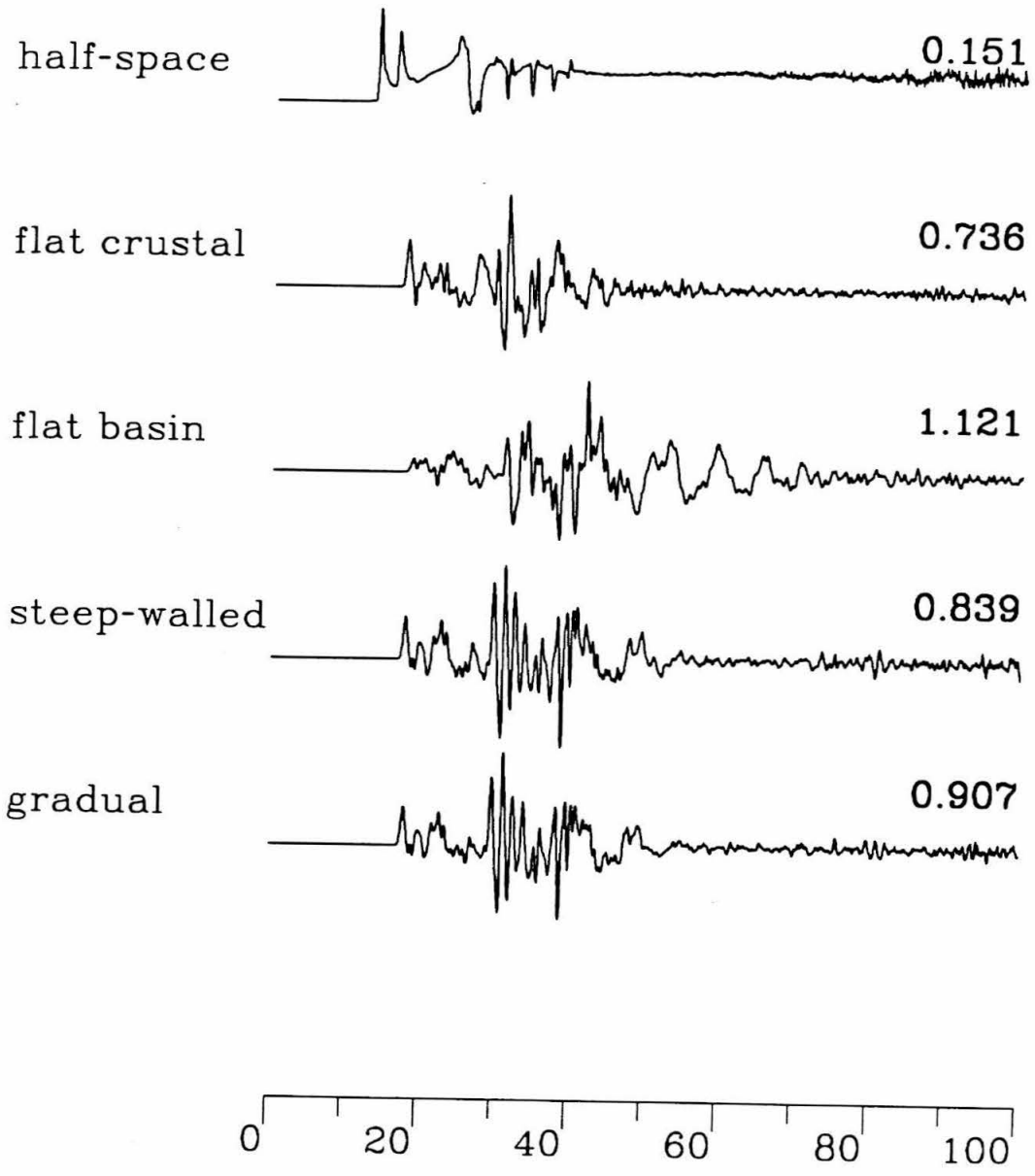

Figure 3.22 A comparison of the synthetics at 100 km range from all five models presented in Figure 3.1. The source depth is 13 km, at 52 km from the basin boundary. The mechanism is pure strike-slip and the moment is 10^{25}. The instrument response is broad-band, limited only by the maximum frequency allowed in the FD grid (about 2 Hz here). Peak amplitudes are in cm; time is in seconds. Two components are shown:
a) the radial component and

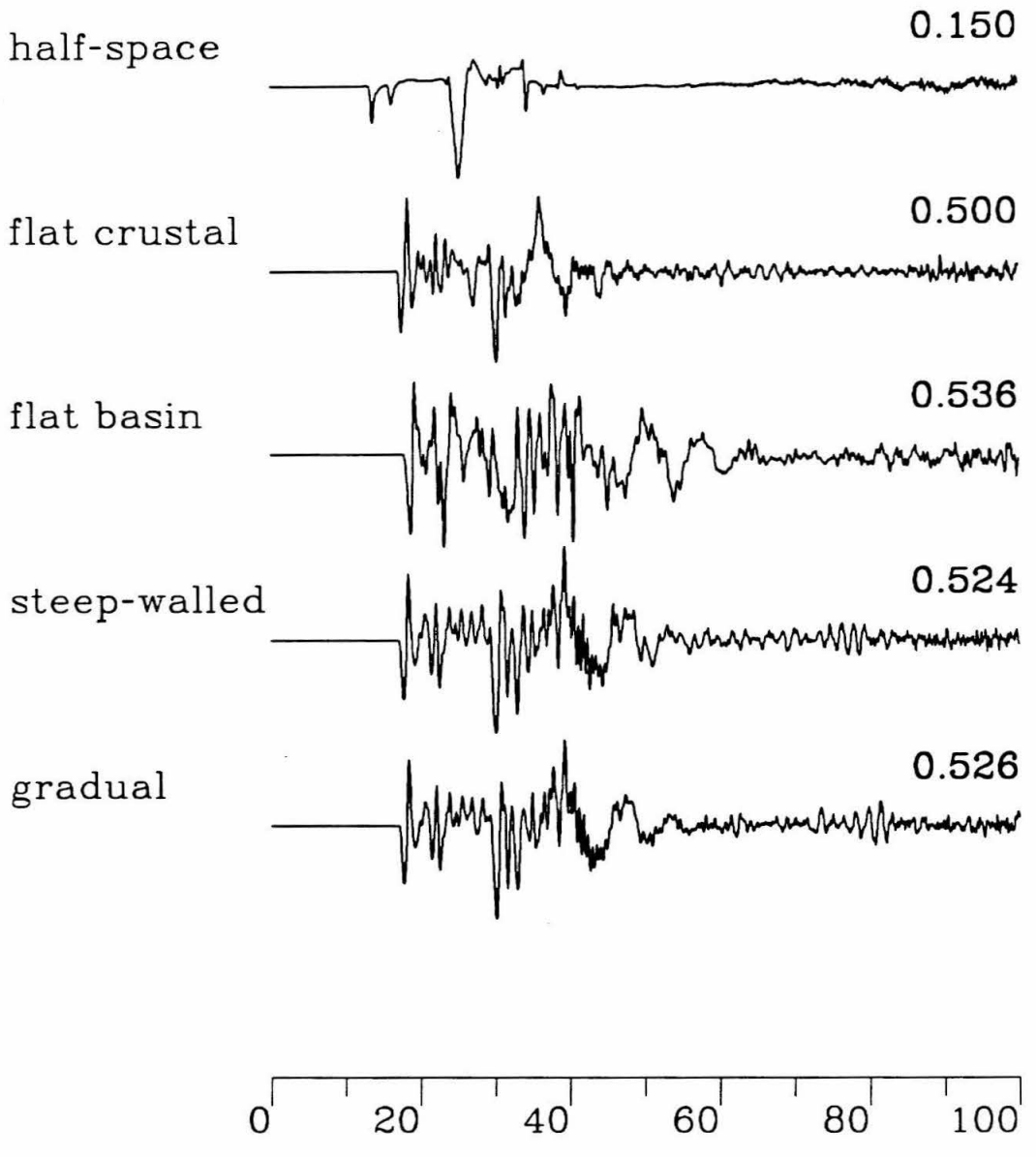

Figure 3.22 b) the vertical component.

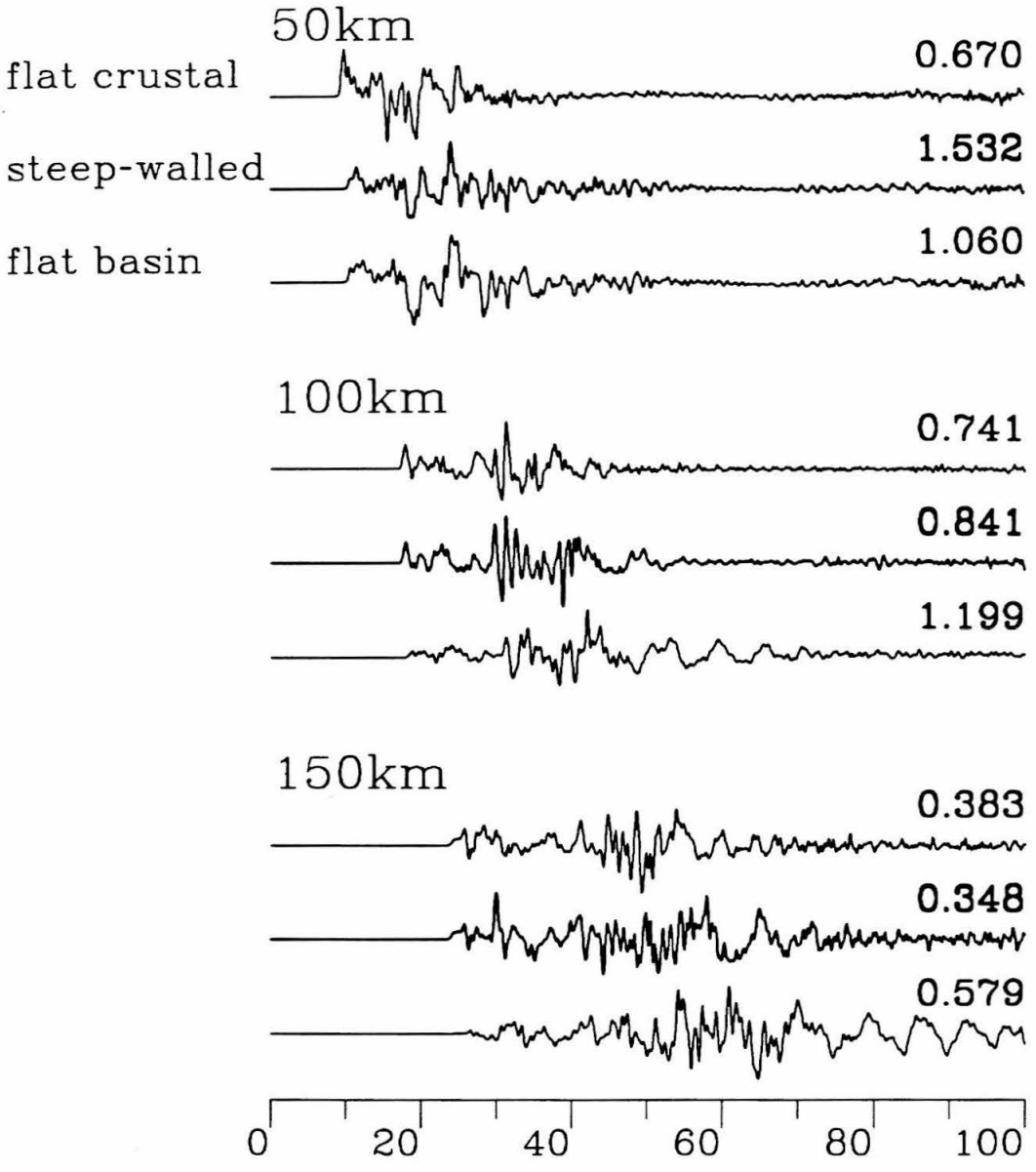

Figure 3.23 A comparison of the regional synthetics for the steep-walled basin structure and both flat-layered structures. The source location, mechanism, moment and instrument response are the same as Figure 3.22. Three ranges are shown, 50 100 and 150 km.
a) the radial component and

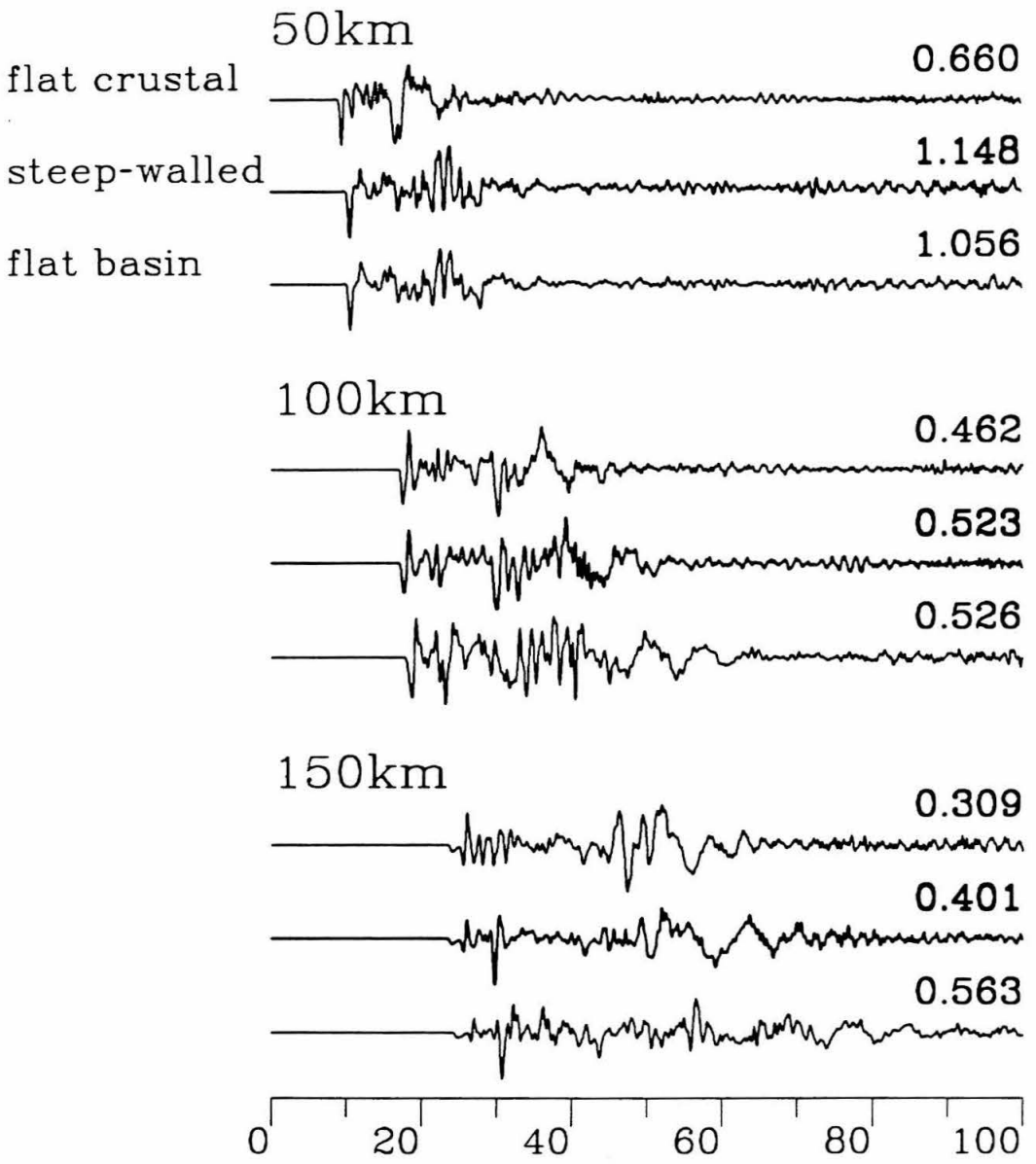

Figure 3.23 b) the vertical component.

This is particularly true of the Rayleigh wave duration and the first five seconds of the P wave. Contrary to what is observed for the SH synthetics, the basin synthetics for the P-SV system are not primarily due to one of the two flat-layered structures. Instead, there is an apparent progression from the flat-layered normal crust through the steep-walled basin model to the flat-layered basin model. While it may be possible to derive an intermediate flat-layered structure that would mimic the synthetics of the laterally varying model, it is unlikely that such a model would work at all ranges. This is because some features of the synthetics for the laterally varying model are dominated by the basin structure, some by the normal crust, and others are affected to varying degrees by both. For example, the shape of the first few swings of the Rayleigh wave is similar to that for the crustal structure, but its timing and duration are intermediate between the two flat-layered structures. The initial P-wave is identical to that for the crustal model, but the SV-wave resembles the synthetics of neither one of the two flat-layered models. Therefore, it is less likely here than in the SH case that flat-layered structures can be used to produce an accurate model of the propagation effects and structure. The same comparison is shown for a shallow source (3 km) in Figure 3.24. Here, the synthetics for the steep-walled basin bear little resemblence to either of the flat-layered models, at the ranges 100 and 150 km. (The synthetics at 50 km, for the steep-walled basin and the flat-layered basin model, are once again nearly identical, since the receiver is 2 km in front of the basin boundary.) Part of the interpretation may be that the Rayleigh wave develops in the basin; then at the boundary it drives a crustal Rayleigh wave train that is similar to the basin Rayleigh wave train at that point. Then, this wave train travels along the surface without much

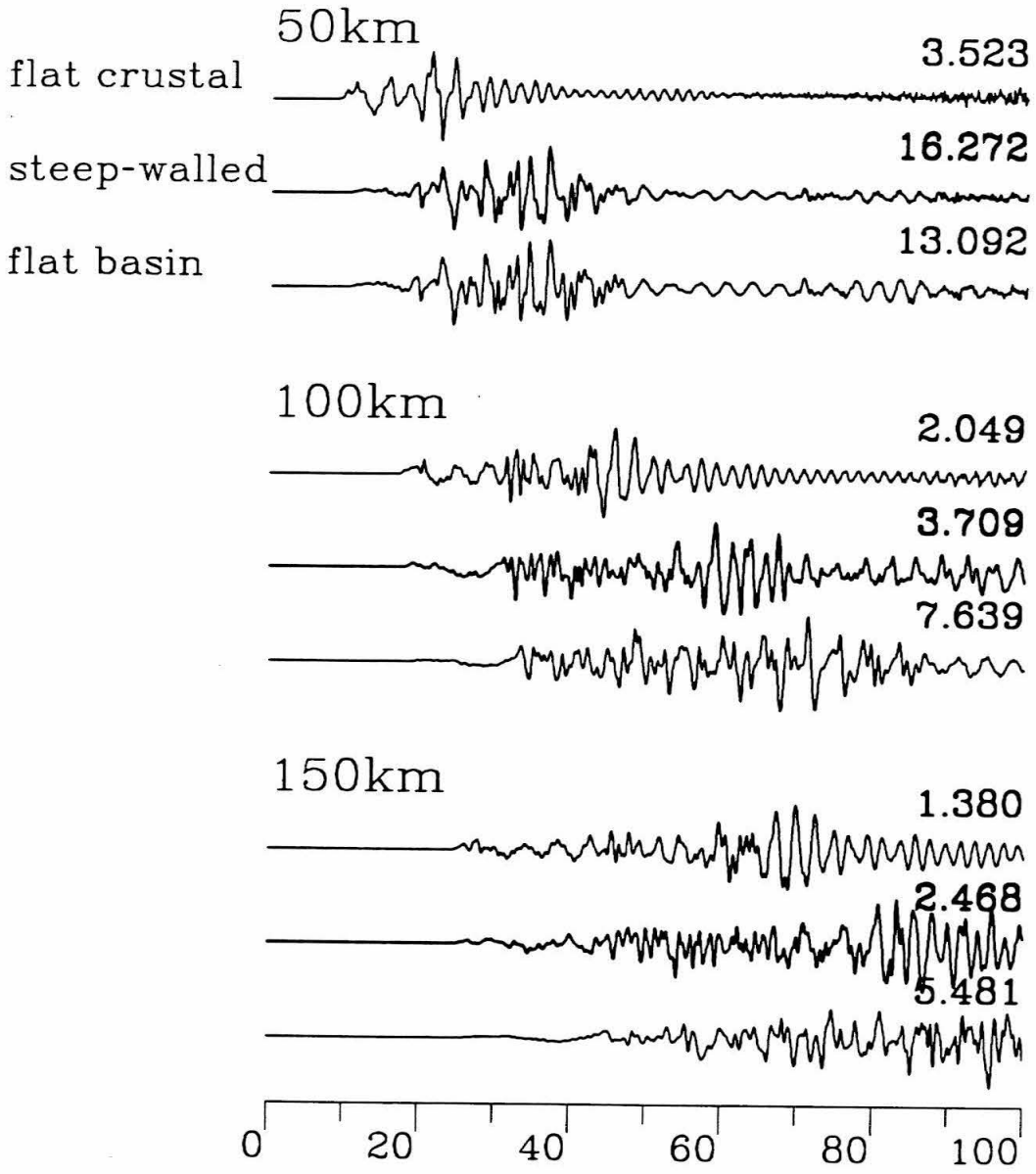

Figure 3.24 A comparison of the regional response for the steep-walled basin and both flat-layered models. The mechanism, moment and instrument are the same as Figure 3.22, but the source location is shallow, 3 km. The source is 52 km from the basin boundary. Three ranges are shown, 50, 100 and 150 km. Compare to Figure 3.23 for the effect of source depth.

a) the radial component and

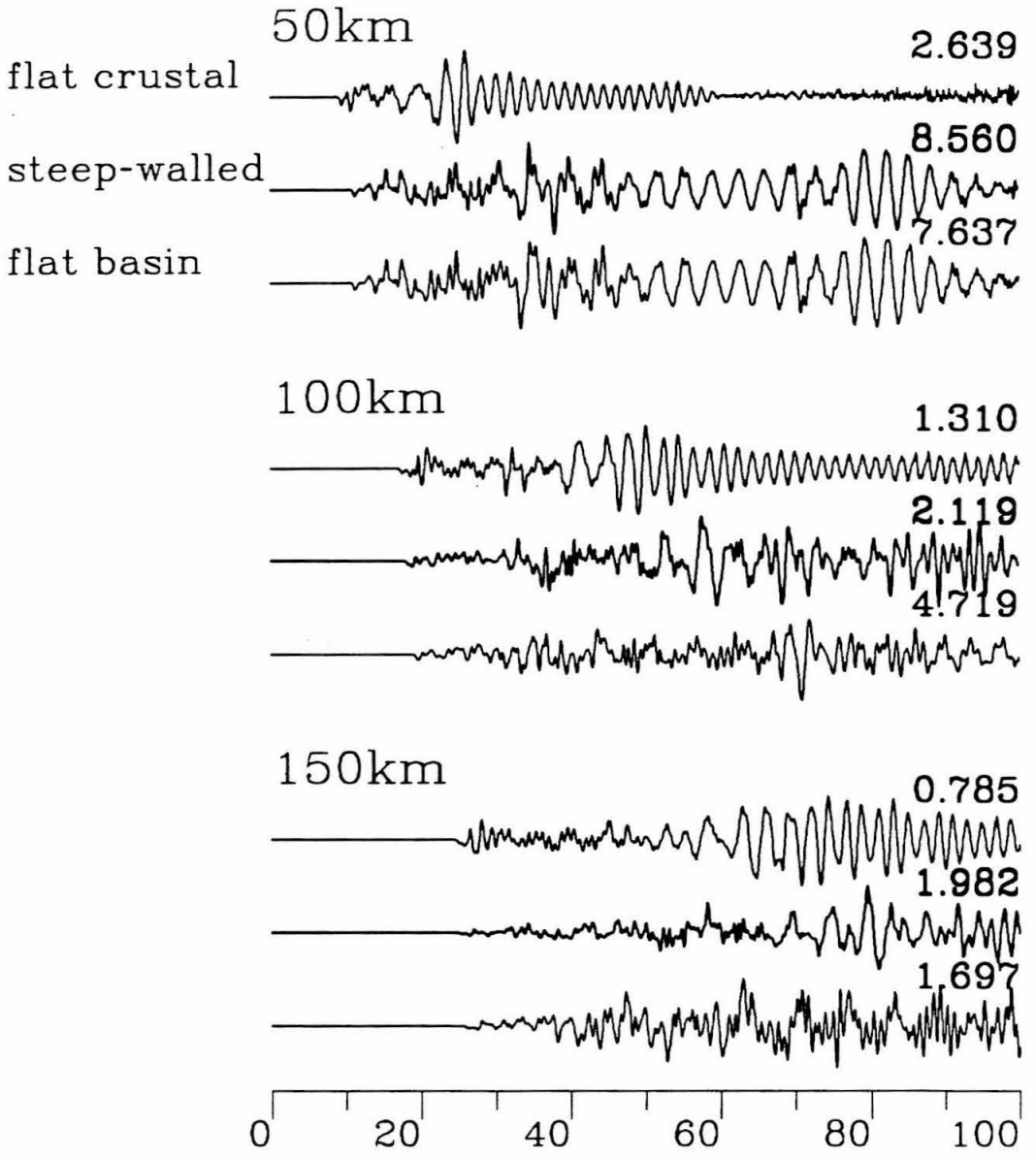

Figure 3.24 b) the vertical component.

modification. The long ringing at the fundamental period for this structure (there is no attenuation and there is a low-velocity flat wave guide at the top) cannot develop for sources outside the crustal medium. Of course, this long ringing is unrealistic; in a natural situation, attenuation or a small amount of lateral variation would destroy this. Another feature of these synthetics, at 100 and 150 km, is the large number of multiples arriving between the inital P phases and the start of the Rayleigh wave. These are produced in the basin structure and then propagate normally to the receiver. While flat-layered models can provide reasonable bounds for laterally varying P-SV models, they are unlikely to provide accurate synthetics. The large variations in waveform and the reduction in amplitude for the steep-walled basin compared to the flat-layered basin structure implies that a lot energy is scattered at the basin boundary.

As in the SH case, two laterally varying models are compared for P-SV case, to investigate the effect of basin termination geometry. Figures 3.25 for the deep source (13 km) and 3.26 for the shallow source (3 km) are comparisons of the steep and gradually dipping basin termination models. While there is little difference between the two models for the deep (13 km) source, the shallowest (3 km) source produces a Rayleigh wave that is generally slightly longer in duration and larger in amplitude for the gradual basin boundary. This is in contrast to the results of simpler canonical models presented in Chapter 1 of this thesis. Apparently, the steep boundary is a more effective scatterer in this case than the gradual boundary. It is interesting that the increase in Rayleigh wave amplitude at 100 km is found on the vertical component, while that at 150 km is found on the radial component. This is most likely due to slight phase shifting of different periods that

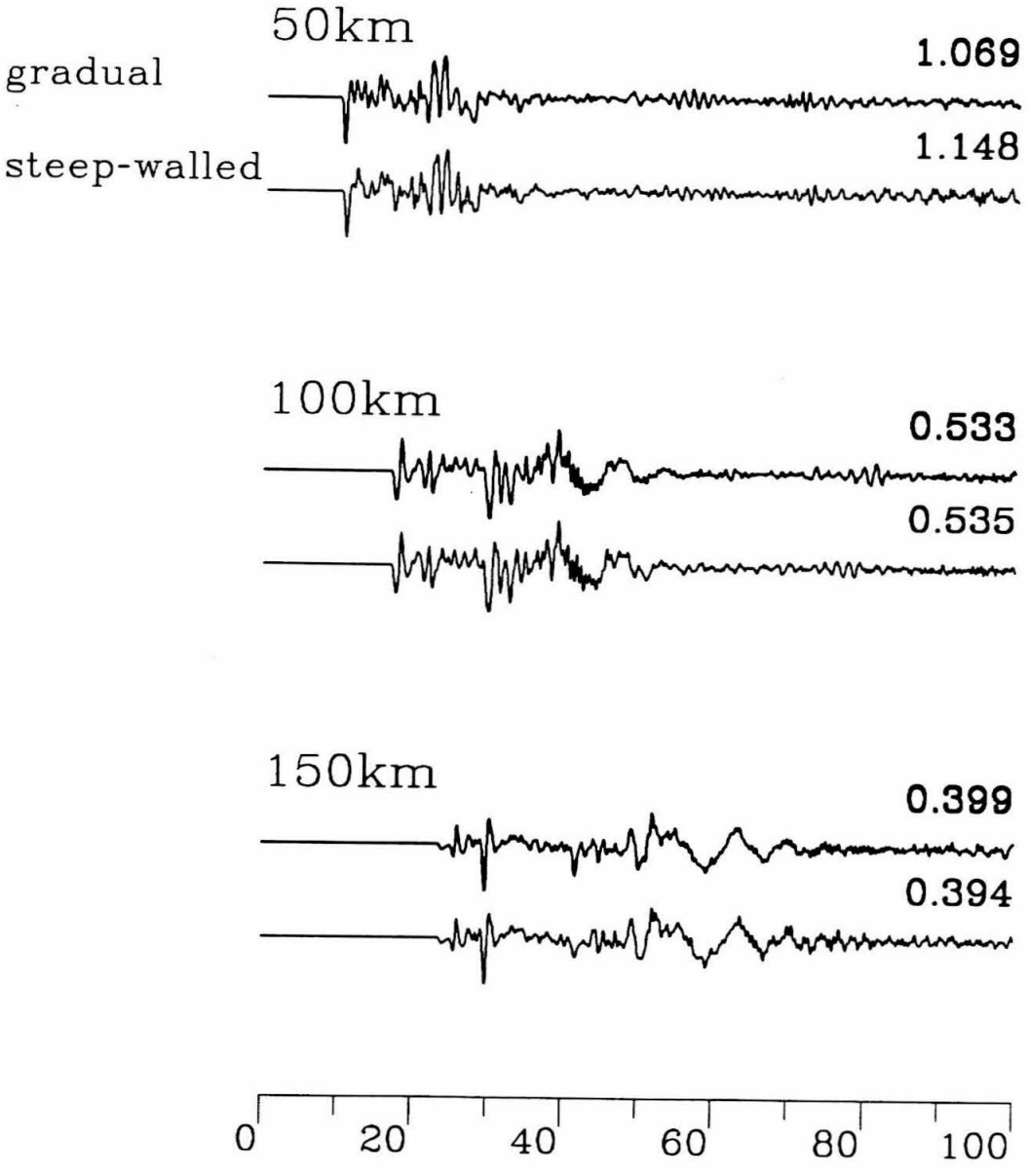

Figure 3.25 A comparison of the two basin boundaries, steep and gradual, at regional distances. The source location, depth, mechanism, instrument, moment and ranges are the same as Figure 3.23.

a) the radial component and

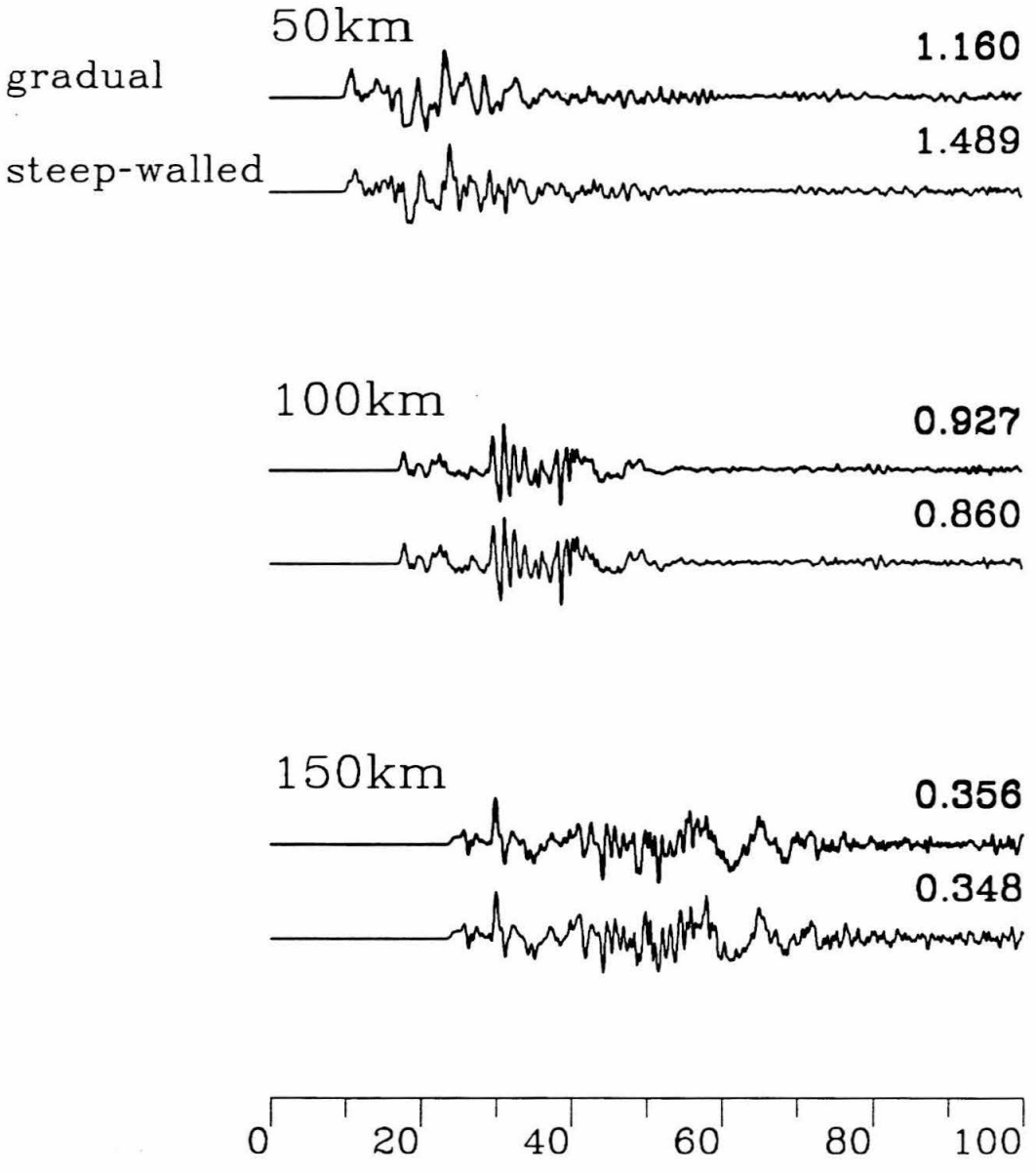

Figure 3.25 b) the vertical component.

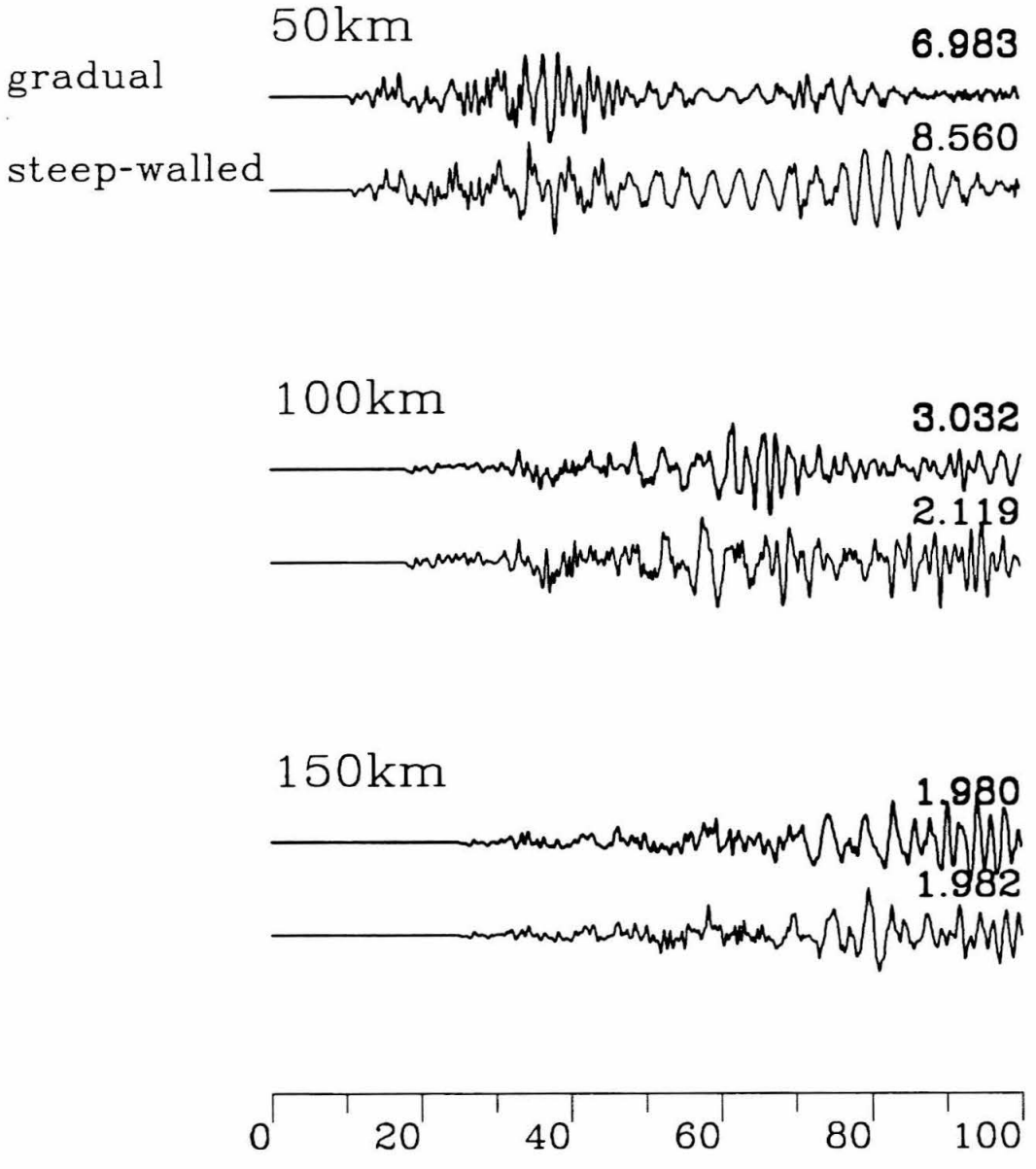

Figure 3.26 A comparison of the two basin boundaries, steep and gradual, at regional distances. The source location, depth, mechanism, instrument, moment and ranges are the same as Figure 3.24. The effect of source depth is illustrated by comparing this to Figure 3.25.

a) the radial component and

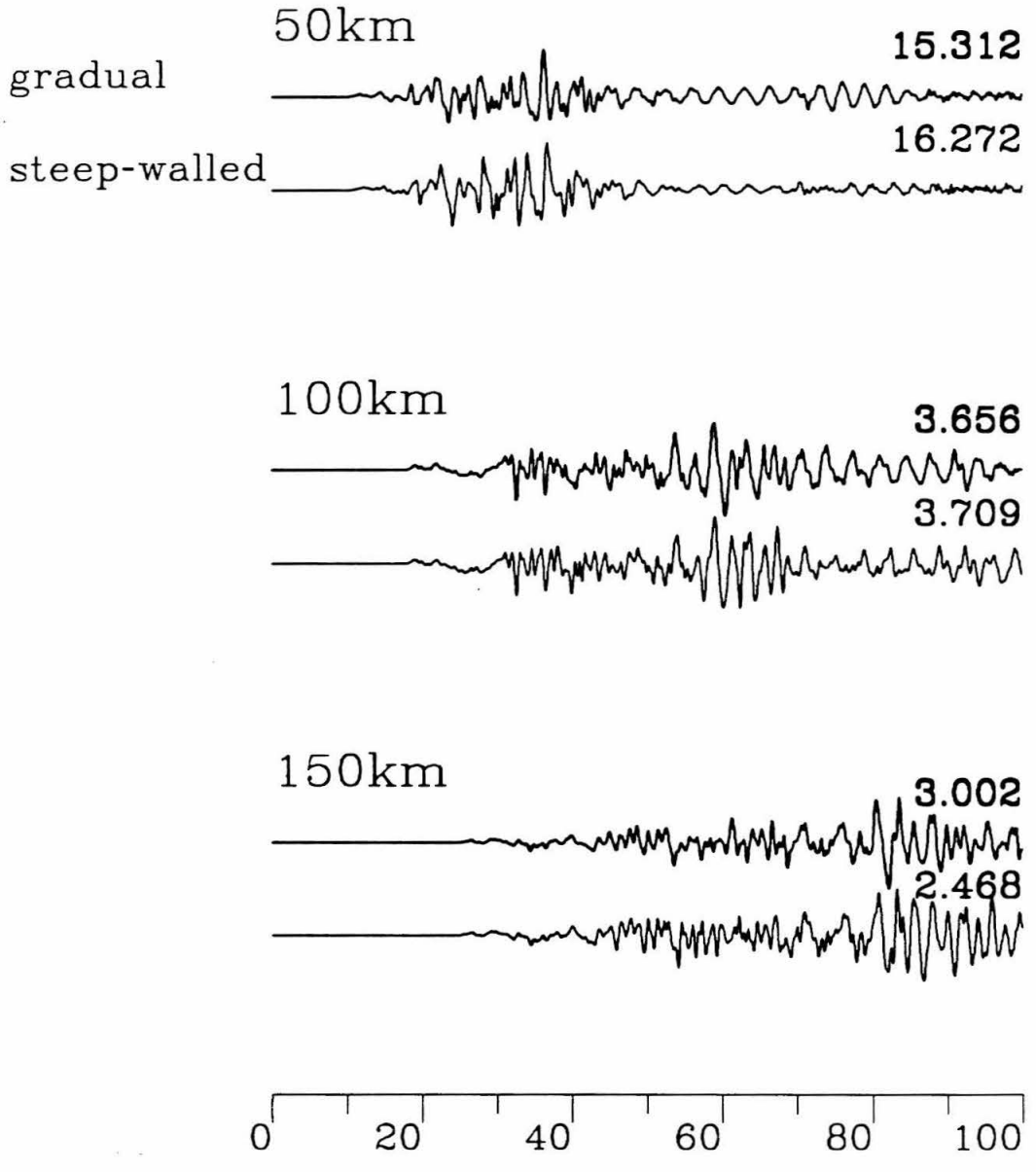

Figure 3.26 b) the vertical component.

compose the full Rayleigh wave. Different Rayleigh periods will encounter the gradual basin boundary at different ranges because the depth profile for each Rayleigh period is different. There should be no such shifting for the steep basin boundary; all periods encounter the velocity contrast at the same time.

Another important variable here is the distance between the source and the basin boundary, for the reason discussed in the introduction above. Figure 3.27 compares two such distances, 52 and 22 km, for a source 5 km deep in the gradually terminating basin. The synthetics for the flat-layered normal crust are also shown for comparison. The evidence for the offset between the source and the basin boundary is apparent in the timing of the Rayleigh wave. There is other evidence here in the body phases, but these would be difficult to reduce from data. The duration of the Rayleigh wave is also indicative of the source to boundary offset. These points are important, since they are evidence that along with the SH data, P-SV data may be used to locate the source relative to structure near the source. This could lead to more accurate locations from regional data for an area where the structure is relatively well-understood.

Figure 3.28 compares the teleseismic synthetics for the same two sources used for Figure 3.27. This figure shows the basic characteristics of the teleseismic P-SV synthetics for deep basins. The various portions of the figure show the comparison for P and SV waves separately and for both WWSSN long-period and short-period instruments. The P waves are convolved with a t^* operator using $t^*=1$, while the SV waves use $t^*=4$. Figure 3.28a shows the P-wave synthetics for a short-period WWSSN instrument. As in the SH case, the synthetics for a 22 km source-to-basin boundary offset creates the

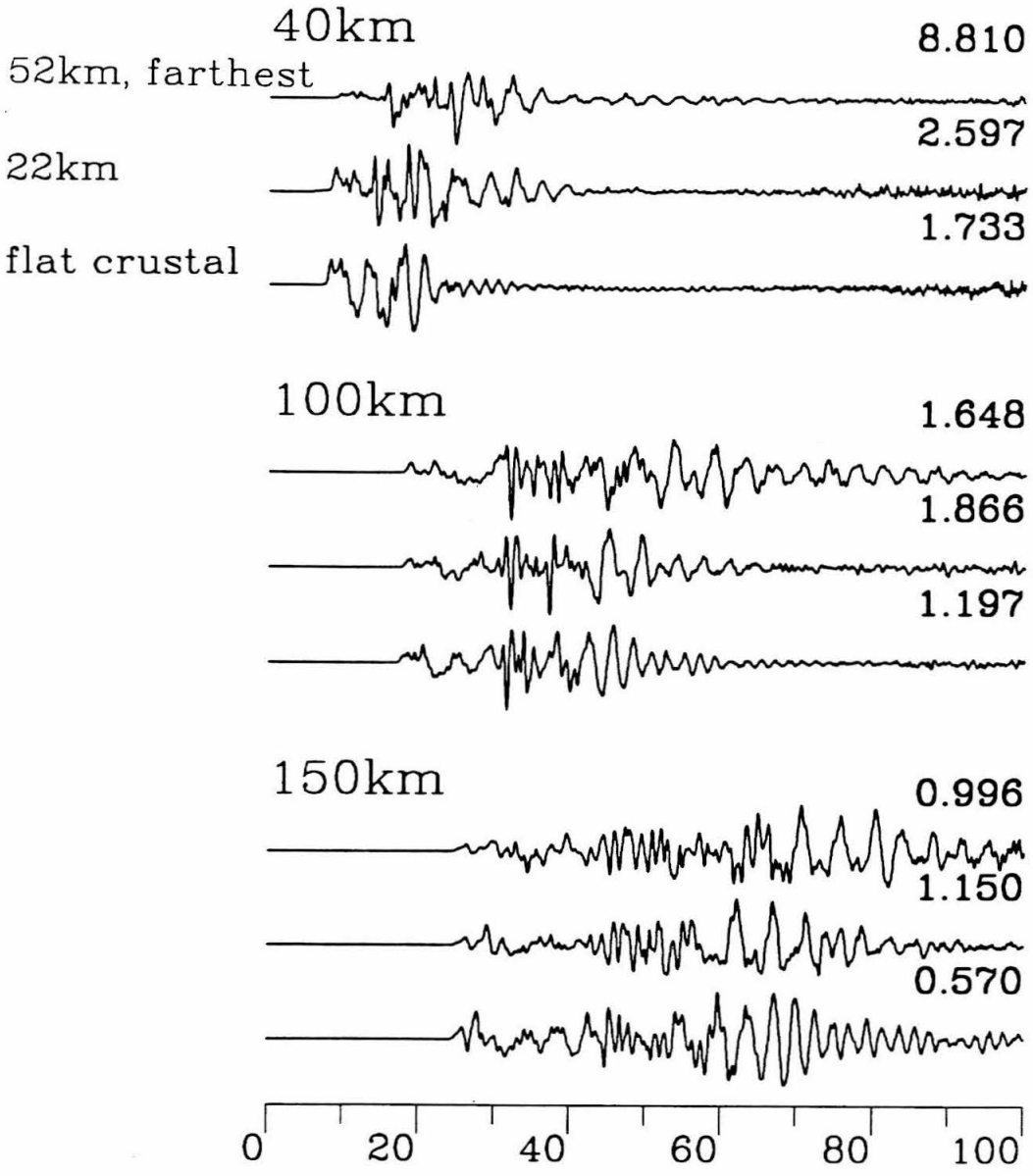

Figure 3.27 A comparison of regional synthetics to demonstrate the effect of distance between the source and basin boundary. Three cases are compared, 22 and 52 km source-to-basin boundary offset and the flat-layered crustal model (which produces results nearly identical to those for basin sources very near the basin boundary). The comparison is done at three ranges, 50, 100 and 150 km for a source at a depth of 5 km. The mechanism is strike-slip, with a moment of 10^{25}. The instrument is broad-band. The basin boundary here is steep.

a) the radial component and

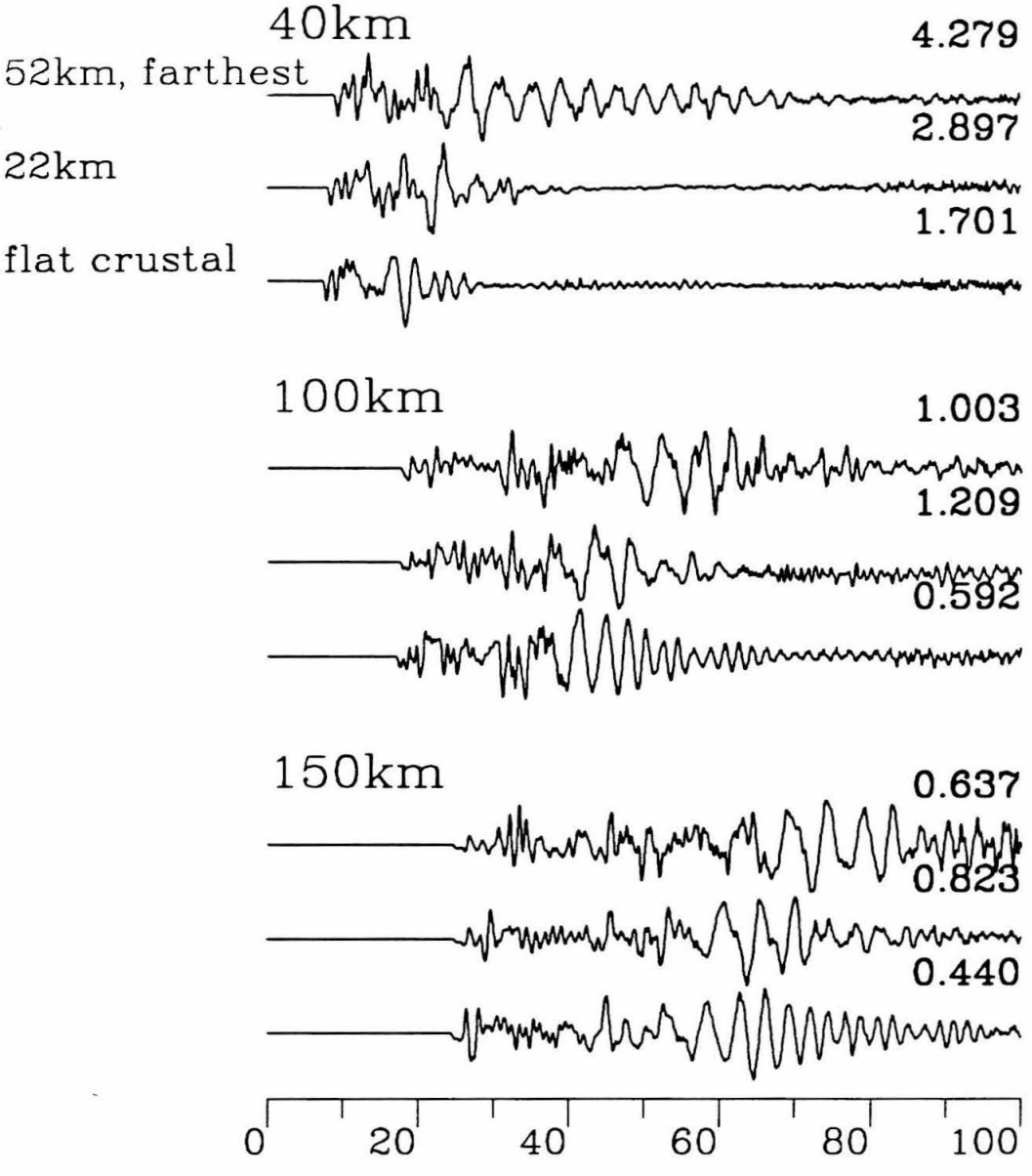

Figure 3.27 b) the vertical component.

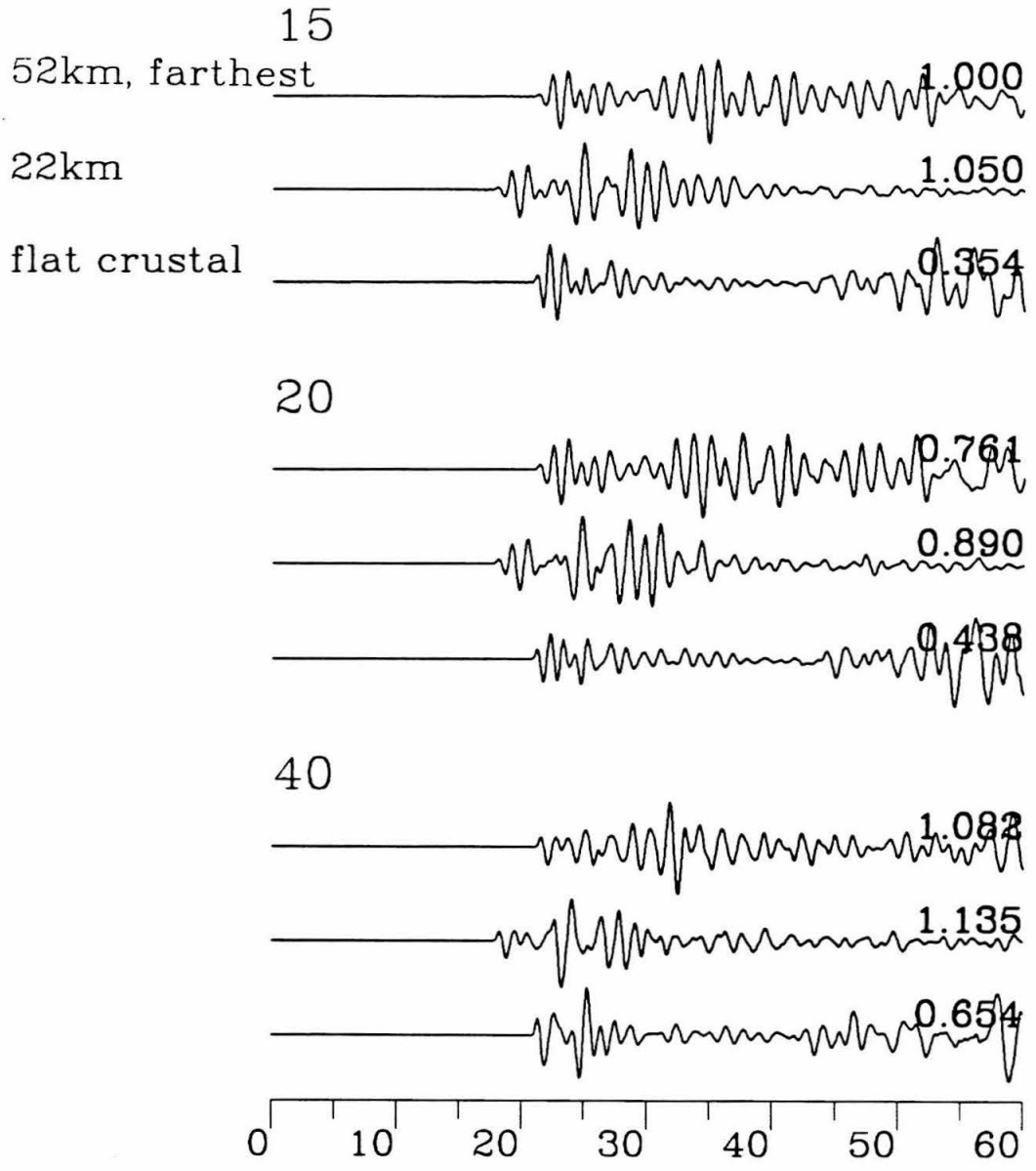

Figure 3.28 A comparison of teleseismic synthetics to demonstrate the effect of distance between the source and basin boundary. Three cases are compared, 22 and 52 km source-to-basin boundary offset and the flat-layered crustal model (which produces results nearly identical to those for basin sources very near the basin boundary). The comparison is done at three take-off angles, 15, 20 and 40 degrees for a source at a depth of 5 km. The basin boundary here is steep, and the mechanism is strike-slip. The traces are all scaled to the peak amplitude of the first trace on each plot.

a) P-wave synthetics for the WWSSN short-period instrument. Attenuation is for $t^*=1$.

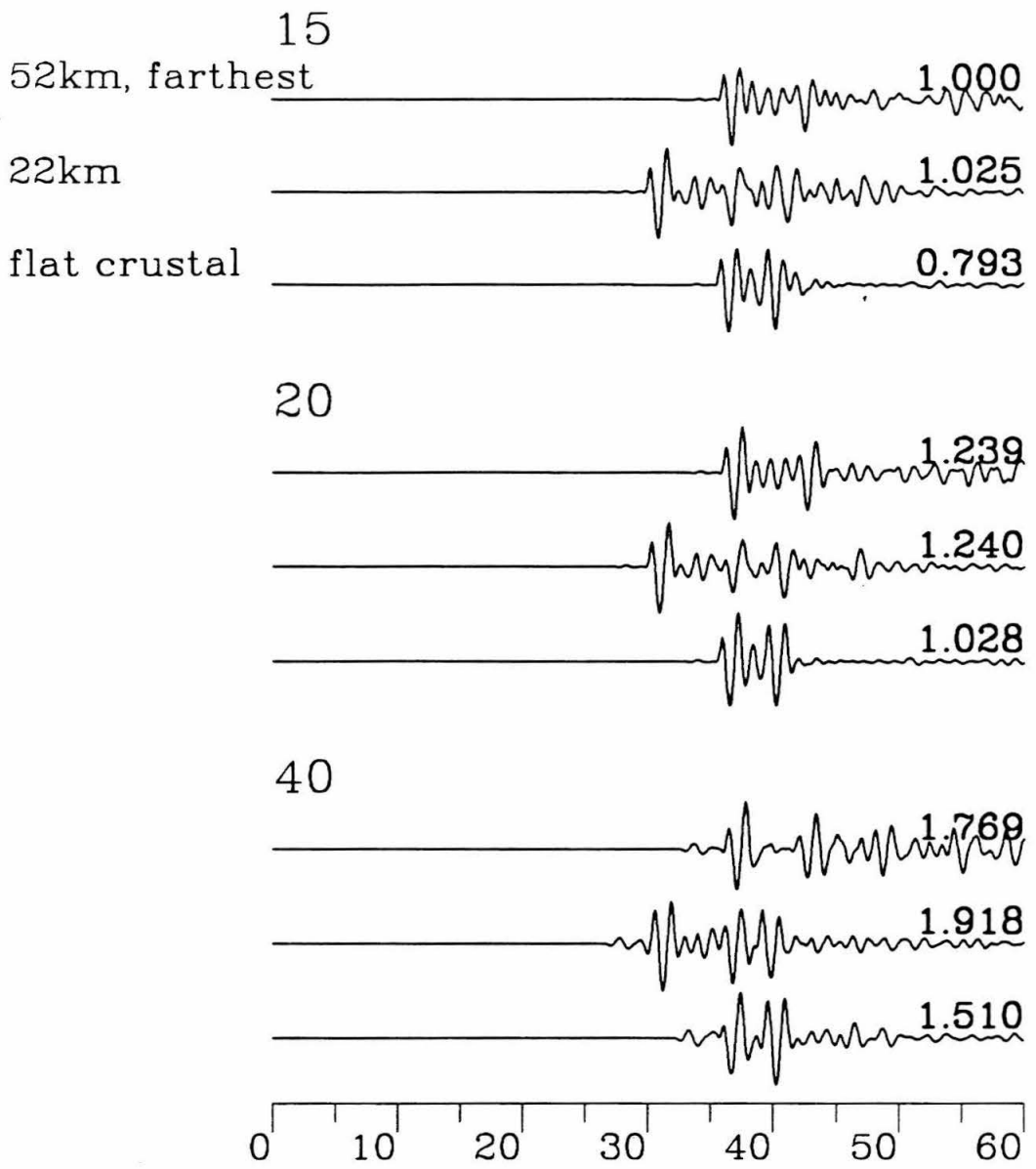

Figure 3.28 b) SV-wave synthetics for the WWSSN short-period instrument. Attenuation is for t*=4.

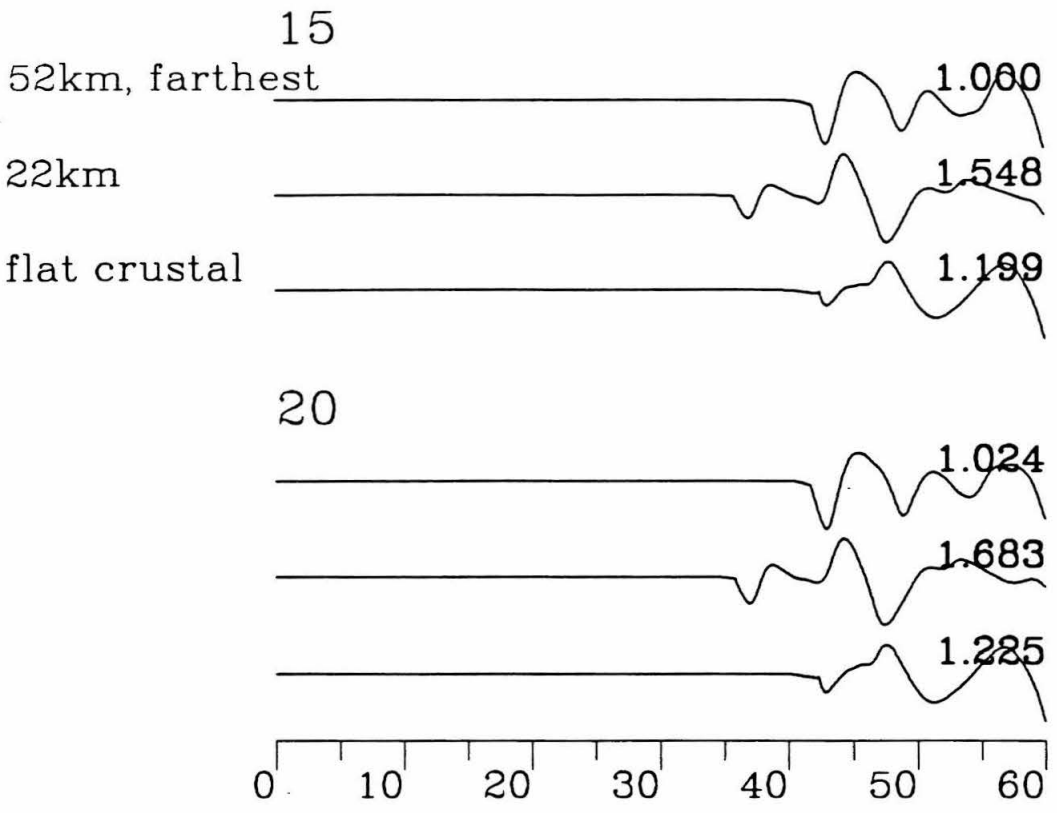

Figure 3.28 c) SV-wave synthetics for the WWSSN long-period instrument. Attenuation is for t*=4. Only take-off angles of 15 and 20 degrees are shown.

largest amplitude of scattered energy. Again, the reason is that the source must be at sufficient offset to allow the Rayleigh wave to form, but not so far that it is substantially reduced in amplitude by further propagation. In this case, further propagation in the basin primarily disperses the Rayleigh wave, so that the scattered energy is lower in amplitude but much longer in duration for the source at 52 km offset. The timing is significant here as well. The timing of the scattered energy relative to the phases P, pP and sP provides information on the source-to-basin boundary offset. The energy that appears to arrive at about 25 seconds after P is noise (a limitation of the methods used here) and can be ignored. The short-period instrument is satisfactory here because the mantle attenuation is so much less for P waves than for S waves, and therefore, there is sufficient energy at the instrument's peak frequency band. Note that the range to the basin boundary has far more effect on the resulting synthetics than 5 degrees in take-off angle. This means that most teleseismic stations along a particular azimuth from the source should show similar effects from near-source scattering, making analyses of these records for near-source structure more robust. Figure 3.28b shows the SV-wave synthetics for the conditions as Figure 3.28a, except that the attenuation is larger ($t^*=4$, as above). The first phases are S, pS and sS, and only the synthetics for the source offset 22 km from the basin boundary show much evidence of scattered Rayleigh waves. There is some scattered energy for the 52 km offset at 40 degrees take-off angle, but this take-off angle will not reach teleseismic distances. Of course, as mentioned above, the short-period instrument is inappropriate for S waves, so the long-period instrument is used in Figure 3.28c. There are differences between the 22 km offset synthetics and the others, but measurable evidence of source-to-basin

boundary offset is lacking. While it may be necessary to consider these scattering effects to create accurate synthetics, the teleseimic SV data probably cannot be used to measure lateral structure.

3.5 Discussion

The above analysis demonstrates the principal features of synthetic SH (tangential component) seismograms generated for earthquake sources in deep continental basins and for receivers at regional (far from the basin boundary) and teleseismic distances. The SH results are then compared to some P-SV results. The variables investigated include source depth, source distance from the basin boundary, source mechanism, instrument response, regional distance from the source to the receiver, teleseismic take-off angle and basin-boundary geometry. These variables are shown to have varying effects on the resultant synthetics, and they often interact with each other. The comparison of the synthetics to controls (half-space and flat-layered models) aids in the identification of basin effects.

The effect of basin boundary geometry is suprisingly small for SH synthetics. The results of Chapter 1 of this thesis for simpler media but for the P-SV system indicates that boundary geometry is important. Although the media here are more complex (12 types of media as opposed to 2), the waveform variation is less because conversions are not available. For the P-SV system three distinct types of waves are free to convert one to another, but the SH case contains only one type of wave showing two types of behavior. Only the sources at optimal ranges and depths create synthetics with variations that are distinct for different boundary geometries. Optimal ranges are those far enough from the boundary to allow surface waves to

develop, but close enough that the surface waves are not significantly reduced by geometric spreading before they are scattered. This range is found to be about 20 to 50 km for the models used here. As for optimal depth, the shallowest sources produce the strongest Love waves (less than 5 km depth in this study). This observation has important implications for the study of data from events similar to the model presented here. The teleseismic records of such events can be modeled using a basin structure but without knowledge of the boundary geometry. In addition, the body phases on the regional SH synthetics are independent of the boundary geometry. The later multiples do, however, demonstrate some dependence on basin boundary geometry, which is strongest for sources optimally located. It is the surface waves that show the greatest variation with boundary geometry. The steep termination scatters surface waves a little more more effectively than the gradual boundary but because of the large shear attenuation of the mantle, most of this information for S-waves is lost before reaching teleseismic ranges. This contrasts with the results of Chapter 1 where the gradual boundary is a more effective scatterer. Clearly, the scattering capacity of different boundary geometries depends on the velocity profiles and possibly the type of source.

For SH-waves the effect of mechanism is to change to generation of the Love wave, which in turn affects all the scattering phenomena. Thus, the regional synthetics show a Love wave with a very different appearance for the strike-slip and dip-slip cases. For the strike-slip case the maximum in the radiation pattern is horizontal and the minima are vertical. This creates large-amplitude Love waves which begin to appear at very short ranges. For teleseismic records, the vertical node makes the direct S and sS small, causing

the scattered-to-direct amplitude ratio to be relatively large. The exact opposite occurs for the dip-slip case for teleseismic records. As for regional records, the Love waves tend to be small until much greater ranges where energy from take-off angles nearer to vertical contributes more significantly to the formation of the Love wave. Although no results are presented in the P-SV case for mechanisms other than strike-slip, similar effects may be expected, with additional complications. The strike-slip source is nodal for both P and SV (as well as SH) vertically. The complications would arise for other mechanisms such as a 90 degree dipping, dip-slip mechanism. For such a mechanism, P is still nodal, but SV is a maximum vertically. For a 45 degree dipping dip-slip mechanism, P is maximum, and SV is nodal vertically. It is due to the plethora of such combinations and their interaction with Rayleigh wave generation that these are not explored above. It is sufficient to realize that any mechanism with strong vertical radiation will conceal scattered energy more effectively than strike-slip.

The regional effect of source depth is to create larger-amplitude surface waves for shallower sources. This provides more energy for scattering. Thus, at teleseismic distances, the effect of source depth is to increase the amplitude of scattered energy relative to direct body phases. This ratio may not be directly applicable to data because other factors may affect it, such as the size and velocity contrast of the basin. Yet, a series of sources in a basin could be distinguished in depth on this basis.

The effect of distance between the source and basin boundary on the regional synthetics is to allow the surface wave to develop and disperse to different extents before encountering the basin boundary. Yet, the surface waves, particulary the Love wave, change dramatically at the boundary, and

thereafter continue to develop more like the surface waves in the flat-layered normal crustal model. This rapid conversion is due to the scattering of energy at the boundary. This scattered energy appears on the teleseismic records, strongest for sources optimally located (as described above).

The effect of the teleseismic take-off angle is negligible in most cases. This implies that the teleseismic modeling is relatively robust, and slight variations in take-off angle (because of a dipping Moho or some other structural effect) are not important in the generation of the synthetic. It also implies that for the same azimuth, all teleseismic records of a given event (corrected for instrument, site response, etc.) should be the same.

The effect of range for the SH regional records is best interpreted in terms of flat-layered behavior. Only in the immediate vicinity of the boundary are any strong deviations from such behavior displayed. The behavior of the P-SV regional synthetics is more complex and may indicate that flat-layered models would be insufficient to interpret regional P-SV data for regions having strong lateral variations in structure.

The effect of instrument response is to remove information. A long-period instrument (such as the Press-Ewing 30-90 instrument) for the regional synthetics can resolve information only about the distance between the source and basin boundary for large basins like the one modeled here. It completely swamps much of the other information. Yet, longer-period characteristics of the seismogram are well-resolved, and this is an aid to modeling the vertical structure. This is especially true of Sn, in this case. A mid- to long-period instrument (such as the 6 second Wood-Anderson torsion) seems to be ideal among limited-band instruments. The finer features of the seismogram are not swamped by the slow response of the instrument, yet the

phases are still distinct, relatively simple pulses. Most of the information about the basin is preserved. The short-period instruments (such as the 0.8 second Wood-Anderson) remove long-period phases, like the Love wave and Sn, and destroy the simple, pulse nature of the other phases. The records for short-period instruments show the greatest dependence on structure and source position, but this information would be very difficult to interpret. For teleseismic records, mantle attenuation leaves little choice of instrument response when studying S waves; only the long-period instruments can be used. For P-waves, on the other hand, the short-period instrument is ideal because mantle attenuation is not nearly as strong for P as for S, and the timing, duration and waveform of the scattered energy are more easily determined at short periods.

3.6 Conclusions

This chapter presents a systematic, synthetic investigation of the effects of a deep continental basin on regional and teleseismic SH and P-SV waveforms. For regional records, the presence of a basin greatly alters the overall trace, but much of this alteration can be interpreted in terms of the presence of two different vertical structures, particularly for the SH case. Up-going waves demonstrate form and timing appropriate for the basin structure, while down-going waves show that appropriate for the surrounding crust. The body phases could be modeled using a generalized ray approach, which separates the rays along these lines and combines the results for a final synthetic. The surface waves have waveforms that vary between the two structures, but become more like the flat-layered normal crust surface waves the farther they propagate through the normal crust. For teleseismic records

the presence of scattered energy is difficult to detect except for source located such that the surface wave is well-developed but has not been greatly reduced by geometric spreading.

Several variables affect the basin response. Source position determines the character of the surface wave when it encounters the basin boundary, which in turn affects the degree to which the presence of the basin is observable in the seismograms. The shape of the basin boundary is relatively unimportant under most conditions. The best mechanism for producing basin scattering effects is strike-slip because it has a maximum along the horizontal. For regional records, the best instrument response for analyzing these effects is broad-band, but failing that, one should choose a mid- to long-period response, such as the longer-period torsion instruments. Teleseismic S does not permit a choice of instrument, but teleseismic P should be studied on short-period instruments.

References for Chapter 3

Benz, H. M., and R. B. Smith (1988). Elastic-wave propagation and site amplification in the Salt Lake Valley, Utah, from simulated normal faulting earthquakes, *Bull. Seism. Soc. Am.*, **78,** 1851-1874.

Vidale, J. E., and D. V. Helmberger (1988). Elastic finite-difference modeling of the 1971 San Fernando, California earthquake, *Bull. Seism. Soc. Am.*, **78,** 122-141.

Chapter 4

Numerical modeling of Imperial Valley, California earthquakes recorded at Pasadena, California

4.1 Introduction

The Imperial Valley region of California is historically an area of unusually high seismicity. In particular, this region produces frequent moderate (M_L between 5.0 and 7.0) earthquakes, which are of interest in seismic hazard assessment. Yet, for many years, this area was poorly instrumented, and the area has never been densely populated. For these reasons, little is known about many of the moderate earthquakes that occurred before the Borrego Mountain earthquake of 1968, with the exception of the 1940 Imperial Valley earthquake. Nevertheless, there are many good records of these earlier events and their aftershocks from stations in the southern California array operated since 1929. The station at Pasadena (PAS) has been in continuous operation since 1927, with a wide variety of instruments recording. Recently (January, 1988), a broad-band instrument has been installed at PAS, providing the most accurate and detailed seismograms ever available. It is proposed here that forward modeling of historic earthquakes recorded at PAS and constrained by broad-band records of very recent, well-located events, will provide more information on the historic events. This will lead to more accurate locations, depths, magnitudes and mechanisms for these events, and allow these events to be more accurately associated with the various faults of the region.

A variety of seismological studies exist that deal with the seismicity and structure of the Imperial Valley, yet only one previous study (Ho-liu, 1988) attempts to model any of the historical events recorded at the stations of the southern California array, particularly PAS. Modern events are typically modeled only for stations in Imperial Valley (Vidale, 1987, Heaton and Helmberger, 1977, Heaton and Helmberger, 1978, Hadley and Helmberger, 1980, Hartzell and Helmberger, 1982, Frankel and Wennerberg, 1989) or for teleseismic stations (Bent, et al., 1989, Burdick and Mellman, 1976, Butler, 1983, among others). While such studies provide valuable information on the sources and processes of modern events, they do not provide many clues to the nature of the older events (those occurring before the Borrego Mountain earthquake of 1968).

Table 4.1 provides a list of the historic and current events considered for this study. The origin times and locations are those from the catalog of the southern California array (Hileman, et al., 1973, and subsequent addenda). The locations, origin times, depths and magnitudes of the older events are approximations, in that a uniform one-dimensional model is routinely used to locate all events in southern California. This model is least accurate for the Imperial Valley, where the best available velocity studies (Fuis, et al., 1982) indicate a structure quite different from other regions of southern California. In addition, the older events are recorded on less than 10 stations, far from the Imperial Valley (all stations $>$ 100km away), and having poor azimuthal coverage (all stations within 90 degrees of azimuth). If La Jolla (LJC) and Palomar (PLM), neither of which have records that span seismic recording in southern California, are eliminated, the available stations span less than 45 degrees of azimuth and all but one (Riverside, RVR) are greater than 200 km

Table 4.1. Imperial Valley earthquakes

date	origin time GCT	latitude degrees N	longitude degrees E	depth km	magnitude
02/26/30	02:29	33.00	-115.50	16.0	5.0
03/27/37	07:42	33.47	-116.58	16.0	4.5
10/21/42	16:22	32.97	-116.00	16.0	6.5
10/21/42	19:10	32.97	-116.00	16.0	4.5
10/22/42	01:50	33.23	-115.72	16.0	5.5
10/22/42	18:13	32.97	-116.00	16.0	5.0
10/29/42	16:21	32.97	-116.00	16.0	4.5
10/30/42	05:35	32.97	-116.00	16.0	4.5
01/08/46	18:54	33.00	-115.83	16.0	5.4
07/27/50	11:29	33.12	-115.57	16.0	4.8
01/24/51	07:17	32.98	-115.73	16.0	6.4
06/14/53	04:17	32.95	-115.72	16.0	5.5
03/19/54	09:54	33.28	-116.18	16.0	6.2
03/23/54	04:14	33.28	-116.18	16.0	5.1
04/25/57	22:24	33.18	-115.85	16.0	5.1
05/23/63	06:36	32.90	-115.68	1.0	4.5
05/23/63	09:06	32.97	-115.55	25.0	4.6
04/09/68	02:28	33.18	-116.12	11.0	6.4
04/09/68	08:00	33.10	-116.00	4.0	4.5
04/09/68	18:31	33.30	-116.30	13.0	4.7
04/28/69	23:20	33.33	-116.33	20.0	6.1
08/11/76	15:24	33.48	-116.52	15.0	4.3
11/04/76	10:41	33.08	-115.60	6.0	5.3
11/04/76	14:12	33.15	-115.63	12.0	4.4
06/05/78	16:03	33.42	-116.70	12.0	4.4
02/12/79	04:48	33.45	-116.43	4.0	4.2
10/15/79	23:16	32.63	-115.33	12.0	7.0
10/16/79	03:10	32.96	-115.54	9.0	4.9
10/16/79	03:39	32.97	-115.55	10.0	4.9
10/16/79	05:49	33.02	-115.57	5.0	5.6
10/16/79	09:36	32.90	-115.45	5.0	3.4
10/16/79	11:46	32.90	-115.55	5.0	5.2
10/16/79	23:16	33.07	-115.57	7.0	5.5
04/25/81	07:03	33.12	-115.65	10.0	4.4
04/26/81	12:09	33.13	-115.65	6.0	6.3
11/24/87	01:54	33.08	-115.78	5.0	5.7
11/24/87	13:15	33.01	-115.84	2.0	6.0
01/28/88	02:54	32.91	-115.68	6.0	4.6
05/17/88	19:38	33.24	-116.25	8.0	3.8
07/02/88	00:26	33.49	-116.44	12.0	4.1
03/06/89	22:16	33.17	-115.59	1.0	4.7

away. Thus, the usual methods of array seismology break down. Routine array seismology relies on a dense distribution of a large number of stations to control errors. The statistics are best for a dense station distribution close to the event, covering all azimuths. Given the available data, the best course of action is to model modern waveforms recorded at the same stations that recorded the historic events, and to use the knowledge gained to model those historic events. This method improves statistics by increasing the number of phases considered as well as the number of properties of each phase such as amplitude and phase shift. If phases that are due to structure in the vicinity of the source can be identified, then statistics are improved, in a sense, by moving the station closer to the event. Teleseismic studies are limited by the number of good records available, and by the periods available in these records. In general, source properties can be distinguished only to within the smallest wavelength available in the records modeled. For these reasons, in this study, we consider the seismograms of Imperial Valley earthquakes as recorded at PAS. Table 4.2 provides the distances and azimuths from PAS for the events listed in Table 4.1. This station is by far the most reliable of the historic stations of the southern California array, and it provides the greatest diversity of instruments as well as the recent installation of broad-band recording.

However, there are some good studies that apply array methods to examine historical seismicity in the Imperial Valley. The most notable of these is Doser and Kanamori (1986). The technique used in that study was to locate modern events using the best available velocity structures, then to apply the resulting station residuals in the relocation of the historic events. The paper describes in detail the limitations of such efforts. The authors do

Table 4.2. Imperial Valley earthquakes and Pasadena (PAS)

date	origin time GCT	distance from PAS km	azimuth from PAS degrees, clockwise from N
Feb 26, 1930	02:29	278.82	116.43
Mar 27, 1937	07:42	165.46	116.59
Oct 21, 1942	16:22	240.29	122.33
Oct 21, 1942	19:10	240.29	122.33
Oct 22, 1942	01:50	249.08	113.44
Oct 22, 1942	18:13	240.29	122.33
Oct 29, 1942	16:21	240.29	122.33
Oct 30, 1942	05:35	240.29	122.33
Jan 8, 1946	18:54	251.95	119.70
Jul 27, 1950	11:29	266.95	114.56
Jan 24, 1951	07:17	261.12	119.06
Jun 14, 1953	04:17	263.62	119.58
Mar 19, 1954	09:54	208.22	116.99
Mar 23, 1954	04:14	208.22	116.99
Apr 25, 1957	22:24	240.61	115.85
May 23, 1963	06:36	269.70	120.19
May 23, 1963	09:06	276.29	117.49
Apr 9, 1968	02:28	218.49	118.86
Apr 9, 1968	08:00	232.64	119.37
Apr 9, 1968	18:31	197.33	117.94
Apr 28, 1969	23:20	193.28	117.48
Aug 11, 1976	15:24	169.93	115.39
Nov 4, 1976	10:41	266.43	115.68
Nov 4, 1976	14:12	260.46	114.44
Jun 5, 1978	16:03	158.43	120.23
Feb 12, 1979	04:48	178.91	115.16
Oct 15, 1979	23:16	313.44	121.70
Oct 16, 1979	03:10	277.65	117.60
Oct 16, 1979	03:39	276.29	117.49
Oct 16, 1979	05:49	272.00	116.66
Oct 16, 1979	09:36	288.24	117.94
Oct 16, 1979	11:46	280.13	118.88
Oct 16, 1979	23:16	269.43	115.62
Apr 25, 1981	07:03	260.26	115.28
Apr 26, 1981	12:09	259.77	115.06
Nov 24, 1987	01:54	251.58	117.42
Nov 24, 1987	13:15	250.58	119.60
Jan 28, 1988	02:54	269.12	119.99
May 17, 1988	19:38	204.67	118.94
Jul 2, 1988	00:26	176.15	113.99
Mar 6, 1989	22:16	262.88	113.65

not report locations on 34 of their 75 events between 1932 and 1973 because of lack of resolution. Of the locations they report, those before 1950 are estimated to have resolution of about 10 to 20 km. Despite these limitations, the new information was sufficient to make new conclusions regarding spatial and temporal variation of Imperial Valley seismicity. If the location resolution could be improved to perhaps 5 km and more events located to within limits of resolution, then individual events could be associated with faults more accurately, and better information on foreshock and aftershock distributions could be derived. A similar study reported by Sanders, et al. (1986) for the San Jacinto fault system (west and northwest of the Imperial Valley) also found large uncertainties (10 to 15 km) and problems with resolution. Nevertheless, in that study, the authors map seismicity along the fault very accurately and define aftershock zones. Both studies use P and S times for stations in the southern California array. Neither study uses PAS or any stations at greater distances. Doser and Kanamori (1986) use Tucson (TUO) at greater than 400 km, mainly to improve azimuthal coverage, but assign it their smallest weight. PAS and the other more distant stations are not used because they are a short distance beyond the Pn and Sn crossover distances; thus the first arrivals are small and emergent. In fact, Sn cannot be picked on the relatively short-period instruments used in these investigations. Other S phases are difficult to pick accurately and may be affected by lateral variation.

The main difficulty in locating and modeling these earthquakes is the lack of good velocity and density profiles for several areas of southern California. Several studies have looked at this problem, but because of various limitations in the data and methods, the resulting structures often are over-

simplified, attempt to cover too large a region, or are inconsistent with other studies. Some areas of southern California have not been examined for seismic structure. In other areas, detailed information is available, for example, Fuis, et al. (1982) present detailed models of several refraction profiles in the Imperial Valley. Their structural model is shown to work well for modeling waveforms of both the refraction data (McMechan and Mooney, 1980) and the 1968 Borrego Mountain earthquake as recorded in the Imperial Valley (Vidale, 1987). The average structure for southern California has been the subject of many studies (Gutenberg, 1944, 1951, 1952, 1955; Richter, 1950; Shor, 1955; Press, 1956, 1960; Roller and Healy, 1963; Kanamori and Hadley, 1975), but southern California, like other parts of western North America, is made up of several tectonic provinces, which may bear little structural similarity between them. Thus, an average structure is one that is not likely to do very well for any particular portion of the region. Some studies have produced models for particular regions such as the Transverse Ranges (Hadley and Kanamori, 1977), the Mojave (Hadley and Kanamori, 1979) and the Peninsular Ranges (Hadley and Kanamori, 1979, Hadley and Combs, 1974). The models derived for some of these regions are presented in Table 4.3. These regions should be divided into subregions; the variations within the regions are mentioned by the authors of these studies. Some regions (for example, the Los Angeles Basin) have not been studied for deep crustal structure. The transitions between areas of differing structures have not been addressed. Hearn and Clayton (1986a and 1986b) attempt to investigate Pn and Pg structure for southern California, using a variation of the tomographic technique. There is ambiguity in these inversions between the velocity of the MOHO and the depth to the MOHO. As for Pg, it is

Table 4.3. Some velocity models for southern California

Transverse Ranges Hadley and Combs, 1974		Southern CA Kanamori and Hadley, 1975		Southern CA Hadley and Kanamori, 1979	
P	thickness	P	thickness	S	thickness
5.5	1.0	5.5	6.0	3.2	4.0
5.8	5.0	6.3	21.4	3.5	21.0
6.2	10.0	6.8	5.0	4.1	5.0
6.8	17.0	7.8	∞	4.6	∞
7.8	∞				

generally recognized that there is no single discontinuity accounting for this phase; any and every midcrustal refractor can generate Pg, and the refractors vary widely in depth, velocity and extent. Other geophysical techniques, such as gravity, have been applied to the problem of structure in southern California, but all have well-recognized limitations.

The lack of information on seismic structure is matched by a lack of information on deep geologic structure. There exists a large body of literature on the surface geology of southern California. This is useful in regional modeling because hard (fast) and soft (slow) formations are identified and located. Knowledge of structure probably extends down to about 2 km in most places. Thus, the seismologist can estimate surface velocities to about that depth, and allow for the lateral variation present. Such structure affects site response for the seismometers and can alter higher-frequency surface waves. Surface waves of more than a 2 second period will not be strongly affected by variations within 2 km of the surface. Because of the ranges involved in this study, higher-frequency surface waves cannot be modeled accurately. Such surface waves have wavelengths much smaller than the distance traveled to PAS, and are scattered off-azimuth, requiring three-dimensional modeling. Therefore, it is the deeper large-scale structures that are most important to this study. Such information is difficult to obtain in southern California. The basement structure in low areas is often buried by very thick sediments over large areas. Two examples of this are the Imperial Valley and the Los Angeles basin. The thickness of these sediments can only be estimated, and there is no knowledge of the basement below them. Another difficulty is the existence of extensive thrust sheets across broad regions of southern California. Some workers hypothesize multiple thrusts

overlying each other in some areas. These sheets can have very large offsets. Combined with a long history of strike-slip faulting and possible terrain accretion, slabs and slices of a variety of basement rocks may be shuffled throughout southern California. The problem exists to such a degree that neither the geologic nor seismologic structure is known in detail beneath PAS, despite its location on hard rock (granodiorite) and its more than 60 years of broad-band seismic recording. Structural geologists are now working with techniques to continue observed surface structures downward to great depth, relying on laws of conservation and reconstruction. Yet, even these modern techniques are often limited; for example, most cannot account for lateral motion (strike-slip or the horizontal component of oblique-slip), which is so prevalent in southern California.

In general, this lack of structural knowledge presents serious difficulties in regional waveform modeling. Even for the 2D methods employed below, the number of variables is very large. For example, a 2D finite-difference model that can produce periods as small as 2 seconds at a range of 250 km would require about a million nodes. At each of these, a P-velocity, S-velocity and density may be specified. This is a far greater problem than that faced in one-dimensional modeling where the media properties are specified for some small number of layers as well as layer thicknesses. The most successful studies of the response of laterally varying media (Stead and Helmberger, 1988; Vidale and Helmberger, 1988; among others) have quite a bit of structural information available to the depths and at the wavelengths appropriate for the study. But it is possible to limit the allowed variations in structure to examine what may be appropriate structures. It is this approach, combined with information from canonical modeling (see also

Chapter 3 of this thesis), that we use in this study.

There are several things that could be resolved by employing 2D laterally varying structures to model the historic earthquakes of the Imperial Valley. The first of these is the location of the events. As mentioned above, this topic has already been addressed (Doser and Kanamori, 1986; Sanders, et al., 1986) by fitting travel times for the few available records. Here, by using the alternate method of waveform modeling, the locations may be better defined, provided a sufficiently accurate structure is obtained. By using the entire waveform, on all components (vertical, radial and tangential), the mechanism may be determined for a single event at a single station. This is because the waveform contains the relative amplitudes of P, SH and SV motion at several take-off angles. Of course, complex time histories, unfavorable orientations, poorly modeled impedance contrasts and off-azimuth phases seriously hamper the determination of single station mechanisms. A good match in waveform between synthetic and observed provides the moment of an event by scaling the amplitude of the synthetic to match the data. Therefore, this study addresses the effects on seismic wave propagation that are due to the presence and termination of the deep continental basin occupying the Imperial Valley.

4.2 Historical Seismicity

This section presents the data collected at PAS for the historical and modern events listed in Tables 4.1 and 4.2. For the four most recent events listed, the data are obtained from the Pasadena Streckeisen digital, broadband, wide-dynamic-range instrument. The recent appearance of these instruments provides seismologists with unparalleled data access and data

quality. These four events are located by the southern California network, currently and jointly operated by Caltech and the U. S. Geological Survey, and consisting of over 250 stations telemetered to Caltech and digitally recorded. The epicenters are accurate to within 2 km, although depth control on the hypocenter is problematic because of the large lateral variations in seismic structure in and around the Imperial Valley region. Because the records are very high-quality and the epicenters are very accurate, these events are used as calibration events for this study. Another aspect of these events which makes them well-suited to calibration is that their magnitudes are small. In general, earthquakes of small magnitude have shorter, simpler time histories than larger events, allowing precise resolution in time, they are less likely to show time-varying mechanisms, and the fault surface involved has smaller area, giving better spatial precision. The usual drawback of using smaller events is a decrease in the signal-to-noise ratio, but in this case that is offset by the improved technology of the instrument. The earlier instruments operated at PAS do not produce useful waveforms for events this small in the Imperial Valley because of limitations in recording apparatus, recording medium and instrument sensitivity. Figure 4.1 shows the data collected for these four events. The very broad-band displacements are convolved with instrument responses for some of the instruments that have been operated at PAS. This is to show how the seismogram would appear as recorded on these more band-limited instruments. While it is possible to make convolutions of the vertical record with the torsion responses, the actual torsion instruments record only horizontal motions. Several points can be made here about the usefulness of the three instruments. First, the 0.8 second torsion completely obscures the longer-period surface waves, making

Figure 4.1 Rotated broad-band and filtered seismograms for four recent Imperial Valley earthquakes: January 28, 1988, May 17, 1988, July 2, 1988 and March 6, 1989. Event date and time are at the upper left of each row, peak amplitude in cm is at the upper right of each trace. Refer to Tables 4.1 and 4.2 for more information.

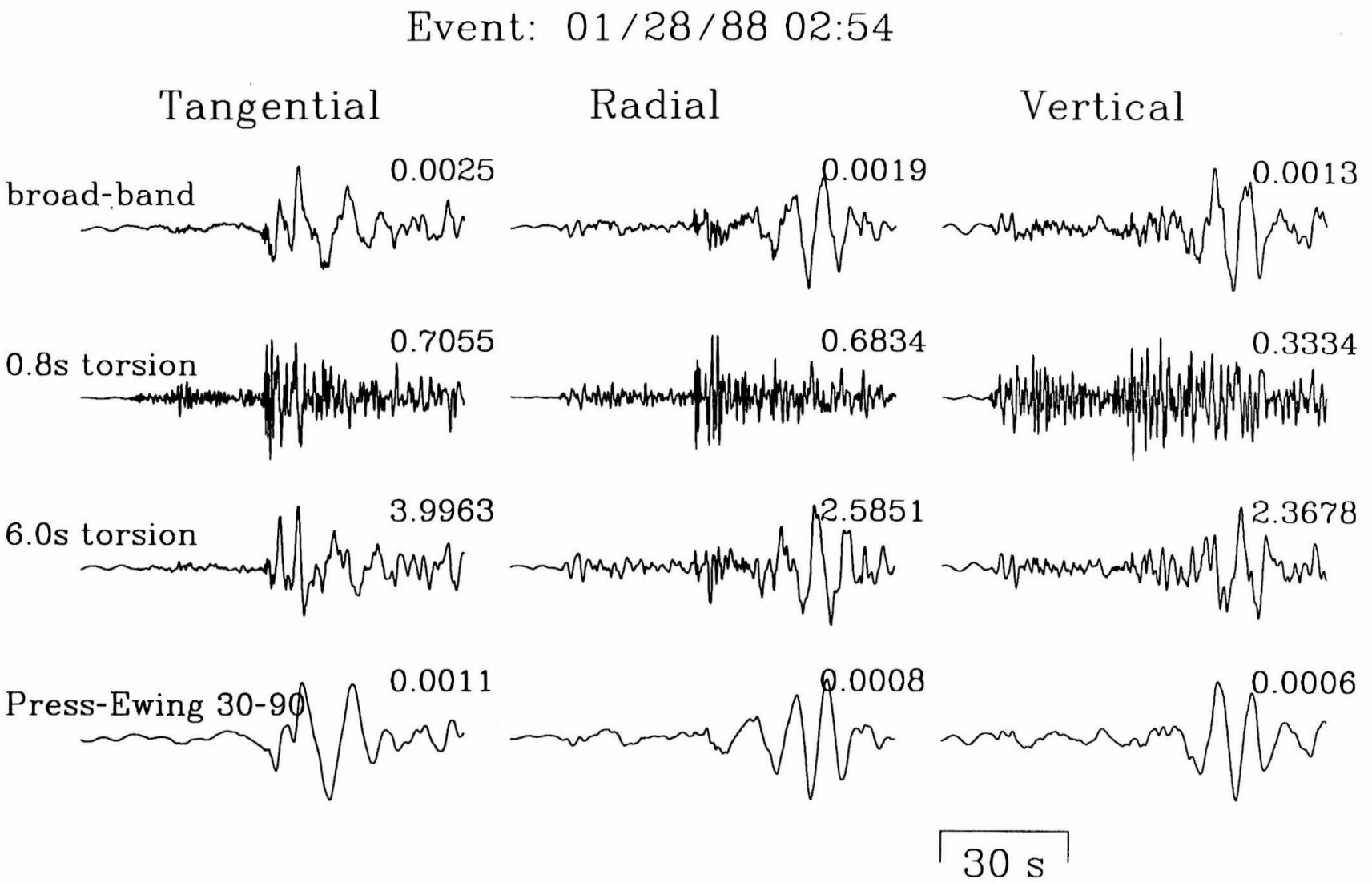
Event: 01/28/88 02:54
Tangential
Radial
Vertical
broad-band
0.0025
0.0019
0.0013
0.8s torsion
0.7055
0.6834
0.3334
6.0s torsion
3.9963
2.5851
2.3678
Press-Ewing 30-90
0.0011
0.0008
0.0006
30 s

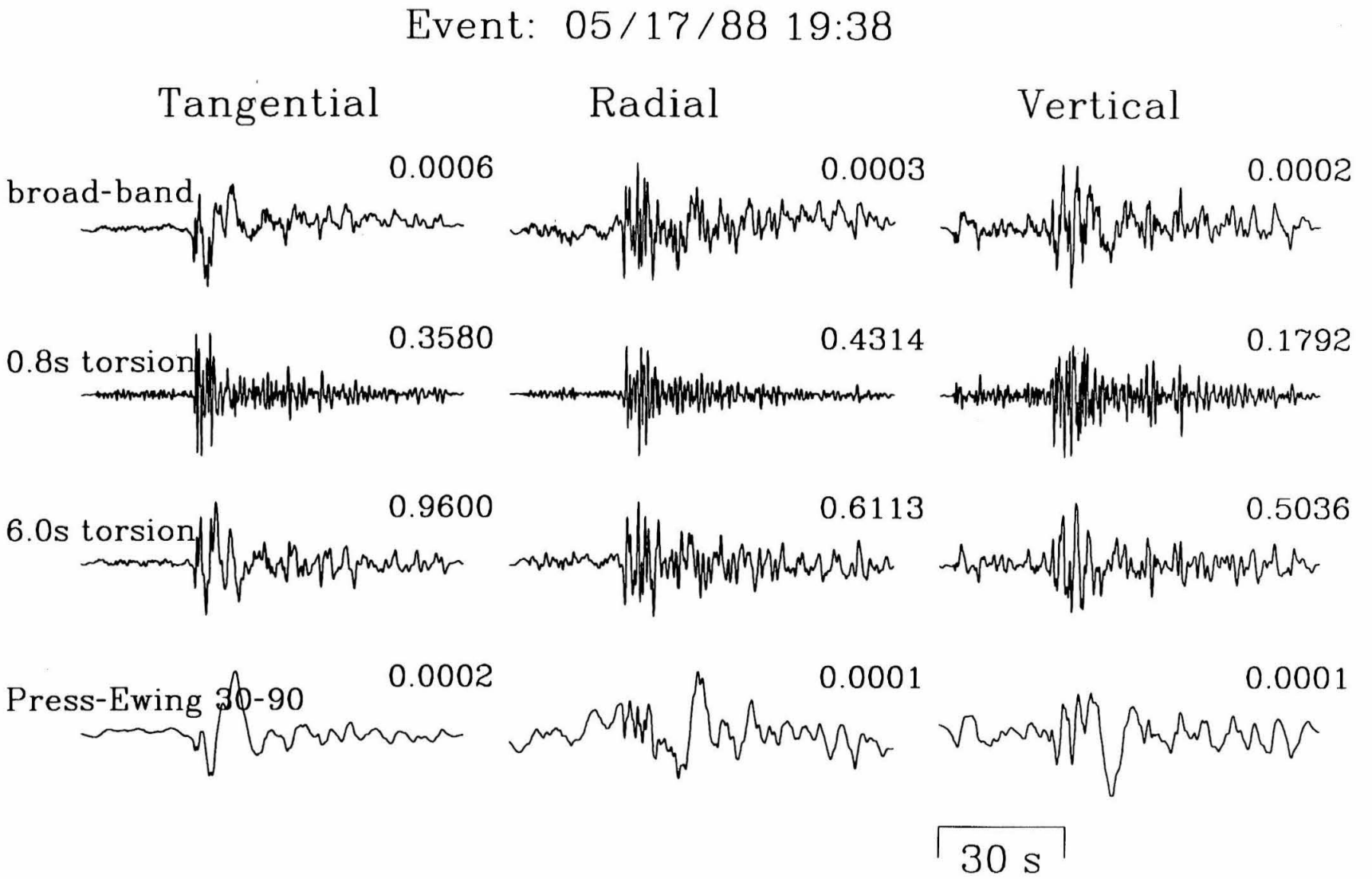
Event: 05/17/88 19:38
Tangential
Radial
Vertical
broad-band
0.0006
0.0003
0.0002
0.8s torsion
0.3580
0.4314
0.1792
6.0s torsion
0.9600
0.6113
0.5036
Press-Ewing 30-90
0.0002
0.0001
0.0001
30 s

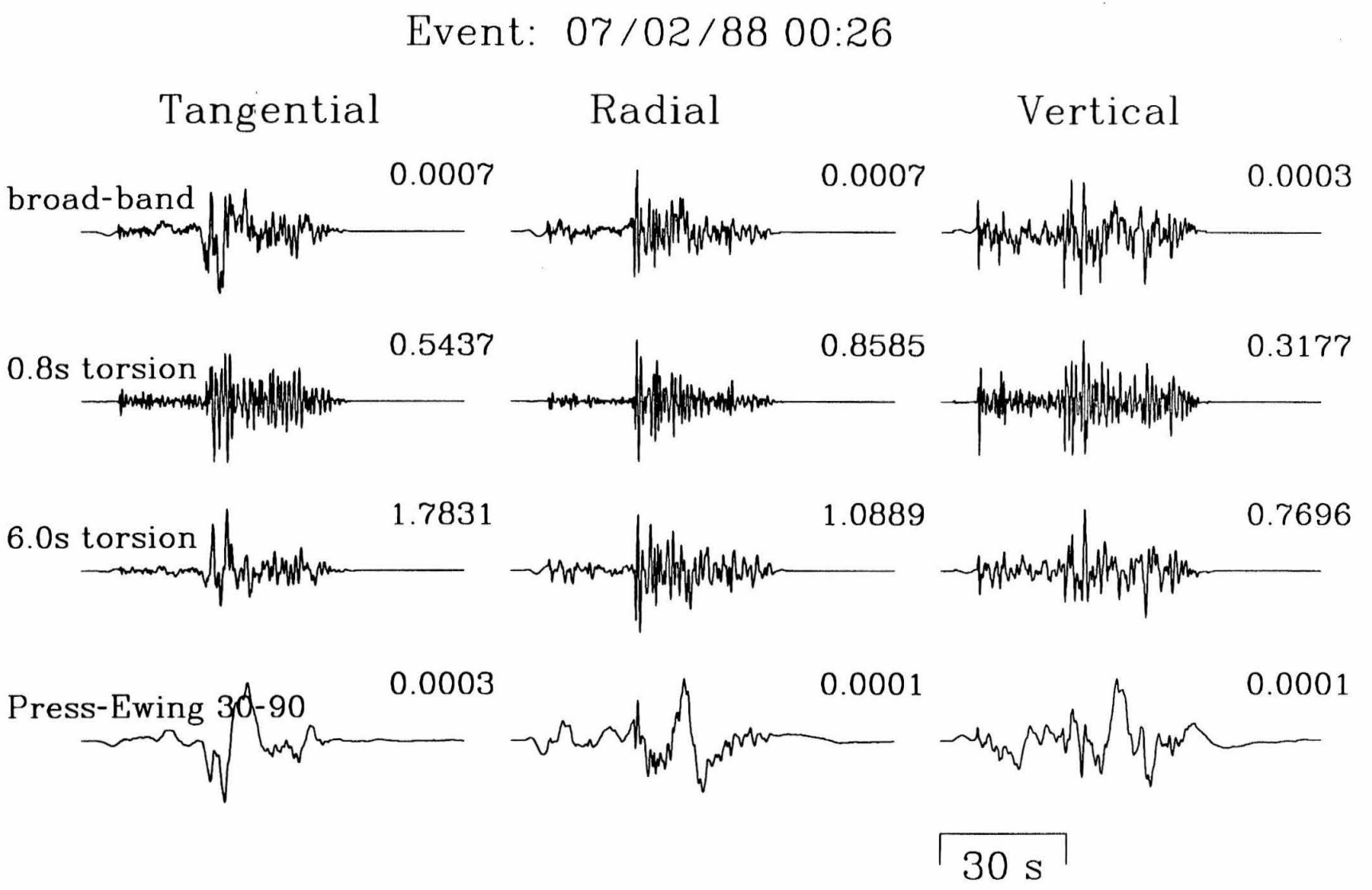
Event: 07/02/88 00:26
Tangential
Radial
Vertical
broad-band
0.0007
0.0007
0.0003
0.8s torsion
0.5437
0.8585
0.3177
6.0s torsion
1.7831
1.0889
0.7696
Press-Ewing 30-90
0.0003
0.0001
0.0001
30 s

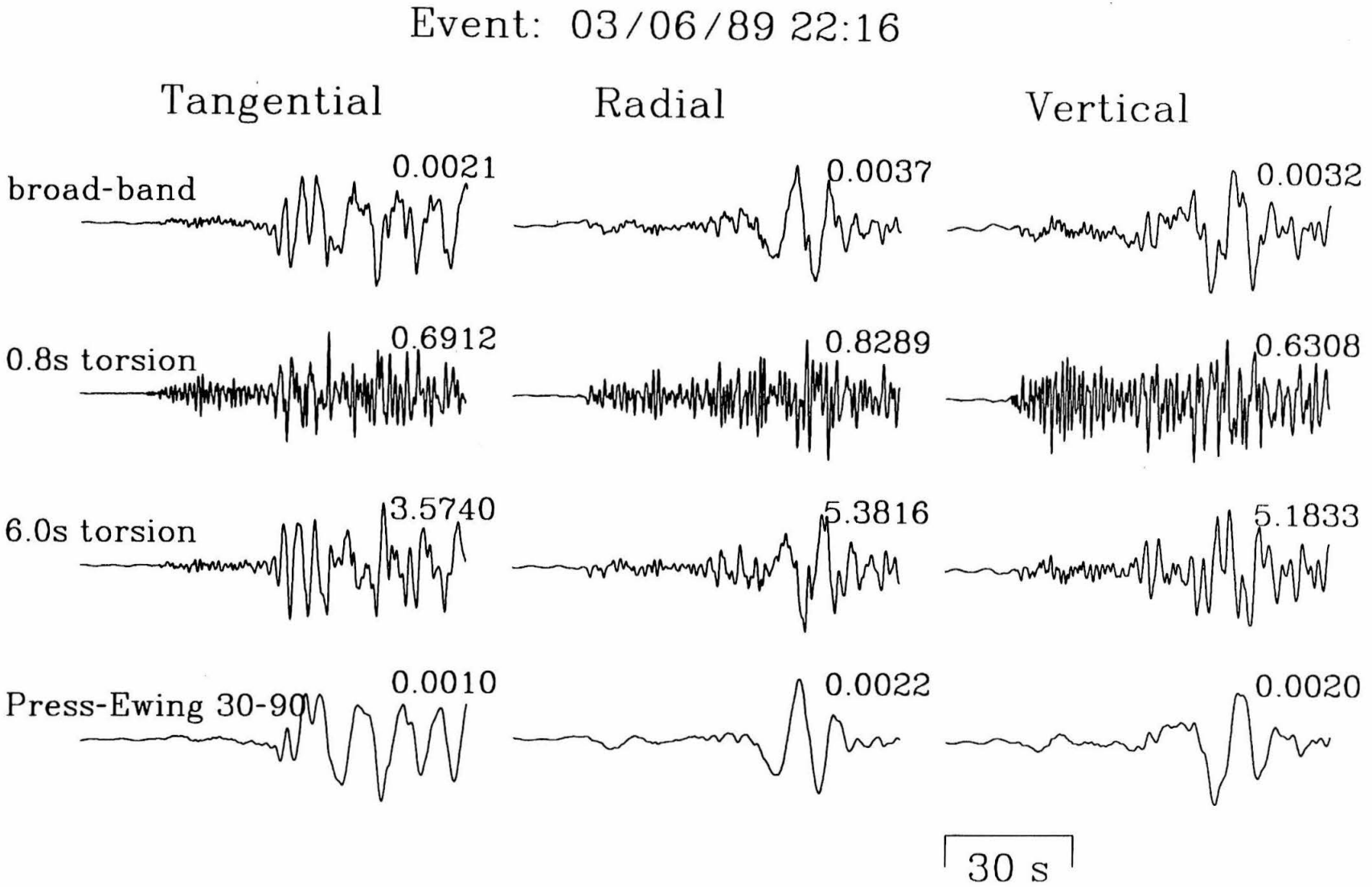
Event: 03/06/89 22:16
Tangential
Radial
Vertical
broad-band
0.0021
0.0037
0.0032
0.8s torsion
0.6912
0.8289
0.6308
6.0s torsion
3.5740
5.3816
5.1833
Press-Ewing 30-90
0.0010
0.0022
0.0020
30 s

this instrument a poor choice for comparing synthetic surface waves. The Press-Ewing, on the other hand, obscures body phases. The 6.0 second torsion appears ideal because both the body and surface waves are preserved for regional events in this magnitude range (M_L between 3.5 and 6.0). This is primarily because of the characteristic source time functions for earthquakes of this size, and this is also evident in the similarity of the broad-band and 6.0 second torsion seismograms.

Figure 4.2 shows some of the three-component Press-Ewing 30-90 records collected and digitized for this study. Figure 4.3 shows the corresponding rotated horizontal components. The records are presented in order of increasing range from PAS, according to catalog location. The events shown are hand-digitized from the original paper records, as are the seismograms from the torsion instruments. No filtering is applied to the hand-digitized records. The filtered broad-band records are interspersed in the profiles for the purpose of calibration. The 30-90 is the longest period of the instruments considered here. It is useful because much of the higher frequency scattered energy is eliminated, allowing for clearer interpretation of the broad regional structure. The records have been roughly aligned at the MOHO S head wave (Sn), to enhance the visual comparison. The order of the traces is determined by the range of the catalog location from PAS, with the closest events at the top of each component record section. Each trace is labeled with its catalog origin time and the peak amplitude in cm. At the periods characteristic of regional seismograms written by this instrument, the traces vary only slightly with range. There is greater similarity between the tangential traces than between either the radial or vertical traces. This is expected because of complexities of the P-SV-Rayleigh wave system.

Figure 4.2 North, east and vertical components from the Press-Ewing 30-90 instrument at PAS. Recent broad-band records filtered with this instrument response are interspersed in the profiles. Event date and time are at the upper left of each trace, peak amplitude in cm is at the upper right. Refer to Tables 4.1 and 4.2 for more information.

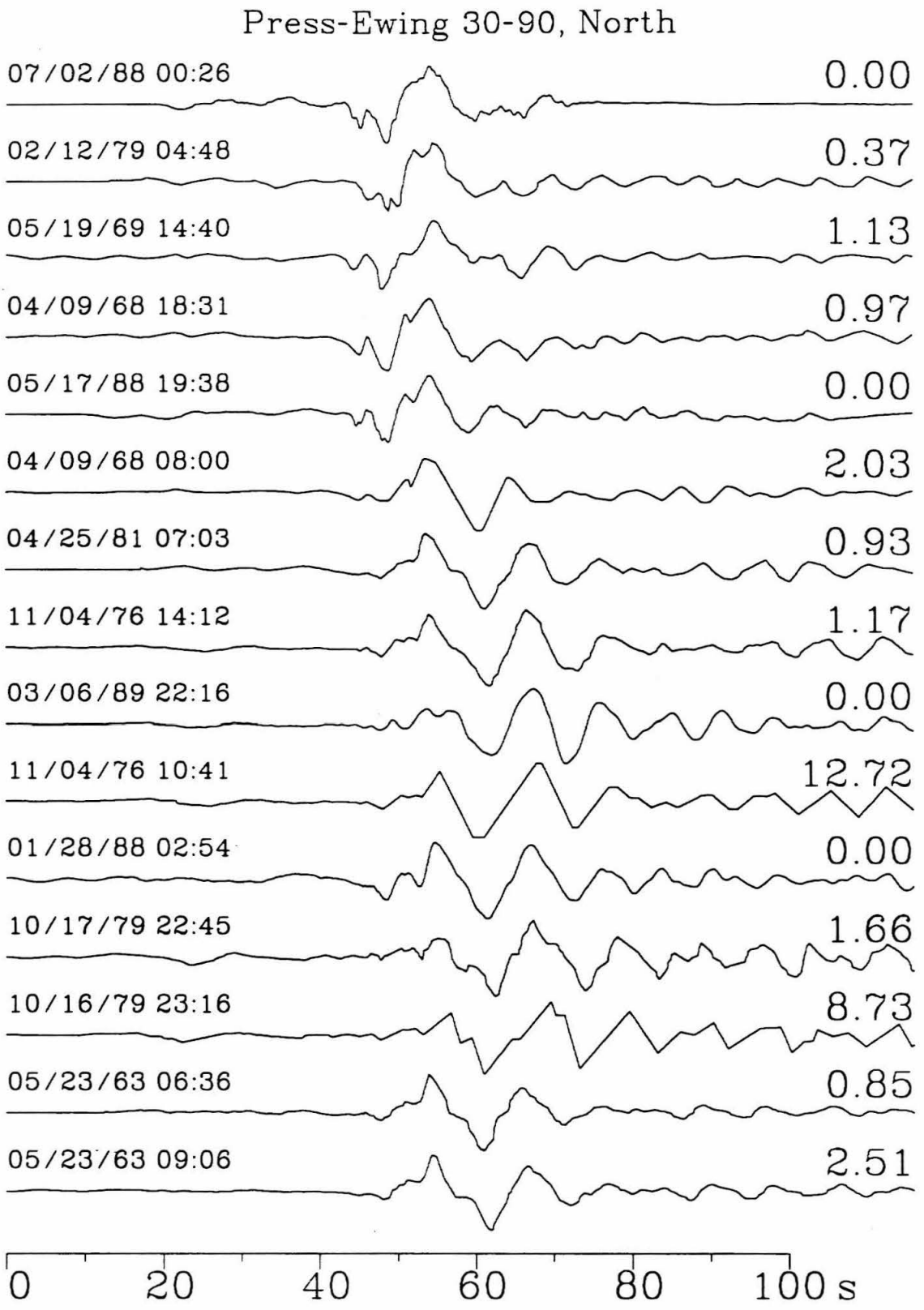
Press-Ewing 30-90, North
07/02/88 00:26
0.00
02/12/79 04:48
0.37
05/19/69 14:40
1.13
04/09/68 18:31
0.97
05/17/88 19:38
0.00
04/09/68 08:00
2.03
04/25/81 07:03
0.93
11/04/76 14:12
1.17
03/06/89 22:16
0.00
11/04/76 10:41
12.72
01/28/88 02:54
0.00
10/17/79 22:45
1.66
10/16/79 23:16
8.73
05/23/63 06:36
0.85
05/23/63 09:06
2.51
0
20
40
60
80
100 s

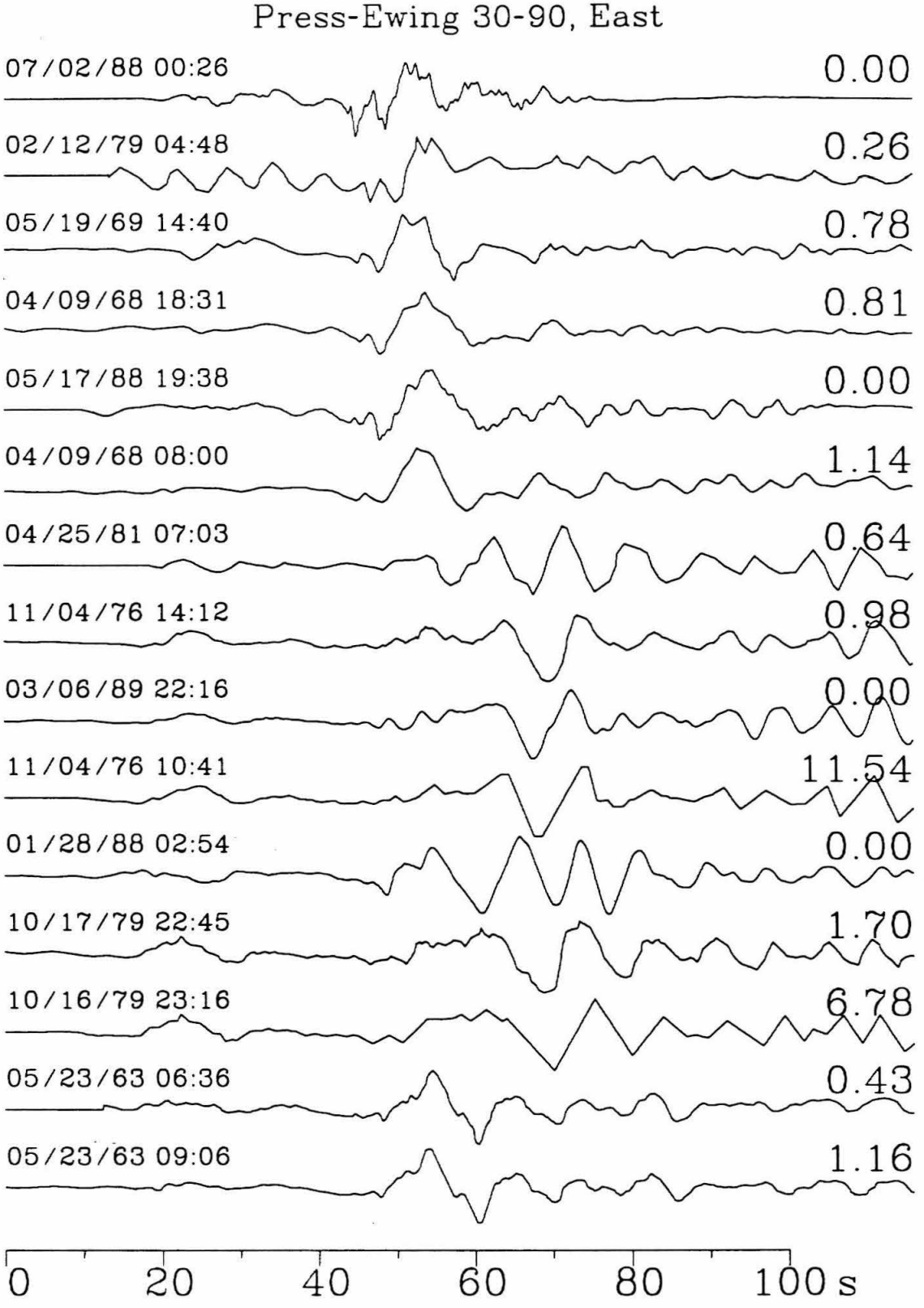
Press-Ewing 30-90, East
07/02/88 00:26
0.00
02/12/79 04:48
0.26
05/19/69 14:40
0.78
04/09/68 18:31
0.81
05/17/88 19:38
0.00
04/09/68 08:00
1.14
04/25/81 07:03
0.64
11/04/76 14:12
0.98
03/06/89 22:16
0.00
11/04/76 10:41
11.54
01/28/88 02:54
0.00
10/17/79 22:45
1.70
10/16/79 23:16
6.78
05/23/63 06:36
0.43
05/23/63 09:06
1.16
0
20
40
60
80
100 s

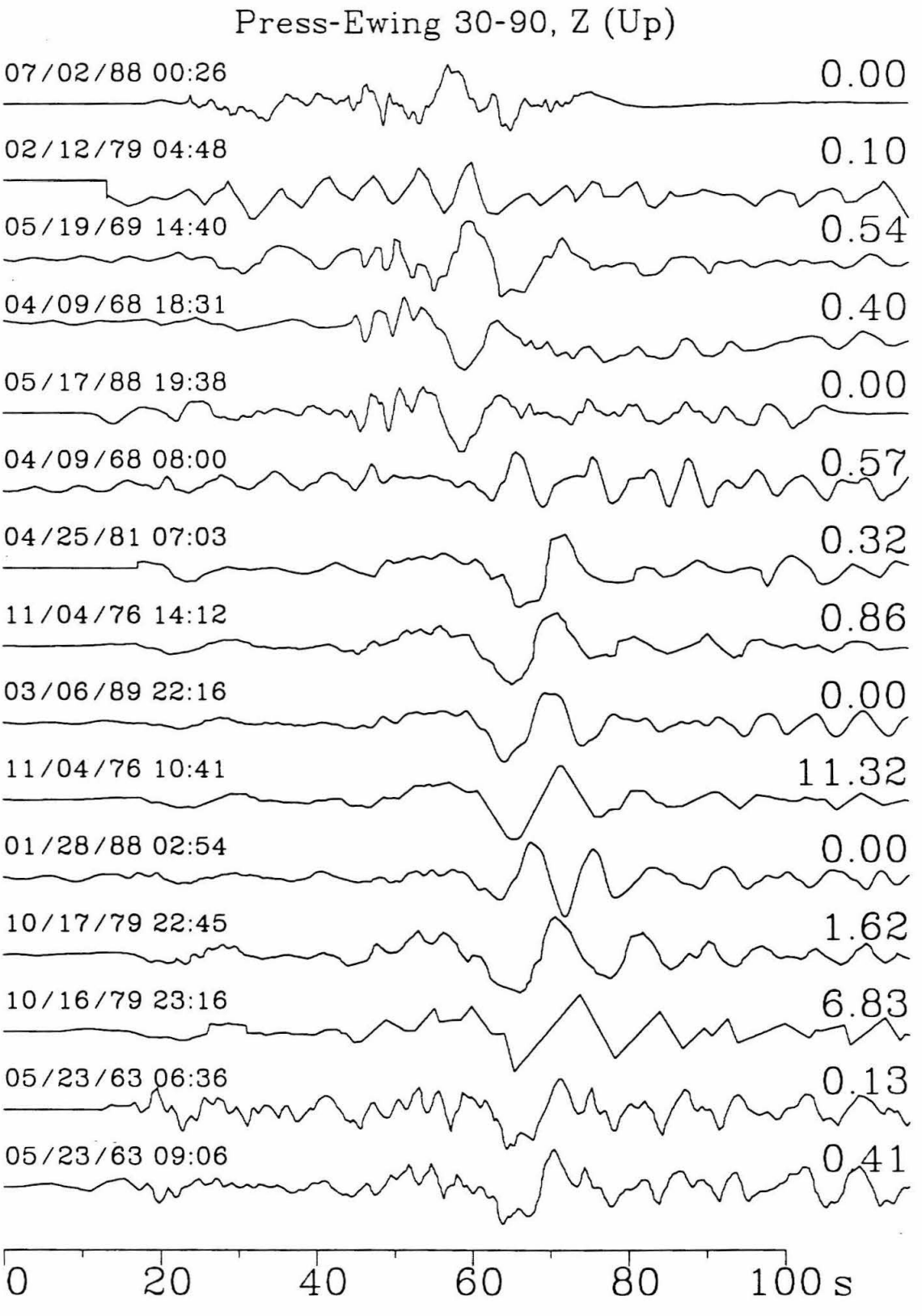
Press-Ewing 30-90, Z (Up)
07/02/88 00:26
0.00
02/12/79 04:48
0.10
05/19/69 14:40
0.54
04/09/68 18:31
0.40
05/17/88 19:38
0.00
04/09/68 08:00
0.57
04/25/81 07:03
0.32
11/04/76 14:12
0.86
03/06/89 22:16
0.00
11/04/76 10:41
11.32
01/28/88 02:54
0.00
10/17/79 22:45
1.62
10/16/79 23:16
6.83
05/23/63 06:36
0.13
05/23/63 09:06
0.41
0
20
40
60
80
100 s

Figure 4.3 Rotated tangential and radial components from the Press-Ewing 30-90 instrument at PAS. Recent broad-band records filtered with this instrument response are interspersed in the profiles. Event date and time are at the upper left of each trace; peak amplitude in cm is at the upper right. Refer to Tables 4.1 and 4.2 for more information.

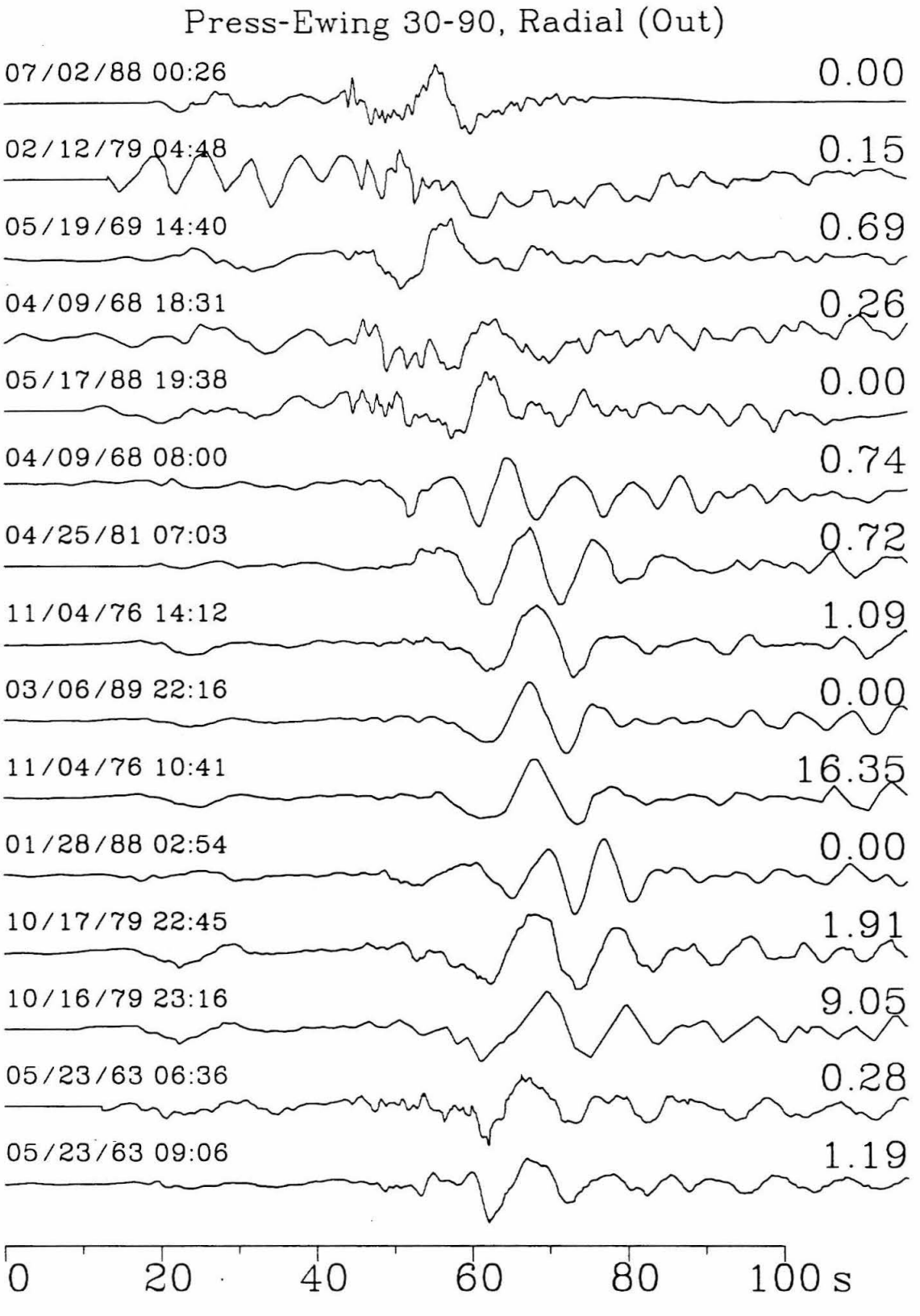
Press-Ewing 30-90, Radial (Out)
07/02/88 00:26
0.00
02/12/79 04:48
0.15
05/19/69 14:40
0.69
04/09/68 18:31
0.26
05/17/88 19:38
0.00
04/09/68 08:00
0.74
04/25/81 07:03
0.72
11/04/76 14:12
1.09
03/06/89 22:16
0.00
11/04/76 10:41
16.35
01/28/88 02:54
0.00
10/17/79 22:45
1.91
10/16/79 23:16
9.05
05/23/63 06:36
0.28
05/23/63 09:06
1.19
0
20
40
60
80
100 s

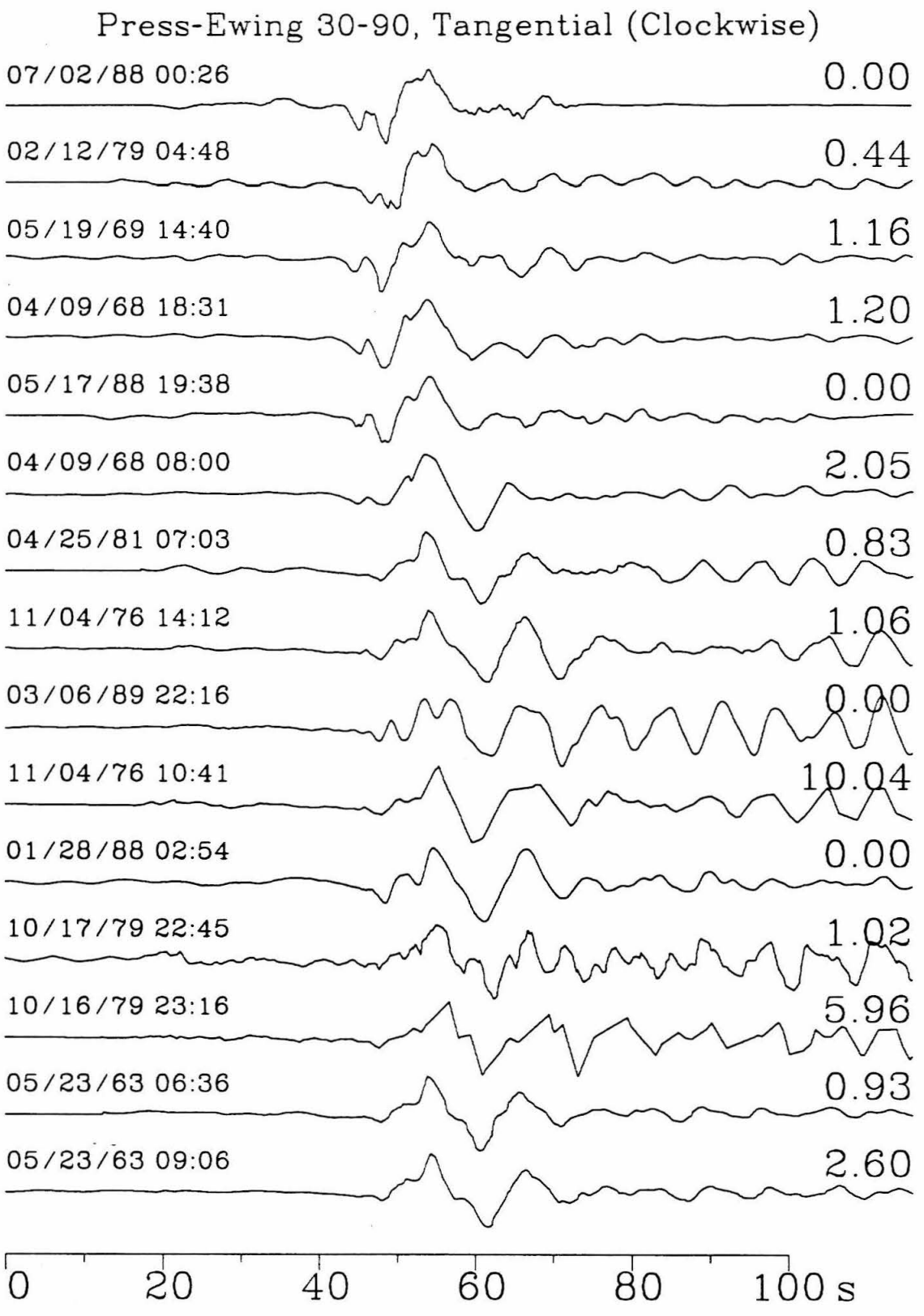
Press-Ewing 30-90, Tangential (Clockwise)
07/02/88 00:26
0.00
02/12/79 04:48
0.44
05/19/69 14:40
1.16
04/09/68 18:31
1.20
05/17/88 19:38
0.00
04/09/68 08:00
2.05
04/25/81 07:03
0.83
11/04/76 14:12
1.06
03/06/89 22:16
0.00
11/04/76 10:41
10.04
01/28/88 02:54
0.00
10/17/79 22:45
1.02
10/16/79 23:16
5.96
05/23/63 06:36
0.93
05/23/63 09:06
2.60
0
20
40
60
80
100 s

Another interesting feature is that the ratios of the peak amplitudes between the various components are not constant. This is most likely due to variations in mechanism and source depth. Variations in source mechanism can directly change these ratios, but will also change the waveform, since different arrivals can change polarity independently. Source depth, on the other hand, affects the Love and Rayleigh amplitudes differently, affecting peak-amplitude ratios. Because of the predominance of strike-slip mechanisms in the Imperial Valley region, if several events at similar ranges have similar waveforms, then depth must be the controlling factor in determining the amplitude ratios. No effort is made here to sort the data according to source depth, because the catalog source depths are poorly constrained for most of the events. Since the 30-90 instrument does not have as long a history as the torsion instruments, no events are recorded in the transitional region between the San Jacinto fault and the Superstition Hills fault. The events fall in separate groups according to range: those between 175 and 200 km, and those beyond 260 km. This explains the appearance of two groups based on waveform. Also important is the fact that the events beyond 260 km are all in or beneath the basin structure, whereas the closer events are not. The similarity between waveforms for both range groups indicates that the structure responsible for the waveform is not sensitive to small variations in source location. It also indicates that the mechanisms of most of the events are similar (strike-slip). This information is useful when constructing models.

Some of the seismograms collected and digitized for the 6.0 second Wood-Anderson torsion instrument are presented in Figure 4.4, along with the rotated components. There is no vertical component to this instrument.

Figure 4.4 North, east and rotated tangential and radial components from the Wood-Anderson 6.0 second torsion instrument at PAS. Recent broad-band records filtered with this instrument response are interspersed in the profiles. Event date and time are at the upper left of each trace; peak amplitude in cm is at the upper right. Refer to Tables 4.1 and 4.2 for more information.

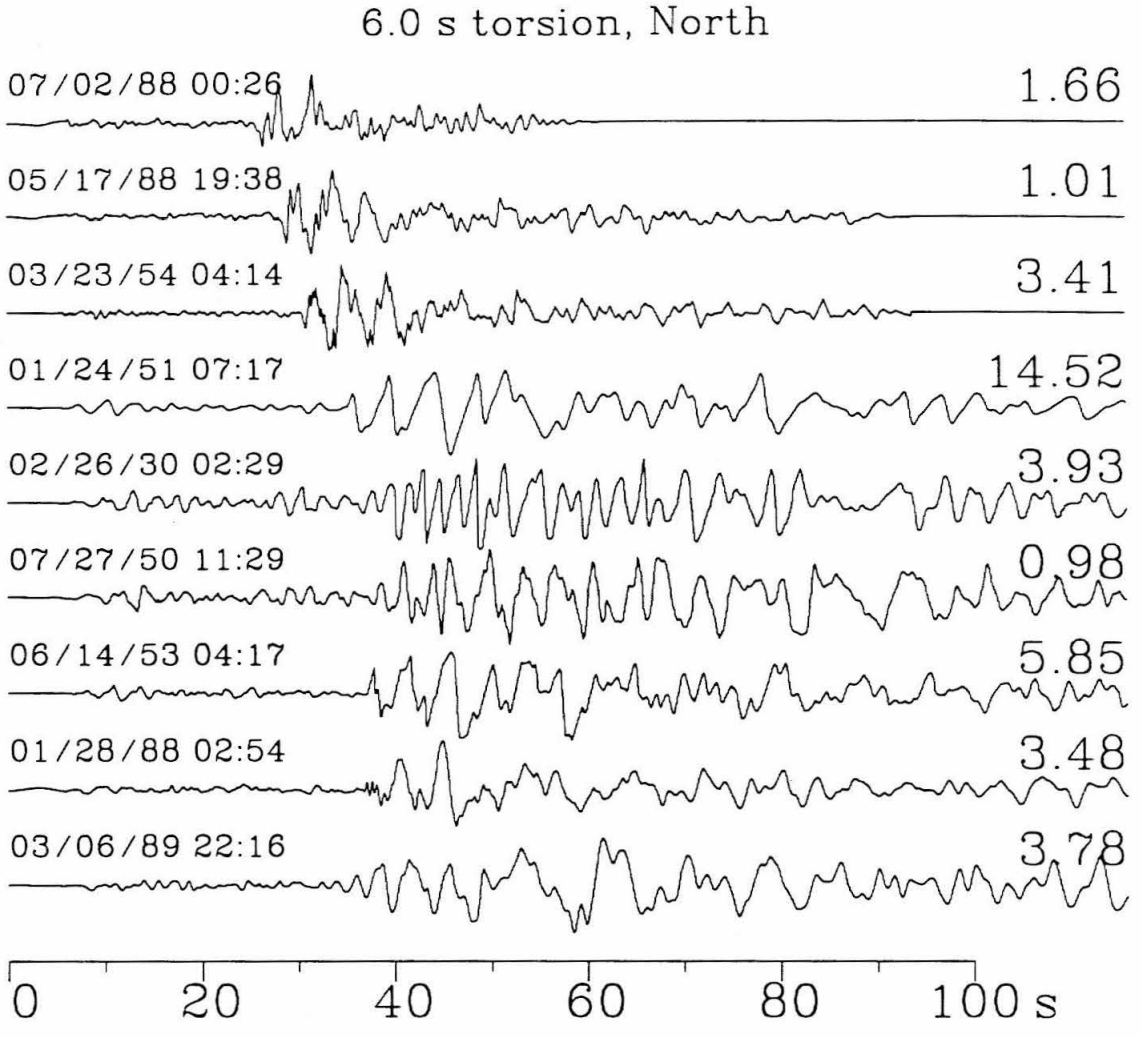
6.0 s torsion, North
07/02/88 00:26
1.66
05/17/88 19:38
1.01
03/23/54 04:14
3.41
01/24/51 07:17
14.52
02/26/30 02:29
3.93
07/27/50 11:29
0.98
06/14/53 04:17
5.85
01/28/88 02:54
3.48
03/06/89 22:16
3.78
0
20
40
60
80
100 s

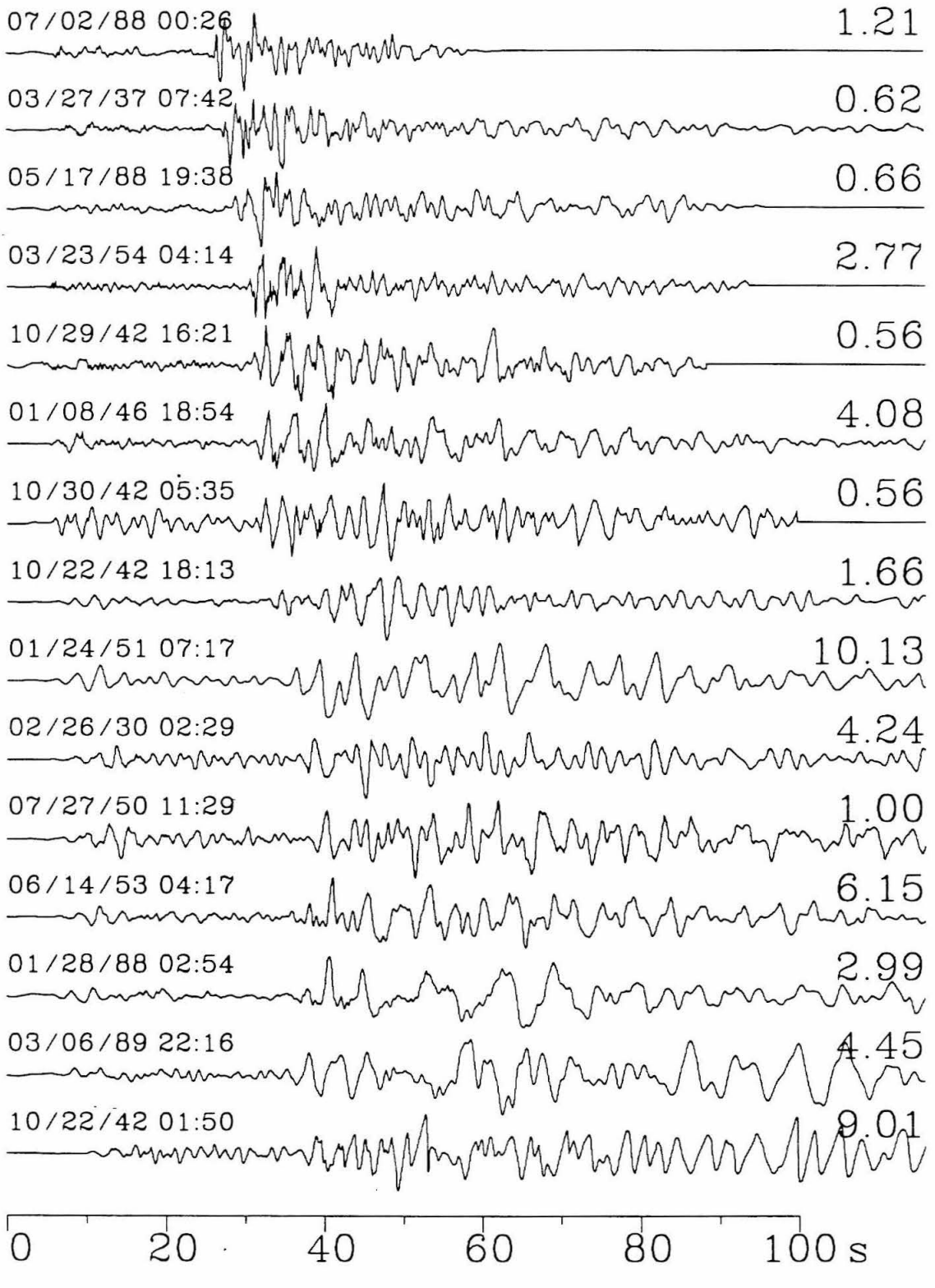
6.0 s torsion, East
07/02/88 00:26
1.21
03/27/37 07:42
0.62
05/17/88 19:38
0.66
03/23/54 04:14
2.77
10/29/42 16:21
0.56
01/08/46 18:54
4.08
10/30/42 05:35
0.56
10/22/42 18:13
1.66
01/24/51 07:17
10.13
02/26/30 02:29
4.24
07/27/50 11:29
1.00
06/14/53 04:17
6.15
01/28/88 02:54
2.99
03/06/89 22:16
4.45
10/22/42 01:50
9.01
0
20
40
60
80
100 s

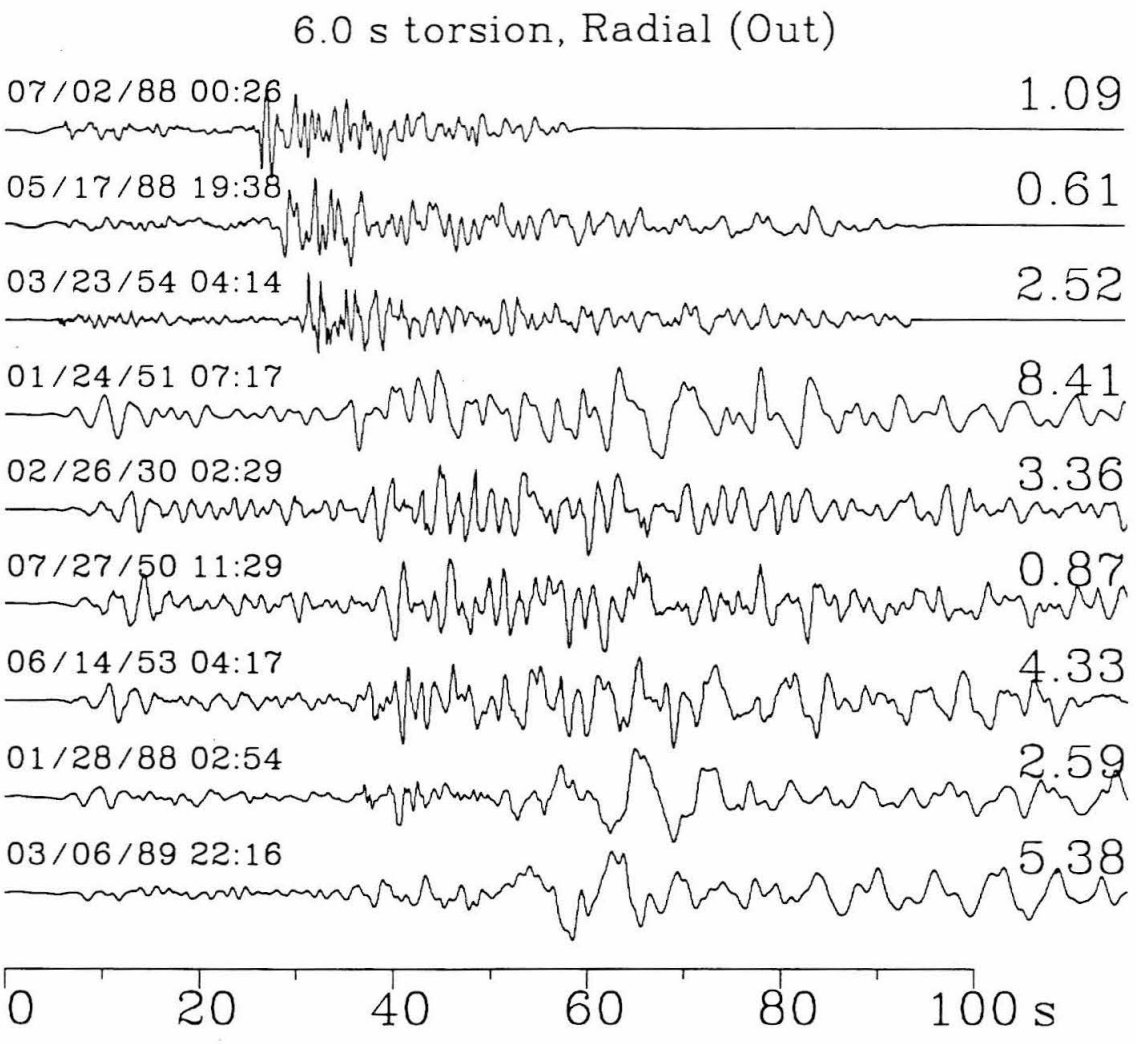
6.0 s torsion, Radial (Out)
07/02/88 00:26
1.09
05/17/88 19:38
0.61
03/23/54 04:14
2.52
01/24/51 07:17
8.41
02/26/30 02:29
3.36
07/27/50 11:29
0.87
06/14/53 04:17
4.33
01/28/88 02:54
2.59
03/06/89 22:16
5.38
0
20
40
60
80
100 s

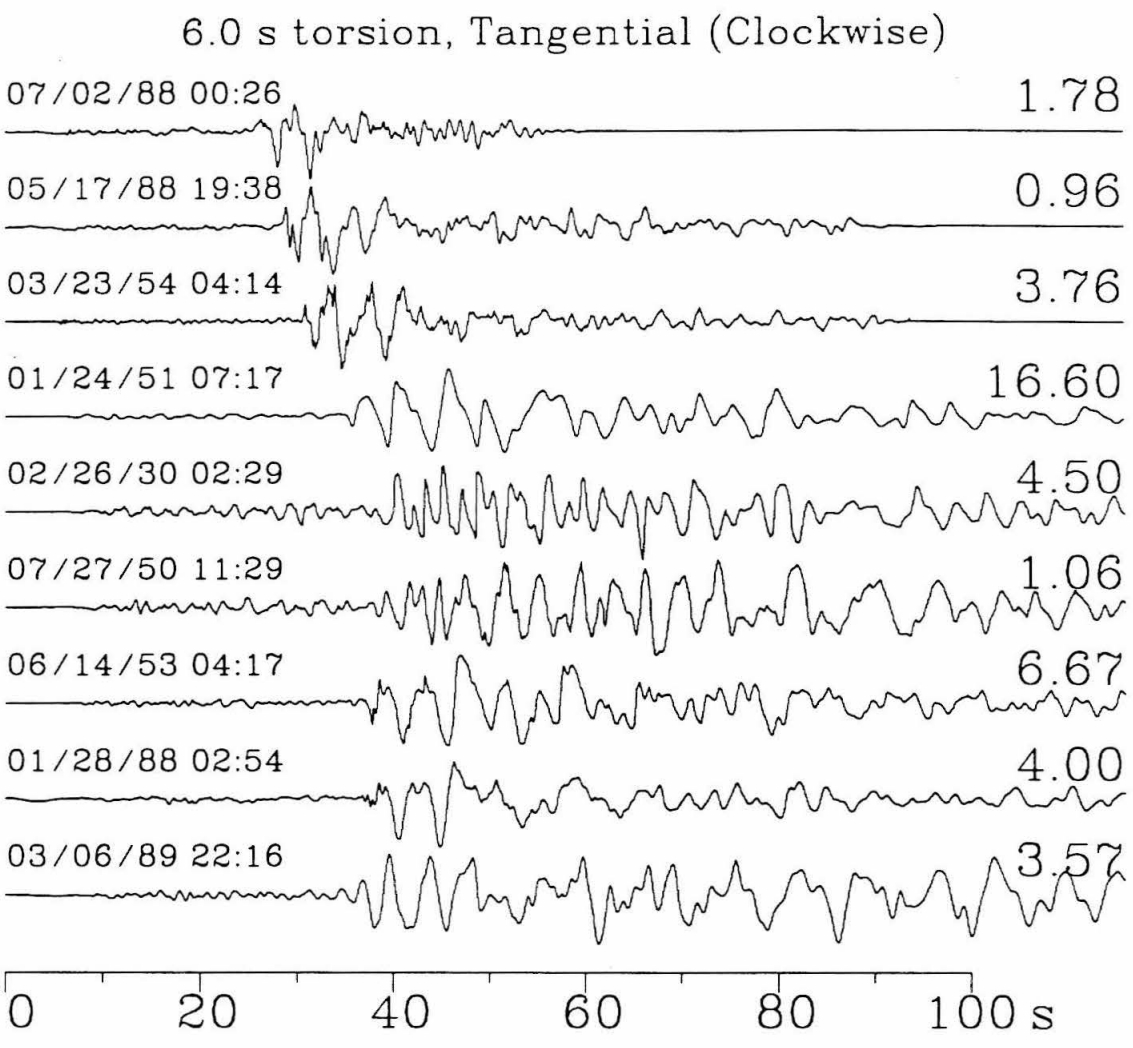
6.0 s torsion, Tangential (Clockwise)
07/02/88 00:26
1.78
05/17/88 19:38
0.96
03/23/54 04:14
3.76
01/24/51 07:17
16.60
02/26/30 02:29
4.50
07/27/50 11:29
1.06
06/14/53 04:17
6.67
01/28/88 02:54
4.00
03/06/89 22:16
3.57
0
20
40
60
80
100 s

The east component shows more records than the north because only the east component was operated at PAS from 1932 until the 1950s (the north was operated intermittently in the 1940s). The instrument was removed on July 9, 1954. (It was installed for a short while as northeast, southeast pair.) Because the principal P and S phases are visible in most of the records shown, the records are ordered according to apparent S-P time, for phases which could be traced through the records. In the presentation of the broad-band data above, the 6.0 second torsion is shown to be an ideal instrument for studying waveforms of intermediate to large regional events. The data presented support this assertion. While many features can be traced through several events, the waveforms of each event remain distinct. This means that most of the record is due to the regional structure, and the phases produced by this structure span sufficient range to be represented on several seismograms. Most of the complications in waveform are not due to complicated source time histories, since such histories are usually not repeatable. The differences between records as a function of range are the information necessary to construct an accurate model of the structure. Some conclusions regrading the nature of the older events can be gained by examining these data alone. Two pairs of events are nearly identical. These are 1930 and 1950 as one pair, and 1953 and January, 1988 as a second. The correspondence between the records of each pair is much greater than that between any other pair of events in the collection. This indicates that the events must have nearly identical locations and mechanisms to within the resolution of a wavelength corresponding to the dominant periods in the records (about 10 km). Another interesting feature of the data presented here is the collection of east components for aftershocks of the 1942 Borrego

Valley earthquake. The waveforms, and apparent S-P times, vary across the entire collection from ranges of 200 to 270 km. This is interesting in the light of the difficulty this earthquake sequence has presented in the past in terms of location. Apparently, the aftershocks are spread over several 10s of km, and probably a wide range of depths. Therefore, to fully understand this series, many more events should be examined and compared according to waveform to each other and to some calibration events so that the events may be sorted into distinct groups for relocation. This way, groups of similar events might be identified with structures in the Imperial Valley, and a model for the progression of the series could be developed. One more note of interest is the duration and amplitude of the surface waves. Large amplitudes for long durations indicate events that are far into the basin structure and are possibly shallow. The two most extreme of these events are the 1989 Niland earthquake and the 1:50 GMT aftershock on October 22, 1942. The Niland event has a catalog location that places it at the southeast shore of the Salton Sea, which is indeed far into the basin. The 1942 aftershock's true location is not known, but has been suggested to be beneath the Salton Sea.

The final instrument examined here is the standard 0.8 second Wood-Anderson torsion. Some of the data collected and digitized are shown in Figure 4.5, along with rotated versions. Here, as in the 30-90 presentation, the records are ordered by range from PAS according to catalog locations. There is little in these records that corresponds between events. At these frequencies, the structure is too fine, and changes in location and depth both rapidly change the waveform. Therefore, there is little that can be modeled in these records. There is something that can be done. While deconvolution of these

Figure 4.5 North, east and rotated tangential and radial components from the Wood-Anderson 0.8 second torsion instrument at PAS. Recent broad-band records filtered with this instrument response are interspersed in the profiles. Event date and time are at the upper left of each trace; peak amplitude in cm is at the upper right. Refer to Tables 4.1 and 4.2 for more information.

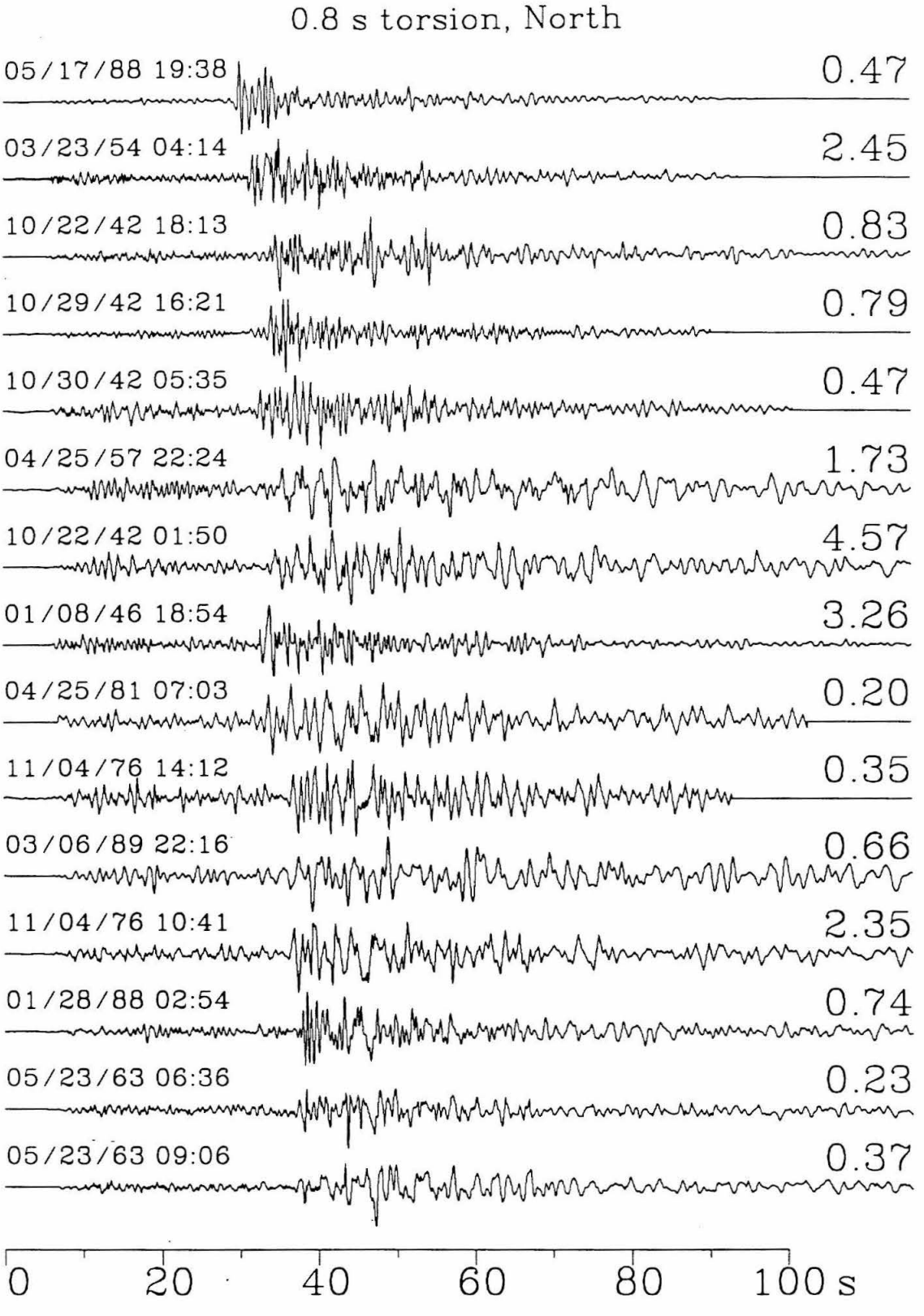
0.8 s torsion, North
05/17/88 19:38
0.47
03/23/54 04:14
2.45
10/22/42 18:13
0.83
10/29/42 16:21
0.79
10/30/42 05:35
0.47
04/25/57 22:24
1.73
10/22/42 01:50
4.57
01/08/46 18:54
3.26
04/25/81 07:03
0.20
11/04/76 14:12
0.35
03/06/89 22:16
0.66
11/04/76 10:41
2.35
01/28/88 02:54
0.74
05/23/63 06:36
0.23
05/23/63 09:06
0.37
0
20
40
60
80
100 s

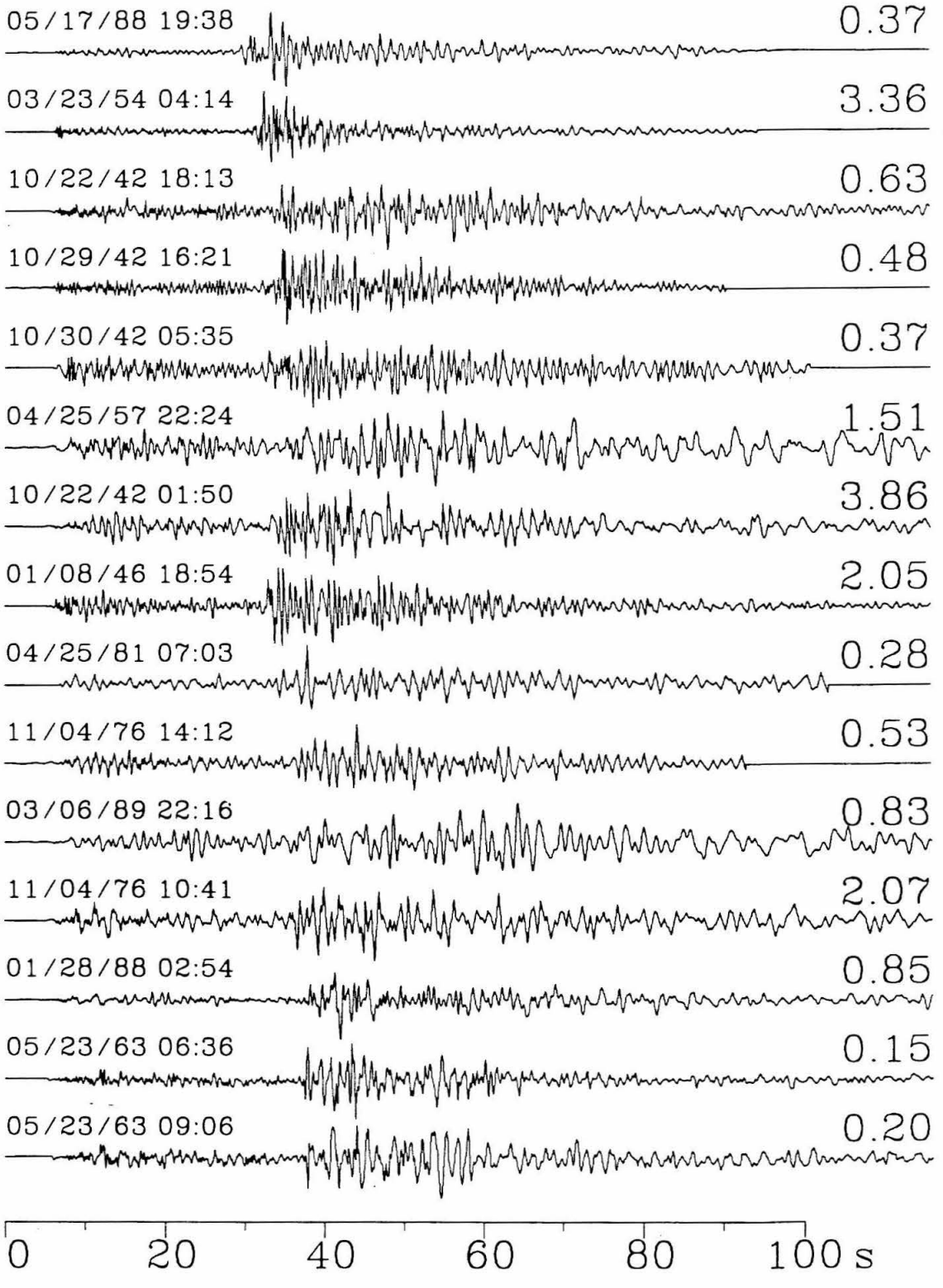
0.8 s torsion, East
05/17/88 19:38
0.37
03/23/54 04:14
3.36
10/22/42 18:13
0.63
10/29/42 16:21
0.48
10/30/42 05:35
0.37
04/25/57 22:24
1.51
10/22/42 01:50
3.86
01/08/46 18:54
2.05
04/25/81 07:03
0.28
11/04/76 14:12
0.53
03/06/89 22:16
0.83
11/04/76 10:41
2.07
01/28/88 02:54
0.85
05/23/63 06:36
0.15
05/23/63 09:06
0.20
0
20
40
60
80
100 s

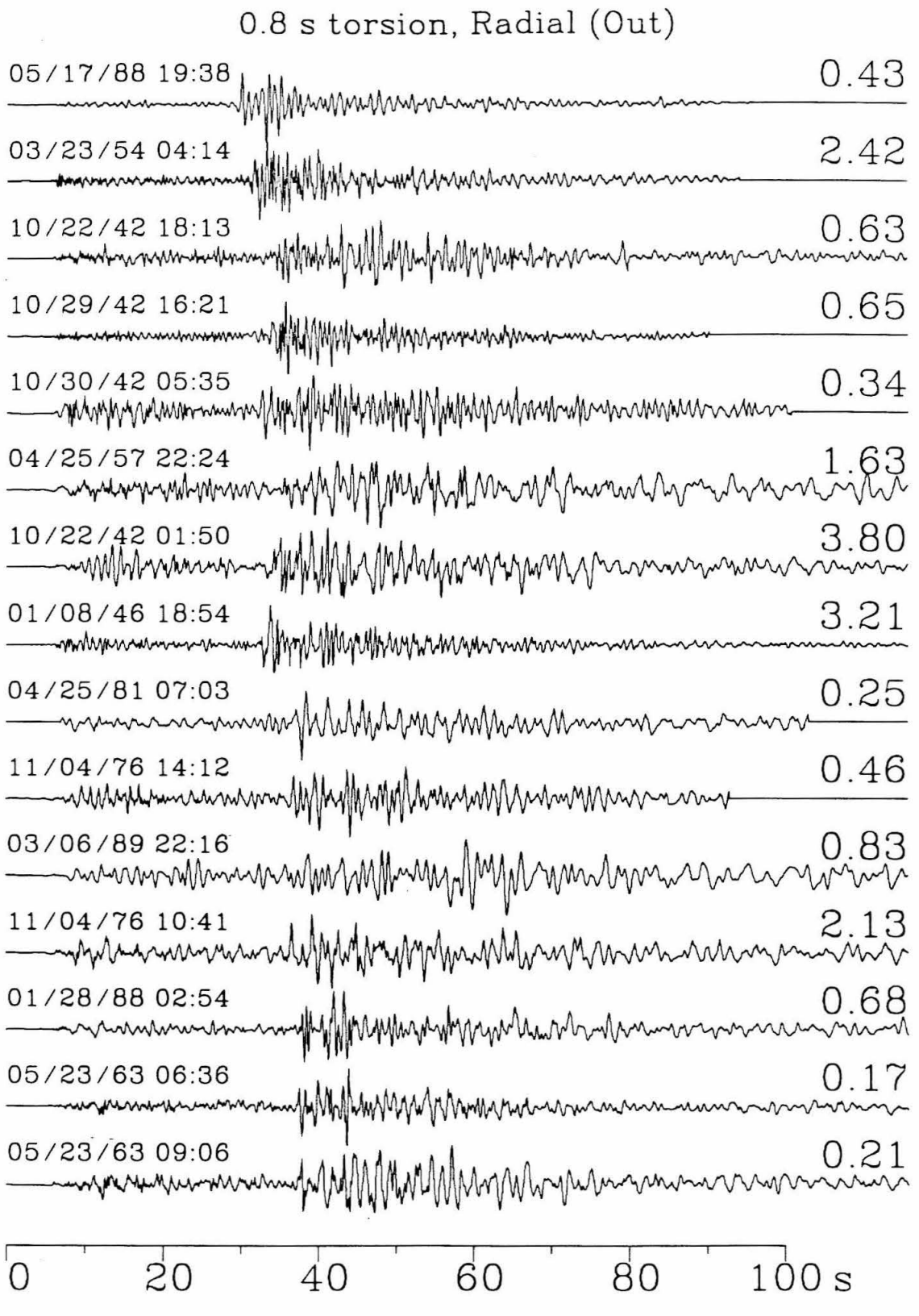
0.8 s torsion, Radial (Out)
05/17/88 19:38
0.43
03/23/54 04:14
2.42
10/22/42 18:13
0.63
10/29/42 16:21
0.65
10/30/42 05:35
0.34
04/25/57 22:24
1.63
10/22/42 01:50
3.80
01/08/46 18:54
3.21
04/25/81 07:03
0.25
11/04/76 14:12
0.46
03/06/89 22:16
0.83
11/04/76 10:41
2.13
01/28/88 02:54
0.68
05/23/63 06:36
0.17
05/23/63 09:06
0.21
0
20
40
60
80
100 s

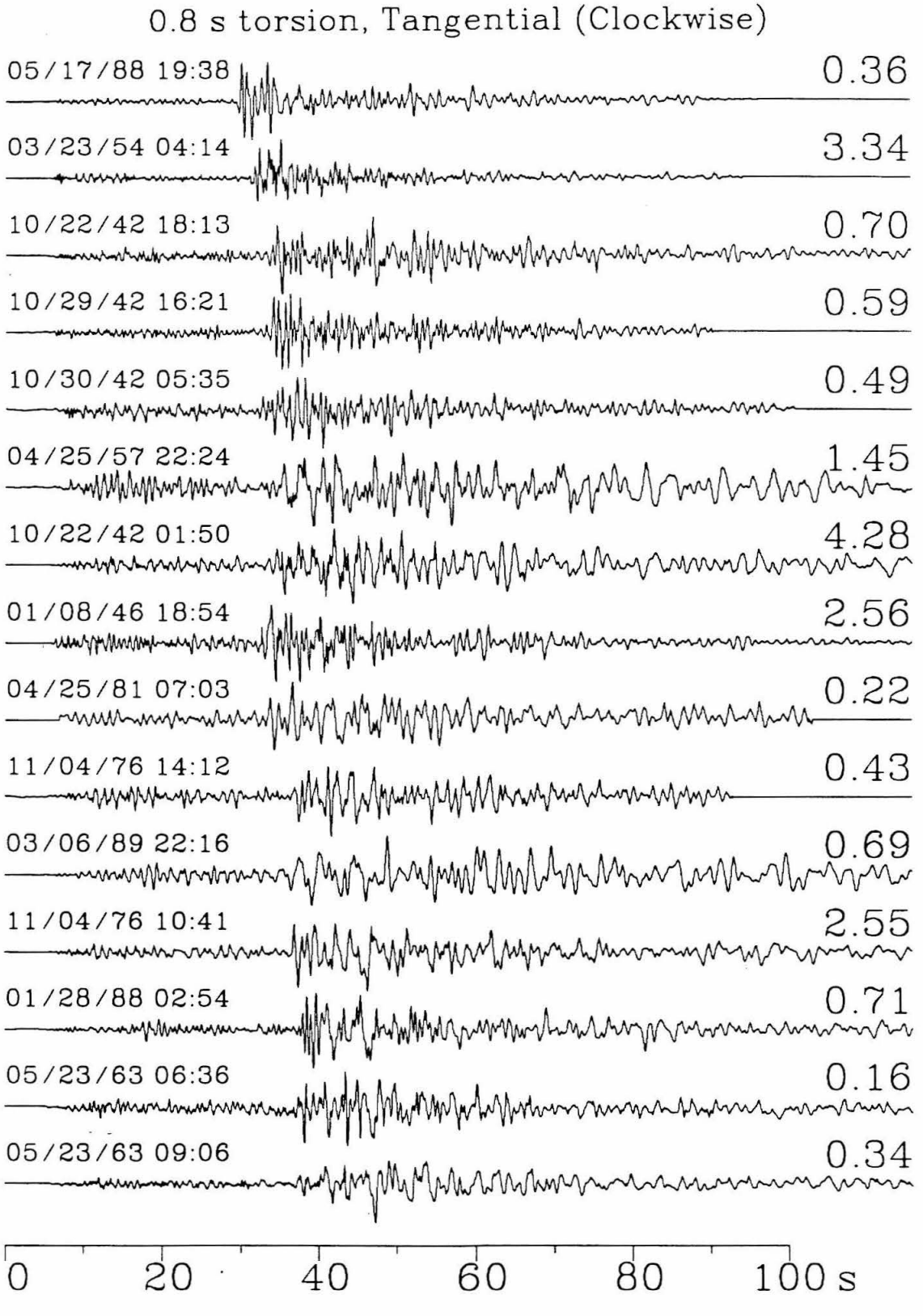
0.8 s torsion, Tangential (Clockwise)
05/17/88 19:38
0.36
03/23/54 04:14
3.34
10/22/42 18:13
0.70
10/29/42 16:21
0.59
10/30/42 05:35
0.49
04/25/57 22:24
1.45
10/22/42 01:50
4.28
01/08/46 18:54
2.56
04/25/81 07:03
0.22
11/04/76 14:12
0.43
03/06/89 22:16
0.69
11/04/76 10:41
2.55
01/28/88 02:54
0.71
05/23/63 06:36
0.16
05/23/63 09:06
0.34
0
20
40
60
80
100 s

records produces unsatisfactory results, deconvolution followed by convolution with a suitable instrument, in this case the 6.0 second torsion, provides very good waveforms that compare well to the recorded 6.0 second torsions, when available. These processed seismograms and the rotated versions are shown in Figure 4.6. Most of the desired features from 6.0 second torsion records are seen in the processed 0.8 second torsion records. In fact, events that are known to be similar, such as the two 1963 events, now appear very similar. Some of the features visible in the collection of 6.0 second torsion records can be seen in the processed seismograms. Also apparent here is the mislocation of some of the events, since the waveforms do not form a smooth progression and some are clearly out of order in range by apparent S-P times.

Not all of these events are not addressed in this chapter. The main purpose in displaying these records is to show the character of the data and its variation with source location. The presentation provides evidence that regional modeling of these events is practical, in that there are many features in the data that are reproduced throughout several events. It provides evidence that modeling is profitable, in that each event shows a distinct waveform. An accurate model will produce the features that appear throughout the data, and will permit precise determination of location, mechanism, etc., by adjusting these parameters to fit each distinct waveform. In the next section, we attempt to produce such a model, using the broadband seismograms to verify it.

4.3 FD Modeling

In this section, we present several models that are used in studying the data. The synthetics for these models are computed using a 2D finite

Figure 4.6 North, east and rotated tangential and radial components from the Wood-Anderson 0.8 second torsion instrument at PAS. The data are deconvolved and then convolved with a 6.0 second torsion response Recent broad-band records filtered with this instrument response are interspersed in the profiles. Event date and time are at the upper left of each trace; peak amplitude in cm is at the upper right. Refer to Tables 4.1 and 4.2 for more information.

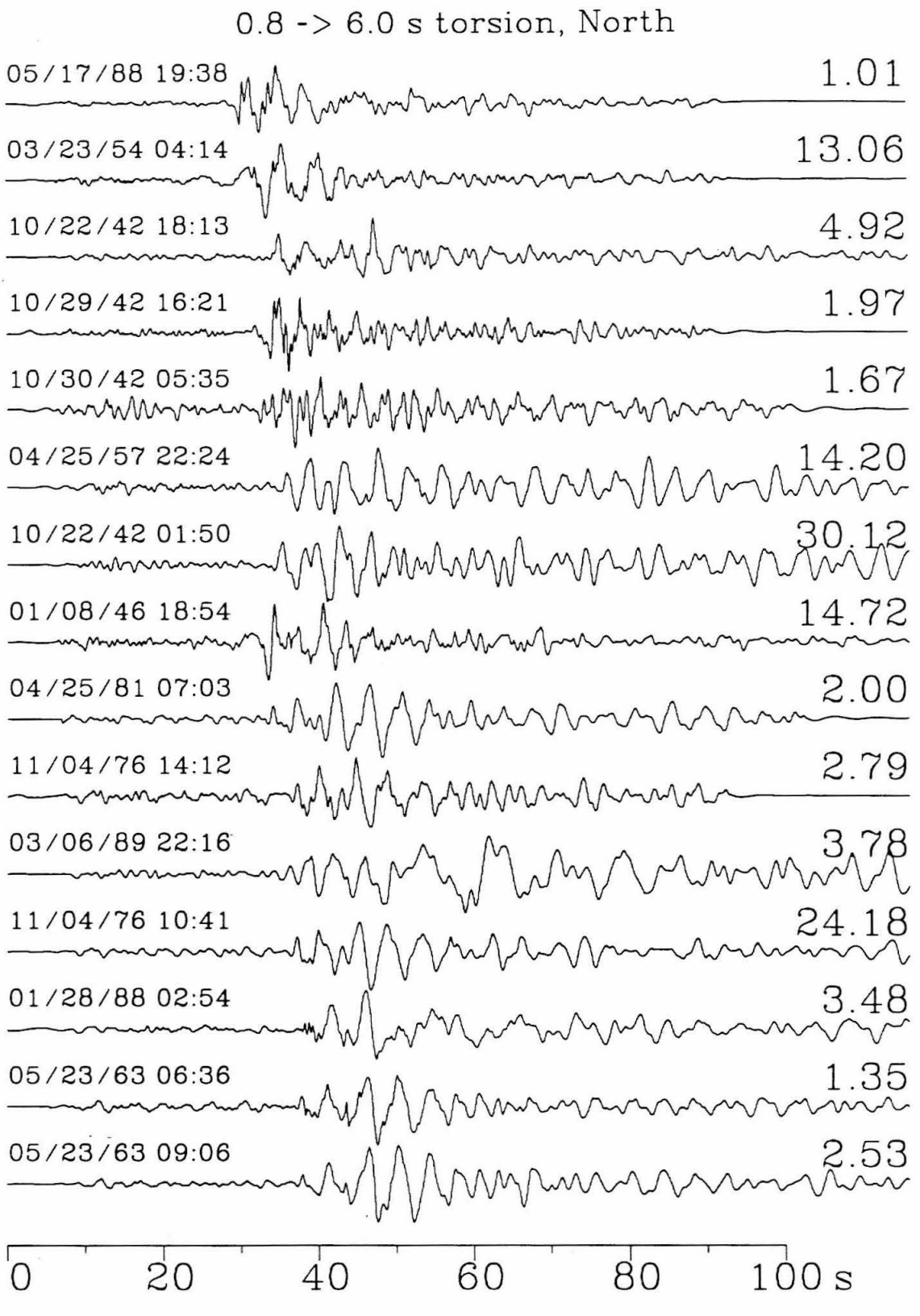
0.8 -> 6.0 s torsion, North
05/17/88 19:38
1.01
03/23/54 04:14
13.06
10/22/42 18:13
4.92
10/29/42 16:21
1.97
10/30/42 05:35
1.67
04/25/57 22:24
14.20
10/22/42 01:50
30.12
01/08/46 18:54
14.72
04/25/81 07:03
2.00
11/04/76 14:12
2.79
03/06/89 22:16
3.78
11/04/76 10:41
24.18
01/28/88 02:54
3.48
05/23/63 06:36
1.35
05/23/63 09:06
2.53
0
20
40
60
80
100 s

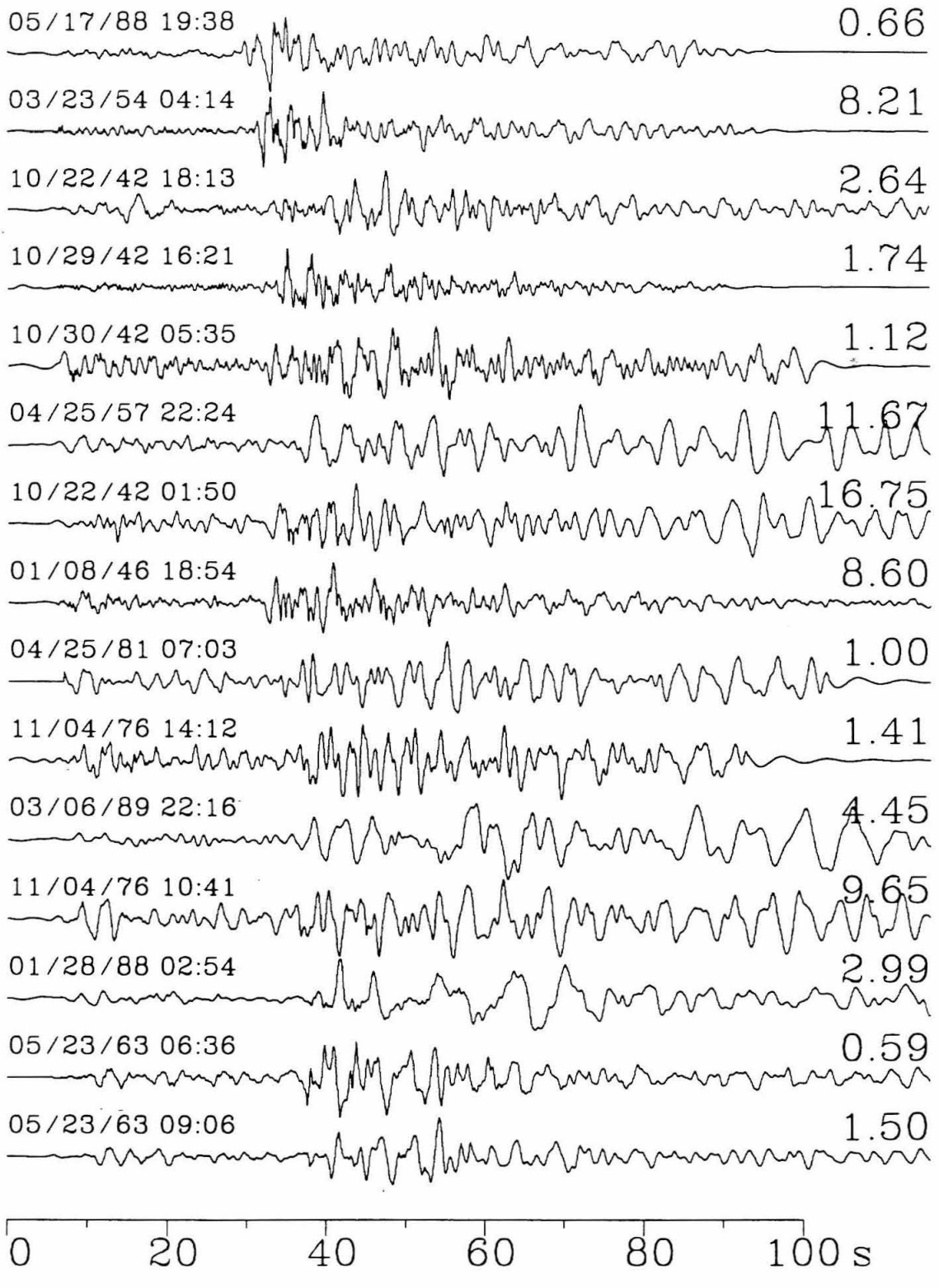
0.8 -> 6.0 s torsion, East
05/17/88 19:38
0.66
03/23/54 04:14
8.21
10/22/42 18:13
2.64
10/29/42 16:21
1.74
10/30/42 05:35
1.12
04/25/57 22:24
11.67
10/22/42 01:50
16.75
01/08/46 18:54
8.60
04/25/81 07:03
1.00
11/04/76 14:12
1.41
03/06/89 22:16
4.45
11/04/76 10:41
9.65
01/28/88 02:54
2.99
05/23/63 06:36
0.59
05/23/63 09:06
1.50
0
20
40
60
80
100 s

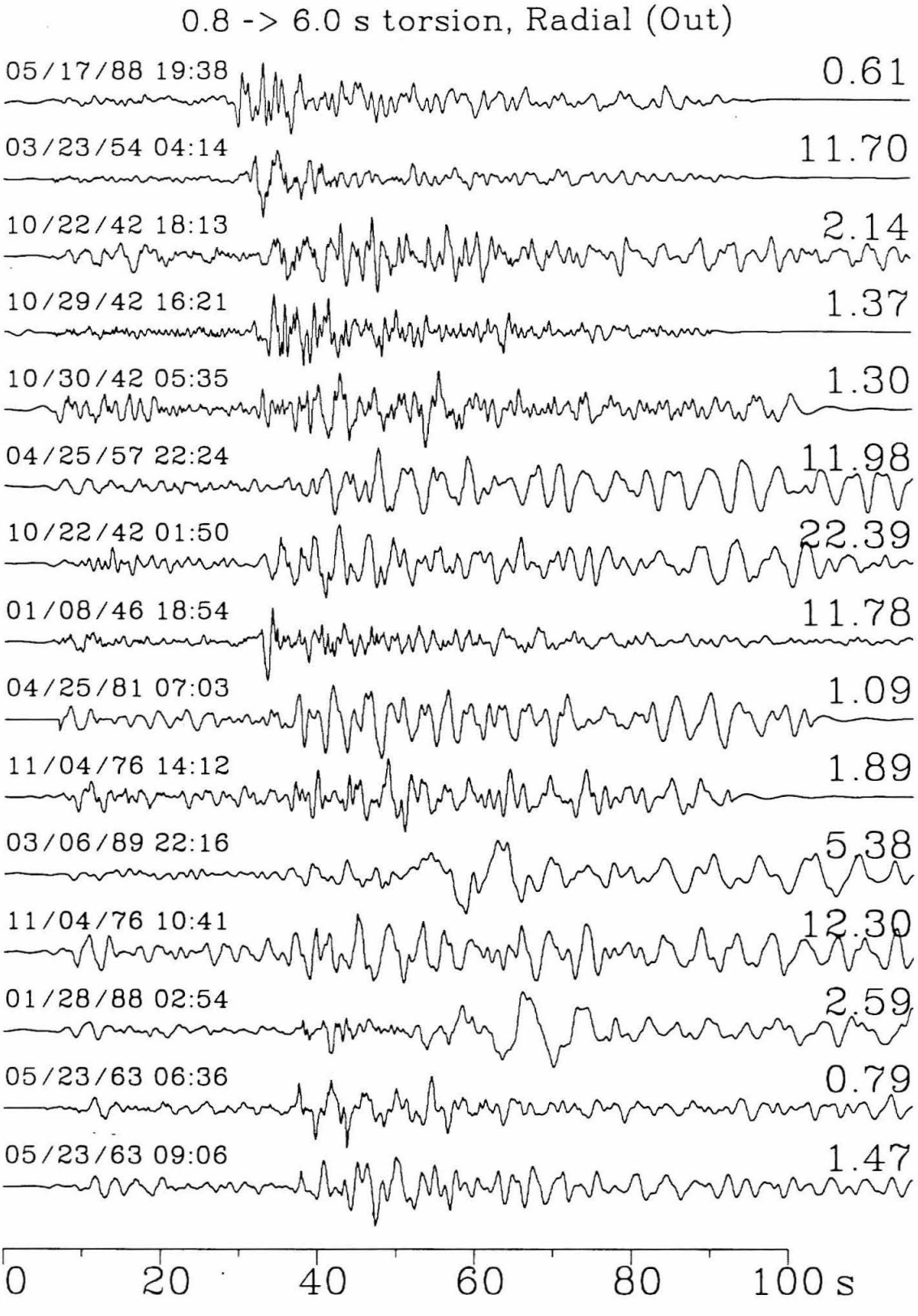
0.8 -> 6.0 s torsion, Radial (Out)
05/17/88 19:38
0.61
03/23/54 04:14
11.70
10/22/42 18:13
2.14
10/29/42 16:21
1.37
10/30/42 05:35
1.30
04/25/57 22:24
11.98
10/22/42 01:50
22.39
01/08/46 18:54
11.78
04/25/81 07:03
1.09
11/04/76 14:12
1.89
03/06/89 22:16
5.38
11/04/76 10:41
12.30
01/28/88 02:54
2.59
05/23/63 06:36
0.79
05/23/63 09:06
1.47
0
20
40
60
80
100 s

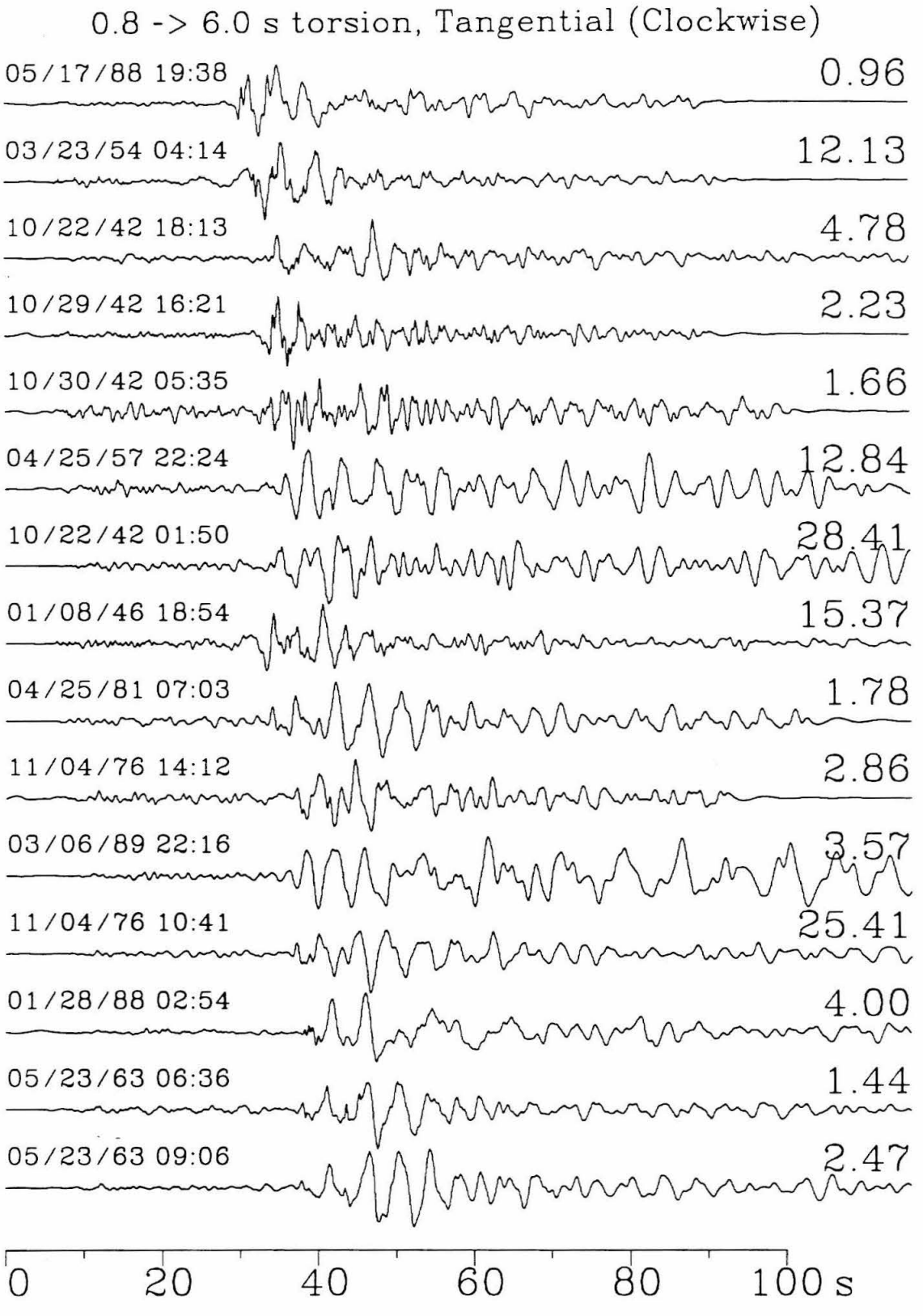
0.8 -> 6.0 s torsion, Tangential (Clockwise)
05/17/88 19:38
0.96
03/23/54 04:14
12.13
10/22/42 18:13
4.78
10/29/42 16:21
2.23
10/30/42 05:35
1.66
04/25/57 22:24
12.84
10/22/42 01:50
28.41
01/08/46 18:54
15.37
04/25/81 07:03
1.78
11/04/76 14:12
2.86
03/06/89 22:16
3.57
11/04/76 10:41
25.41
01/28/88 02:54
4.00
05/23/63 06:36
1.44
05/23/63 09:06
2.47
0
20
40
60
80
100 s

difference (FD) technique. FD is used because it produces the full solution for an arbitrary structure, which is important for modeling the complex structure of southern California. We start with the model of Ho-Liu (1988), a FD model for long-period SH waves recorded at PAS from the Imperial Valley. It is necessary to modify this model, because the Imperial Valley basin structure as presented by Ho-Liu (1988) includes velocity contrasts that are large enough to introduce instabilities in the FD grid. In particular, the instability is generated by the specification of the upper two layers: layer 1 having an S-velocity of 1.0 km/s and a density of 1.4 g/cc, and layer 2 having an S-velocity of 2.34 km/s and a density of 2.3 g/cc, and their abutment against the uppermost crustal layer of S-velocity 3.38 km/sec and density 2.7 g/cc. These contrasts require a few grid points of gradation across the boundaries in order to produce a stable result. The symptoms of instability in this case are not exponential growth in the signal or grid dispersion, but are seen in the extreme dependence of the model on the variation of the media at very few grid points. Empirically, it is found that a flat interface of the velocity contrast for layers 1 and 2 in the basin above is stable, but an interface with the same contrast that is not flat is often unstable. The maximum contrast in the above example (a velocity ratio of 3.38 and density ratio of 1.92) is very unstable for interfaces that are not flat. This largest contrast occurs only across 3 grid points near the free surface in the above model; otherwise it would produce an exponentially growing signal that would swamp any other energy in the grid. Therefore, this basin structure is modified for our starting model by introducing the intermediate media necessary to insure stability. This basin is shown in Figure 4.7 and is referred to as basin 1. The figure also shows the initial crustal model. The model has a

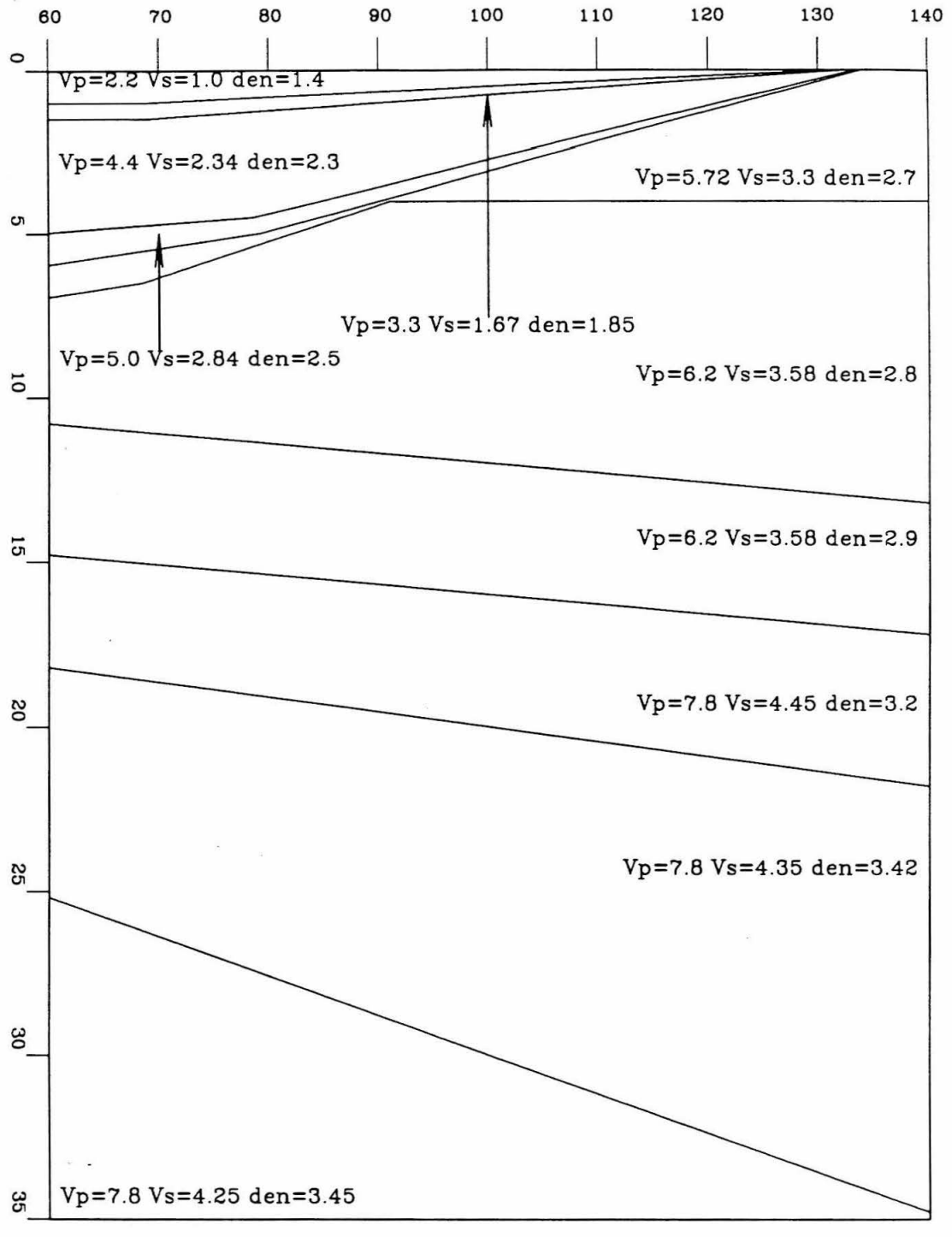

Figure 4.7 Initial basin structure used for FD models for the Imperial Valley. Velocities in km/s and densities in g/cc are shown on the figure. Distances are in km from the edge of the FD model. Compare full structure in Figure 4.8.

negative gradient beneath the MOHO designed to reduce the amplitude of Sn. The distances labeled at the top of the figure are measured in kilometers from the edge of the whole grid, and may be compared to subsequent figures of the whole grid.

The models are first compared to an aftershock of the Superstition Hills sequence that occurred on January 28, 1988. This event is significant because it is the first event in the Imperial Valley of sufficient magnitude to record well at PAS since the installation of the broad-band seismometer. The mechanism of this aftershock is one of the few for earthquakes in the Imperial Valley region that is not necessarily strike-slip. Magistrale (personal communication, 1989) finds that a thrust mechanism with both planes perpendicular to the strike of the Superstition Hills fault is required to explain this event. For SH-waves recorded at PAS, such a thrust (dip=75 degrees, rake=50 degrees for a northeast strike) cannot be distinguished from strike-slip motion on a plane parallel to the Superstition Hills fault. Therefore, in the discussion below, only pure strike-slip mechanisms are used for modeling the SH data. Figure 4.8 shows a diagram of the starting model (see also Figure 4.7) with the chosen source and station positions for this comparison. Below are comparisons for the broad-band displacement record (instrument response has been deconvolved) and filtered versions of this record using the responses of three historic seismometers that have been operated at PAS: 0.8 and 6.0 second Wood-Anderson torsion instruments and the Press-Ewing 30-90 second instrument (tangential components, positive clockwise). These data are compared to the FD synthetics generated for the starting model for the selected source and receiver (source depth 10 km, range 266 km), using the same instrument responses. The moment for the synthetics is 8×10^{22},

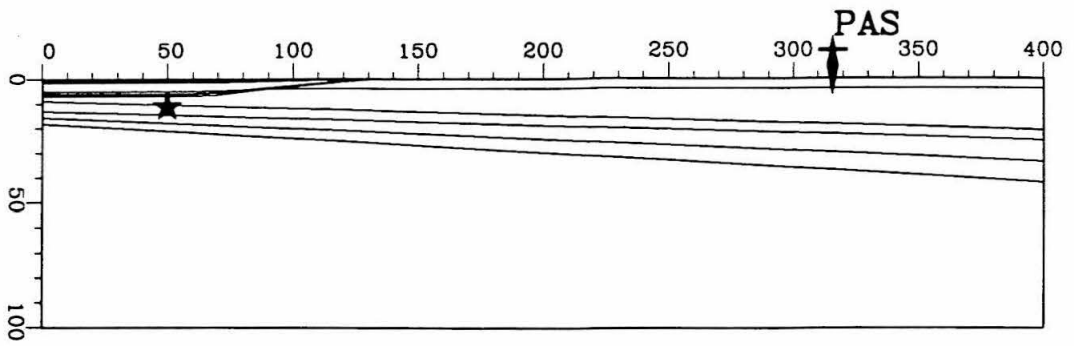

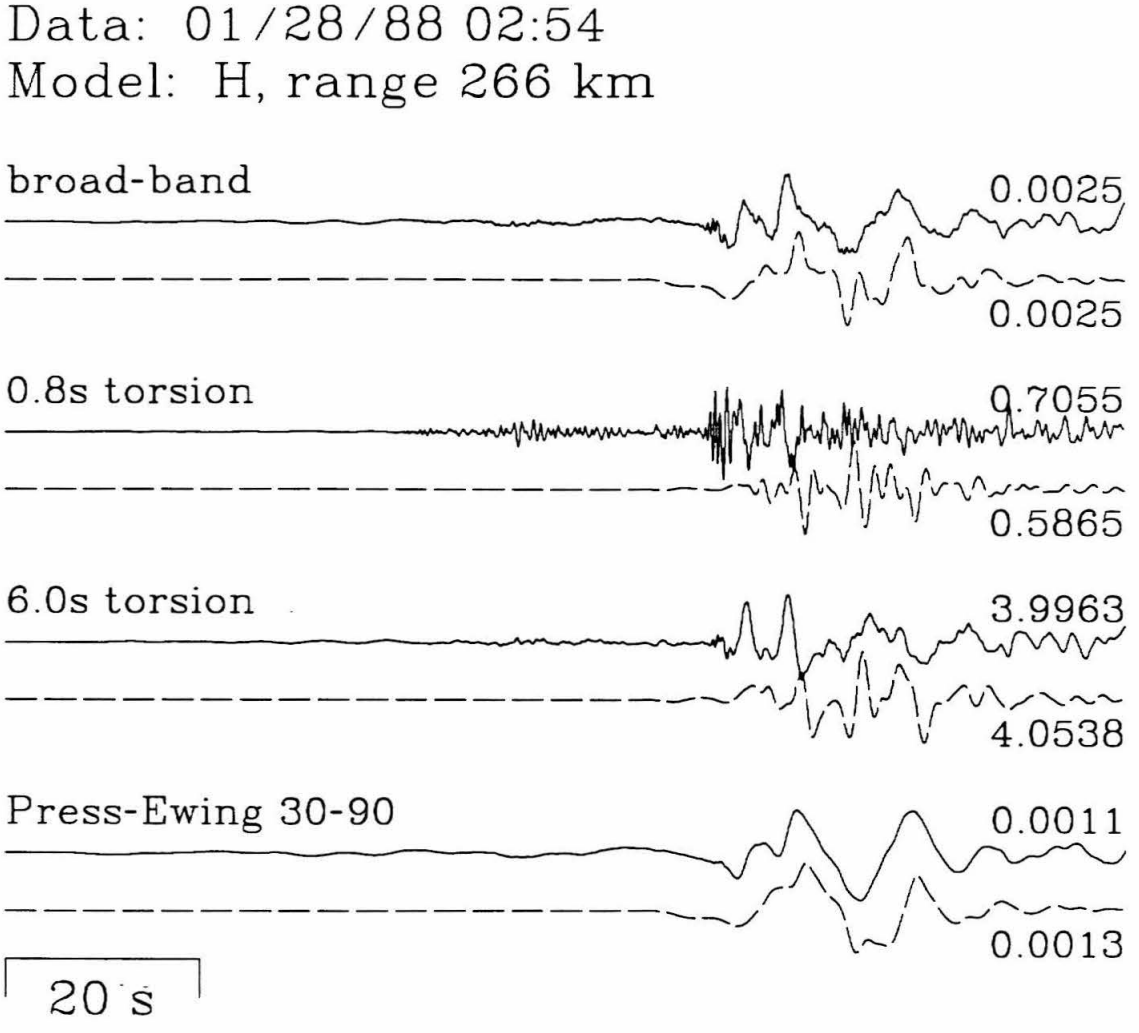

Figure 4.8 Results for initial 2d FD model of SH structure from Imperial Valley to PAS as compared to the calibration event from January 28, 1988.

derived by matching amplitudes. This moment corresponds to an M_L of 4.6, by the moment - M_L relation of Thatcher and Hanks (1973), and agrees precisely with the catalog value. The Gaussian source time function has a half-width at 1/e amplitude of 0.75 s. The mechanism is pure strike-slip, at 161° azimuth from the fault strike. The fault strike is taken from the teleseismic solution of Bent, et al. (1989) for the largest subevent of the Superstition Hills mainshock (the location of the aftershock is near the southern portion of the Superstition Hills fault). The comparison shows that several phases are comparable, including the Love wave, through a range of frequencies, but timing of the phases and amplitude ratios between phases are not exact and are, in some cases, poor. Overall, it is unlikely that this model improves on a best-fitting, flat-layered model, except for the surface wave. The lack of higher frequencies in the synthetic for the 0.8 s torsion is due to both the source time function and the lack of high wave number variations in the model medium. Finally, the model appears slightly slow for this event.

Suspecting that some of the failings of the above model are due to an inaccurate specification of the basin, we modify the basin to alter phases reflected off the surface. By carefully comparing the model of Fuis, et al. (1982) to the propagation, a new basin is inserted in the model, see Figure 4.9. This basin is referred to as basin 2. It does not approach PAS as far as basin 1; it is thinner directly above the chosen source location, and its boundary is not as smooth as basin 1. All these factors may contribute to the alteration of the surface reflections sSn and sSmS, the MOHO refracted and reflected phases off the free surface. Figure 4.10 shows the result, and the fit has improved in absolute time, but is worse in amplitude ratios between the phases. The waveform fit to the Love wave has improved, particularly at the

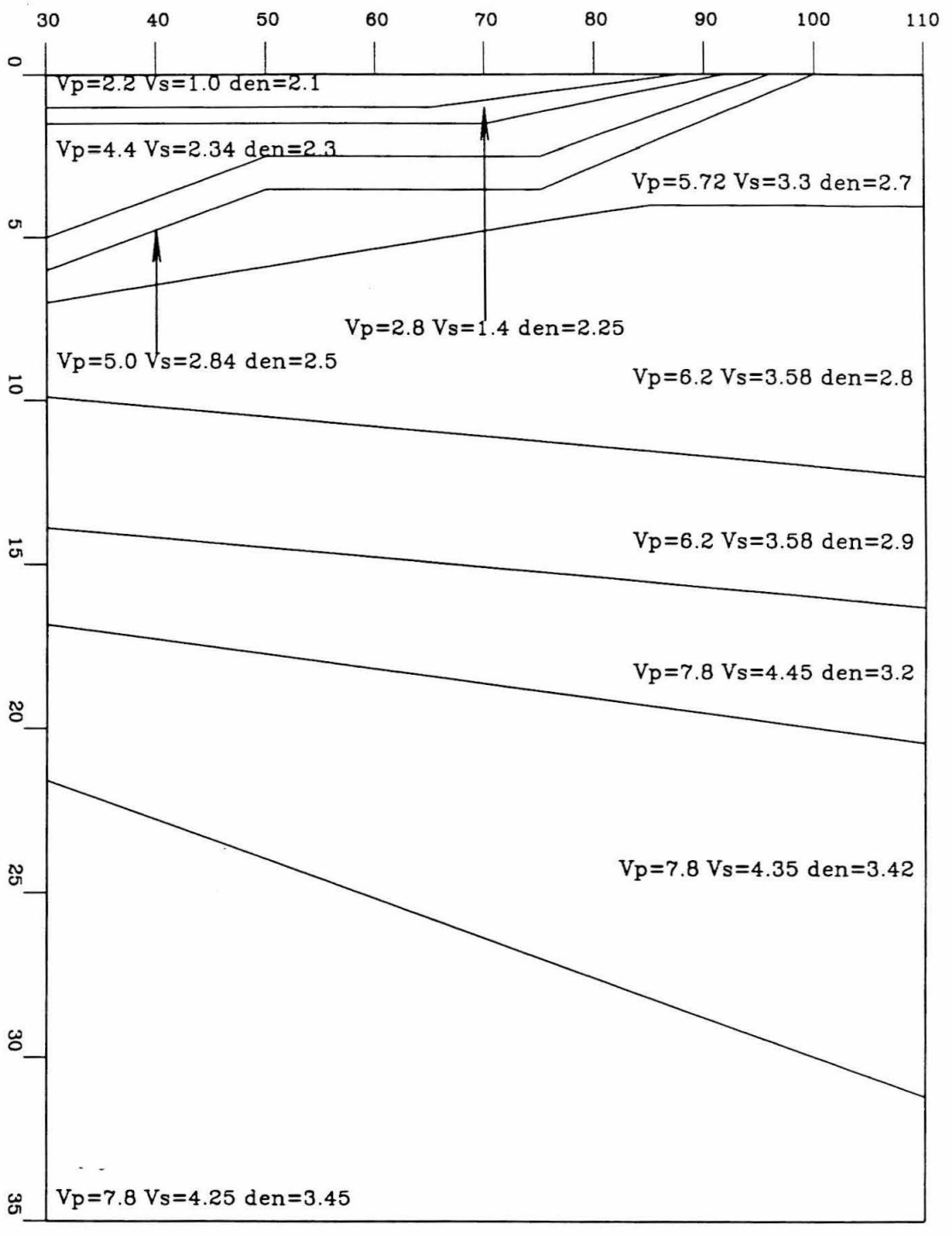

Figure 4.9 Second basin structure used for FD models for the Imperial Valley. Velocities in km/s and densities in g/cc are shown on the figure. Distances are in km from the edge of the FD model. Compare full structure in Figure 4.10.

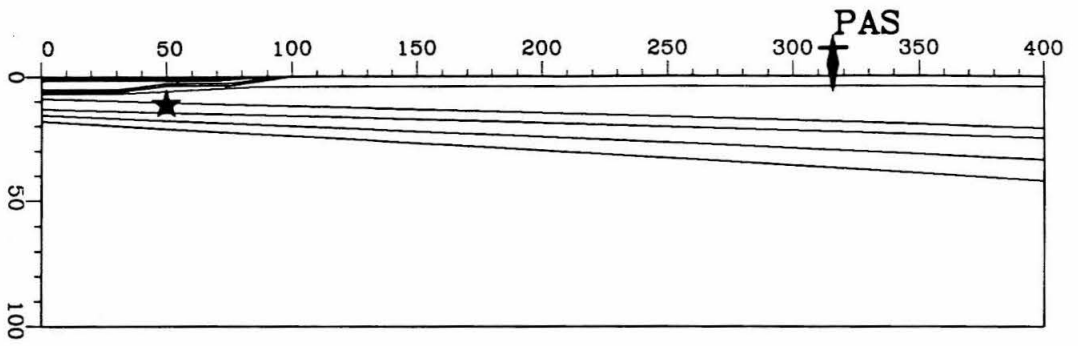

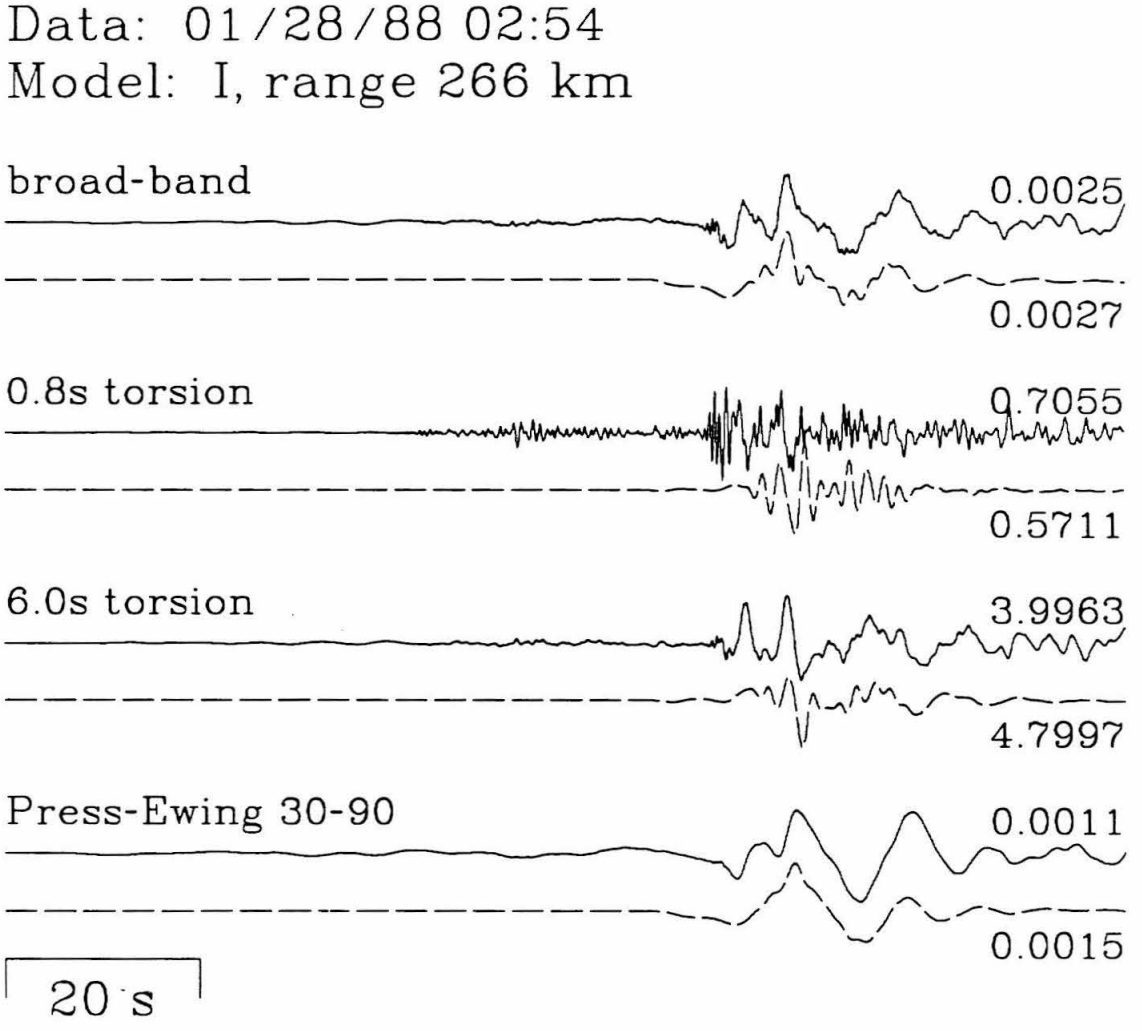

Figure 4.10 Results for second 2d FD model of SH structure from Imperial Valley to PAS as compared to the calibration event from January 28, 1988.

higher frequencies. The interpretation is that neither model is very accurate. Other variables need to change to fit all the phases simultaneously. Model I models the Love wave particularly well; therefore some specifications of this model are accurate. These are probably the depth of the basin, the distance from the source to the edge of the basin, the depth of the source and the velocity profile in the basin. In general, once the Love wave has passed the basin boundary, it experiences little modification traveling across the surface of the model, because the crustal model is a flat layer over a thick midcrustal layer. The timing of the Love-wave means that the velocities of those two layers and the thickness of the upper layer are correct, although the Love wave samples the structure as an average, which means that the velocity profile is only one of a family of profiles that produce identical Love wave behavior.

The large phase in Model I that is poorly modeled is probably sSmS. It may be adjusted independent of the rest of the model by modifying its surface bounce point. This is Model K, as displayed in Figure 4.11. The modification employed is to extend the lower velocity medium under the basin boundary away from the boundary. Since the bounce point is in the vicinity of the basin boundary; this modification should force more of the energy away from the basin boundary. The comparison between the synthetics and data in this example shows that the modification has made the phase more extreme, the opposite of the original intent. There is no geological support for a fast blob at the basin boundary, so an experiment designed to push the bounce point toward the basin is not performed. It is important to verify the model for sources in the vicinity of the basin boundary. Fortuitously, an earthquake of sufficient size occurred near Borrego Springs on May 17, 1988,

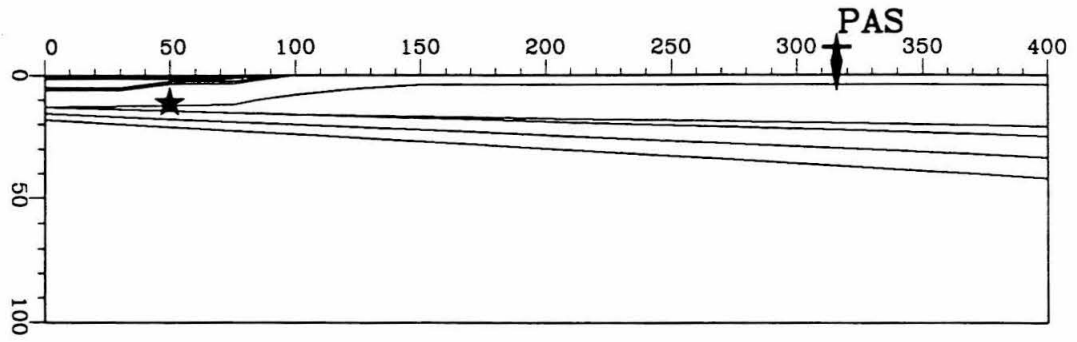

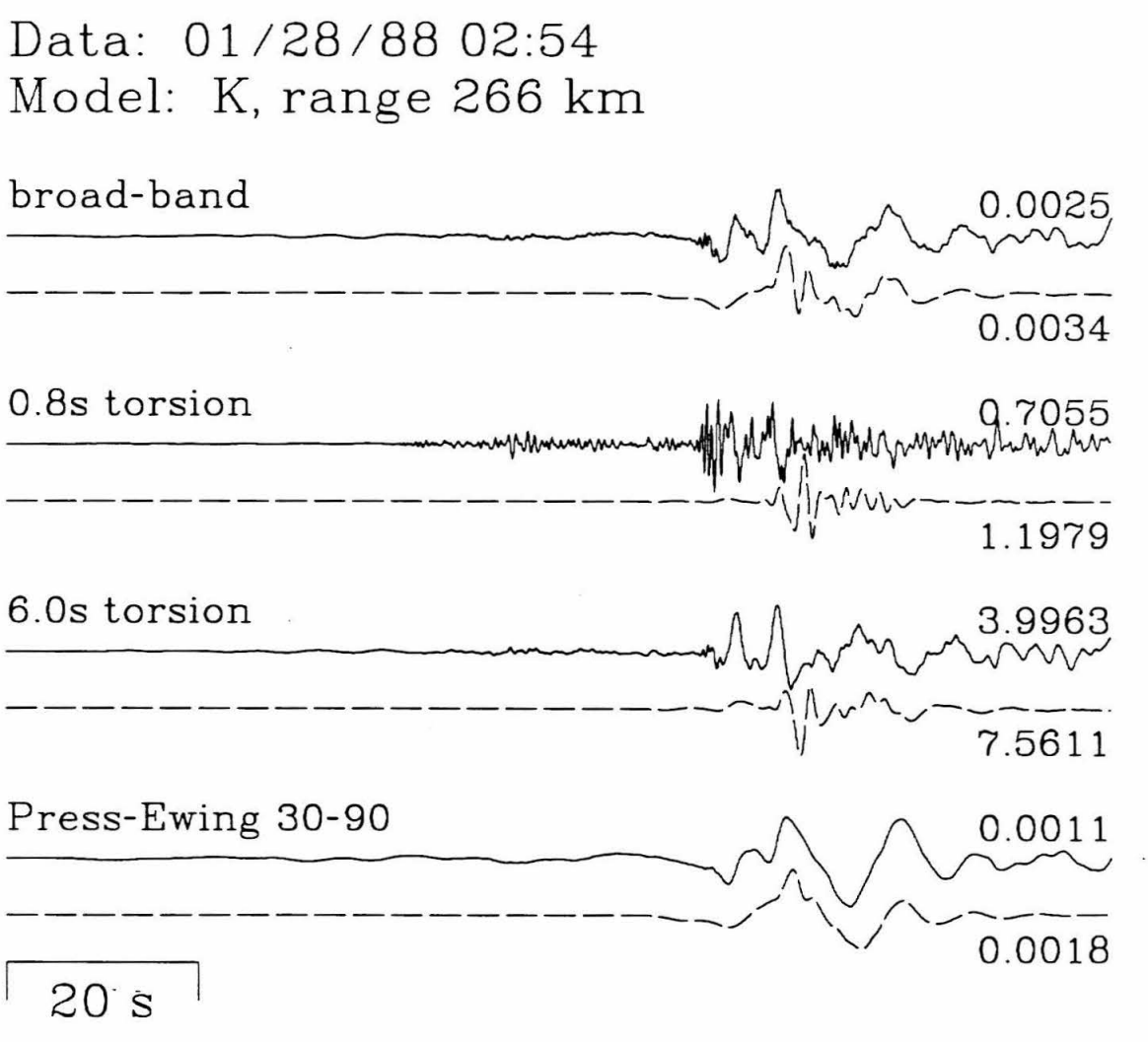

Figure 4.11 Results for 2d FD model K of SH structure from Imperial Valley to PAS as compared to the calibration event from January 28, 1988.

and was recorded by the broad-band instrument at PAS. Figure 4.12 compares that data to the current model (K) for a range of 206 km. All other source parameters are identical to the above for the Superstition Hills aftershock. The moment is 1×10^{22} (M_L about 4.0), found by amplitude comparison. This is larger than the catalog value. The station (PAS) is 169° azimuth from the fault strike, where the fault strike is assumed to be identical to that found by Burdick and Mellman (1976) for the Borrego Mountain, 1968, earthquake. While the timing appears close, it is clear from the waveform comparison that the region in the vicinity of the boundary needs adjustment, and that the MOHO is poorly modeled as well.

The above suggestions are carried out in model N, as displayed in Figure 4.13. The source has been moved closer to the MOHO because the surface wave amplitude is very small. The basin has also been altered slightly to account for a slight difference in azimuth between the Superstition Hills aftershock and the Borrego Springs event. Once again, the fit is poor, in absolute timing as well as in waveform. One way to change the timing is to move the MOHO to greater depth. Since the depth to the MOHO in the previous examples is somewhat shallow when compared to accepted depths for this region, this is a reasonable experiment. This is likely to make MOHO phases late for the Superstition Hills aftershock, but may improve the overall waveform. Altering the MOHO is also an alternative to altering the surface bounce-point when improving the fit in time and amplitude of such phases as sSmS.

The model (P) and results are shown in Figure 4.14. Again, the source has been moved to greater depth to improve the timing of the phases, and it is now 16 km deep. There is some improvement here, but the model does not

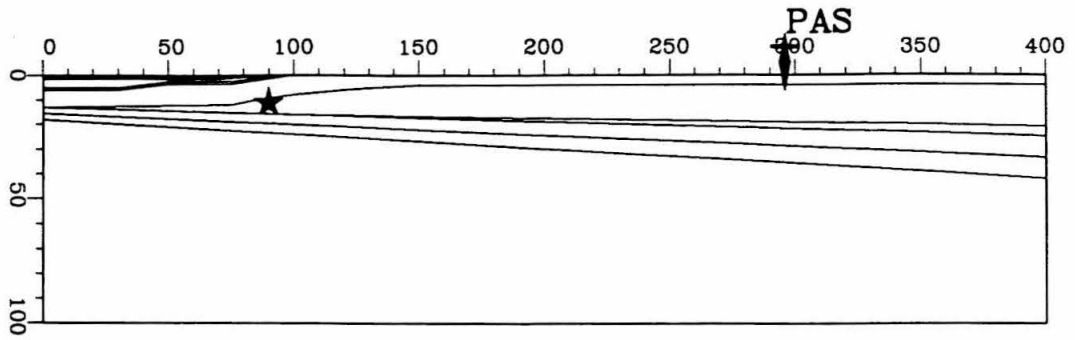

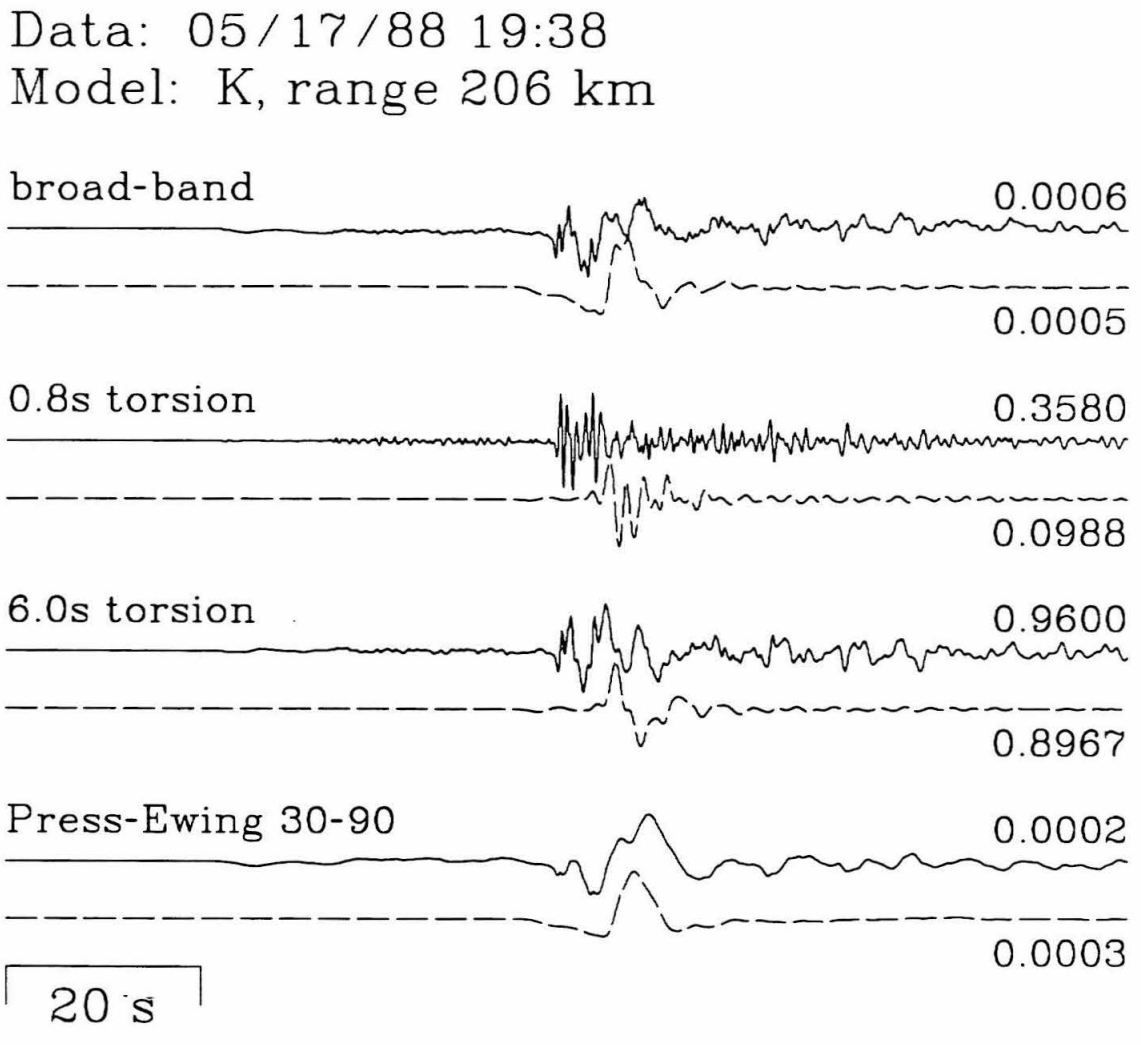

Figure 4.12 Results for 2d FD model K of SH structure from Imperial Valley to PAS as compared to the calibration event from May 17, 1988.

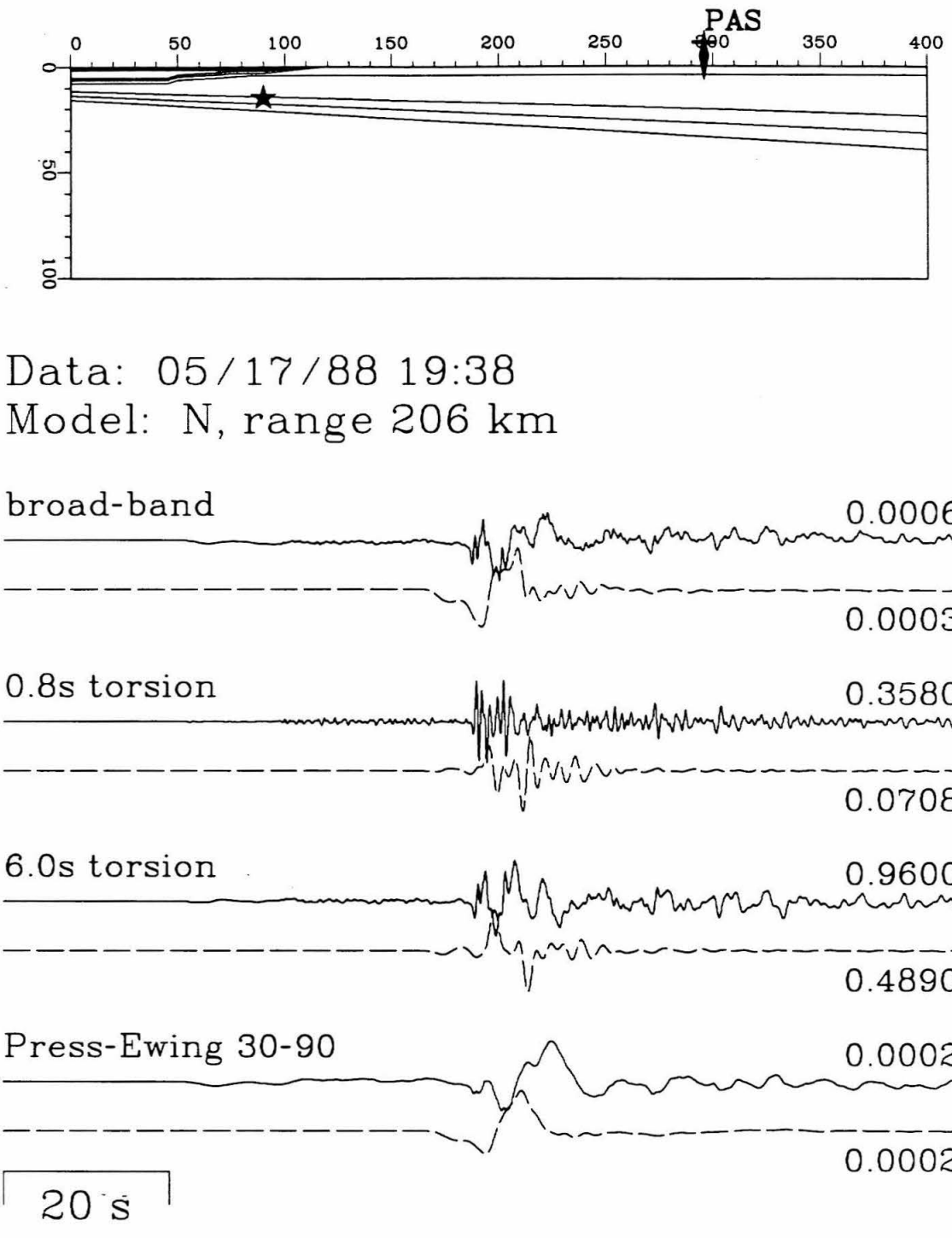

Figure 4.13 Results for 2d FD model N of SH structure from Imperial Valley to PAS as compared to the calibration event from May 17, 1988.

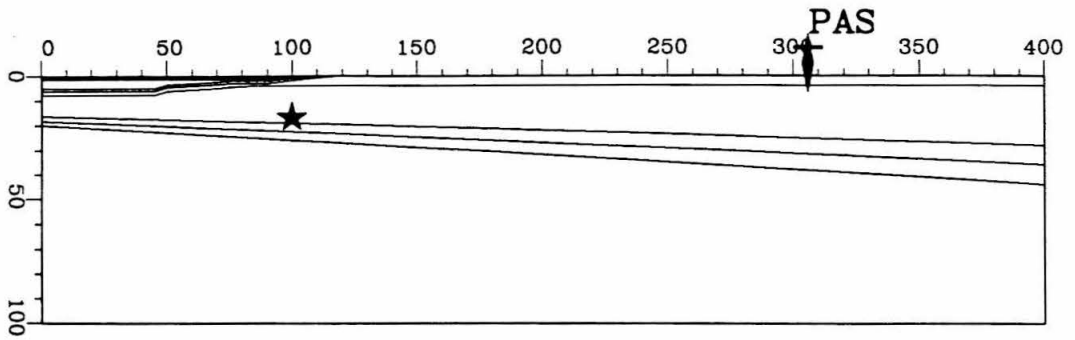

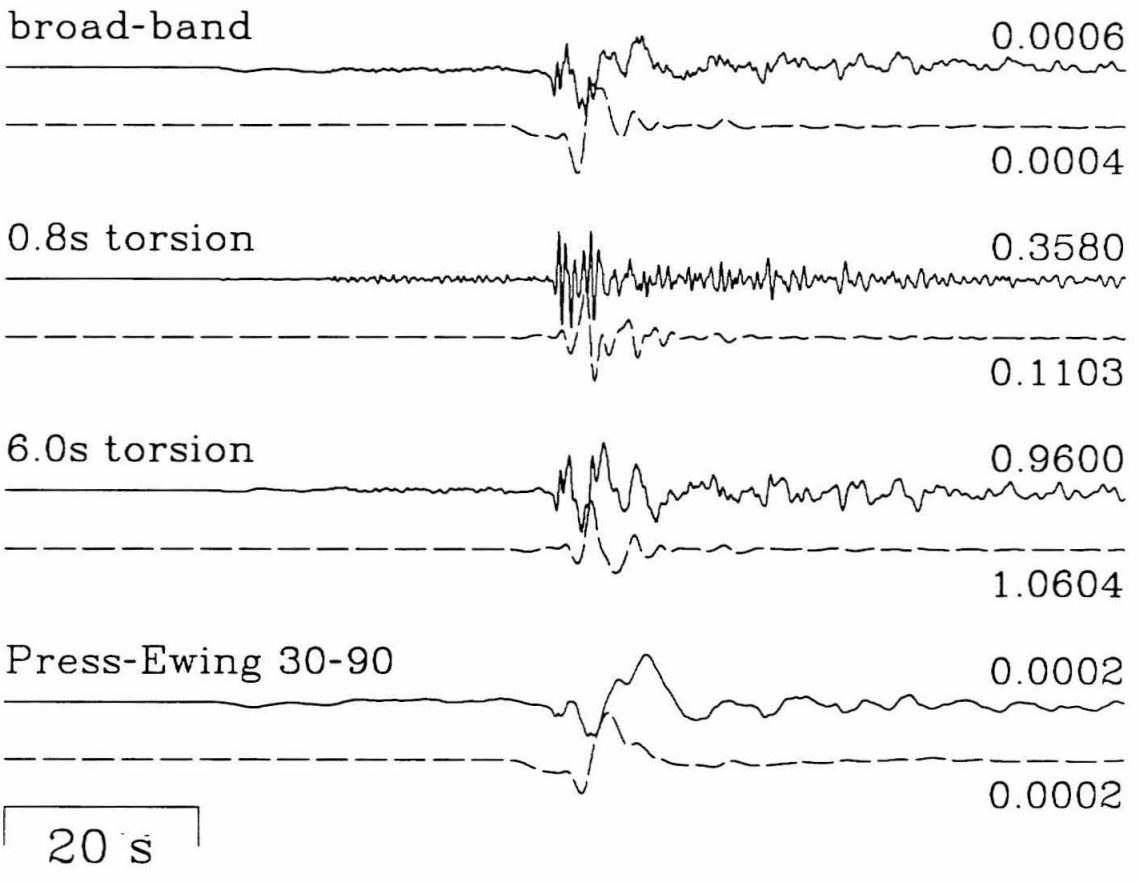

Figure 4.14 Results for 2d FD model P of SH structure from Imperial Valley to PAS as compared to the calibration event from May 17, 1988.

yet produce a good fit. The most improvement is seen for the 6.0 s torsion response where the dominant phases are now present, and the timing of these pulses has improved over model N. An examination of the other instrument responses shows that absolute timing has improved for all frequencies except for the highest and lowest frequencies present.

At this point, the timing error indicates that the model is too fast. Yet, as mentioned above, the crustal model appears satisfactory for the propagation of the Love wave. The next step, therefore, is to reduce velocities in the vicinity of the basin. This will delay the phases initially without affecting further propagation toward PAS. A model (J) that has reduced velocity beneath the basin is displayed in Figure 4.15. The base model for model J is model I, with a medium of Vp=6.1 km/s, Vs=3.5 km/s, and density=2.8 g/cc inserted beneath the basin, replacing the midcrustal layer. The medium above this is extended in depth and toward PAS. The synthetics are compared for the Superstition Hills aftershock to verify two things: that the change in velocity has a significant effect for sources under the basin (otherwise the modification cannot alter sources nearer the edge of the basin), and that the timing is not so strongly affected as to make the model unacceptable. This comparison shows that neither of these points is satisfied; see Figure 4.10.

To test this further, the velocities across the entire model are reduced. This model (C) is shown in Figure 4.16. The structure for the basin is that for model H, basin 1. The crustal profile has four media: Vp=(6.0, 6.5, 7.0, 7.4) km/s, Vs=(3.08, 3.48, 4.0, 4.08) km/s, and density=(2.7, 2.8, 3.2, 3.42) km/s. Crustal velocities this low are a very poor model. The entire record is very late; none of the phases match the data in waveform, and the Love

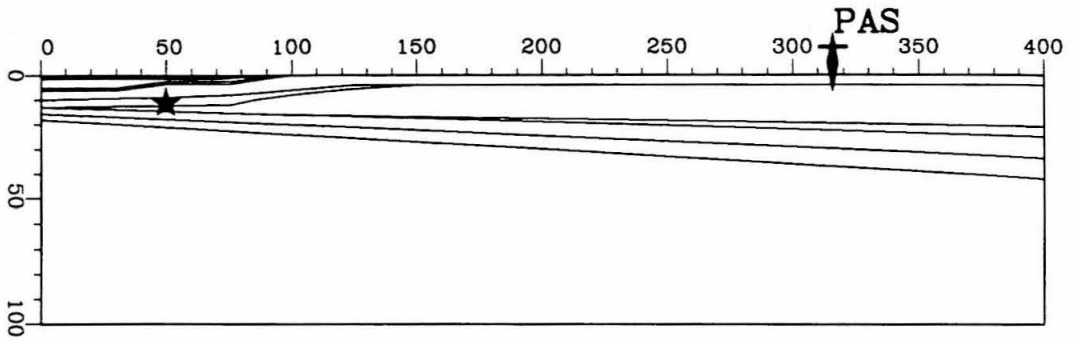

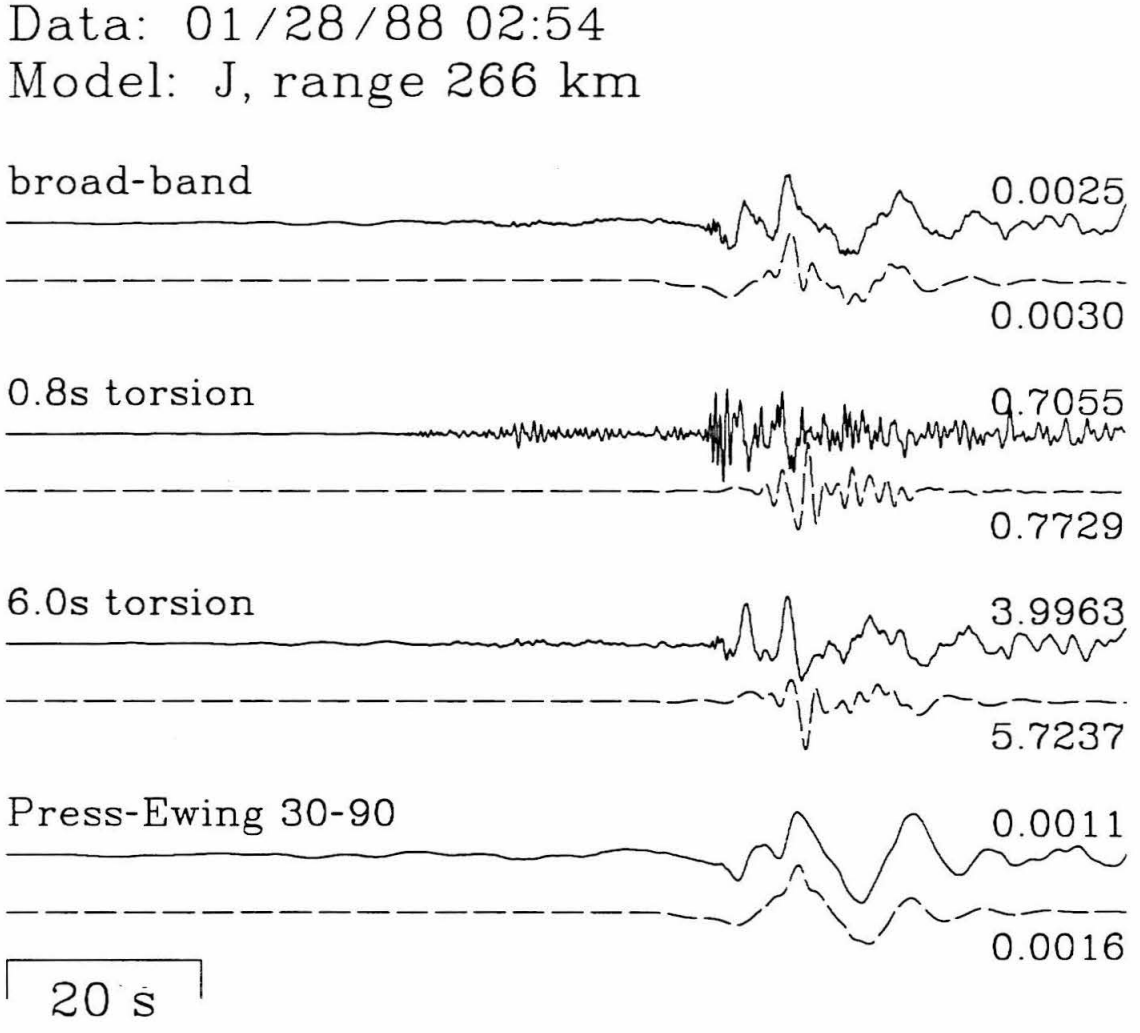

Figure 4.15 Results for 2d FD model J of SH structure from Imperial Valley to PAS as compared to the calibration event from January 28, 1988.

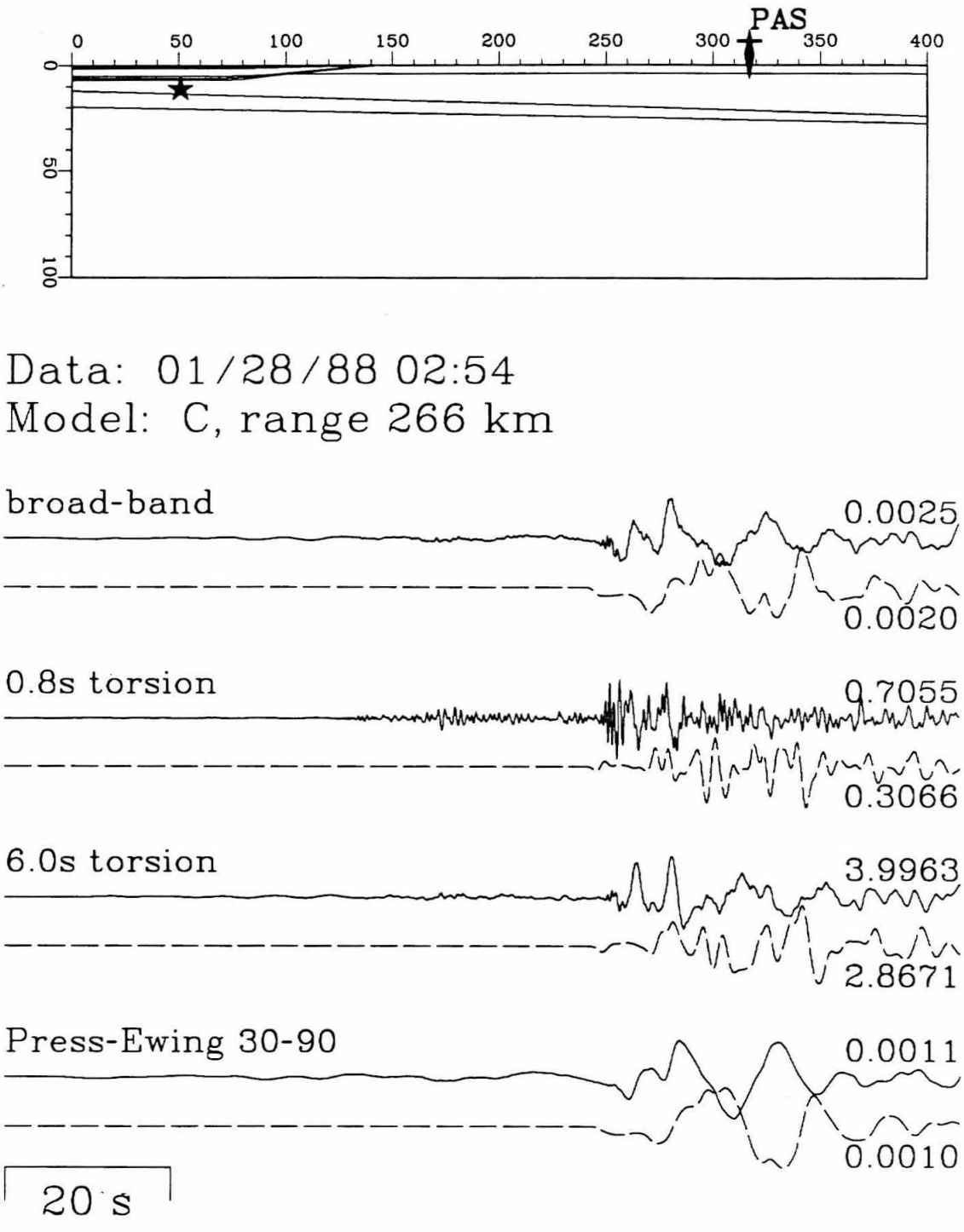

Figure 4.16 Results for 2d FD model C of SH structure from Imperial Valley to PAS as compared to the calibration event from January 28, 1988.

wave in particular is greatly distorted.

All the above models are simple by FD standards. They contain only uniform media with sharp contrasts between media. The boundaries are relatively smooth in geometry and the free surface is flat. Because the above models span a wide variety of such structures, and none of these produce a particularly good fit to either of two calibration events, it is necessary to explore more complex models. As mentioned above, the surface reflections are a problem in fitting the waveform. An alternative to varying the media at the surface is to vary the geometry of the surface. This is done by simulating topography. We simulate topography by creating an interface within the grid that simulates a free surface. The density is reduced across this interface until it is nearly zero. Velocities remain constant. Trials show that the density for an interface that is not flat may only be reduced by a factor of 2.5 for each grid point away from the interface. Spreading the contrast across 8 points produces a reduction in density by a factor of 1500. In constructing the model, care must be taken to insure that step down in density completely separates the medium above and below; that is, media that contrast by more than a factor of 2.5 must be more than 1 grid point apart in all directions. Figure 4.17 demonstrates the proper technique. Note that the free surface of the medium exists at the last grid point that has the appropriate density; this is where surface receivers are placed.

The profile between the Imperial Valley and PAS passes through the Peninsular Ranges, one of southern California's rugged mountain chains. Model G simulates the topography along this profile, using the principles discussed above. The topography is coarsely sampled because of the chosen grid spacing (0.5 km). The model is shown in Figure 4.18. The gradation to "air"

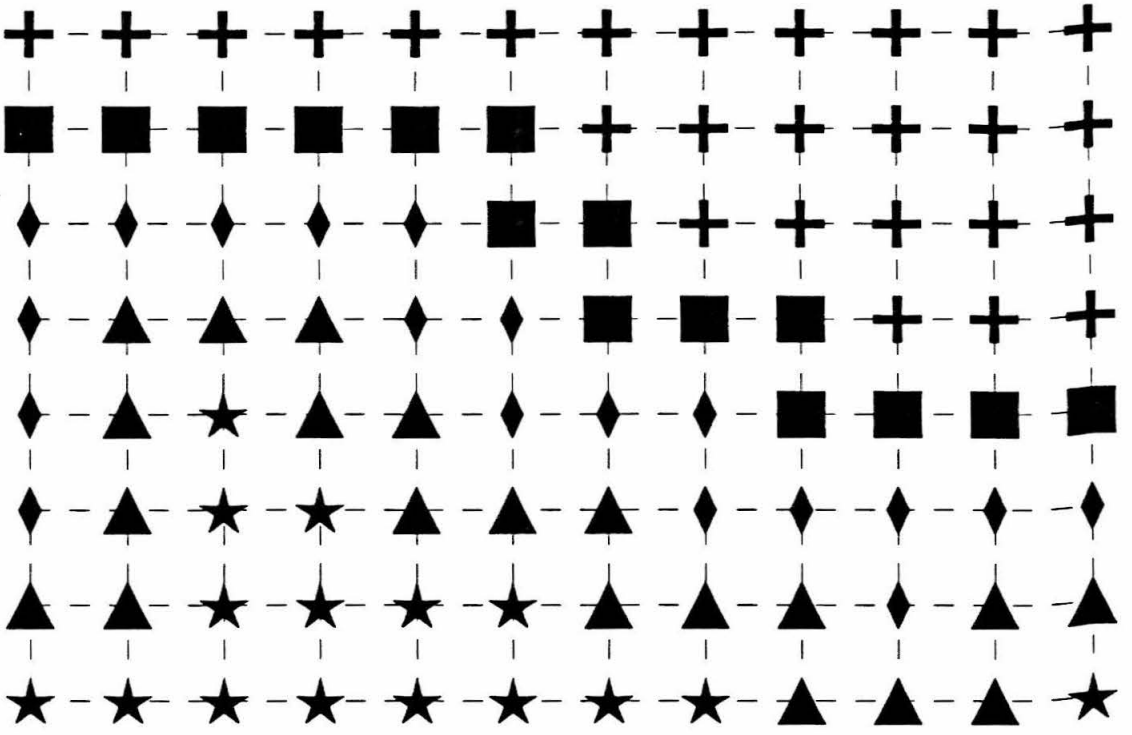

Figure 4.17 Example of topography specification for FD. The stars represent grid points of the solid medium; seismograms may be obtained at any of these grid points. Crosses represent the air medium, All other symbols represent intermediate media necessary for stability. Each of these media has a density ratio compared to neighboring media of no more than 2.5.

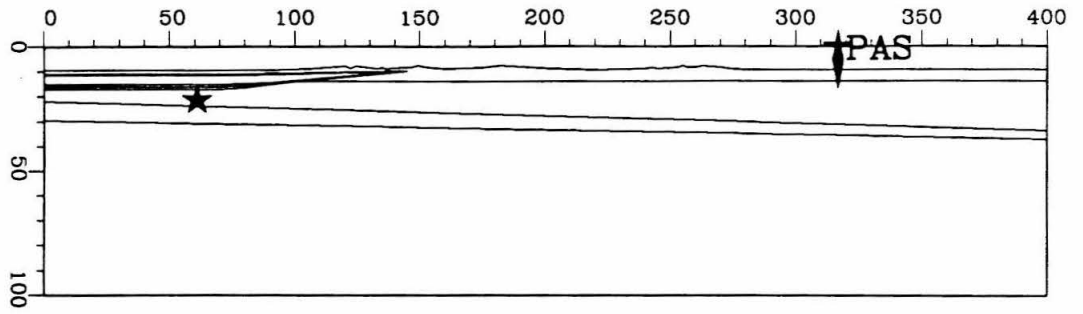

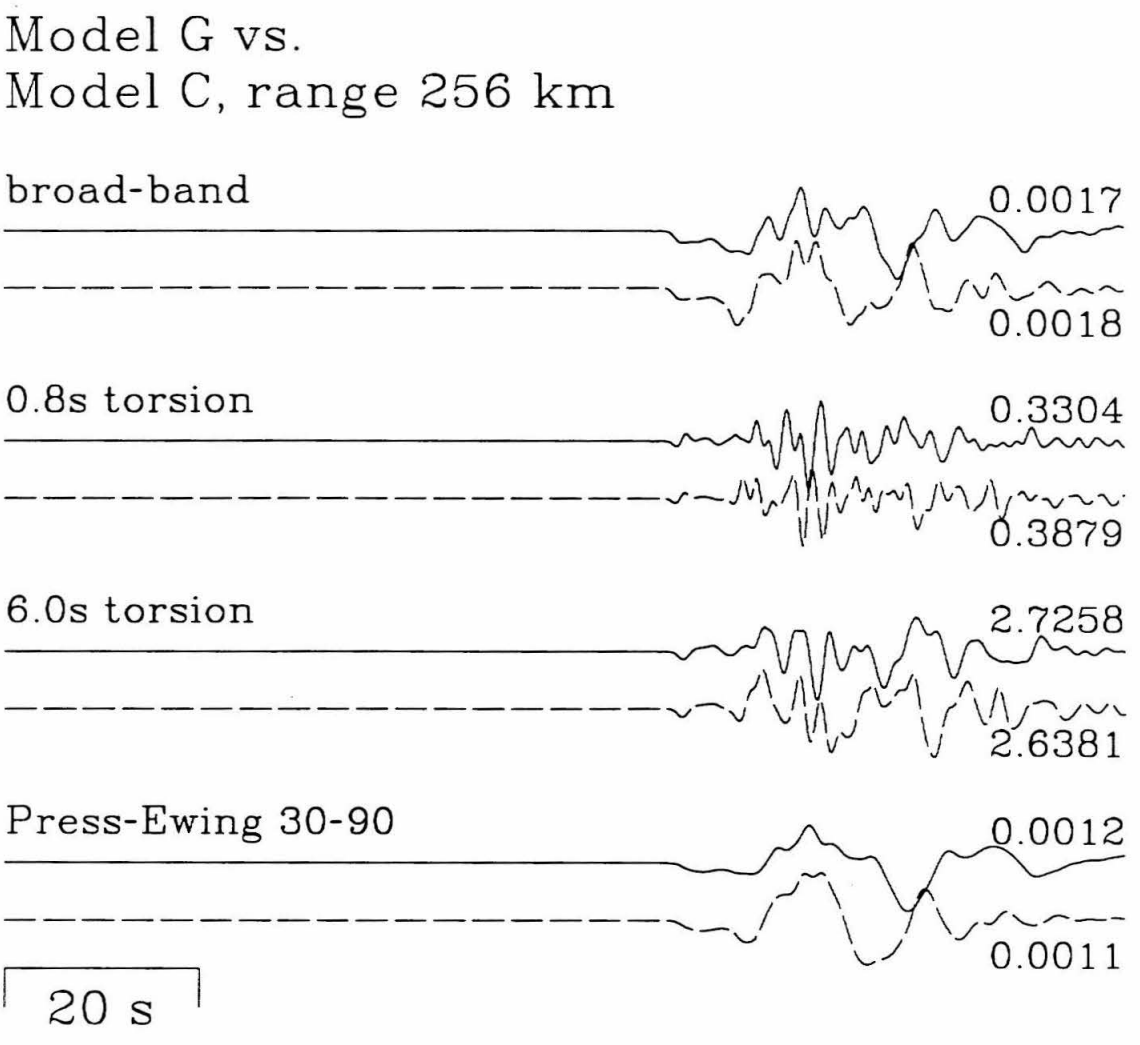

Figure 4.18 Results for 2d FD model with topography compared to base model (C).

is not shown, only the position of the simulated free surface. The base model used here is model C. Although this model produced a poor fit as discussed above, that is not important here. The purpose is to determine if the Peninsular Ranges topography has a significant effect on the results. There are no data in the comparison of seismograms in the figure. The results for the topographic model (G) and the original model (C) are compared at 256 km range. The source used is appropriate for the Superstition Hills aftershock. The primary modification to the synthetics occurs in the Love wave. The remainder of the record is nearly unaffected. This is not surprising, since the Love wave must interact with the surface along its entire propagation path, while a few other phases only reflect off it. Yet, the Love wave in the above examples appeared to fit well, so modification of the Love wave is undesirable. Also, because the technique used here creates cylindrical symmetry about a vertical axis through the source, the real topography will have less effect on the waveform than a 2D slice through it. This is because variation as a function of azimuth would require topography to be treated in an azimuthly averaged sense.

Another complexity of structure to test is the use of gradients rather than uniform media. This has the effect of changing the behavior of interfaces as a function of frequency. In the model (L) presented in Figure 4.19, gradients are used to model the upper crust and the MOHO. The gradient beneath the MOHO has Vp from 7.8 to 7.7 km/s, Vs from 4.45 to 4.25 km/s and density from 3.2 to 3.45 g/cc, with the highest velocities directly beneath the MOHO (which has Vp=8.0 km/s, Vs=4.6 km/s, density=3.2 g/cc). The gradient zone beneath the MOHO varies from 3 to 15 km thickness, and the MOHO layer is 2 km thick. The gradient in the crust is Vp from 5.4 to

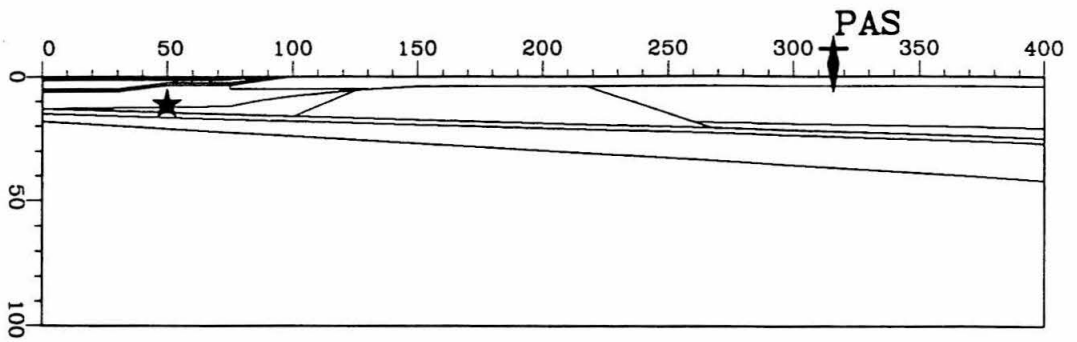

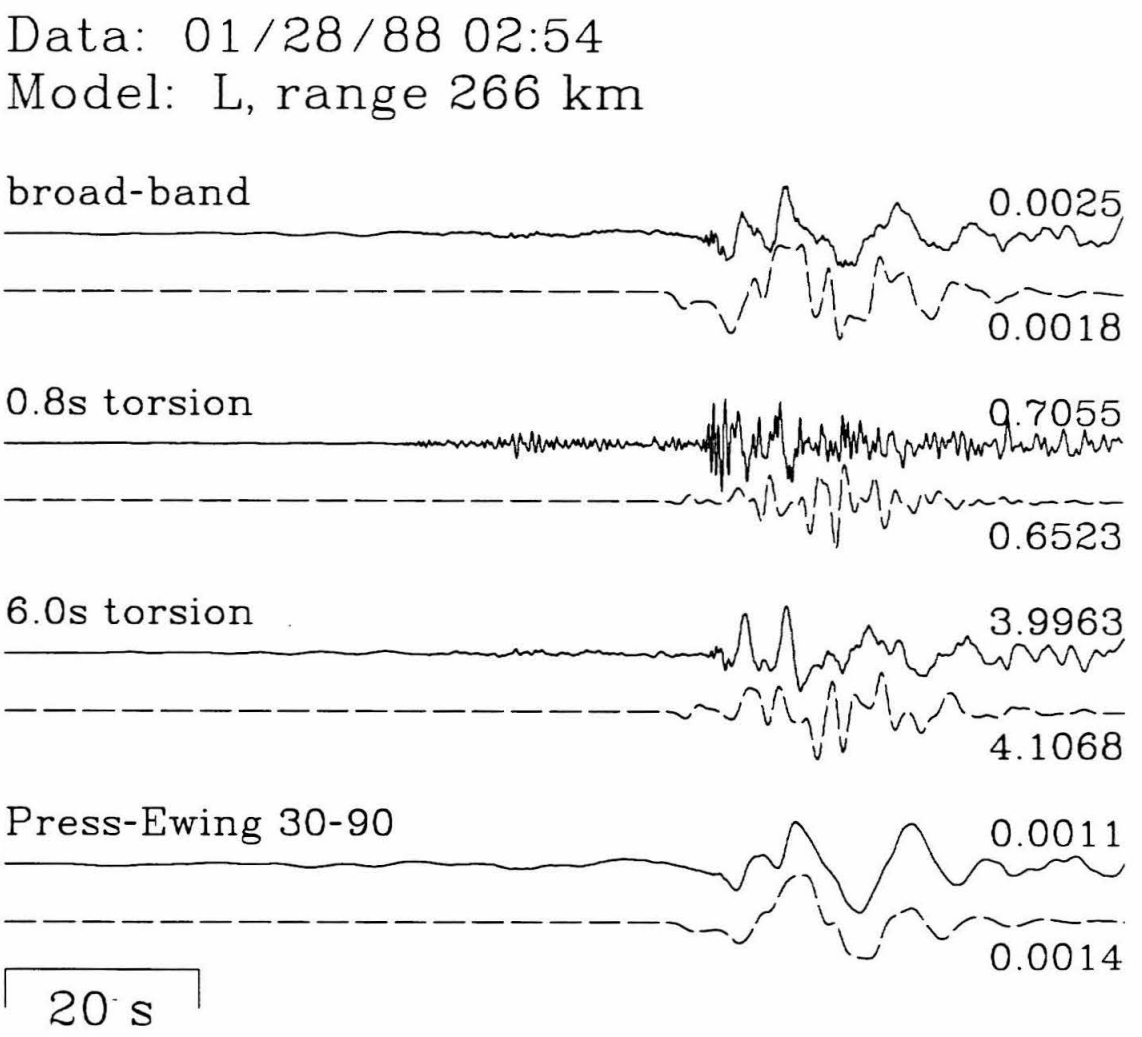

Figure 4.19 Results for 2d FD model L of SH structure from Imperial Valley to PAS as compared to the calibration event from January 28, 1988.

5.8 km/s, Vs from 3.1 to 3.4 km/s and density from 2.67 to 2.72 g/cc, over a depth of 5 km. There is also a fast mid-crust region beneath the Peninsular Ranges which has Vp=6.6 km/s, Vs=3.81 km/s and density=2.95 g/cc. The remainder of the crust is similar to that of model I. The results are mixed. The Love wave does not fit as well as model I, but there is some improvement to the front of the record in the vicinity of SmS. The 6.0s torsion synthetic is no longer dominated by a single SH body phase and the broadness of the peaks in the 30-90 record matches the data more accurately.

Since model L shows some possibility of improving the fit, we pursue it further with model M, shown in Figure 4.20. Model M is a modification of model L, where the dip of the MOHO has been modified and the crust under the Peninsular ranges made faster (Vp=6.7 km/s, Vs=3.87 km/s). The gradient at the surface has been modified to make the surface slower (Vp=5.2 km/s, Vs=3.0 km/s). Again, the fit has improved, and the Love wave is not as poorly modeled here as for model L. There are several problems with the model. Sn is too strong, so the MOHO structure is incorrect. The body phases on the 6.0 s torsion are apparently somewhere between the two models L and M. This indicates that the midcrust structure is approximately correct, but needs further modification. The fact that the Love wave fits better for model I and M than model L is puzzling. There is no upper-crust gradient in model I, and the gradient for model M is stronger than that for model L. It is possible that later multiples off the MOHO are responsible for distorting the Love wave in model L.

It is interesting that the above model (M) shows some correspondence to the data. It is a model based to a certain extent on existing hypotheses of the regional structure between the Imperial Valley and PAS. This leads to

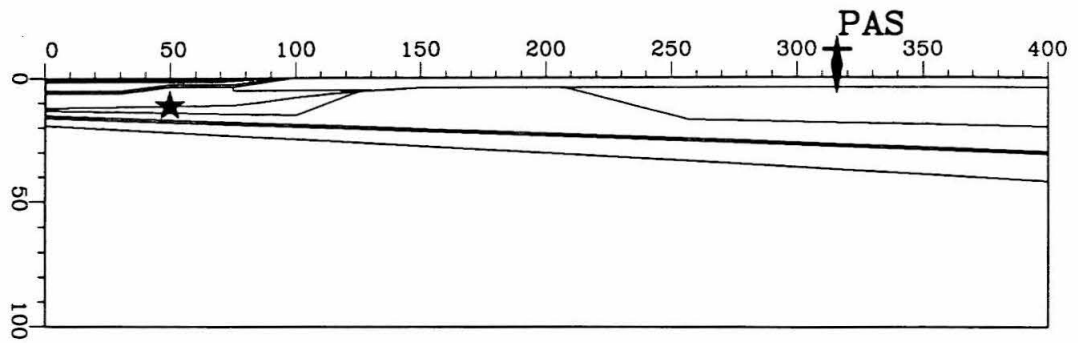

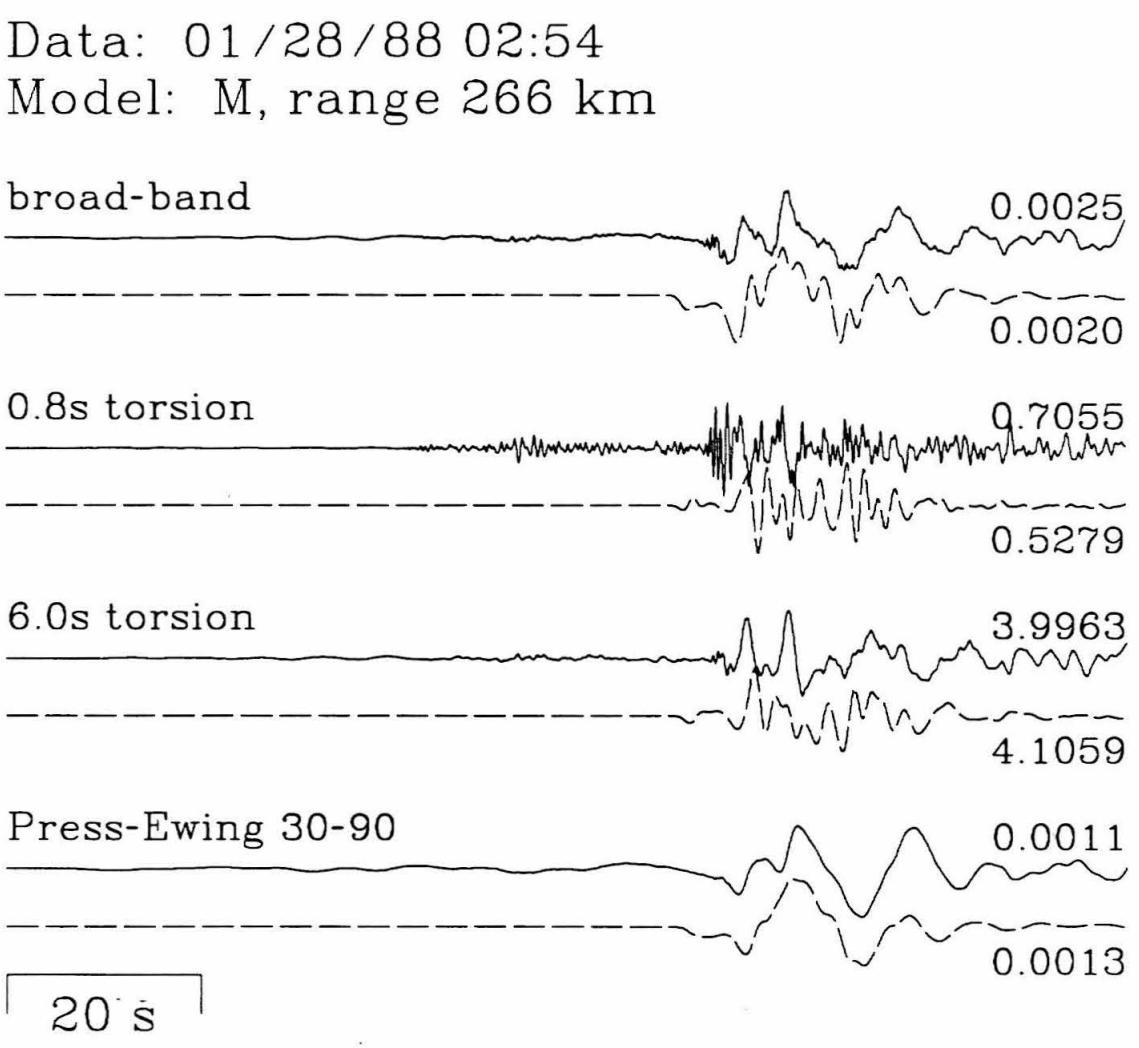

Figure 4.20 Results for 2d FD model M of SH structure from Imperial Valley to PAS as compared to the calibration event from January 28, 1988.

the hypothesis that a model based entirely on existing hypotheses of structure may best fit the data. Toward that end, model E is an attempt to incorporate naively every existing structural model along the path into one structure. The various structures that are combined here are mentioned above in the introduction. The final structure is not shown because a full specification of this model is too complicated. A comparison of the synthetics produced by this model to the Superstition Hills aftershock is shown in Figure 4.21. Although the range for the synthetic is 10 km closer than most of the above comparisons, this should have little effect on the result. The model is very unsuccessful at fitting the data. The reason for this is the naive construction, of the model which attempts to weld together models that are often conflicting, or that are supported by very little evidence. A better approach is to create a model where the structure is an average of several of the best models and differs along the path in the relative weight assigned each model, according to how appropriate a model should be for any given part of the profile. This approach is used in constructing model R. The results (Figure 4.22) show substantial improvement over model E, but the fit is no better than most of the simpler models discussed above.

Although the above structures fail to model most features in the tangential records from the two calibration events chosen, some features in the data are successfully modeled by some of the structures. It is interesting to see how well the corresponding structures for the P-SV system model the data. The fit here is more sensitive to variations in mechanism, distance and depth than the SH analysis above. It is important to consider this when comparing the data and synthetics for the Superstition Hills aftershock, for example, because of the questions mentioned above regarding its mechanism.

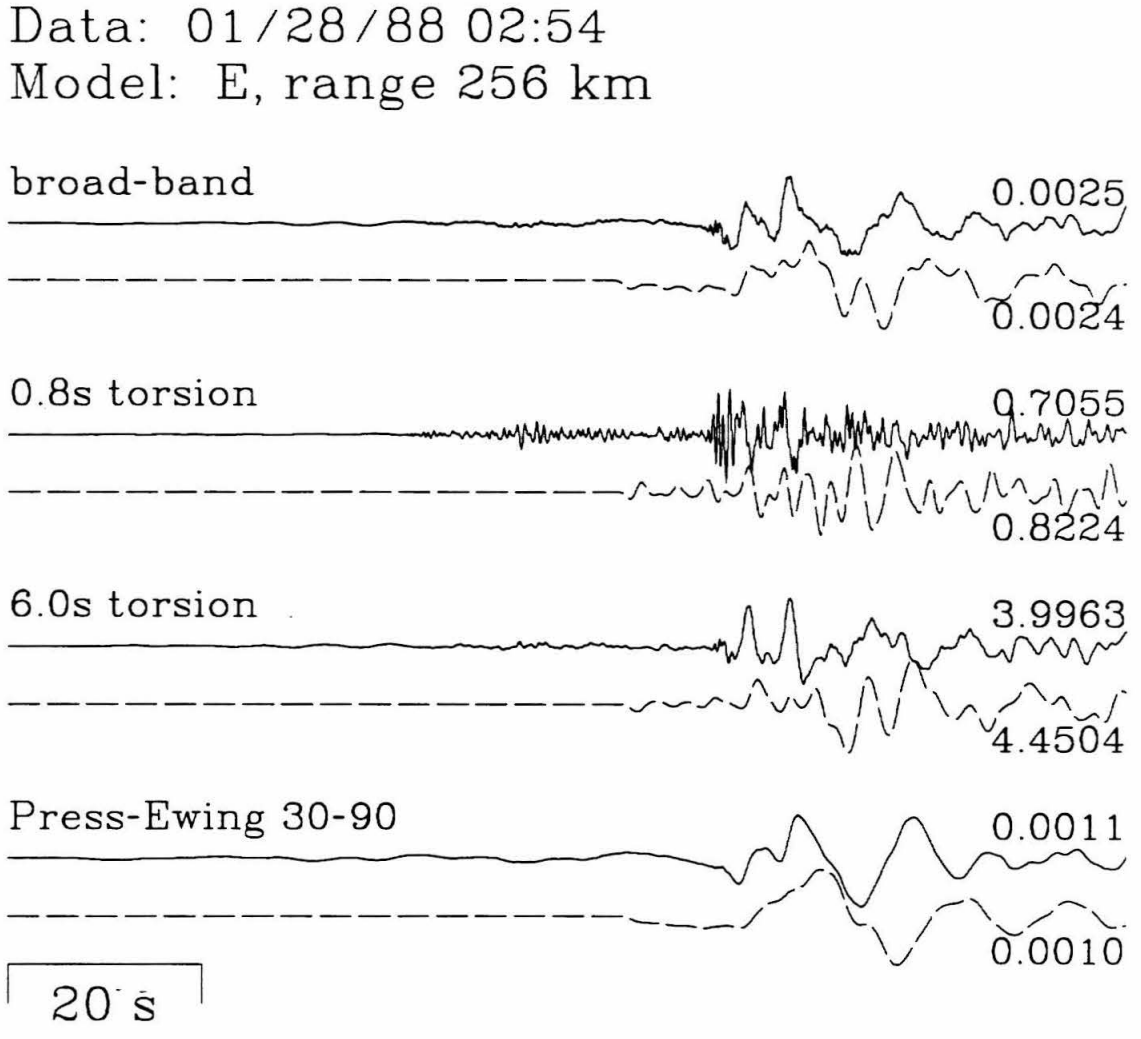

Figure 4.21 Results for 2d FD model E of SH structure from Imperial Valley to PAS as compared to the calibration event from January 28, 1988. The structure is very complex and is not shown.

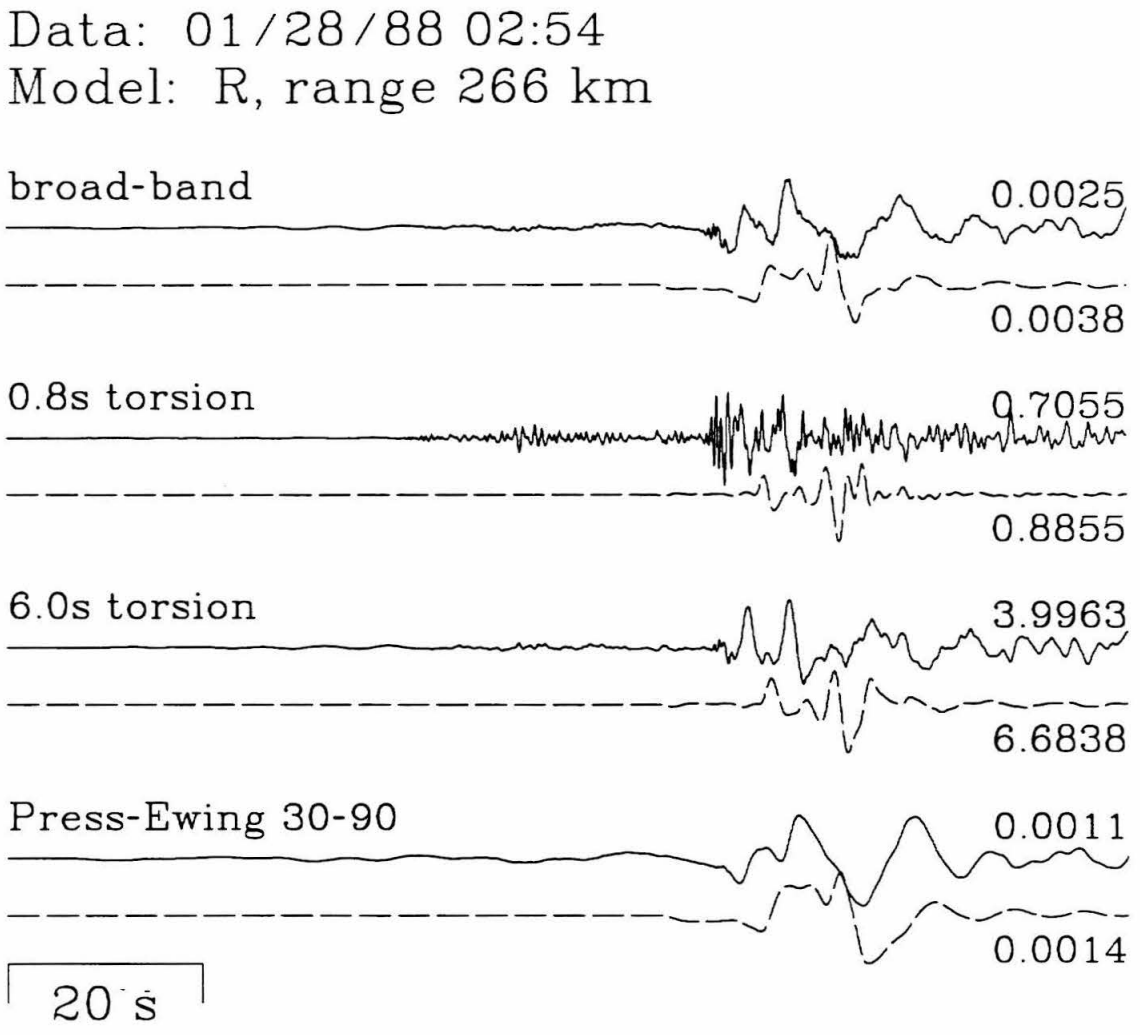

Figure 4.22 Results for 2d FD model R of SH structure from Imperial Valley to PAS as compared to the calibration event from January 28, 1988. The structure is very complex and is not shown.

We first examine the P-SV synthetics for model H, the first model examined for the SH case above. Figure 4.23 shows the results for a pure strike-slip mechanism at 266 km range and 10 km depth. The moment used is the same as that for the SH case above, 8×10^{22}. It is clear that the model does not fit the data very well. The Rayleigh wave is particularly problematic because the lack of fit appears incompatible between the two components. Probably, this is partly due to the mechanism, but the velocity structure is clearly not accurate.

To investigate this further, the data are compared to P-SV synthetics for the model (I) with basin 2. This comparison is shown in Figure 4.24. Here, the timing is somewhat improved, indicating that the shape and position of the basin is more accurate, but mechanism is still a problem. In Figure 4.25, the comparison is made again for the mechanism suggested for this earthquake in the SH analysis above. The waveforms are certainly different, but they do not fit the data any better than the pure strike-slip. The timing for these models is poor enough so as to eliminate the possibility of inverting for the mechanism using these synthetics. Therefore, no attempt is made here to find the best fitting mechanism.

There is another calibration event at approximately the same range which is more likely to be strike-slip. This is the Niland earthquake of March 6, 1989. The azimuth to this event is significantly different from that to the Superstition Hills aftershock, but given that the structure was poorly known and did not fit the latter event, we will use the same source and receiver pair to compare to the Niland event. The first comparison for this event is to model H in Figure 4.26. The model fits this event much better than it fits the Superstition Hills aftershock. The interpretation is simple,

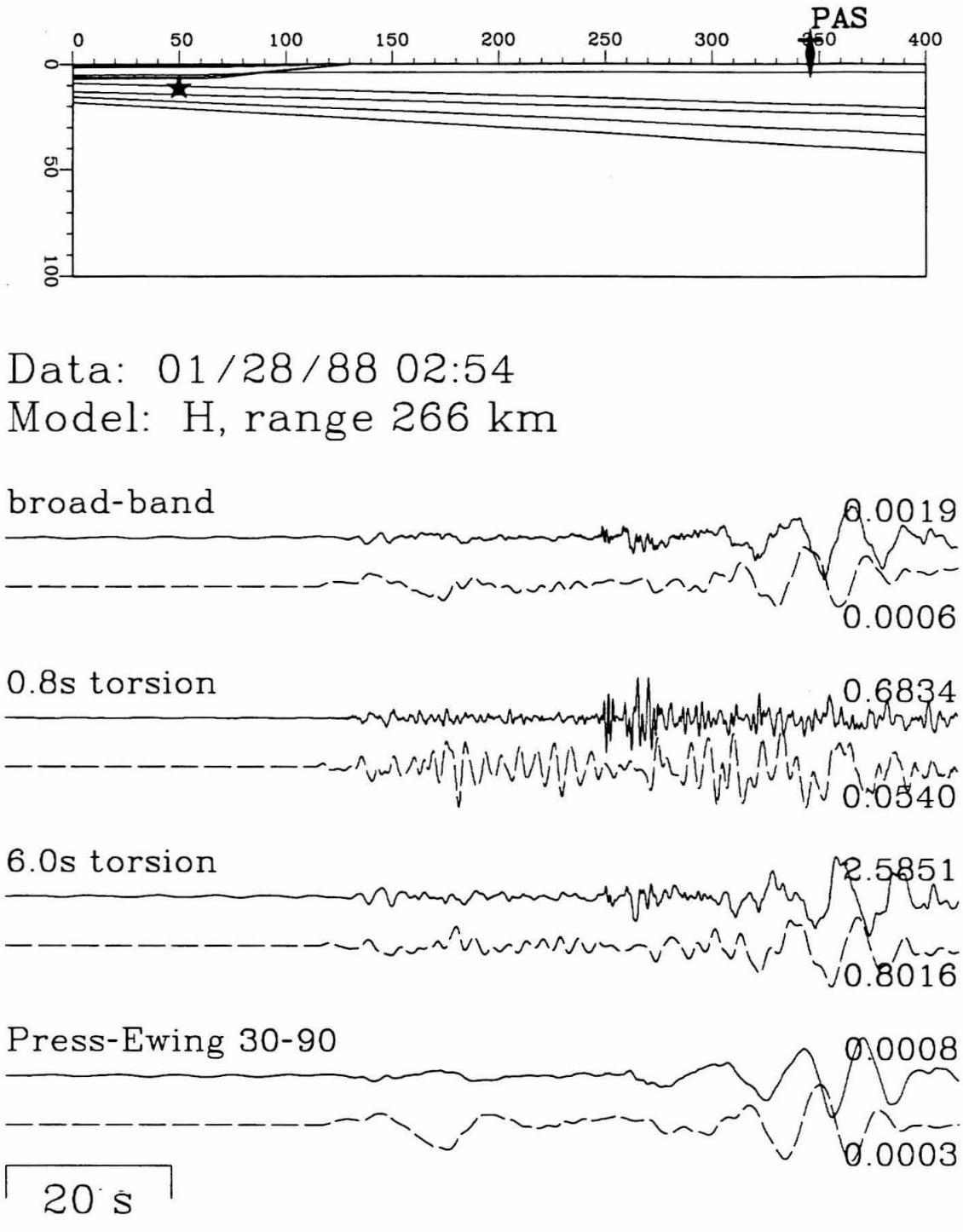

Figure 4.23 Results for 2d FD model H of P-SV structure from Imperial Valley to PAS as compared to the calibration event from January 28, 1988.
a) Radial component

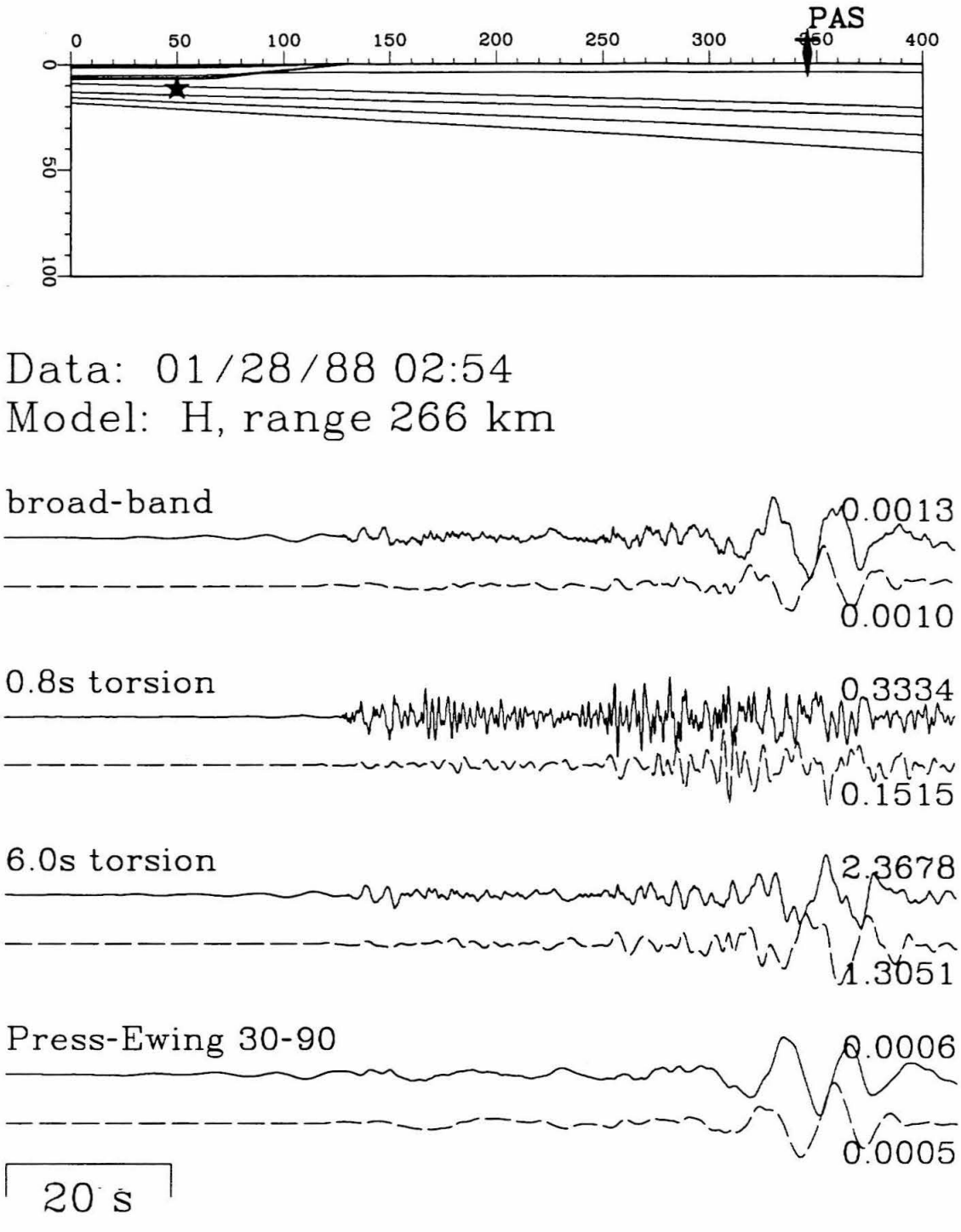

Figure 4.23 continued.
b) Vertical component

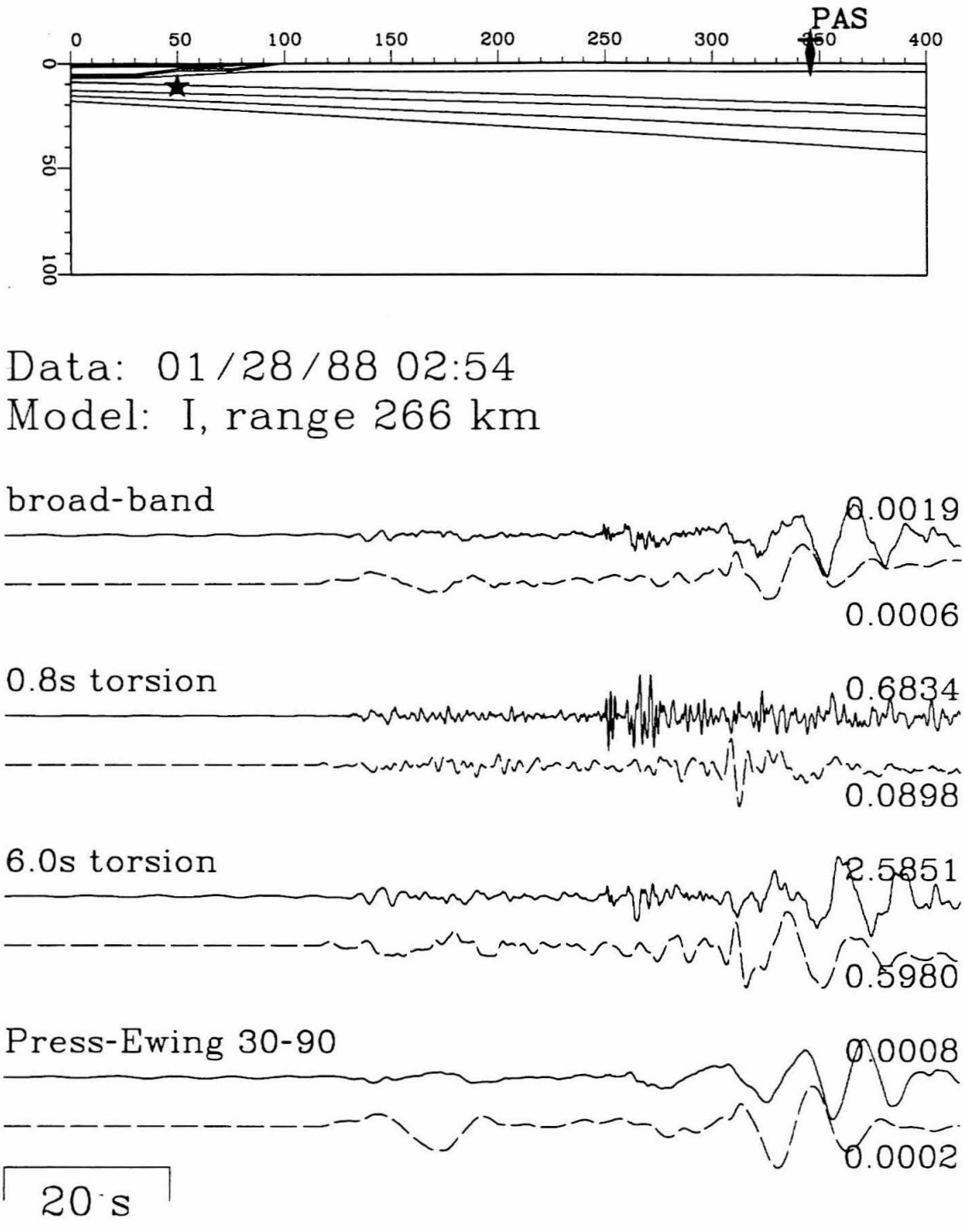

Figure 4.24 Results for 2d FD model I of P-SV structure from Imperial Valley to PAS as compared to the calibration event from January 28, 1988.
a) Radial component

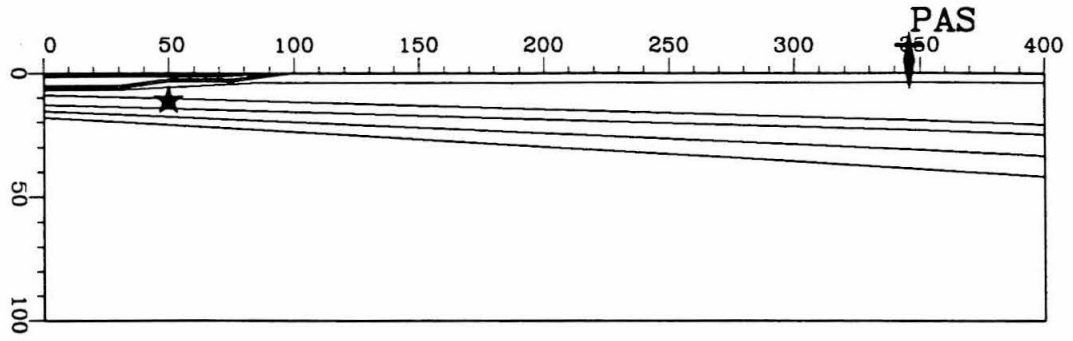

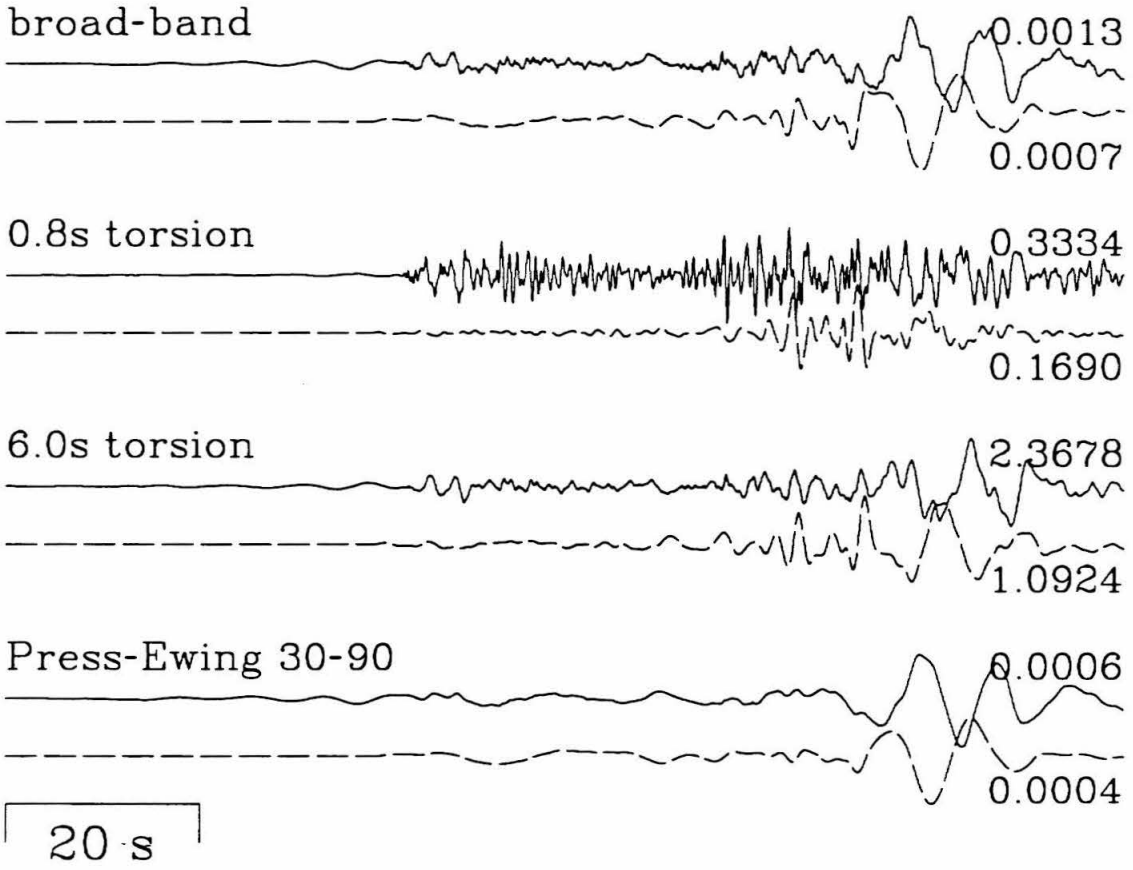

Figure 4.24 continued.
b) Vertical component

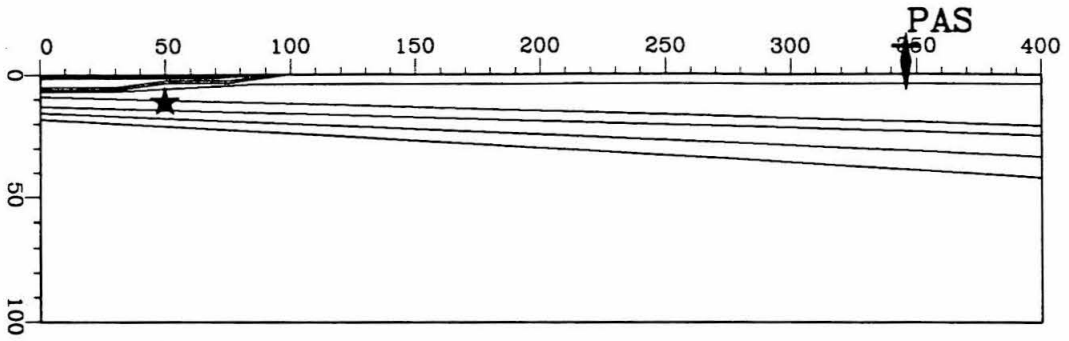

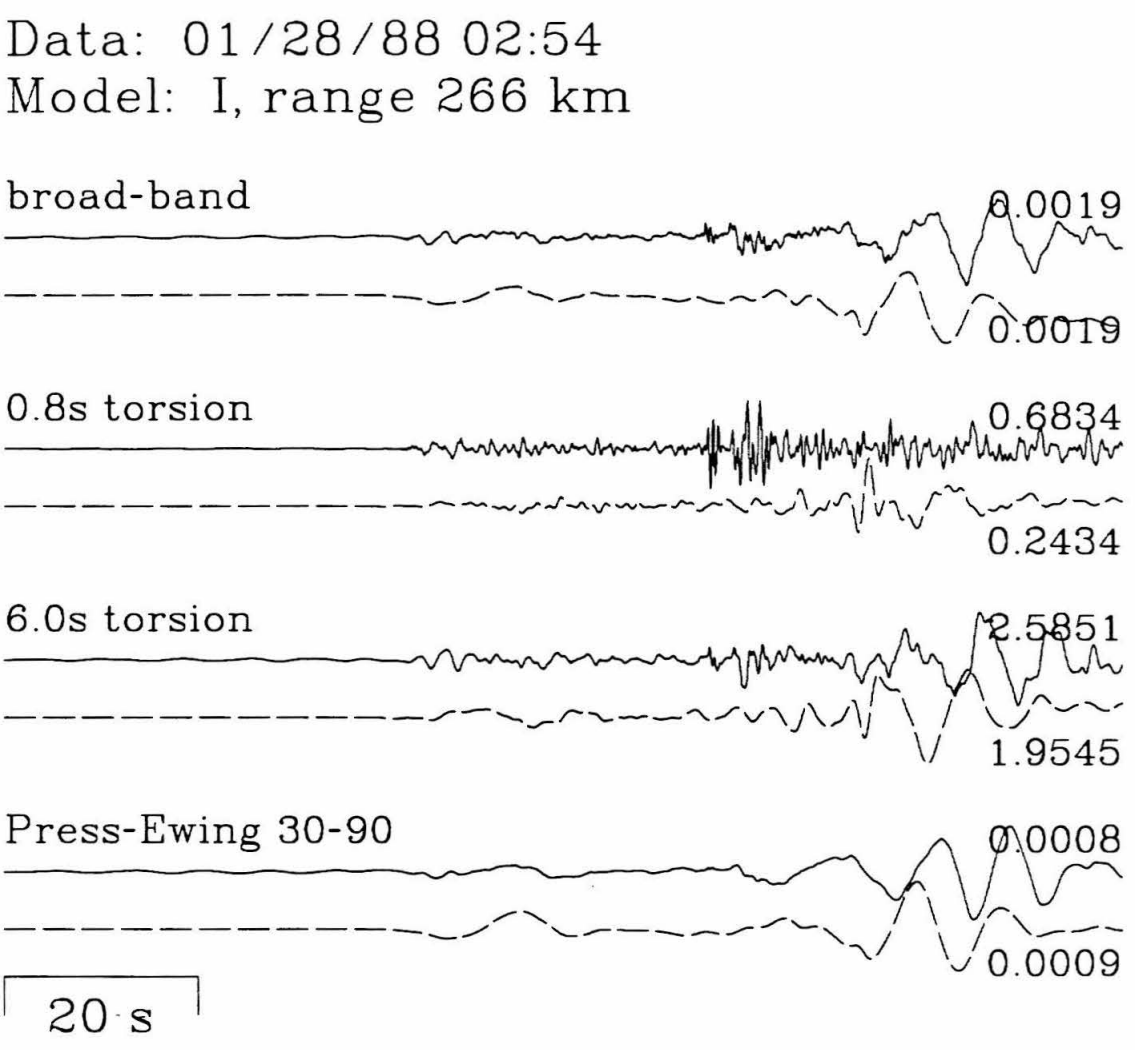

Figure 4.25 Results for 2d FD model I of P-SV structure from Imperial Valley to PAS as compared to the calibration event from January 28, 1988. The mechanism for this figure is thrust, as opposed to strike-slip.
a) Radial component

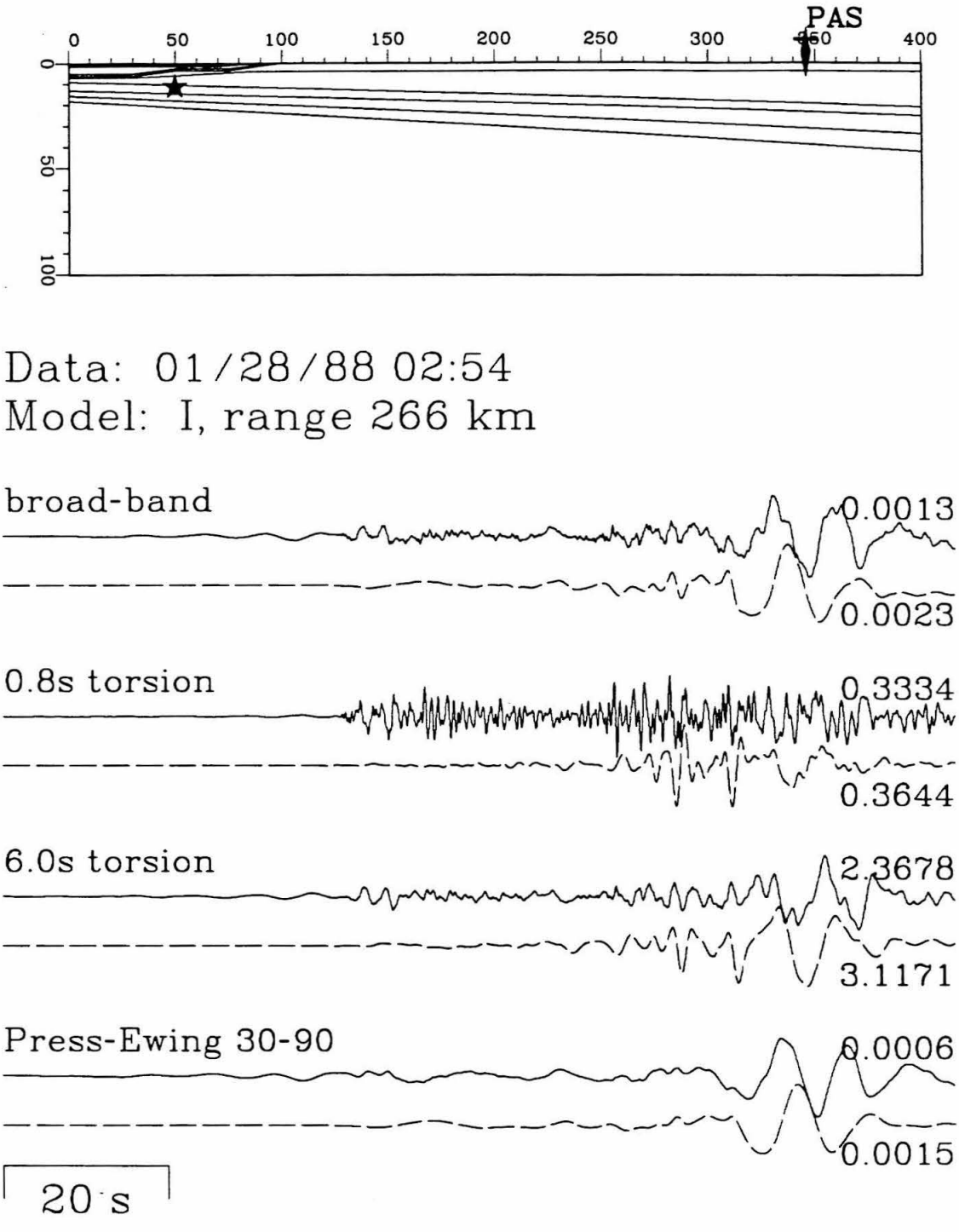

Figure 4.25 continued.
b) Vertical component

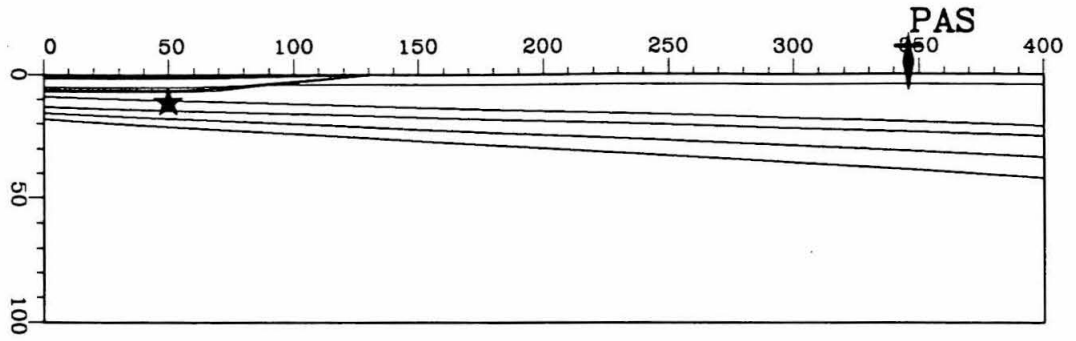

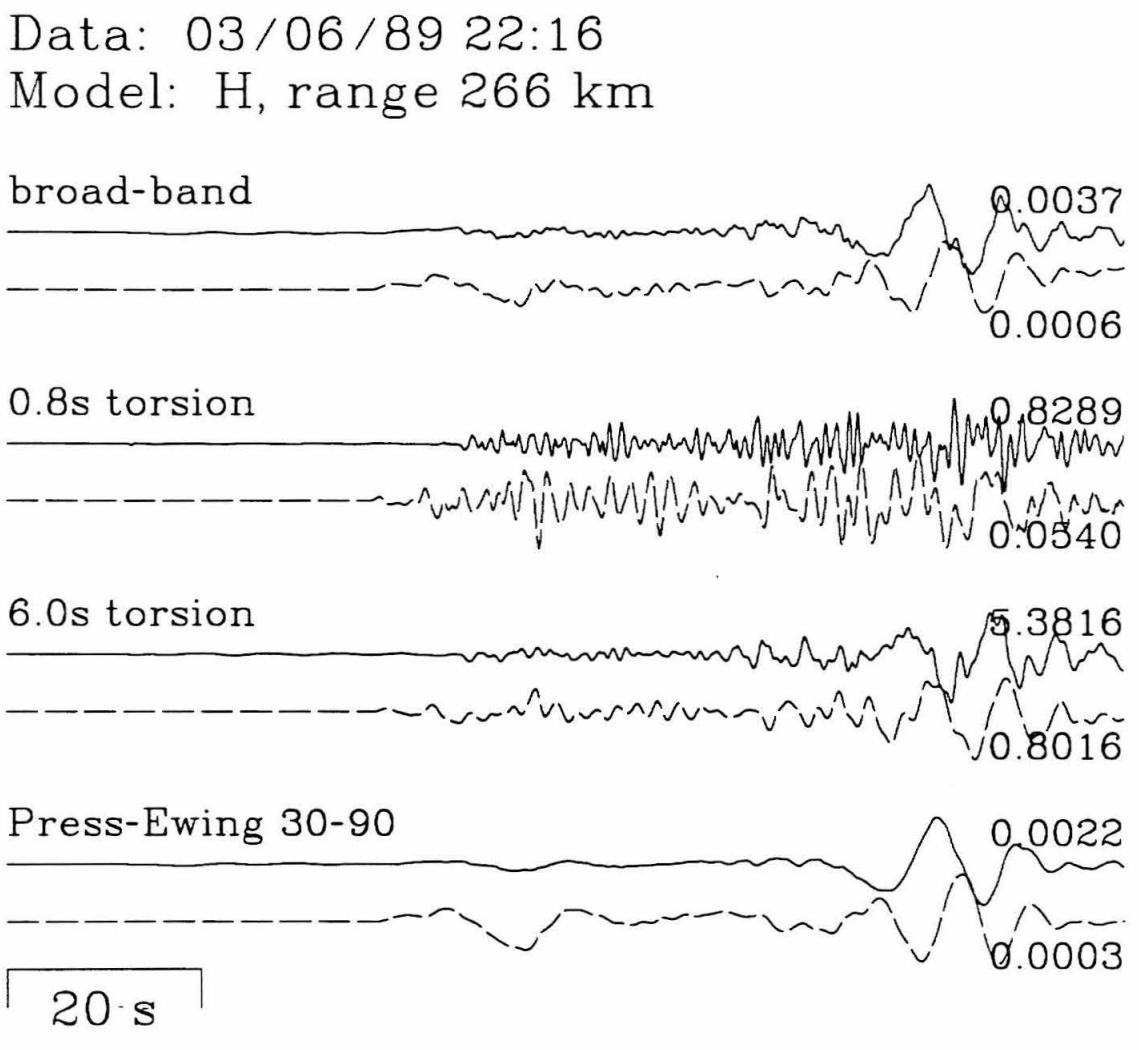

Figure 4.26 Results for 2d FD model H of P-SV structure from Imperial Valley to PAS as compared to the calibration event from March 6, 1989.
a) Radial component

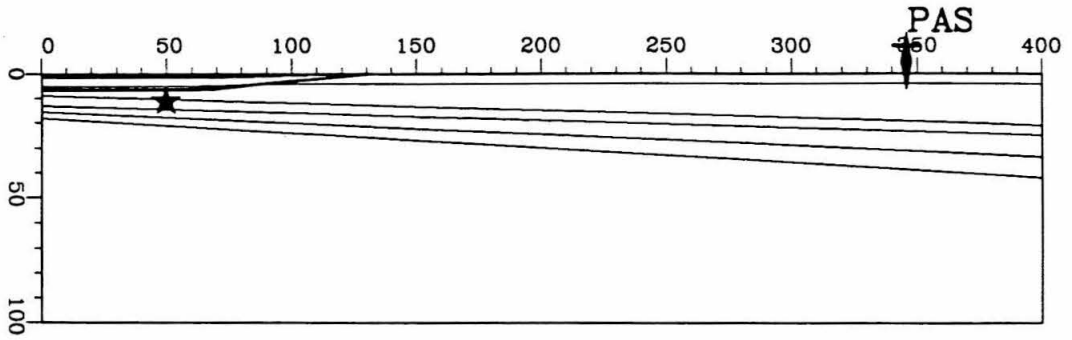

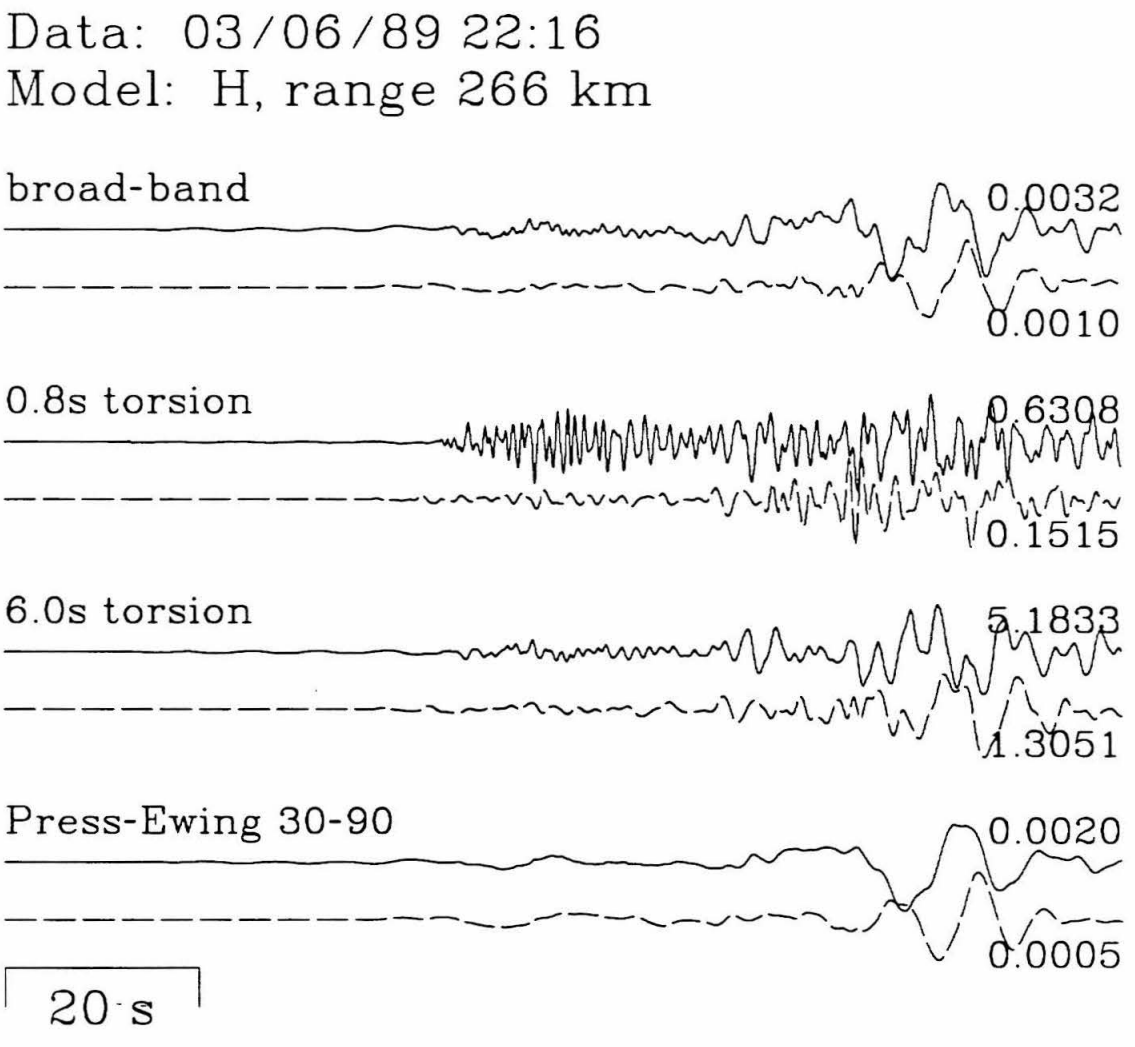

Figure 4.26 continued.
b) Vertical component

the P wave is too fast and the Rayleigh wave is too slow. Both components agree with respect to the direction and timing of the misfit. The gross characteristics of the waveforms of the data correspond to the synthetics.

The next comparison for the Niland event data is against model L. This model is a reasonable choice because the fast midcrust region beneath the Peninsular Ranges should advance the Rayleigh wave. The results in Figure 4.27 demonstrate that the timing of the Rayleigh wave has improved. Nevertheless, the P-wave is still too fast. The reason for this is probably related to MOHO geometry. If Pn had to travel farther to reach the MOHO, then it would be delayed without affecting the Rayleigh wave timing.

4.4 Discussion and recommendations

The high goals of this study are not met. The aim is to find new insight on seismic hazard and microtectonics of the Imperial Valley region through more accurate knowledge of historical seismicity. This requires an accurate model and such a model proves elusive. Nevertheless, the data support the effort to find such a model. Therefore, this study must be analyzed for its failure and new hypotheses proposed.

The goals of this study are motivated by evidence in the data and rely on analysis of the data to produce an accurate model. Although a large number of events are shown here, only a few are recent enough to have sufficiently accurate locations, magnitudes, mechanisms, etc. Much more data should be collected on modern instruments to provide more detailed calibration of the data. It would be useful to address other stations as well. While it is true that only a few have as long a history as PAS, and none yet have broad-band recording, the additional constraints would allow better

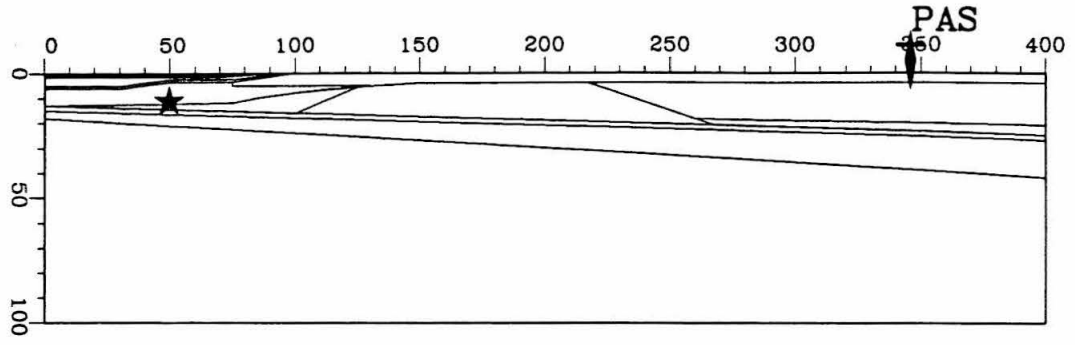

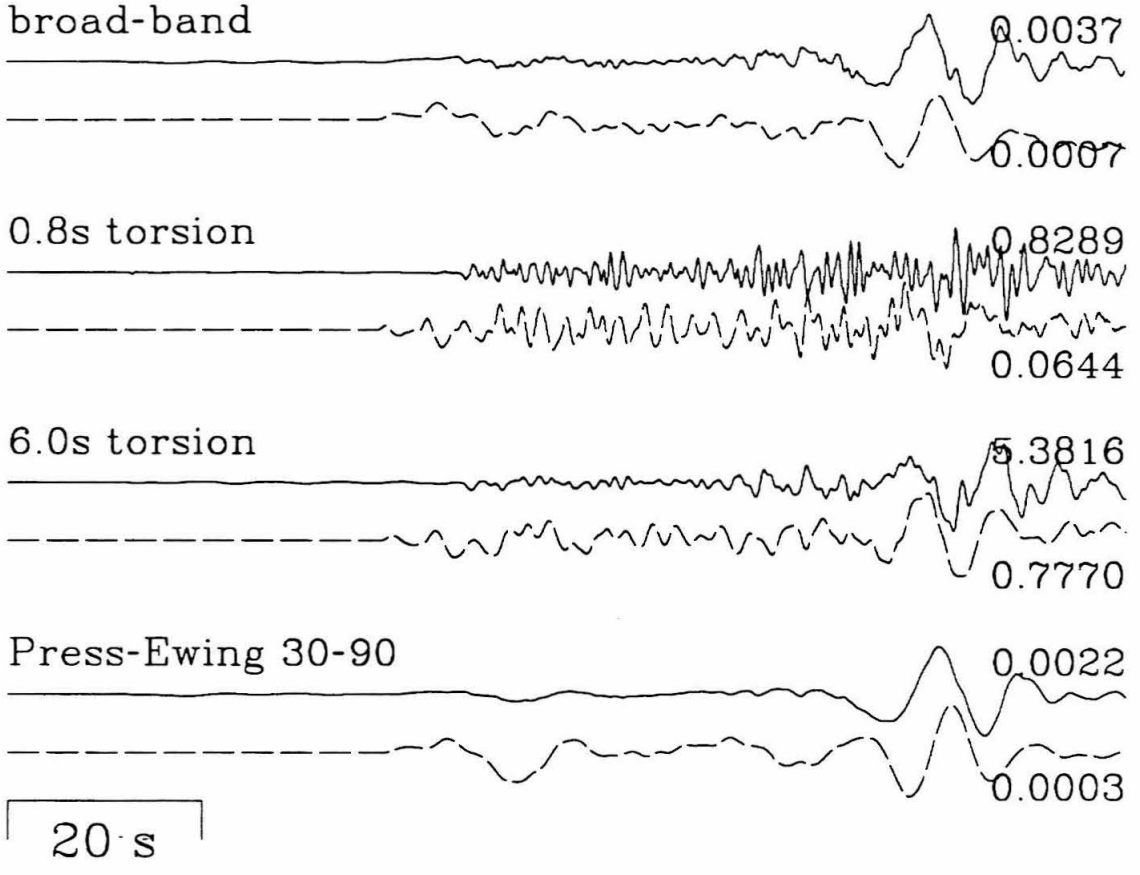

Figure 4.27 Results for 2d FD model L of P-SV structure from Imperial Valley to PAS as compared to the calibration event from March 6, 1989.
a) Radial component

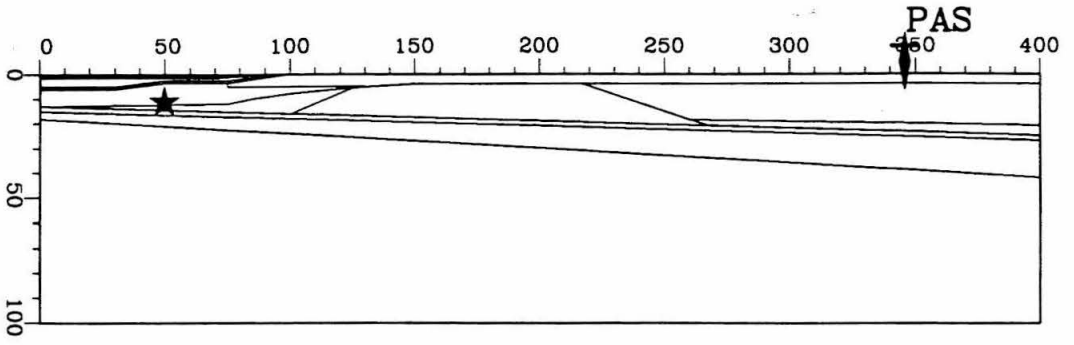

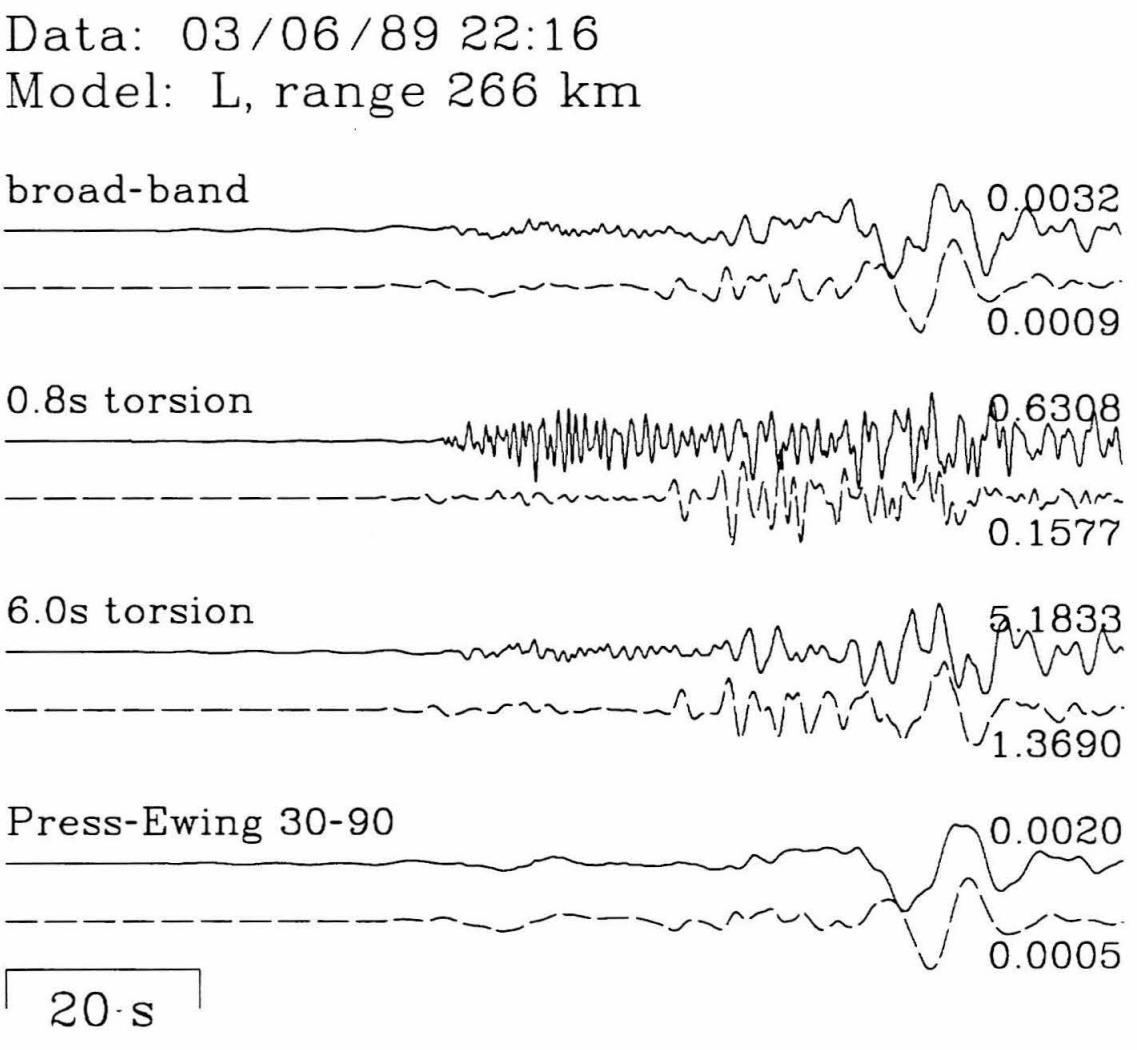

Figure 4.27 continued.
b) Vertical component

separation of the data according to mechanism and distance from the basin boundary. More data would also allow the kind of event association only partly explored in the above presentation of the 6.0 second torsion data. Thus, events could be classed into location/depth/mechanism groups and then modeled as a whole. Also, the quality of the hand-digitized records should be improved. The technology exists for automatic digitization of such information, provided that the necessary software is written. Careful examination of the paper records shows that scanning up to 1200 bpi for black and white may be required to fully describe the waveform as recorded, but gray-scale scanning would require less resolution. Once scanned, the algorithms for reducing this information to vector form exist, including filling in gaps in the record and sorting out line crossings, but this would have to be implemented for the specific application of seismic digitizing. Of course, operator intervention would lessen the need for sophisticated software. Overall, such a system is feasible, and would be quite valuable to seismology by providing relatively fast, easy access to digital seismograms from the past century of seismic recording.

The lack of structural information is a strong limitation in this study. As is evident in the free pursuit of a wide variety of 2d models above, there is little constraint on structure available. It would be useful to have more high-quality seismic reflection and refraction work around southern California to better define structure down to the MOHO. It is possible that 2d modeling will not provide useful information. This would be the case if the 3d effects are of the same order or larger than the 2d effects. There is some evidence that this may be the case. The profile crosses the Peninsular Ranges at an angle close to 45 degrees. This is as far from a 2d cross section as

possible. Profiles perpendicular to structure are ideal for 2d modeling, and profiles parallel to structure are mainly affected by focusing and defocusing, but otherwise have little off-azimuth effect. More evidence that the profile may be strongly 3d is that the profile runs along the trace of the Elsinore Fault and then between the Los Angeles and San Gabriel basins. Nowhere does the profile intersect structure at 90 degrees. If there is topography on the MOHO, as suggested by the differences between proposed flat-layer models, such variations are likely to cross the profile at a variety of angles. All these factors have two primary effects. First, energy will arrive at PAS off-azimuth (polarization analysis may detect this). Second, the energy arriving at PAS will represent an average of several paths that vary somewhat in such things as MOHO topography. This second effect presents at PAS what appears to be a smeared structure, which may be best modeled by a gradational, flat-layered model rather than a 2d model. This leads to a final point: The variety of one-dimensional models that can explain some of the data should be fully explored before turning to more studies of lateral variation. Finally, teleseismic data should be analyzed for evidence of scattered energy. Such evidence would demonstrate the need for lateral variation in the structure. If the evidence is not present, it could indicate that either scattering is relatively unimportant, and flat-layered models will suffice, or scattering is weakened by 3d variations in the scattering structure.

References for Chapter 4

Bent, A. L., D. V. Helmberger, R. J. Stead, and P. Ho-Liu (1989). Waveform modeling of the November 1987 Superstition Hills earthquakes, *Bull. Seism. Soc. Am.*, **79,** 500-514.

Burdick, L. J. and G. R. Mellman (1976). Inversion of the body waves from the Borrego Mountain earthquake to the source mechanism, *Bull. Seism. Soc. Am.*, **66,** 1485-1499.

Butler, R. H. (1983). Surface wave analysis of the 9 April 1968 Borrego Mountain earthquake, *Bull. Seism. Soc. Am.*, **73,** 879-883.

Doser, D. I. and H. Kanamori (1986). Spatial and temporal variations in seismicity in the Imperial Valley (1902-1984), *Bull. Seism. Soc. Am.*, **76,** 421-438.

Frankel, A. and L. Wennerberg (1989). Rupture process of the M_S 6.6 Superstition Hills, California, earthquake determined from strong-motion recordings: application of tomographic source inversion, *Bull. Seism. Soc. Am.*, **79,** 515-541.

Fuis, G. S., W. D. Mooney, J. H. Healy, G. A. McMechan and W. J. Lutter (1982). Crustal structure of the Imperial Valley region in *the Imperial Valley, California earthquake of Oct. 15, 1979, U. S. Geol. Survey Prof. Paper,* **1254,** 25-49.

Gutenberg, B. (1944). Travel times of principal P and S phases over small distances in southern California, *Bull. Seism. Soc. Am.*, **34,** 13-32.

Gutenberg, B. (1951). Revised travel times in southern California, *Bull. Seism. Soc. Am.*, **62,** 427-439.

Gutenberg, B. (1952). Waves from blasts recorded in southern California, *Trans. Am. Geophys. Union,* **33,** 427-431.

Gutenberg, B. (1955). Wave velocities in the earth's crust, *Geol. Soc. Am. special paper,* **62,** 19-34.

Hadley, D. and J. Combs (1974). Microearthquake distribution and mechanisms of faulting in the Fontana-San Bernardino area of southern California, *Bull. Seism. Soc. Am,* **64,** 1477-1499.

Hadley, D. and H. Kanamori (1977). Seismic structure of the Tranverse Ranges, California, *Bull. Geol. Soc. Am.,* **88,** 1469-1478.

Hadley, D. and H. Kanamori (1979). Regional S-wave structure for southern California from the analysis of teleseismic Rayleigh waves, *Geophys. J. R. astr. Soc.,* **58,** 655-666.

Hadley, D. M. and D. V. Helmberger (1980). Simulation of strong ground motions, *Bull. Seism. Soc. Am.,* **70,** 617-630.

Hartzell, S. and D. V. Helmberger (1982). Strong-motion modeling of the Imperial Valley earthquake of 1979, *Bull. Seism. Soc. Am.,* **72,** 571-596.

Hearn, T. M. and R. W. Clayton (1986a). Lateral velocity variations in southern California. II. Results for the upper crust from Pg waves, *Bull. Seism. Soc. Am.,* **76,** 495-509.

Hearn, T. M. and R. W. Clayton (1986b). Lateral velocity variations in southern California. II. Results for the lower crust from Pn waves, *Bull. Seism. Soc. Am.,* **76,** 511-520.

Heaton, T. H. and D. V. Helmberger (1977). A study of the strong ground motion of the Borrego Mountain, California, earthquake, *Bull. Seism. Soc. Am.,* **67,** 315-330.

Heaton, T. H. and D. V. Helmberger (1978). Predictablility of strong ground motion in the Imperial Valley: modeling the M4.9, November 4, 1976 Brawley earthquake, *Bull. Seism. Soc. Am.,* **68,** 31-48.

Hileman, J. A., C. R. Allen and J. M. Nordquist (1973). *Seismicity of the southern California region 1 January 1932 to 31 December 1972,* Seismological Laboratory, California Institute of Technology, Pasadena, CA.

Ho-Liu, P. (1988). I. Attenuation tomography II. Modeling regional Love waves: Imperial Valley to Pasadena, Ph.D. thesis, California Institute of Technology, Pasadena, CA, 160pp.

Kanamori, H. and D. Hadley (1975). Crustal structure and temporal velocity change in southern California, *Pageoph,* **113,** 257-280.

McMechan, G. A. and W. D. Mooney (1980). Asymptotic ray theory and synthetic seismograms for laterally varying structure: Theory and application to the Imperial Valley, California, *Bull. Seism. Soc. Am.,* **70,** 2021-2035.

Press, F. (1956). Determination of crustal structure from phase velocity of Rayleigh waves, part I: southern California, *Bull. Geol. Soc. Am.,* **67,** 1647-1658.

Press, F. (1960). Crustal structure in the California-Nevada region, *J. Geophys. Res.,* **65,** 1039-1051

Richter, C. F. (1950). Velocities of P at short distances, *Bull. Seism. Soc. Am,* **40,** 281-289.

Roller, J. C. and J. H. Healy (1963). Seismic refraction measurements of crustal structure beneath Santa Monica Bay and Lake Mead, *J. Geophys. Res.,* **68,** 5837-5848.

Sanders, C. O., H. Magistrale and H. Kanamori (1986). Rupture patterns and preshocks of large earthquakes in the southern San Jacinto fault zone, *J. Geophys. Res.,* **76,** 1187-1206.

Shor, G. G. (1955). Deep reflections from southern California blasts, *Trans.*

Am. Geophys. Union, **36,** 133-138.

Stead, R. J., and D. V. Helmberger (1988). Numerical-analytical interfacing in two dimensions with applications to modeling NTS seismograms. *J. Pure and Appl. Geophys.,* **128,** 101-193.

Thatcher, W. and T. C. Hanks (1973). Source parameters of southern California earthquakes, *J. Geophys. Res.,* **78,** 8547-8576.

Vidale, J. E. (1987). Application of two-dimensional finite-difference wave simulation to earthquakes, earth structure and seismic hazard, Ph.D. thesis, California Institute of Technology, Pasadena, CA, 150pp.

Vidale, J. E., and D. V. Helmberger (1988). Elastic finite-difference modeling of the 1971 San Fernando, California earthquake, *Bull. Seism. Soc. Am.,* **78,** 122-141.

Appendix A: Analytic source function for two-dimensional finite differences

Asymptotic source theory produces P-wave point-source displacement potentials in three dimensions of the following forms, assuming a step function source:

$$\phi_P(x,z,t) = \frac{\sqrt{2}}{\pi\sqrt{x}}\left[\frac{1}{\sqrt{t}} * \mathrm{Im}\left(\frac{\sqrt{p}}{\eta}\frac{dp}{dt}\right)\right], \tag{A.1}$$

and for a delta-function source

$$\phi_P(x,z,t) = \frac{\sqrt{2}}{\pi\sqrt{x}}\frac{d}{dt}\left[\frac{1}{\sqrt{t}} * \mathrm{Im}\left(\frac{\sqrt{p}}{\eta}\frac{dp}{dt}\right)\right]. \tag{A.2}$$

In these equations, p is given by

$$p = \frac{xt}{R^2} + \iota\sqrt{t^2-(R/\alpha)^2}\frac{|z|}{R^2}, \tag{A.3}$$

and η is given by

$$\eta = \frac{|z|}{R^2}t - \iota\sqrt{t^2-(R/\alpha)^2}\frac{x}{R^2}. \tag{A.4}$$

The conventions are x positive to the right, u positive to the right, z positive down, but w positive up. The variables are: x, u horizontal distance and displacement; z, w vertical distance and displacement; α P-wave velocity; ϕ potential; and $R = (x^2+z^2)^{1/2}$.

The method used in this paper requires the delta function response in displacement, which is obtained by taking derivatives of the potential.

$$u_P = \frac{\partial\phi_P}{\partial x} \qquad w_P = -\frac{\partial\phi_P}{\partial z} \tag{A.5}$$

To simplify the taking of these derivatives, first take the Laplace transform of Equation A.2.

$$\bar{\phi}_P = \frac{\sqrt{2}}{\sqrt{\pi x}} \frac{s}{\sqrt{s}} \mathrm{Im} \int e^{-s(px+\eta|z|)} \frac{\sqrt{p}}{\eta} \frac{dp}{dt} dt \tag{A.6}$$

Now, taking the derivatives A.5 of Equation A.6 and keeping only the far-field terms

$$\bar{u}_P = \frac{\partial \bar{\phi}_P}{\partial x} = (-sp)\bar{\phi}_P, \text{ and } \bar{w}_P = -\frac{\partial \bar{\phi}_P}{\partial z} = (s\eta\epsilon)\bar{\phi}_P, \tag{A.7}$$

where ϵ is the signum function.

$$\epsilon = sgn(z) = \begin{cases} +1 & z > 0 \\ -1 & z < 0 \end{cases}$$

Returning A.7 to the time domain,

$$u_P = -\frac{d}{dt} Re(p\,\phi_P) \text{ and } w_P = \frac{d}{dt} Re(\eta\epsilon\phi_P). \tag{A.8}$$

Part of Equation A.2 can be evaluated before assembling the displacements; that is,

$$\mathrm{Im}\left(\frac{1}{\eta}\frac{dp}{dt}\right) = \frac{H(t-R/\alpha)}{\sqrt{t^2-(R/\alpha)^2}}. \tag{A.9}$$

A final stipulation is that one derivative with respect to time will be applied later to the source time function before convolving it with the result, so one derivative can be dropped here. Then using A.2 and A.9 in Equation A.8:

$$u_P = \frac{\sqrt{2}}{\pi\sqrt{x}} \frac{d}{dt} \left[\frac{1}{\sqrt{t}} * \left(\frac{H(t-R/\alpha)}{\sqrt{t^2-(R/\alpha)^2}} Re(-p\sqrt{p}) \right) \right], \tag{A.10}$$

and

$$w_P = \frac{\sqrt{2}}{\pi\sqrt{x}} \frac{d}{dt} \left[\frac{1}{\sqrt{t}} * \left(\frac{H(t-R/\alpha)}{\sqrt{t^2-(R/\alpha)^2}} Re(\eta\epsilon\sqrt{p}) \right) \right]. \tag{A.11}$$

Now let

$$u_P = \frac{-1}{\sqrt{x}} \frac{d}{dt}\left[\frac{1}{\sqrt{t}} * u_{FD}\right] \quad \text{and} \quad w_P = \frac{-1}{\sqrt{x}} \frac{d}{dt}\left[\frac{1}{\sqrt{t}} * w_{FD}\right]. \tag{A.12}$$

Then, combining A.10 and A.11,

$$\begin{pmatrix} u \\ w \end{pmatrix}_{FD} = \frac{\sqrt{2}}{\pi} \frac{H(t-R/\alpha)}{\sqrt{t^2-(R/\alpha)^2}} \mathrm{Re}\begin{pmatrix} p\sqrt{p} \\ -\eta\epsilon\sqrt{p} \end{pmatrix}. \tag{A.13}$$

Approximate $\sqrt{p}$ as

$$\sqrt{p} \sim \frac{\sqrt{p_0}}{2}\left(1+\frac{p}{p_0}\right),$$

or, more generally,

$$\sqrt{p} \sim \sqrt{p_0}\left(1-k_f+k_f\frac{p}{p_0}\right), \tag{A.14}$$

where k_f is a parameter that allows a better fit to $\sqrt{p}$ over selected ranges of take-off angle. Using this approximation, set

$$\begin{aligned} Re\,(p\sqrt{p}) &= \mathrm{Re}\left[p\sqrt{p_0}\left(1-k_f+k_f\frac{p}{p_0}\right)\right] \\ &= (1-k_f)\sqrt{p_0}\frac{xt}{R^2} + \frac{k_f}{\sqrt{p_0}} Re\,(p^2) \\ &= (1-k_f)\sqrt{p_0}\frac{xt}{R^2} + \frac{k_f}{\sqrt{p_0}}\left[\frac{t^2}{R^4}(x^2-z^2)+\frac{z^2}{R^2}\frac{1}{\alpha^2}\right]. \end{aligned} \tag{A.15}$$

Similarly,

$$Re\,(\eta\epsilon\sqrt{p}) = (1-k_f)\sqrt{p_0}\frac{|z|}{R^2}t\epsilon + \frac{k_f}{\sqrt{p_0}}\frac{t^2}{R^4}\left[2|z|x - |z|x\frac{R^2}{\alpha^2 t^2}\right]\epsilon. \tag{A.16}$$

If i is the take-off angle (the direction of R), measured counter-clockwise from positive z; then $p_0 = sin(i)/\alpha$. Take $p_0 = 1/\alpha$ for $i \sim \pi/2$ in Equations A.15 and A.16, and apply these to Equation A.13,

$$\begin{pmatrix} u \\ w \end{pmatrix}_{FD} = \frac{\sqrt{2}}{\pi\sqrt{\alpha}} \frac{H(t-R/\alpha)}{t(1-(R/\alpha t)^2)^{1/2}} \frac{t}{R^2} \left[(1-k_f) \begin{pmatrix} x \\ -|z|\epsilon \end{pmatrix} + k_f \frac{\alpha t}{R^2} \begin{pmatrix} x^2 - z^2 + z^2 (R/\alpha t)^2 \\ -2x|z|\epsilon + x|z|(R/\alpha t)^2 \epsilon \end{pmatrix} \right].$$

Let $(R/\alpha t)^2 = T_\alpha$ and $|z|\epsilon = z$, then

$$\begin{pmatrix} u \\ w \end{pmatrix}_{FD} = \frac{\sqrt{2}}{\pi R^2 \sqrt{\alpha}} \frac{H(t-R/\alpha)}{(1-T_\alpha)^{1/2}} \left[(1-k_f) \begin{pmatrix} x \\ -z \end{pmatrix} + k_f \frac{\alpha t}{R^2} \begin{pmatrix} x^2 - z^2 + z^2 T_\alpha \\ (T_\alpha - 2)xz \end{pmatrix} \right]. \tag{A.17}$$

It is instructive at this point to do dimensional analysis on Equation A.17. Let units of length be denoted l and units of time t. Then,

$$\begin{aligned} \begin{pmatrix} u \\ w \end{pmatrix}_{FD} &= \frac{1}{l^2} \frac{\sqrt{t}}{\sqrt{l}} \left[l + \frac{l}{t} \frac{t}{l^2} l^2 \right] \\ &= \frac{1}{l^2} \frac{\sqrt{t}}{\sqrt{l}} l \\ &= \frac{\sqrt{t}}{\sqrt{l^3}}. \end{aligned} \tag{A.18}$$

Convert this result to point-source form using Equation A.12.

$$\begin{aligned} \begin{pmatrix} u \\ w \end{pmatrix}_{P} &= \frac{1}{\sqrt{l}} \frac{1}{t} \frac{1}{\sqrt{t}} \frac{\sqrt{t}}{\sqrt{l^3}} t \\ &= \frac{1}{l^2} \end{aligned} \tag{A.19}$$

Now convolve the result with the correct time function, the reduced

displacement potential (RDP) function. The definition of the RDP is

$$\phi(R,t) = \frac{-\psi(t)}{R} \quad \text{where} \quad \psi(t) = \psi_\infty(1-e^{-kt})(1+kt+...), \tag{A.20}$$

where ψ_∞ has dimensions of volume. From Equation A.5, displacement is

$$u = \frac{\partial\phi}{\partial R} = \frac{\psi}{R^2} + \frac{1}{R\,\alpha}\frac{d\,\psi}{dt}. \tag{A.21}$$

Applying this to the derivation above, true displacement is expressed as

$$u(R,t) = -\psi(t) * \frac{d\,\phi_P}{dR}, \tag{A.22}$$

where the derivative is equivalent to the expression of Equation A.19. Continuing with the dimensional analysis, Equations A.19 and A.22 give the result,

$$u = l^3\frac{1}{l^2}t = lt. \tag{A.23}$$

But, in the derivation of Equations A.10 and A.11, one time derivative was dropped in order that it could be applied later to the source time function. Replacing ψ with $d\,\psi/dt$ in Equation A.22, Equation A.23 becomes

$$u = \frac{l^3}{t}\frac{1}{l^2}t = l, \tag{A.24}$$

which is correct for displacement. Instead of using the RDP, a moment could be applied to the filtered result. Replace $\psi(t)$ with $M_0 10^{-10}/4\pi\rho\alpha^2$, where M_0 is moment in dyne-cm, ρ is density in g/cc, and α is P-velocity in km/s for displacement in cm.

When applying this source to the finite-difference method, the full form of the source is assembled in stages. The form of the source entered into the finite difference grid is given in Equation A.17. The value of k_f is chosen at

the start of the run to best fit the required range of take-off angles. Of course, since the parameter k_f governs a linear combination between two source terms, an isotropic line explosion and a dipole line force, the results of two runs differing only in k_f may be combined to give any desired k_f (the effect of varying k_f is shown in Chapter 2). Since Equation A.17 is singular at $T_\alpha=1$, that is $t=R/\alpha$, the corresponding point for the numerical time series must be found by integrating the equation and matching area. This singular nature also introduces energy at frequencies too high for the grid to propagate. To correct this, the numerical time series is convolved with a Gaussian filter before it is propagated.

The finite difference results must be subjected to a line-source to point-source conversion filter. This filter is given by Equation A.12. It is restated here where U_{line} and U_{point} are line-source and point-source wave fields.

$$U_{\text{point}} = \frac{1}{\sqrt{x}} \frac{d}{dt} \left[\frac{1}{\sqrt{t}} * U_{\text{line}} \right] \tag{A.25}$$

This may not be the best teleseismic form, considering the approximation (Equation A.14) of $\sqrt{p}$. Starting with Equation A.2, use Equation A.9 and rearrange terms to obtain

$$\phi_{\text{P}} = \frac{\sqrt{2}}{\sqrt{x}} Re\,(\sqrt{p}\,) \left[\frac{1}{\pi\sqrt{t}} * \frac{\delta(t-R/\alpha)}{\sqrt{t^2-(R/\alpha)^2}} \right]. \tag{A.26}$$

As t approaches R/α,

$$\phi_{\text{P}} = \frac{\sqrt{2}}{\sqrt{x}} Re\,(\sqrt{p}\,) \frac{1}{\sqrt{2R/\alpha}} \left[\frac{1}{\pi\sqrt{t}} * \frac{1}{\sqrt{t-R/\alpha}} \right]$$

$$= \frac{\sqrt{\alpha}}{\sqrt{Rx}} Re\,(\sqrt{p}\,) H(t-R/\alpha). \tag{A.27}$$

Use Equation A.14 with $k_f = 0.5$ and the approximations

$$p \sim \frac{\sin i}{\alpha} \quad \text{and} \quad p_0 \sim \frac{\sin i_0}{\alpha} \tag{A.28}$$

to get the form

$$\phi_P = \frac{1}{2\sqrt{xR}} \left[\sqrt{\sin i_0} + \frac{\sin i}{\sqrt{\sin i}} \right] H(t - R/\alpha). \tag{A.29}$$

The reference take-off angle i_0 is along positive x; that is, $\sin i_0 = 1$. In this case, the final form is

$$\phi_P = \frac{1}{2\sqrt{xR}} (1 + \sin i) H(t - R/\alpha). \tag{A.30}$$

An ideal line-to-point filter would cause ϕ_P in Equation A.30 to be $H(t - R/\alpha)/R$ for all angles i between 0° and 180°. A better filter can be found by inspection. Replace $\sqrt{x}$ in Equation A.30 as follows:

$$\phi_P = \frac{1}{2\sqrt{R}} \frac{2}{\sqrt{x} + \sqrt{R}} (1 + \sin i) H(t - R/\alpha). \tag{A.31}$$

Then for both $i = 0°$ and $i = 90°$ it is immediately found that ϕ_P is $H(t - R/\alpha)/R$. Finally, applying the substitution used to obtain Equation A.31 to the filter given in Equation A.25,

$$U_{\text{point}} = \frac{2}{\sqrt{R} + \sqrt{r}} \frac{1}{\sqrt{t}} * \frac{d}{dt} U_{\text{line}}. \tag{A.32}$$

Appendix B: Synthetic verification of the "2D Kirchhoff" formula

Several workers in theoretical elastodynamics have reservations regarding the derivation of our formulation of the representation theorem, which we refer to as 2D Kirchhoff. The questions concern the validity of extending a solution from a heterogeneous medium into a homogeneous medium, using a boundary integral formulated for a homogeneous region. This is a difficult technical point, which we do not attempt to prove rigorously. Yet, it is incumbent upon us to show that the formula as derived works satisfactorily for the application in which we apply it. Therefore, we present herein a synthetic study of various complex structures containing strong scatterers, point diffractors (modeled as nearly as possible using finite difference, FD) and refractors designed to test the technique in the extreme. We find the technique to be remarkably successful, even improving upon FD, and we conclude that use of the technique is certainly justified for our application.

Three test cases are examined. In each case, FD is compared to the 2D Kirchhoff integral. This was done by running a large FD grid, observing the seismograms near the bottom of the model. The wave functions necessary for the 2D Kirchhoff were sampled (the artificial Kirchhoff interface) just far enough below the upper structure to avoid complications, and then used to obtain the response at the same place as the FD receivers.

There are some important general considerations to note before examining the results. First, the FD records will be time-differentiated twice to obtain acceleration, because this is what the 2D Kirchhoff produces for the elastic case. It is easier to differentiate the FD records than to integrate the Kirchhoff records and to have to consider numerical drift. Second, we use

Clayton-Enquist absorbing boundary conditions. These produce P-to-S and S-to-P conversions for wave fronts nearly perpendicular to the boundary. The examples run are all isotropic explosions, so in a deep FD grid, direct P will be small on the radial, while S off the boundary will be large. The Kirchhoff will not show this since most of the effect occurs after the waves have crossed the Kirchhoff line. This might be considered an advantage of the 2D Kirchhoff.

The first case is a large "point" diffractor. Two enclosed bodies with strong velocity contrast are abutting each other. This will act as a secondary source with a radiation pattern. Two cases are run: a deep, narrow box and a box twice as wide to show the effect of the absorbing boundaries. There is no free surface. Both acceleration and acceleration corrected to point source are shown. The second case contains two lenses to provide focusing and conversions. The final case is an admixture of many effects, designed to produce a diversity of diffractors, reflectors and focusing bodies.

The method is quite satisfactory, taking the aforementioned boundary condition problem into account. (This is not discussed in Chapter 1 of this thesis, since it is a FD problem which has been sufficiently addressed in the literature, and the models used here are designed to minimize it.) The main merits of the new integral are fast and efficient computation and conceptual simplicity. For these reasons, even if problems arise for some cases, the method is worth consideration.

Figure B.1 is a schematic of the run. The discussion of the figure that follows describes elements common to the schematics of all the runs. The star indicates source position (2D isotropic line explosion); the dashed line indicates the position of the Kirchhoff contour; and the inverted triangles

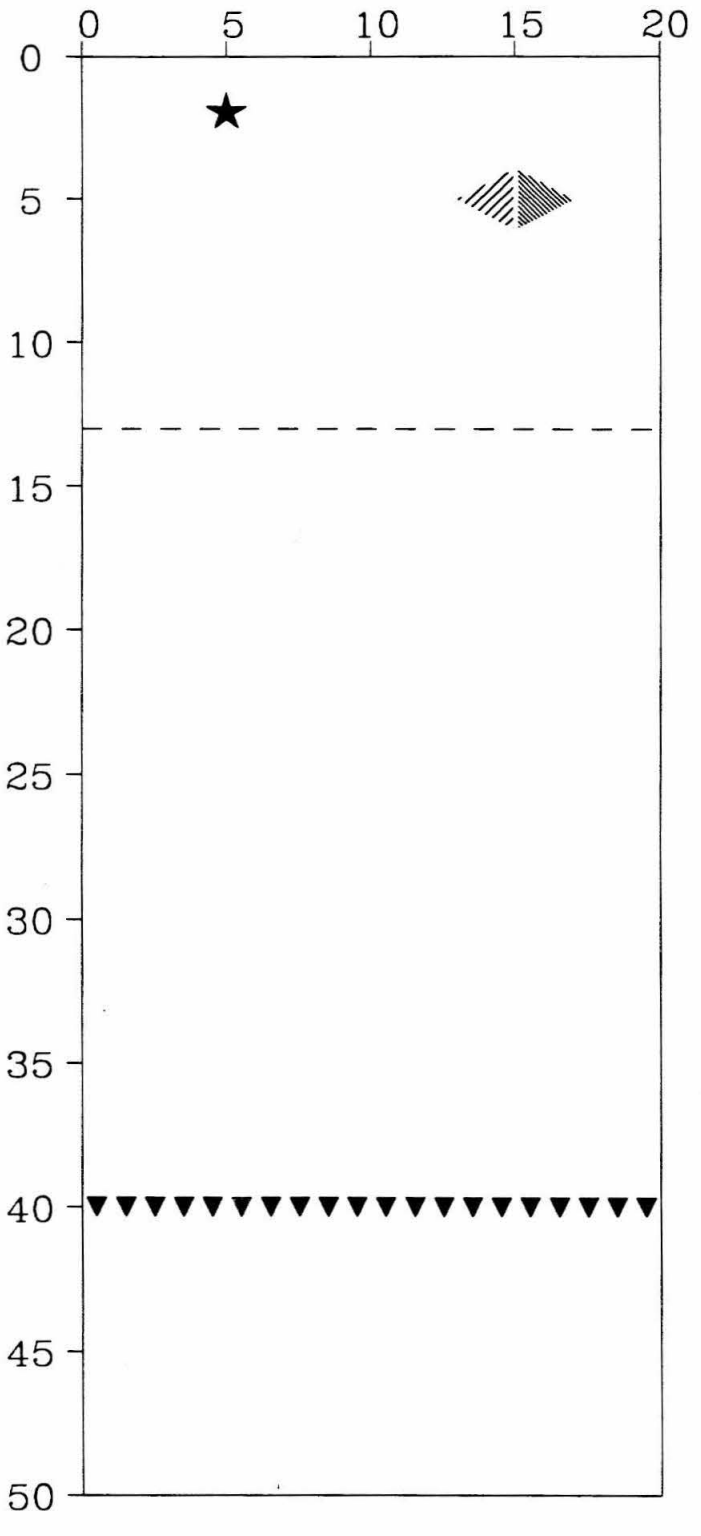

Figure B.1 First test model.

indicate the receiver positions. The numbers along the border of the diagram are distance (radial and depth) in km. The unshaded region is a uniform background medium. Clayton-Enquist absorbing boundaries form the left, right and bottom boundaries.

For this run, the top is absorbing, also. The background has P-velocity (Vp) of 6.0 km/s, S-velocity (Vs) of 4.0 km/s and density (den) of 3.0 g/cc. (These units and this notation are used below.) The shaded triangle on the left is a low-velocity region; Vp=1.1, Vs=0.8, den=1.0. The right triangle is fast; Vp=13.0, Vs=10.0, den=8.0,. Both regions have gradational boundaries to prevent the FD from becoming unstable; the boundaries are 4 grid points wide (0.4 km). The purpose of this run is to observe a single, strong scatterer.

Figure B.2 is the raw FD output (displacement), uncorrected for source effects. All seismograms are plotted as follows. The time scale is shown for reference. There are two columns: The left column is radial displacement (positive is rightward motion); the right column is vertical displacement (positive is downward motion). This column convention is followed for all subsequent presentations of results in this section. The records from top to bottom are for the receivers located in the schematic from left to right, respectively. The peak amplitude is given to the right of each trace. Figure B.3 is displacement corrected to point-source form. This correction is derived in Appendix A. Note that it is not very accurate for this case. The correction is derived to be most accurate horizontally, and it is least accurate vertically. Hence, the amplitudes for stations immediately below the source are somewhat high. The reflections off the absorbing boundaries are stronger on the side of the model as the source, so the amplitudes are further enhanced.

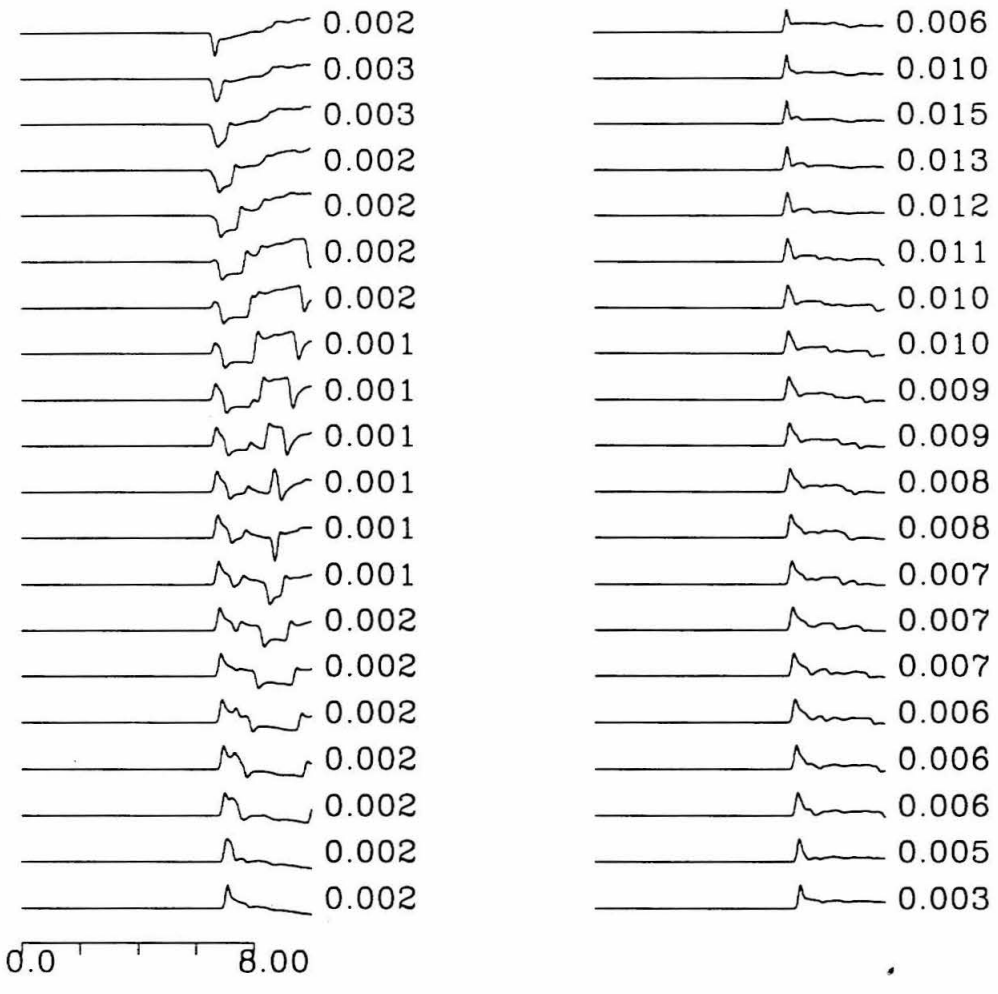

Figure B.2 FD line-source displacements for first model.

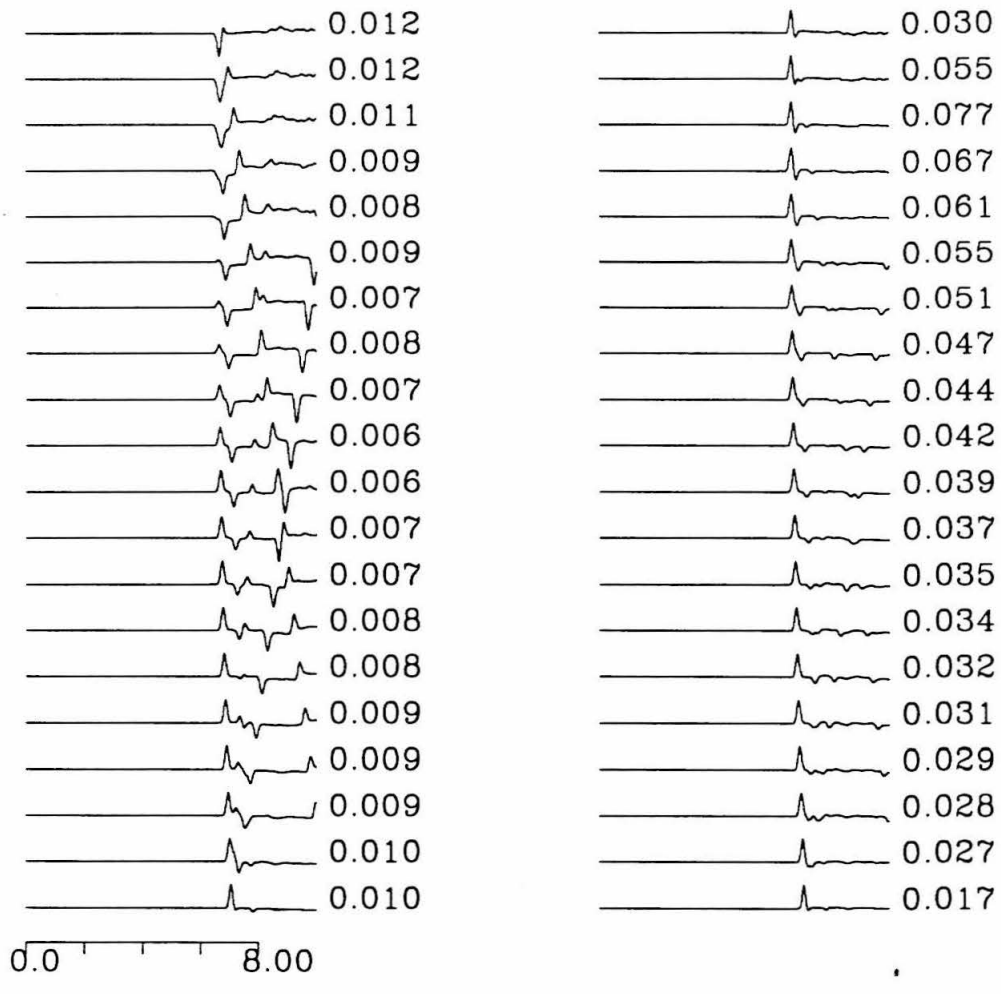

Figure B.3 FD point-source displacements for first model.

Figure B.4 is acceleration from FD, uncorrected. Note very strong absorbing boundary p-to-s conversions on the radial. These are a tenth to a fifth the amplitude of direct P (mostly on vertical). Figure B.5 is Kirchhoff accelerations, for the same conditions as Figure B.4. Note the absence of absorbing boundary effects. Note another advantage of this method here: While the FD is run only long enough to obtain about 4 s of the record after direct P, the Kirchhoff shows 8 s after direct P. This is, of course, because the waves must travel longer to get to the receivers than to the contour. This was the reason for developing the method. Figures B.6 and B.7 are the point-source corrected records corresponding to B.4 and B.5, respectively. The correction tends to de-emphasize long periods and alters phase somewhat by removing line-source tails. This makes records easier to interpret, so only point-source accelerations are shown for the remaining test cases. The Kirchhoff records also suffer somewhat from amplitude effects because of the inaccuracies of the range correction. Contrary to the effect on the FD seismograms, the Kirchhoff seismograms may show too little amplitude variation. The errors in the range correction are averaged across the entire Kirchhoff interface. Apart from the range correction problem, both the waveforms and absolute amplitudes are directly comparable here. Without the conversion to point-source form, the amplitudes are not directly comparable.

Figure B.8 shows a modified model of the first test case. This is to further demonstrate the absorbing boundary effect, and this run is identical to the preceding run, except that the boundaries are moved out 10 km on both the right and left. Figure B.9 and B.10 correspond to B.6 and B.7, respectively. Note that the absorbing boundary effect has been moved back and slightly reduced in amplitude. This model is run for 50% more time to

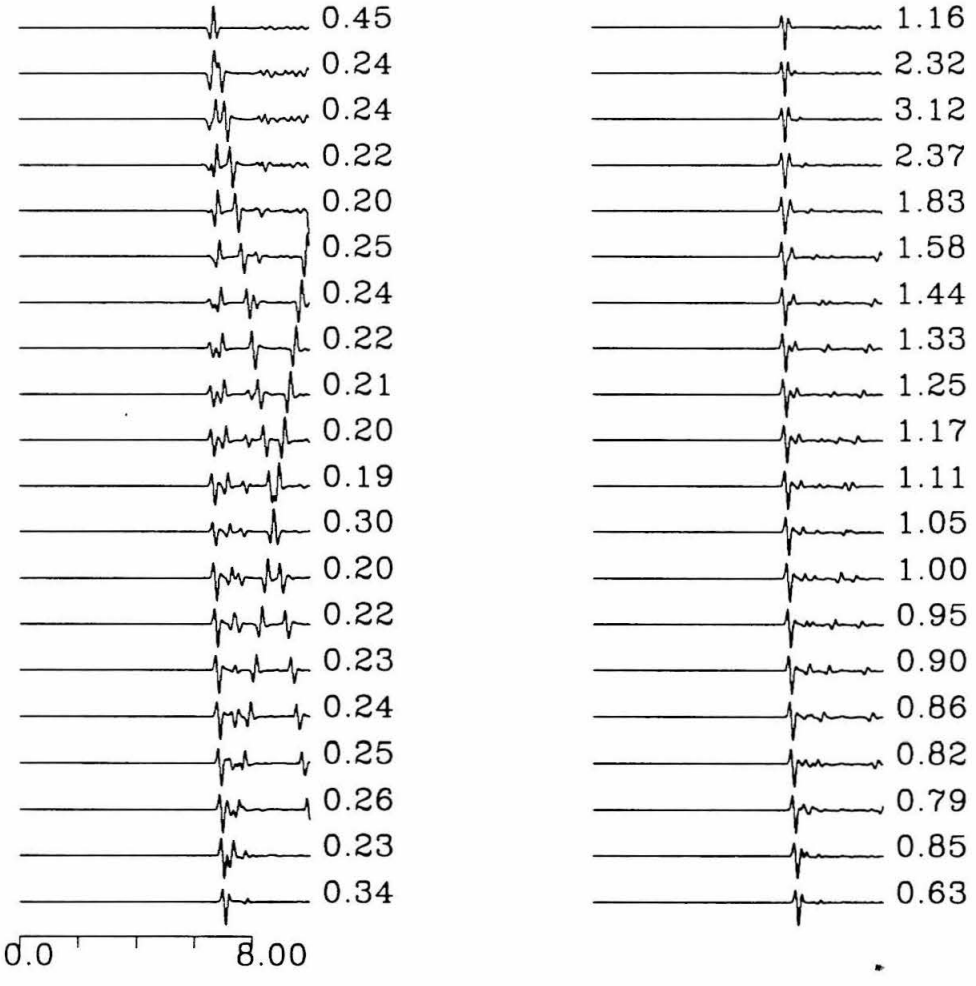

Figure B.4 FD line-source accelerations for first model.

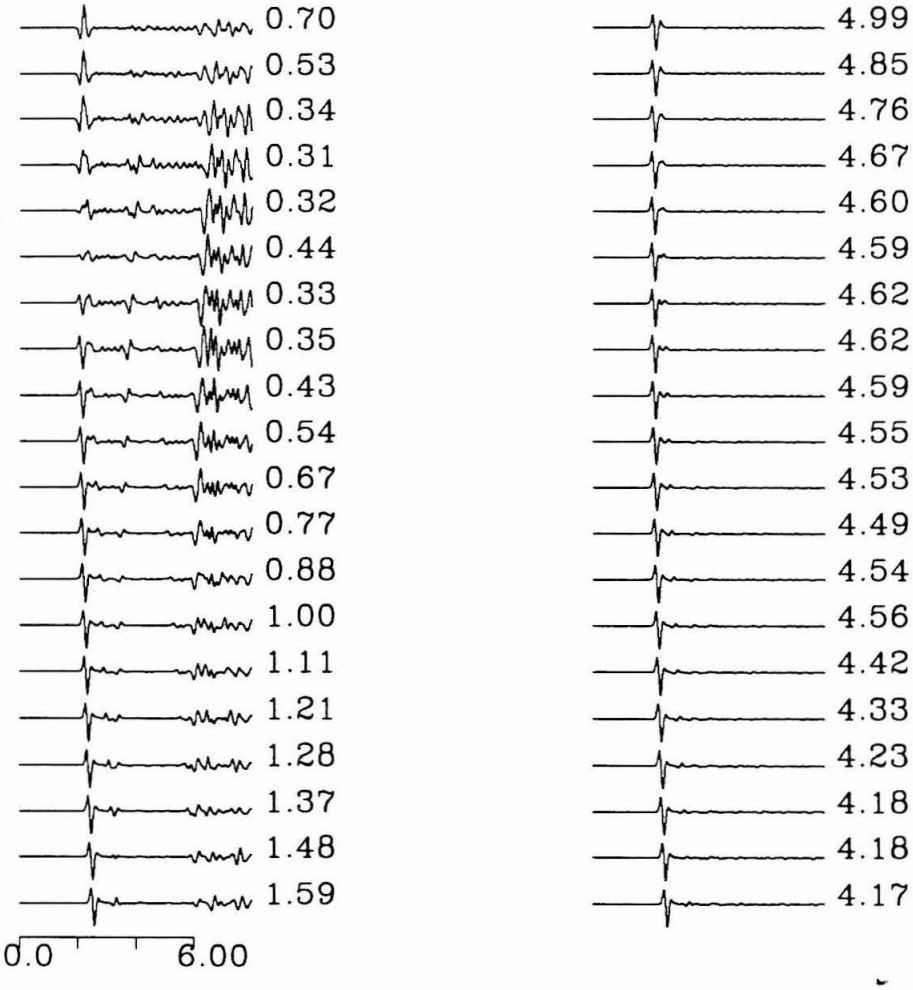

Figure B.5 2D Kirchhoff line-source accelerations for first model.

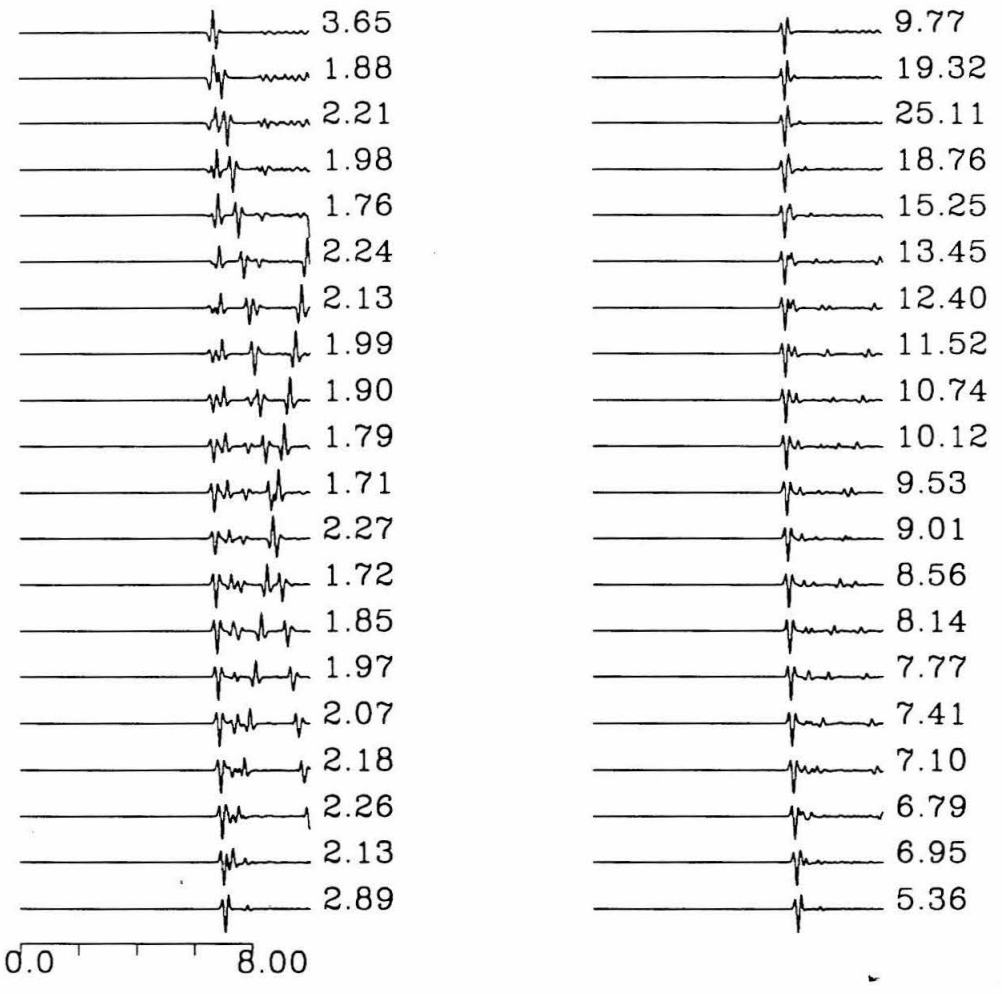

Figure B.6 FD point-source accelerations for first model.

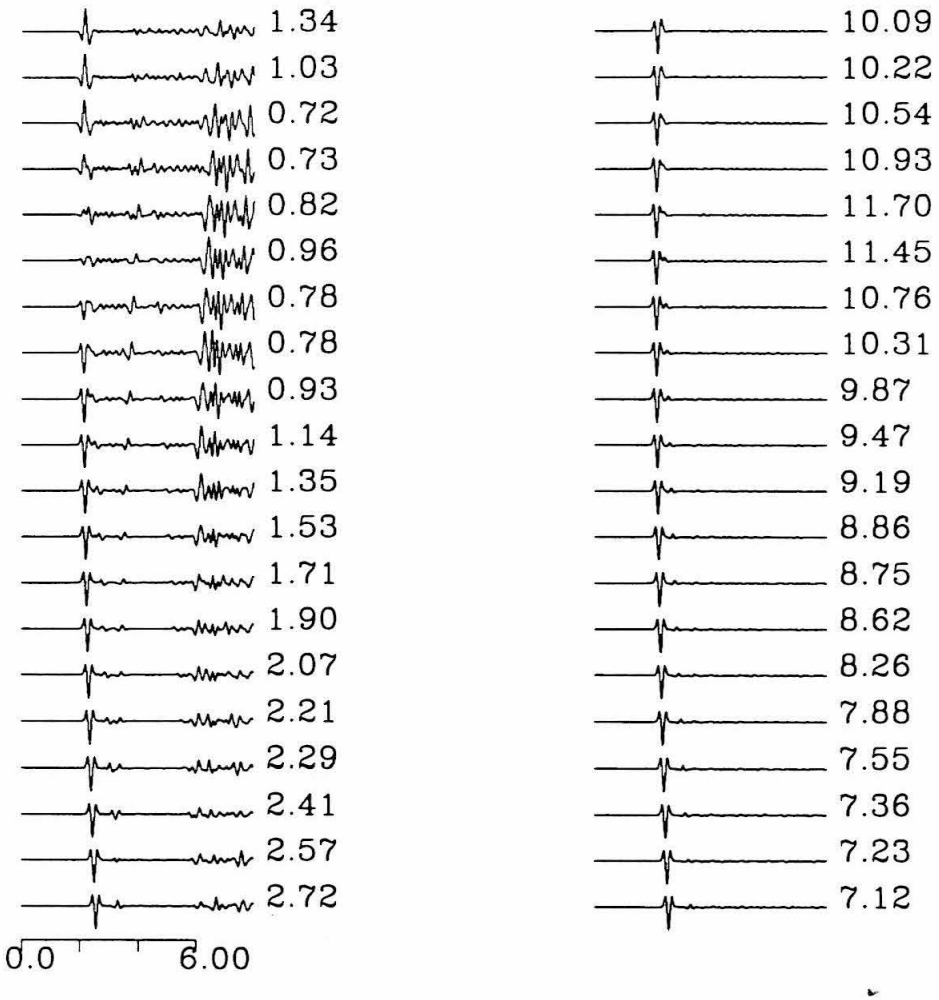

Figure B.7 2D Kirchhoff point-source accelerations for first model.

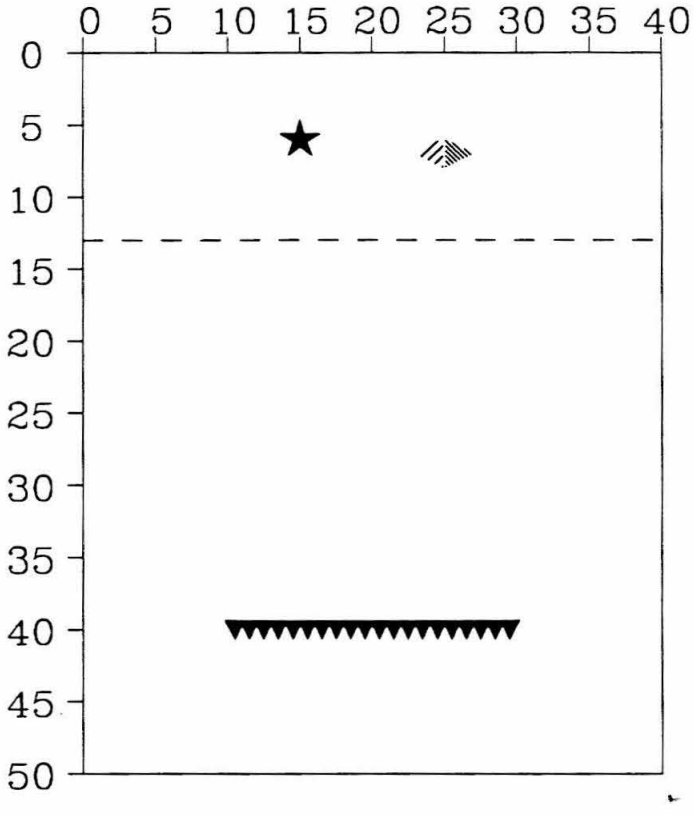

Figure B.8 Modified version of first model.

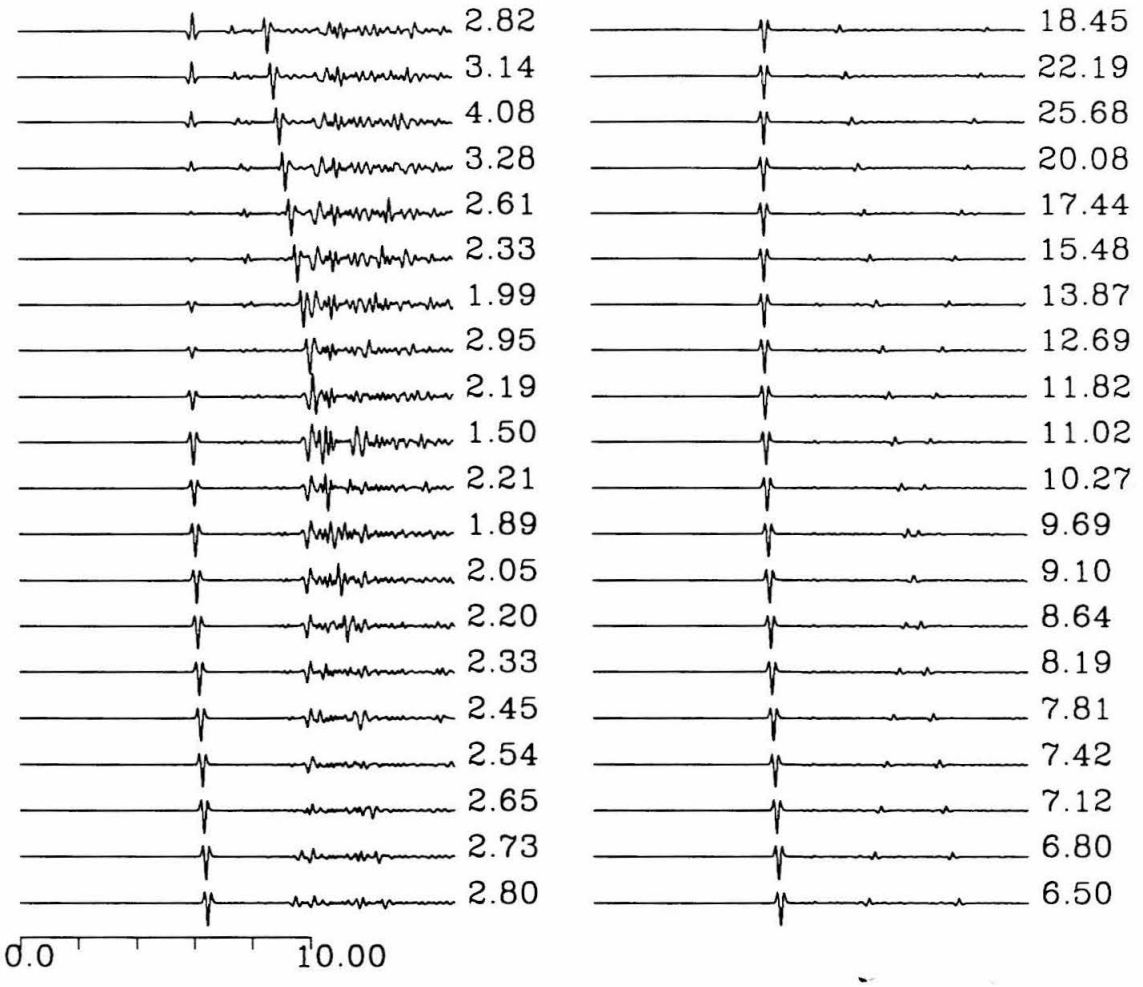

Figure B.9 FD point-source accelerations for modified model.

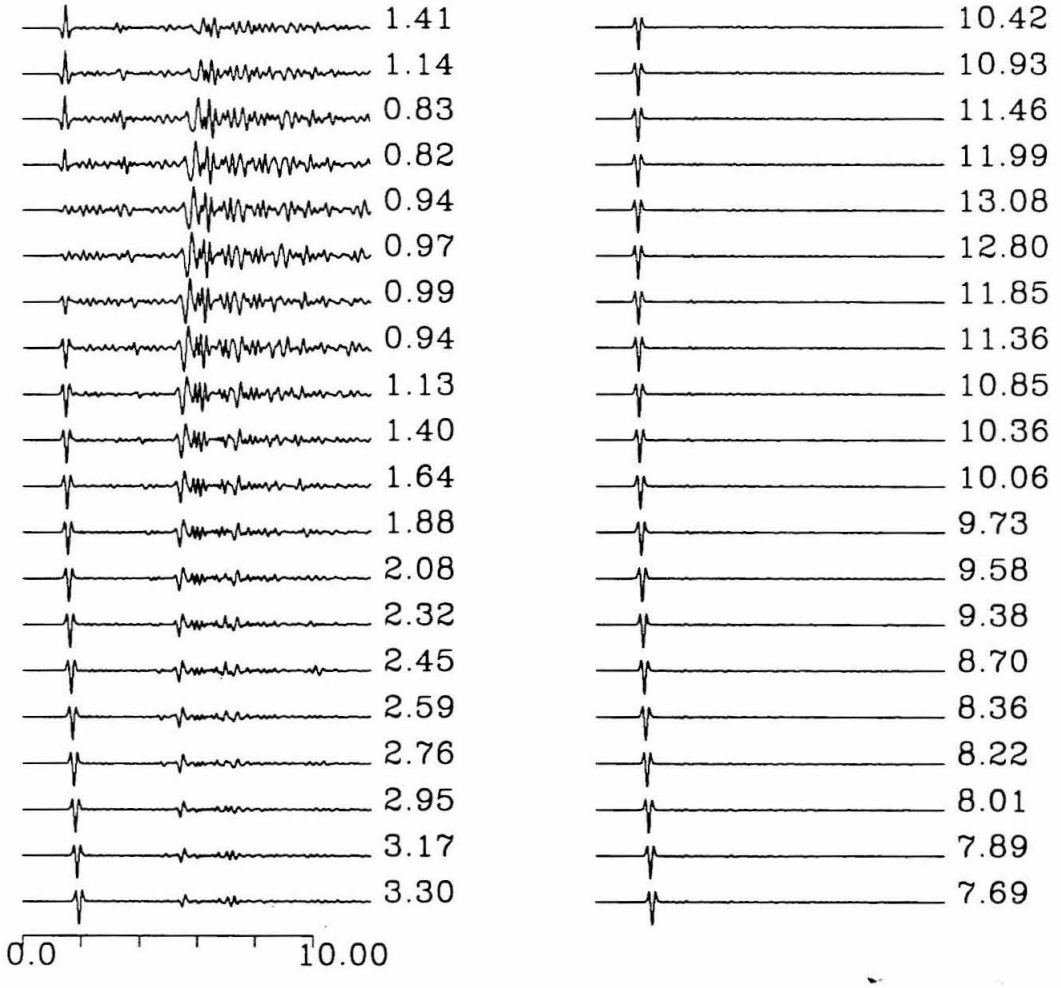

Figure B.10 2D Kirchhoff point-source accelerations for modified model.

allow more of the scattered waves to arrive on the FD records.

Figure B.11 is a schematic for the second test: fast and slow lenses. The left lens is fast (zigzag pattern), with Vp=9.0, Vs=6.0 and den=3.0. The right is slow (checkered pattern), with a Vp=3.9, S=1.8 and den=2.0. The top boundary is absorbing. For this case, we deliberately produce incorrect source functions in a further attempt to corrupt the Kirchhoff integral. Media properties appropriate for the fast lens are used to generate the source, which is in the background medium (Vp=6.0, S=3.3, den=2.5). This affects timing between the grid points of the source, setting them out of phase in such a way as to produce higher-order radiation pattern effects. Such a source is still a solution to the 2D wave equation, but its take-off angle dependence and wave-number content are unusual. We do not offer an analysis of this here. Figures B.12 and B.13 are the FD and Kirchhoff accelerations, respectively, for this second model. Mismatch in this case is due to absorbing boundaries and multiples off the boundaries.

Figure B.14 shows the structure for the final case examined here. This model shows a number of effects combined. The background medium has Vp=6.0 Vs=4.0 den=3.0. The patterned star-shaped region (scattering and diffracting) has Vp=5.0 Vs=2.5 den=2.5. The wedge at the top (free-surface disturbance) has Vp=4.0 Vs=1.0 den=1.5. The lowermost medium (reflections and focusing) has Vp=8.0 Vs=6.4 and den=4.0. The entire top is a free surface. Figures B.15 and B.16 are the FD and Kirchhoff accelerations, respectively, for this model. Mismatch in this case is again due to absorbing boundaries.

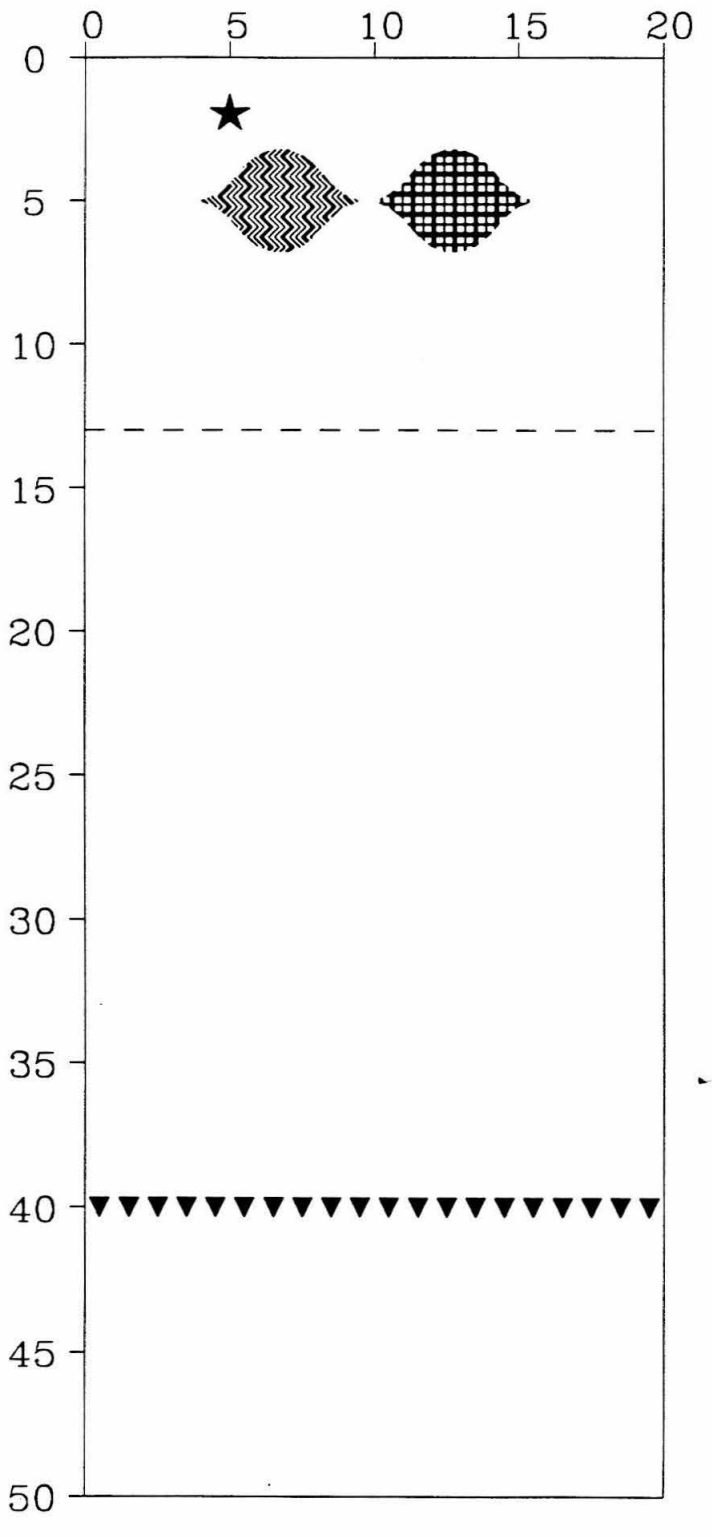

Figure B.11 Second test model.

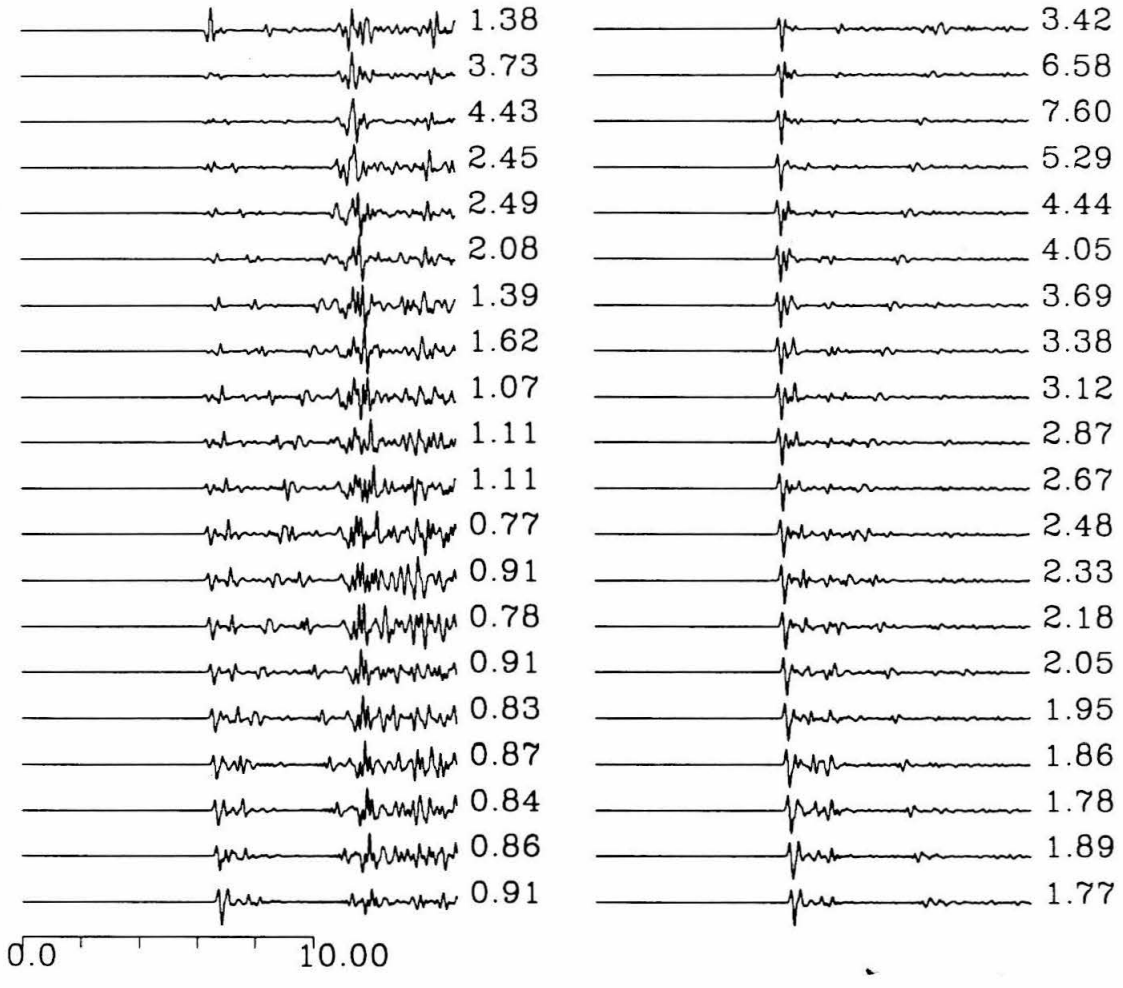

Figure B.12 FD point-source accelerations for second model.

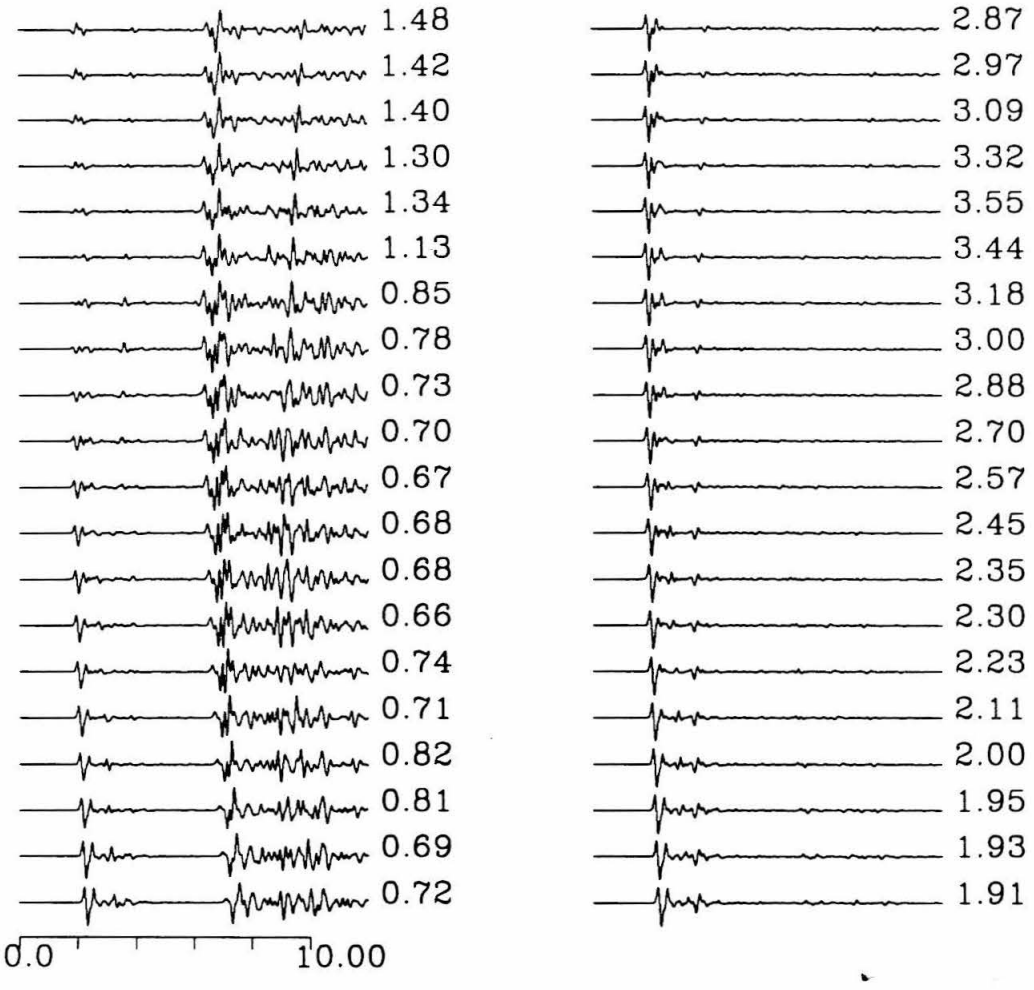

Figure B.13 2D Kirchhoff point-source accelerations for second model.

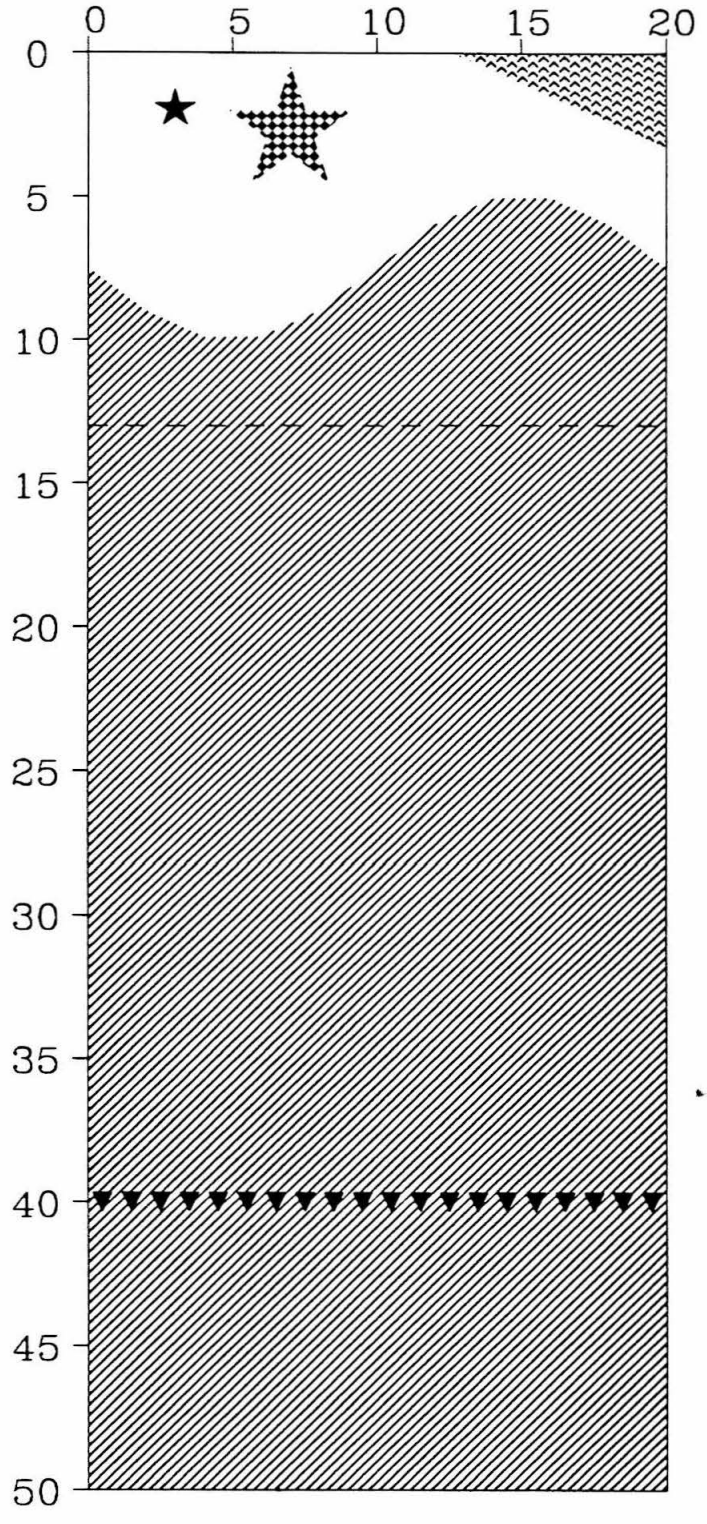

Figure B.14 Third test model.

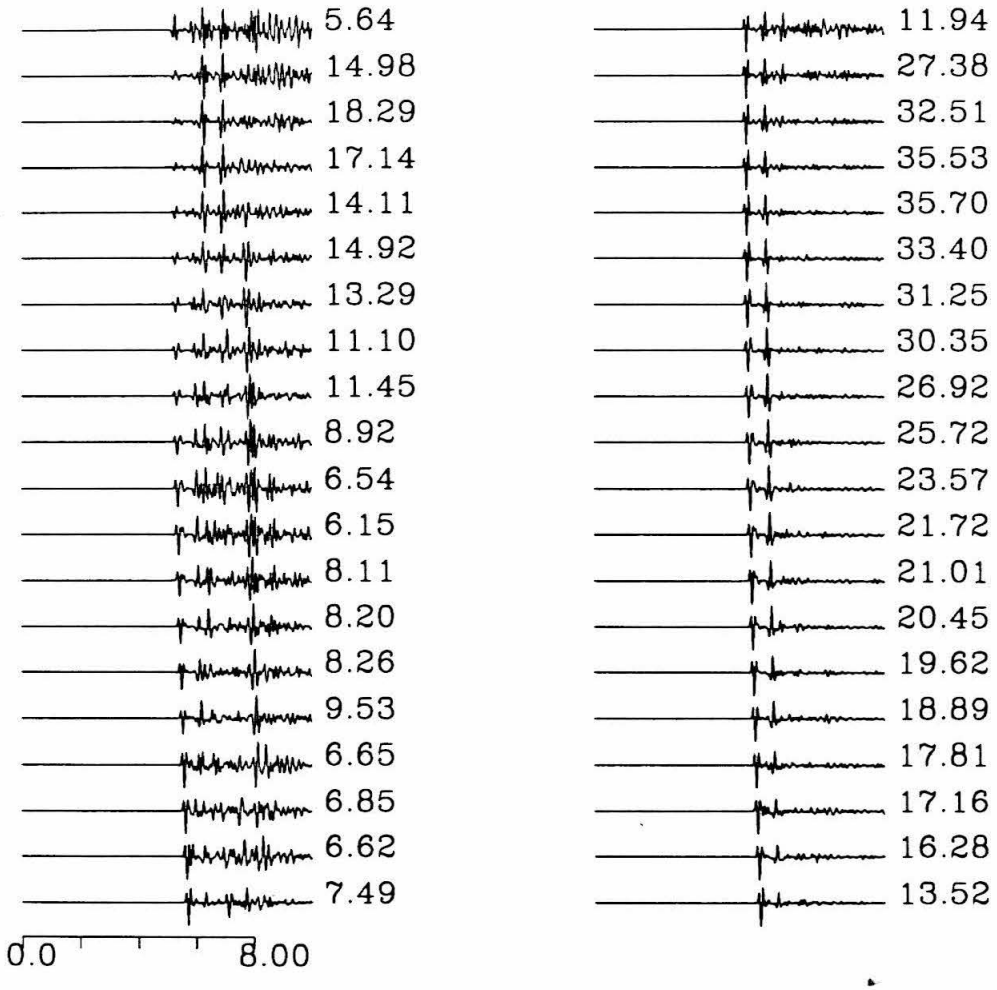

Figure B.15 FD point-source accelerations for second model.

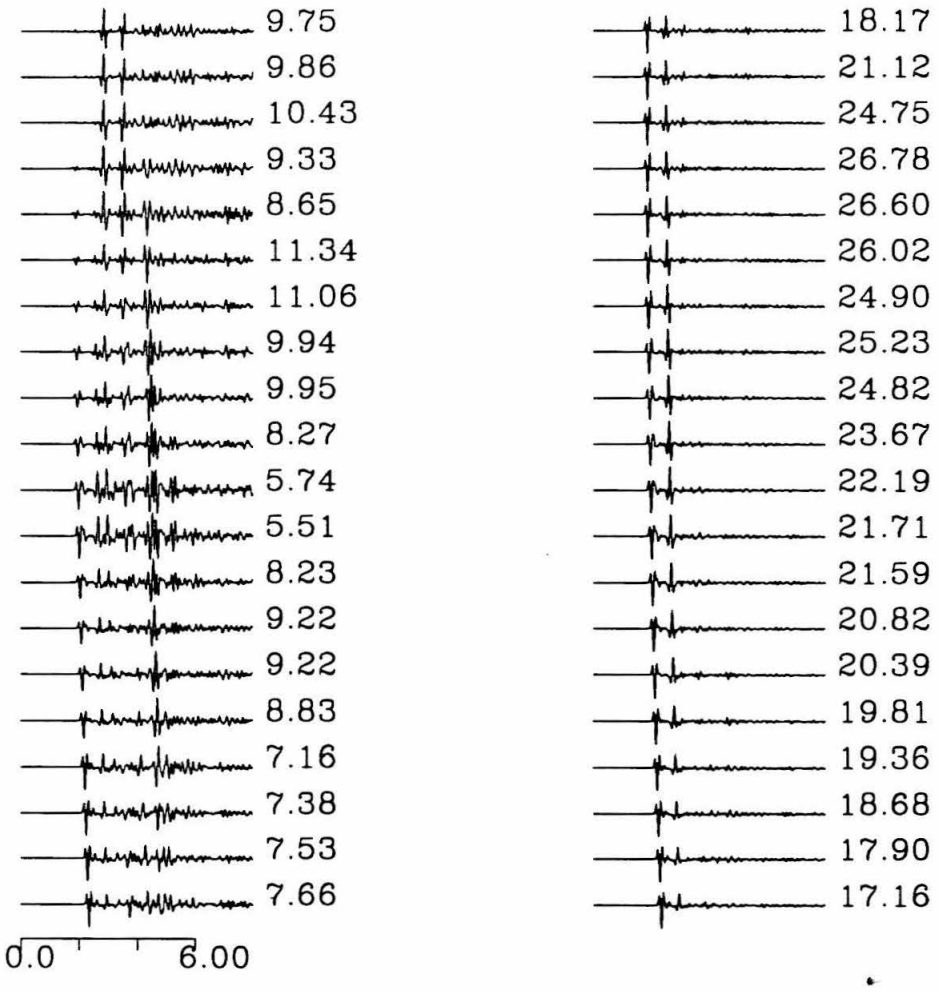

Figure B.16 2D Kirchhoff point-source accelerations for second model.

Appendix C: Dense profiles of synthetic seismograms for basin structures

We present herein a few profiles of synthetic SH seismograms representative of the finite difference (FD) models discussed in Chapter 3 of the thesis. The purpose is to show the moveout of various phases as a function of range, and to show the effects in the immediate vicinity of a basin boundary. A complete collection for all the source positions, models, mechanisms and instruments considered is far too large to present here (over 300 profiles) and would serve only to obscure the more important effects. This is intended primarily as a visual display, a more detailed discussion of the effects of various parameters is found in Chapter 3. Only a brief description of each selected profile is given in the figure caption to allow the reader to follow the structure. All record sections begin with a receiver 10 km from the source and then one receiver for each 10 km. The records are broad-band displacements. The moment used is 1×10^{25} and the amplitudes are in cm. The first several record sections are for SH waves (tangential). The last few are for the P-SV system (radial and vertical). Note here that for the P-SV double-couple source, the higher-order terms in the source expression grow exponentially with time. This introduces a drift in the synthetic, which is normally removed using polynomial regression. However, a single specification of the regression parameters is usually not successful for an entire record section. Therefore, some of the P-SV synthetics in each record section remain uncorrected for drift. (Here the order of the polynomial is 7, regressed only to the first zero crossing from the right side of the trace.)

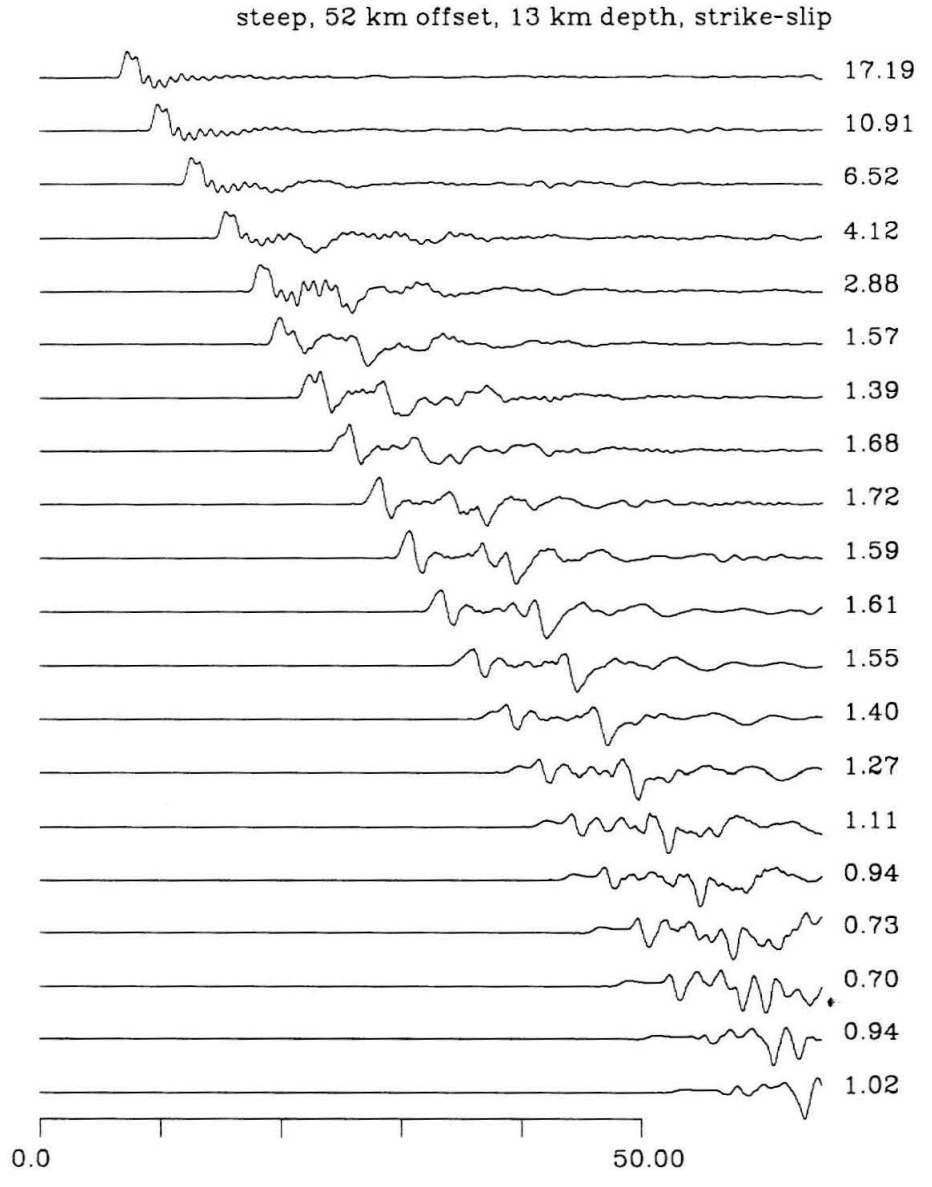

Figure C.1 SH synthetics for strike-slip source 52 km from the steep boundary, 13 km deep.

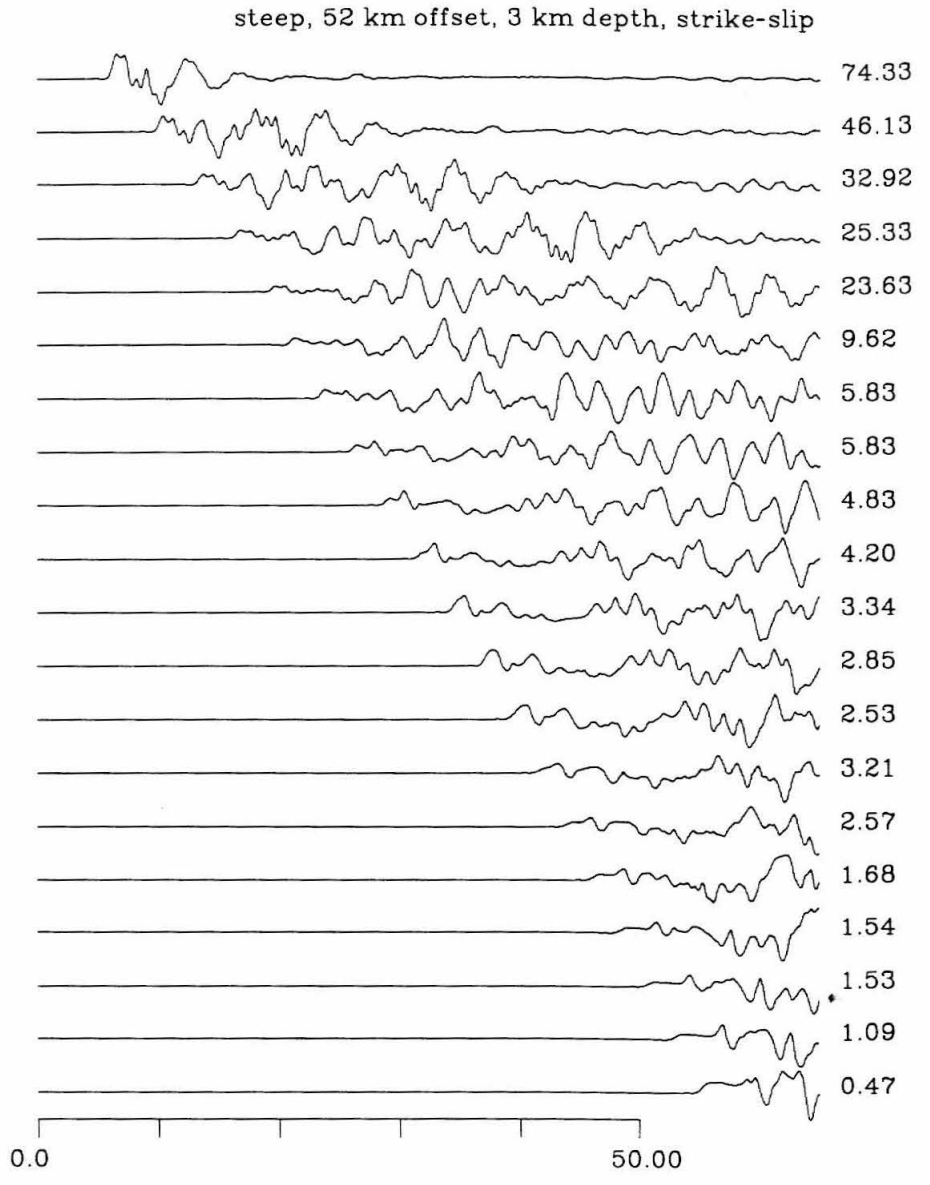

Figure C.2 SH synthetics for strike-slip source 52 km from the steep boundary, 3 km deep.

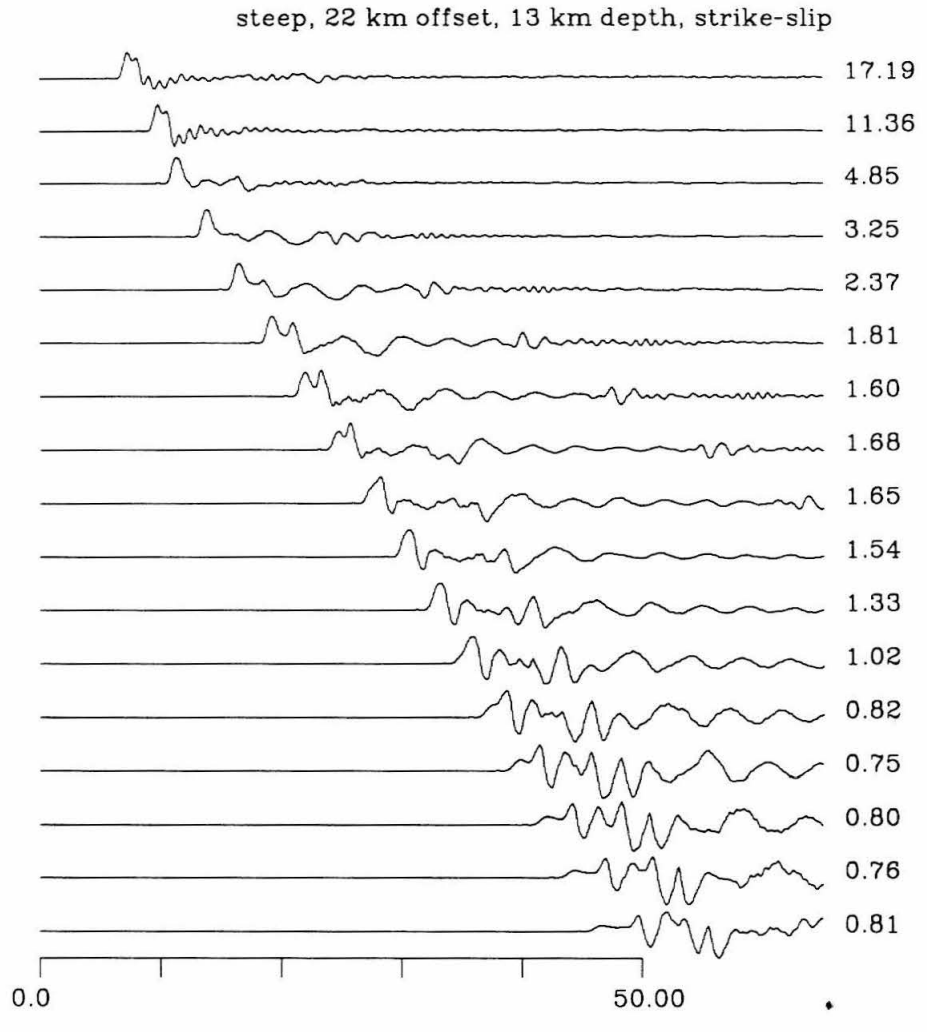

Figure C.3 SH synthetics for strike-slip source 22 km from the steep boundary, 13 km deep.

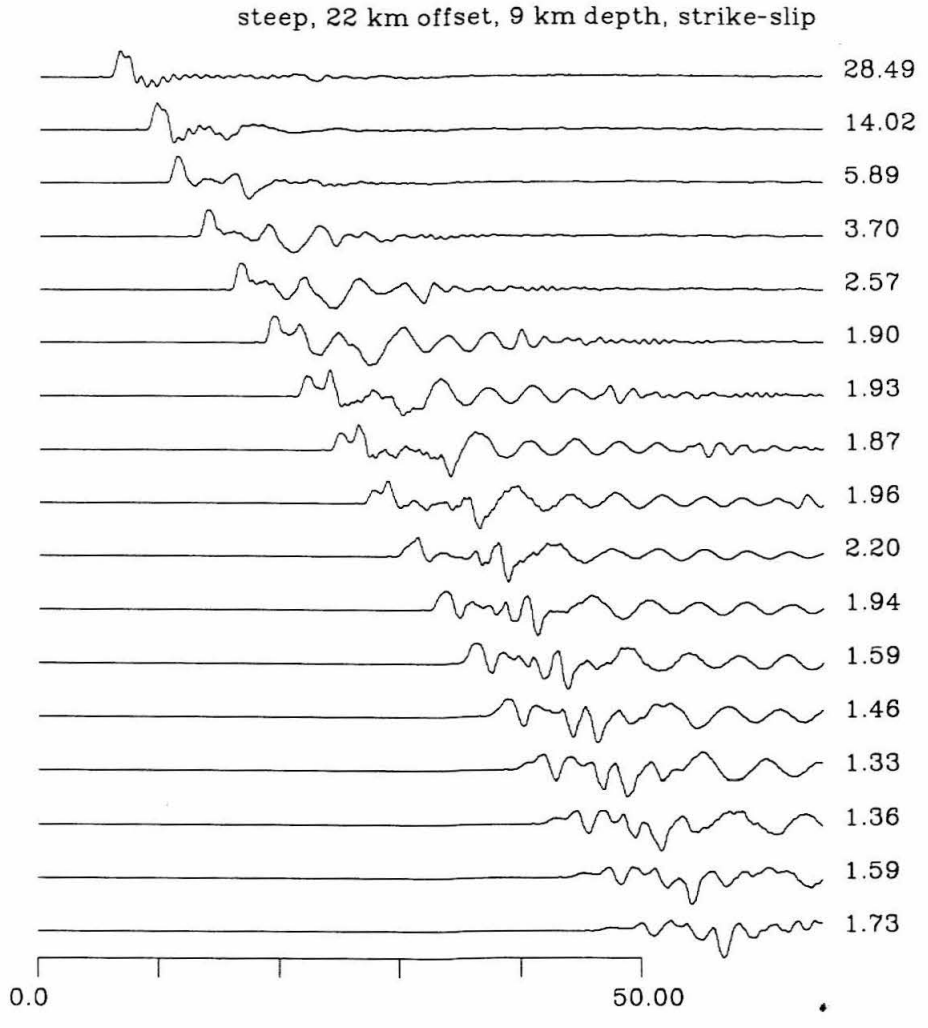

Figure C.4 SH synthetics for strike-slip source 22 km from the steep boundary, 9 km deep.

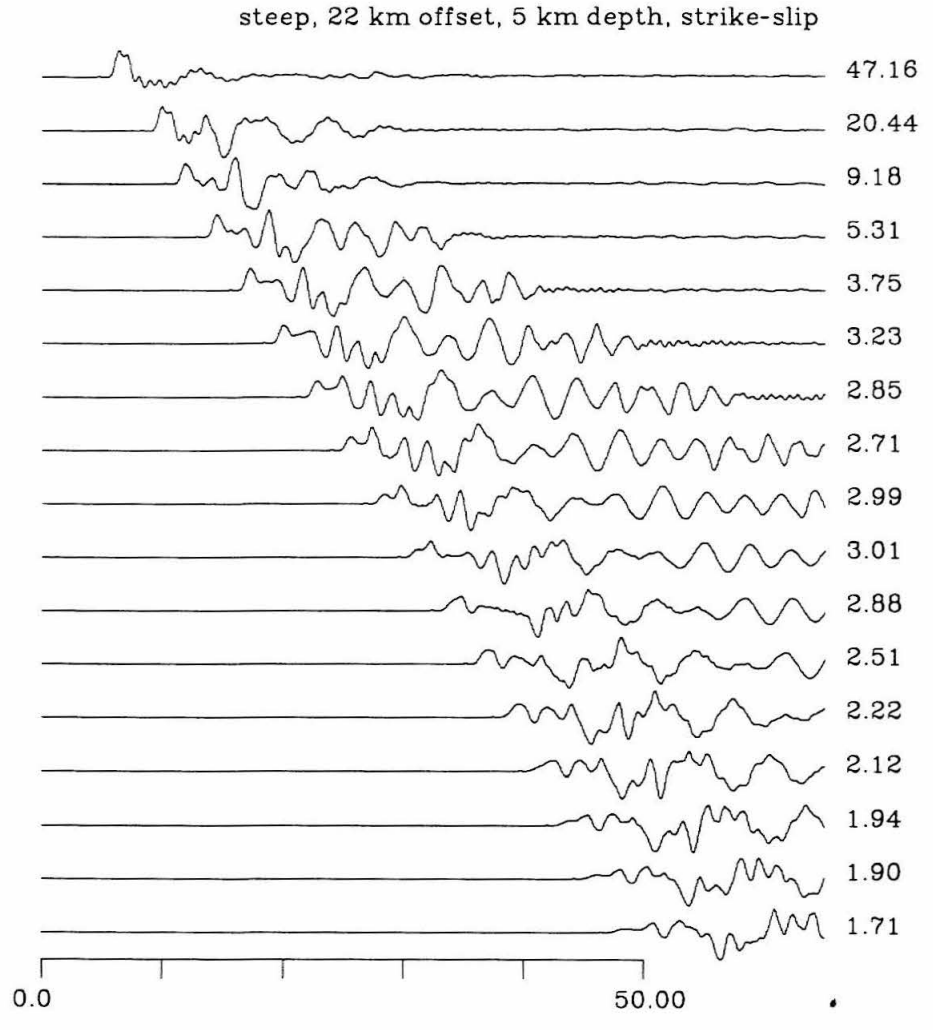

Figure C.5 SH synthetics for strike-slip source 22 km from the steep boundary, 5 km deep.

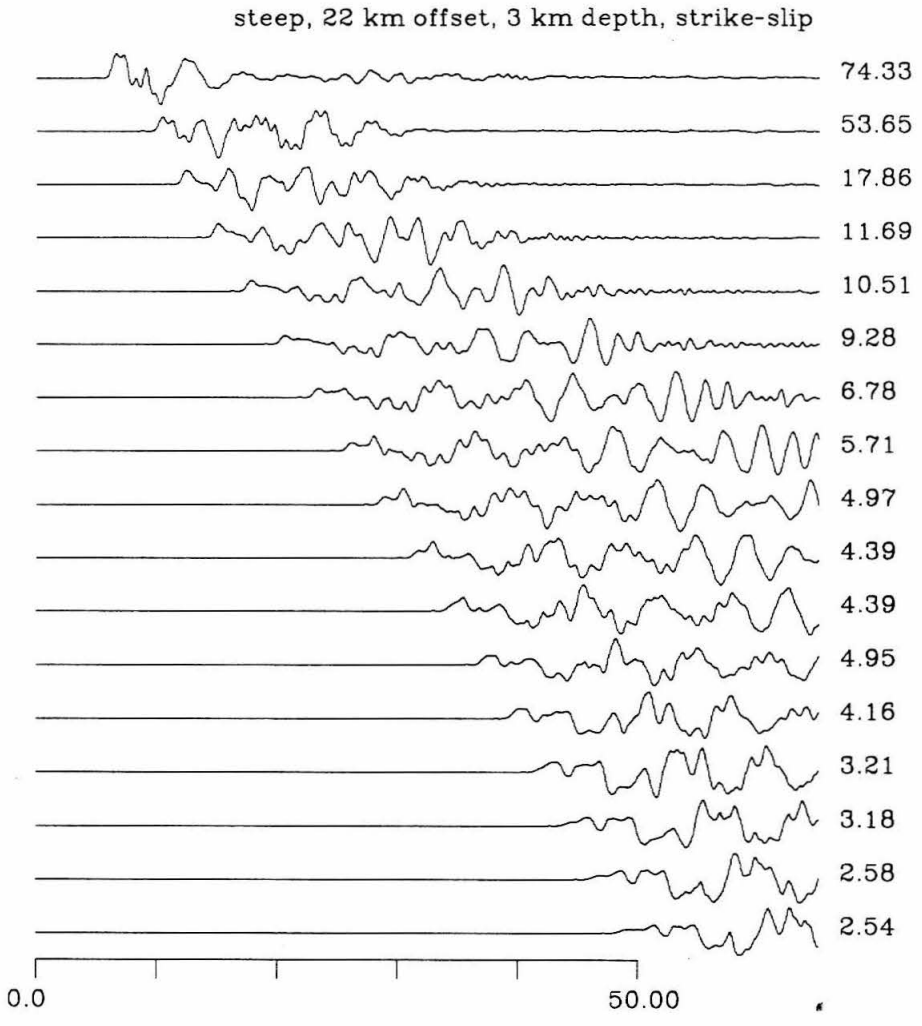

Figure C.6 SH synthetics for strike-slip source 22 km from the steep boundary, 3 km deep.

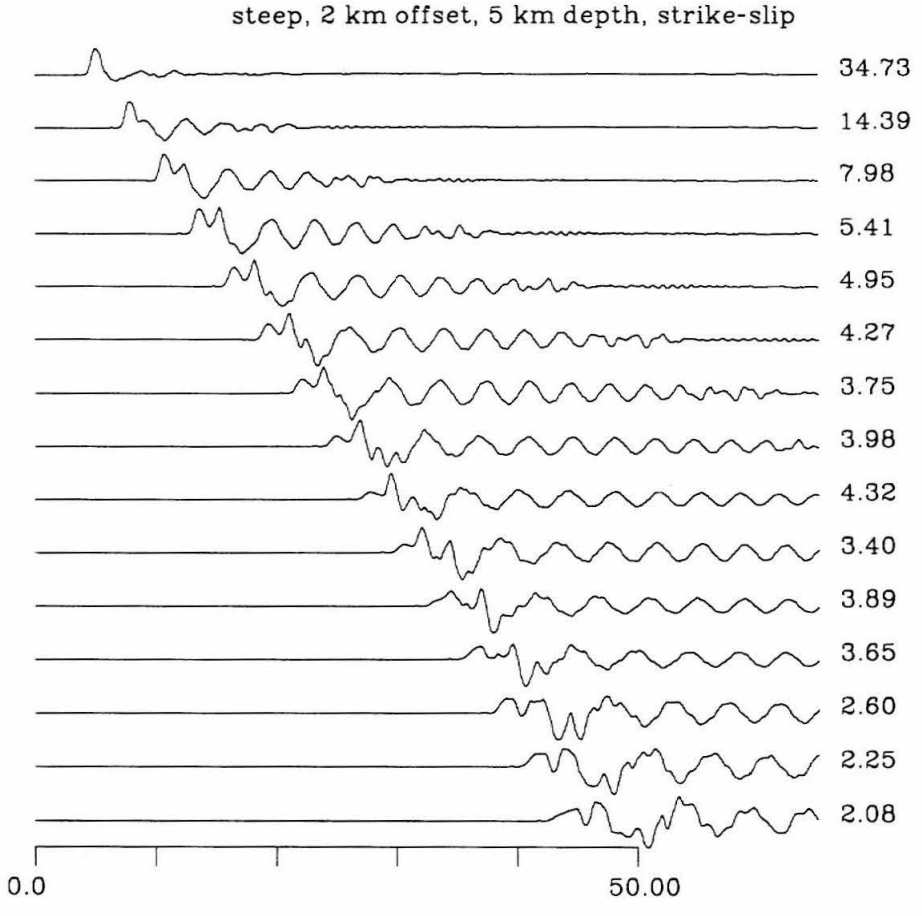

Figure C.7 SH synthetics for strike-slip source 2 km from the steep boundary, 5 km deep.

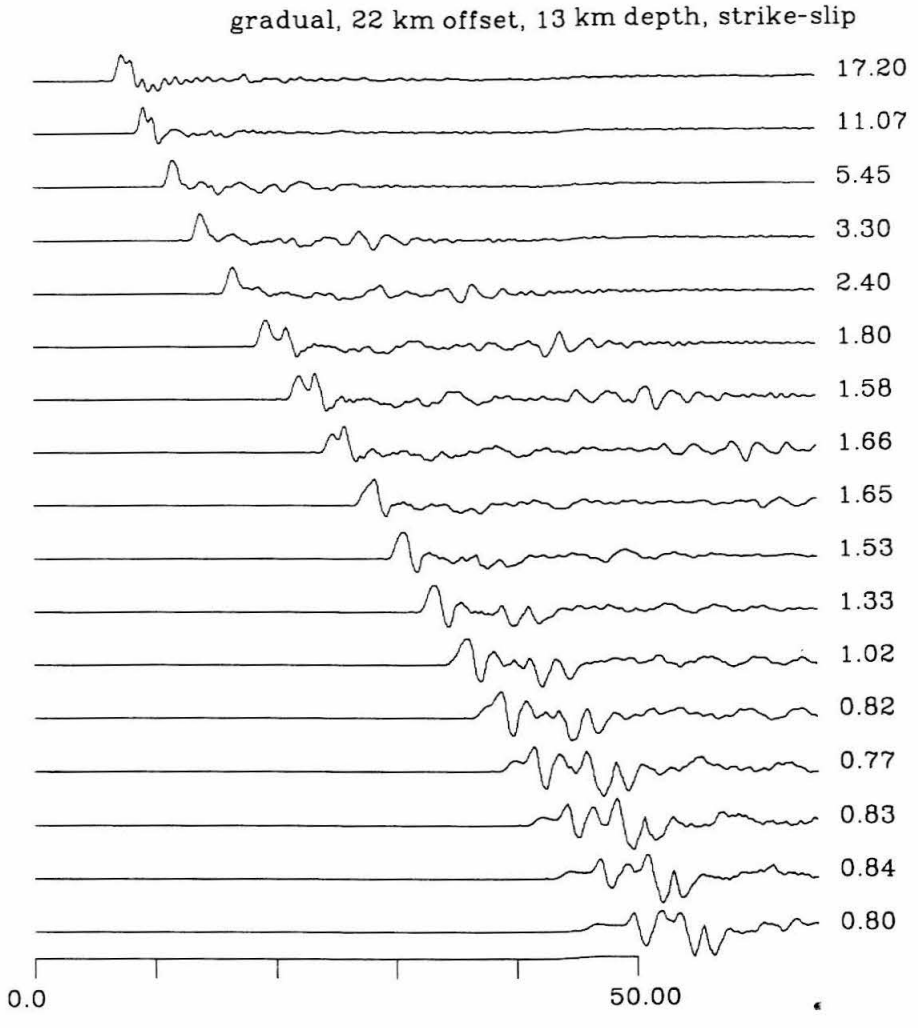

Figure C.8 SH synthetics for strike-slip source 22 km from the gradual boundary, 13 km deep.

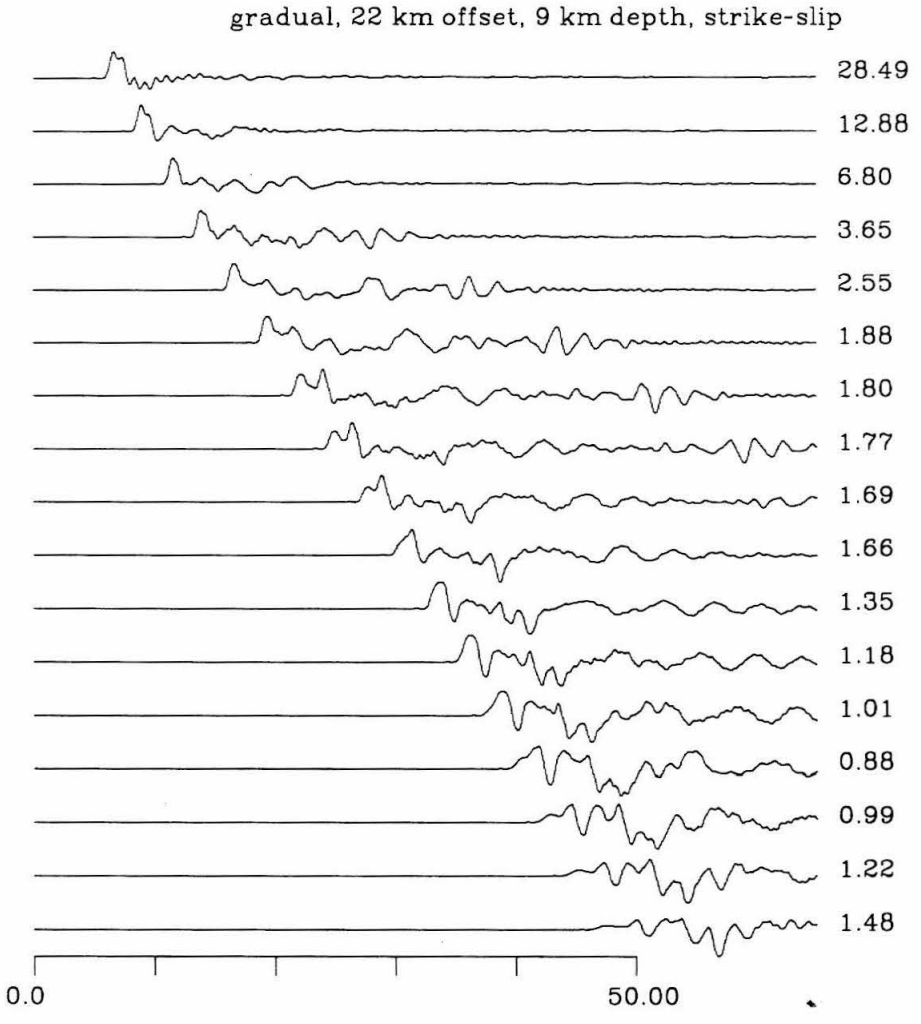

Figure C.9 SH synthetics for strike-slip source 22 km from the gradual boundary, 9 km deep.

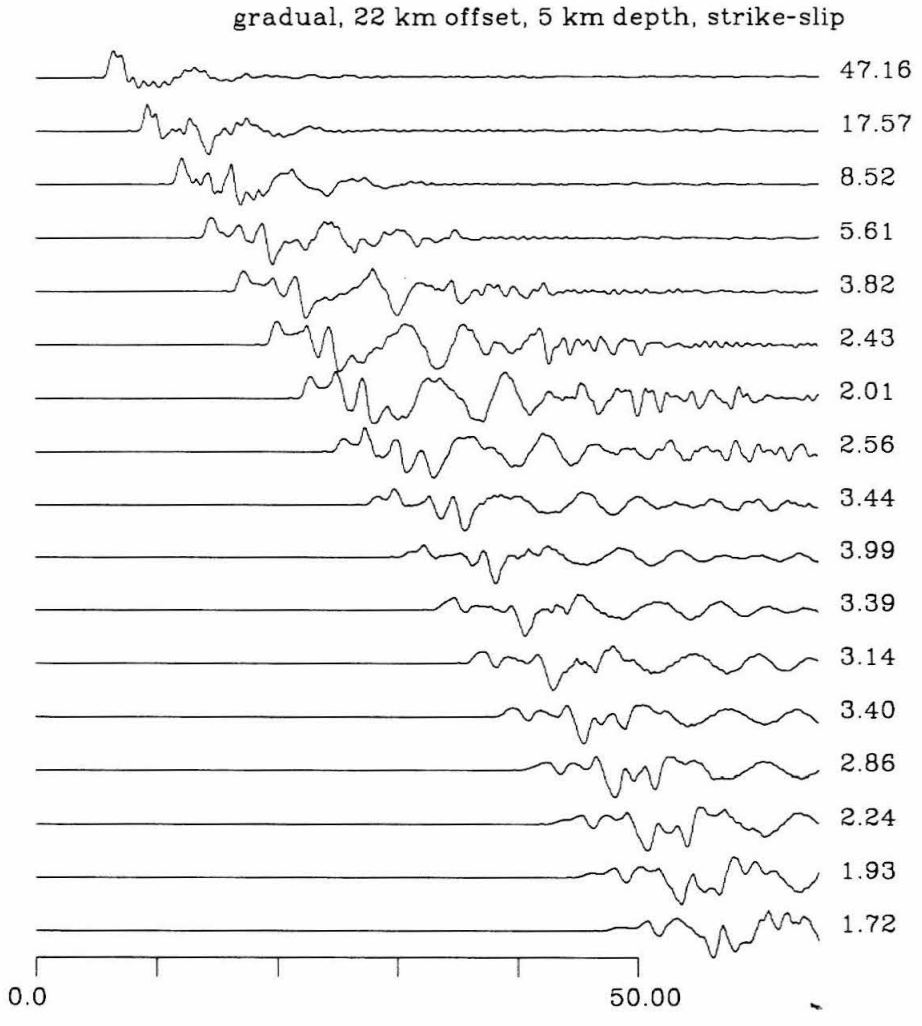

Figure C.10 SH synthetics for strike-slip source 22 km from the gradual boundary, 5 km deep.

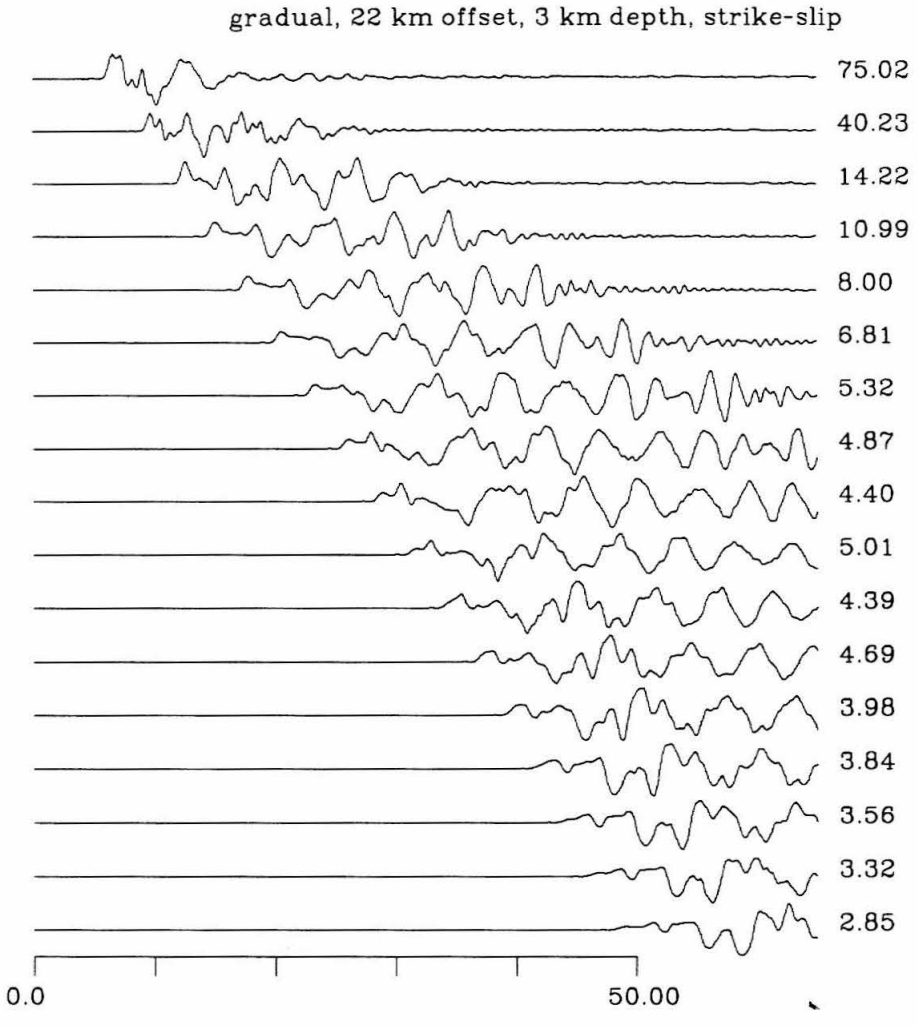

Figure C.11 SH synthetics for strike-slip source 22 km from the gradual boundary, 3 km deep.

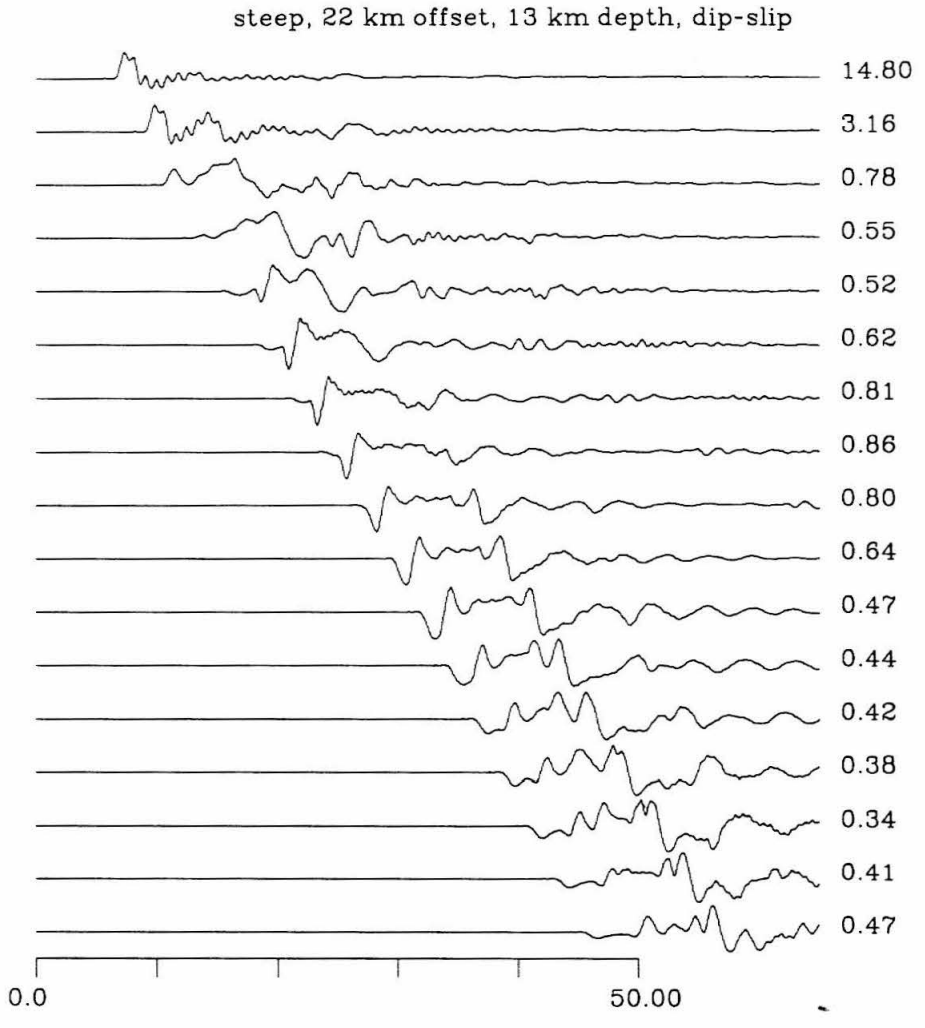

Figure C.12 SH synthetics for dip-slip source 22 km from the steep boundary, 13 km deep.

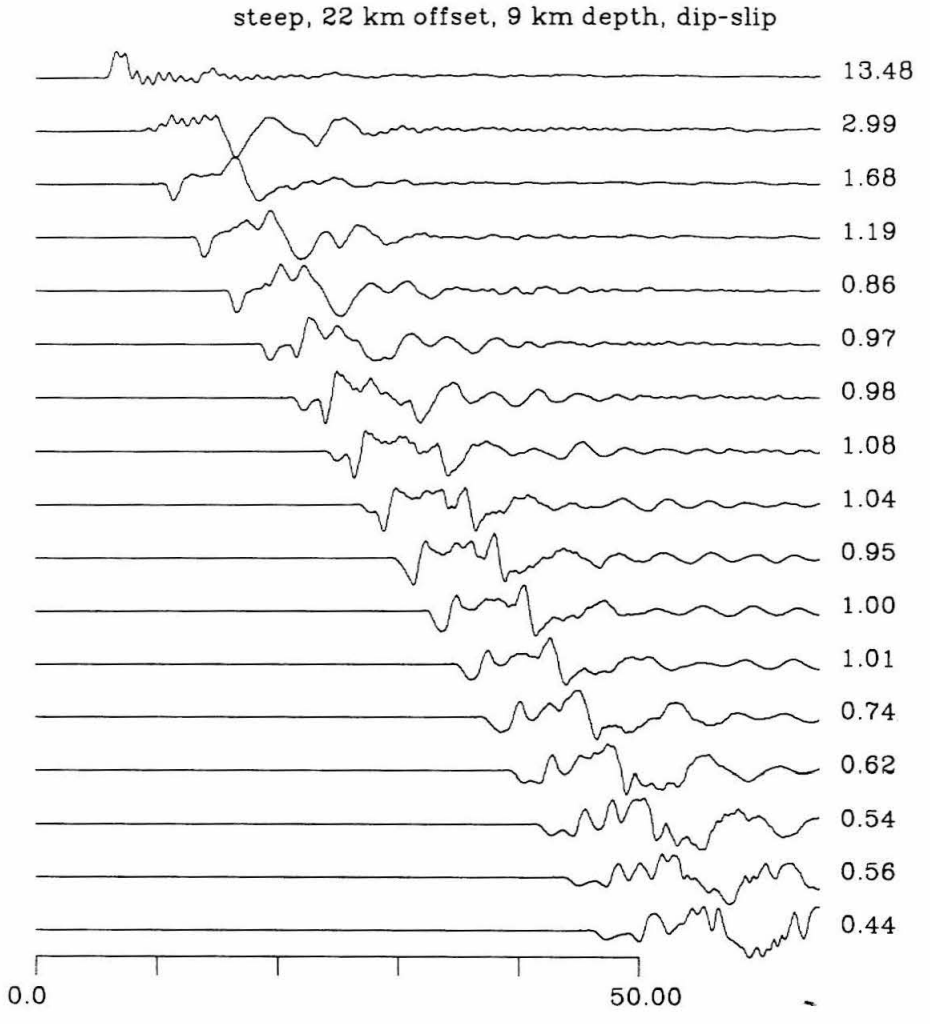

Figure C.13 SH synthetics for dip-slip source 22 km from the steep boundary, 9 km deep.

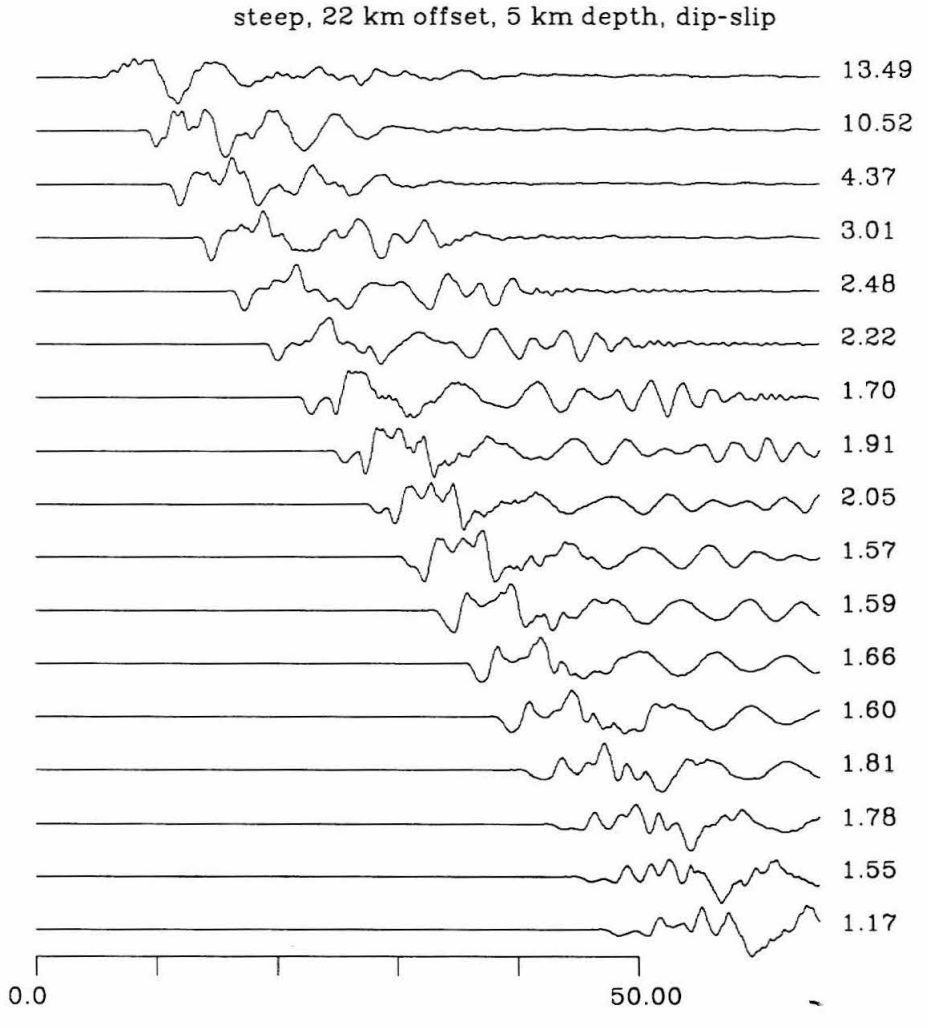

Figure C.14 SH synthetics for dip-slip source 22 km from the steep boundary, 5 km deep.

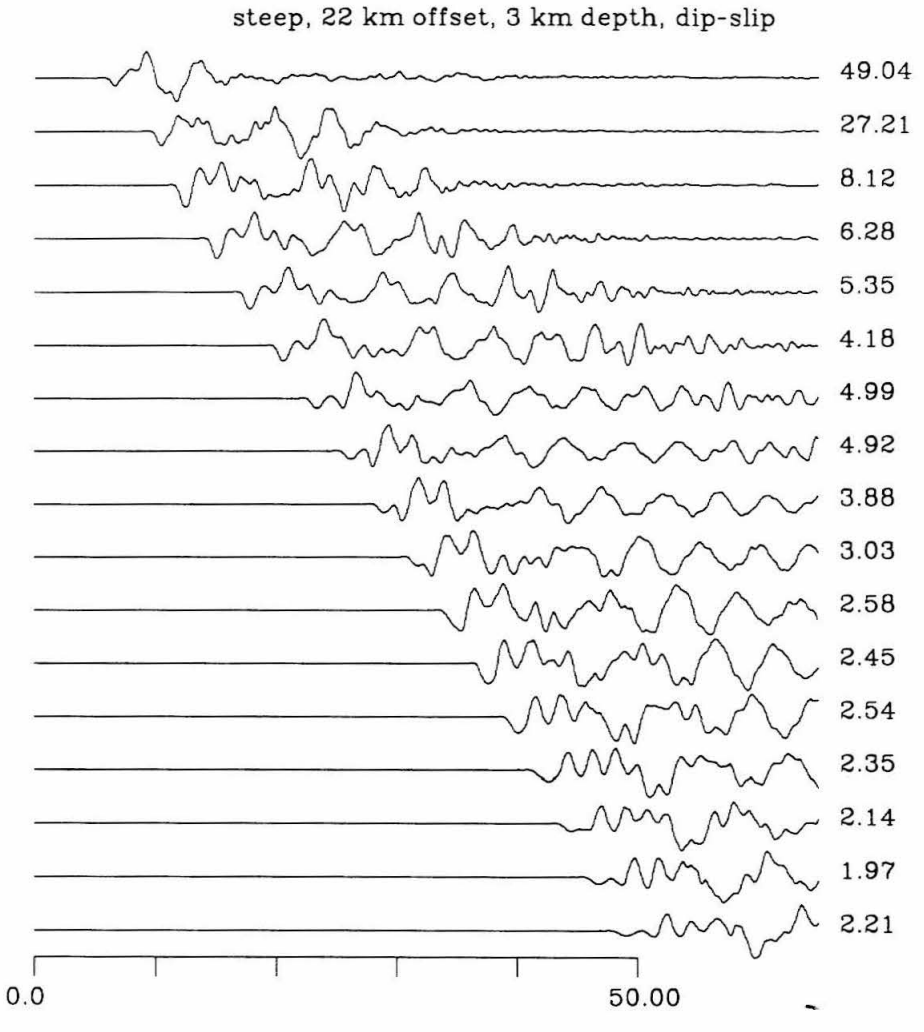

Figure C.15 SH synthetics for dip-slip source 22 km from the steep boundary, 3 km deep.

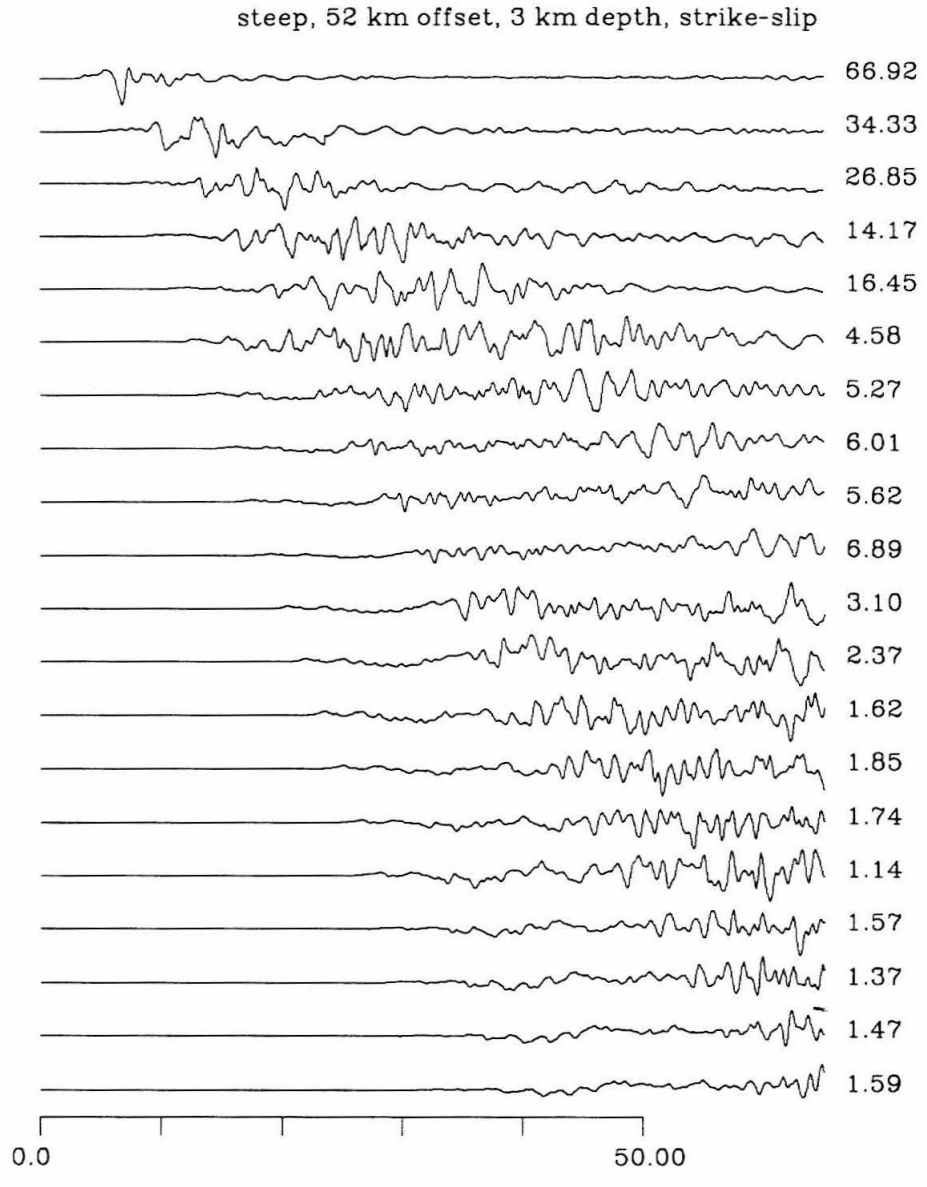

Figure C.16 P-SV radial synthetics for strike-slip source 52 km from the steep boundary, 3 km deep.

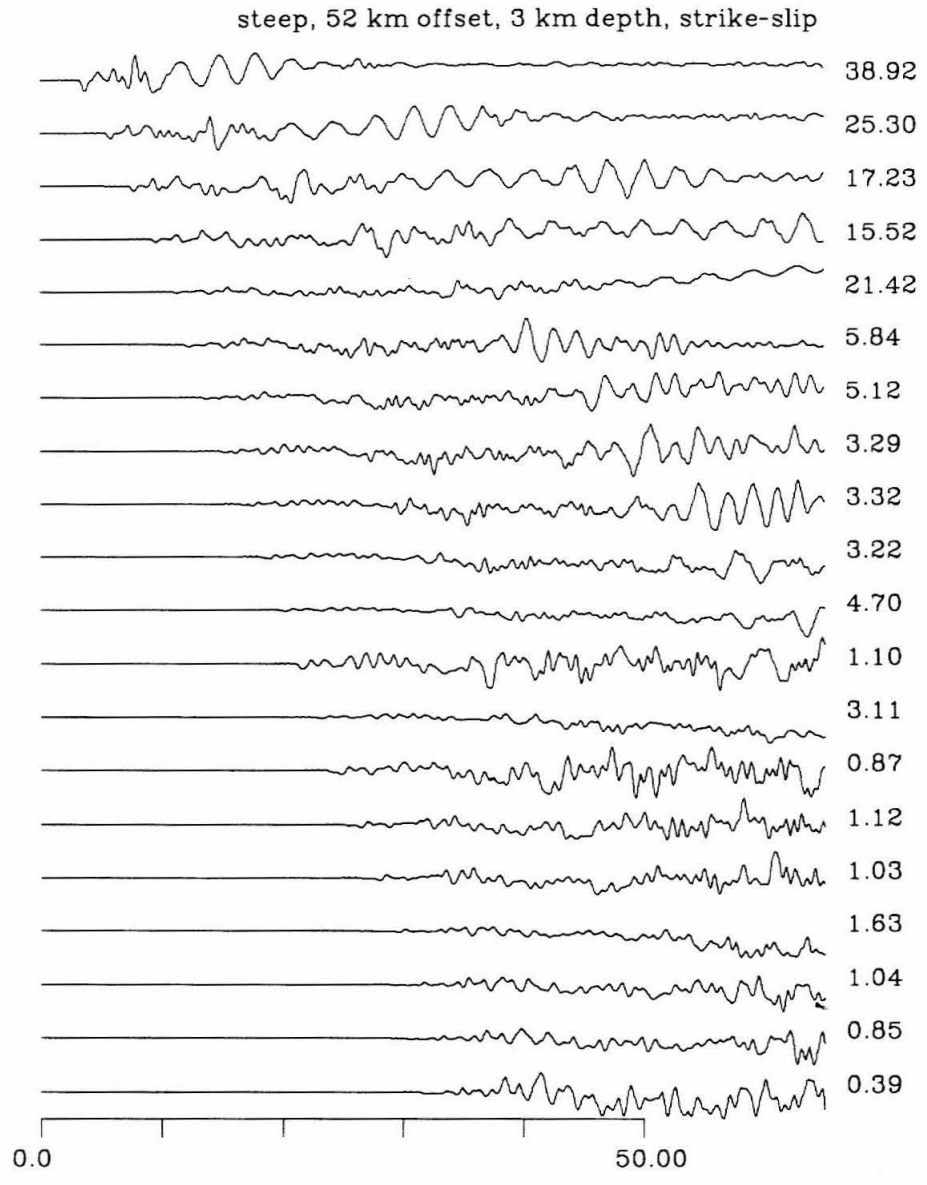

Figure C.17 P-SV vertical synthetics for strike-slip source 52 km from the steep boundary, 3 km deep.

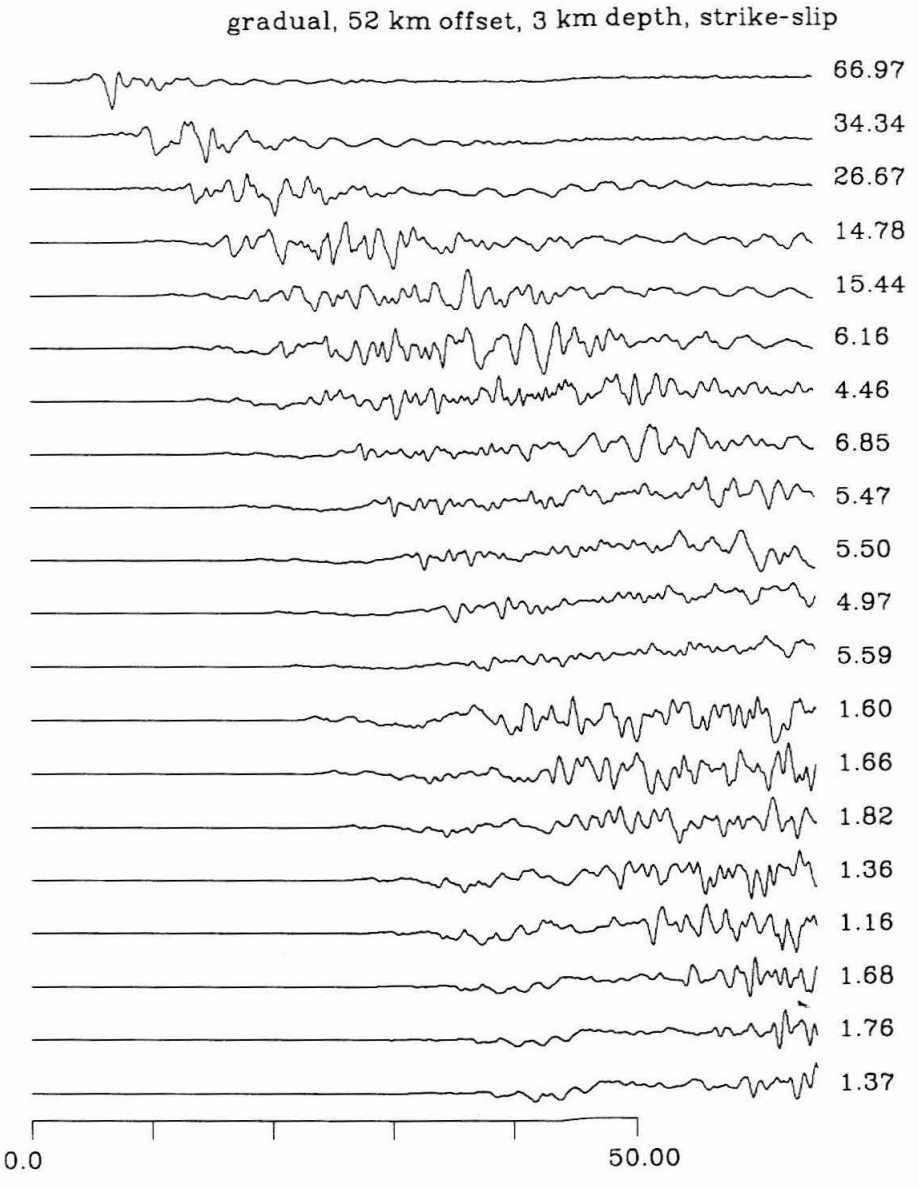

Figure C.18 P-SV radial synthetics for strike-slip source 52 km from the gradual boundary, 3 km deep.

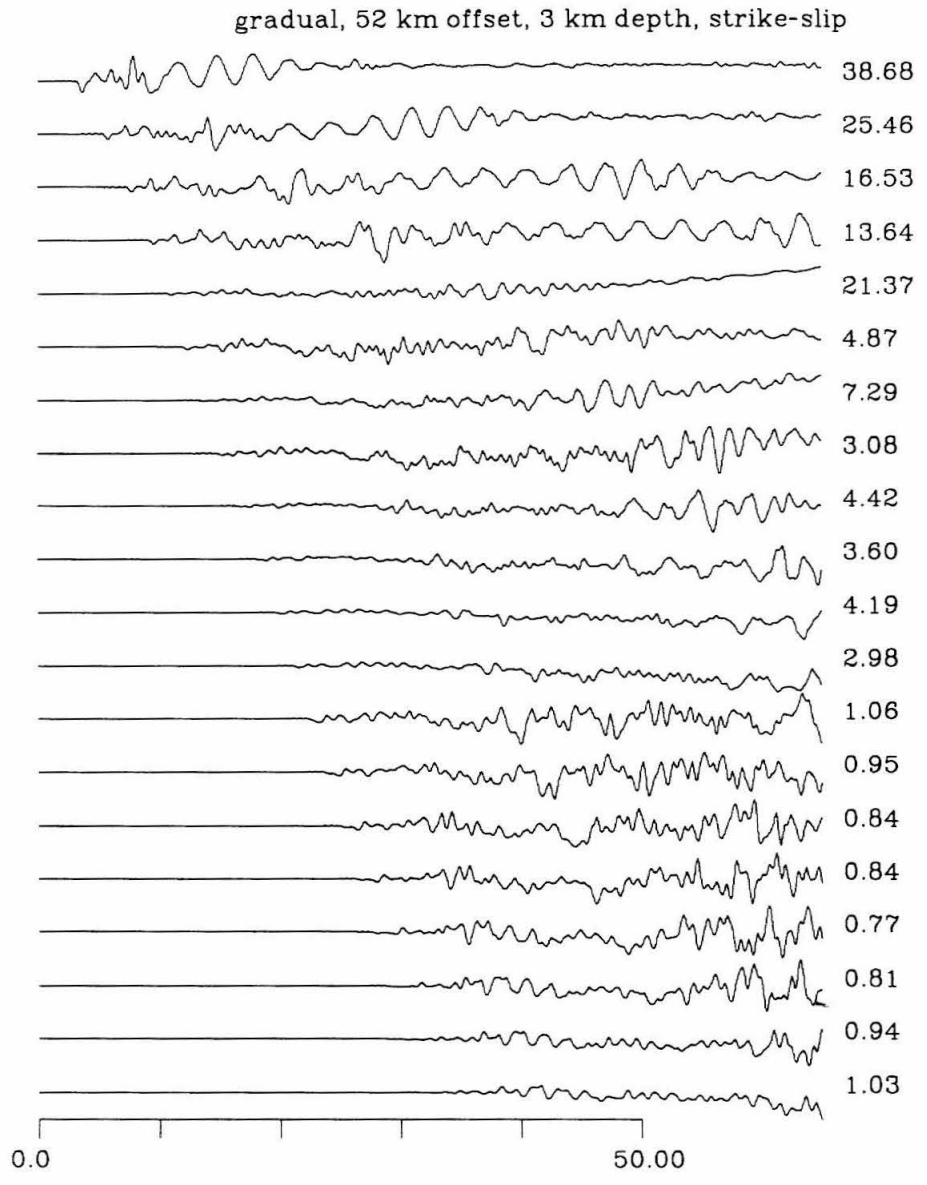

Figure C.19 P-SV vertical synthetics for strike-slip source 52 km from the gradual boundary, 3 km deep.

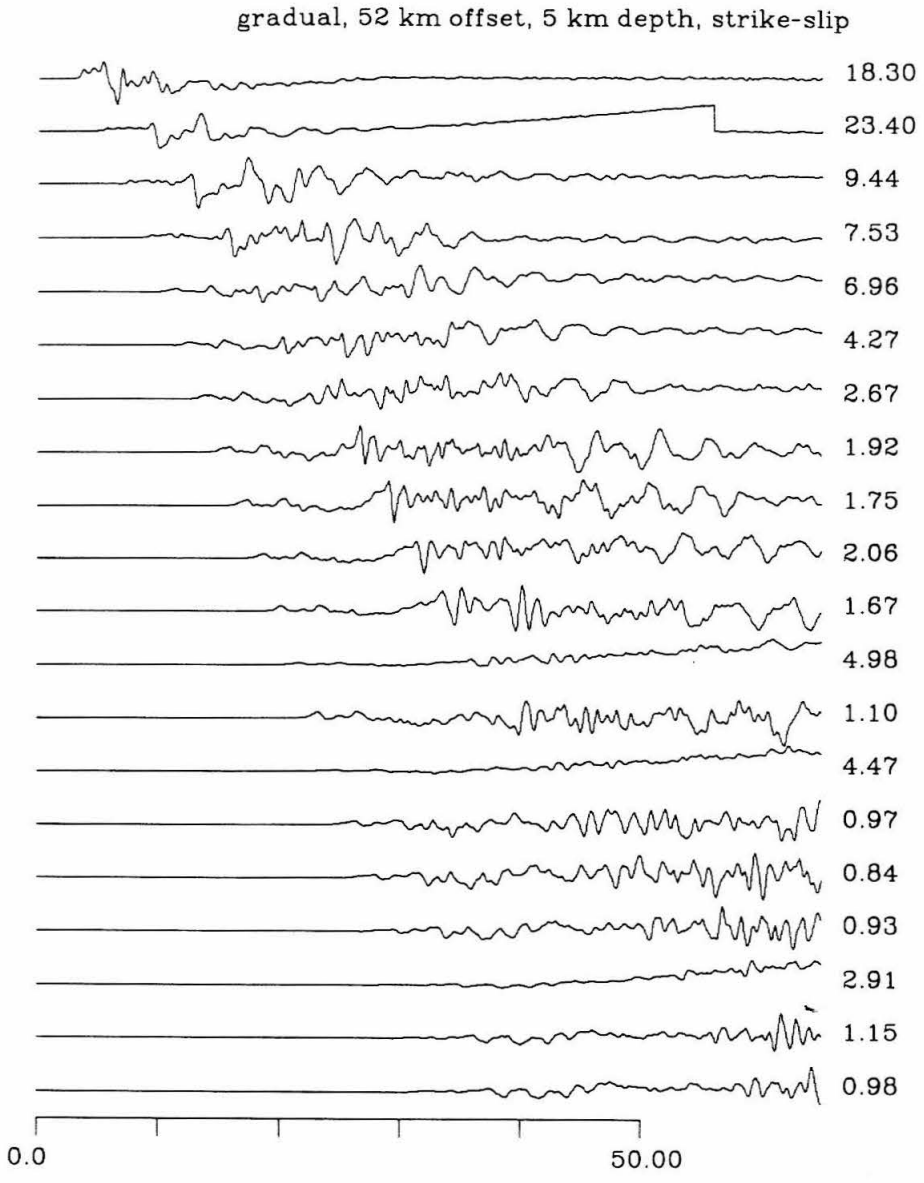

Figure C.20 P-SV radial synthetics for strike-slip source 52 km from the gradual boundary, 5 km deep.

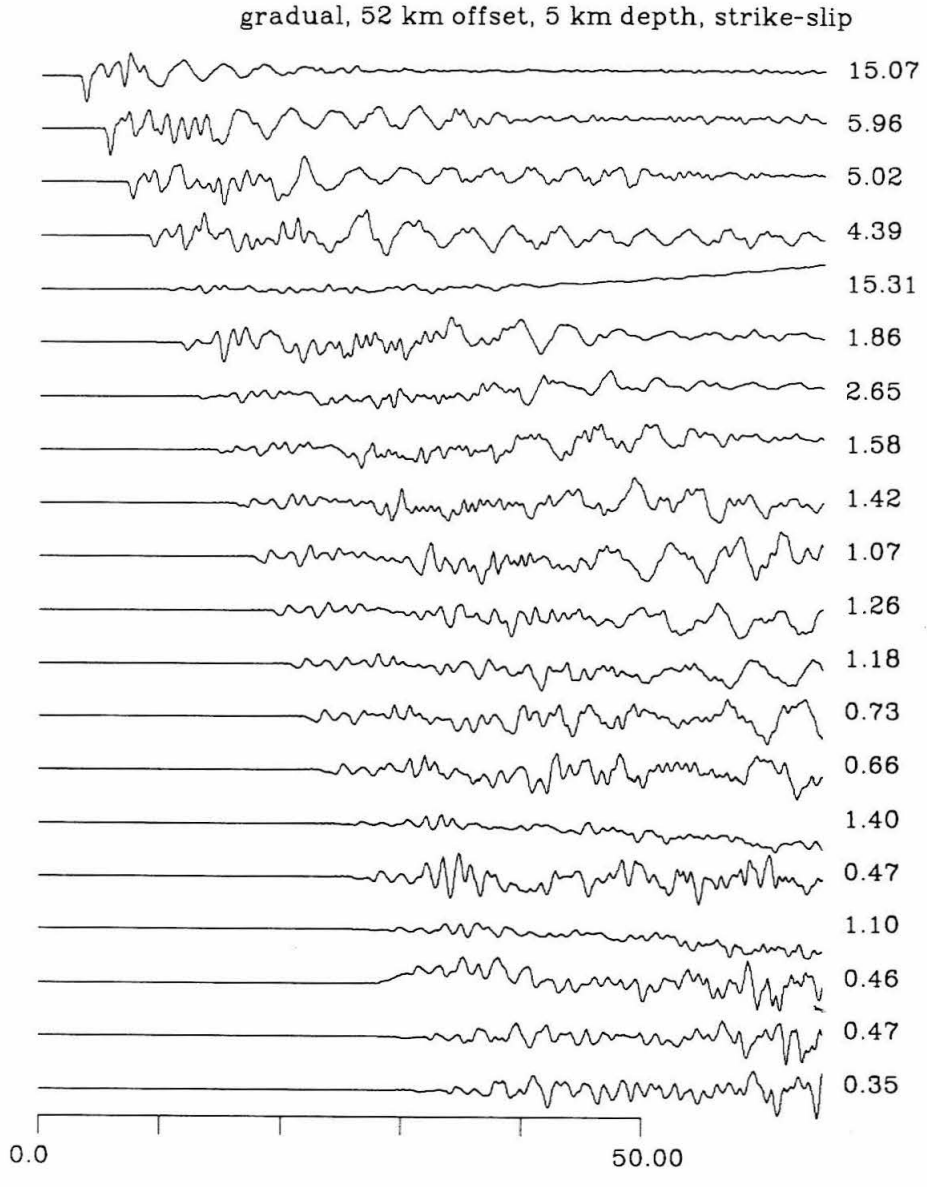

Figure C.21 P-SV vertical synthetics for strike-slip source 52 km from the gradual boundary, 5 km deep.

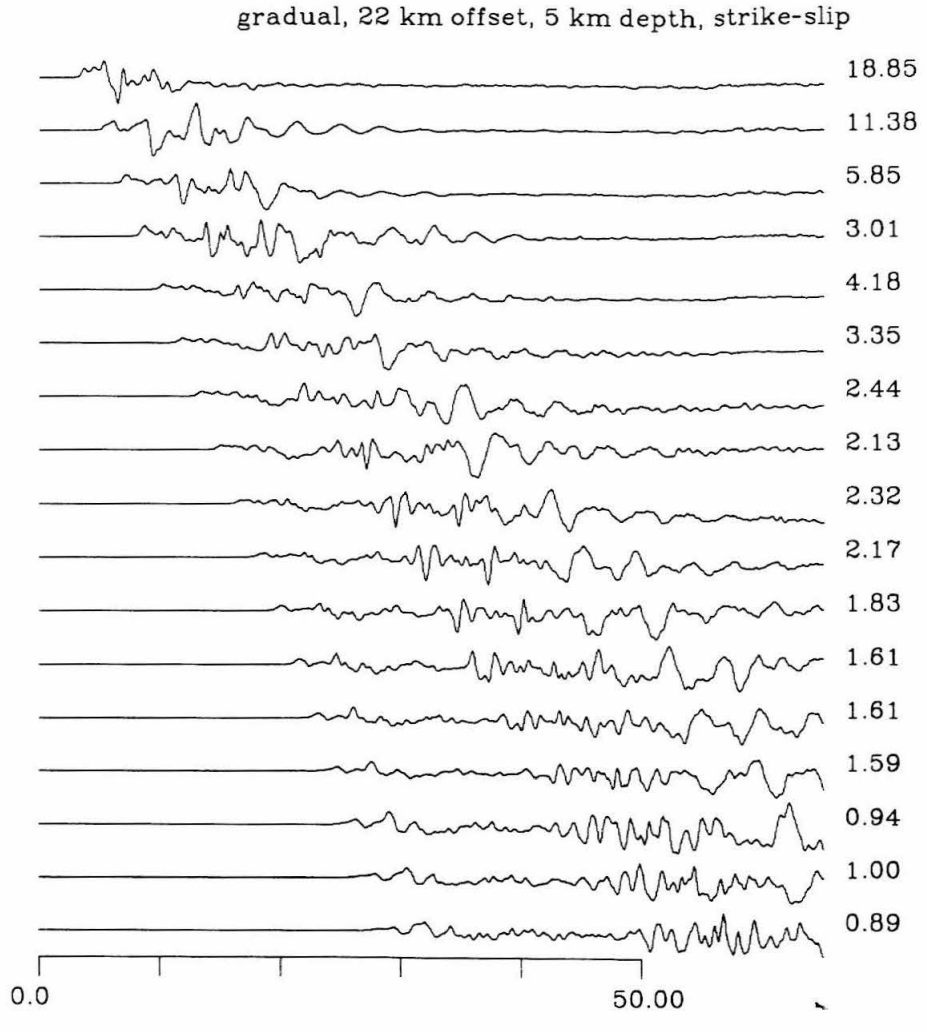

Figure C.22 P-SV radial synthetics for strike-slip source 22 km from the gradual boundary, 5 km deep.

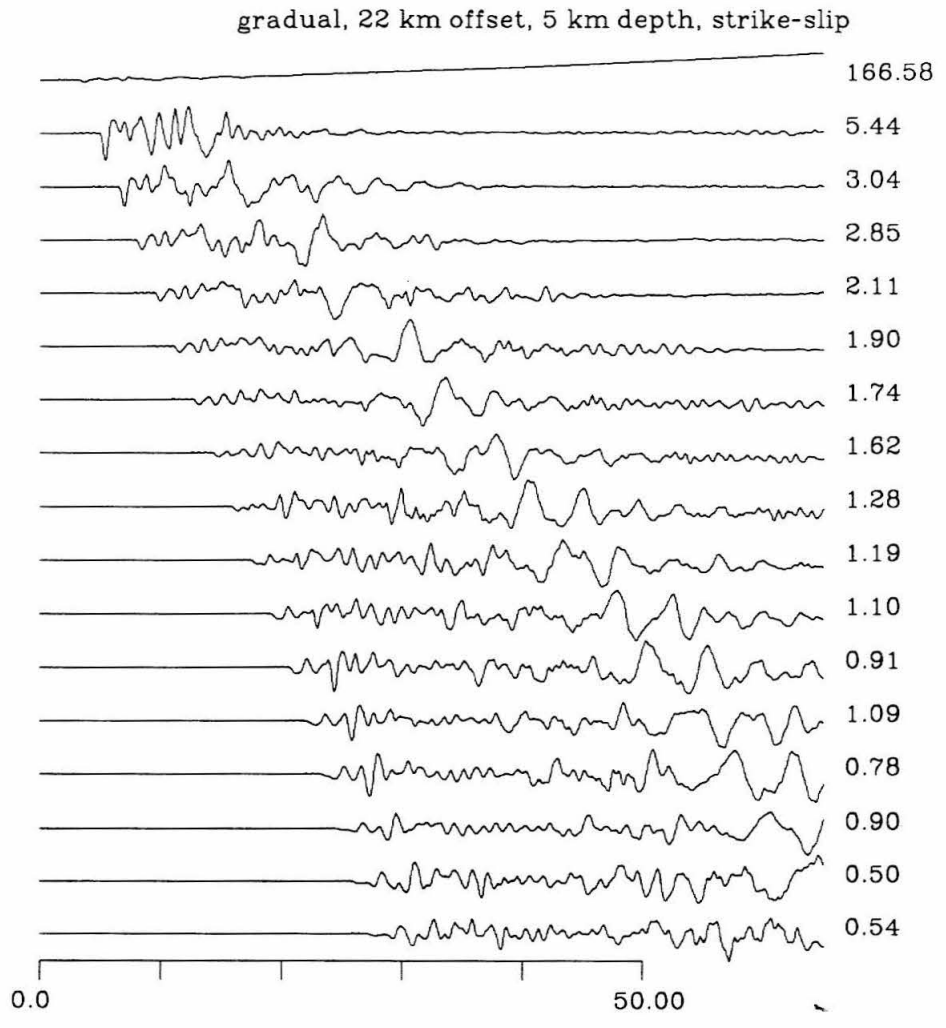

Figure C.23 P-SV vertical synthetics for strike-slip source 22 km from the gradual boundary, 5 km deep.

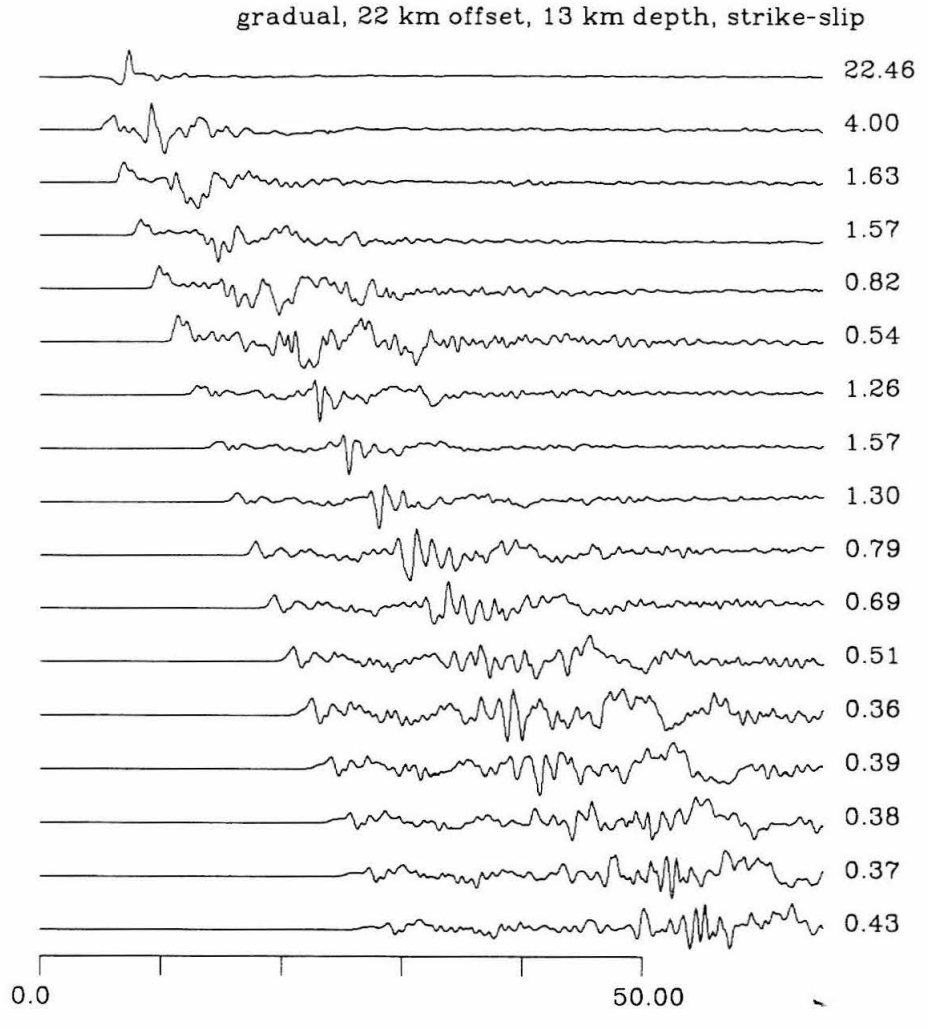

Figure C.24 P-SV radial synthetics for strike-slip source 22 km from the gradual boundary, 13 km deep.

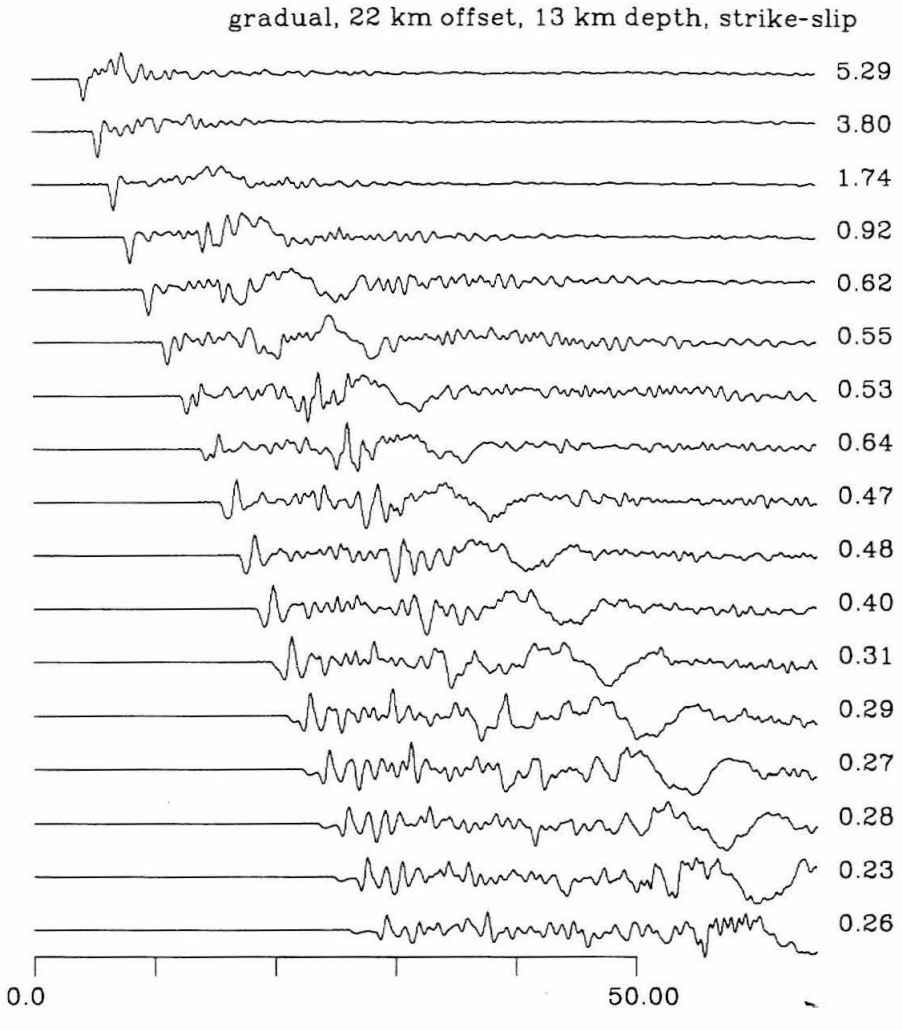

Figure C.25 P-SV vertical synthetics for strike-slip source 22 km from the gradual boundary, 13 km deep.